I. R. IRAN

ISSN: 1728-1431
e-ISSN: 1735-9244

International Journal of Engineering

Journal Homepage: www.ije.ir

MERC

TRANSACTIONS A: BASICS

Volume 35, Number 07, July 2022

Materials and Energy Research Center

In the Name of God

INTERNATIONAL JOURNAL OF ENGINEERING
Transactions A: Basics

DIRECTOR-IN-CHARGE
A. R. Khavandi

EDITOR-IN-CHIEF
G. D. Najafpour

ASSOCIATE EDITOR
A. Haerian

EDITORIAL BOARD

S.B. Adeloju, Charles Sturt University, Wagga, Australia
K. Badie, Iran Telecomm. Research Center, Tehran, Iran
M. Balaban, Massachusetts Ins. of Technology (MIT), USA
M. Bodaghi, Nottingham Trent University, Nottingham, UK
E. Clausen, Univ. of Arkansas, North Carolina, USA
W.R. Daud, University Kebangsaan Malaysia, Selangor, Malaysia
M. Ehsan, Sharif University of Technology, Tehran, Iran
J. Faiz, Univ. of Tehran, Tehran, Iran
H. Farrahi, Sharif University of Technology, Tehran, Iran
K. Firoozbakhsh, Sharif Univ. of Technology, Tehran, Iran
A. Haerian, Sajad Univ., Mashhad, Iran
H. Hassanpour, Shahrood Univ. of Tech., Shahrood, Iran
W. Hogland, Linnaeus Univ, Kalmar Sweden
A.F. Ismail, Univ. Tech. Malaysia, Skudai, Malaysia
M. Jain, University of Nebraska Medical Center, Omaha, USA
M. Keyanpour rad, Materials and Energy Research Center, Meshkindasht, Karaj, Iran
A. Khavandi, Iran Univ. of Science and Tech., Tehran, Iran
A. Mahmoudi, Bu-Ali Sina University, Hamedan, Iran
O.P. Malik, University of Calgary, Alberta, Canada
G.D. Najafpour, Babol Noshirvani Univ. of Tech. ,Babol, Iran
F. Nateghi-A, Int. Ins. Earthquake Eng. Seis., Tehran, Iran
S. E. Oh, Kangwon National University, Korea
M. Osanloo, Amirkabir Univ. of Tech., Tehran, Iran
M. Pazouki, Material and Energy Research Center, Meshkindasht, Karaj, Iran
J. Rashed-Mohassel, Univ. of Tehran, Tehran, Iran
S. K. Sadrnezhaad, Sharif Univ. of Tech, Tehran, Iran
R. Sahraeian, Shahed University, Tehran, Iran
A. Shokuhfar, K. N. Toosi Univ. of Tech., Tehran, Iran
R. Tavakkoli-Moghaddam, Univ. of Tehran, Tehran, Iran
T. Teng, Univ. Sains Malaysia, Gelugor, Malaysia
L. J. Thibodeaux, Louisiana State Univ, Baton Rouge, U.S.A
P. Tiong, Nanyang Technological University, Singapore
X. Wang, Deakin University, Geelong VIC 3217, Australia

EDITORIAL ADVISORY BOARD

S. T. Akhavan-Niaki, Sharif Univ. of Tech., Tehran, Iran
M. Amidpour, K. N. Toosi Univ of Tech., Tehran, Iran
M. Azadi, Semnan university, Semnan, Iran
M. Azadi, Semnan University, Semnan, Iran
F. Behnamfar, Isfahan University of Technology, Isfahan
R. Dutta, Sharda University, India
M. Eslami, Amirkabir Univ. of Technology, Tehran, Iran
H. Hamidi, K.N.Toosi Univ. of Technology, Tehran, Iran
S. Jafarmadar, Urmia Univ., Urmia, Iran
S. Hesaraki, Material and Energy Research Center, Meshkindasht, Karaj, Iran
A. Kheyroddin, Semnan Univ., Semnan, Iran
N. Latifi, Mississippi State Univ., Mississippi State, USA
H. Oraee, Sharif Univ. of Tech., Tehran, Iran
S. M. Seyed-Hosseini, Iran Univ. of Sc. & Tech., Tehran, Iran
M. T. Shervani-Tabar, Tabriz Univ., Tabriz, Iran
E. Shirani, Isfahan Univ. of Tech., Isfahan, Iran
A. Siadat, Arts et Métiers, France
C. Triki, Hamad Bin Khalifa Univ., Doha, Qatar
S. Hajati, Material and Energy Research Center, Meshkindasht, Karaj, Iran

TECHNICAL STAFF
M. Khavarpour; M. Mohammadi; V. H. Bazzaz, R. Esfandiar; T. Ebadi

DISCLAIMER
The publication of papers in International Journal of Engineering does not imply that the editorial board, reviewers or publisher accept, approve or endorse the data and conclusions of authors.

International **J**ournal of **E**ngineering *Transactions A: Basics* (ISSN 1728-1431) (EISSN 1735-9244)
International **J**ournal of **E**ngineering *Transactions B: Applications* (ISSN 1728-144X) (EISSN 1735-9244)
International **J**ournal of **E**ngineering *Transactions C: Aspects* (ISSN 2423-7167) (EISSN 1735-9244)
Web Sites: www.ije.ir & www.ijeir.info E-mails: ije.editor8@gmail.com, Tel: (+9821) 88771578, Fax: (+9821) 88773352
Materials and Energy Research Center (MERC)

ISSN: 1728-1431, e-ISSN: 1735-9244

International Journal of Engineering, Volume 35, Number 07, July 2022

CONTENTS

Transactions A: Basics

ISSN: 1728-1431, e-ISSN: 1735-9244

International Journal of Engineering, Volume 35, Number 07, July 2022

International Journal of Engineering

Journal Homepage: www.ije.ir

Influence of Project and Affected Local Community Interests Level on Social Conflicts in Indonesian Infrastructure Projects

H. B. Sanggoro*, S. W. Alisjahbana, D. Mohamad

Civil Engineering Doctoral Program, University of Tarumanagara, Jakarta, Indonesia

P A P E R I N F O

Paper history:
Received 06 January 2022
Received in revised form 26 February 2022
Accepted 09 March 2022

Keywords:
Environmental and Social Framework
Project Interests
Community Interests
PLS-SEM
Infrastructure Project

A B S T R A C T

Poor economic growth due to Covid-19 pandemic in the last two years has resulted in a decline in indicators of public welfare. The construction industry sector also experienced a severe decline in productivity; thus, adjustments had to be made to survive the crisis situation. In addition, environmental problems due to development activities also threaten the lives and incomes of people who depend on natural products. These conditions encourage the escalation of interests that affect infrastructure projects in Indonesia. This study aimed to predict the influence of project and affected local community's interests on infrastructure projects social conflicts. Data were obtained by questionnaire from 68 project managers as respondents and analyzed using PLS-SEM. The findings of this study are that the influence of affected community is more dominant than that of project interests on project social conflicts. This shows the important role of communities in the concept of sustainable development with environmental and social perspectives. The results of this study will be useful in drafting the concept of an integrated and standardized environmental and social safeguard framework. To achieve an appropriate framework, further research is needed to examine the framework concept as a moderation of the relationship between interests and project social conflicts.

***doi**: 10.5829/ije.2022.35.07a.01*

1. INTRODUCTION

The health crisis due to the Covid-19 pandemic that has hit the world in the last two years has resulted in a severe economic downturn. This condition is experienced by all countries including Indonesia. Negative growth as a result of Covid-19 pandemic has an impact on the level of community welfare. Statistics Indonesia (BPS) data show an increase in the number of poor people during 2020 and 2021 by 2.75 million compared to Q4/2019. Several other welfare indicators also show stagnation and even worsening due to slowing national and global economic growth as a result of the spread of Covid-19 [1]. This condition also resulted in a decline in construction business activities [2]. BPS recorded a significant slowdown in the construction sector during the pandemic. Thus, many construction industries must carry out performance efficiency which has an impact on increasing internal interests that have the potential to affect the overall project performance and include the potential to intersect with other interests around the project [3].

In addition to economic and social issues, environmental issues are also a topic of special concern from countries in the world in improving the quality of life and controlling climate change [4]. Meanwhile, in the last few decades, infrastructure development has become one of the causes of land use changes and has resulted in a reduction in the buffer zones [5, 6]. The loss of part of the forest area has an impact on the deterioration of environmental quality which results in disruption of the livelihoods of people who depend on the results of processingnatural resources. This serious attention to environmental and climate change issues can be seen in the results of the COP26 Climate Change Summit in

*Corresponding Author Institutional Email: heru.328201007@stu.untar.ac.id (H. B. Sanggoro)

Please cite this article as: H. B. Sanggoro, S. W. Alisjahbana, D. Mohamad, Influence of Project and Affected Local Community Interests Level on Social Conflicts in Indonesian Infrastructure Projects, ***International Journal of Engineering, Transactions A: Basics***, Vol. 35, No. 07, (2022) 1217-1226

Glasglow, where one of the important points is ending deforestation.

However, the reality of Indonesia's infrastructure needs and quality, which is still below expectations, has resulted in the development program becoming a major dilemma in its implementation. The quality of Indonesia's road infrastructure based on the Global Competitiveness Report on 2019 is ranked 50 out of 141 countries. This condition will need serious attention from the government and project stakeholders in Indonesia. Developments that deal with environmental impacts have the potential to cause conflicts and social disputes in their implementation [7].

This study was developed from the previous research by Sanggoro et al. [8], where conflicts are mostly caused by differences of interests between the project and the affected local communities. So that this study is limited to the aspects and criteria that have been previously disclosed, to measure the influence of the interests that arise from the project itself and the interests that arise due to the social conditions of the affected local communities. This study aimed to predict the effect of the interests of projects' internal environment and affected local communities on social conflicts on infrastructure projects in Indonesia. The interests of local communities in terms of economic, social, environmental, and cultural aspects are based on a statistical index published by the Statistics Indonesia (BPS). Measurement using this statistical data and index will make it easier for project actors to obtain an actual representation of the relevant local community conditions used to measure the level of community interest in project activities. It is hoped that the results of this study will assist project actors in mapping and planning project work programs based on local community empowerment. With proper planning, collaboration between a project and the affected local community can be optimized to achieve project targets.

2. LITERATURE REVIEW

2. 1. Internal Project Interests

Interests are basically the other form or can be referred to as a collection of demands, expectations, needs, and values expected from each stakeholder [9]. Meanwhile, Zhang and El-Gohary [3], explained that the project objective is one of the values expected by stakeholders. Therefore, project objectives are project interests that will affect the overall project performance. Based on PMBOK [10], project objectives are generally determined by the achievement of costs, quality, time, and customer satisfaction. However, in its development, the achievement of K3 performance is also widely used as a project success parameters.

In addition, construction as a business entity also has its own interest to survive in the face of the times and the rapidly changing business environment [11]. This business interest is generally influenced by profitability targets, financial capability, annual turnover, and business diversification [12, 13]. Another thing that is considered as a factor of internal interest is the characteristics of the project. In their research, Min et al. [14] argued that project characteristics are factors that contribute to conflict in projects. As a unique activity, projects have different characteristics and require different management [10]. Projects can be distinguished by complexity, scale, scope of the work [15], type of contract [16] and project location [17].

The argument strengthens the research of Al-Sibaie et al. [18], that internal conflict is one of the factors that negatively affects project performance. The strong influence between conflicts and project performance shows that the causal link between the two factors is very high [19-21]. Based on the discussion above, the first hypothesis is structured as follows:

H1. The higher the project interests, the higher the positive effect on the increase in project social conflicts

2. 2. Interests of Affected Communities

The construction industry is one of the business entities whose activities are in direct contact with the community as stakeholders. According to Project Management Institute (PMI) [10], the community is one of the main project stakeholders who exert influence from outside the system (external stakeholder). Therefore, the community will have their own interests that affect the project [22].

In the last decade, sustainable development has continued to be developed as a concept of equitable development. The concept of collaboration between the business aspect and the social responsibility aspect is not only profit-oriented but also for the benefit of people's lives and the environment. Wang et al. [23] mentioned three aspects that are the focus of the concept of sustainable development, namely (a) social, (b) environmental, and (c) economic aspects. These three aspects are also factors that influence the birth of interests or the occurrence of conflicts as studied by Chan and Oppong [9], Silvius and Schipper [24], Xiahou et al. [25], Zhuang et al. [26].

Furthermore, Hartono et al. [27] stated that social diversity is one of the factors that influence the occurrence of conflicts. This is related to Xue and Xiang's opinion [28], that local communities are one of the risk factors that can create conflicts and ultimately lead to social instability. Another factor revealed in the study of Meng et al. [29], Lückmann and Färber [30], is that different cultures have different effects on a project.

Based on the discussion, the importance of the affected community is measured through indexes and data related to the condition of the economic, social, environmental, and cultural aspects of the community around the project published by the Institution/Ministry and BPS (see Table 1). Referring to the opinion above, then this study proposes the second hypothesis as follows:

H2. The higher the interests of the affected community, the higher the positive effect on an increase in project social conflicts

2. 3. Project Social Conflicts According to Omenge et al. [31], conflicts can occur due to the interaction of interdependent people who feel incompatible goals. Conflict is also a common and unavoidable consequence of a social interaction in society and in organizations. It is seen as an indication of failed functions [32]. Project performance is influenced by conflicts that occur, including (a) task-related conflict and (b) emotional conflict [27]. Another opinion was conveyed by Wu et al. [19] who stated that conflicts that affect project performance are task conflict, relationship conflict, and process conflict.

Riley and Ellegood [33] also proved in their study that (a) task conflict and (b) relationship conflict have a negative impact on a project. According to them, when working together in the implementation of a project, an individual or an entity has common goals as well as their respective goals through the interests attached to the parties. Periodically, the parties involved will feel tension in their duties or interference from other parties. There may also be feelings of hostility resulting from interpersonal and socioemotional factors. Meanwhile, Prasad and Junni [34] used different variables in measuring conflict, namely cognitive conflict and affective conflict. Sanggoro et al. [8] stated that the conflict between a project and the community can be divided based on the causes, namely (1) task-related conflict, (2) rule-related conflict, (3) affective conflict, and (4) value-related conflict.

The results of the study reveal that conflict is an excess of the interaction of several people or groups in the project. In this study, the parameters of the interests of the affected community as measured by official data and indexes from BPS and Ministries/Government Institutions are new solutions that are offered for ease of measuring conflict opportunities based on the conditions and perceptions of the community around the project. Therefore, the measurement of the level of public interest in the 4 aspects reviewed can be precise and in line with data officially recognized by the government.

3. MATERIALS AND METHOD

3. 1. Data Collection and Sample This study focuses on infrastructure projects managed by the Ministry of Public Works and Public Housing (Ministry of PUPR) of the Republic of Indonesia in period of 2019-2021. In each fiscal year, the Ministry of PUPR is the largest development budget manager in Indonesia. The annual increase in the infrastructure development budget has also increased the number of social conflicts due to the projects being undertaken. In addition to the ability of project actors to manage conflict risk, the right strategy is needed to mediate the interests that affect project implementation in Indonesia [8].

This study used the point of view of the project manager as one of the main actors of a project. Determination of the sample was determined randomly representing the territory of Indonesia, namely the western, central, and eastern parts. The collection of the primary data in this study was carried out by using a questionnaire sent by email and post to respondents. Meanwhile, secondary data, namely data on the condition of affected local communities, was obtained from BPS and other ministries/government agencies.

$$\frac{Z^2 p(1-p)}{d^2} \tag{1}$$

where :

Z^2 = confidence level at 95% (standard value of 1.96)

p = estimated prevalence or proportions of project area (based on perliminary research of 0.04)

d^2 = desired precision (0.05)

The research sample was determined by using the Lemeshow formula (Equation (1)), with a standard deviation of 0.04 (based on preliminary research), minimum sample as required is 60 respondents. The research questionnaire was sent to 80 potential respondents representing regions and infrastructure projects in Indonesia. However, only 68 questionnaires were sent back or with a response rate of 85%. However, there were 2 respondents who did not meet the expected expert qualifications so they were not included in the analysis and only used data from 66 respondents. The response rate was good and meet to the minimum sample as required.

3. 2. Measurement and Instrumentation Various influence factors and impact of conflict in the project have been investigated by previous researchers.

Figure 1. Conceptual model based on research hypotheses

TABLE 1. Research variables and measurement criteria

VARIABLE/DIMENSION	DEFINITION	
X-1 Internal Project Interests		
X-1.1 PRJ Project Performance	Interests resulting from the performance targets set in project implementation: cost achievement (PRJ1), quality conformity (PRJ2), timeliness (PRJ3), K3 performance achievement (PRJ4), and customer satisfaction (PRJ5)	
X-1.2 BUS Company business performance	Interests coming from company's performance targets that are the burden of the project as its business unit as measured by: achievement of profitability (BUS1), financial capability (BUS2), achievement of turnover (BUS3), and business diversification (BUS4)	
X-1.3 CHR Project characteristics	The project's interests as a result of project complexity (CHR1), project scale (CHR2), contract type (CHR3), scope of work (CHR4), and project location (CHR5)	
X-1.4 PER Personal and team interests	Interests resulting from the level of satisfaction of personnel and teams with respect to the promotion system (PER1), income/salary (PER2), performance benefits and rewards (PER3), job descriptions (PER4), regulations and employment status (PER5), training and competency improvement (PER6), and the conditions of co-workers/teamwork (PER7)	
X-2 Interests of Affected Communities		
X-2.1 ECO Economic conditions	Public interests that are caused by economic conditions determined by the unemployment rate (ECO1), the regional minimum wage (ECO2), poverty rate (ECO3), Gini ratio (ECO4), regional economic growth rate (ECO5), and income per capita (ECO6) (BPS)	
X-2.2 SOC Social conditions	Public interests that are caused by social conditions determined by the human development index (SOC1), high school net enrollment rate (SOC2), home ownership level (SOC3), disaster risk index (SOC4), food security index (SOC5), vulnerability index politics (SOC6) and number of health facilities (SOC7) (BPS)	
X-2.3 ENV Environmental conditions	Community interests that are caused by environmental conditions determined by water quality index (ENV1), air quality index (ENV2), land cover quality index (ENV3), environmental quality index (ENV4), rice field area (ENV5), plantation area (ENV6), dry field area (ENV7), and village forest area (ENV8) (Ministry of Environment and Forestry or Ministry of LHK; Ministry of Agriculture)	
X-2.4 CUL Cultural conditions	Community interests that are caused by cultural conditions determined by the percentage of the majority religion (CUL1), majority ethnicity (CUL2), users of the national language in daily conversation (CUL3), and the level of information disclosure (CUL4) (BPS)	
Impact of Project Social Conflicts		
Y – Project social conflict	The conflict impacts caused by project activities are as follows.	
	Y-1.1 PSC1.1	task conflict, determined by the impact on the number of days lost
	Y-1.2 PSC1.2	task conflict, determined by the impact on cost overrun due to conflict
	Y-2 PSC2	conflict of rules, namely conflict due to the application of company and project rules in completing work
	Y-3 PSC3	affective conflict, namely interpersonal conflict, including personal interaction, involving the emotions and sentiments of each party
	Y-4 PSC4	conflict values conflict due to the system and values prevailing in the social order as seen from its impact on CSR costs

However, the use of indexes as parameters in determining the level of interest that affects social conflict in projects, generally lack empirical studies, especially in Indonesia. Based on the literature reviews and previous research [8], the conflict of interest in the project was rearranged in this study to measure the effects of the interest condition based on the socio-community indexes around the project. The theoretical model was developed using factors of interest and conflict that have been resulted in the previous study by the Soft System Methodology.

Based on the conceptual model (Figure 1) and discussion above, this study was generated from the project interests as a variable and affected community interests as the other variable, each of which is compiled by measuring indicators (Table 1). A Likert scale of 1 to 5 was used to measure the indicators with criteria of interests from "Very Low" to "Very High". Variables X-1 and Y represent the level of project interests and the level of impact caused by project social conflicts which were obtained based on the responses to the proposed questionnaire. While X-2 is an illustration of the level of interest of the affected community obtained from data for each project area from official government ministries/agencies of the Republic of Indonesia, such as BPS-Statistics Indonesia, Ministry of Environment and

Forestry, Ministry of Agriculture, National Board for Disaster Management (BNPB), and The General Election Supervisory Agency (BAWASLU).

3. 3. Method of Data Analysis A research model (Figure 1) was developed with the aim of predicting the impact of project social conflicta (Y) from the influence of project interests (X1.1 - X1.4) and affected community interests (X2.1 - X2.4). Referring to Hair et al. [35], PLS-SEM is a statistical analysis technique based on variance and is appropriate for descriptive and prediction-oriented models. Since the number of samples used in this study is 68 respondents, it means it is more appropriate to use PLS-SEM as the method of analysis. Chin et al. [36] stated that 30-100 samples is the minimum required by PLS-SEM to obtain consistency in model analysis. Furthermore, PLS-SEM is more consistent in predicting estimates without requiring the assumption of a normal distribution.

Based on the above theory, PLS-SEM is an analytical method that is in accordance with the research objective to predict the effect of interests on the impact of project social conflicts. SmartPls 3 was used in the estimation and measurement of the research model.

4. RESULTS AND DISCUSSION

4. 1. Respondent Demography Respondents in this study were project managers throughout Indonesia who were currently or had worked on infrastructure projects under the Ministry of PUPR RI. The demographics of the 68 participating respondents can be seen in Table 2.

TABLE 2. Respondent demography

RESPONDENT CHARACTERISTIC	FREQ.	%
Experience as Project Manager		
5 - 10 years	14	21.21%
11 - 15 years	11	16.67%
16 - 20 years	6	9.09%
≥ 20 years	35	53.03%
Education degree		
Bachelor in Civil Engineer	54	81.82%
Master	12	18.18%
Type of Project		
Road and Bridge	38	57.58%
Building	9	13.64%
Dam and Water Resource	19	28.79%

4. 2. PLS-SEM Model Evaluation The estimation and measurement process with SmartPls was carried out in two stages:
1). assessment of the measurement model (outer model)
2). assessment of the structural model or (inner model).

In assessing the measurement model, several criteria were used: internal consistency (Cronbach's alpha, composite reliability, rho-A), convergent validity (indicator reliability, AVE), and discriminant validity (cross loading and Fornell-Larker Criterion). Meanwhile, in testing the structural model, the coefficient of determination (R-Square), predictive relevance (Q-square), multicollinearity test (VIF), and hypothesis testing (T-statistical significance and p-value) were used as criteria [37].

4. 3. Assessing of the Measurement Model (Outer Model) The first test of this study model was to evaluate the measurement model or outer model. In the model (Figure 1), it is stated that all dimensions have reflective indicators, so the test was conducted to look at the loading value. Smartpls requires loading values > 0.7 and AVE > 0.5. However, Hair et al. [35] stated that indicators with a loading factor of less than 0.4 should be eliminated, and indicators with a loading factor of 0.4 – 0.7 can be deleted if it is intended to increase the value of AVE, composite reliability (CR), and Cronbach's Alpha. With these considerations in mind, this study eliminated indicators that have a loading factor > 0.5.

Cronbach's Alpha (CA) and composite reliability (CR) were used to measure internal consistency reliability. This criterion adhered to the opinion of Hair et al. [35] where the model is declared reliable if it has Cronbach's Alpha and composite reliability values > 0.7. The loading factor value of the dimensions/variables that have CA and CR values below 0.7 must be reviewed again on the indicator. Meanwhile, discriminant validity was determined by the correlation value of each indicator to its dimensions/variables which must be higher than the correlations with other dimensions/variables. The discriminant validity test can be seen in the cross loading value or the Fornell-Larcker Criterion.

The VIF value was used to see the symptoms of multicollinearity in the model. According to Hair et al. [38], multicollinearity can be predicted if the VIF value is > 5, but the threshold commonly used for the 0.10 tolerance value is the VIF value of 10. According to the opinion above, in this research model, the VIF criteria > 10 was used to indicate severe multicollinearity symptoms. Indicators that were suspected of not meeting the validity and reliability criteria above must be removed at this stage. After fulfilling the validity testing phase, the results are shown in Table 3.

4. 4. Assessing of the Structural Model (Inner Model) Testing of the structural model (inner model) began by looking at the value of the coefficient of determination (R-square). The coefficient of determination (R2) is used to determine the magnitude of the ability of endogenous variables to explain the diversity of exogenous variables [39]. The R-square value generated from the estimation of this model (Figure 3) was 0.544, which means that 54.4% of the Project Social Conflict variable (Y) can be explained by the independent variables used. Meanwhile, the 45.6% (1-0.544) is explained by other factors that were not included in this research model. R-square was also used to calculate the predictive relevance estimate (Q-square). The value of Q2 indicates how well the observed values were generated by the model and also the estimated parameters. Q2 value greater than 0 (zero) indicates that the model is considered good enough. To determine Q-square the following formula was used.

$$Q^2 = \sqrt{R^2 \text{ x AVE}}$$
$$Q^2 = \sqrt{0.544 \text{ x } 0.830} = 0.672 \quad (2)$$

The analysis at this stage was continued by determining the significant level using t-statistics and p-values. To see the direction of the relationship between the independent variables on the dependent variable, the path coefficient (Table 4) was used.

TABLE 3. Measurement model (outer model) assessment result

FACTOR	LF	CA	CR	AVE	VIF
X1.1 PRJ		0.918	0.928	0.721	6.031
X1.1.1 PRJ1	0.832				
X1.1.2 PRJ2	0.892				
X1.1.3 PRJ3	0.844				
X1.1.4 PRJ4	0.949				
X1.1.5 PRJ5	0.710				
X1.2 BUS		0.913	0.945	0.852	7.813
X1.2.1 BUS1	0.908				
X1.2.2 BUS2	0.915				
X1.2.3 BUS3	0.945				
X1.3 CHR		0.829	0.898	0.746	4.878
X1.3.1 CHR1	0.804				
X1.3.4 CHR4	0.858				
X1.3.5 CHR5	0.924				
X1.4 PER		0.964	0.971	0.825	2.559
X1.4.1 PER1	0.917				
X1.4.2 PER2	0.821				
X1.4.3 PER3	0.928				
X1.4.4 PER4	0.879				
X1.4.5 PER5	0.925				
X1.4.6 PER6	0.962				
X1.4.7 PER7	0.919				
X2.1 ECO		1.000	1.000	1.000	1.342
X2.1.1 ECO1	1.000				
X2.2 SOC		1.000	1.000	1.000	1.675
X2.2.3 SOC3	1.000				
X2.3 ENV		1.000	1.000	1.000	1.316
X2.3.6 ENV6	1.000				
X2.4 CUL		0.845	0.928	0.866	1.098
X2.4.2 CUL2	0.934				
X2.4.3 CUL3	0.920				
Y - PSC		0.948	0.961	0.830	
Y-1.1 PSC1.1	0.845				
Y-1.2 PSC1.2	0.957				
Y-2 PSC2	0.894				
Y-3 PSC3	0.906				
Y-4 PSC4	0.949				

Notes: LF = loading factor; CA = Cronbach's alpha; CR = composite reliability; AVE = average variance extracted; VIF = variance inflation factor

4. 5. Hypotheses and Discussion

The results in this study showed different findings from several previous studies. Significant and positive influence of project performance [19-21], the company's business interests [40, 41], and the interests of personnel and teams [18, 40] as variables are not supported based on this research model. However, the relationship between interests and the characteristics of the project as variables can be proven to have a relationship and influence on the impact of project social conflicts [14, 16].

In the category of the interests of affected communities, it showed the opposite result. Effect of economic conditions, environmental conditions [9, 24-26], and cultural conditions [28-30] showed a positive direction and significant relationship to the impact project social conflicts. Meanwhile, the social conditions of affected communities proved different from the study of Chan and Oppong [9], Silvius and Schipper [24], Xiahou et al. [25], and Zhuang et al. [26] who stated that there is a significant relationship to conflict in the project.

The biggest influence on social conflict is given by the variable interest characteristics of the project with a contribution of 0.435 and then followed by cultural conditions of 0.327, environmental conditions of 0.312, and economic conditions of 0.286. The magnitude of the influence of the variables of interests on the impact of project social conflicts is expressed by an R-square of 0.544 (54.4%) with an error factor of 45.6%. The ability of the variables to relevantly predict the project's social conflict variables is also quite high, with a Q-square value of 0.672 (67.2%).

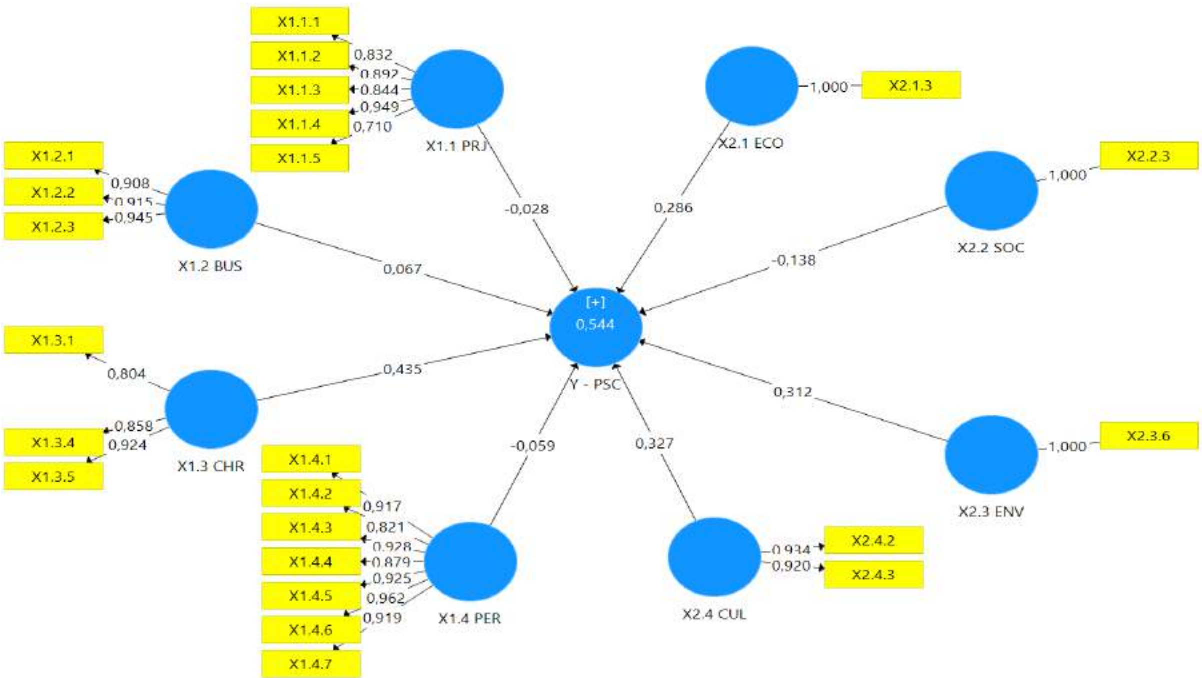

Figure 3. Path coefficient dan R-square model

TABLE 4. Structural model (inner model) assessment result

STRUCTURAL PATH	PATH COEF.	T-STAT.	P-VALUES	SIGN. LVL.	CONCLUSION
X1.1 PRJ → Y - PSC	-0.028	0.136	0.892	n.s	H.1a. not supported
X1.2 BUS → Y - PSC	0.067	0.323	0.747	n.s	H.1b. not supported
X1.3 CHR → Y - PSC	0.435	2.552	0.011	Significant	H1c. supported
X1.4 PER → Y - PSC	-0.059	0.441	0.659	n.s	H.1d. not supported
X2.1 ECO → Y - PSC	0.286	3.176	0.002	Significant	H.2a. supported
X2.2 SOC → Y - PSC	-0.138	1.428	0.154	n.s	H.2b. not supported
X2.3 ENV → Y - PSC	0.312	3.166	0.002	Significant	H.2c. supported
X2.4 CUL → Y - PSC	0.327	3. 692	0.000	Significant	H.2d. supported

Note: Notes: n.s = not significant; t-stat. ≥ 1.96 or p-value ≤ 0.05 significant

The results of this study showed that the interests of affected communities dominate the impact on project social conflicts. The basic difference between this study and previous research is that in this study, internal (projects) and external (communities) interests are jointly developed to be tested on project social conflicts. In previous studies, the model was arranged partially between internal and external interests. However, the differences in the results of this study provide new information, that communities as social entities in the projects have a great influence on project conflict conditions. This finding corroborates Siregar and Utomo's study [42] that for the environmental and social safeguard framework, as an effort to minimize development conflicts, communities must be the subject. The absence of an integrated and standardized environmental and social framework in Indonesia is also an important note in the effort to realize sustainable development with environmental and social perspectives [8]. As generally, this model can be used in all industrial activities that are project-based which have a limited time life cycle, and potentially to intersect with community social activities. However, all the measurement parameters should meet the measurement intervals that were used in this study.

The relationships between the interests of project performance, business performance, and personnel and teams which are not significant to the impact of project social conflicts indicates the level of project and company flexibility to make adjustments to their policies. Projects and construction companies as business entities will consider a smaller impact on the concept and objectives of the project and business compared to rigidity in implementing policies. Meanwhile, project characteristics are variables whose measurement criteria are difficult to change and adjust. Therefore, the interests that arise from the characteristics of the project tend to be rigid and have the potential to create conflicts in the implementation. This is corroborated by indicators that shape the importance of project characteristics, namely project complexity, scope of work, and location. The all three have definite technical and managerial risks to the project based on the level of difficulty.

Meanwhile, the relationship with the interests of affected communities shows the importance of economic, environmental, and cultural aspects for communities. Fluctuating economic conditions as a result of the Covid-19 pandemic have contributed to communities' interests in projects to earn better income. Local communities' interests in environmental aspects show a high level of dependence on natural resources. Cultural aspects are also proven to still have a strong influence on the lives of local people. This proves that culture and customs still dominates social forces in people's lives in Indonesia [43]. What is interesting in the findings of this study is that there is no evidence of a significant influence of social conditions on project social conflicts. Measurement of social conditions through indicators of the level of home ownership that is not significant explains that for local people, home ownership does not determine the status and level of social importance. In the life of local communities, a family house that has been occupied for generations by several generations is actually a matter of pride. Several others built their houses on land inherited from their ancestors as proof of appreciation for the efforts of their ancestors in obtaining family assets. Thus, in the context of this social interest, the indicators used to measure it cannot be proven to have a significant effect on project social conflicts.

5. CONCLUSION

The findings of this study provide a detailed description of the conditions of interests in the implementation of infrastructure projects in Indonesia by involving project and affected community interests. Social conflicts in the project are more dominantly influenced by the interests of the affected communities compared to the interests of the internal project. This is proven by the significant influence of economic, environmental, and cultural aspects on the project's social conflicts. This influence places the social conditions of the affected communities as essential in determining the size of the potential conflict that can occur in project implementation. It also proves that the EIA concept in Indonesia which places the community as an object of protection needs to be reviewed. Meanwhile, project characteristics are a factor of project internal interest that has a significant effect on project social conflicts. Internal interests in aspects of project performance, company business performance, and the interests of personnel and teams have not been proven to have a significant effect on creating social conflicts in the project. This shows the project's ability to adjust the achievement targets to be more realistic to the situation and conditions. The project interprets that failure to manage conflict will have a worse impact on the business performance of the project and its corporation than staying on business interests..

Based on the results of this research, the project is expected to be able to maximize information on the condition of the local community around the project in its implementation. Therefore, it can determine the strategy and concept of empowerment and community involvement in the project appropriately. Meanwhile, the EIA concept which still places the role of the affected community as an object of protection must be immediately transformed by placing the community as a subject who is actively involved in the development process and protection against social and environmental impacts. To achieve an appropriate safeguard framework, further research is needed to examine the framework concept as a moderation of the relationship between interests and project social conflicts. Thus, the conceptual framework proposed as an effort to manage and control conflicts can be tested for its ability and reliability in accommodating the interests of both parties. The concept of this framework is then referred to as "compromise of interests" or "middle way interests" in managing project social conflicts with dignity.

6. REFERENCES

1. Pereirinha, J.A.C. and Pereira, E., "Social resilience and welfare systems under covid-19: A european comparative perspective", ***Global Social Policy***, Vol. 21, No. 3, (2021), 569-594, https://doi.org/10.1177/14680181211012946
2. Zamani, S.H., Rahman, R., Fauzi, M. and Yusof, L., "Effect of covid-19 on building construction projects: Impact and response mechanisms", in IOP Conference Series: Earth and Environmental Science, IOP Publishing. Vol. 682, No. 1, (2021), 012049.
3. Zhang, L. and El-Gohary, N.M., "Discovering stakeholder values for axiology-based value analysis of building projects", ***Journal of Construction Engineering and Management***, Vol. 142, No. 4, (2016), 04015095, https://doi.org/10.1061/(ASCE)CO.1943-7862.0001004
4. File, D.J. and Derbile, E.K., "Sunshine, temperature and wind: Community risk assessment of climate change, indigenous knowledge and climate change adaptation planning in ghana", ***International Journal of Climate Change Strategies and***

Management, (2020), https://doi.org/10.1108/IJCCSM-04-2019-0023

5. Austin, K.G., Schwantes, A., Gu, Y. and Kasibhatla, P.S., "What causes deforestation in indonesia?", ***Environmental Research Letters***, Vol. 14, No. 2, (2019), 024007, https://doi.org/10.1088/1748-9326/aaf6db
6. Alamgir, M., Campbell, M.J., Sloan, S., Suhardiman, A., Supriatna, J. and Laurance, W.F., "High-risk infrastructure projects pose imminent threats to forests in indonesian borneo", ***Scientific Reports***, Vol. 9, No. 1, (2019), 1-10, https://doi.org/10.1038/s41598-018-36594-8
7. Yu, J. and Leung, M.-y., "Structural stakeholder model in public engagement for construction development projects", ***Journal of Construction Engineering and Management***, Vol. 144, No. 6, (2018), 04018046, https://doi.org/10.1061/(ASCE)CO.1943-7862.0001462
8. Sanggoro, H.B., Alisjahbana, S.W. and Mohamad, D., "Soft system methodology: Project vs local community interests in project social conflict", https://doi.org/10.5829/ije.2021.34.09c.08
9. Chan, A.P. and Oppong, G.D., "Managing the expectations of external stakeholders in construction projects", ***Engineering, Construction and Architectural Management***, (2017), https://doi.org/10.1108/ECAM-07-2016-0159
10. Verzuh, E. and Association, A.P., "A guide to the project management body of knowledge: Pmbok guide", (2021).
11. Ho, P.H., "Analysis of competitive environments, business strategies, and performance in hong kong's construction industry", ***Journal of Management in Engineering***, Vol. 32, No. 2, (2016), 04015044, https://doi.org/10.1061/(ASCE)ME.1943-5479.0000399
12. Jang, Y., Jeong, I.-B., Cho, Y.K. and Ahn, Y., "Predicting business failure of construction contractors using long short-term memory recurrent neural network", ***Journal of Construction Engineering and Management***, Vol. 145, No. 11, (2019), 04019067, https://doi.org/10.1061/(ASCE)CO.1943-7862.0001709
13. Kim, D.G. and Choi, S.O., "Impact of construction it technology convergence innovation on business performance", ***Sustainability***, Vol. 10, No. 11, (2018), 3972, https://doi.org/10.3390/su10113972
14. Min, J.H., Jang, W., Han, S.H., Kim, D. and Kwak, Y.H., "How conflict occurs and what causes conflict: Conflict analysis framework for public infrastructure projects", ***Journal of Management in Engineering***, Vol. 34, No. 4, (2018), 04018019, doi. https://doi.org/10.1061/(ASCE)ME.1943-5479.0000625
15. Liu, B., Huo, T., Liang, Y., Sun, Y. and Hu, X., "Key factors of project characteristics affecting project delivery system decision making in the chinese construction industry: Case study using chinese data based on rough set theory", ***Journal of Professional Issues in Engineering Education and Practice***, Vol. 142, No. 4, (2016), 05016003, https://doi.org/10.1061/(ASCE)EI.1943-5541.0000278
16. Vaux, J.S. and Kirk, W.M., "Relationship conflict in construction management: Performance and productivity problem", ***Journal of Construction Engineering and Management***, Vol. 144, No. 6, (2018), 04018032, https://doi.org/10.1061/(ASCE)CO.1943-7862.0001478
17. Dao, B., Kermanshachi, S., Shane, J., Anderson, S. and Hare, E., "Exploring and assessing project complexity", ***Journal of Construction Engineering and Management***, Vol. 143, No. 5, (2017), 04016126, https://doi.org/10.1061/(ASCE)CO.1943-7862.0001275
18. Al-Sibaie, E.Z., Alashwal, A.M., Abdul-Rahman, H. and Zolkafli, U.K., "Determining the relationship between conflict factors and performance of international construction projects", ***Engineering, Construction and Architectural Management***, (2014), https://doi.org/10.1108/ECAM-03-2014-0034
19. Wu, G., Zhao, X. and Zuo, J., "Effects of inter-organizational conflicts on construction project added value in china", ***International Journal of Conflict Management***, (2017), https://doi.org/10.1108/IJCMA-03-2017-0025
20. Wu, G., Zhao, X. and Zuo, J., "Relationship between project's added value and the trust–conflict interaction among project teams", ***Journal of Management in Engineering***, Vol. 33, No. 4, (2017), 04017011, https://doi.org/10.1061/(ASCE)ME.1943-5479.0000525
21. Chen, Y.Q., Zhang, Y.B. and Zhang, S.J., "Impacts of different types of owner-contractor conflict on cost performance in construction projects", ***Journal of Construction Engineering and Management***, Vol. 140, No. 6, (2014), 04014017, https://doi.org/10.1061/(ASCE)CO.1943-7862.0000852
22. Archer, P., "Towards a theory of interest claims in constructing social problems", ***Qualitative Sociology Review***, Vol. 11, No. 2, (2015), 46-60.
23. Wang, H., Zhang, X. and Lu, W., "Improving social sustainability in construction: Conceptual framework based on social network analysis", ***Journal of Management in Engineering***, Vol. 34, No. 6, (2018), 05018012, https://doi.org/10.1061/(ASCE)ME.1943-5479.0000607
24. Silvius, G. and Schipper, R., "Planning project stakeholder engagement from a sustainable development perspective", ***Administrative Sciences***, Vol. 9, No. 2, (2019), 46, https://doi.org/10.3390/admsci9020046
25. Xiahou, X., Tang, Y., Yuan, J., Chang, T., Liu, P. and Li, Q., "Evaluating social performance of construction projects: An empirical study", ***Sustainability***, Vol. 10, No. 7, (2018), 2329, https://doi.org/10.3390/su10072329
26. Zhuang, T., Qian, Q.K., Visscher, H.J. and Elsinga, M.G., "Stakeholders' expectations in urban renewal projects in china: A key step towards sustainability", ***Sustainability***, Vol. 9, No. 9, (2017), 1640, https://doi.org/10.3390/su9091640
27. Hartono, B., Dzulfikar, L. and Damayanti, R., "Impact of team diversity and conflict on project performance in indonesian start-ups", ***Journal of Industrial Engineering and Management***, Vol. 13, No. 1, (2020), 155-178, https://doi.org/10.3926/jiem.3037
28. Xue, Y. and Xiang, P., "The social risk of high-speed rail projects in china: A bayesian network analysis", ***Sustainability***, Vol. 12, No. 5, (2020), 2087, https://doi.org/10.3390/su12052087
29. Meng, J., Yan, J. and Xue, B., "Exploring relationships between national culture and infrastructure sustainability using qca", ***Journal of Construction Engineering and Management***, Vol. 144, No. 9, (2018), 04018082, https://doi.org/10.1061/(ASCE)CO.1943-7862.0001463
30. Lückmann, P. and Färber, K., "The impact of cultural differences on project stakeholder engagement: A review of case study research in international project management", ***Procedia Computer Science***, Vol. 100, (2016), 85-94, https://doi.org/https://doi.org/10.1016/j.procs.2016.09.127
31. Omenge, P.M., Obwoyere, G.O., Eshiamwata, G.W., Makindi, S.M. and Nathwani, J., "Environmental and social impact assessment procedural steps that underpin conflict identification: Reference to renewable energy resource development in kenya", ***International Journal of Energy Production and Management***, Vol. 5, No. 2, (2020), 157-174, https://doi.org/10.2495/EQ-V5-N2-157-174
32. Khalid, S. and Fatima, I., "Conflict types and conflict management styles in public and private hospitals", ***PAFMJ***, Vol. 66, No. 1, (2016), 122-126.
33. Riley, J.M. and Ellegood, W.A., "Relationship conflict, task conflict and teams' transactive memory systems", ***International***

Journal of Educational Management, (2019), https://doi.org/10.1108/IJEM-01-2019-0003

34. Prasad, B. and Junni, P., "Understanding top management team conflict, environmental uncertainty and firm innovativeness: Empirical evidence from india", ***International Journal of Conflict Management***, (2017), https://doi.org/10.1108/IJCMA-02-2016-0006
35. Hair Jr, J.F., Hult, G.T.M., Ringle, C.M. and Sarstedt, M., "A primer on partial least squares structural equation modeling (pls-sem), Sage publications, (2021).
36. Chin, W.W., How to write up and report pls analyses, in Handbook of partial least squares. 2010, Springer.655-690.
37. Garson, G.D., *Partial least squares. Regression and structural equation models*. 2016, Statistical Publishing Associates.
38. Hair, J., Black, W., Babin, B., Anderson, R. and Tatham, R., "Multivariate data analysis: A global perspective (6th editio)", ***Upper Saddle Rider: Pearson Education***, (2010).
39. Ali, I., Musawir, A.U. and Ali, M., "Impact of knowledge sharing and absorptive capacity on project performance: The moderating role of social processes", ***Journal of Knowledge Management***, (2018), https://doi.org/10.1108/JKM-10-2016-0449
40. Panahi, B., Moezzi, E., Preece, C.N. and Zakaria, W.N.W., "Value conflicts and organizational commitment of internal construction stakeholders", ***Engineering, Construction and Architectural Management***, (2017), https://doi.org/10.1108/ECAM-01-2016-0006
41. Wang, Y. and Xiang, P., "Investigate the conduction path of stakeholder conflict of urban regeneration sustainability in china: The application of social-based solutions", ***Sustainability***, Vol. 11, No. 19, (2019), 5271, https://doi.org/10.3390/su11195271
42. Siregar, M. and Utomo, S., "Environmental impact assessment as a regulation and equator principles as an initiative", in IOP Conference Series: Earth and Environmental Science, IOP Publishing. Vol. 399, No. 1, (2019), 012081.
43. Sanggoro, H.B., Widyaningsih, N. and Bintoro, B.P., "Analysis influence factors of domination, competency and interpersonal skill in the stakeholder interaction to infrastructure project success", ***International Journal of Engineering & Technology***, Vol. 9, No. 1, (2020), 164-174, https://doi.org/10.14419/ijet.v9i1.30153

Persian Abstract

چکیده

رشد اقتصادی ضعیف به دلیل همه‌گیری کووید-۱۹ در دو سال گذشته منجر به کاهش شاخص‌های رفاه عمومی شده است. بخش صنعت ساختمان نیز کاهش شدید بهره وری را تجربه کرد. بنابراین، برای زنده ماندن در شرایط بحرانی باید تنظیماتی انجام می شد. علاوه بر این، مشکلات زیست محیطی ناشی از فعالیت های عمرانی نیز زندگی و درآمد افراد وابسته به محصولات طبیعی را تهدید می کند. این شرایط باعث افزایش منافعی می شود که بر پروژه های زیرساختی در اندونزی تأثیر می گذارد. این مطالعه با هدف پیش‌بینی تأثیر پروژه و منافع جامعه محلی تأثیرگذار بر تعارضات اجتماعی پروژه‌های زیربنایی انجام شد. داده ها با استفاده از پرسشنامه از ٦٨ مدیر پروژه به عنوان پاسخگو به دست آمد و با استفاده از PLS-SEM تجزیه و تحلیل شد. یافته های این مطالعه حاکی از آن است که تأثیر جامعه متاثر از منافع پروژه بر تعارضات اجتماعی پروژه بیشتر است. این امر نشان دهنده نقش مهم جوامع در مفهوم توسعه پایدار با دیدگاه های زیست محیطی و اجتماعی است. نتایج این مطالعه در پیش نویس مفهوم چارچوب حفاظت محیطی و اجتماعی یکپارچه و استاندارد شده مفید خواهد بود. برای دستیابی به یک چارچوب مناسب، تحقیقات بیشتری برای بررسی مفهوم چارچوب به عنوان تعدیل رابطه بین منافع و تضادهای اجتماعی پروژه مورد نیاز است.

IJE TRANSACTIONS A: Basics Vol. 35, No. 05, (July 2022) 1227-1236

International Journal of Engineering

Journal Homepage: www.ije.ir

Structural Stiffness Matching Modeling and Active Design Approach for Multiple Stepped Cantilever Beam

M. H. Zhang*, Z. C. Cao, F. C. Xia, Z. Yao

Northwest Institute of Mechanical and Electrical Engineering, Xianyang, China

PAPER INFO

Paper history:
Received 09 January 2022
Received in revised form 03 March 2022
Accepted 05 March 2022

Keywords:
Cantilever Beam
Stiffness Match
Active Design
Stiffness Index
Optimization

ABSTRACT

Aiming at the problem that it is difficult to realize the optimal design due to the fuzzy mapping relationship for the structural stiffness of multiple stepped cantilever beam; a stiffness matching modeling and active stiffness design approach was proposed. Firstly, by deriving out the continuous coordination conditions and the load extrapolation expressions of the cantilever joint, the stiffness analytical model and the recursive model were established for multiple cantilever beam segments, and the stiffness influence coefficient of those composition parameters were obtained by the sensitivity analysis. Then, the active stiffness optimization design process was constructed according to the stiffness design level of the stepped cantilever beam, and those implementation procedures were clearly figured out. Finally, the comparison and verification of the stiffness design of the stepped cantilever beam was carried out through numerical simulations, finite element analysis and bench test. The obtained results showed that the established models and the active stiffness design method are reasonable and effective. The stiffness match parameters are easy to meet the stiffness index requirements, and the safety factor is greater than 1; when the number of steps is not more than 5. The relative error between the match stiffness and the test stiffness is less than 15%, which can be reduced to less than 5% by adding redundancy coefficient (1.05, 1.15).

***doi**: 10.5829/ije.2022.35.07a.02*

1. INTRODUCTION

With the gradual transition from the secondary load-bearing structure to the primary load-bearing structure of the multi-step cantilever beam, the rapid calculation and preliminary optimization of its structural stiffness has become a key issue in engineering application [1, 2]. The current stiffness design mainly adopts the empirical coefficient method, which includes the experience designing, stiffness checking and the modifying steps. But it is often blind to a certain extent, and it is unavoidable that insufficient or redundant stiffness occurs. Although some researches have used the optimization design method; since the structural stiffness match models of the multi-step cantilever beam has not yet been found in the relevant literature. It is still challenging to establish the objective function and constraint conditions according to the level of stiffness design, such as the continuous coordination conditions and the load extrapolation expressions are not clear. Therefore, it is of great significance to carry out the active stiffness design research on the stepped cantilever beam. On the basis of mastering the equivalent mapping relationship between the cantilever parameters and the structural stiffness, the deformation of the cantilever beam segments can be efficiently controlled to achieve the designed requirements at one time, which could promote the application of stepped cantilever beam to aerospace, robotics and other fields.

The existing researches [3-5] on the stiffness design of some characteristic structures mainly focus on the active design method or the forward design method. Li et al. [6] proposed the beam-frame model aeroelastic optimization method and the three-dimensional model conversion method for designing the global stiffness of a high aspect ratio wing. Ke et al. [7] established the

*Corresponding Author Institutional Email: kun836520839@163.com (M. H. Zhang)

Please cite this article as: M. H. Zhang, Z. C. Cao, F. C. Xia, Z. Yao, Structural Stiffness Matching Modeling and Active Design Approach for Multiple Stepped Cantilever Beam, ***International Journal of Engineering, Transactions A: Basics***, Vol. 35, No. 07, (2022) 1227-1236

matching relationship between the key parameters of layer scheme and the stiffness of composite leaf spring, and also, its structural layout was designed for the matching stiffness target. Shi et al. [8] put forward a top-down design method for the static and dynamic stiffness of precision horizontal machining centers. By summarizing those researches, it is worth noting that although those stiffness design methods could preliminarily achieve the control of structural deformation, the distribution of structural internal force, etc., but many application restrictions still appear when combining with the stepped cantilever structure. The structural stiffness match model of multiple stepped cantilever beam has not been found in relevant literatures, and the mapping relationship is not clear between the structural stiffness and different scale or characteristic parameters. The existing stiffness design methods are mainly for machine tools and other specific devices [9, 10], the design process should be adjusted for multiple stepped beam.

In order to realize the structural stiffness match and active stiffness design of multi-step cantilever beams, the continuous coordination conditions and the load extrapolation expressions are derived out through the motion and deformation modeling of the cantilever structure, and the stiffness match models shown in section 2 are constructed by using the elastic mechanics theory, of which includes the explicit expression of double stepped beam and the recursive expression of multiple stepped beam. On this basis, the stiffness coefficient of various composition parameters is obtained with the sensitivity analysis. In section 3, the active stiffness design process is constructed according to the stiffness requirements of the stepped cantilever structure, and the key implementation elements are also presented. Finally, the reliability of the established stiffness match models and the rationality of the active design process are verified according to the numerical simulations, the finite element simulations and the bench test of the cantilever beam sample in section 4. Meanwhile, the high-precision and high-confidence application mode of the established active stiffness design method is pointed out, which is helpful to promote the robust design and reliable application of multi-step cantilever beams. In addition, section 1 is the introduction, section 5 is the conclusion, section 6 is the acknowledgment, section 7 is the list of references.

2. STIFFNESS MATCH MODEL

According to the practical application situation, the parametric model of the stepped cantilever structure composed of multiple beam is shown in Figure 1. To simplify the modeling process, principle hypothesizes are as follows: (a) the length, width and height parameter of the rectangle section of n-steps $(n \geq 2)$ beams are L_k, B_k, H_k $(k=1,\cdots,n)$ respectively; (b) the fixed and the free ends of the whole cantilever structure satisfy the boundary conditions; (c) the combined area $S_1,\cdots,S_{n-1}$ satisfy deformation coordination conditions.

Based on the stiffness index concept [11], the geometric analysis mainly focusses on the maximum allowable deformation under the external load. The stiffness coefficient expression can be expressed as:

$$K = P/w \tag{1}$$

where, P is the external load, which could be the concentrated force, distributed force, moment and torque, etc. w is the maximum deformation, angle, etc.

2. 1. Motion and Deformation Modeling In the simple-beam framework of elastic mechanics, the bending modeling assumption of rectangular beam can be pointed out as follows: (a) the bending deformation is always in the main plane or cross section with respect to its body coordinate system, the shear and torsional deformation can be ignored; (b) the cross section could keep as plane during the motion, and it is perpendicular to the axis of the deformation beam; (c) the rotational kinetic energy of beam unit can be ignored, and also, the shear deformation potential energy can be ignored compared with bending deformation potential energy.

Taking the uniform beam with rectangle section as the object, the basic models corresponding to one-dimensional bending problem can be expressed as:

$$\kappa = \frac{\mathrm{d}^2 w}{\mathrm{d}x^2}, M = EI\frac{\mathrm{d}^2 w}{\mathrm{d}x^2}, Q = EI\frac{\mathrm{d}^3 w}{\mathrm{d}x^3}, q = EI\frac{\mathrm{d}^4 w}{\mathrm{d}x^4} \tag{2}$$

where, $w(x)$ is the deflection function of the mid plane, κ is the deformation curvature of the mid plane, M is the bending moment and Q is the transverse shear force on the section, E is the elastic modulus and I is the bending inertia moment, q is the transverse force.

(1) Single cantilever beam

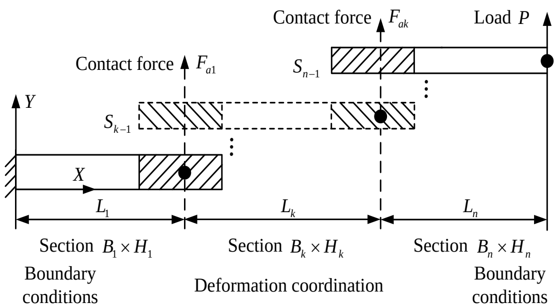

Figure 1. Component and parametric model of multiple stepped cantilever beam

The single cantilever beam can be equivalent to a curved beam element, and the boundary conditions of its fixed end are given by:

$$w(x)\big|_{x=0}=0,\quad \mathrm{d}w(x)/\mathrm{d}x\big|_{x=0}=0 \tag{3}$$

Combining to the concentrated load that located at the free end, the motion model and the maximum deformation can be expressed as follows:

$$\frac{EI}{L^3}\begin{bmatrix}12 & -6L\\ -6L & 4L^2\end{bmatrix}\begin{bmatrix}w_L\\ \theta_L\end{bmatrix}=\begin{bmatrix}P\\ 0\end{bmatrix},\theta_L=\frac{3w_L}{2L},\ w_L=\frac{PL^3}{3EI} \tag{4}$$

Then, the equivalent structural stiffness of the single cantilever beam can be expressed as follows:

$$K_L=3EI/L^3 \tag{5}$$

(2) Double stepped cantilever beam

When the double stepped cantilever beam has a separation trend under the external load, and the combined area is similar with the fixed boundary form, the deflection equation of the first-step beam can be expressed as follows:

$$\begin{cases} w\big|_{x=L_1}=\dfrac{F_aL_1^{\,3}}{3E_1I_1},\quad \theta\big|_{x=L_1}=\dfrac{F_aL_1^{\,2}}{2E_1I_1}\\ w(x)=\dfrac{F_ax^2}{6E_1I_1}(3L_1-x)\end{cases} \tag{6}$$

where, F_a is the contact force of the combined area.

Through the fixed constraint of the combined area, the motion model of the second-step beam can be expressed as follows:

$$E_2I_2\frac{\mathrm{d}^2W}{\mathrm{d}X^2}=\hat{P}(L_1+L_2-X),\quad X\in[L_1,L_1+L_2] \tag{7}$$

By using the direct differential method, the deflection equation can be derived and expressed as follows:

$$W(X)=\frac{\hat{P}}{E_2I_2}\left[-\frac{X^3}{6}+\frac{(L_1+L_2)X^2}{2}+\tilde{C}_1X+\tilde{C}_2\right] \tag{8}$$

After substituting the deformation coordination conditions of the displacement and the section rotation into Equation (8), it can be simplified and given by the following expression:

$$W(X)\big|_{X=L_1}=w\big|_{x=L_1},\ \left.\frac{\partial W}{\partial X}\right|_{X=L_1}=\theta\big|_{x=L_1} \tag{9}$$

$$W_2(L_1+L_2)=\frac{F_a}{3E_1I_1}L_1^{\,3}+\frac{\hat{P}L_2^{\,3}}{3E_2I_2}+\frac{F_a}{2E_1I_1}L_1^{\,2}L_2 \tag{10}$$

where, $W_2(L_1+L_2)$ is the maximum deformation.

Besides, the contact force F_a can be determined with the modified concentrated load [12] method, which could be constructed by the constraint relationship of the combined area and expressed as follows:

$$\begin{aligned}&Q_a\hat{P}+Q_a{}'F_a=0,\ \ Q_a=\frac{1}{2}\frac{I_1}{I_2}\left[3\frac{L_2}{L_1}-2\right]\\ &Q_a{}'=-\left[1+\frac{I_1}{I_2}\right],\ \ F_a=\frac{1}{2}\frac{I_1}{(I_1+I_2)}\left[3\frac{L_2}{L_1}-2\right]\hat{P}\end{aligned} \tag{11}$$

Then, the equivalent structural stiffness of double stepped cantilever beam can be expressed as follows:

$$K_{L_1+L_2}=\frac{E_1E_2I_2}{\dfrac{E_2I_2}{(I_1+I_2)}\left[\dfrac{3}{4}L_1L_2^{\,2}-\dfrac{1}{3}L_1^{\,3}\right]+\dfrac{1}{3}E_1L_2^{\,3}} \tag{12}$$

(3) Multiple stepped cantilever beam

With the same bending modeling assumption, the recursive function can be used to derive the equivalent stiffness of multiple cantilever beam.

Firstly, relative to the reference coordinate system, the motion models and the deflection equations of the n-step $(n\geq 3)$ cantilever beam are given by the following expression:

$$\begin{cases} W_1(X)=F_{a1}\dfrac{X^2(3L_1-X)}{6E_1I_1},X\in[0,L_1]\\ E_2I_2\dfrac{\mathrm{d}^2W_2}{\mathrm{d}X^2}=F_{a2}(L_1+L_2-X),X\in[L_1,L_1+L_2]\\ E_nI_n\dfrac{\mathrm{d}^2W_n}{\mathrm{d}X^2}=\hat{P}(L_1+\cdots+L_n-X),\\ \qquad X\in[L_1+\cdots+L_{n-1},L_1+\cdots+L_n]\end{cases} \tag{13}$$

Secondly, based on the deformation coordination conditions of the combined areas $X=L_k(k=1,\cdots,n-1)$, those $n-1$ contact forces can be also derived from the modified concentrated loads and expressed as follows:

$$\begin{cases} Q_{n-1}\hat{P}+Q'_{n-1}F_{a(n-1)}+Q''_{n-1}F_{a(n-2)}=0\\ Q_kF_{a(k+1)}+Q'_kF_{ak}+Q''_kF_{a(k-1)}=0\\ Q_1F_{a2}+Q'_1F_{a1}=0\end{cases} \tag{14}$$

$$\begin{cases} Q_k=\dfrac{I_k}{2I_{k+1}}\left[\dfrac{3L_{k+1}}{(L_1+\cdots+L_k)}-2\right]\\ Q'_k=-\left[1+\dfrac{I_k}{I_{k+1}}\right],\ k=1,\cdots,n-1\\ Q''_k=\dfrac{1}{2}\left[\dfrac{I_{k-1}}{I_k}\right]^2\left[3-\dfrac{(L_1+\cdots+L_{k-1})}{(L_1+\cdots+L_k)}\right]\end{cases} \tag{15}$$

$$\begin{bmatrix} Q'_{n-1} & Q''_{n-1} & 0 & \cdots & \cdots & \cdots & \cdots & 0 \\ Q_{n-2} & Q'_{n-2} & Q''_{n-2} & 0 & \cdots & \cdots & \cdots & 0 \\ 0 & Q_{n-3} & Q'_{n-3} & Q''_{n-3} & 0 & \cdots & \cdots & 0 \\ \vdots & \vdots & \cdots & \ddots & \cdots & \cdots & \vdots & \vdots \\ \vdots & \vdots & \cdots & \cdots & \ddots & \cdots & \vdots & \vdots \\ 0 & \cdots & \cdots & \cdots & 0 & Q_2 & Q'_2 & Q''_2 \\ 0 & \cdots & \cdots & \cdots & \cdots & 0 & Q_1 & Q'_1 \end{bmatrix} \begin{bmatrix} F_{a(n-1)} \\ F_{a(n-2)} \\ F_{a(n-3)} \\ \vdots \\ F_{a3} \\ F_{a2} \\ F_{a1} \end{bmatrix} = \begin{bmatrix} -Q_{n-1}\hat{P} \\ 0 \\ 0 \\ \vdots \\ 0 \\ 0 \\ 0 \end{bmatrix} \quad (16)$$

Finally, the implicit expression of the equivalent stiffness of the multiple stepped cantilever beam can be expressed as follows:

$$K_{L_1+\cdots+L_n} = \frac{\hat{P}}{W_n\left(L_1+\cdots+L_n\right)} \quad (17)$$

For the stiffness match model given in Equation (17), since the end deflection contains the higher-order term of the external load variable, the constant term in the load extrapolation expression cannot be completely offset. However, when the scale parameters, mechanical parameters and external force parameters of the cantilever structure are determined, the maximum deformation can be obtained recursively, and the stiffness characteristics can be figured out by the slope between the maximum deformation and the external load. In the existing researches, the composite element method is used to establish the overall stiffness matrix of the cantilever beam [3, 5], or the nonlinear characterization test results [13] of stepped cantilever structure are used to establish a fitting model to obtain the linear term and cubic term of stiffness coefficients. Compared with the existing methods, the established models introduce the continuous coordination condition and the load extrapolation relationship of the cantilever joint, which avoids the complex calculation of the overall stiffness matrix and the requirement of the physical model test system, and can be directly applied to the rapid calculation and optimization of the stiffness of the cantilever structure.

2. 2. Stiffness Influence Coefficient After establishing the structural stiffness match model of multiple stepped cantilever beam, the stiffness influence coefficient of different composition parameters can be obtained by using the sensitivity analysis method [14].

Taking the double stepped cantilever beam as the object, the stiffness match model that given in Equation (12) can be expressed as follows:

$$\begin{aligned} & I_\alpha = \frac{1}{12}B_\alpha H_\alpha{}^3, \quad \Delta L = \frac{1}{16}L_1{}^2L_2 - \frac{1}{36}L_1{}^3 \\ & K_{L_1+L_2} = \frac{E_1E_2B_2H_2{}^3}{\dfrac{E_2B_2H_2{}^3}{\left(B_1H_1{}^3+B_2H_2{}^3\right)}\Delta L + \dfrac{1}{36}E_1L_2{}^3} \end{aligned} \quad (18)$$

$$\begin{aligned} & \bar{K} = \psi_B \cdot B_1 \ \text{or}\ \bar{K} = \psi_E \cdot E_1 \\ & \bar{K} = \psi_H \cdot H_1{}^3 \ \text{or}\ \bar{K} = \psi_D \cdot L_1{}^{-3} \end{aligned} \quad (19)$$

$$\begin{aligned} & \lambda_B = \frac{B_2}{B_1},\ \lambda_e = \frac{E_2}{E_1},\ \lambda_h = \frac{H_2}{H_1},\ \lambda_L = \frac{L_2}{L_1} \\ & \psi_B = \frac{\lambda_B E_1E_2H_2{}^3}{\dfrac{\lambda_B E_2H_2{}^3}{\left(H_1{}^3+\lambda_B H_2{}^3\right)}\Delta L + \dfrac{1}{36}E_1L_2{}^3} \\ & \psi_E = \frac{\lambda_e B_2H_2{}^3}{\dfrac{\lambda_e B_2H_2{}^3}{\left(B_1H_1{}^3+B_2H_2{}^3\right)}\Delta L + \dfrac{1}{36}L_2{}^3} \\ & \psi_H = \frac{E_1E_2B_2\lambda_h{}^3}{\dfrac{E_2B_2\lambda_h{}^3}{\left(B_1+B_2\lambda_h{}^3\right)}\Delta L + \dfrac{1}{36}E_1L_2{}^3} \\ & \psi_D = \frac{36E_1E_2B_2H_2{}^3}{\dfrac{E_2B_2H_2{}^3}{\left(B_1H_1{}^3+B_2H_2{}^3\right)}\left[\dfrac{9}{4}\lambda_L - 1\right] + E_1\lambda_L{}^3} \end{aligned} \quad (20)$$

It can be found that when the scale and mechanical parameters of each beam are proportional, the structural stiffness is positively linear with the width *B* and the elastic modulus *E*, and also it is positively cubic with the height *H*, but it is negatively cubic with the effective length *L*.

In addition, Equation (18) can be transformed with the slender ratio η and given by the following equations:

$$\begin{aligned} & L_j = \eta_j H_j,\ \Delta\eta = \frac{1}{16}\eta_2 H_2 - \frac{1}{36}\eta_1 H_1 \\ & K_{L_1+L_2} = \frac{E_1E_2B_2}{\dfrac{E_2B_2\eta_1{}^2H_1{}^2}{\left(B_1H_1{}^3+B_2H_2{}^3\right)}\Delta\eta + \dfrac{1}{36}E_1\eta_2{}^3} \end{aligned} \quad (21)$$

$$\begin{aligned} & \frac{\partial K_{L_1+L_2}}{\partial \eta_1} = -C_\eta H_\eta \eta_1\left[\frac{1}{8}\eta_2 H_2 - \frac{1}{12}\eta_1 H_1\right] \\ & \frac{\partial K_{L_1+L_2}}{\partial \eta_2} = -C_\eta\left[\frac{1}{16}H_\eta\eta_1{}^2H_2 + \frac{1}{12}E_1\eta_2{}^2\right] \\ & C_\eta = \frac{E_1E_2B_2}{\left[H_\eta\eta_1{}^2\Delta\eta + \dfrac{1}{36}E_1\eta_2{}^3\right]^2} \\ & H_\eta = \frac{E_2B_2H_1{}^2}{B_1H_1{}^3+B_2H_2{}^3} \end{aligned} \quad (22)$$

It can be concluded that when the scale constraint $\left(L_2/8 - L_1/12\right) < 0$ is satisfied, the structural stiffness has a positive correlation with the slender ratio η_1 of the first-step beam. Otherwise, it would have a negative correlation. Under the arbitrary constraint conditions, the structural stiffness has a negative correlation with slender ratio η_2 of second-step beam.

Based on Equation (17), the stiffness influence coefficient of those composition parameters of multiple stepped beam can be also obtained by using the sensitivity analysis and the chain derivation method, while those analytical expressions are omitted.

2. ACTIVE STIFFNESS OPTIMIZATION DESIGN

Combined to detailed decomposition of structural stiffness requirements, such as the bending parameter of gun barrel and the critical deformation parameter of ballistic missile body, etc., the active stiffness optimization design flowchart is constructed and shown in Figure 2. Omitting most of the match modeling process, the key to the implementation procedures for stiffness optimization [15] of multi-step cantilever beam is shown in Figure 3.

(1) Selecting and implementing the optimal design method. In general, the optimization design includes design variables, objective functions, constraints and algorithms. Besides, both mature multi-objective optimization algorithms and the improved algorithm [16] can be used. The implementation process can be achieved by the self programming and the mature software, such as ANSYS optimization module, UG parametric module, etc.

(2) Presenting and applying the stiffness design parameters. The materialization process of the stiffness index involves the structural form, the control of the structure weight and so on. It is necessary to determine the most ideal cantilever structural parameters within the optional configuration system.

(3) Checking the difference between the actual stiffness characteristics and the stiffness index. For the preliminary design parameters, it is necessary to figure out the stiffness error and the impact on the overall stiffness performance. And then, the local corrections could be carried out to modify the actual stiffness characteristics of multiple stepped cantilever beam.

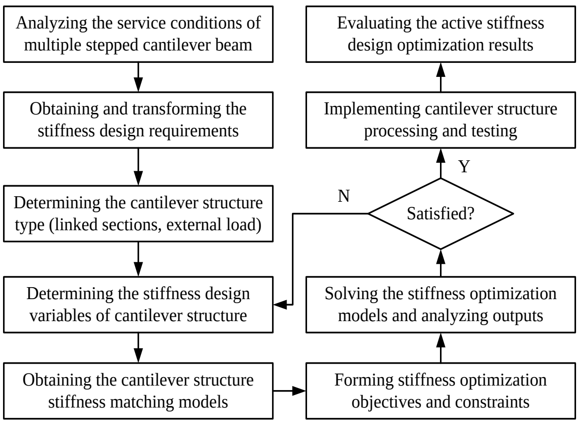

Figure 2. Active stiffness design flowchart

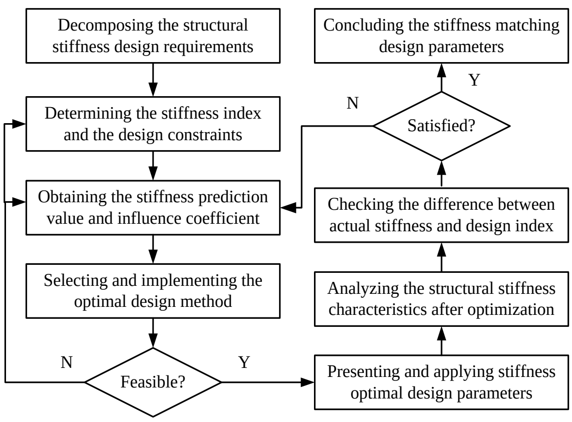

Figure 3. Key procedures of stiffness optimization

4. SIMULATION ANALYSIS AND TEST VERIFICATION

4. 1. Numerical Simulations and Analysis Based on the equivalent stiffness given in Equations (12), (18) and (21), the structural stiffness match results of double stepped cantilever beam are easy to obtain and shown in Figure 4. Besides, the benchmark parameters are as follows: the length, width and height of first-step beam is set to $64 \times 12 \times 6$ mm respectively. Its elastic modulus is set to 2.0E+05 MPa ; the corresponding scale parameters and elastic modulus of the second-step beam is $60 \times 12 \times 5$ mm, 2.0E+05 MPa .

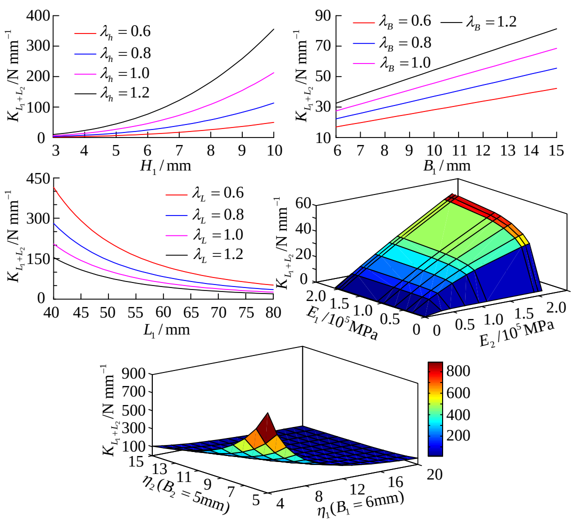

Figure 4. Stiffness match results of double stepped cantilever beam

It can be seen that when the structural parameters of first-step beam are used as the benchmark, the structural stiffness of the double stepped beam has a non-uniform mapping with different composition conditions, of which includes the non-linear relationship with the height and the length, as well as the linear rule with the width and the elastic modulus. From the viewpoint of sensitivity analysis, the stiffness growth rate is large with the height and its proportion coefficient, and it is very small with the elastic modulus. Without considering the proportion coefficient, the sensitivity is arranged from high to low in terms of height, length, width and elastic modulus, which means that it is feasible to change structural stiffness by increasing or decreasing the height conveniently. From the perspective of nonlinear characterization, the change trend of cantilever structure stiffness with scale parameters is a smooth curve, but there is a local jump relative to the change trend of elastic modulus and proportional coefficient. In addition, the structural stiffness also has a non-linear relationship with the slender ratio, and the sensitivity of the slender ratio of second-step beam is larger than that of the first-step beam, the stiffness variation tends to be smooth with an increase in the slender ratio.

Then, the double stepped beam is still taken as the object, and the active stiffness design simulation is carried out sequentially. It may be assumed that the material properties do not change, the effective length and the working load corresponded to the layout mode do not change. At this moment, the optimization model under the lightweight requirement is stated in the following.

The constant parameters are given by $E = 2.0\text{E+05 MPa}, \rho = 7850 \text{ kg m}^{-3}, L_1 = 108 \text{ mm}$, $L_2 = 78 \text{ mm}, \tilde{P} = 75 \text{ N}$, and the design variables are given by $B_1 B_2, H_1 H_2$, the maximum deformation should be less than 2.5 mm. Among them, the minimization objective functions that contain the weight, the scale and the stiffness constraints are:

$$\min: \begin{cases} g_1 = \rho\left(B_1 H_1 L_1 + B_2 H_2 L_2\right) \\ g_2 = B_2 - B_1,\ g_2 \le 0 \\ g_3 \in \left[-30,\ 0\right] \\ g_3 = \dfrac{\tilde{P}}{\left[f\right]} - \dfrac{36E^2 B_2 H_1{}^2 H_2{}^3}{36 H_\eta H_2{}^3 \Delta L + E H_1{}^2 L_2{}^3} \end{cases} \tag{26}$$

$$s.t. \quad \begin{cases} 10\text{mm} \le B_1 \le 20\text{mm},\ 10\text{mm} \le B_2 \le 16\text{mm} \\ 3\text{mm} \le H_1 \le 21\text{mm},\ \ 3\text{mm} \le H_2 \le 15\text{mm} \end{cases}$$

The multi-objective optimization model given in Equation (26) can be solved through the NSGA-II algorithm [17], where the population number is set to 200 and the maximum evolution algebra is set to 200 times. The optimization design results are shown in Figure 5 and Table 1.

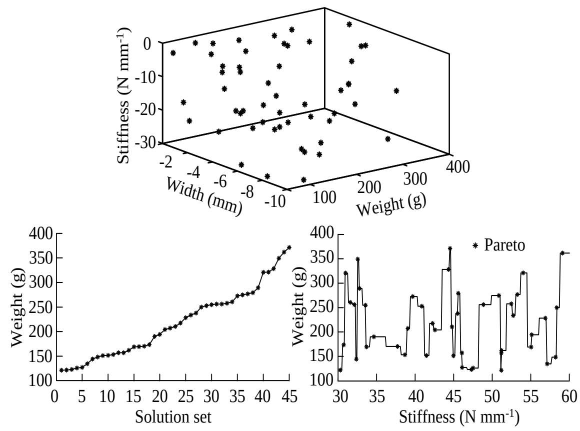

Figure 5. Active stiffness design results of double stepped cantilever beam

TABLE 1. Feasible solutions of the stiffness design

Variable	Pareto-1	Pareto-2	Pareto-3	Pareto-4
B_1 / mm	14.5117	16.6063	15.1705	15.8131
B_2 / mm	13.1158	11.6706	13.7044	12.1791
H_1 / mm	5.4649	8.7993	10.9754	10.3794
H_2 / mm	6.7842	6.3507	5.8456	7.4089
Weight (g)	121.7175	169.2641	190.2119	194.3999
Scale (mm)	-1.3959	-4.9357	-1.4661	-3.6340
Stiffness (N mm^{-1})	30.2928	33.6758	34.6324	55.1330

It should be noted that the Pareto front shown in Figure 5 are in the scale constraint space and the stiffness constraint space, the rest of the non-dominated solutions beyond the limitation range are not listed. The feasible parameters are summarized in Table 1. The optimal selection results by using diversity criteria method [18], of which pareto-1 can be rounded up and the stiffness matching design parameters can be expressed as follows:

$$\begin{aligned} &B_1 = 14.5 \text{ mm},\ B_2 = 14 \text{ mm},\ H_1 = 6 \text{ mm} \\ &H_2 = 6.5 \text{ mm},\ L_1 = 108 \text{ mm},\ L_2 = 78 \text{ mm} \\ &W = 129.5 \text{ g},\ \left[K\right] = 30.52 \text{ N mm}^{-1} \end{aligned} \tag{27}$$

The Pareto solution set is shown in Figure 5; that indicates that based on the proposed design method, the number of the non-dominant individuals does not have a coincident trend. For the constraints beyond the limitation range, the dominant individuals could reduce and control them within the allowed band. For the allowable constraints, the dominant individuals could make those close to the limitation values. Different stiffness matching results could correspond to the same weight constraint, and different weight distributions may receive the same stiffness constraint of the stepped cantilever structure. Moreover, the diversity screening result of Equation (27) comes from engineering application requirements, while the rounding result closest to the design goal is $B_1 = 14.5$ mm, $B_2 = 13.2$ mm, $H_1 = 5.5$ mm, $H_2 = 6.8$ mm, $W = 122.6$ g, $[K] = 30.27$ N mm^{-1}, but those parameters are not meet the ergonomics requirements.

4. 2. Bench Test Verification Through the stiffness design parameters given in Equation (27), the finite element model and its bench test are constructed respectively. As shown in Figure 6, the materials are set to structural steel, and the boundary conditions are approximate between the verification experiments.

After processing the transient structural analysis results and bench test results with the linear approximation method [11], the comparison verification of the structural stiffness of double stepped beam are shown in Figure 7 and Table 2. For the comparison subjects in Table 2, the stiffness index is consistent with the above mentioned optimization model, the match stiffness is obtained by substituting the round parameters into the established models, the FEM stiffness is determined by fitting the finite element results, and the test stiffness is determined by fitting the test results.

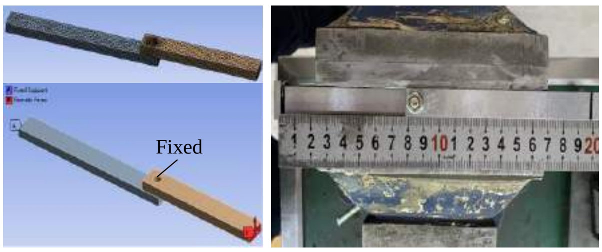

Figure 6. Finite element model and bench test of double stepped cantilever beam

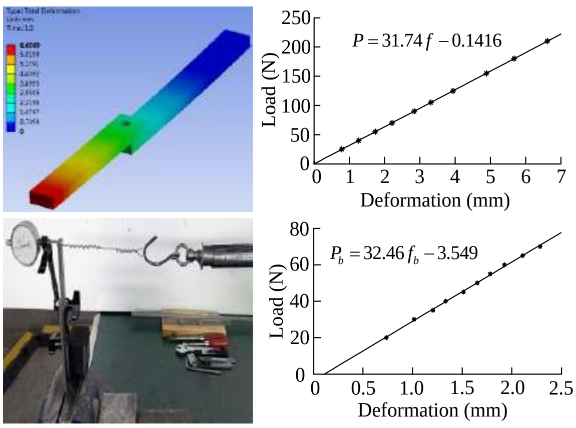

Figure 7. Structural stiffness test of double stepped beam

TABLE 2. Stiffness comparison verification of double stepped cantilever beam

Types	Index	Match	FEM	Test
Value (N mm^{-1})	30	30.52	31.74	32.46
Error (%)	--	+1.73%	+5.80%	+8.20%

Moreover, the stiffness index is used to derive the relative errors.

It is known that when the structural stiffness index is clear to the double stepped beam, its design parameters can be obtained through integrating the active stiffness design and engineering experience, which can ensure that the relative error between the match stiffness and the stiffness index is less than 2%. The relative error of the FEM stiffness is less than 6%, which indicates that the active design parameters are easier to meet the stiffness index. The relative error of the test stiffness is less than 9%, which shows that both the stiffness match models and the active design flowchart are practicable. Meanwhile, the match stiffness is less than the FEM stiffness and the test stiffness, which shows that the established models could meet the stiffness design requirements at one time, the safety factor is greater than 1, which is helpful to improve the reliability of stiffness design.

4. 3. Discussion and Application It can be concluded that the active stiffness optimization design performance of cantilever structure can not entirely consistent with the actual stiffness characteristics when the active design parameters applied to the engineering situation, the reasons are as follows.

(1) The bending modeling assumptions are derived from the simple-beam framework, and the influence of shear deformation is not taken into account. In general, the increase of the slender ratio would reduce the shear factor of beam, thus decreasing its influence on the whole deflection. But for the short beam, the cross section of beam can not keep as plane during the motion process, and the influence of the shear factor may be gradually increasing with the rise of the order of the deflection equations. At the same time, the action area of external force would not completely in the middle surface of the stepped structure, and then the cantilever structure produces torsion, which affects the accuracy of the match models.

(2) When the modified concentrated loads method is used to determine the contact forces of the combined areas, the assumptions are that the adjacent beams only contact at the end part, and the combined areas have the same deflection during the motion process. On the one hand, it is difficult to meet the full contact conditions in the actual application situation, which will lead to the smaller equivalent structural stiffness. On the other hand,

the cantilever joint could also be separated when the external load is large enough. It would cause the cantilever beam systems to gradually degenerate into complete sliding motion, which affects the calculation accuracy of the match models.

To quantitatively analyze the error range and the confidence boundary of stiffness match model, the numerical simulations are adopt to figure out the influence of the slender ratio and the beam' steps, and the relative finite element simulations are conducted. The comparison results are shown in Figure 8. Besides, the width and height of each section is 12×6 mm, the elastic modulus is $2.0E{+}05$ MPa, and the range of the slender ratio is set to (5, 20), the number of the steps is set to (3, 5).

It can be known that for the same slender ratio, the increase of the number of steps would reduce its equivalent structure stiffness, but if the slender ratio is large enough, the reduction trend is not obvious, and this situation is also indirectly verified in Figure 3. The verified stiffness based on the finite element simulations are larger than the match stiffness based on the proposed models, and the relative error ranges are $E_{n=3} \in [5\%, 8\%]$, $E_{n=4} \in [6\%, 11\%]$ and $E_{n=5} \in [7\%, 15\%]$ respectively. Also, it can be inferred that the maximum error with the bench test is no more than 15% through analyzing the test results of double stepped beam. The error results shown in Figure 8 are arranged in descending order, where dose not have a consistent one-to-one match between each relative error and each slender ratio.

Furthermore, it can be drawn that when carrying out the active stiffness optimization design of multiple stepped cantilever beam, the redundancy coefficient that belongs to $\sigma \in [1.05, 1.15]$ should be added to the stiffness match models, which could avoid the actual stiffness performances exceeding the design requirements too much.

As shown in Figure 9 and Table 3, the bench test of three stepped cantilever beam sample is conducted to verify the reliability of redundancy coefficient. It can be found that when the coefficient is set to 1.05, the relative error between the match stiffness and the FEM stiffness

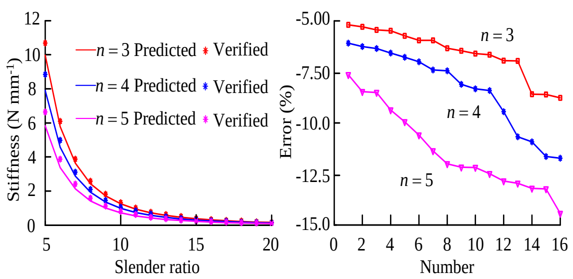

Figure 8. Multifactor analysis of structural stiffness error

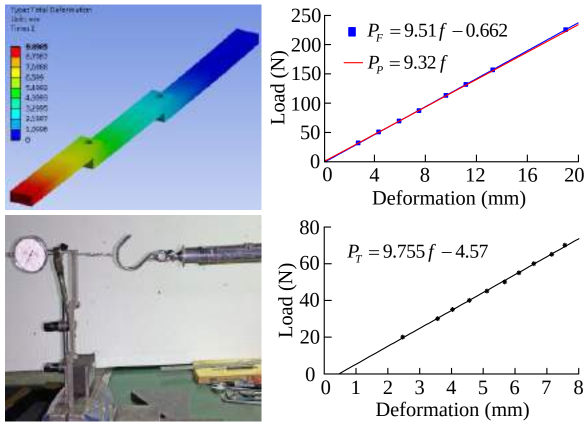

Figure 9. Bench test of three stepped cantilever beam

TABLE 3. Stiffness verification of three stepped beam

Types	Match	FEM	Test
Value (N mm^{-1})	9.32	9.51	9.755
Error (%)	--	+2.04%	+4.67%

can reduce to 2%, the relative error between the test stiffness and the match stiffness can reduce to 5%, which means that the stiffness redundancy can be improved effectively, both the accuracy of the established stiffness models and the feasibility of the presented active stiffness design flowchart are able to achieve the stiffness design of multiple stepped cantilever beam preferably. As the cantilever structure with more than 6 steps (except the stepped shaft structure) does not have engineering practical value, its stiffness change law will not be shown in detail here.

Finally, taking the test results of the double stepped beam and the three stepped beam as the object, and the Iwan model that given in literature [13] is used to process the raw data and generate the linear term of the stiffness coefficient, the comparison results are obtained and shown in Table 4.

It can be seen that under the unified test sample, the Iwan stiffness coefficient is less that the test stiffness, but also greater than the match stiffness. When the redundancy coefficient is not added to the double stepped beam, the relative error between the match stiffness and the Iwan stiffness coefficient is 5.3%, while the relative error reduces to 3.4% when taking in account the redundancy coefficient for the three stepped beam.

TABLE 4. Comparison results of different stiffness design methods

Types	Match	Test [11]	Iwan [13]
Double stepped beam	30.52	32.46	32.14
Three stepped beam	9.32	9.76	9.64

Moreover, the average error between the test stiffness and the Iwan stiffness coefficient is about 1%, which shows that the established models could reduce the demand for the physical model test system and retain high stiffness match accuracy.

3. CONCLUSIONS

This paper provided a structural stiffness matching modeling and active design approach for multiple stepped cantilever beam, and the validity was verified through simulations and bench test.

The stiffness match models were constructed according to the motion and deformation of multiple stepped cantilever beam, which included the analytical model of double stepped beam and recursive model of multiple stepped beam. Meanwhile, the qualitative stiffness influence coefficient of different scale and mechanical parameters were figured out through the sensitivity analysis. Through the stiffness requirements conversion, both the active stiffness optimization design flowchart and its implementation modes are presented for stiffness design of multiple stepped beam.

The simulations and bench test results showed that for the multiple stepped beam with rectangle section, the stiffness influence coefficient are arranged from high to low in terms of height, length, width and elastic modulus. Based on the same active stiffness design parameters, the FEM results are larger than the match results, the stiffness index are easier to achieve during the active stiffness design process. The relative error between the test stiffness and the stiffness index is less than 9%, and the redundancy coefficient that belongs to (1.05, 1.15) can be adopt to avoid the actual stiffness exceeding design requirements overmuch.

The overall results indicated that the proposed method is effectiveness and it is useful to reduce the redundant stiffness and increase the insufficient stiffness of the multiple stepped cantilever beam.

4. ACKNOWLEDGMENT

This research did not receive any specific grant from funding agencies in the public, commercial, or not-for-profit sectors.

5. REFERENCES

1. Righettini, P. and Strada, R., "Driving Technologies for the Design of Additive Manufacturing Systems" ***HighTech and Innovation Journal***, Vol. 2, No. 1, (2021), 20-28. DOI: 10.28991/HIJ-2021-02-01-03.
2. Strömberg, L. J., "Battery Pot Plants with Magnets and Adjacent Balloon as Substitutes for Light" ***Journal of Human, Earth, and Future***, Vol. 2, No. 2, (2021), 136-139. DOI: 10.28991/HEF-2021-02-02-05.
3. Xie, J. R., Zhou, C. Y., Cheng, Y. and Lv, Z. R., " A New Method for Solving Free Vibration of Cantilever Beam with Multiple Steps and Its Experimental Validation" ***Earthquake Resistant Engineering and Retrofitting***, Vol. 34, No. 4, (2012), 52-60. DOI: CNKI:SUN:GCKZ.0.2012-04-010.
4. Parate, B. A., "Propellant Actuated Device for Parachute Deployment during Seat Ejection for an Aircraft Application" ***HighTech and Innovation Journal***, Vol. 1, No. 3, (2020), 112-120. DOI: 10.28991/HIJ-2020-01-03-03.
5. Bhat J. A., "Improved Strength and Stiffness Characteristics of Cross-laminated Poplar Timber Columns" ***International Journal of Engineering, Transactions A: Basics***, Vol. 34, No. 4, (2021), 803-810. DOI: 10.5829/ije.2021.34.04a.06.
6. Li, X. Y., Wan, Z. Q., Wang, X. Z. and Yang, C.,"Aeroelastic Optimization Design of the Global Stiffness for a Joined Wing Aircraft" ***Applied Sciences***, Vol. 11, (2021), 11800. DOI: 10.3390/app112411800.
7. Ke, J., Shi, W. K., Chen, Z. Y, Gao, B., Yuan, K. and Zhou, G., "Matching Design Method for Stiffness of Composite Auxiliary Spring" ***Acta Materiae Compositae Sinica***, Vol. 33, No. 5, (2016), 1119-1124. DOI:10.13801/ j.cnki.fhclxb.20151225.003.
8. Shi, Y. G., Zhao, X. Y., Zhang, H. J., Nie, Y. X. and Zhang, D. W., "A New Top-Down Design Method for the Stiffness of Precision Machine Tools" ***The International Journal of Advanced Manufacturing Technology***, Vol.83, (2016), 1887-1904. DOI: 10.1007/s00170-015-7705-y.
9. Saindane, U. V., Soni, S. and Menghani, J. V., "Dry Sliding Behavior of Carbon-based Brake Pad Materials" ***International Journal of Engineering, Transactions B: Applications***, Vol. 34, No. 11, (2021), 2517-2524. DOI: 10.5829/IJE.2021.34.11B.14.
10. Saindane, U. V., Soni, S. and Menghani, J. V., "Friction and Wear Performance of Brake Pad and Optimization of Manufacturing Parameters using Grey Relational Analysis" ***International Journal of Engineering, Transactions C : Aspects***, Vol. 35, No. 3, (2022), 552-559. DOI: 10.5829/IJE.2022.35.03C.07.
11. Wang, X.C., Finite element method, Beijing: Tsinghua University Press, 2003.
12. Ke, J., Wu, Z. Y., Liu, Y. S., Xiang, Z. and Hu, X. D., "Design Method, Performance Investigation and Manufacturing Process of Composite Helical Springs: A Review" ***Composite Structures***, Vol. 252, (2020), 112747. DOI: 10.1016/ j.compstruct.2020.112747.
13. Ahmadian, H. and Jalali, H., "Generic Element Formulation for Modelling Bolted Lap Joints" ***Mechanical Systems and Signal Processing***, Vol. 21, No. 5, (2007), 2318-2334. DOI: 10.1016/j.ymssp.2006.10.006
14. Lee, J. S., Ha, M. Y. and Min, J. K., "A Finite-Volume Based Topology Optimization Procedure for an Aero-thermal System with a Simplified Sensitivity Analysis Method" ***International Journal of Heat and Mass Transfer***, Vol. 163, (2020), 120524. DOI: 10.1016/j.ijheatmasstransfer.2020.120524.
15. Yuan, N., He, J. W. and Zhao, J., "Research on the Design for Structure Stiffness Center Line Using Method of Active Stiffness" ***Aircraft Design***, Vol. 34, (2014), 23-27. DOI: CNKI:SUN:FJSJ.0.2014-06-005.
16. Mohammadi, S. and Babagoli, M., "A Hybrid Modified Grasshopper Optimization Algorithm and Genetic Algorithm to Detect and Prevent DDoS Attacks" ***International Journal of Engineering, Transactions A: Basics***, Vol. 34, No. 4, (2021), 811-824. DOI: 10.5829/ije.2021.34.04a.07.
17. Deb, K., Pratap, A., Agarwal, S. and Meyarivan, T., "A Fast and Elitist Multiobjective Genetic Algorithm: NSGA-II" ***IEEE Transactions on Evolutionary Computation***, Vol. 6, No. 2, (2002), 182-197. DOI:10.1109/4235.996017.

18. Mohsin, M. S., Alwash, N. A. and Kadhum M. M., "Comparative Study on Structural Behavior of Reinforced Concrete Straight Beam and Beams with out Plane Parts" ***International Journal of Engineering, Transactions A: Basics***, Vol. 34, No. 10, (2021), 2280-2293. DOI: 10.5829/ije.2021.34.10a.09.

Persian Abstract

چکیده

با هدف این مشکل که به دلیل رابطه نقشه‌برداری فازی برای سختی ساختاری تیرهای چند پله‌ای کنسول، دستیابی به طراحی بهینه دشوار است. یک مدل سازی تطبیق سختی و رویکرد طراحی سختی فعال پیشنهاد شده است. ابتدا، با استخراج شرایط هماهنگی پیوسته و عبارات برون یابی بار اتصال کنسول، مدل تحلیلی سختی و مدل بازگشتی برای قطعات تیرهای چندگانه کنسول ایجاد شد و ضریب تأثیر سختی آن پارامترهای ترکیب با تجزیه و تحلیل حساسیت به دست آمد. سپس، فرآیند طراحی بهینه‌سازی سختی فعال با توجه به سطح طراحی سختی تیر کنسول پلکانی ساخته شد و این روش‌های اجرایی به وضوح مشخص شدند. در نهایت، مقایسه و تایید طراحی سختی تیر کنسول پلکانی از طریق شبیه‌سازی عددی، تحلیل اجزای محدود و تست رومیزی انجام شد. نتایج به‌دست‌آمده نشان داد که مدل‌های ایجاد شده و روش طراحی سختی فعال معقول و مؤثر هستند، پارامترهای مطابقت سختی برای برآوردن الزامات شاخص سختی آسان هستند و ضریب ایمنی بیشتر از ۱ است. زمانی که تعداد مراحل بیشتر از ۵ نباشد، خطای نسبی بین سختی مطابقت و سختی تست کمتر از ۱۵ درصد است که با افزودن ضریب افزونگی (۱.۰۵، ۱.۱۵) می‌توان به کمتر از ۵ درصد کاهش داد.

IJE TRANSACTIONS A: Basics Vol. 35, No. 05, (July 2022) 1237-1245

International Journal of Engineering

Journal Homepage: www.ije.ir

Experimental Study on Performance of Ductile and Non-ductile Reinforced Concrete Exterior Beam-column Joint

S. Ravikumar*, S. Kothandaraman

Civil Engineering Department, Puducherry Technological University, Puducherry, India

P A P E R I N F O

Paper history:
Received 19 February 2022
Received in revised form 11 March 2022
Accepted 24 March 2022

Keywords:
Beam-Column Joint
Displacement Ductility
Hysteresis Curve
Energy Dissipation
Reinforced Concrete

A B S T R A C T

The purpose of this study is to evaluate the behaviour and the performance of reinforced concrete (RC) exterior Beam-Column Joints (BCJ) experimentally under reverse quasi-static cycle displacement test conducted for ductile and non-ductile detailed reinforcement. Two columns (one upper and one lower) and one beam were used to construct the specimen; the beam end is free, while the other ends are fixed. These specimens were subjected to reverse cyclic quasi-static stress till failure. At each cycle, the hysteresis curve, cracking loads, ultimate loads, deflection of the loaded at the free end of the beam, crack patterns, and failure mechanisms of BCJ were recorded and studied. Additionally, all specimens' energy dissipation and stiffness deterioration were addressed. The experimental results reveal that the ductile joint (DJ) performance is more satisfactory in all the parameters than the non-ductile joint (NDJ). The ultimate load and energy dissipation of DJ is approximately 20% higher than the NDJ. However, expected beam failure occurred in the ductile joint, and the non-ductile joint underwent undesirable joint failure.

doi: *10.5829/ije.2022.35.07a.03*

NOMENCLATURE

L_d	development length in tension	σ_s	Stress in beam bar
f_y	yield stress of bar	τ_{bd}	Design bond stress
LVDT	Linear Variable Differential Transduser	δ_1, δ_2	Elongation/shortening of beam in tension and Compression
μ	Displacement ductility	$\Delta_{u,y}$	Ultimate and Yield displacement
θ	Joint rotation	d	Vertical distance between the transducers
D_n	Damage Index	$K_{i,n}$	Initial Stiffness and nth cycle stiffness

1. INTRODUCTION

Beam-Column Joints (BCJ) are considered a critical element of reinforced concrete (RC) structures, especially in seismic regions. Because of its region transfer the beam load to column member, complex behaviour under seismic force, complicated in construction due to dense reinforcement. The numerous reconnaissance survey on past earthquakes revealed that many RC framed structures were failure because of BCJ failure. During earthquakes, the BCJ undergoes high shear stress through seismic forces, which cause cyclic action. Kassem et al. [1, 2] were discussed all the vulnerabilities of buildings that cause the failure of the structures in earthquake zones. The lateral forces induced the shear stress cause the diagonal cracks at the joints, resulting in joint shear failure. Initially, the beam reinforcement bars yield under earthquake forces, then bars in joint region yields and bond-slip cause the deterioration of joint strength. Joint failure is undesirable as the joint portion is considered part of the column; the column failures cause the global failure of structures. Many experimental and numerical studies were carried out to understand beam-column joint behaviour under seismic forces and influencing parameters of joint strength [3]. Hanson and Connor [4] are pioneers in

*Corresponding Author Institutional Email: srktce@pec.edu (S. Ravikumar)

Please cite this article as: S. Ravikumar, S. Kothandaraman, Experimental Study on Performance of Ductile and Non-ductile Reinforced Concrete Exterior Beam-column Joint, ***International Journal of Engineering, Transactions A: Basics***, Vol. 35, No. 07, (2022) 1237-1245

understanding the behaviour of beam-column joints. The outcome of the research experiment was defined as the horizontal joint shear. Park and Paulay [5, 6] described the joint shear resisting by two mechanisms of strut and truss mechanism. First, the strut mechanism contributed by the diagonal portion of concrete in joint to resist the joint shear; second, the truss mechanism contributed by vertical and horizontal reinforcement in joint through the bond between concrete and reinforcement. Kim and LaFave [7] proposed using these mechanisms to predict the joint shear strength. Some other researchers experimentally investigated beam-column joint behaviour [8, 9]. Based on these research outcomes international code of practice was prepared for design of beam column joints [10]. Kusuhara and Shiohara [11] loaded ten half-scale reinforced concrete beam-column joint sub-assemblages to investigate using statically cyclic loading to acquire essential data, such as stress in yielding bars and joint deformation. It was discovered that the specimen with transverse beams enhanced its narrative shear capacity when the joint was severely damaged.

Additionally, if the joints were severely damaged, the bond actions of beam bars travelling through them remained lower than the bond strength. Megget and Brooke [12] conducted the joint under cyclic loading to simulate seismic force with various anchorage reinforcement detailing standard 90-degree hook and U bar. Inadequate anchoring length of beam bars at external joints resulted in decreased story shear capacity, column reinforcement yielding, and severe joint damage. In all the above-mentioned experimental studies, the performance of various joints was measured in terms of ultimate strength, ductility factor, energy dissipation, stiffness degradation, and joint rotation.

2. MATERIALS

The specimens were cast in M30 grade concrete. Concrete was made using Ordinary Portland Cement (OPC) 43-grade confirming to IS 8112-2013 [13], M-sand, and crushed stone aggregate with a maximum size of 12 mm. Longitudinal reinforcement was provided by reinforcement steel of grade Fe 500 IS 1786-2008 [14], while transverse reinforcement was provided by plain mild steel bars of grade Fe 250 IS 432 Part1-1982 [15]. Potable water was used in the manufacture and curing of concrete. Manual mixing was done in the laboratory. The concrete design mix of materials by weight for a cubic meter of concrete is given in Table 1. Chemical admixture of superplasticizer of 2.5 liter per cubic meter of concrete used to reduce water content in concrete as per design mix. The average compressive strength of a cube of 150x 150 x 150 mm results in an equal 36MPa after 28days of curing.

TABLE 1. Concrete Design Mix per Cubic meter

Material	Cement	Fine Aggregates	Coarse Aggregates	Water
Weight (kg/m^3)	400	710	1170	470

3. DESCRIPTION OF TEST SPECIMENS

Two sets of exterior beam-column joint (BCJ) subassemblies were prepared for testing. First set specimens were designed using the following strong-column weak-beam concept. Murty et al. [16] with ductile detailing as per IS 13920 [17] with full anchorage length and additional close spacing transverse reinforcement. Another set of specimens resembled current construction practice with the limited anchorage length within the depth of beam in insufficient anchorage length and less transverse reinforcement. Beams and columns were designed based on procedures in IS: 456-2000 [18]. The reinforcement details are illustrated in Figure1 and are also given in Table 2.

3. 1. Specimen Designation

Ductile Joint - This category specimen is designed based on the special moment-resisting frame as a ductile structure for the special ductile joint [14, 15], as shown in Figure 1. Therefore, this category specimen is designed for ductile behaviour, designated as Ductile Joint (DJ). The anchorage length is provided with full required development length in *tension* plus 10 times of bar diameter, i.e. **anchorage length** $= \mathbf{L_d + 10\emptyset}$**.**

Non-ductile Joint- This category of test specimen resembles current construction practice for joint details with limited anchorage length within the available beam depth, as shown in details. In addition, this category specimen resembles the non-ductile behaviour, designated as Non-Ductile Joint (NDJ). Both the top and bottom bars of the beam had their anchoring lengths extended beyond the inner face of the column, with a 90° bending towards the joint core. Therefore, the following equation is used to calculate the development length under IS: 13920-1993 [19]:

$$L_d = \frac{\emptyset \sigma_s}{4\,\tau_{bd}} \tag{1}$$

where Ld, development length in tension, Ø-diameter of the bar, σs -stress in the bar (equals to 0.87 times of fy yield stress of bar), τbd- bond stress of plain bars in tension depending on the concrete grade, as given in IS 456: 2000 [18].

All control specimens were cast monolithically at one go in a prepared waterproof coated plywood mould for this research. Firstly, the test specimens were demoulded after 24 hours of casting. Then, the specimen was cured for about 28 days. Curing was accomplished by covering

TABLE 2. Reinforcement details

Specimen Name	Column details		Beam details		Anchorage length
	Longitudinal	Transverse	Longitudinal	Transverse	
Ductile Joint (DJ)	4 # 10mm	4 mm dia @ 30 & 60mm c/c	2#10mm @ top & bottom	4 mm dia @ 37.5 & 75mm c/c	(Ld+10ϕ =) 553mm
Non-Ductile Joint (NDJ)		6 mm dia @ 120mm c/c		6mm @ 100mm c/c	Anchored till the depth of the beam.

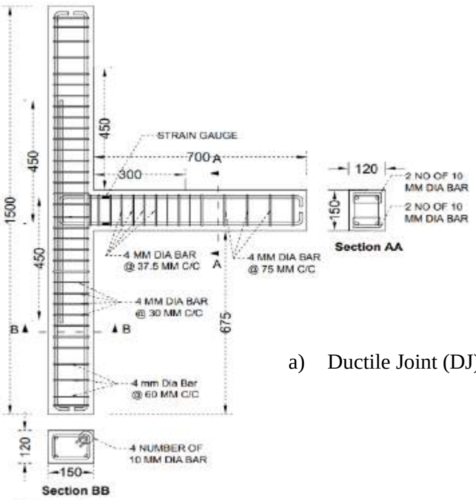

a) Ductile Joint (DJ)

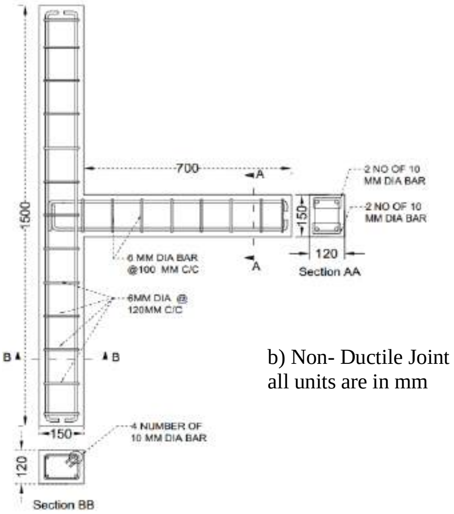

b) Non- Ductile Joint (NDJ), all units are in mm

Figure 1. Test Specimen Reinforcement Details

the specimens daily with moist gunny bags at regular intervals, as shown in Figure 2.

4. TEST SETUP AND PROCEDURE

The reverse cyclic test schematic representation of the test setup is shown in Figure 3. Servo-controlled non-hydraulic actuator made exclusive for this project first of

(a) Prepared Plywood Mould for casting

(b) Prepared specimen during casting and curing

Figure 2. Preparation of mould and specimen

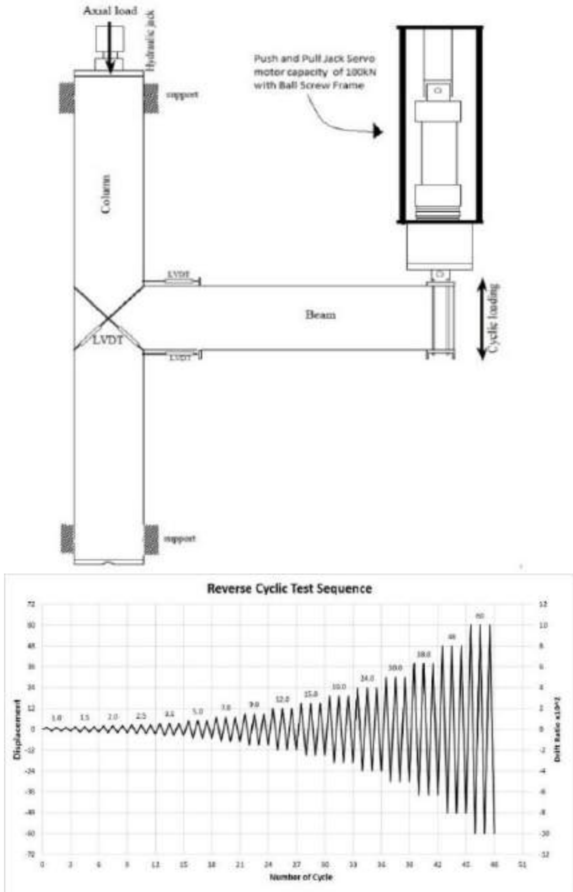

Figure 3. Testing setup and loading sequence

its kind of capacity 100 kN was used for applying cyclic load on the specimen. The peak displacement capacity of the instrument used was ±60 mm. Columns were placed in a vertical position supported on the roller, and the beam was placed in a horizontal position fixed with the actuator. In the present investigation, 10 % capacity of column capacity was applied as the axial load on the column head before starting the test by hydraulic jack of capacity of 500kN to represent the gravity load. The complete setup of the experimental setup is illustrated in Error! Reference source not found..

4. 1. Reverse Cyclic Loading Test Sequence The Push and Pull jack capacity of the 100kN actuator were placed at the beam end to apply the reversible cyclic loading. The main LVDT and loadcell were mounted with an actuator with the reverse cyclic loading history were applied in displacement in the current study, as specified in Figure 3. The reverse cyclic test was conducted in the increment displacements from 1mm to 60mm (0.15 to 9.52 % drift ratio respectively) in 16 number displacements, as shown in Figure 3. Each displacement runs three times a cycle; therefore, 48 displacement cycles are applied to each specimen. The drift ratio is between displacement at the beam end and beam length. The increment of drift ratio is maintained between 1.25 to 1.5.

The downward displacement direction and force (push) have positive signs. On the other hand, the upward displacement direction and force (pull) has negative sign assigned to the loadcell value. All sensors (LVDT and load cell) were linked to a datalogger throughout the test to capture continuous data at regular intervals and store it in the Data Acquisition (DAQ) system. Once the concrete cover began to spall, the four LVDT sensors were removed. However, the data logger is configured to record data continuously without interfering with the primary instrumentation (main LVDT and loadcell) throughout loading and until the last cycle. After that, the test will be terminated either complete test cycle or till the joint collapse, whichever occurs early.

5. EXPERIMENTAL RESULTS AND DISCUSSION

The performance of beam-column joint specimens was evaluated with the following parameters: Hysteresis curve, Ultimate load, Envelope curve, Stiffness degradation, Displacement ductility, Energy dissipation, Damage index, and Crack pattern.

5. 1. Load Deformation Behaviour Hysteresis curve is a graph plotted between the load and displacement at the beam end, and all test specimens were presented in Figure 5 and 6. Additionally, the envelope curves are constructed by connecting the peak load locations of each displacement cycle. The hysteresis curve is used to describe the overall behaviour of elastic and plastic areas. The stable load-displacement curves for ductile and non-ductile joint specimens in the elastic area were obtained during the first loading stage, i.e. at a lower drift level. DJ specimens with stable hysteresis loops illustrate the strength of the link between reinforcement and joint concrete. Pinching began at the very early cyclic loading stage of the NDJ specimens in the downward direction.

The ultimate load of DJ specimen in the positive direction, 13.1kN at the 12 mm displacement 1st cycle, in the negative direction, is 20.5kN at the displacement of 48 mm displacement 1st cycle. The ultimate load of NDJ specimen in the positive direction, 11.6 kN at the 7 mm displacement 1st cycle, in the negative direction, is 15.94 kN at the displacement of 30 mm displacement 1st cycle. The load-carrying capacity of DJ is 20 % higher than NDJ in the positive direction and 11 % higher in the

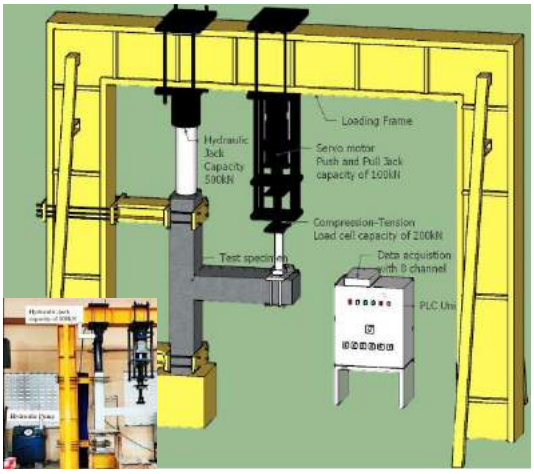

Figure 4. Illustrated the experimental setup

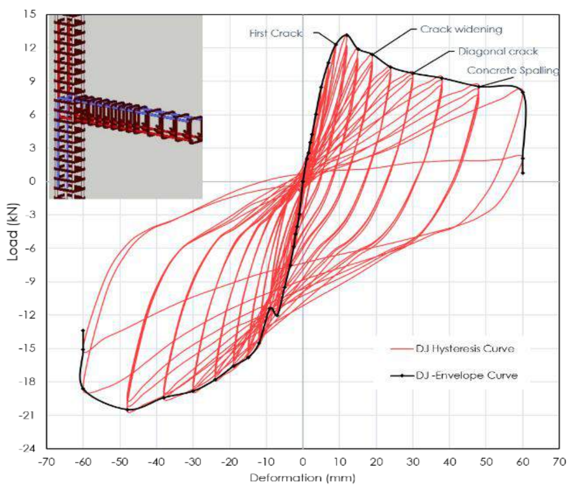

Figure 5. Ductile Joint (DJ) Hysteresis Curve

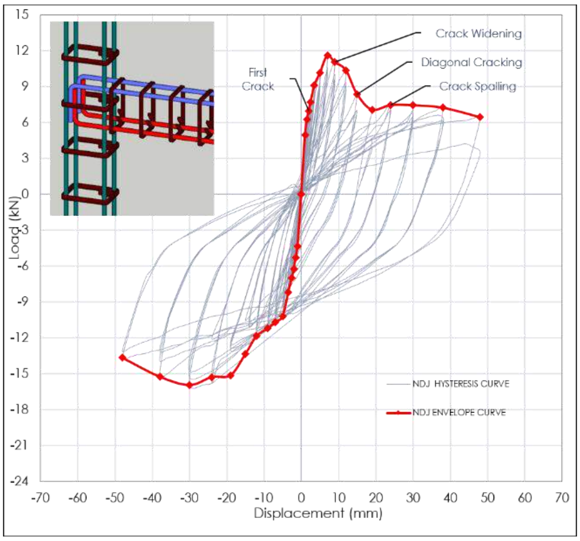

Figure 6. Non-Ductile Joint (DJ) Hysteresis Curve

Negative direction. The DJ has obtained an ultimate capacity of nearly 2% drift ratio, but NDJ obtained at a low drift ratio of 1.1% due to less transverse reinforcement and inadequate anchorage length at the joint.

Figures 5 and 6 show hysteresis behaviour; the DJ specimen has high strength and a fatter hysteresis curve than the NDJ specimen, representing the desirable ductile behaviour. On the other hand, the NDJ specimen has low and sudden significant strength reduction, which is undesirable behaviour of the joint.

5. 2. Crack Pattern and Mode of Failure In the DJ specimen, the first hairline crack occurs at the beam-column joint interface during the 9mm displacement cycle at the load of 12.3kN. Then, multiple hairline cracks occurred at the beam region. Next, the crack at the interface slowly starts widening at the displacement of 19 mm cycle of the load of 11.4kN. Then, the first diagonal cracks appeared in the joint region during the 30mm displacement cycle at the load 9.7kN. Finally, the concrete starts spalling during a 48mm displacement cycle at load 20.5kN. The crack pattern and propagation are presented in Figure 7. From the crack pattern of the DJ specimen, it started with longitudinal bar yielding, then slowly hairlines formed at the joint region, then the cracks at beam and interface widen the beam near joint region. The small concrete spalling started at a 38 mm displacement cycle, and significant concrete spalling occurred at a 60 mm displacement cycle. DJ specimen were cracked pattern increases to beam and beam hinge was developed. It shows that failure mode of DJ specimens beam failure (beam bar yielded before the shear failure at joint).

On the contrary, the NDJ specimen cracks appeared at an early displacement of 2.5 mm at the beam-column joint interface. After that, the beam-column interface crack widened, and concrete started the spalling at 19 mm displacement. For NDJ specimens after the first crack, diagonal cracks were developed as hairlines and slowly started widening with an increment of displacement. NDJ specimen concrete spalling started earlier at 24 mm, beam bars got pulled out of the joint, and bars were cut at 48 mm displacement cycle. So, reverse cycle tests were stopped at this stage. The detailed crack propagation of the first crack, crack widening, diagonal crack formation and concrete spalling out of specimens with respective displacements are shown in Figure 7, and loads are listed in Table 3.

Figure 7 clearly shows that cracks in the DJ specimen were slower than the NDJ specimen from the first crack to concrete spalling. This crack formation in ductile joints is delayed, and the crack widens than the NDJ specimen due to improvement of ductility factor.

5. 3. Displacement Ductility Ductility is defined as the structure's capacity to withstand considerable deformation without losing its significant strength. The structure's ductility helps diffuse the energy generated by

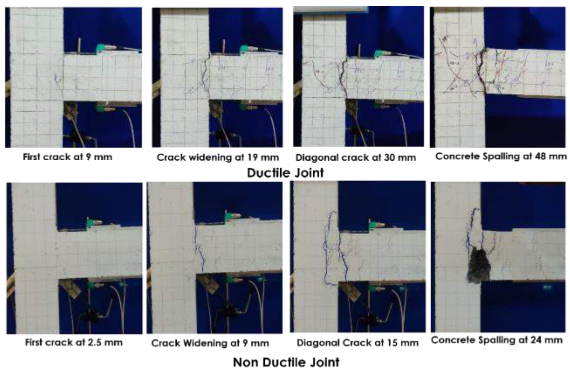

Figure 7. Crack Pattern of Specimen

TABLE 3. Crack Pattern load and displacement

Specimen	First Crack		Crack Widening		Diagonal Crack		Concrete Spalling	
	Δ (mm)	P (kN)	Δ (mm)	P (kN)	Δ (mm)	P (kN)	Δ (mm)	P (kN)
DJ	9	13.4	19	16.6	30	18.8	60	18.6
NDJ	2.5	6.97	9	11.05	15	13.05	24	15.27

an earthquake. The displacement ductility ratio is a standard way to assess the ductility of a structure. The ultimate displacement to yield displacement ratio is the displacement ductility ratio. The ultimate and yield displacement is identified from the hysteresis curve envelope. To evaluate ultimate and yield displacement, many methods were recommended by Park [20].

In this research, the ultimate displacement is found by the ultimate load with significant reduction after the peak load method. The ultimate displacement is defined as a slight reduction in maximum load by 80 % after the peak load (see Figure 8a). The yield displacement is identified by the reduced stiffness equivalent elasto-plastic yield method (see Figure 8b). First, the maximum load point is traced horizontally as a reference; then, a point is marked on the envelope with secant stiffness at 75% of the maximum load (Hu); then, a line is plotted from origin to pass through the respective point to the reference line, with that respective point displacement is yield displacement. The respective ultimate displacement, yield displacement and displacement ductility of the specimens are specified in Table 4.

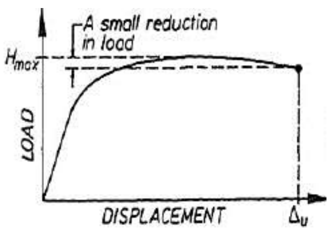

(a) Ultimate displacement

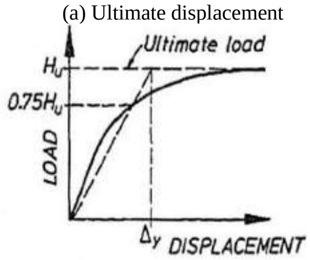

(b) Yield Displacement

Figure 8. a) Ultimate Displacement-Ultimate load Significant load capacity after peak load, b) Yield displacement- reduced stiffness equivalent Elasto-plastic yield [20]

TABLE 4. Displacement Ductility

Specimen Name	Ultimate displacement (Δ_u) mm		Yield Displacement (Δ_y) mm		Displacement Ductility Factor (μ)	
	+	-	+	−	+	−
DJ	23.6	60	8.2	18	2.87	3.33
NDJ	14	49	6	17	2.33	2.88

where, + ve means downward direction displacement, -ve upward direction displacement.

5. 4. Energy Dissipation The area encompassed by the load versus deflection graph (hysteresis curve) was used to calculate the energy dissipated during each cycle. The area included inside each cycle was determined as energy dissipation (kN-mm). The energy dissipation during the first cycle was expected to be about zero for all specimens. However, the energy dissipated throughout a cycle increased when the specimen was supplied with a more significant cyclic load. Figure 9 depicts the rate of increase in energy dissipated for all specimens at each cycle. For specimen DJ, increased energy dissipated at the test start was more significant than increased energy dissipated during the test. The maximum energy dissipated at the 48 mm displacement cycle and was reduced after concrete spalling out. The cumulative energy dissipation increased by 40% for the specimen DJ than the specimen NDJ. The experimental results indicate closed spaced stirrups inside the beam-column connection significantly improved energy dissipation.

5. 5. Stiffness Degradation The stiffness of the beam-column joint under cyclic load can be defined as it resists deformation due to an applied force. Usually, the joint stiffness reduces under cyclic/repeated loading [21]. Figure 10 presents the relationship between beam-column joint stiffness and cycle number for all specimens. The stiffness of beam-column joints under reverse cyclic load is calculated by dividing the peak load by its respective displacement in the experiment. The finding shows that the stiffness of the beam-column junction and the displacement cycle number is inversely related. The degree of damage determines the remaining stiffness. The rigidity of the beam-column joints rises as the fraction of the stirrup's joint increases. The testing results showed that the stirrups enhanced joint shear and load-carrying capacity with less restrained deformations [22]. The stiffness degradation NDJ occurred earlier due

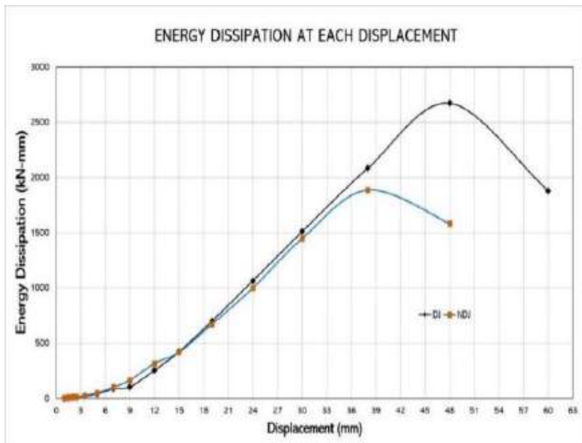

Figure 9. Energy dissipation of respective displacement

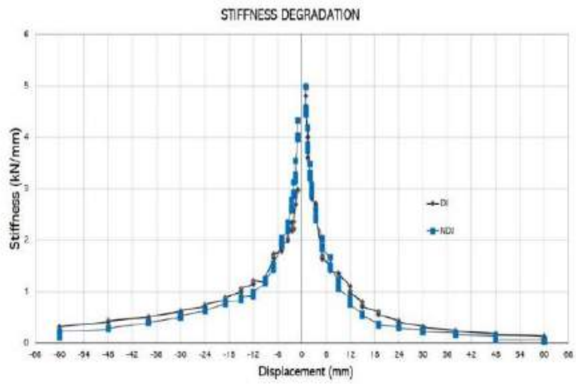

Figure 10. Stffness Degradation

to concrete contribution lost after early cracks, but for the DJ specimen, stiffness was slowly degraded due to its more anchorage length and stirrups at the joint.

5. 6. Damage Index The Damage Index, Dn is a parameter that defines the specimen that sustains the damage through the ratio of its stiffness at a specific cycle to its initial stiffness [23]. Effective confinement of column and beam reduce the damages of specimen [24]. The damage index is found by Equation (2).

$$D_n = 1 - \frac{k_n}{k_i} \tag{2}$$

where ki and kn are the initial stiffness and stiffness at the nth cycle of the specimen, respectively. Figure 11 shows that the NDJ specimen has a large damage index because that section loses the concrete contribution for part to joint stiffness after cracking. NDJ specimens ultimately failed at 48 mm displacement, and DJ did not completely collapse until the last displacement of 60mm.

5. 7. Beam Moment and Rotation Relationship The joint rotations were calculated at the distance of 100mm from the face of the column using the LVDT placed on top and bottom of the beam shown in Figure 12. This portion of the beam undergoes maximum moment and high stress during an increase in the displacement cycle. The joint rotation θ was calculated using the following equation.

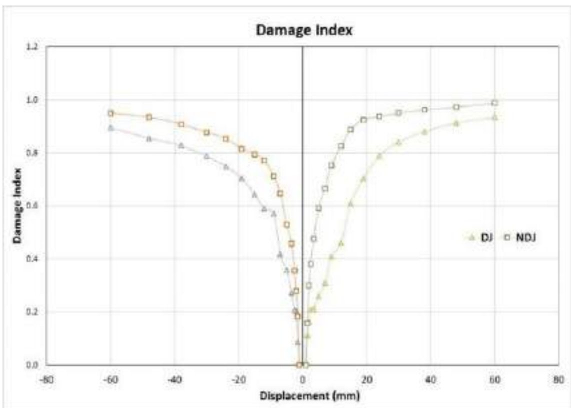

Figure 11. Damage Index

$$\theta = \frac{\delta_1 + \delta_2}{d} \tag{3}$$

where, δ_1 is the elongation on the tensile face of the beam, δ_2 is the shortening on the compressive face of the beam, and d is the vertical distance between the transducers (160 mm). The beam rotation angle at 100 mm from the column face, in rad, is plotted against the applied moment for the specimens.

Comparison the beam moment-rotation plots reveal that specimen NDJ (Figure 13) exhibited a much lower rotation before beam yielding (at comparable bending moments) than specimen NDJ for the 100 mm long beam segment from the column face. The decreased stiffness of DJ rebars, on the other hand, resulted in more significant rotations in the DJ-reinforced beam at comparable moments than in the steel-reinforced beam. However, because of the DJ specimen's mainly elastic behaviour, there were relatively few residual deformations in the beam [25]. Furthermore, despite many fractures, the level of damage in the beam for specimens DJ shows less spalling than the NDJ specimen beam.

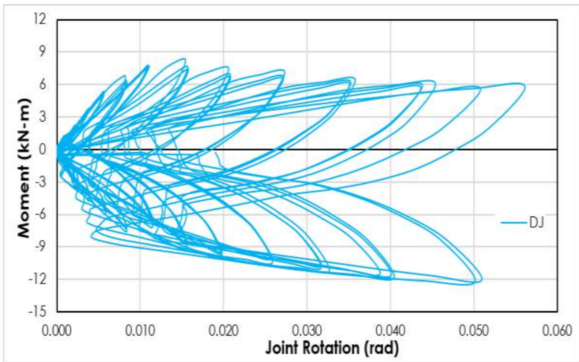

Figure 12. Beam moment Rotation of DJ specimen

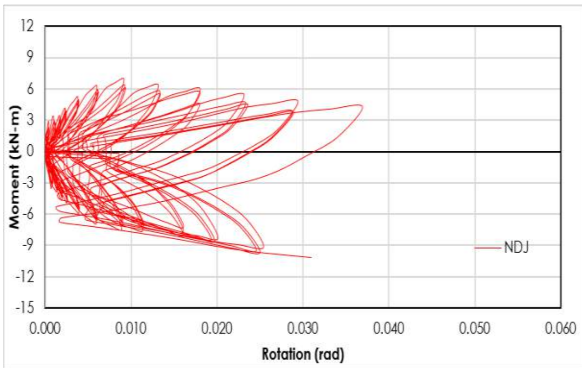

Figure 13. Beam moment Rotation of NDJ specimen

6. CONCLUSIONS

The experimental investigation on the performance of RC beam-column joints subjected reversed cyclic loading, as the simulation of seismic forces. The present experimental study included two exterior reinforced concrete beam-column joint specimens. The displacement cycle was applied at the free end of the beam. The specimens were put through a total of 48 cycles with 16 displacements at each cycle. This research aimed to find the effect of anchorage length of beam reinforcement and the effect of transverse reinforcement on joint performance improvement in terms of the hysteresis curve, envelope curve, crack patterns, mode of failure, and failure. The following findings may be taken from research conducted in this study.

- It was found that for DJ specimens with more stirrups in the joint as ductile detail, the first crack of the joint was delayed, but for NDJ specimens, cracks developed earlier than DJ specimens.
- It was noticed that the hysteresis curve of the DJ specimen was recorded till the last cycle of 60mm displacement without collapse, but NDJ specimens had collapsed at 48 mm displacement cycle.
- Due to insufficient anchorage length of beam bars and no proper anchorage system in the NDJ specimen, the beam bars got pulled out at the higher displacement cycle and caused the joint failure.
- The anchorage length and transverse reinforcement play a significant role in transferring the load and load-carrying capacity of the DJ specimen to 20 % higher than that of the NDJ specimen.
- Energy dissipation capacity is 40% higher for the DJ specimen than that of the NDJ specimen.
- Beam moment versus rotation of beam plots indicated that NDJ resists less moment than DJ specimen with the relative rotation.
- The beam moment versus joint rotation shows the precise formation of plastic hinges in beam for DJ specimen with high deformation, but NDJ specimen has formed failure mechanism of joint.
- This study reveals that closed spaced stirrups plays significant role in the ultimate load capacity and ductility of structure, so it is highly recommended to consider in the beam-column joint design.

7. ACKNOWLEDGEMENTS

The research was financially supported by the AICTE (All India Council for Technical Education) - RPS NDF Grant and Pondicherry Engineering College research funding. The authors gratefully acknowledge these supports.

8. REFERENCES

1. M. M. Kassem, F. M. Nazri, E. N. Farsangi, and B. Ozturk, "Improved Vulnerability Index Methodology to Quantify Seismic Risk and Loss Assessment in Reinforced Concrete Buildings," ***Journal of Earthquake Engineering.,*** **2021**.
2. M. M. Kassem, F. Mohamed Nazri, E. N. Farsangi, and B. Ozturk, "Development of a uniform seismic vulnerability index framework for reinforced concrete building typology," ***Jounral of. Build. Engineering***., vol. 47, 2022.
3. S. Ravikumar, S. Kothandaraman, Influencing Parameters of Exterior Reinforced Concrete Beam-Column Joint Shear Strength: A Depth Review of Recent Advances, ***International Journal of Engineering, Transactions B: Applications***, Vol. 35, No. 05, (2022) 931-942. doi: 10.5829/ije.2022.35.05b.09.
4. N. Hanson and H. Conner, "Seismic Resistance of Reinforced Concrete Beam-Column Joints," ***Jounral of Structural. Divison***., vol. 93, no. 5, pp. 533–560, 1967.
5. R. Park and T. Paulay, "Behaviour of reinforced concrete external beam-column joints under cyclic loading," in Proceedings Fifth World Conference on Earthquake Engineering, 1973, p. 10.
6. R. Park and T. Paulay, *Design Concrete Structures*. John Wiley & Sons, New York., 1975.
7. J. Kim and J. LaFave, "Probabilistic joint shear strength models for design of RC beam-column connections," ***ACI Structural jounral***, vol. 105, no. 6, pp. 770–780, 2008.
8. J. Yu and K. H. Tan, "Special detailing techniques to improve structural resistance against progressive collapse," ***Journal of Structural Engineering*** *(United States)*, vol. 140, no. 3, pp. 1–15, 2014.
9. S. Chidambaram and G. Thirugnanam, "Comparative Study on Behaviour of Reinforced Beam-Column Joints with Reference to Anchorage Detailing," ***Journal of Civil Engineering Research,*** vol. 2, no. 4, pp. 12–17, 2012.
10. S. Ravikumar and S. Kothandaraman, "Design of Reinforced Concrete Beam-Column Joint," ***Interantional. Journal of Engineering Trends and Technology***., vol. 70, no. 3, pp. 85–94, 2022. doi:10.14445/22315381/IJETT-V70I3P210
11. F. Kusuhara and H. Shiohara, "Tests of RC Beam-Column Joint with Variant Boundary Conditions and Irregular Details on Anchorage of Beam Bars," ***14th World Conference on Earthquake Engineering,*** pp. 1–8, 2008.
12. L. M. Megget and N. J. Brooke, "Beam-column joint tests with grade 500E reinforcing," no. ***NZSEE conference*** 41, 2004.
13. IS: 8112 – 1989, "Specification for 43 grade Ordinary Portland Cement," ***Bureau of Indian Standard (BIS),*** *Delhi*, p. 17, 2013.
14. IS 1786, "High Strength Deformed Steel Bars and Wires for Concretereinforcement— Specification," ***Bureau of Indian Standard (BIS)***, *New Delhi*, pp. 1–12, 2008.
15. IS 432, "Indian standard specification for mild steel and medium tensile steel bars and hard-drawn steel wire for concrete reinforcement," ***Bureau of Indian Standard (BIS),*** p. 9, 1982.
16. C. V. . Murty and V. V. M. Murty, C. V. R., Rupen, Goswami., A. R. Vijayanarayanan., *Some Concepts Earthquake Behaviour of Buildings*. ***GSDMA***, 2012.
17. IS:13920-2016, "Ductile Design and Detailing of Reinforced Concrete Structures Subjected to Seismic Forces — Code of Practice," ***Bureau of Indian Standard (BIS)***,. *New Delhi*, no. July, pp. 1–121, 2016.
18. IS 456-2000, "Plain and Reinforced Concrete," ***Bureau of Indian Standard (BIS)***. *Dehli*, pp. 1–114, 2000.
19. IS:13920, *Ductile Design and Detailing of Reinforced Concrete Structures Subjected to Seismic Forces*, no. July. ***Bureau of Indian***

Standard (BIS), 1993.

20. R. Park, "Ductility evaluation from laboratory and analytical testing," *Proceedings of* ***the 9th World Conference on Earthquake Engineering***, *2-9 August*. pp. 605–616, 1988.
21. N. Ganesan, P. V. Indira, and R. Abraham, "Steel fibre reinforced high performance concrete beam-column joints subjected to cyclic loading," ***ISET J. Earthq. Technol.***, vol. 44, no. 3–4, pp. 445–456, 2007.
22. C. Marthong, A. Dutta, and S. K. Deb, "Effect of Cyclic Loading Frequency on the Behavior of External RC Beam-Column Connections," ***Journal of Earthquake Engineering***., vol. 20, no. 7, pp. 1126–1147, 2016.
23. J. Lemaitre and R. Desmorat, *Engineering Damage Mechanics: Ductile, Creep, Fatigue and Brittle Failures*. ***Springer Science & Business Media***, 2006.
24. S. T. Nemati Aghamaleki, M. Naghipour, J. Vaseghi Amiri, M. Nematzadeh, Experimental Study on Compressive Behavior of Concrete-filled Double-skin Circular Tubes with Active Confinement, ***International Journal of Engineering***, ***Transactions A: Basics*** Vol. 35, No. 04, (2022) 819-829
25. T. K. and H. F. Sefatullah Halim, Susumu Takahashi, Toshikatsu Ichinose, Masaomi Teshigawara, "179-192 Amorn Pimanmas," ***Preeda Chaimahawa Journal of Advance Concrete Technology***, vol. 12, no. 4, pp. 146–157, 2014.

Persian Abstract

چکیده

هدف از این مطالعه ارزیابی رفتار و عملکرد اتصالات تیر-ستون خارجی (BCJ)بتن مسلح (RC)تحت آزمایش جابجایی چرخه شبه استاتیک معکوس انجام شده برای آرماتورهای دقیق شکل‌پذیر و غیر شکل‌پذیر است. برای ساخت نمونه از دو ستون (یکی بالا و دیگری پایین) و یک تیر استفاده شد. انتهای تیر آزاد است، در حالی که انتهای دیگر ثابت است. این نمونه ها تا زمان شکست تحت تنش شبه استاتیکی چرخه ای معکوس قرار گرفتند. در هر چرخه، منحنی پسماند، بارهای ترک، بارهای نهایی، انحراف بارگذاری شده در انتهای آزاد تیر، الگوهای ترک و مکانیسم‌های شکست BCJ ثبت و مورد مطالعه قرار گرفتند. علاوه بر این، تمام اتلاف انرژی و زوال سفتی نمونه ها مورد بررسی قرار گرفت. نتایج تجربی نشان می‌دهد که عملکرد اتصال شکل‌پذیر (DJ)در تمام پارامترها نسبت به اتصال غیر شکل‌پذیر (NDJ)رضایت‌بخش‌تر است. بار نهایی و اتلاف انرژی DJ تقریباً ۲۰٪ بیشتر از NDJ است. با این حال، شکست تیر مورد انتظار در اتصال شکل‌پذیر رخ داد و اتصال غیر شکل‌پذیر دچار شکست مفصلی نامطلوب شد.

IJE TRANSACTIONS A: Basics Vol. 35, No. 05, (July 2022) 1246-1256

International Journal of Engineering

Journal Homepage: www.ije.ir

Implementation of Total Productive Maintenance to Improve Overall Equipment Effectiveness of Linear Accelerator Synergy Platform Cancer Therapy

D. I. Sukma*, H. A. Prabowo, I. Setiawan, H. Kurnia, I. M. Fahturizal

Industrial Engineering Depertment, Faculty of Engineering, Universitas Mercu Buana, Jakarta, Indonesia

PAPER INFO

Paper history:
Received 20 February 2022
Received in revised form 21 March 2022
Accepted 25 March 2022

Keywords:
Health Service
Linear Accelerator
Overall Equipment Effectiveness
Six Big Losses
Total Productive Maintenance

ABSTRACT

The Jakarta Government Hospital provides cancer services with several available types of equipment, one of which is the Linear accelerator (LINAC) Synergy Platform (SP) machine. The phenomenon of this machine experiencing a low effectiveness value because it is not able to handle the patient queue so it is not able to reduce the severity of cancer. The purpose of this study was to determine the factors causing the low value of Overall Equipment Effectiveness (OEE) and provide suggestions for improvement to increase the OEE value. The new approach of this research is using the Total Productive Maintenance (TPM) approach with OEE analysis as a success parameter because TPM is more identical in the manufacturing industry. Another update is using Failure Mode and Effect Analysis (FMEA) through Focus Group Discussions (FGD) with experts. The results of the study found that the factors that influenced the low OEE value on the LINAC SP machine were caused by breakdown loss of 76.29%, setup loss of 9.59%, idling and minor stop of 8.80%, and a decrease in speed of 5.29%. The continuous and consistent implementation of the TPM Pillar has increased the OEE value of the LINAC SP machine.

doi: *10.5829/ije.2022.35.07a.04*

NOMENCLATURE

LT	Loading Time	*PE*	Performance Efficiency
AR	Availability Ratio	*QR*	Quality Rate

1. INTRODUCTION

The medical equipment is the most important part of health service activities both in hospitals and other health facilities. A medical device is an instrument, equipment, or machine that has a function to assist nurses, doctors in diagnosing, detecting, measuring, curing, preventing, and repairing parts of the human body for health purposes. Medical equipment is a very vital medical device so this tool must require training in its use, calibration and maintenance must be carried out periodically. Medical equipment is usually managed by technical personnel. Medical equipment does not include implants and disposable [1]. Medical equipment also has an important role in handling various types of diseases that exist in hospitals in addition to the role of medical personnel, doctors, and nurses. Therefore, it becomes very important for hospitals to maintain the availability and reliability of equipment. Health services, especially in hospitals, are carried out by scheduling nurse performance which consists of scheduling patient services, providing satisfaction, and fulfilling nurse needs [2].

The Jakarta government hospital is one of the hospitals that provides cancer services with several available types of equipment, one of which is the LINAC SP. Based on initial observations, this machine experienced a low effectiveness value because it was unable to handle the patient queue so it was unable to reduce the severity of cancer. The inability to service the LINAC SP machine is due to the overall effectiveness of the LINAC SP machine being below the standard set by the ministry of health of 85%. LINAC SP machine as a

*Corresponding Author Email: diasirawati2005@gmail.com (D. I. Sukma)

Please cite this article as: D. I. Sukma, H. A. Prabowo, I. Setiawan, H. Kurnia, I. M. Fahturizal, Implementation of Total Productive Maintenance to Improve Overall Equipment Effectiveness of Linear Accelerator Synergy Platform Cancer Therapy, ***International Journal of Engineering, Transactions A: Basics***, Vol. 35, No. 07, (2022) 1246-1256

radiotherapy machine for the treatment of cancer is often found experiencing damage that varies from year to year.

The LINAC SP machine breakdown data for 2021 was 76% exceeding the target set by management; which is 35% of the time loss parameter and the OEE value of under 80%. Based on these problems, it is necessary to make improvements to get reliable equipment to be able to improve cancer patient services [3]. Applying the TPM concept is one of the best ways to overcome OEE values below 80%, so the implementation of TPM is a new thing in the hospital service industry because the TPM concept is more attached to the manufacturing industry. The implementation of TPM depends on the sincerity of all employees involved in TPM activities, from employees to management. Discipline in carrying out procedures and maintenance guidelines that have been made will greatly help the achievement of each TPM pillar [4].

The implementation of the TPM stage can bring other non-economic benefits such as increased safety and facilitation of repairs; thanks to work standardization based on 3 main pillars of TPM, namely focussed maintenance, autonomous maintenance, and planned maintenance [5]. Performance improvement is not only pursued by the industrial sector but also in the health care sector to reduce maintenance costs and increase operational efficiency [6].

TPM has characteristics that are measured by three parameters, namely improving overall equipment, maintenance by all human resources and activities carried out by small groups. The involvement of Human Resources (HR) is a key factor in TPM performance [7]. The effectiveness of the traditional overall tool is by considering the performance of human resources and the performance of equipment [8]. Another study used the Kaizen approach to improve maintenance elements, performance, and equipment availability [9, 10]. Modern medical machines and equipment have complex characteristics and different parts [11].

Therefore, TPM is a priority maintenance action by hospitals to analyze problems so that it can be seen how to improve OEE on equipment/machines. Increasing the effectiveness of the tool can be done by looking for six big losses, implementing TPM pillars and 5S foundation to increase the OEE value. Implementation of FMEA is used to analyze problems and determine improvement priorities. This study refers to research by Sharma et al. [12] where the TPM approach is used to increase the effectiveness of machines in the industry so that companies can survive, compete and dominate the global market. The research conducted by Xiang and Feng [13], Pacaiova and Izarikova [14], Thorat and Mahesha [15] applied the pillars of TPM in the manufacturing industry to increase machine effectiveness.

Reducing total network costs and maximizing responsiveness to customer requests in advance and reverse case, based on performance metrics and statistical hypotheses [16]. The TPM method can be combined with the Plan Do Check Action (PDCA) cycle in the manufacturing industry [17]. But in this study, the TPM method is combined with FMEA in the health services industry. The strength of this research will implement the pillar of TPM on one of the machines in the health service so that it becomes a new approach in this research.

This study aims to find the causal factors that affect the low OEE value and provide suggestions for improvements that must be made to increase the OEE value on the LINAC SP machine by using the TPM approach. The next sub-section contains a literature review as an understanding of the method used, methodology as a flow of problem-solving in this study, results, and discussion as a section for analysis, improvement, and discussion of this research, and conclusion as a section that collects research findings and results.

2. LITERATURE REVIEW

In this section, we will discuss the literature review that is still related to the materials and methods taken in this study. This grouping of literature studies should be focused and conceptualized between the research methods taken and the literature review used.

2. 1. LINAC SP Machine The LINAC SP machine is an ionizing radiotherapy medical machine that is used as a cancer therapy. Cancer treatment with this device uses radiation from radioactive particles to treat and control cancer growth. According to Ahmed Ali Omer [18] this machine requires high energy radiation so that it can be used to treat cancer with electricity utilizing fast-moving subatomic particles. LINAC machine produces beams of X-rays and radiate them to the patient's cancerous region [19]. Complex beam delivery techniques for patient care using clinical LINAC can result in variations in the photon spectrum, which can lead to dosimetric differences in patients that cannot be explained by current Treatment Planning Systems (TPS) [20]. Dosymmetrical Characterization of the Elekta LINAC SP that can be used for cancer therapy [21]. The simulation includes all components of the LINAC head and a homogeneous water ghost that yields in terms of depth dose and lateral dose profiles are presented for the 6 Megavolts [22].

2. 2. TPM According to Nakajima [23] TPM is defined as a popular approach used on equipment/machines for maintenance, preventing machine trouble, improving performance, and promoting maintenance by machine operators through daily maintenance activities involving all personnel from operators to top management.

The TPM implementation has many benefits for the workforce including sharpening knowledge and skills related to maintenance, improving internal communication, increasing teamwork, preparing equipment diagnosis so that they can prepare for inspection audits. TPM extends equipment life, zero defects, and zero accidents by involving operators [14]. The TPM implementation is based on the 5S foundation and 8 pillars [4, 24]. The eight pillars of TPM namely autonomous maintenance, planned maintenance, focussed maintenance, quality maintenance, training and education, office maintenance, occupation health and safety maintenance, and early equipment maintenance [25]. TPM method in various manufacturing industries as an approach to machine consistency in productivity and machine efficiency improvement [7, 26].

The implementation of the triple bottom line concept in production scheduling can result in the continuous solution of the Distributed Permutation Flow Store Scheduling Problem (DPFSP) [27]. a mixed-integer mathematical programming model was proposed to minimize cycle time and environmental costs, while a metaheuristic approach based on fruit fly optimization (FOA) algorithm was developed to find a fuzzy unloading scheduling scheme [28]. Other research has applied the design of experiment (DOE) method and a mathematical modeling approach based on the fuzzy possibility regression integrated (FPRI) model [29].

2. 3. OEE OEE is a method of measuring the effectiveness of an equipment/machine consisting of availability, performance, and quality factors [23, 28]. OEE is generally measured from the three losses, namely the availability function, machine performance level, and production line. The operating conditions of production machines/equipment will not be displayed accurately if it is only based on the calculation of one factor, such as performance efficiency [17]. However, the other six factors in the six losses should be included in the OEE analysis. The actual condition of the machine/equipment can be seen accurately. Through the Japan Institute of Planned Maintenance (JIPM), the OEE value that has met international standards is 85% [29]. An increase in OEE value can also be applied to the DMAIC approach at the analysis stage before and after improvement [6].

2. 4. FMEA According to Stamatis [30] FMEA is an analytical method that is intended to analyze, determine, and identify failure factors and problems of a process, product, and service in a manufacturing or service industry. FMEA is an analysis that an organization can decide that any Risk Priority Number (RPN) above 200 creates an unacceptable risk [31, 32]. RPN calculation is based on three elements, namely severity (S), occurrence (O), and detection (D). The FMEA method can be included in the DMAIC approach, namely at the Analyst stage, which was previously carried out by FGD in determining the RPN value [33, 34]. Improvements in service quality can also use the FMEA method in the service industry [35]. The use of the FMEA analysis method is one of the most practical techniques with high reliability in HSE risk assessment integrated with fuzzy system [32].

The gap between this study and other studies is the use of the kaizen concept consisting of Pareto diagrams, fishbone diagrams, and FMEA combined with the implementation of the TPM concept in taking corrective actions to increase the OEE value of LINAC SP machines in the health care industry. In contrast to other research related to industrial health services, it is more directed to TPS [20]. The contribution of this research can provide alternative inputs in increasing the value of OEE on machines in hospitals, especially those related to patient care. Other studies also use the PDCA approach so that it is more conceptual and focused which is combined with the TPM concept to increase the OEE value in the manufacturing industry [17]

3. METHODOLOGY

This research was conducted in the health care industry in the cancer service unit. The focus of this research is on the LSP machine of the ionizing radiation beam. This type of research is mixed methods. The design of this research is descriptive exploratory which aims to determine the causes of the emergence of losses/loss of machine operating time and how to make repairs. The types of data needed in this study are primary data and secondary data. Primary data was obtained from FGD with 5 experts consisting of 2 electromedical informants, 1 field Quality Control (QC) of medical physics, and 2 radiotherapists. Primary data is also obtained online from the electronic implementation of medical devices. While secondary data were obtained from literature, previous research, books, and company reports such as the number of defects, downtime, and total maintenance time.

This study uses systematic steps so that this research is focused and directed. This research step is divided into 4 stages, namely as follows:

Stage 1: Explain the phenomenon of problems that occur on LSP machines. Set research objectives to fix problems. Conduct a literature review on the TPM approach, FMEA, and OEE methods. The literature study is intended to deepen the theory used as a method of problem-solving.

Stage 2: Analyzing six big losses for OEE calculations by measuring the loading time used during the study, while the loading time formula is as follows:

$$\text{LT} = \text{Number of working days x } \frac{\text{Working hours}}{\text{Days}} \text{ x } \frac{\text{Minutes}}{\text{Hours}} \tag{1}$$

The next step is to calculate the baseline OEE before the repair, using the following formula:

$$AR = \frac{(\text{Loading Time} - \text{Unplanned Downtime})}{\text{Loading Time}} \text{ x } 100\% \quad (2)$$

$$PE = \frac{(\text{Idle Run Time x Total Production Part})}{\text{Operating Time}} \text{ x } 100\% \quad (3)$$

$$QR = \frac{(\text{Total Produced Parts} - \text{Total Defect Parts})}{\text{Total Produced Parts}} \text{ x } 100\% \quad (4)$$

$$\text{OEE} = \text{AR x PE x QR} \quad (5)$$

The next step is to make a Pareto diagram from the results of the Six Big Losses analysis with the help of Minitab 19 software. Based on the Pareto diagram then create a Fishbone diagram to determine the causes of the main problems through FGD.

Stage 3: FMEA analysis is carried out through FGD with 5 experts. The purpose of FMEA is to determine the priority failure mode based on the Risk Priority Number (RPN), which is calculated based on the risk factors for occurrence (O), severity (S), and detection (D). Give each score with an integer from 1 to 10 through the assessment of the expert. Next, the RPN calculation is carried out with the formula (6):

$$\text{RPN} = \text{S x O x D} \quad (6)$$

After the priority ranking is known, then make improvements by applying the TPM pillar.

Stage 4: Performing OEE calculations after improvement in Jul–Oct 2021 in the same way in the second stage and finally the conclusions of this research are obtained.

The new approach of this research is that the type of machine used in analyzing the OEE value is the LINAC SP machine, while the method used when determining the RPN value with FMEA analysis uses FGD with experts in their field [17]. But the kaizen method will also be systematic in the Pareto diagram, FMEA, and OEE methods because it includes quantitative research and uses FGD and Fishbone diagrams which are qualitative research. The framework can be seen in Figure 1.

4. RESULT AND DISCUSSION

In this section, we will discuss data collection starting from measurement loading time data as the basis for calculating six big losses. Calculation of OEE value data starting from AR, PE, and QR. Then to determine the biggest six big losses, using the Pareto diagram. After the dominant problem is known, the Fishbone diagram is used to find the main cause of a problem with FGD meeting was held to determine the priority values of the RPN using the FMEA method. Finally, the TPM method is used to determine corrective actions and prevent problems from recurring.

4. 1. Six Big Losses Analysis In this study, the six big losses on the LINAC SP machine are explained according to the operating time loss conditions. Breakdown loss on a LINAC SP machine is a time and quantity failure/loss caused by a faulty machine that cannot be operated. While the setup is the loss of setting and adjustment time when the LINAC SP machine warms up before use. Idling and minor loss is a loss when the machine is operating due to a shortstop or the process is temporarily interrupted. Reduce speed loss is the loss of time in the patient's therapy process due to additional time due to late admission. Reject loss is the loss of time due to the patient's treatment results being failed/rejected or canceled. Rework loss is the machine working again due to electrical problems or data is not stored. This first section will discuss the results of the calculation of loading time carried out during this research. Calculation of loading using formula (1). The results are summarized in Table 1.

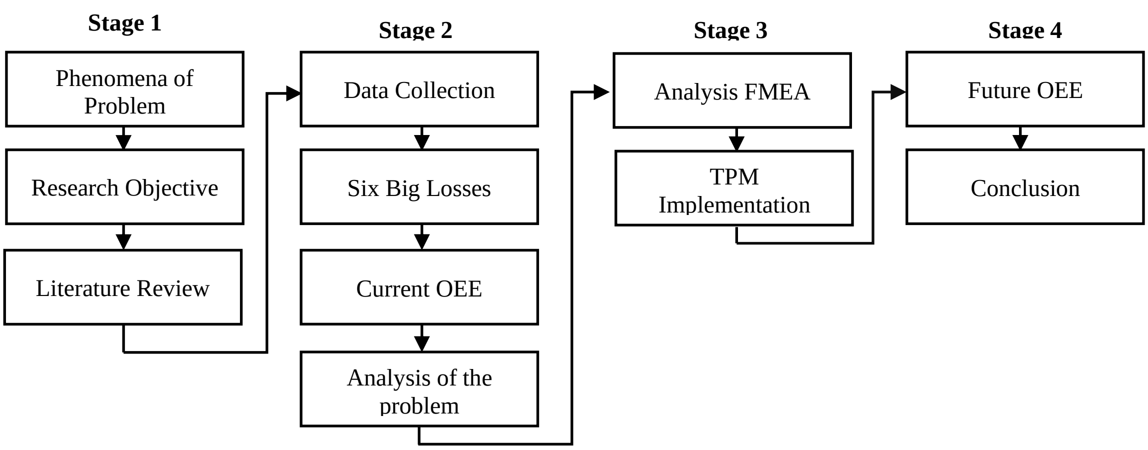

Figure 1. Research framework

TABLE 1. Measurement of data loading time before improvement

Month	Number of working days	Working hours/ days	Minute/ hour	Loading Time (minute)
Jan 21	20	8	60	9,600
Feb 21	19	8	60	9,120
Mar 21	22	8	60	10,560
Apr 21	20	8	60	9,600
Total	81	8	60	39,360

TABLE 2. Calculation of six big losses before improvement

Month	Downtime Loss (minute)			Speed Loss (minute)			Quality Loss (minute)		
	Breakdown loss	Setup loss	Sum	Idling & minor loss	Reduce speed loss	Sum	Reject loss	Rework loss	Sum
Jan 21	1,765	230	1,995	200	125	325	0	0	0
Feb 21	1,965	215	2,180	210	125	335	0	0	0
Mar 21	1,875	245	2,120	240	140	380	0	0	0
Apr 21	1,670	225	1,895	190	115	305	0	0	0
Total	7,275	915	8,190	840	505	1,345	0	0	0

Table 1 shows that the number of working days for LINAC SP machines are 81 days with 8 machine operating hours and 60 machine operating minutes/hour. The total loading time before the repair was 39,360 minutes. Next, analyze the six big losses generated from the checksheet done by the LINAC SP machine operator. The results of the report can be seen in Table 2.

Table 2 shows that the downtime loss includes breakdown and setup loss with a total of 8,190 minutes. Speed losses include idling & minor loss with a total of 1,345 minutes. Meanwhile, reject loss and rework loss do not lose time. Based on the data of six big losses, then data processing is carried out using the Pareto diagram. Based on the Pareto diagram in Figure 2, it can be seen that the highest loss/time loss occurred in the breakdown loss, which was 76.3%. So this breakdown loss will be evaluated for improvement.

Table 2 shows the results that the quality rate is 0, which means that there is no reject loss in the form of printouts from the LINAC SP machine and there is no rework in the process of working on cancer therapy at the hospital. This is because the output on the LINAC SP machine is a patient, not a product. While Figure 2 shows that the dominant problem is breakdown time which is very high at 76.3%.

4. 2. OEE Calculation In this section, the baseline OEE value is calculated using secondary data, namely health service annual report data. The data used is data from Jan-Apr 2021. The calculation of the OEE value before the improvement (January sample) using the formulas (2), (3), (4) and (5) is as follows:

$$AR = \frac{(9{,}600-1{,}995)}{9{,}600} \text{ x } 100\% = 79.22\%$$

$$PE = \frac{(15 \; x \; 465)}{7605} \; x \; 100\% = 91.78\%$$

$$QR = \frac{(640-0)}{640} \; x \; 100\% = 100\%$$

OEE (%) = 79.22% x 91.78% x 100% = 72.71%

Based on the calculation with formulas (2), (3), (4) and (5) the OEE value is 72.71%. The value of this calculation is carried out on the January sample. The recapitulation of OEE values from Jan-Apr 2021 (before improvement) can be seen in Table 3.

4. 3. Problem Cause Analysis In this section, the results of the Fishbone diagram obtained from brainstorming will be explained including machine operators, inspectors, and other medical personnel. The results of the Fishbone diagram can be seen in Figure 3.

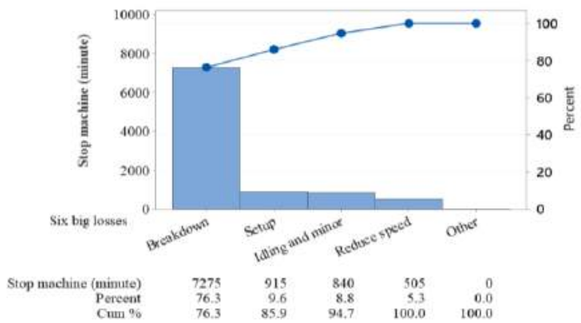

Figure 2. Pareto diagram of six big losses

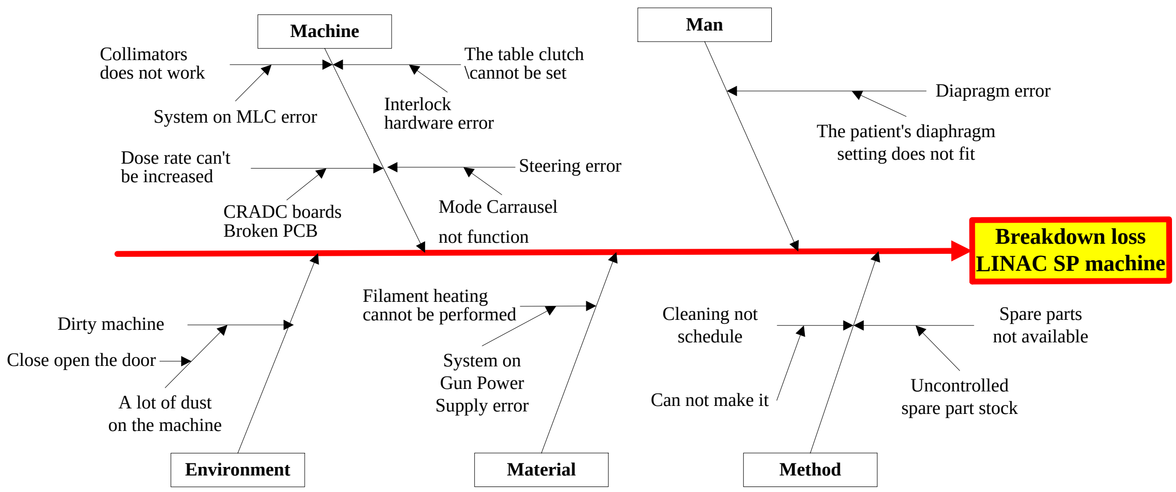

Figure 3. Fishbone diagram of breakdown losses

TABLE 4. FMEA analysis of breakdown losses

Potential Failure Mode	Sev	Potential Failure Effects	Occ	Potential Cause of Failure	Det	RPN	Rank
Multi-Leaf Collimators (MLC) not working	9	Machine off	8	System on MLC error	7	504	1
The table can't go up and down	8	The table cannot be set	9	Interlock hardware	7	504	2
Filament heating cannot be performed	8	Gun Filament not working	7	System on gun power supply error	9	504	3
Spare part not available	7	Permanent machine off	8	Uncontrolled spare part stock	9	504	4
Steering error	7	Carrousel mode not working	8	Carrousel locking pin doesn't fit the hole	6	343	5
Dirty machine	5	Machine restarted frequently	8	There is dust on the table, 5S is lacking	6	240	6
Control System	5	Dose rate can't be increased	6	Board CRADC PCB is broken	6	180	7
Diaphragm error	5	Machine often hangs	8	The patient's diaphragm setting is not up to standard	4	160	8
Unscheduled cleaning	4	Dirty machine	8	Bad scheduling	5	160	9

4. 4. Analysis of FMEA This FMEA analysis is carried out to determine the priority ranking of problems that will be repaired. FMEA analysis is based on the calculation of the RPN where the scorer is carried out by 5 experts. The FGD was conducted to determine the priority ranking and how to determine corrective action by applying the TPM pillar so that the expected improvements were obtained, namely increasing and maintaining the OEE value in controlling LINAC SP machines in health services. The results of the FMEA analysis can be seen in Table 4.

4. 5. Implementation of Pilar TPM After obtaining the priority value for the potential failure, further improvements, and implementation will be carried out by applying the TPM pillar. Maintenance activities in the industry directly impact output, production quality, production costs, safety, and environmental performance [36]. Several improvement implementations must be critical points to implement TPM in the health care industry, especially in increasing the OEE value on LINAC SP machines. The improvements made by referring to the principles of the TPM pillar are as follows:

4. 5. 1. Autonomous Maintenance (AM) The concept of implementing autonomous maintenance must involve all personnel from the operator level to top management. AM activities by providing knowledge to operators regarding the understanding of LINAC SP machines from technicians and experts. Operators will get material on basic understanding of machines, machine operations, machine safety systems, basic machine maintenance, to more advanced stages of machines. There are critical points in carrying out autonomous maintenance aimed at operators, including:

- Able to run the machine correctly
- Clean the machine regularly
- Knowing the inspection points to check on the machine
- Able to perform lubrication on machine parts
- Checking parts that are prone to abnormality and able to take early preventive action
- Perform machine startup and machine shutdown correctly.

4. 5. 2. Planned Maintenance (PM) Planned maintenance aims to control the damage of each machine component to avoid more severe damage. Based on the problem in the breakdown, it is necessary to schedule an earlier to prevent abnormality from occurring. The following schedule of preventive activities resulting from the FGD can be seen in Table 5.

TABLE 5. LINAC SP machine preventive schedule

Activity	Before Improvement	After Improvement
System control on MLC	6 month	1 month
Periodic control of gun power supply system	3 month	2 month
Hardware interlock check	3 month	2 month
Procurement of spare parts	6 month	2 month

4. 5. 3. Kaizen/Focused Maintenance (FM) This pillar section implements changes to the existing Standard Operation Procedure (SOP). The problem with the carrousel mode during setup is that there is no standardization in the SOP so maintenance is not optimal.

Changes to the SOP were made by adding several standardizations, including setting the carrousel mode during setup and making One Point Lessons.

4. 6. OEE Calculation After Improvement In this section, the calculation of the OEE value after improvement is carried out. However, before going to this section, the results of the loading time inspection carried out in this study will be explained in Table 6. After the loading time results are obtained, then a loss/time loss analysis is carried out through the six big losses which have been filled in by the LINAC SP machine operator. The calculation of six big losses can be seen in Table 7. Based on the loading time data in Table 5 and the six big losses data in Table 7, the OEE value can then be calculated after the improvement. The calculation of OEE value after improvement (May 2021 sample) is as follows:

AR = $\frac{(8{,}640-1{,}185)}{8{,}640}$ x 100% = 86.28%

PE = $\frac{(15\ x\ 471)}{7.445}\ x$ 100% = 94.90%

QR = $\frac{(471-0)}{471}\ x$ 100% = 100%

OEE (%) = 76.28% x 94.90% x 100% = 81.88%

Based on the calculation with formulas (2), (3), (4) and (5) the OEE value is 81.88%. The value of this calculation is carried out on the May sample. The recapitulation of OEE values from May to August (after improvement) can be seen in Table 3.

TABLE 6. Measurement of data loading time after improvement

Month	Number of working day	Working hours/ days	Minute/ hour	Loading Time (minute)
May 21	18	8	60	8,640
Jun 21	21	8	60	10,080
Jul 21	21	8	60	10,080
Aug 21	20	8	60	9,600
Total	81	8	60	38,880

TABLE 7. Calculation of six big losses after improvement

Month	Downtime Loss (minute)			Speed Loss (minute)			Quality Loss (minute)		
	Breakdown loss	Setup loss	Sum	Idling & minor loss	Reduce speed loss	Sum	Reject loss	Rework loss	Sum
May 21	980	205	1,185	185	95	280	0	0	0
Jun 21	975	210	1,185	210	120	330	0	0	0
Jul 21	925	215	1,140	210	125	335	0	0	0
Aug 21	920	220	1,140	195	105	300	0	0	0
Total	3,800	850	4,650	800	445	1,245	0	0	0

TABLE 3. Recapitulation data before and after improvement

	Month	Availability	Performance	Quality	OEE
Before	January 2021	79.21%	91.78%	100%	72.70%
	February 2021	76.09%	92.16%	100%	70.13%
	March 2021	79.92%	92.80%	100%	74.16%
	April 2021	80.26%	92.98%	100%	74.62%
	Average	78.94%	92.98%	100%	73.39%
After	May 2021	86.28%	94.90%	100%	81.88%
	June 2021	88.24%	96.86%	100%	85.47%
	July 2021	88.69%	97.00%	100%	86.02%
	August 2021	88.12%	97.85%	100%	86.23%
	Average	87.89%	97.85%	100%	86.00%

Table 3 shows that the OEE value before improvement is 73.39% and after improvement is 86.00%. This increased the OEE value of 14.6% and it can be discussed that this success rate has met the target of the Indonesian Ministry of Health of 86% of the 85% target.

4. 7. Discussion with Previous Research Based on the improvements made in the previous section, maintenance management must pay attention to the availability of equipment spare parts to minimize the risk of increased downtime due to the replacement of spare parts. Investments are needed for repairing medical equipment and machinery infrastructure to properly support the TPM program and increase productivity, however, the hospital's managerial insight must fully support and approve the improvement program that results in this comprehensive increase in OEE value. This is in line with the research of Sutoni et al. [37]. Investment in training and socialization is also needed so that AM becomes a work culture for all medical personnel. Scheduling of component replacement activities in the PM program requires the availability of the required components. The implementation of PM using the time-based maintenance method will facilitate the planning for the supply of the required components. This is in line with the research performed by Bekar et al. [38].

The purchase of components needs to be planned properly so that when the schedule for the replacement implementation arrives, the required components are already available. This is in line with the research of Patil et al. [39]. Management can maximize maintenance scheduling by combining the TPM method with advanced optimization algorithms such as heuristics or metaheuristics. This is in line with the research of Dulebenets [40, 41]. The implementation of two-hybrid meta-heuristic algorithms can overcome the design problem of a two-channel closed-loop supply chain network in the tire industry [42].

The distribution of this research related to the implementation of TPM on the LINAC SP machine in the hospital service industry can provide a reference with the 3 pillars of TPM namely AM, PM, and FM which is carried out consistently by hospital service workers and fully supported by the management, it will create an increase OEE value so that cancer therapy services can run well.

4. 8. Research Gap Analysis This study used the direct improvement Kaizen method according to existing needs, while other studies use the PDCA approach so that it is more conceptual and focused [17]. But the Kaizen method also has a synergetic relation with Pareto diagram, FMEA, and OEE methods for quantitative method and with FGD and Fishbone diagrams for qualitative method.

The Synergy Platform machine through various thicknesses of graphite and lead is measured using an ion chamber so that there is an ion space response as a function of photon energy obtained by using the MC method in the Geant4 simulation code [20]. Simulate the radiotherapy process using LINAC machine to perform dosimetric analysis and this simulation uses the Monte Carlo (MC) method which has been proven to provide realistic results in terms of accuracy [19]. However, present the strategy to simulate a clinical linear accelerator based on the geometry provided by the manufacturer and summarize the corresponding experimental validation. Simulations were performed with the Geant4 MC code under a grid computing environment [43].

The other research gap is the implementation of the MC method in the treatment of cancer therapy patients in the LINAC SP machine [20, 19, 43]. The difference with this study is more directed at improving the service of cancer therapy patients by increasing the OEE value of the LINAC SP machine. In this study, it has been successful in the implementation of the TPM Pillar that is continuous and consistent has increased the OEE value of the LINAC SP machine in the hospital service industry.

5. CONCLUSION

Based on the analysis in the previous section, several conclusions were obtained. The conclusions obtained in this study include finding that there are factors that affect the low OEE value on the LSP machine, namely the breakdown loss factor of 76.29% setup loss of 9.59%, idling and minor stops of 8.80%, and reduced speed of 5.29%. Based on the FGD with the experts, the improvement in this research is to apply the pillars of sustainable TPM. Controlling the system on the MLC periodically once a month, setting the carrousel mode at the time of setup must be according to standards, controlling the gun power supply system periodically every 2 months, providing scheduled spare parts where spare parts that are difficult to procure must be stocked at least 5 pcs, checking interlocks hardware every 2 months so that the table setting can go up and down smoothly, cleaning the Printed Circuit Board (PCB) board is done every 2 months during machine maintenance. Setting the patient's diaphragm by making a One Point Lesson (OPL).

The limitation of this research is that it only uses 1 machine and the limited permission to analyze this machine is very limited because it is under strict supervision by the hospital. The continuous and consistent implementation of the TPM Pillar has increased the OEE value of LINAC SP machines in the hospital service industry. These results give satisfaction to the health management because it has been able to provide effective patient care and cost savings inefficient machine repairs. For further research, suggestions and recommendations that can be given are to apply TPM which refers to technology 4.0 on the same type of machine or other types of machines in the health industry. The installation of sensors on the machine is expected to can predict early damage such as abnormal temperatures and vibrations with the help of signals/sirens.

6. REFERENCES

1. R. Bahreini, L. Doshmangir, and A. Imani, "Influential factors on medical equipment maintenance management: In search of a framework," ***Journal of Quality in Maintenance Engineering***, Vol. 25, No. 1, (2019), 128-143, doi: 10.1108/JQME-11-2017-0082.
2. M. Mohammadian, M. Babaei, M. A. Jarrahi, and E. Anjomrouz, "Scheduling nurse shifts using goal programming based on nurse preferences: A case study in an emergency department," ***International Journal of Engineering, Transactions A: Basics***, Vol. 32, No. 7, (2019), 954-963, doi: 10.5829/ije.2019.32.07a.08.
3. I. Setiawan, "Integration of Total Productive Maintenance and Industry 4.0 to increase the productivity of NC Bore machines in the Musical Instrument Industry," in Proceedings of the 11th Annual International Conference on Industrial Engineering and Operations Management Singapore, 4701-4711, (2021).
4. H. A. Prabowo, Y. B. Suprapto, and F. Farida, "The Evaluation of Eight Pillars Total Productive Maintenance (TPM) Implementation and Their Impact on Overall Equipment Effectiveness (OEE) and Waste," ***Sinergi,*** Vol. 22, No. 1, (2018), 13-18, doi: 10.22441/sinergi.2018.1.003.
5. J. D. Morales Méndez and R. S. Rodriguez, "Total productive maintenance (TPM) as a tool for improving productivity: a case study of application in the bottleneck of an auto-parts machining line," ***International Journal of Advanced Manufacturing Technology***, Vol. 92, No. 1-4, (2017), 1013-1026, doi: 10.1007/s00170-017-0052-4.
6. A. Rozak, C. Jaqin, and H. Hasbullah, "Increasing overall equipment effectiveness in automotive company using DMAIC and FMEA method," ***Journal Européen des Systèmes Automatisés,*** Vol. 53, No. 1, (2020), 55-60, doi: 10.18280/jesa.530107.
7. L. Setiawan, "Literature Review of the Implementation of Total Productive Maintenance (TPM) in various Industries in Indonesia," ***Indonesian Journal of Industrial Engineering Management***, Vol. 2, No. 1, (2021), 16-34, doi: doi.org/10.22441/ijiem.v2i1.10328.
8. M. Nakhla, "Designing extended overall equipment effectiveness: application in healthcare operations," ***International Journal of Management Science and Engineering Management,*** Vol. 13, No. 4, (2018), 227-236, doi: 10.1080/17509653.2017.1373377.
9. M. Suryaprakash, M. Gomathi Prabha, M. Yuvaraja, and R. V. Rishi Revanth, "Improvement of overall equipment effectiveness of machining centre using tpm," ***Materials Today Proceedings***, (2020), doi: 10.1016/j.matpr.2020.02.820.
10. M. Abbasghorbani, Prioritization of Transmission Network Components Based on their Failure Impact on the Reliability of Composite Power Systems, ***International Journal of Engineering, Transactions C: Aspects*** Vol. 35, No. 03, (2022) 502-509. doi: 10.5829/ije.2022.35.03c.02
11. K. A. Mkalaf, "Total Productive Maintenance: A Safety Approach to Optimize the Anesthesia Device Outcomes," ICITM-9th International Conference on Industrial Technology Management, (2020), 122-126, doi: 10.1109/ICITM48982.2020.9080374.
12. R. Sharma, J. Singh, and V. Rastogi, "The impact of total productive maintenance on key performance indicators (PQCDSM): A case study of automobile manufacturing sector," ***International Journal of Productivity and Quality Management***, Vol. 24, No. 2, (2018), 267-283, doi: 10.1504/IJPQM.2018.091794.
13. Z. Tian Xiang and C. Jeng Feng, "Implementing Total Productive Maintenance in a Manufacturing Small or Medium-Sized Enterprise," ***Journal of Industrial Engineering Management***, Vol. 14, No. 2, (2020), 152-175, doi: https://doi.org/10.3926/jiem.3286.
14. H. Pacaiova and G. Izarikova, "Base principles and practices for implementation of total productive maintenance in automotive industry," ***Quality Innovation Prosperity***, Vol. 23, No. 1, (2019), 45-59, doi: 10.12776/QIP.V23I1.1203.
15. R. Thorat and G. T. Mahesha, "Improvement in productivity through TPM Implementation," ***Materials Today Proceedings***, Vol. 24, (2020), 1508-1517, doi: 10.1016/j.matpr.2020.04.470.

16. M. Fasihi, R. Tavakkoli-Moghaddam, S. E. Najafi, and M. Hahiaghaei-Keshteli, “Developing a Bi-objective mathematical model to design the fish closed-loop supply chain,” ***International Journal of Engineering, Transactions B: Applications***, Vol. 34, No. 5, (2021), 1257-1268, doi: 10.5829/ije.2021.34.05b.19.

17. C. Jaqin, A. Rozak, and H. H. Purba, “Case Study in Increasing Overall Equipment Effectiveness on Progressive Press Machine Using Plan-do-check-act Cycle,” ***International Journal of Engineering, Transactions B: Applications***, Vol. 33, No. 11, (2020), 2245-2251, doi: 10.5829/ije.2020.33.11b.16.

18. M. Ahmed Ali Omer, “Instrumental Quality Control of Therapeutic Linear Accelerator Performance,” ***American Journal of Physics and Applications,*** Vol. 5, No. 5, (2017), 66-78, doi: 10.11648/j.ajpa.20170505.12.

19. S. Francis, D. Suresh, S. Nath, S. Lakshmi, B. Jayaraj, N. Puzhakkal, and P. Pournami, “Monte Carlo Simulation of Linear Accelerator for Dosimetry Analysis,” 6th International Conference for Convergence in Technology, I2CT, (2021), doi: 10.1109/I2CT51068.2021.9418059.

20. H. J. Choi, H. Park, C. Y. Yi, B. C. Kim, W. G. Shin, and C. H. Min, “Determining the energy spectrum of clinical linear accelerator using an optimized photon beam transmission protocol,” ***Medical Physics***, Vol. 46, No. 7, (2019), 3285-3297, doi: 10.1002/MP.13569.

21. D. B. Patil and M. K. Zope, “A Dosimetric Characterization of an Elekta Synergy Platform Linear Accelerator,” ***IOSR Journal of Dental and Medical Sciences,*** Vol. 18, No. 5, (2019), 40-46, doi: 10.9790/0853-1805114046.

22. D. Samir, M. Zerfaoui, A. Moussa, Y. Benkhouya, and M. El Ouartiti, “Grid Monte Carlo Simulation of a Medical Linear Accelerator,” ***European Journal of Engineering and Technology Research,*** Vol. 3, No. 12, (2018), 40-43, doi: 10.24018/ejers.2018.3.12.1001.

23. Nakajima, *Introduction to Total Productive Maintenance*. Cambridge: Productivity Press, Inc, 1988.

24. A. Y. Ali, “Application of Total Productive Maintenance in Service Organization,” ***International Journal of Research in Industrial Engineering,*** Vol. 8, No. 2, (2019), 176-186, doi: 10.22105/riej.2019.170507.1076.

25. A. M. Fathollahi-Fard, L. Woodward, and O. Akhrif, “Sustainable distributed permutation flow-shop scheduling model based on a triple bottom line concept,” ***Journal of Industrial Information Integration,*** Vol. 24, No. 12, (2021), doi: 10.1016/J.JII.2021.100233.

26. G. Yuan, Y. Yang, G. Tian, and A. M. Fathollahi-Fard, “Capacitated multi-objective disassembly scheduling with fuzzy processing time via a fruit fly optimization algorithm,” ***Environmental Science and Pollution Research International***, (2022), https://doi.org/10.21203/rs.3.rs-1075510/v1

27. H. Gholizadeh, A. M. Fathollahi-Fard, H. Fazlollahtabar, and V. Charles, “Fuzzy data-driven scenario-based robust data envelopment analysis for prediction and optimisation of an electrical discharge machine’s parameters,” ***Expert Systems with Applications,*** Vol. 193, No. 1, (2022), doi: 10.1016/j.eswa.2021.116419.

28. A. P. Herry, F. Farida, and N. I. Lutfia, “Performance analysis of TPM implementation through Overall Equipment Effectiveness (OEE) and Six Big Losses,” IOP Conference Series: Materials Science Engineering, Vol. 453, No. 1, (2018), doi: 10.1088/1757-899X/453/1/012061.

29. S. Sunadi, H. H. Purba, and E. Paulina, “Overall Equipment Effectiveness to Increase Productivity of Injection Molding Machine : A Case Study in Plastic Manufacturing Industry,” ***ComTech: Computer, Mathematics and Engineering Applications***, Vol. 12, No. 1, (2021), 53-64, 2021, doi: 10.21512/comtech.v12i1.6706.

30. D. H. Stamatis, *Failure Mode and Effect Analysis FMEA from Theory to Execution*. Wisconsin: ASQC Quality Press, 1995.

31. M. A. Bennett, R. McDermott, and M. Beauregard, *The Basics of FMEA*, 2017. Productivity Press https://doi.org/10.1201/b16656

32. A. Ardeshir, P. F. Ahmadi, and H. Bayat, “A Prioritization Model for HSE Risk Assessment Using Combined Failure Mode and Effect Analysis and Fuzzy Inference System: A Case Study in Iranian Construction Industry,” ***International Journal of Engineering, Transactions C: Aspects***, Vol. 31, No. 9, (2018), 1487-1497, doi: 10.5829/ije.2018.31.09c.03.

33. H. Kurnia, C. Jaqin, H. H. Purba, and I. Setiawan, “Implementation of Six Sigma in the DMAIC Approach for Quality Improvement in the Knitting Socks Industry,” ***Tekstilvemuhendis***, Vol. 28, No. 124, (2021), 269-278, doi: 10.7216/1300759920212812403.

34. H. Kurnia, C. Jaqin, and H. Manurung, “Implemantation of the DMAIC Approach for Quality Improvement at the Elastic Tape Industry,” ***J@ti Undip Jurnal Teknik Industri***, Vol. 17, No. 1, (2022), 40-51, doi: 10.14710/jati.17.1.40-51.

35. A. Niñerola, M. V. Sánchez-Rebull, and A. B. Hernández-Lara, “Quality improvement in healthcare: Six Sigma systematic review,” ***Health Policy (New York)***., Vol. 124, No. 4, (2020), 438-445, doi: 10.1016/j.healthpol.2020.01.002.

36. H. Gholizadeh, H. Fazlollahtabar, A. M. Fathollahi-Fard, and M. A. Dulebenets, “Preventive maintenance for the flexible flowshop scheduling under uncertainty: a waste-to-energy system,” ***Environmental Science and Pollution Research,*** Vol. 1, No. 9, (2021), doi: 10.1007/s11356-021-16234-x.

37. A. Sutoni, W. Setyawan, and T. Munandar, “Total Productive Maintenance (TPM) Analysis on Lathe Machines using the Overall Equipment Effectiveness Method and Six Big Losses,” ***Journal of Physics: Conference Series,*** Vol. 1179, No. 1, (2019), 1-7, doi: 10.1088/1742-6596/1179/1/012089.

38. E. T. Bekar, A. Skoogh, and N. Cetin, “Prediction of Industry 4.0’s Impact on Total Productive Maintenance Using a Real Manufacturing Case,” in Proceedings of the International Symposium for Production Research 2018, (2019), 136-149, doi: 10.1007/978-3-319-92267-6.

39. B. B. Patil, A. S. Badiger, and A. H. Mishrikoti, “A Study on Productivity Improvement through Application of Total Productive Maintenance in Indian Industries-A Literature Review,” ***IOSR Journal of Mechanical and Civil Engineering,*** Vol. 15, No. 3, (2018), 13-23, doi: 10.9790/1684-1503041323.

40. M. A. Dulebenets, “A Delayed Start Parallel Evolutionary Algorithm for just-in-time truck scheduling at a cross-docking facility,” ***International Journal of Production Economics***, Vol. 212, No. 6, (2019), 236-258, doi: 10.1016/J.IJPE.2019.02.017.

41. M. A. Dulebenets, J. Pasha, O. F. Abioye, M. Kavoosi, E. E.Ozguven, R. Moses, W. R. Boot, and T. Sando, “Exact and heuristic solution algorithms for efficient emergency evacuation in areas with vulnerable populations,” ***International Journal of Disaster Risk Reduction,*** Vol. 39, No. 10, (2019), 101-114, doi: 10.1016/J.IJDRR.2019.101114.

42. A. M. Fathollahi-Fard, M. A. Dulebenets, M. Hajiaghaei-Keshteli, R. Tavakkoli-Moghaddam, M. Safaeian, and H. Mirzahosseinian, “Two hybrid meta-heuristic algorithms for a dual-channel closed-loop supply chain network design problem in the tire industry under uncertainty,” ***Advanced Engineering Informatics,*** Vol. 50, No. 10, (2021), doi: 10.1016/j.aei.2021.101418.

43. S. Didi, K. Bahhous, M. Zerfaoui, Z. Aboulbanine, H. Ouhadda, and A. Halimi, “Experimental validation of a linac head Geant4 model under a grid computing environment,” ***Biomedical Physics & Engineering Express***, Vol. 8, No. 2, (2022), 25-37, doi: 10.1088/2057-1976/AC4DD2.

Persian Abstract

چکیده

بیمارستان دولتی جاکارتا خدمات سرطان را با چندین نوع تجهیزات موجود ارائه می دهد که یکی از آنها دستگاه پلتفرم هم افزایی (SP) شتاب دهنده خطی (LINAC) است . پدیده ای که این دستگاه ارزش اثربخشی پایینی را تجربه می کند زیرا قادر به رسیدگی به صف بیماران نیست بنابراین قادر به کاهش شدت سرطان نیست .هدف از این مطالعه تعیین عوامل ایجاد کننده ارزش پایین اثربخشی کلی تجهیزات (OEE) و ارائه پیشنهادهایی برای بهبود برای افزایش مقدار OEE بود .رویکرد جدید این تحقیق استفاده از رویکرد نگهداری کل تولیدی (TPM) با تحلیل OEE به عنوان پارامتر موفقیت است زیرا TPM در صنعت تولید یکسان تر است .به روز رسانی دیگر استفاده از حالت شکست و تجزیه و تحلیل اثر (FMEA) از طریق گفتگوهای گروهی متمرکز (FGD) با کارشناسان است .نتایج این مطالعه نشان داد که عواملی که بر مقدار OEE پایین در ماشین LINAC SP تأثیر می گذارند، ناشی از افت خرابی 76.29 درصد، افت راه اندازی 9.59 درصد، در حالت آرام و توقف جزئی 8.80 درصد و کاهش سرعت 5.29 است .٪ .کاربرد مداوم و مداوم ستون TPM باعث افزایش ارزش OEE دستگاه LINAC SP شده است.

IJE TRANSACTIONS A: Basics Vol. 35, No. 05, (July 2022) 1257-1267

International Journal of Engineering

Journal Homepage: www.ije.ir

A New Texture Segmentation Method with Energy-driven Parametric Active Contour Model Based on Jensen-Tsallis Divergence

M. Nouri, Y. Baleghi Damavandi*

Department of Electrical & Computer Engineering, Babol Noshirvani University of Technology, Babol, Iran

PAPER INFO

Paper history:
Received 18 December 2021
Received in revised form 18 Merch 2022
Accepted 28 March 2022

Keywords:
Co-occurrence Matrix
Parametric Active Contour Model
Jensen -Tsallis Divergence
Balloon Energy
Texture Segmentation

ABSTRACT

Texture image segmentation plays an important role in various computer vision tasks. Active contour models are one of the most efficient and popular methods for identifying the purpose and segmentation of objects in the image. This paper presents a parametric active contour model (PACM) with a robust minimization framework based on image texture energy. First, the texture features of the original image are extracted using gray level co-occurrence matrix (GLCM). Subsequently, based on the GLCM texture features inside and outside the active contour, Jensen-Tsallis divergence of energies is calculated. The Jensen-Tsallis divergence is added to the parametric active contour using the balloon equation. The divergence is maximum at the boundary between the foreground and background of the image, which results in minimizing the active contour equation at the boundary of the target object. This global minimization energy function with texture feature can avoid the existence of local minima in the PACM models. Also, as opposed to previous models, the proposed model only requires the initial contour and is not dependent on the distance of the initial contour from the target object. In terms of segmentation accuracy and efficiency, experiments with synthetic and natural images demonstrate that the proposed approach obtains more satisfactory results than the previous state-of-the-art methods.

***doi**: 10.5829/ije.2022.35.07a.05*

1. INTRODUCTION

Segmentation is one of the prime parts of image processing. Boundary detection plays an important role in machine vision applications, such as control of urban transportation systems [1], video surveillance [2], medical diagnosis [3-6], identifying military targets [7], plants monitoring [8-10] and object tracking [11-15]. One of the important areas in image segmentation is the division of an image into areas with different textural features [16]. This has been the focus of researchers for a long time. So far, no identified method has been proposed for segmenting images with non-uniform textures that can segment all textures. In general, the quality of textural image segmentation depends on the performance of texture description algorithms as well as the choice of segmentation method [17]. Many methods for segmenting images have been introduced, including region growth, division, integration, neural networks (ANN), active contour (ACM) models, etc [18]. Active contour models are recognized as one of the most successful methods for segmenting images [19, 20]. Active contour models have many advantages over other algorithms [21, 22]. First, active contour models show the coordinates of boundary pixels well. Second, it is possible to add image region information to the active contour to improve the quality of texture segmentation. Third, the resulting contour is a closed and regular contour that is very suitable for applications such as segmentation, detection, and analysis of an image [23].

Based on basic equations for active contours, the models of active contours can be divided into geometric [24] and parametric [25] categories. The basic equations of active contour models consist of two parts: internal energy, and external energy. Internal energy is not dependent on image and is simply a mathematical definition of a discrete contour [26]. External energy is an equation that is derived from the content of the image and helps to converge the active contour to the object boundary [25]. Researchers have so far been able to define external energy equations in edge-based (traditional) and region-based methods [18]. Edge-based

*Corresponding Author Institutional Email: y.baleghi@nit.ac.ir (Y. Baleghi Damavandi)

Please cite this article as: M. Nouri, Y. Baleghi Damavandi, A New Texture Segmentation Method with Energy-driven Parametric Active Contour Model Based on Jensen-Tsallis Divergence, ***International Journal of Engineering, Transactions A: Basics***, Vol. 35, No. 07, (2022) 1257-1267

active contours use an edge detection algorithm to stop the active contour from moving at the target object boundary [16]. Therefore, edge-based methods will be incapable of dealing with images with weak borders. To overcome this problem, researchers have tried to use region information to improve the performance of the active contour [27-29]. Region-based active contours are stronger when facing low-contrast images (weak edges) and are also less sensitive to the position of the starting points of the active contour [23].

Therefore, to overcome this problem in low-edge images, Ivins and Porrill [30] and Schaub and Smith [31] introduced different models of color active contour. In turn, Hamarneh et al. [32] introduced a type of color active contour in which inflatable energy is used to guide the contour towards the target. This energy uses normalized RGB color space or HSV color space to produce color pressure energy. This model used an active contour in medical images to segment oral lesions. In this method, the energy of color pressure is added to the energy function of the parametric active contour model. The energy is directed to the target object with a specific color using the new energy function of the active contour. The technique was used in medical image segmentation and mobile image lighting. This method makes it possible to segment targets that have weak borders. In this method, the target and the background should have the same color. However, the color pressure energy cannot segment targets with complex colors or textures.

Recent studies have examined external energies based on texture properties since color-based external energies have difficulty dealing with complex textured images. Researchers have shown that by adding new balloon energy based on texture properties to parametric active contour models, it is possible to segment texture objects in the textured background [27].

Vard et al. [33] presented an active contour based on texture properties, which used region information to enhance its ability to capture object boundaries in the image using the texture energy moment equations. Vard et al. [27] also used Walsh Hadamard's transform in another study to obtain region information and obtained better results.

Moallem et al. [28] used the Gabor filter to add image texture information to the active contour. Based on their results, the active contour method which uses a Gabor filter has a better response than the active contour method using a moment.

The above methods are effective for segmenting synthetic images, but they are not accurate enough in order to segment natural images. To overcome this problem, Wu et al. [23] proposed a combination of the Gabor filter and the GLCM algorithm. This combination was used to obtain region information and to construct a new model for a geometric active contour. Due to the GLCM algorithm and geometric active contour, this method is very slow. By combining local variation degree (LVD) of intensity and Gabor features, Gao et al. [34] added new texture energy to the active contour. Due to the use of a level set contour, this method is very slow, too. Subudhi and Mukhopadhyay [35] presented a statistical region-based Active Contour Model (ACM) that considered the correlation between local and global image statistics to segment cluttered images. Wu et al. [36] proposed Deep Parametric Active Contours (DPAC). Using such high-dimensional features may improve segmentation accuracy, however, calculations of these high-level features burden high computational cost. Subudhi and Mukhopadhyay [16] introduced a new energy using discrete cosine transforms, directing the active contour towards the object boundary. Also Badoual [37] introduced the contour which was directed to the boundary of the target object by including a circle wavelet in the active model.

Due to the high calculation requirements of geometric models [16], the focus of this paper is on active contour models for object segmentation in the textural environment. With the help of the Jensen-Tsallis divergence, new texture properties are added to the parametric active contour model. Jensen-Tsallis divergence (JTD) calculates the distance between two probability density functions, and it is maximal at the boundary between the two probability density functions. If an image consists of two different textures, then the image histogram has two probability density functions, an object probability density function, and a background probability density function. Since the Jensen-Tsallis divergence at the boundary between the two density functions is at a maximum level, if we add it to the active contour, the contour energy equation at the boundary between the target object and the background is minimized.

The structure of this paper is as follows. The mathematical background which contains three parts of ACM, GLCM, and JTD is presented in section 2. In section 3, the proposed method of the active contour model based on JTD is described. The experimental results and validation of the proposed method are discussed in section 4, and the conclusion follows in section 5.

2. BACKGROUND

2. 1. Mathematical Description of the Parametric Active Contour Model

In the parametric active contour model, the contour or surface is specified in parametric form during the deformation process. Parametric active contours are open or closed contours [25], as described in Equation (1):

$$S(u) = I(x(u), y(u) \quad , \quad u \in [0 , 1] \tag{1}$$

The points of the contour move in coordinate space (x, y) until they match the desired properties of the object. It is necessary to take the vector discrete function S(u) in the set of points [22] where i = 0,1,..., M, where M is the number of points on the contour. In the following, the interpolation of discrete points results in a continuous contour in the final stage. Based on the sum of the two internal energies $E_{int}(S(u))$ and the external energy $E_{ext}(S(u))$, the contour energy $E(S(u))$ is calculated as follows:

$$E(S(u)) = E_{int}(S(u)) + E_{ext}(S(u)) \tag{2}$$

An effective boundary for segmentation is when the energy from the above equation is the lowest. Thus, finding the boundary of the object will correspond to minimizing the contour energy function. The amount of elasticity and bending of the contour is determined by the internal energy, which is calculated as follows:

$$E_{int} = \frac{\alpha}{2}\left|\frac{\partial}{\partial u}S(u)\right|^2 + \frac{\beta}{2}\left|\frac{\partial^2}{\partial u^2}S(u)\right|^2 \tag{3}$$

Internal energy prevents the points of contour from oscillating and keeps them at a constant distance from one another. The first and second parts of the internal energy respectively prevent excessive elasticity and bending of the contour and keep it cohesive and smooth. In this case, the obtained flexible model will act as a string with both elasticity and strength properties. By adjusting the weighting parameters α and β, it is possible to adjust the two properties of elasticity and bending concerning each other.

External energy is defined in the scope of the image. It is responsible for absorbing contours into the desired features in an image, such as lines, corners, and other image properties. Therefore, external energy is also known as image energy ($E_{img}(S(u))$). As a result, the parametric active contour energy is defined according to Equation (4):

$$E = \frac{\alpha}{2}\oint\left|\frac{\partial}{\partial u}S(u)\right|^2 du + \frac{\beta}{2}\oint\left|\frac{\partial^2}{\partial u^2}S(u)\right|^2 du + \oint E_{img}(S(u))\, du \tag{4}$$

In the traditional model of a parametric active contour, the active contour is deformed enough to capture the actual boundaries of the object to an acceptable extent. For this reason, in the initial active contour models, the image energy was proposed in proportion to the edge characteristic [12, 20]. It was described according to Equation (5) [25] and Equation (6) [38]:

$$E_{img} = E_{edge} = -|\nabla I(s)|^2 \tag{5}$$

$$E_{img} = E_{edge} = -\gamma\left|\nabla\left(G_\sigma(s) \times I(s)\right)\right|^2 \tag{6}$$

Equation (6) is used to reduce noise in which γ is a parameter that controls the amount of image energy. ∇ is Gradient operator and $G_\sigma(s) \times I(s)$ shows image convolution with a Gaussian filter including standard deviation σ.

2. 2. Gray-Level Co-Occurrence Matrix The gray-level co-occurrence matrix is used to extract second-order statistics from an image. The co-occurrence matrix represents the number of times two pixels occur in an image in the direction of a given vector, called the displacement vector. By changing the direction of the vector, we can obtain different characteristics for the texture. The co-occurrence matrix for an image I (x, y) is defined as Equation (7) [23]:

$$P(x,y) = Pr(x,y|d,\theta,G,W) \tag{7}$$

In the above equation, d is the distance; θ is the direction of movement; G is the quantization level; and W is the window size. Once the co-occurrence matrix is formed, various properties can be calculated. In this paper, a new feature is calculated by the Jensen-Tsallis divergence, which is described in the next section.

2. 3. Jensen -Tsallis Divergence Information theory is one of the new scientific branches in applied mathematics and electrical engineering in which information is quantified and studied from a mathematical point of view. Information theory is based on the science of statistics and probability, in which entropy is a fundamental quantity. According to this theory, the concept of entropy is introduced as a branch of image processing that estimates the amount of information in an image. Entropy can provide a sufficient level of image information. Since probabilities are represented by entropy, this is a meaningful measure for texture.

The desired entropy can be calculated from the distribution of the gray level of the image. Since the new external energy is defined based on it, entropy helps the active contour to be better absorbed towards the object boundary. In this case, if each gray level r occurs with a probability of p, then the occurring probability of a pixel can be defined as follows:

$$p_k = \frac{n_k}{N \times M} \quad k = 0, \dots, L-1 \tag{8}$$

n_k indicates the number of pixels on the gray surface k, and L represents the number of gray levels. M, N also represents the number of rows and columns in the image, respectively [39].

2. 4. Relative Entropy (Divergence) Shannon defined entropy for discrete random variables for the first time in 1948 [40]. This entropy is known as Shannon entropy that is described as follows:

$$S(P) = \sum_{k=0}^{L-1} P_k \, log(P_k^{-1}) \quad k = 0,1,2, \dots L-1 \tag{9}$$

Visually, entropy measures the amount of formation or uncertainty in a random variable related to a natural process. Divergence, also known as relative entropy, is the distance between two probability distribution functions. Divergences have been proposed as a measure of similarity between two probability distribution functions. In information theory, the most important divergence is the Kullback-Leibler (KLD) Divergence between P and Q [41], which is defined as follows:

$$KLD(P \parallel Q) = \sum_{k=0}^{L-1} log \frac{p_i}{q_i} \quad (10)$$

In classical information theory, this function, known as reciprocal entropy or directional divergence, measures uncertainty in relative rather than absolute terms [42]. The relative entropy is always non-negative and is zero only if P = Q. However, this is not a real distance between distributions since it is not symmetric and does not satisfy the triangle inequality [43]. When the Kullback-Leibler divergence is zero, we can expect similar (not exactly the same) behavior from two distributions, while a value of 1 indicates that the two distributions have opposite behaviors. A Jensen-Shannon Divergence (JSD) is a finite, symmetric, and smooth version of the Kullback-Leibler Divergence [44], that is defined as follows:

$$JSD(P \parallel Q) = \frac{1}{2} KLD(P \parallel Q) + \frac{1}{2} KLD(Q \parallel M) \quad (11)$$

where M = (P + Q) / 2 in probability information theory and statistics, JSD is a popular method for determining the similarity of two probability distributions. Jensen-Shannon divergence has the following properties: (A) it has mathematical properties and KLD divergence interpretations, and it offers simple interpretations within the framework of statistical physics and information theory; (B) it is symmetrical and works in a metric space; (C) it can be generalized to more than two distributions [45].

Various generalizations of Shannon entropy have been proposed in recent years. The generalization of the Shannon entropy standard is called the Tsallis Entropy as defined below [46]:

$$T^{\kappa}(P) = \frac{1 - \sum_{k=0}^{L-1} p_k^{\kappa}}{\kappa - 1} \qquad \kappa > 0, \kappa \neq 1 \quad (12)$$

The new form of divergence can be introduced by substituting Tsallis entropy with Shannon entropy in Equation (13). It is known as Jensen-Tsallis divergence and is defined as follows [45]:

$$JTD^{\kappa}(P, Q) = T^{\kappa}\left(\frac{P+Q}{2}\right) - \frac{1}{2}[T^{\kappa}(P) + T^{\kappa}(Q)] \quad (13)$$

In a picture with a background and a target object, an image histogram diagram shows the image content using two bell-shaped curves (probability density functions), one for the background and the other for the target object. We can separate the pixels related to background and target objects if we can calculate the boundary between these two probability density functions. Different methods have been proposed to obtain the distance between two probability density functions, such as Kolbeck-Liber, Cauchy-Schwarz, Jensen-Shannon, and Jensen-Tsallis Divergences [47]. This paper shows that the maximum Jensen-Tsallis divergence occurs at the boundary of two density functions, and thus can be recognized as a threshold between target and background objects. Jensen-Tsallis divergence is used by the proposed method to calculate new energy that, when added to Equation (2), will minimize the energy of the active contour exactly at the object boundary. This is described in the following section.

3. THE PROPOSED MODEL OF ACTIVE CONTOUR BASED ON JENSEN-TSALLIS DIVERGENCE BALLOON ENERGY

In this paper, a new active contour model based on Jensen-Tsallis divergence is proposed. As described previously, Jensen-Tsallis divergence can be used to determine the boundary between two textures in an image. Since the Jensen-Tsallis divergence is described based on the brightness level of an image, it does not work well in images with inhomogeneous textures. First, the image is described using the co-occurrence matrix algorithm, and then using the Jensen-Tsallis divergence, a new property is extracted from the co-occurrence matrix, which can mention the distinction between two textures in the image. This property is utilized to generate new balloon energy that greatly increases the convergence power of the active parametric contour toward the object boundary.

3. 1. Balloon Energy Based on Texture As described in section 1, the active contour model is expressed as Equation (2). The balloon energy based on the texture feature is added to the external energy of the contour equation to increase the strength of the active contour. Therefore, the new external energy is defined by Equation (14):

$$E_{ext} = E_{img} + \lambda \cdot E_{bal} \quad (14)$$

the balloon energy factor λ helps the active contour cross local minima. In the proposed method, E_{bal} is Equation (15):

$$E_{bal} = -\, T_{JTD}\big(I(s)\big) \times \vec{n}(s) \quad (15)$$

$\vec{n}(s)$ is the unit normal vector of the contour point.

3. 2. Algorithm for Segmentation Based on the Proposed Method The flowchart in Figure 1 illustrates how to segment a textured object in a textured background. The first step is to create the initial contour around the target object in the image. As Equation (4) moves this contour towards the boundary of the target object, an update to Equation (4) is required for a better

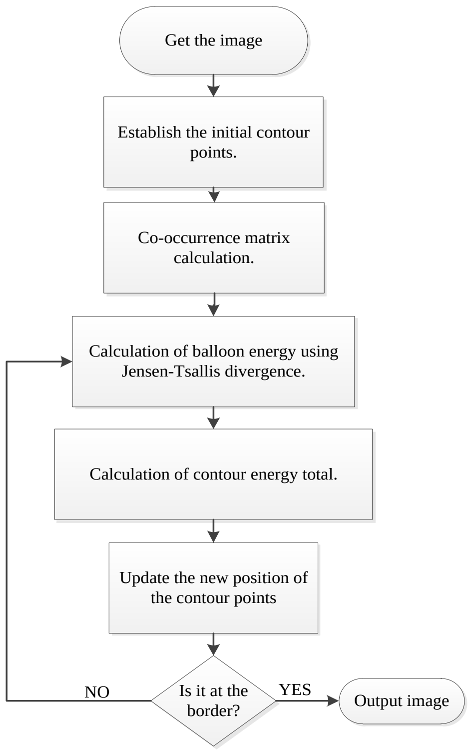

Figure 1. The flowchart for the proposed algorithm

active contour function. To achieve this, balloon energy is added to the active contour energy of Equation (4), which improves the active contour's function. The balloon energy is derived from the Jensen-Tsallis divergence. Jensen-Tsallis divergence is calculated by using the texture feature of the image. An image's texture feature can be computed using the GLCM matrix. Therefore, by combining the texture feature and Jensen-Tsallis divergence, novel balloon energy is created. By replacing the existing balloon energy in Equation (4), the total active contour energy equation will be updated. Since the Jensen-Tsallis divergence peaks at the boundary between two texture regions, and the Balloon energy is negative in Equation (15), the total contour equation (Equation (4)) is minimized at that boundary, leading to the active contour stopping.

4. EXPERIMENTS AND ANALYSIS OF RESULTS USING VISUAL AND MATHEMATICAL MEASURES

In this section, first under section 4.1, the divergence performance of Jensen-Tsallis is evaluated. According to the experiments, the divergence of Jensen-Tsallis at the boundary between two texture regions is maximum, so the active contour can better determine the boundary between the two regions. In section 4.2, the value of each variable used in the simulations is suggested based on the table. In section 4.3, the proposed method is compared to active contour methods based on discrete cosine conversion [16] and active contour methods based on filter bank properties [37]. Simulations are carried out in MATLAB R2016. In the experiments, two groups of images were used. The first group is artificial images from the Brodatz database [48], which consists of two types of textures. The second group is images from the Berkeley database that represent natural images. Images are selected in 256 × 256 sizes.

4. 1. Jensen-Tsallis Divergence Function

One texture image from Brodatz database is shown in Figure 2. The histogram shows that the gray levels of the image are L = 0, ..., 174. A part of another texture is placed inside the previous image to create an image with two textures. As can be seen in the second image, two bell-shaped curves indicate the two textures. As shown in Figure 2, the histogram has been enhanced with gray levels 174 to 221. This means that level 174 is the optimal threshold for detecting boundaries between textures. By applying the Jensen-Tsallis algorithm to the second image, it can be seen that the algorithm is maximized at the level of 168, which can be considered approximating the gray level 168 as the segmentation threshold. Based on the obtained threshold, it can be concluded that the Jensen-Tsallis algorithm can be useful for segmenting such images.

4. 2. Selecting Parameters

Before performing the tests, six significant parameters need to be adjusted.

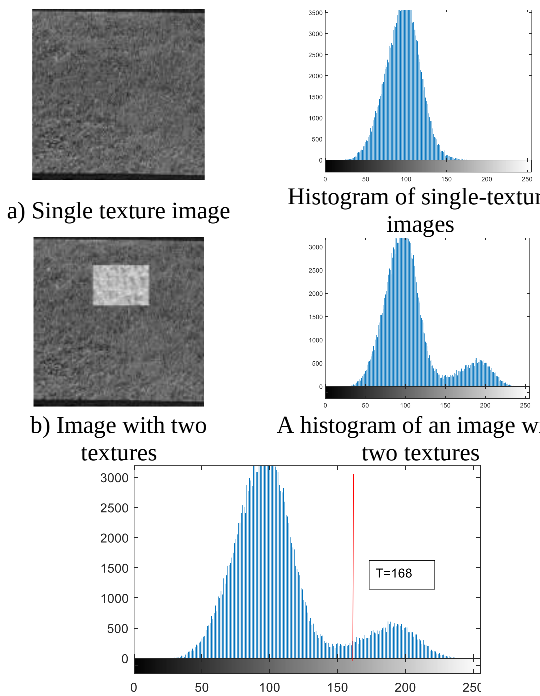

a) Single texture image

Histogram of single-texture images

b) Image with two textures

A histogram of an image with two textures

C) The result of Jensen-Tsallis divergence

Figure 2. Jensen-Tsallis divergence function

First, it examines the α and β parameters, which are the weights used to calculate the internal energy of a contour. Both the α and β coefficients are fixed and positive. A value of α is between [0,1] and a value of β is between [0,0.1]. A contour's length and its evolution rate are controlled by the α parameter, while its curvature is controlled by the β parameter. The active contour jumps over the object boundary if a large value of α is selected. The active contour becomes very slow and reaches the limit with a significant number of iterations if a value of α is set too small. In light of other parameters, a value of α between [0.2,0.5] is suggested. Generally, the second parameter β is chosen close to 0, otherwise, it might increase contour oscillation, which is undesirable. γ represents the energy factor of the image that helps the active contour move toward the object boundary. This value is chosen between [0.01, 0.001]. When the active contour faces a local minimization problem, the balloon energy factor λ helps the active contour cross local minima. The value of λ is selected between [0,1]. K is the coefficient of the Jensen-Tsallis function for determining the appropriate threshold for separating objects from backgrounds. An amount greater than zero is chosen. LCM is calculated by selecting a window around each pixel image. The size of that window is determined by W. We should not be too large as it will increase computations and the algorithm will slow down. If W is selected too small, the texture pattern may not be found. As described in the following Table 1, the above parameters have been used for this paper.

4. 3. Jensen-Tsallis K Parameters Selection

Section 4.1 explains that divergences create a threshold that the active contour can be used to locate the boundary of an object in the image. This paper uses the Jensen-Tsallis divergence for this purpose. A Jensen-Tsallis divergence is a generalized form of Jensen-Shannon divergence that has an adjustment parameter known as k. When the k-parameter is changed, a distinct threshold is created that can help the contour move to the boundary of the target object. If k = 1, the divergence is the same as the Jensen-Shannon divergence, and based on that, the segmentation operation is performed. The best value for k is chosen based on the images for which Ground Truth is available, along with the flowchart of Figure 3. Initially, k_0 is assumed for the parameter k, and the new position of the contour in the image is determined based on this assumption. Depending on the position of the contour and how many setpoints of the active contour have reached the boundary, the decision is made to update K, or to complete the process selection of parameter K. To update parameter K, it is increased one unit, then the percentage of setpoints that reach the boundary is calculated. This process is repeated until the contour approximates the object boundary or matches it. For updating K, adding one unit to the value of k, and calculating the percentage of points touching the boundary is adjusted. This process is repeated until the contour approximates the object boundary or matches it. The value of k at which the most contour setpoints reach the boundary is used as the divergence parameter (k). Next, other images are segmented using the K selected in the previous step. It is significant to note that the value of k is between zero and one. The k parameter in this study is selected by incrementing it by 0.0015 for each iteration and the most accurate value for k is about 0.08.

TABLE 1. Parameters values of the proposed algorithm

α	β	γ	λ	W
0.2	0.05	0.001	0.2	5

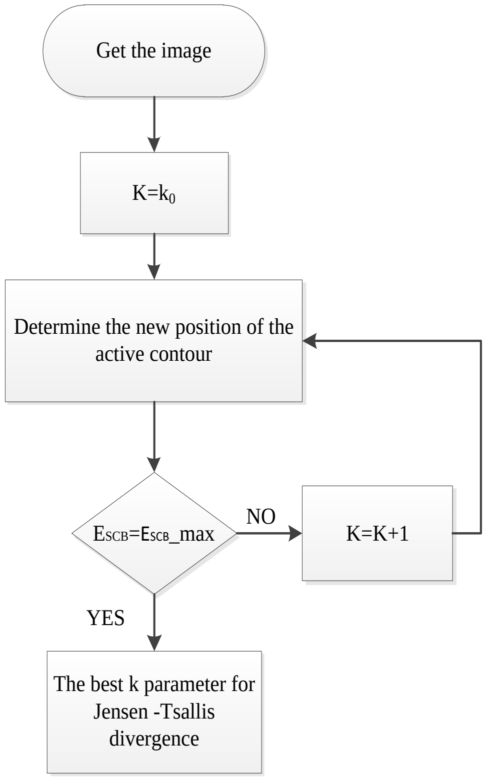

Figure 3. A flowchart for determining the best parameter K for the Jensen-Tsallis divergence function

4. 4. Test Results

In this section, the proposed method is applied to two groups of images (artificial images and natural images). Figure 4 demonstrates the superiority of Jensen- Tsallis divergence segmentation over other divergences. Figure 5 shows four artificial images with different textures, the first row of which shows the initial contour, and the fourth row shows the segmentation results for each image. In Figure 5, the second and third rows compare segmentation results for methods using discrete cosine conversions [16] and filter

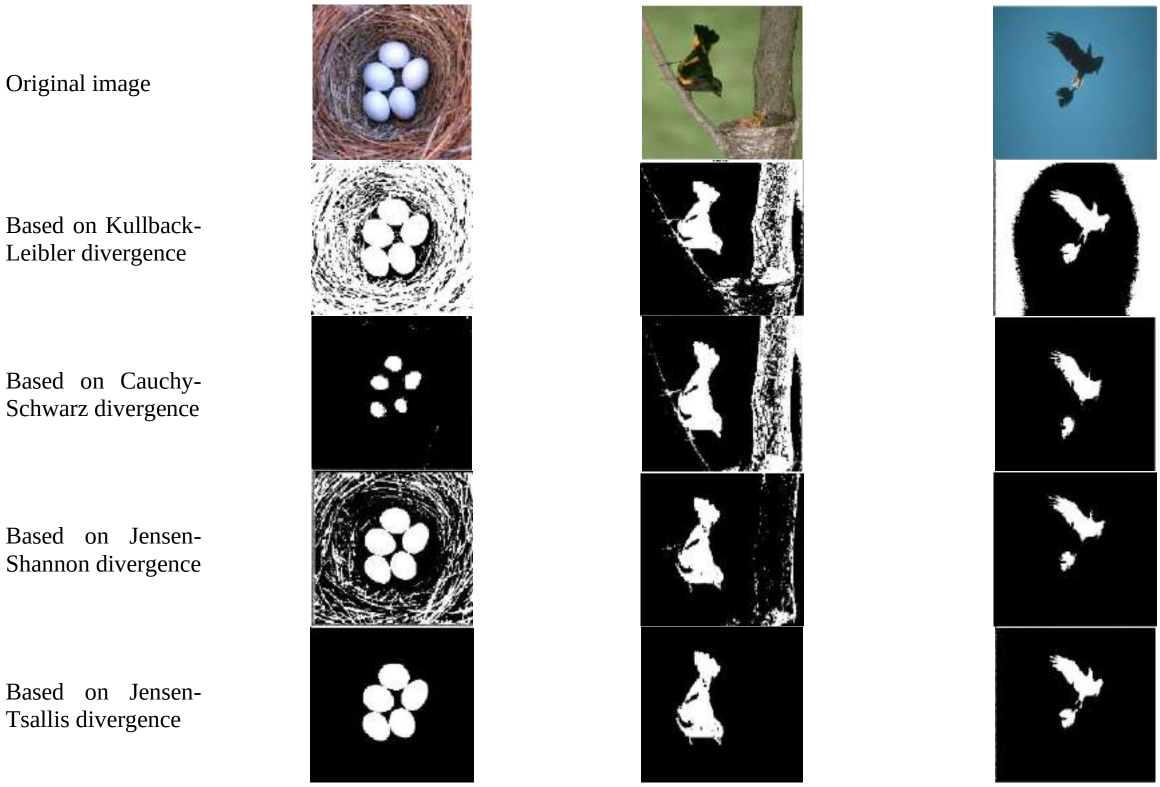

Figure 4. Segmented results of three images using four divergences

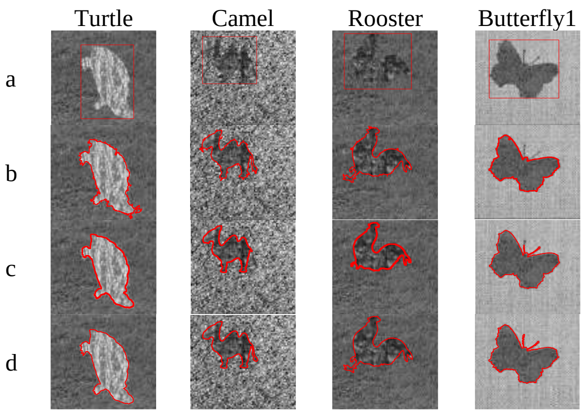

Figure 5. Comparison of segmentation results for synthetic images, a) initial contour, b) based on DCT [16], c) based on filter banks [37], and d) the proposed method

bank texture properties [37]. These simulations visually demonstrate the superiority of the proposed method over other methods. In Figure 6, the simulation results of the proposed method are shown on a variety of natural texture images to analyze its performance further.

4. 5. Performance of Jensen-Tsallis Divergence Compared to Other Divergences In section 3.2, various methods are described for obtaining the distance between two probability density functions, such as the Kullback-Leibler, Cauchy-Schwarz, Jensen-Shannon, and Jensen- Tsallis divergences. Distance between two probability density functions is crucial for distinguishing two areas within an image. Equation (13) states that the Jensen-Tsallis divergence function has a variable parameter k. The variable parameter allows the algorithm to better find the boundary between the two areas of the image and will allow the best segmentation to occur. When k is 1, the Jensen- Tsallis divergence is the same as the Jensen-Shannon divergence.

4. 6. Quantitative Evaluation When evaluating the performance of a method, just a visual comparison will not suffice, and the results should be analyzed through various parameters. Two quantitative parameters were used to compare our method with the previous approaches. The first of these is the Maximum Distance of the obtained Active contour from the Desired contour (MDAD) [49], which is defined as follows:

$$\mathrm{MDAD} = \max\left(\min\left(\mathrm{d}\left(\mathrm{C}(\mathrm{s}).\hat{\mathrm{C}}\right)\right)\right) \tag{16}$$

In this equation, d (C (s).C´) is the distance between the active contour and the desired contour C. Second, E_{SCB} [28] is used, whose equation is as follows:

$$E_{SCB} = \frac{SCB(N)}{N} \tag{17}$$

In Equation (17), N is the number of contour points and SCB(N) is the number of contour points that fall on the object boundary.

In Table 2, the MDAD values for all of the above images are shown after applying the three methods. In all images, a small amount of MDAD indicates a contour that is closer to the actual contour, which means better segmentation of the subject. In Table 3, a comparison of the E_{SCB} percentages for all test images is shown. Table 3 shows that, unlike the other two approaches, the proposed method has a higher E_{SCB} percentage, which means that more contour points are correctly located at the boundary.

4. 7. Robustness to Noise

To evaluate the noise performance, the proposed method was tested by adding two types of noise to a textured image. In the first experiment, Gaussian noise with zero mean and different variances was applied to the image and the robustness of the proposed method was evaluated. In Figure 7, the first row shows the Gaussian noisy images as well as the segmentation results. The next experiment included Salt and Pepper noise of various densities, added to the image for robustness evaluation.

TABLE 2. A comparison between the MDAD parameter in the proposed method and two other methods for segmenting textural images

Test images	Methods		
	DCT energy-based [16]	based on filter banks [37]	Proposed
Turtle	6.4	6.1	5.4
Camel	5.2	4.6	4.2
Rooster	5.0	4.7	4.5
Butterfly1	5.2	5.8	5.1
Tiger	11.2	3.3	3.2
Dog1	10.7	11.0	4
Dog2	9.7	10.1	9.6
Butterfly2	5.1	5.5	4.4

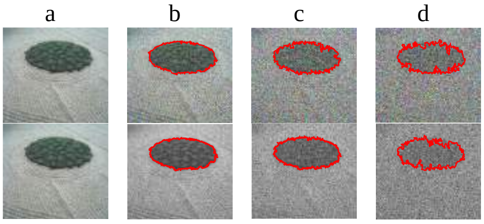

Figure 7. The effect of two types of noise on the input image and the segmentation results using the proposed method. Gaussian: a) original image, b) $\sigma^2 = 0.1$, c) $\sigma^2 = 1$, d) $\sigma^2 = 1.9$, Salt & Pepper: a) original image, b) d = 0.1, c) d = 0.5, d) d = 0.7

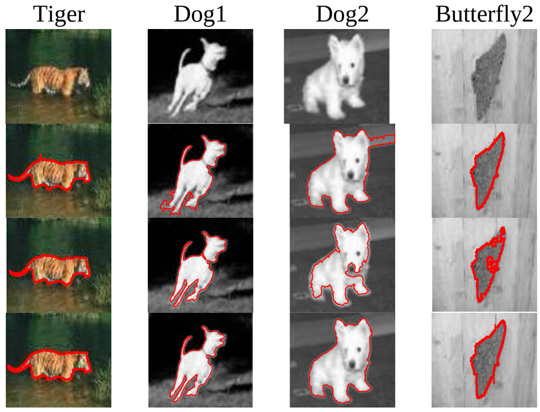

Figure 6. Comparison of segmentation results for natural images, a) original image, b) based on DCT [16], c) based on filter banks [37], and d) the proposed method

TABLE 3. A comparison between the E_{SCB} parameter in the proposed method and two other methods for segmenting textural images

Test images	Methods		
	DCT energy-based [16]	based on filter banks [37]	Proposed
Turtle	88.7	90.6	95
Camel	88.6	78.4	95
Rooster	87.3	77.9	94
Butterfly1	75	93.2	94.3
Tiger	91	83.1	93
Dog1	79.3	80.1	96.0
Dog2	75	83.3	87
Butterfly2	90.3	92.2	92

The second row shows noisy images and results of segmentation at noise densities of d = 0.1, 0.5, and 0.7, where, for example, d = 0.1 means 10% of the pixels in the image are noisy. Based on these experiments, the proposed method is typically able to segment objects correctly even if noise levels are high.

4. 8. Comparison of the Speed of the Proposed Method with other Methods

In this subsection, the time consumed for execution of the proposed algorithm is compared with two previous works. These three methods were tested on textured images with different and complex objects. The test images have 256 × 256 dimensions. For these eight images, Table 4 shows the convergence time of the three methods. According to Table 4, the proposed method takes less time than the other compared methods. Thus, the proposed algorithm is faster for the purpose of detecting textured objects.

TABLE 4. Comparing the convergence time of two previous methods and the proposed algorithm

Test images	Methods	Execution time (s)
Turtle	DCT energy-based [16]	44
	based on filter banks [37]	65
	Proposed	35
Camel	DCT energy-based [16]	43
	based on filter banks [37]	62
	Proposed	34
Rooster	DCT energy-based [16]	47
	based on filter banks [37]	64
	Proposed	36
Butterfly1	DCT energy-based [16]	45
	based on filter banks [37]	63
	Proposed	35
Tiger	DCT energy-based [16]	47
	based on filter banks [37]	66
	Proposed	34
Dog1	DCT energy-based [16]	45
	based on filter banks [37]	66
	Proposed	33
Dog2	DCT energy-based [16]	42
	based on filter banks [37]	63
	Proposed	32
Butterfly2	DCT energy-based [16]	43
	based on filter banks [37]	64
	Proposed	33

5. CONCLUSION

In this paper, a novel active contour model based on the Jensen-Tesalis divergence is presented that can be applied to artificial texture images as well as natural textures. To improve the active contour performance, the old external energy of the active contour has been combined with the new external energy based on the area information of the image. because information about the area helps the contour to be better absorbed towards the object's edge. The external energy is calculated based on the features extracted from the integration of the co-occurrence matrix method and Jensen-Tsallis divergence, and it corrects the previous external energy. MATLAB software was used to conduct the simulations. Experimental results show that segmentation results are better for both artificial and natural textures.

In addition to converging the contour to the exact boundary of the object, this method also solves the problem of local minimization. The method uses a parametric active contour, so it is faster than methods that use a level set contour. However, the use of the GLCM algorithm slows down the segmentation process, so it cannot be applied to online applications. The proposed model is limited in segmentation of one object at a time and is not developed for multiple objects simultaneously. This is the main limitation of all parametric active contour models. We plan to implement a new active contour model based on more flexible divergences in the future works.

6. REFERENCES

1. Eng, H.-L., Thida, M., Chew, B.-F., Leman, K. and Anggrelly, S.Y., "Model-based detection and segmentation of vehicles for intelligent transportation system", in 2008 3rd IEEE Conference on Industrial Electronics and Applications, IEEE. (2008), 2127-2132. https://doi.org/10.1109/ICIEA.2008.4582895
2. Huang, K. and Tan, T., "Vs-star: A visual interpretation system for visual surveillance", ***Pattern Recognition Letters***, Vol. 31, No. 14, (2010), 2265-2285, https://doi.org/10.1016/j.patrec.2010.05.029.
3. Salimi, A., Pourmina, M.A. and Moin, M.-S., "Fully automatic prostate segmentation in mr images using a new hybrid active contour-based approach", ***Signal, Image and Video Processing***, Vol. 12, No. 8, (2018), 1629-1637, doi.
4. Jabbari, S. and Baleghi, Y., "Segmentation of skin lesion images using a combination of texture and color information", ***Journal of Soft Computing and Information Technology***, Vol. 8, No. 4, (2020), 87-97, doi.
5. Mahdiraji, S.A., Baleghi, Y. and Sakhaei, S.M., "Skin lesion images classification using new color pigmented boundary descriptors", in 2017 3rd International Conference on Pattern Recognition and Image Analysis (IPRIA), IEEE. (2017), 102-107. https://doi.org/10.1109/PRIA.2017.7983026
6. Mahdiraji, S.A., Baleghi, Y. and Sakhaei, S.M., "Bibs, a new descriptor for melanoma/non-melanoma discrimination", in Electrical Engineering (ICEE), Iranian Conference on, IEEE. (2018), 1397-1402. https://doi.org/10.1109/ICEE.2018.8472701
7. Chen, Q., Sun, Q.-S., Heng, P.A. and Xia, D.-S., "Two-stage object tracking method based on kernel and active contour", ***IEEE Transactions on Circuits and Systems for Video Technology***, Vol. 20, No. 4, (2010), 605-609, https://doi.org/10.1109/TCSVT.2010.2041819.
8. Nikbakhsh, N., Baleghi, Y. and Agahi, H., "Maximum mutual information and tsallis entropy for unsupervised segmentation of tree leaves in natural scenes", ***Computers and electronics in Agriculture***, Vol. 162, (2019), 440-449, https://doi.org/10.1016/j.compag.2019.04.038.
9. Nikbakhsh, N., Baleghi, Y. and Agahi, H., "A novel approach for unsupervised image segmentation fusion of plant leaves based on g-mutual information", ***Machine Vision and Applications***, Vol. 32, No. 1, (2021), 1-12.
10. Nikbakhsh, N., Baleghi Damavandi, Y. and Agahi, H., "Plant classification in images of natural scenes using segmentations fusion", ***International Journal of Engineering***, Vol. 33, No. 9, (2020), 1743-1750.
11. Asvadi, A., Mahdavinataj, H., KARAMI, M.R. and Baleghi, Y., "Online visual object tracking using incremental discriminative

color learning", ***The CSI Journal on Computer Science and Enginering***, Vol. 12, No. 24, (2014), 16-28, doi.

12. Asvadi, A., Karami-Mollaie, M., Baleghi, Y. and Seyyedi-Andi, H., "Improved object tracking using radial basis function neural networks", in 2011 7th Iranian Conference on Machine Vision and Image Processing, IEEE. (2011), 1-5. https://doi.org/10.1109/IranianMVIP.2011.6121604
13. Asvadi, A., Karami, M. and Baleghi, Y., "Efficient object tracking using optimized k-means segmentation and radial basis function neural networks", ***International Journal of Information and Communication Technology Research***, Vol. 4, No. 1, (2012), 29-39, doi.
14. Asvadi, A., Karami, M. and Baleghi, Y., "Object tracking using adaptive object color modeling", in Proceeding of 4th Conference on Information and Knowledge Technology. (2012), 848-852.
15. Asvadi, A., Mahdavinataj, H., Karami, M. and Baleghi, Y., "Incremental discriminative color object tracking", in International Symposium on Artificial Intelligence and Signal Processing, Springer. (2013), 71-81.
16. Subudhi, P. and Mukhopadhyay, S., "A fast texture segmentation scheme based on active contours and discrete cosine transform", ***Computers & Electrical Engineering***, Vol. 62, (2017), 105-118, https://doi.org/10.1016/j.compeleceng.2017.04.021.
17. Sagiv, C., Sochen, N.A. and Zeevi, Y.Y., "Integrated active contours for texture segmentation", ***IEEE Transactions on Image Processing***, Vol. 15, No. 6, (2006), 1633-1646, https://doi.org/10.1109/TIP.2006.871133.
18. Abdelsamea, M.M., Gnecco, G. and Gaber, M.M., "An efficient self-organizing active contour model for image segmentation", ***Neurocomputing***, Vol. 149, (2015), 820-835, https://doi.org/10.1016/j.neucom.2014.07.052.
19. Shantkumari, M. and Uma, S., "Grape leaf segmentation for disease identification through adaptive snake algorithm model", ***Multimedia Tools and Applications***, Vol. 80, No. 6, (2021), 8861-8879.
20. Fu, X., Fang, B., Zhou, M. and Li, J., "Hybrid active contour driven by double-weighted signed pressure force for image segmentation", in ICASSP 2020-2020 IEEE International Conference on Acoustics, Speech and Signal Processing (ICASSP), IEEE. (2020), 2463-2467. https://doi.org/10.1109/ICASSP40776.2020.9054627
21. Cremers, D., Rousson, M. and Deriche, R., "A review of statistical approaches to level set segmentation: Integrating color, texture, motion and shape", ***International Journal of Computer Vision***, Vol. 72, No. 2, (2007), 195-215, doi.
22. Wang, Y. and Zeng, R., "Image segmentation algorithm based on geometric flow bandelets transformation particle replanting", ***Pattern Recognition Letters***, Vol. 116, (2018), 200-204, https://doi.org/10.1016/j.patrec.2018.10.021.
23. Wu, Q., Gan, Y., Lin, B., Zhang, Q. and Chang, H., "An active contour model based on fused texture features for image segmentation", ***Neurocomputing***, Vol. 151, (2015), 1133-1141, https://doi.org/10.1016/j.neucom.2014.04.085.
24. Caselles, V., Kimmel, R. and Sapiro, G., "Geodesic active contours", ***International Journal of Computer Vision***, Vol. 22, No. 1, (1997), 61-79, doi.
25. Kass, M., Witkin, A. and Terzopoulos, D., "Snakes: Active contour models", ***International Journal of Computer Vision***, Vol. 1, No. 4, (1988), 321-331, doi.
26. Nisirat, M.A., "A new external force for snake algorithm based on energy diffusion", ***International Journal of Machine Learning and Computing***, Vol. 9, (2019), 316-321.
27. Vard, A., Monadjemi, A., Jamshidi, K. and Movahhedinia, N., "Fast texture energy based image segmentation using directional walsh–hadamard transform and parametric active contour models", ***Expert Systems with Applications***, Vol. 38, No. 9, (2011), 11722-11729, https://doi.org/10.1016/j.eswa.2011.03.058.
28. Moallem, P., Tahvilian, H. and Monadjemi, S.A., "Parametric active contour model using gabor balloon energy for texture segmentation", ***Signal, Image and Video Processing***, Vol. 10, No. 2, (2016), 351-358, doi.
29. Bae, H.-J. and Jung, S.-H., "Image retrieval using texture based on dct", in Proceedings of ICICS, 1997 International Conference on Information, Communications and Signal Processing. Theme: Trends in Information Systems Engineering and Wireless Multimedia Communications (Cat., IEEE. Vol. 2, (1997), 1065-1068.
30. Ivins, J. and Porrill, J., "Active region models for segmenting medical images", in Proceedings of 1st International Conference on Image Processing, IEEE. Vol. 2, (1994), 227-231.
31. Schaub, H. and Smith, C.E., "Color snakes for dynamic lighting conditions on mobile manipulation platforms", in Proceedings 2003 IEEE/RSJ International Conference on Intelligent Robots and Systems (IROS 2003)(Cat. No. 03CH37453), IEEE. Vol. 2, (2003), 1272-1277.
32. Hamarneh, G., Chodorowski, A. and Gustavsson, T., "Active contour models: Application to oral lesion detection in color images", in Smc 2000 conference proceedings. 2000 ieee international conference on systems, man and cybernetics.'cybernetics evolving to systems, humans, organizations, and their complex interactions'(cat. no. 0, IEEE. Vol. 4, (2000), 2458-2463.
33. Vard, A.R., Moallem, P. and Nilchi, A.R.N., "Texture-based parametric active contour for target detection and tracking", ***International Journal of Imaging Systems and Technology***, Vol. 19, No. 3, (2009), 187-198, https://doi.org/10.1002/ima.20194.
34. Gao, M., Chen, H., Zheng, S. and Fang, B., "Feature fusion and non-negative matrix factorization based active contours for texture segmentation", ***Signal Processing***, Vol. 159, (2019), 104-118, https://doi.org/10.1016/j.sigpro.2019.01.021.
35. Subudhi, P. and Mukhopadhyay, S., "A statistical active contour model for interactive clutter image segmentation using graph cut optimization", ***Signal Processing***, Vol. 184, (2021), 108056, https://doi.org/10.1016/j.sigpro.2021.108056.
36. Wu, X., Tan, G., Li, K., Li, S., Wen, H., Zhu, X. and Cai, W., "Deep parametric active contour model for neurofibromatosis segmentation", ***Future Generation Computer Systems***, Vol. 112, (2020), 58-66, https://doi.org/10.1016/j.future.2020.05.001.
37. Badoual, A., Unser, M. and Depeursinge, A., "Texture-driven parametric snakes for semi-automatic image segmentation", ***Computer Vision and Image Understanding***, Vol. 188, (2019), 102793, doi: 10.1016/j.cviu.2019.102793.
38. Prince, J.L. and Xu, C., "A new external force model for snakes", in Proc. 1996 Image and Multidimensional Signal Processing Workshop, Citeseer. Vol. 3, No. 31, (1996), 1.
39. Mehri, A., Jamaati, M. and Mehri, H., "Word ranking in a single document by jensen–shannon divergence", ***Physics Letters A***, Vol. 379, No. 28-29, (2015), 1627-1632, https://doi.org/10.1016/j.physleta.2015.04.030.
40. Shannon, C.E., "A mathematical theory of communication", ***The Bell System Technical Journal***, Vol. 27, No. 3, (1948), 379-423.
41. Mezard, M. and Montanari, A., "Information, physics, and computation, Oxford University Press, (2009).
42. Klir, G., "Uncertainty and information: Foundation of generalized information theory: John willey and sons, new jersey", (2006).
43. Kieffer, J., "Elements of information theory (thomas m. Cover and joy a. Thomas)", ***SIAM Review***, Vol. 36, No. 3, (1994), 509-511.

44. Endres, D.M. and Schindelin, J.E., "A new metric for probability distributions", ***IEEE Transactions on Information Theory***, Vol. 49, No. 7, (2003), 1858-1860, https://doi.org/10.1109/TIT.2003.813506.

45. Angulo, J., Antolín, J., López-Rosa, S. and Esquivel, R., "Jensen–tsallis divergence and atomic dissimilarity for ionized systems in conjugated spaces", ***Physica A: Statistical Mechanics and its Applications***, Vol. 390, No. 4, (2011), 769-780, https://doi.org/10.1016/j.physa.2010.11.005.

46. Rajinikanth, V., Dey, N., Satapathy, S.C. and Ashour, A.S., "An approach to examine magnetic resonance angiography based on tsallis entropy and deformable snake model", ***Future Generation Computer Systems***, Vol. 85, (2018), 160-172, https://doi.org/10.1016/j.future.2018.03.025.

47. Baleghi, Y. and Rousseau, D., "An analytical proof on suitability of cauchy-schwarz divergence as the aggregation criterion in region growing algorithm", ***Image and Vision Computing***, Vol. 115, (2021), 104312, https://doi.org/10.1016/j.imavis.2021.104312.

48. Hersey, I., "Textures: A photographic album for artists and designers by phil brodatz", ***Leonardo***, Vol. 1, No. 1, (1968), 91-92.

49. Subudhi, P. and Mukhopadhyay, S., "A pyramidal approach to active contours implementation for 2d gray scale image segmentation", in 2016 International Conference on Wireless Communications, Signal Processing and Networking (WiSPNET), IEEE., (2016), 752-757.

Persian Abstract

چکیده

بخش بندی تصاویرِ بافتی، نقش مهمی در عملیات مختلف بینایی ماشین ایفا می کند. مدل‌های کانتور فعال یکی از کارآمدترین و محبوب‌ترین روش‌ها برای شناسایی هدف و بخش‌بندی اشیا در تصویر هستند. این مقاله یک مدل کانتور فعال پارامتری (PACM) با یک چارچوب کمینه‌سازی مقاوم بر اساس انرژی بافت تصویر ارائه می‌کند. ابتدا، ویژگی‌های بافت تصویر اصلی با استفاده از GLCM (ماتریس هم‌رخدادی سطح خاکستری) استخراج می‌شوند. پس از آن، بر اساس ویژگی‌های بافت GLCM در داخل و خارج از کانتور فعال، واگرایی جنسن–تسالیس انرژی‌ها محاسبه می‌شود. واگرایی جنسن–تسالیس با استفاده از معادله بالون به کانتور فعال پارامتریک اضافه می شود. واگرایی در مرز بین پیش زمینه و پس‌زمینه تصویر حداکثر است، که منجر به به حداقل رساندن معادله کانتور فعال در مرز جسم هدف می‌شود. این تابع انرژی کمینه سازی با ویژگی بافت می تواند از وجود حداقل های محلی در مدل های PACM جلوگیری کند. همچنین، برخلاف مدل‌های قبلی، مدل پیشنهادی فقط به کانتور اولیه نیاز دارد و به فاصله کانتور اولیه از شی هدف وابسته نیست. از نظر دقت و کارایی بخش‌بندی، آزمایش‌ها با تصاویر مصنوعی و طبیعی نشان می‌دهند که رویکرد پیشنهادی نتایج رضایت‌بخش‌تری نسبت به روش‌های اخیر به دست آورده است.

IJE TRANSACTIONS A: Basics Vol. 35, No. 05, (July 2022) 1268-1282

International Journal of Engineering

Journal Homepage: www.ije.ir

Location Sensitivity of Non-structural Component for Channel-type Auxiliary Building Considering Primary-secondary Structure Interaction

M. M. Rahman[a,b], T. T. Nahar[b], D. Kim*[c], D. W. Park[a]

[a] *Department of Civil and Environmental Engineering, Kunsan National University, 558 Daehak-ro, Gunsan-si, Jeollabukdo 54150, Republic of Korea*
[b] *Department of Civil Engineering, Pabna University of Science and Technology, Rajapur, Pabna 6600, Bangladesh*
[c] *Department of Civil and Environmental Engineering, Kongju National University, 1223-24 Cheonan-daero, Seobuk-gu, Cheonan, Chungcheongnam-do 31080, Republic of Korea*

PAPER INFO

Paper history:
Received 05 February 2022
Received in revised form 05 March 2022
Accepted 09 March 2022

Keywords:
Non-structural Components
Auxiliary Building
Zero-period Acceleration
Seismic Response
Primary-secondary Structure Interaction
Response Surface Methodology

ABSTRACT

To ensure the safe and stable operation of nuclear power plants (NPP), many non-structural components (NSCs) are actively associated with NPP. Generally, floor response spectrum (FRS) is used to design the NSCs. Nevertheless, it is essential to focus on the mounting position and frequency of NSCs which is normally ignored during the conventional design of NSCs. This paper evaluates the effect of mounting location for NSCs over the same floor in a channel-type auxiliary building. The modal parameter estimation is taken into account to capture the dynamic property of the NPP auxiliary building by the shake table test; which leads to the calibration of the finite element model (FEM). The calibration of FEM was conducted through response surface methodology (RSM) and the calibrated model is verified utilizing modal parameters as well as frequency response spectrum function. Finally, the location sensitivity was investigated by time history analysis (THA) under artificially generated design response spectrum compatible earthquakes and sine sweeps. The result showed that the right choice of location for NSCs can be an important measure to reduce the undesirable responses during earthquakes, which can reduce up to 30% horizontal and 70% vertical zero period acceleration (ZPA) responses in channel-type auxiliary buildings.

***doi**: 10.5829/ije.2022.35.07a.06*

1. INTRODUCTION

Earthquake (EQ) is a natural hazard and loads due to EQ have the greatest influence on nuclear power plant (NPP) structures. Therefore, the safety against EQ of structural and non-structural components (NSCs) in NPP is a critical concern. In particular, the safety concern of the NPP structures has significantly increased since the Fukushima Daiichi nuclear accident in Japan (2011) and the Gyeongju (2016) and Pohang (2017) EQs in South Korea [1, 2]. The auxiliary building (AB) is one of the main parts of NPP systems. AB is generally placed adjacent to the reactor containment structure that supports most of the auxiliary and safety-related systems and components [3]. The configuration for the structural and NSCs in NPP has been reported by Kwag et al. [4] as shown in Figure 1. NSCs are susceptible to earthquakes throughout the last few decades [5]. Some damages of NSCs due to EQ events are depicted in Figure 2, captured by Jiang [5]. The AB contains many substantial NSCs, i.e., pumps, heat exchanger, feedwater tanks, main control room, emergency diesel generator, fuel storage tanks, radioactive waste systems, chemical and volume control systems, etc. [3, 6]. In the context of safety assurance and operating the NPP, the seismic analysis, design, assessment, and evaluation of such NSCs are the most challenging issue. Besides, the distribution of the following NSCs plays a vital role in minimizing the seismic responses without addition and any structural modification.

*Corresponding Author Institutional Email: kim2kie@kongju.ac.kr (D. Kim)

Please cite this article as: M. M. Rahman, T. T. Nahar, D. Kim, D. W. Park, Location Sensitivity of Non-structural Component for Channel-type Auxiliary Building Considering Primary-secondary Structure Interaction, ***International Journal of Engineering, Transactions A: Basics***, Vol. 35, No. 07, (2022) 1268-1282

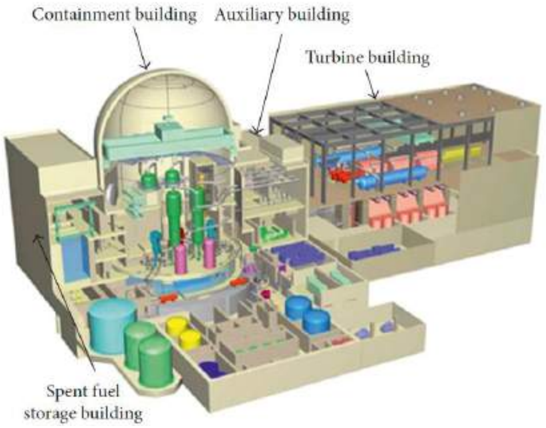

Figure 1. NPP with structural and NSCs systems [4]


Figure 2. Earthquake damage of NSCs [5]

The previous study focuses mainly on the vertical distribution of NSCs. Hur et al. [7] investigated the seismic performance of nonstructural components located in various locations throughout the AB and found that the probability of acceleration of NSCs on the first floor is greater than that of NSCs on the second floor. Mondal and Jain [8] recommend, for the design of NSCs and their attachments, amplification of lateral force that increases with an increase in vertical position of the NSCs should be considered. If the NSC is located on lower building floors and has a natural period equal to or greater than the building's second or third natural period, the responses of NSCs are amplified [9]. Merz and Ibanez [10] reported only for rough estimates of NSCs, floor response spectra (FRS) may be considered but estimating the mounting point response is desirable. According to Pardalopoulos and Pantazopoulou [11], the responses of NSCs are mainly controlled by the developed absolute spectral acceleration at the mounting point on the supporting building. However, there are no considerable investigations on the previous study for the response behavior of NSCs attached at different locations on the same floor.

This type of distribution can be very effective in response measures of NSCs; especially for the asymmetric building which is the main motivation of this study. This study evaluates the location sensitivity on NSCs on the same floor under earthquake excitation considering the primary-secondary structure interaction. To fulfill the objective of this study, the numerical investigations were conducted using a three-dimensional finite element model (FEM) developed by SAP2000 software [12] of a channel type AB. This building was designed and the shake table test program was organized by the Korea Atomic Energy Research Institute (KAERI). Among various modal parameter estimation (MPE) techniques, least-squares complex exponential (LSCE) was utilized for MPE using the shake table test results. LSCE approximates the correlation function using the sum of exponentially decaying harmonic functions [13-16]. After evaluating the modal parameters, the FEM was updated based on test results through a statistical tool, i.e., response surface methodology (RSM). Many researchers employed the RSM for FEM optimization due to its simplicity and effectiveness [17-23]. Then the evaluation was conducted using optimized FEM throughout the study.

2. AUXILIARY BUILDING

As demonstrated in Figure 3(a), this study was conducted using a channel type three-storied AB provided by KAERI. The overall dimension of the main part of the test specimen is 3650mm×2575mm×4570mm. The thicknesses of slabs, walls, and base assembly are 140mm, 150mm, and 400mm, respectively. The detailed dimensions of the test specimen are predicted in Figure 3(b).

2. 1. Shake Table Test The Earthquake Disaster Prevention Center at Pusan National University conducted this experimental program with the shaking table facility. This program was organized by KAERI for joint research on the Round Robin Analysis to evaluate the dynamic characteristics and to verify the numerical model for the AB in NPP. To capture linear response characteristics, natural frequencies, and vibration modes, the model was initially excited by a low-intensity random vibration (peak acceleration is 0.05g) in X and Y-directions separately [24].

The sensors, i.e., the accelerometers were installed as different arrays to record the responses under the excitation in X and Y direction. Figure 4(a) and Figure 4(b) show the accelerometer's location for X and Y-directional responses, respectively. Although the shake table test was directed for the Gyeongju earthquake with a loading sequence as 0.28g - 0.28g - 0.50g - 0.75g - 1.00 g, which was not considered in this study. The random vibration response was utilized for MPE and validates the linear FEM model of the AB.

(a)

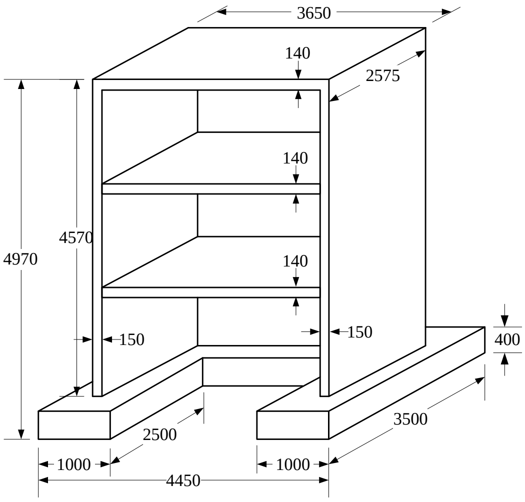

(b)

Figure 1. Test specimen (a) Anchorage system, (b) Dimension details

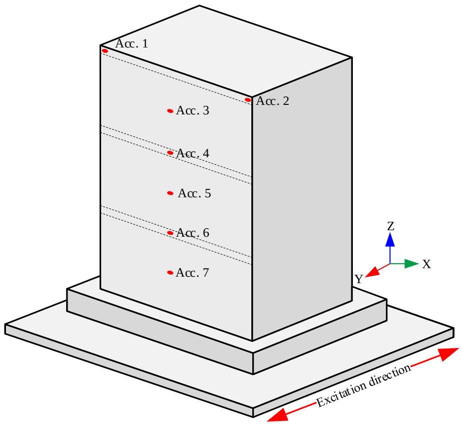

(b)

Figure 4. Sensor's location for record the responses (a) X-direction and (b) Y-direction

Figure 5(a) and Figure 5(b) represent the recorded acceleration response for the X and Y-direction, respectively. Here, the sensors denoted as "Acc. base", "Acc. 6", "Acc. 4" and "Acc. 1" are the sensors for the corresponding base, 1st floor, 2nd floor, and 3rd floor (roof) responses for each case, which is used for MPE.

In the study, the LSCE method was used for MPE. Figure 5(a) and Figure 5(b) illustrate the stabilization diagram for X and Y-direction the input-output responses of shake table test for probable model order and a frequency range up to 30 and 100Hz, respectively. The dot marker specifies the unstable poses whereas plus-shaped shows stable one in frequency and damping, and the circular marker represents the stale poles only in frequency. Furthermore, a solid blue line depicts the average response to help distinguish between physical and non-physical poles. The modal frequency of predominant modes, i.e., mode 1 (X-direction) and mode 2 (Y-direction) are 16.05 Hz and 23.02 Hz (Figure 6). The damping ratio for fundamental modes varies from

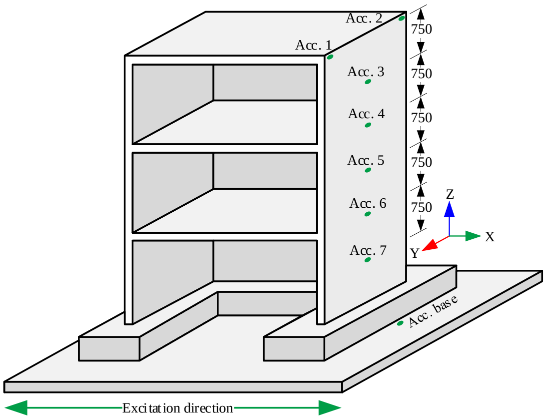

(a)

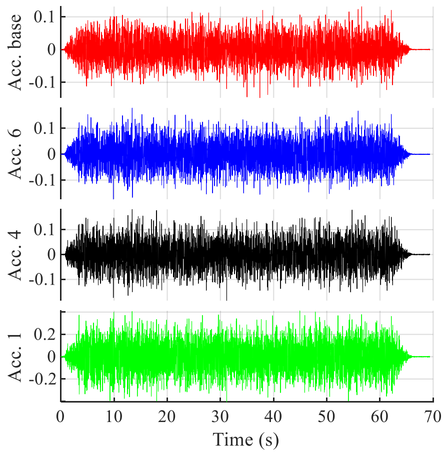

(a)

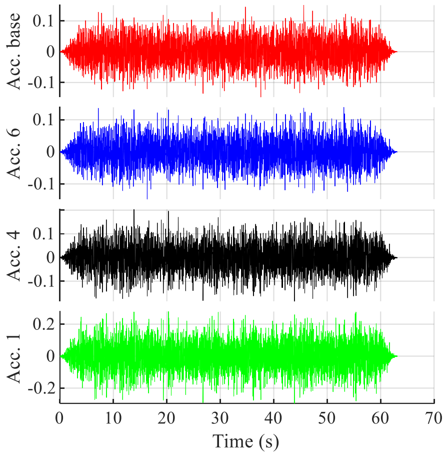

(b)

Figure 5. Stabilization diagram from shake table test results (a) X-direction and (b) Y-direction

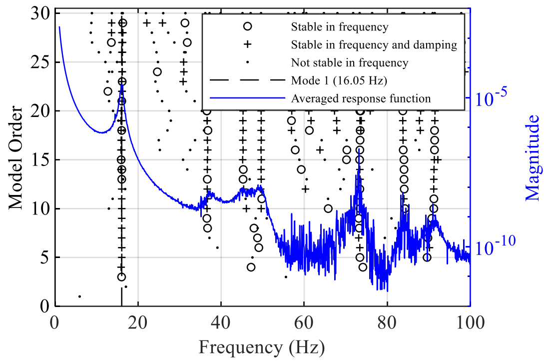

(a)

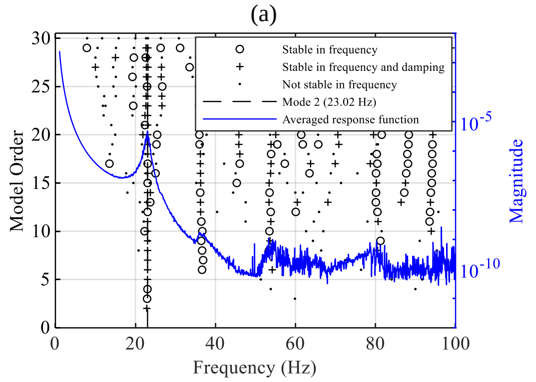

(b)

Figure 6. Stabilization diagram from shake table test results (a) X-direction and (b) Y-direction

3.18 to 3.74% according to the LSCE. Details about MPE using LSCE has been reported by Rahman et al. [24].

2. 2. Numerical Modeling and Updating For the dynamic evaluation of horizontally distributed NSCs, i.e., secondary structures on the KAERI channel type AB, a three-dimensional linear (elastic) FEM developed using commercially available structural analysis and design software SAP2000 is presented in this study [12]. SAP2000 allows the nonlinear behavior of materials to be modeled using either link/support elements or plastic hinges or multilayer shell elements [12, 25]. During the shake table test evaluation, the building was excited under the Gyeongju earthquake (2016) with a loading sequence as 0.28g - 0.50g - 0.75g - 1.00 g. When the excitation level was upto 1.00 g, there was no remarkable damage present in the structure [2]. Also, the maximum floor acceleration i.e., zero period acceleration (ZPA) responses in the incremental dynamic analysis (IDA) as shown in Figure 7, indicates that the building model shows approximately linear behavior up to 1g excitation level of peak table acceleration (PTA). Therefore, in this case, linear analysis was performed.

The slabs and walls were modeled as 4 noded shell elements. And the base assembly was considered as 8 noded solid elements. The maximum mesh size is assumed as 300mm. Figure 8(a) shows the full FEM with mesh view. As the shear wall elements were assumed as elastic, the effective stiffness was considered to reduce the strength for inelastic behaviors. Based on ACI [26], the effective stiffness was applied by reducing the moment of inertia (I_g) of the wall as $0.70I_g$ (as it was in uncracked condition). The NSCs were modeled by the linear spring available in SAP2000 which were rigidly connected with the mounting position as depicted in Figure 8(b). Three translational degrees of freedoms (Ux, Uy, and Uz) were activated at the top of NSCs. The second floor was considered for the placing of NSCs in this case study. The governing equation of motion for linearly modeled structure can be expressed as Equation (1) [27]:

$$M\ddot{u}(t) + C\dot{u}(t) + Ku(t) = -M\ddot{u}_g(t) \quad (1)$$

where $\ddot{u}$, $\dot{u}$, and u represent the acceleration, velocity, and displacement vector of the systems at any instant of time (t). $\ddot{u}_g$ denotes the ground motion excitation acceleration. The compiled mass (M), damping (C) and

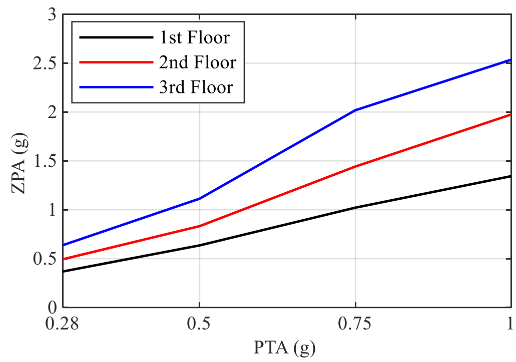

Figure 7. Shake table test, IDA Responses of building under Gyeongju earthquake (2016)

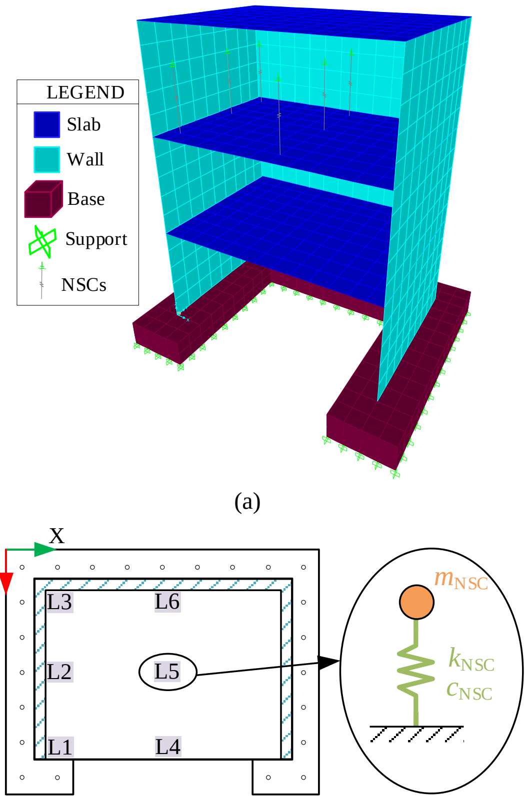

(b)

Figure 2. Numerical modeling (a) FEM with mesh view, and (b) probable location and SDF system of NSC

stiffness (K) matrices considering primary-secondary structure interaction can be expressed by Equation (2) [28]:

$$M = \begin{bmatrix} m_{\text{p}} & 0 \\ 0 & m_{\text{NSC}} \end{bmatrix};\quad C = \begin{bmatrix} c_{\text{p}} & 0 \\ 0 & c_{\text{NSC}} \end{bmatrix};\quad K = \begin{bmatrix} k_{\text{p}} & 0 \\ 0 & k_{\text{NSC}} \end{bmatrix} \tag{2}$$

where the mass matrix for primary and secondary structures are denoted by m_{p} and m_{NSC}, respectively. c_{p} and c_{NSC} denote the damping matrix of primary and secondary structures and finally, the stiffness matrix of primary and secondary structures are symbolized by k_{p} and k_{NSC}, respectively.

For the case study, the height and masses of NSCs are implicit as 1m and 200kg. The global damping matrix (C) of the coupled system was constructed by assuming the same damping ratio (3.4%) for primary and secondary structures. The stiffness of the NSCs was calculated as, $k_{\text{NSC}} = 4\pi^2 f_{\text{NSC}}^2 m_{\text{NSC}}$. The frequency range of NSCs was assumed as 5 to 50Hz. The evaluation was directed by a frequency increment of 5Hz.

Before going to the evaluation stage, the FEM was calibrated using RSM based on the updating of concrete material properties. The RSM is a collection of statistical models that may be used to model, analyze, optimize, and construct an empirical model [29]. It appears to be highly promising in terms of reducing the time and cost of model design and analysis [30].

Based on the statistical and mathematical analysis, RSM investigates the approximate relationship of the input design variables and the outputs in the form of a linear or polynomial equation. According to Rastbood et al. [19], a polynomial of higher-order must be used, if the system has curvatures and in most cases, the second-order is adequate to handle engineering problems [21]. Therefore, a second-order polynomial equation is considered for the RSM as shown in Equation (3) to get the response, y.

$$y = \beta_0 + \sum_{i=1}^{k} \beta_i x_i + \sum_{i=1}^{k} \beta_{ii} x_i^2 + \sum_{i=1}^{k} \sum_{i<j}^{k} \beta_{ij} x_i x_j + \varepsilon \tag{1}$$

where the intercept, linear, quadratic, and interaction terms are represented by β_0, β_i, β_{ii}, and β_{ij}, respectively; k denotes the number of input variables and ε is the offset or residual related to the experiments.

The central composite design (CCD) was used to estimate the number of the experiment of RSM for optimization of multi-objective input variables [31]. The total number of samples of runs of the experiment required for a complete CCD circumscribed is computed by $N = 2^k + 2k + n_c$; where k is the number of factors, i.e., input variables; and 2^k, $2k$, and n_c represent the number of cubic, axial, and center points. Here, each factor is studied at 5 levels as depicted in Figure whereas one center point, two cubic points, and two axial points are established at a distance -α and +α which represent new extreme values. The α value of 1.682 was calculated considering the full factorial CCD by $\alpha = [2^k]^{1/4}$ [32].

A total of 3 factors were used, i.e., Young's modulus (E), mass density (ρ), and Poisson's ratio (μ) as input variables, and 2 parameters are considered as responses, i.e., modal frequency of mode 1 $(F1)$ and mode 2 $(F2)$.

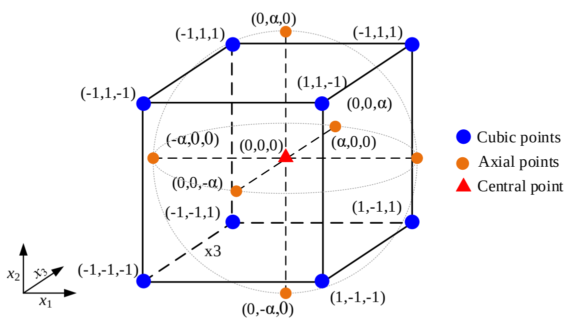

Figure 9. Central Composite Design (CCD) coded points

The lower and upper limit ranges of factors were chosen based on the normal concrete material properties. The range for density and Poisson's ratio was 0.15 to 0.25 [33] and 2200 to 2600 kg/m^3 [34], respectively. The Young's modulus was assumed to be 10 to 25 GPa. The cubic, axial and central points coded and actual values of 3 factors are presented in Table 1.

CCD created a total of 20 design points for E, ρ, and μ. Each set of design points and corresponding responses from FEM are listed in Table 2.

TABLE 1. Factors value range from CCD

Factors	Range	Cubic		Axial		Central
		Min.	Max.	Min.	Max.	
E	CVR	-1	+1	- α	+ α	0
	AVR	10	25	4.89	30.11	17.5
ρ	CVR	-1	+1	- α	+ α	0
	AVR	2200	2600	2063.64	2736.36	2400
μ	CVR	-1	+1	- α	+ α	0
	AVR	0.15	0.25	0.12	0.28	0.20

CVR: Coded value range; AVR: Actual value range; unit for actual values of E and ρ are GPa and kg/m3, respectively.

TABLE 2. Input factors and responses

Run order	Inputs/ Factors			Outputs			
	1	2	3	FEM		RSM	
	E (GPa)	ρ (kg/m3)	μ	F1 (Hz)	F2 (Hz)	F1 (Hz)	F2 (Hz)
1	4.89	2400	0.2	8.74	12.96	8.98	13.32
2	17.5	2400	0.17	16.64	24.71	16.67	24.76
3	10	2200	0.25	13.01	19.30	12.91	19.15
4	10	2600	0.25	11.97	17.75	11.85	17.58
5	17.5	2400	0.2	16.53	24.53	16.53	24.53
6	25	2600	0.25	18.93	28.07	18.98	28.15
7	17.5	2400	0.2	16.53	24.53	16.53	24.53
8	25	2200	0.15	20.71	30.75	20.78	30.86
9	25	2200	0.25	20.57	30.52	20.64	30.62
10	10	2200	0.15	13.10	19.45	13.00	19.30
11	17.5	2400	0.2	16.53	24.53	16.53	24.53
12	17.5	2400	0.2	16.53	24.53	16.53	24.53
13	30.11	2400	0.2	21.69	32.18	21.51	31.93
14	17.5	2400	0.2	16.53	24.53	16.53	24.53
15	17.5	2736.36	0.2	15.48	22.98	15.54	23.06
16	10	2600	0.15	12.05	17.89	11.93	17.71
17	17.5	2400	0.28	16.45	24.39	16.49	24.45
18	25	2600	0.15	19.05	28.29	19.11	28.37
19	17.5	2400	0.2	16.53	24.53	16.53	24.53
20	17.5	2063.64	0.2	17.83	26.46	17.84	26.48

The polynomial relationships between input variables (for E, ρ, and μ) and responses ($F1$ and $F2$) from Equation (3) can be presented by Equations (4). The coefficients for Equations (4) using RSM through the Minitab tool [35] are shown in Table 3.

$$F1 \text{ or } F2 = \beta_0 + \beta_1 E + \beta_2 \rho + \beta_3 \mu + \beta_{11} E^2 + \beta_{22} \rho^2 + \beta_{33} \mu^2 + \beta_{12} E\rho + \beta_{13} E\mu + \beta_{23} \rho\mu \tag{4}$$

The analysis of variance (ANOVA) established by Ronald Fisher in 1918, is an effective method for assessing the model fitness [36, 37]. To clarify the model fitness with data, the probability values (P-value) are compared to their significant level. Model terms with P-values less than 0.05 are considered significant. Model terms are significant if the P-value is less than 0.05. Table 4 indicates that for both responses ($F1$ and $F2$), E, ρ, E^2, and $E * \rho$ are significant model terms. The model F-value of 1409.60 and 1409.09 for $F1$ and $F2$, respectively implies the model is significant. The goodness of fit, i.e., R^2 is 99.92% and also the Predicted R^2 of 99.40% is in reasonable agreement with the Adjusted R^2 of 99.85% for both models (Table 5). Therefore, the model represented in Equation (4) for $F1$ and $F2$ prediction can be used.

To make it easier to grasp, the surface plot function was used to display a three-dimensional perspective of the response when the parameters were changed. Figures 10 and 11 show the response plot (surface and contour) using Equation (4) for corresponding output variables $F1$ and $F2$, respectively. It shows that the changing pattern of responses $F1$ and $F2$ with respect to factors E and ρ is approximately similar.

To get the optimized value of E, ρ, and μ the target values for $F1$ and $F2$ were set to 16.05 and 23.02 Hz. The optimized values for E, ρ, and μ were 15.75 GPa, 2400 kg/m^3, and 0.20, respectively (Figure 13). Figure 13 demonstrates that the values of $F1$ and $F2$ are matched

TABLE 3. Value for coefficients in Equations

Coefficients	Responses	
	$F1$	$F2$
β_0	18.03	26.69
β_1	1.0293	1.529
β_2	-0.00852	-0.01259
β_3	-4.1	-6.1
β_{11}	-0.008071	-0.011979
β_{22}	0.00000142	0.0000021
β_{33}	7.5	10.6
β_{12}	-0.000101	-0.00015
β_{13}	-0.033	-0.056
β_{23}	0.00025	0.00039

TABLE 2. ANOVA of RSM model

Responses	Source	DF	Adj SS	Adj MS	F-Value	P-Value
	Model	9	199.595	22.177	1406.60	0.000
	E	1	189.806	189.806	12038.58	0.000
	ρ	1	6.395	6.395	405.62	0.000
	μ	1	0.042	0.042	2.64	0.135
	E^2	1	2.970	2.970	188.40	0.000
	ρ^2	1	0.047	0.047	2.96	0.116
	μ^2	1	0.005	0.005	0.32	0.584
$F1$	$E*\rho$	1	0.185	0.185	11.72	0.007
	$E*\mu$	1	0.001	0.001	0.08	0.788
	$\rho*\mu$	1	0.000	0.000	0.00	0.956
	Error	10	0.158	0.016		
	Lack-of-Fit	5	0.158	0.032		
	Pure Error	5	0.000	0.000		
	Total	19	199.752			
	Model	9	439.571	48.841	1409.09	0.000
	E	1	417.989	417.989	12059.13	0.000
	ρ	1	14.085	14.085	406.36	0.000
	μ	1	0.120	0.120	3.46	0.093
	E^2	1	6.543	6.543	188.76	0.000
	ρ^2	1	0.101	0.101	2.92	0.118
	μ^2	1	0.010	0.010	0.29	0.602
$F2$	$E*\rho$	1	0.407	0.407	11.75	0.006
	$E*\mu$	1	0.003	0.003	0.10	0.758
	$\rho*\mu$	1	0.000	0.000	0.00	0.954
	Error	10	0.347	0.035		
	Lack-of-Fit	5	0.347	0.069		
	Pure Error	5	0.000	0.000		
	Total	19	439.918			

TABLE 5. RSM model summary

Responses	S	R^2 (%)	Adjusted R^2 (%)	Predicted R^2 (%)
$F1$	0.126	99.92	99.85	99.40
$F2$	0.186	99.92	99.85	99.40

S: standard deviation

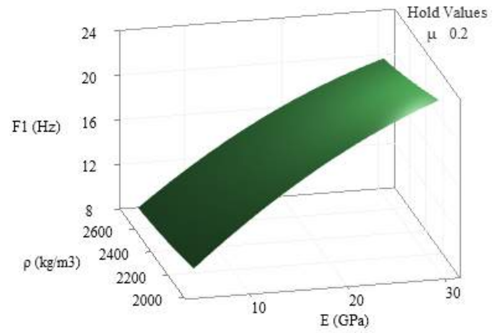

(a)

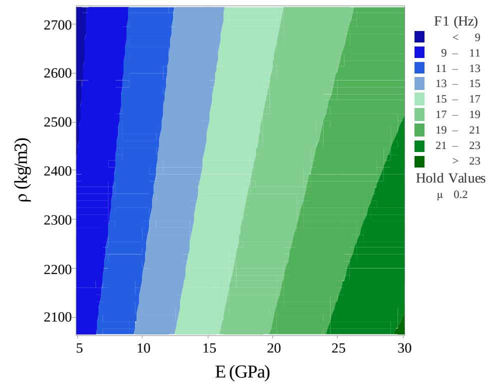

(b)

Figure 10. Response plot for $F1$ Vs E and ρ (a) surface plot and (b) contour plot

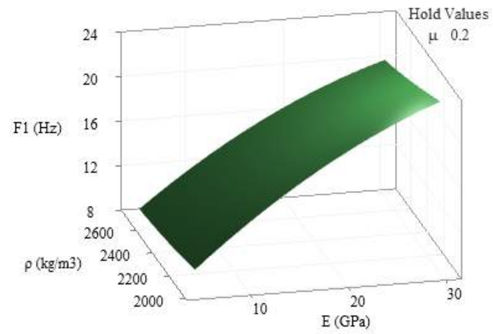

(a)

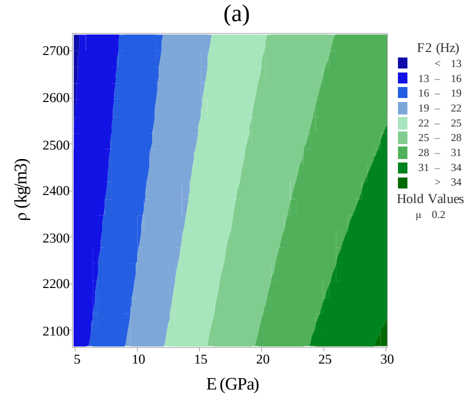

(b)

Figure 11. Response plot for $F2$ Vs E and ρ (a) surface plot and (b) contour plot

about 94 and 98%, respectively with the target values and the composite desirability is matched about 96%. Figure 12(a) depicted the comparison of actual responses of $F1$ and $F2$ were from FEM and the predicted responses using RSM (Equation (4)). The results from both models are near to the diagonal (dotted line), showing a good correlation between the predicted and actual values. Figure 12(b) shows that the maximum error between the fitted values from RSM and the FEM simulation is 2.75%, which also relay the use of the predicted model for further study.

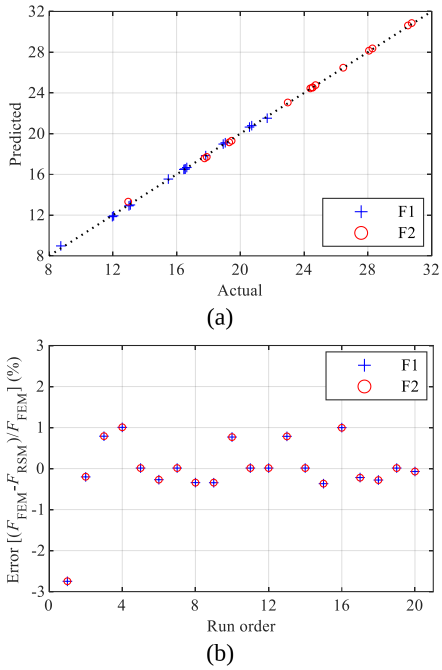

Figure 12. (a) Predicted vs. Actual plot, (b) Error of fitted values from RSM

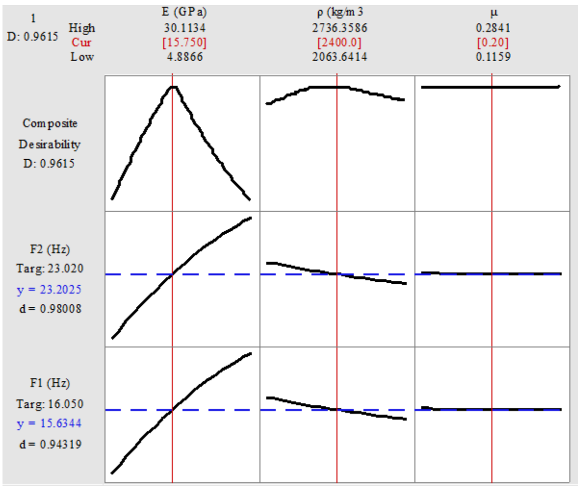

Figure 13. Modal frequency optimization plot (using Minitab tool)

2. 3. Model Validation

The FEM model was validated through the modal parameters and the response function under random seismic excitations. The MPE is the first stage in detecting structural deterioration and performing structural health monitoring (SHM) or assessing dynamic characteristics. The natural frequencies of the AB were obtained through modal analysis, and the results were compared with shake table test results to validate the studied FEM. The most fundamental frequencies (mode 1 and mode 2) are enlisted in Table 6 along with the error compared with test results. The mode shapes (first 6 modes) and their natural frequencies along with modal participation mass ratio (MPMR) from FEM are described in Figure .

Table 6 shows that the maximum error is 2.4%, which indicates the good agreement of the result from FEM in this study with compared to shake table test. Based on the LSCE methods, the magnitudes of the averaged response functions were plotted against frequencies as shown in Figure 15, which also indicate similar dynamic actions between the actual model and FEM. Therefore, the presented model was used for the NSC's location sensitivity evaluation.

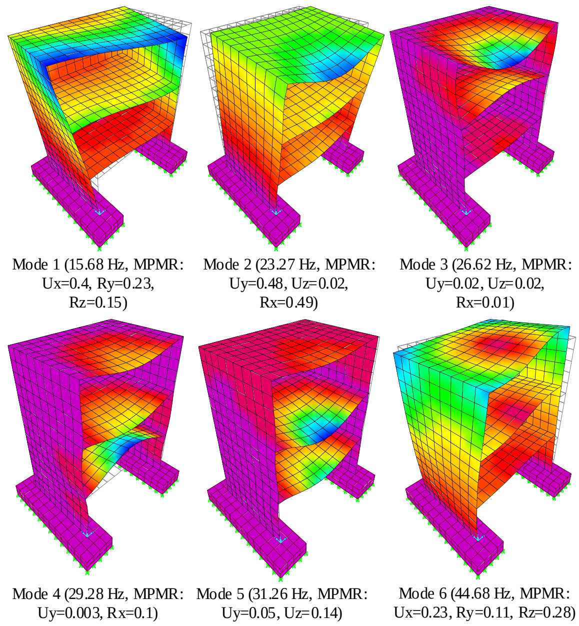

Figure 14. Fundamental mode shapes

TABLE 3. Fundamental frequencies of APR1400 NPP model

Modes	Modal frequency, F (Hz)		
	Shake table test	**FEM**	**Error** $\left(\frac{\lvert F_{test}-F_{FEM}\rvert}{F_{test}}\right)$
Mode 1	16.05	15.68	2.4%
Mode 2	23.02	23.27	1.1%

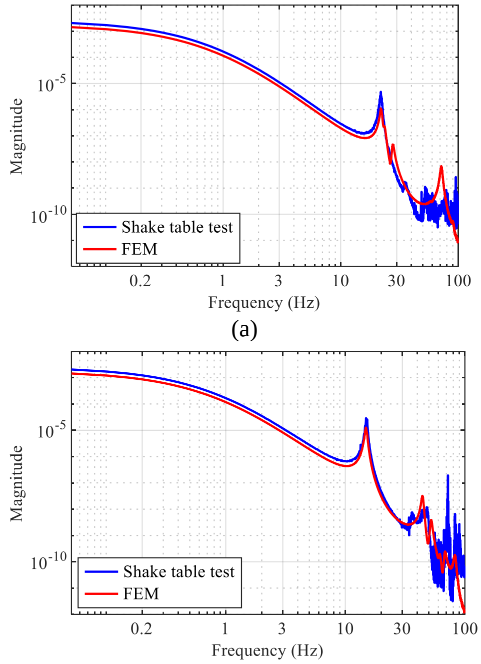

(a)

(b)

Figure 15. Average response function from shake table and FEM results (a) X-direction and (b) Y-direction

3. LOCATION SENSITIVITY ANALYSIS

3. 1. Input Ground Motions (GMs)

To evaluate the response behavior of NSCs, two types of input motions were used, i.e., 1) artificially generated GMs (AGMs) for the reference design response spectrum (DRS), and 2) Sine sweep with exiting frequency range 5 to 50 Hz. The artificial ground motion was generated for the response spectrum compatible accelerogram for the design of NPP, i.e., Regulatory guide 1.60 (RG 1.60) [38]. The GMs were applied in three directions, i.e., horizontal 1, H1 (X-direction); horizontal 2, H2 (Y-direction); vertical, V (Z-direction). The peak acceleration for the horizontal component was considered based on 2400 years of return period for seismic zone I (Korean peninsula), i.e., 0.22g [39]. The vertical component of GM was defined by scaling of the horizontal component by a factor of 2/3, i.e,e., 0.147 [40]. The generation was done using the Matlab-based computer tool "Quake_M" developed by Kim and Quake [41] as represented in Figure 16 and Figure 17(a). The root means square error of AGMs are 1.004%, 1.187%, and 0.729% for H1, H2, and V directions, which indicate the well-matched AGMs with target spectrum (RG 1.60). The sine sweep was used to confirm the response behavior for all excitation modes (target frequency range) of the NSCs. The amplitude of the sine sweep was the same as AGMs. Only the first 3s of sine sweep is presented in Figure 17(b) for the clear visualization, but actually it was 30s with frequency range 5 to 50 Hz.

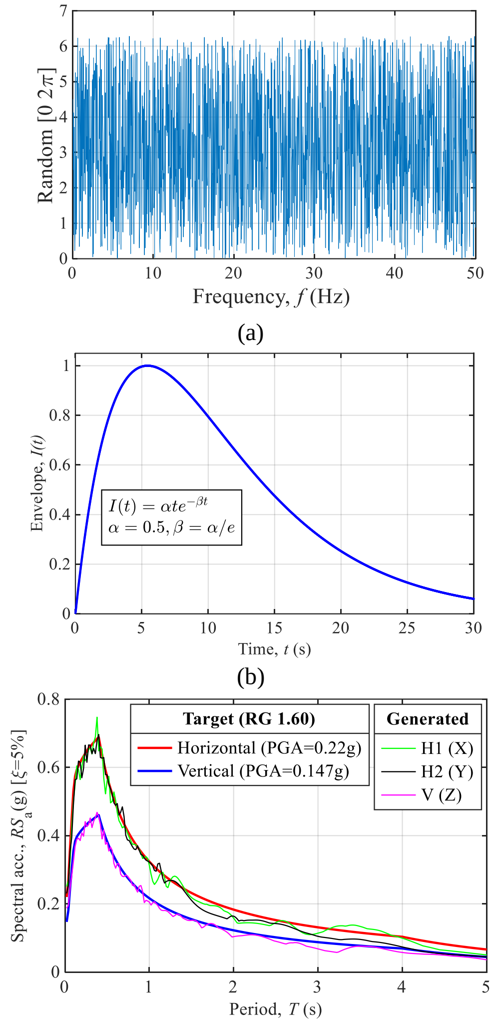

(a)

(b)

(c)

Figure 16. Generation of spectra-matched AGMs (a) Seed function: white noise, (b) Envelope function and (c) Target and generated response spectrum

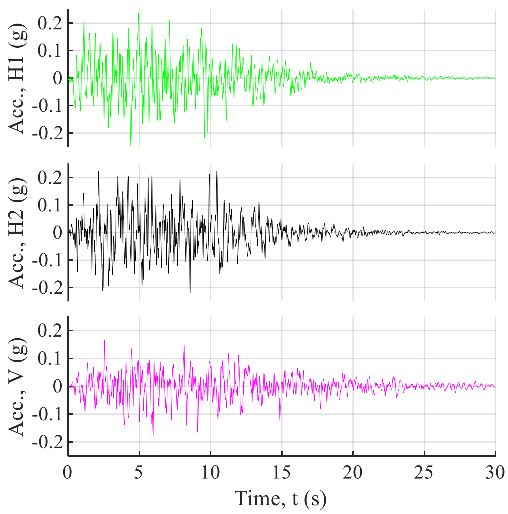

(a)

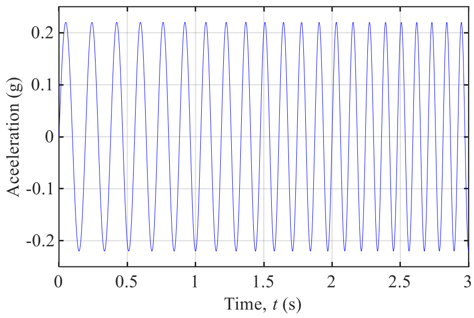

(b)

Figure 17. Input GMs (a) Generated AGMs (target: RG 1.60 DRS) and (b) Sine sweep (0~3s)

3. 2. Location Sensitivity To evaluate the location sensitivity of NSCs, a total of 6 probable locations as shown in Figure 8(b) were considered in this study, i.e., 1) L1 represents the response of outside or exposer corners, 2) L2 denotes the middle of the sidewall, 3) L3 indicates the responses for the inside corners, 4) L4, middle of the exposer side of the building, 5) L5, middle of the floor, 6) L6, which replicates the responses of the middle of the back wall of the AB. The study was conducted assuming the NSCs are distributed only on the second floor.

Zero period acceleration (ZPA) i.e., peak acceleration responses are compared for each direction and each loading. Figure 18 replicates the acceleration responses in X-direction whereas Figure 19 shows the corresponding ZPA of NSCs placed in each credible location, in which the responses for L1 and L4, L2 and L5, and L3 and L6 indicate the similar path under AGM and sine sweep as well. In the case of AGM excitation,

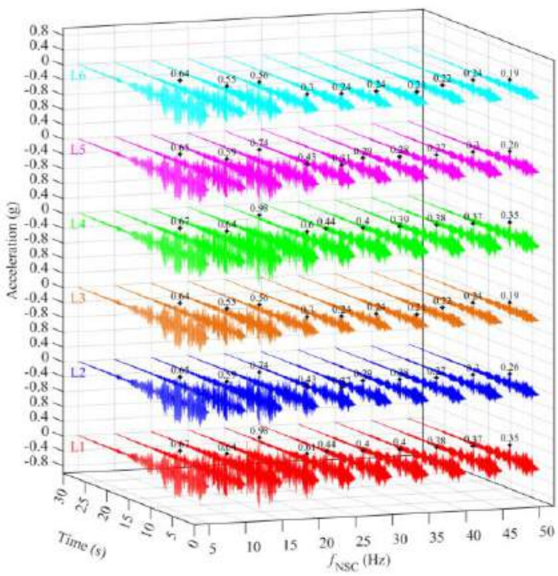

(a)

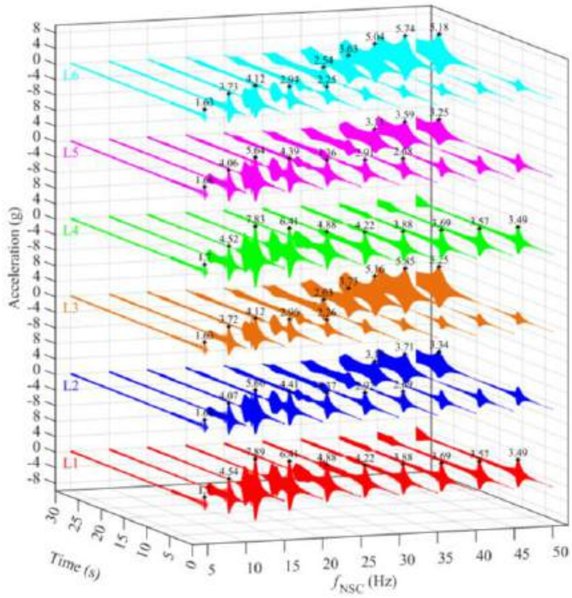

(b)

Figure 18. Acceleration responses in X-direction (a) AGM excitation (b) Sine sweep excitation

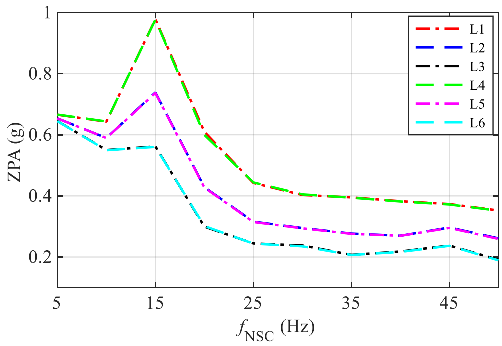

(a)

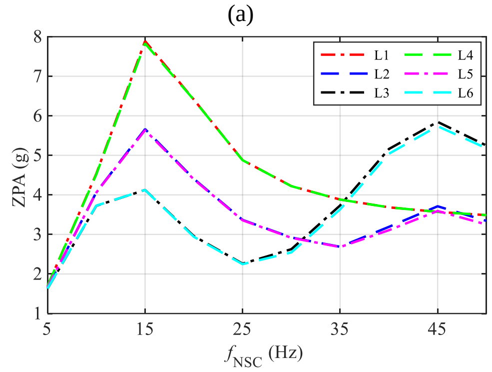

(b)

Figure 19. X-directional ZPA responses of NSC (a) AGM excitation (b) Sine sweep excitation

the NSCs with frequency around 15Hz were more vulnerable (in X-direction) under both excitation for location L1 and L4. Additionally, it confirms that the NSCs with higher frequency, i.e., around 45Hz were more sensitive for location L3 and L6 than others under sine sweep excitation.

In Y-directional response as shown in Figure 20, the AGM excitation indicates that if NSCs frequency is more than the 1st modal frequency of AB, the locations for L1, L2 and L3 are more sensitive than others, whereas the sine sweep excitation reveals that all locations were pursuing approximately the similar track and sensible frequency range was widespread (it may be 15Hz to 35Hz) (Figure 21). Figure 22 explores the time history responses for all considered locations in Z-direction. Figure 23 ensure that in Z-direction the riskier zone was in the middle of the exposure side, i.e., L4, and also the NSCs with frequency around 25Hz in this zone were more hazardous than others.

There are different types of NSCs in NPP, electrical cabinet is one of them, which plays a critical role in the

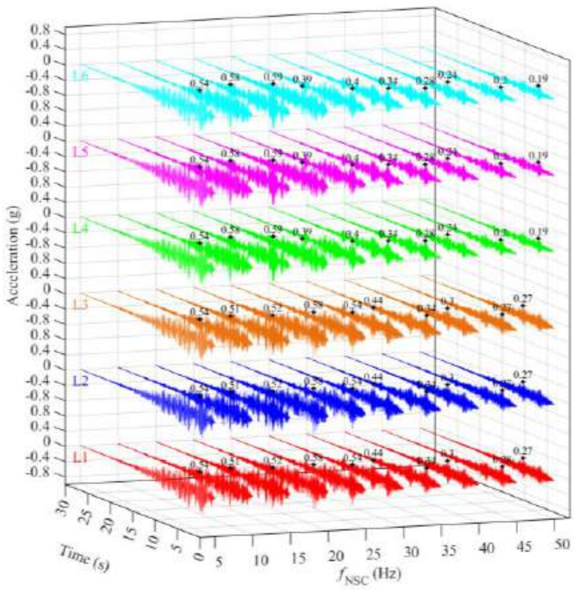

(a)

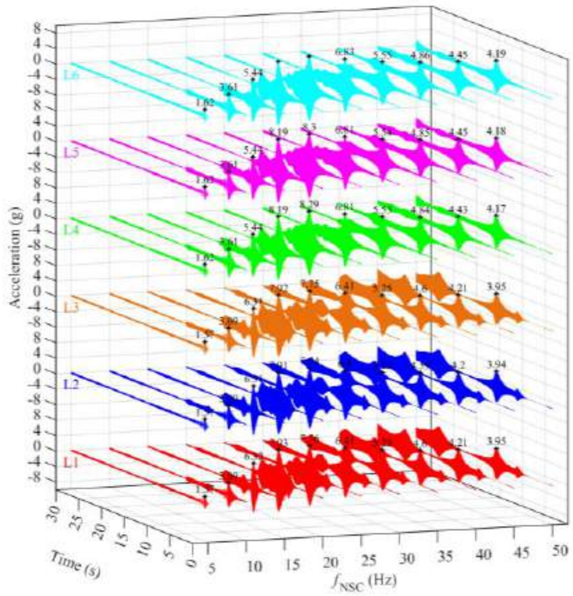

(b)

Figure 20. Acceleration responses in Y-direction (a) AGM excitation (b) Sine sweep excitation

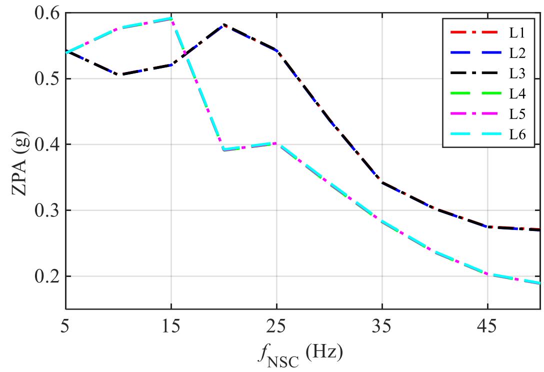

(a)

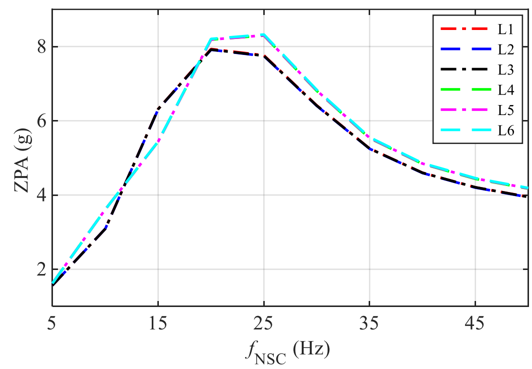

(b)

Figure 21. Y-directional ZPA responses of NSC (a) AGM (b) Sine sweep excitation

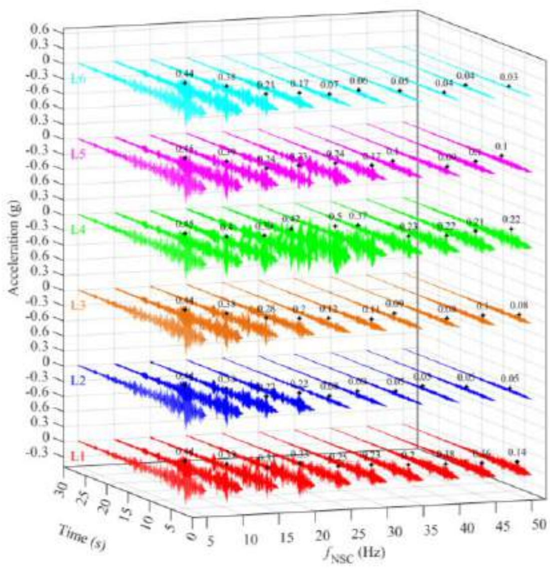

(a)

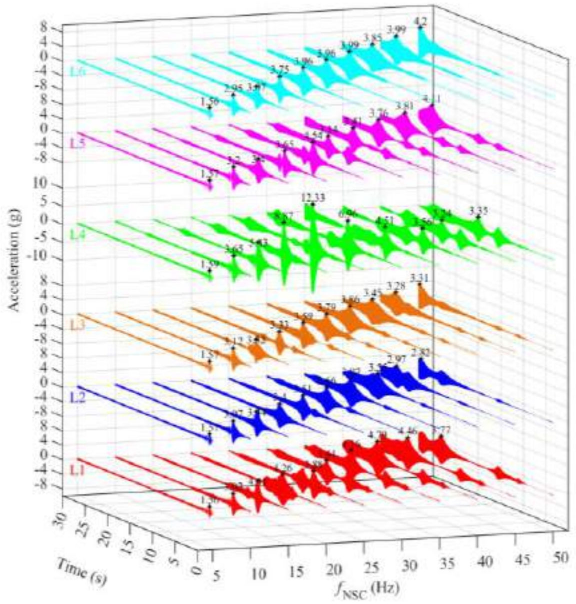

(b)

Figure 22. Acceleration responses in Z-direction (a) AGM excitation (b) Sine sweep excitation

proper functionality of NPP [42]. Like other NSCs, the cabinet is also acceleration sensitive so it can be susceptible to the high-frequency input motions. Here, as a case study, a single electrical cabinet was used to check the location sensitivity on the response under AGMs. The properties, i.e., stiffness (2897kN/m) and mass (287kg) of the cabinet were obtained from Salman et al. [28]. The cabinet was modeled for both directions, i.e., X and Y-directions using same the mass and stiffness values (Z direction was considered as fully stiff). Figure 24(a) shows the cabinet response spectrum under AGMs and it reflects that the location L1 and L4 give 61.8% more peak spectrum acceleration than L3 and L6 for X-direction. Similarly, in Y-directional responses, the L4, L5, and L6 were more sensible (21.5%) than other locations (Figure 24(b)). So, the cabinet or other NSCs distribution over the same floor is very important to get the proper in-cabinet response spectrum for selecting the engineering demand parameters (EDP). From Figure 25, it can be concluded that considering the ZPA as EDP, the L3 location is the best choice for electrical cabinet, which can provide safety of devices in the cabinet by lowering (around 42% in X and 15% in Y-direction) the ZPA responses.

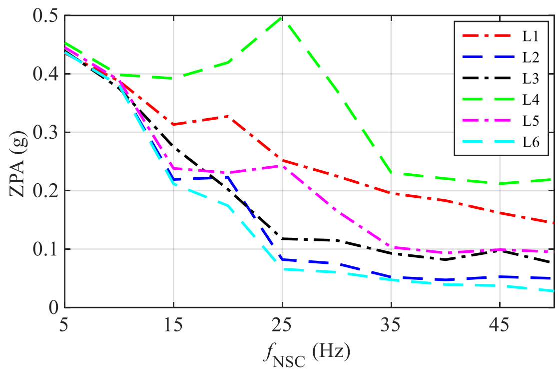

(a)

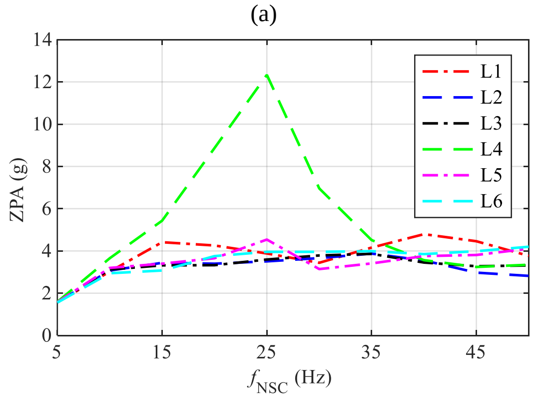

(b)

Figure 23. Z-directional ZPA responses of NSC (a) AGM excitation (b) Sine sweep excitation

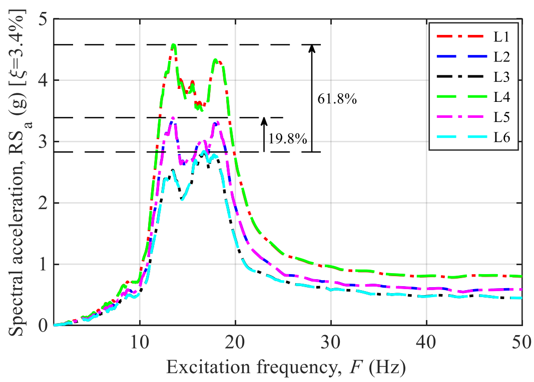

(a)

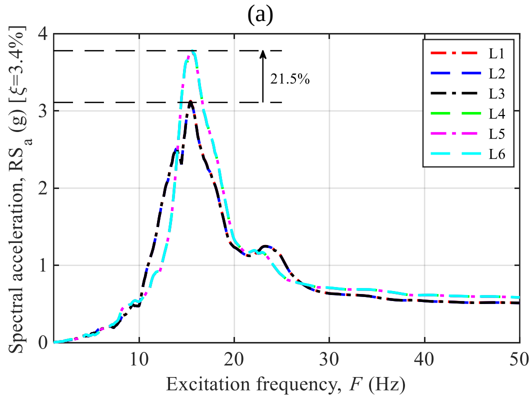

(b)

Figure 24. Response spectra of electrical cabinet under AGM (a) X-direction, (b) Y-direction

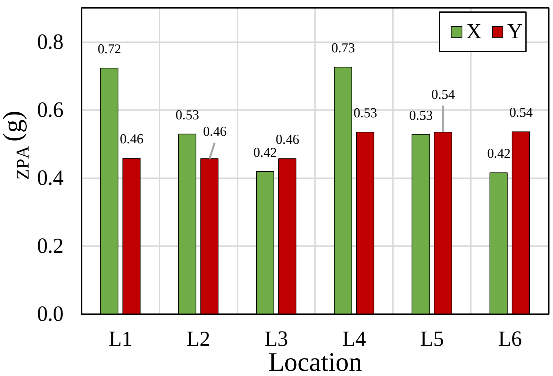

Figure 25. ZPA responses of the cabinet under AGM

4. CONCLUSIONS

The effects of the distribution of NSCs over the same floor in an AB under seismic excitations have been focused. Most of NSCs in NPP are acceleration sensitive and the floor acceleration can differ in the different mounting positions of NSCs. The flexibility of floor and combination of predominant modes with translational and torsional effects (especially in channel-type buildings) can lead to diverse responses of them in different locations. Therefore, the location sensitivity needs to be assessed before placing the NSCs in NPP to reduce the responses. KAERI channel type AB was acted here as the reference for developing the FEM to capture the goal through numerical evaluation. The FEM was calibrated using RSM and the calibrated model was used for seismic analysis under AGMs and sine sweep excitation for NSCs with frequency range 5 to 50Hz, which was rigidly mounted on six different locations. Finally, the sensitivity of the response of NSCs was evaluated for different locations. The key findings and conclusions from the results can be summarized as follows:

• In X-direction, the exposer side corners (L1) and mid positions (L4) are more vulnerable especially if the frequency of NSCs (around 15 Hz) are around the first mode of AB. Although, the inside corners (L3) and middle of the back wall (L4) show lower responses for AGMs whereas sine sweep confirms that after 30 Hz (frequency of NSCs) L3 and L4 increase the responses remarkably (especially around 45 Hz).

• In Y-direction, if the NSCs frequency is less than 15Hz the exposure corners (L1), middle of the sidewall (L2), and inside corners (L3) are more sensitive. If the frequency is more than 20Hz the response behavior changes and in this case, the middle of the exposure side (L4), middle of the floor (L5), and middle of the back wall (L6) show more sensitivity. However, under sine sweep, the sine sweep excitation reveals that all locations are pursuing approximately a similar track and sensible frequency range is widespread (around 2nd and 3rd modes of the AB).

• In Z-direction, the riskier zone in the middle of the exposure side (L4), and also the NSCs with frequency around 25Hz in this zone is more hazardous than others.

• The location selection of NSCs can be reduced up to 30% horizontal (X or Y-direction) and 70% vertical ZPA responses which can lead to the economic design of NSCs as there is no need to consider any additional measures, just the right choice of mounting positions based on their vibration frequency.

• In the case of the cabinet, the inside corners (L3) can be a good choice for the placement and the middle of the exposure side (L4) will be the worst choice. Placing at L3 can reduce the maximum cabinet response spectrum by around 62% in X-direction and 22% in Y-direction, which were measured under AGMs excitation.

4. FUNDING

This work was supported by the National Research Foundation of Korea (NRF) grant funded by the Korea government (MSIT), Grant No.: 2021R1A4A1031509.

5. REFERENCES

1. Kim, N. and Kim, M., "Investigation of existing researches for seismic fragility assessment of fuel assembly in NPPs", in Transactions of the Korean Nuclear Society Virtual spring Meeting, Online, Korean Nuclear Society, (2021), 2021.
2. Kim, M., Jung, J.-W., Ha, J.-G., Hahm, D. and Moon, H.S., *The Shaking Table Test of Shear Wall Structure for Seismic Performance Evaluation of Nuclear Power Plants*. 2021, Korea Atomic Energy Research Institute: Daejeon, Korea.182.
3. NRC, U.S. *Auxiliary building*. 2021 March 09, 2021 [cited 2021 July 01]; Available from: https://www.nrc.gov/reading-rm/basic-ref/glossary/auxiliary-building.html.
4. Kwag, S., Ju, B. and Jung, W., "Beneficial and Detrimental Effects of Soil-Structure Interaction on Probabilistic Seismic Hazard and Risk of Nuclear Power Plant", ***Advances in Civil Engineering***, Vol. 2018, (2018), 2698319. DOI: 10.1155/2018/2698319.
5. Jiang, W., "Direct Method of Generating Floor Response Spectra", University of Waterloo, Civil and Environmental Engineering, Waterloo, Canada, Doctoral Thesis, (2016),
6. KEPCO and KHNP, *Status Report – APR1400*. 2020, Korea Electric Power Corporation and Korea Hydro & Nuclear Power Co., Ltd. .
7. Hur, J., Wang, Z., Shafieezadeh, A. and Kim, M., "Seismic reliability analysis of NPP's nonstructural components using surrogate models", in 13th International Conference on Applications of Statistics and Probability in Civil Engineering, Seoul, South Korea, (2019).
8. Mondal, G. and Jain, S.K., "Design of non-structural elements for buildings: A review of codal provisions", ***The Indian Concrete Journal***, Vol. 79, (2005), 22-28.
9. Chaudhuri, S.R. and Villaverde, R., "Effect of building nonlinearity on seismic response of nonstructural components: A

parametric study", ***Journal of Structural Engineering***, Vol. 134, No. 4, (2008), 661-670. DOI: 10.1061/(ASCE)0733-9445(2008)134:4(661).

10. Merz, K. and Ibanez, P., "Guidelines for estimation of cabinet dynamic amplification", ***Nuclear Engineering and Design***, Vol. 123, No. 2-3, (1990), 247-255. DOI: 10.1016/0029-5493(90)90244-R.
11. Pardalopoulos, S.I. and Pantazopoulou, S.J., "Seismic response of nonstructural components attached on multistorey buildings", ***Earthquake Engineering & Structural Dynamics***, Vol. 44, No. 1, (2015), 139-158. DOI: 10.1002/eqe.2466.
12. CSI, *Getting Started With SAP2000 (Integrated Solution for Structural Analysis and Design)*. 2018, Computers and Structures, Inc.: Berkeley, CA, USA.75.
13. Kim, B.H., Stubbs, N. and Park, T., "A new method to extract modal parameters using output-only responses", ***Journal of Sound and Vibration***, Vol. 282, No. 1, (2005), 215-230. DOI: 10.1016/j.jsv.2004.02.026.
14. Cara, J., "Modal identification of structures from input/output data using the expectation–maximization algorithm and uncertainty quantification by mean of the bootstrap", ***Structural Control and Health Monitoring***, Vol. 26, No. 1, (2019), e2272. DOI: 10.1002/stc.2272.
15. Park, B.-H. and Kim, K.-J., "Vector ARMAX modeling approach in multi-input modal analysis", ***Mechanical Systems and Signal Processing***, Vol. 3, No. 4, (1989), 373-387. DOI: 10.1016/0888-3270(89)90044-7.
16. Brown, D.L., Allemang, R.J., Zimmerman, R. and Mergeay, M., "Parameter estimation techniques for modal analysis", ***SAE Technical Papers***, Vol. 88, No. 1, (1979), 828-846. DOI: doi.org/10.4271/790221.
17. Huang, W., Pei, M., Liu, X., Yan, C. and Wei, Y., "Nonlinear optimization of orthotropic steel deck system based on response surface methodology", ***Research***, Vol. 2020, (2020), 1303672. DOI: doi.org/10.34133/2020/1303672.
18. Cao, A.-T., Nahar, T.T., Kim, D. and Choi, B., "Earthquake risk assessment of concrete gravity dam by cumulative absolute velocity and response surface methodology", ***Earthquakes and Structures***, Vol. 17, No. 5, (2019), 511-519. DOI: 10.12989/eas.2019.17.5.511.
19. Rastbood, A., Gholipour, Y. and Majdi, A., "Finite element based response surface methodology to optimize segmental tunnel lining", ***Engineering, Technology & Applied Science Research***, Vol. 7, No. 2, (2017), 1504-1514. DOI: 10.48084/etasr.1045.
20. Sadeghifar, M., Sedaghati, R., Jomaa, W. and Songmene, V., "Finite element analysis and response surface method for robust multi-performance optimization of radial turning of hard 300M steel", ***The International Journal of Advanced Manufacturing Technology***, Vol. 94, No. 5, (2018), 2457-2474. DOI: 10.1007/s00170-017-1032-4.
21. Nahar, T.T., Cao, A.-T. and Kim, D., "Risk assessment of aged concrete gravity dam subjected to material deterioration under seismic excitation", ***International Journal of Concrete Structures and Materials***, Vol. 14, No. 1, (2020), 53. DOI: 10.1186/s40069-020-00430-z.
22. Tran, T.-T., Cao, A.-T., Nguyen, T.-H.-X. and Kim, D., "Fragility assessment for electric cabinet in nuclear power plant using response surface methodology", ***Nuclear Engineering and Technology***, Vol. 51, No. 3, (2019), 894-903. DOI: 10.1016/j.net.2018.12.025.
23. Dabiry, Y., Nikoi, R. and dabiry, y., "An Experimental Study on the Tensile Behaviors of Ultrasonic Welded T-joints for Polyamide Composite", ***International Journal of Engineering***, ***Transactions C: Aspects,*** Vol. 29, No. 12, (2016), 1783-1790. DOI: 10.5829/idosi.ije.2016.29.12c.18.
24. Rahman, M.M., Nahar, T.T., Baek, G. and Kim, D., "Seismic response characterization of shear wall in auxiliary building of nuclear power plant", ***Journal of the Earthquake Engineering Society of Korea***, Vol. 25, No. 3, (2021), 93-102. DOI: 10.5000/EESK.2021.25.3.093.
25. Ozturk, B., "Seismic behavior of two monumental buildings in historical Cappadocia region of Turkey", ***Bulletin of Earthquake Engineering***, Vol. 15, No. 7, (2017), 3103-3123. DOI: 10.1007/s10518-016-0082-6.
26. ACI, *Building Code Requirements for Structural Concrete* 2011, American Concrete Institute: Michigan, United States.503.
27. Chopra, A.K., "Dynamics of Structures: Theory and Applications to Earthquake Engineering", 4th ed, Hoboken, NJ, USA, Prentice Hall, (2012), 992.
28. Salman, K., Tran, T.-T. and Kim, D., "Grouping effect on the seismic response of cabinet facility considering primary-secondary structure interaction", ***Nuclear Engineering and Technology***, Vol. 52, No. 6, (2019), 1318-1326. DOI: 10.1016/j.net.2019.11.024.
29. Myers, R.H., Montgomery, D.C. and Anderson-Cook, C.M., "Response Surface Methodology: Process and Product in Optimization using Designed Experiments", 4th ed, Hoboken, NJ, USA, John Wiley & Sons, Inc., (2016), 855.
30. Yousefi, M., Safikhani, H., Jabbari, E., Yousefi, M. and Tahmsbi, V., "Numerical modeling and optimization of respirational emergency drug delivery device using computational fluid dynamics and response surface method", ***International Journal of Engineering, Transactions B: Applications,*** Vol. 34, No. 2, (2021), 547-555. DOI: 10.5829/ije.2021.34.02b.28.
31. Sadhukhan, B., Mondal, N.K. and Chattoraj, S., "Optimisation using central composite design (CCD) and the desirability function for sorption of methylene blue from aqueous solution onto Lemna major", ***Karbala International Journal of Modern Science***, Vol. 2, No. 3, (2016), 145-155. DOI: 10.1016/j.kijoms.2016.03.005.
32. Venkata Vishnu, A. and Sudhakar Babu, S., "Mathematical modeling & multi response optimization for improving machinability of alloy steel using RSM, GRA and Jaya algorithm", ***International Journal of Engineering, Transactions C: Aspects***, Vol. 34, No. 9, (2021), 2157-2166. DOI: 10.5829/ije.2021.34.09C.13.
33. Iffat, S., "Relation between density and compressive strength of hardened concrete", ***Concrete Research Letters***, Vol. 6, No. 4, (2015), 182-189.
34. Grünewald, S. and Walraven, J.C., "Properties of fibre reinforced SCC", in Self-Compacting Concrete: Materials, Properties and Applications, R. Siddique (Ed.), Vol., Woodhead Publishing, Sawston, UK, (2020), 309-370, (Chapter 12). DOI: 10.1016/B978-0-12-817369-5.00012-X.
35. Alin, A., "Minitab", ***Wiley Interdisciplinary Reviews: Computational Statistics***, Vol. 2, No. 6, (2010), 723-727. DOI: 10.1002/wics.113.
36. Kazemian, M.E. and Gandjalikhan Nassab, S.A., "Thermodynamic Analysis and Statistical Investigation of Effective Parameters for Gas Turbine Cycle using the Response Surface Methodology", ***International Journal of Engineering, Transactions B: Applications***, Vol. 33, No. 5, (2020), 894-905. DOI: 10.5829/ije.2020.33.05b.22.
37. Sahu, N.K. and Andhare, A.B., "Multiobjective optimization for improving machinability of Ti-6Al-4V using RSM and advanced algorithms", ***Journal of Computational Design and Engineering***, Vol. 6, No. 1, (2018), 1-12. DOI: 10.1016/j.jcde.2018.04.004.
38. NRC, U.S., *Regulatory Guide 1.60: Design Response Spectra for Seismic Design of Nuclear Power Plants*, in *US NRC*. 2014, United States Nuclear Regulatory Commission.13.

39. AIK, *Korean Building Code-Structural*. 2016, Architectural Institute of Korea: Seoul, Korea.

40. Uniform Building CodeTM, "Uniform Building Code: Structural Engineering Design Provisions, Whittier, CA, USA, International Conference of Building Officials, Vol. 2, (1997), 503.

41. Kim, D., *Quake_M: Response Spectra Based Earthquake Generation*. 2013, Structural System Laboratory: Cheonan, Korea.

42. Hur, J.S., Abdollah, "Performance of nonstructural components in NPPs under high-frequency ground motions", in 13th International Conference on Applications of Statistics and Probability in Civil Engineering, Seoul, South Korea, (2019).

Persian Abstract

چکیده

برای اطمینان از عملکرد ایمن و پایدار نیروگاه های هسته ای (NPP)، بسیاری از اجزای غیر ساختاری (NSCs) به طور فعال با NPP مرتبط هستند. به طور کلی، برای طراحی NSC ها، از طیف پاسخ طبقه (FRS) استفاده می شود، با این وجود، تمرکز بر موقعیت نصب و فرکانس NSC ها ضروری است که معمولا در طراحی معمولی NSC ها نادیده گرفته شود. این مقاله اثر محل نصب NSCها را در یک طبقه در یک ساختمان کمکی از نوع کانال ارزیابی می‌کند.تخمین پارامتر مودال برای بدست آوردن ویژگی دینامیکی ساختمان کمکی NPP توسط آزمون میز لرزان در نظر گرفته شده است، که منجر به کالیبراسیون FEM می شود. کالیبراسیون FEM از طریق روش سطح پاسخ (RSM) انجام شد و مدل کالیبره شده با استفاده از پارامترهای مدال و همچنین تابع طیف پاسخ فرکانسی تأیید شده است. در نهایت، حساسیت مکان با استفاده از تجزیه و تحلیل تاریخچه زمانی (THA) تحت زلزله‌های سازگار با طیف پاسخ طراحی و حرکات سینوسی به‌طور مصنوعی مورد بررسی قرار گرفت. نتایج نشان می‌دهد که انتخاب مکان مناسب برای NSCها می‌تواند یک اقدام مهم برای کاهش پاسخ‌های نامطلوب در هنگام زلزله باشد که می‌تواند تا ۳۰٪ پاسخ‌های افقی و ۷۰٪ پاسخ های عمودی شتاب دوره صفر (ZPA) را در ساختمان‌های کمکی نوع کانال کاهش دهد.

International Journal of Engineering

Journal Homepage: www.ije.ir

Dynamic Response of Glass/Epoxy Laminated Composite Plates under Low-velocity Impact

J. Anish Jafrin Thilak*[a], P. Suresh[b]

[a] Department of Mechanical Engineering, Mepco Schlenk Engineering College, Sivakasi, India
[b] Department of Mechanical Engineering, Muthayammal Engineering College, Namakkal, India

PAPER INFO

Paper history:
Received 19 February 2022
Received in revised form 25 March 2022
Accepted 27 March 2022

Keywords:
Glass/epoxy
Impact
LS-DYNA
Laminate
Finite Element

ABSTRACT

In the presented paper, the phenomenon of impact response of glass/epoxy laminates of thickness 5, 7, 10 mm subjected to impact energy of 50, 100, 150 J were numerically analyzed using the commercially available finite element software LS-DYNA. To predict the energy absorption capability and damage response, a finite element model was developed. The impact response was assessed in terms of maximum displacement, contact force at the event of an impact and energy absorption. Laminates with higher thickness showed better results in deformation and contact force generation when compared with thin laminates. The numerical results in terms of displacement and contact force are validated with experimental studies in the literature. Moreover, there is a good agreement between numerical results and experimental studies. In this study chang chang failure criteria were considered for predicting the impact response at low-velocity impact. Based on the observed numerical results, the energy absorption capability and the perforation resistance of the laminated composite structure were revealed. These results can be further referred to in the design and modelling of the composite laminated structure subjected to impact loadings. A grid independent study has been performed in this paper, which will be helpful for the researchers to select an optimized element size to reduce the computational time. In addition, the finite element analysis reasonably predicted the impact load–displacement responses and the perforation energies of laminated plates.

doi: *10.5829/ije.2022.35.07a.07*

1. INTRODUCTION

Glass/epoxy laminated composites are valued for their strength and stiffness concerning their density and are preferable to traditional materials in various applications where weight plays a major role, like aircraft panels, rocket structures. Whereas, the resistance to transversal loads of these materials is poor, especially dynamic loads. Many attempts have been made endlessly in search of materials with relatively high quality and performance. Synthetic fiber-reinforced composites, especially glass/epoxy laminated composites have gained substantial importance in aerospace and defense applications due to their high specific strength, damage tolerance and maturity in processing [1]. Fiber-reinforced polymer (FRP) composites have better fatigue and corrosion resistive performance superior to metals, which in turn reduce the maintenance cost. Moreover these materials have been recognized as effective energy-absorbing materials in impact related applications [2]. But still many researchers have extensively studied laminated composites' performance since an out of plane impact can initiate damage even at very low impact energies [3]. In FRP structures with impact, the damage is one of the major concern in aerospace industries since it can accidentallly happen from dropped tools, hailstone impact, bird strikes and so on [4]. This research work addresses the imapact damage caused either by low-velocity sources like collisions between cars, cargo, maintenance damage, dropped tool or high velocity sources like runway debris, hail, bird strike and having some ballistic impact in military aircraft. The influence of diameter and boundary conditions on low-velocity impact response of CFRP circular laminated plates has

*Corresponding author email: jafrinthilak@gmail.com (J. Anish Jafrin Thilak)

Please cite this article as: J. Anish Jafrin Thilak, P. Suresh, Dynamic Response of Glass/Epoxy Laminated Composite Plates under Low-velocity Impact, ***International Journal of Engineering, Transactions A: Basics,*** Vol. 35, No. 07, (2022) 1283-1290

been investigated [5]. Their results indicate that the higher target stiffness results in more energy absorption and delamination. Recently, the behavior of continuous fiber composite sandwich core plates under low-velocity impact was studied [6]. They revealed that the multi-cell composite corrugated core has increased the energy absorption capacity because of the fibers between adjacent cells. Impact damage detection is a key factor to maintain the structural integrity of composite structures used in the aerospace industry. Impact loads are always considered a threat to laminated structures since it reduces the load bearing capability. The effects of impactor mass, velocity and energy on the contact force, energy absorption and overall damage area of laminates were also investigated [7]. Researchers have also employed active thermography techniques and image processing technology. The pattern and area of the damage zone were determined by the Vibro thermography method [8]. It was established that a flat nose striker causes no crucial damage to the composite laminate, when compared to a conical and spherical nose impactor. In addition, the stiffness behavior [9] of hybrid laminated composites with surface crack has been investigated. Energy balance modeling [10] of high-velocity impact effect and damping response [11] in fabric reinforced composite plate structures were also studied by researchers in the last decades.

Eventually, the results of the low impacts results in a drastic reduction of stiffness and strength of laminates, therefore investigating the material's stiffness and strength at the time of impact is essential. Even though the impact behavior of laminate structures has been investigated by various researchers very few works reported the comparison study on the response on different laminate thickness and impact velocities. In this study, the low-velocity impact response behavior of glass/epoxy composite laminates was numerically investigated with the help of LS-Dyna, commercially available explicit finite element software. The effect of laminate thickness and impact energy on the response behavior was studied.

2. EXPERIMENTAL INVESTIGATION

In this section, the materials used in the sample preparation for material characterization and impact tests were discussed. In addition the experimental test procedures implemented for the low velocity impact testing was also discussed.

2. 1. Materials and Sample Preparation

The materials needed for the preparation of the laminates are glass fiber, epoxy resin and hardener. In the recent studies about composite materials performance the widely used resin and hardener are LY556 and HY951. At room temperature the composites having a density of 1100 kg/m^3 and 1000 kg/m^3, respectively. E-glass plain woven fabric having a thickness of 0.25 mm, 360 GSM was selected as the reinforcement material. Samples were prepared aacording to ASTM D3039 standard and the obtained mechanical properties were used in the finite element modelling of impact response of glass/epoxy laminated composites.

2. 2. Experimental Impact Testing Procedure

The low velocity impact tests were performed using instrumented drop weight impact tester [12]. The glass/epoxy laminates were exposed to low velocity impact using a hemispherical tip steel impactor of 16mm diameter. The ballistic limit velocity of hemispherical tip projectiles was found to be highest as compared to the other shapes such as flat, ogive and conical [13]. In order to measure the force exerted by the laminate on the impactor at the time of impact a transducer of 45 KN capacity was equipped with the striker. By varying the dropping height of the impactor the required impact energies were obtained [14]. The complete results of these experiments such as failure behavior, deformation and energy absorption were taken from literatures and were used in this study for the correlation with numerical results. In order to avoid further damage due to rebound of the impactor it was seized by the catcher system. Moreover piezoelectric sensors were incorporated to record the impact time-histories which provides force versus time plots.

3. FINITE ELEMENT MODELLING

3. 1. Failure Modelling–Theoretical Background

The low velocity impact response of the glass reinforced epoxy composite laminates was performed in the LS-DYNA explicit finite element analysis software. Composite lamina failure theories for can be categorized into three distinct groups namely: Non-interactive or limit theories, Interactive theories and Failure mode based theories. Whereas, the interaction between various stress/strain components in a laminate is accounted by Interactive theories; Tsai-Wu and Tsai-Hill, Tsai-Wu and Chang-Chang failure criterion falls under this category. The damage behavior of composite materials can be easily simulated using LS DYNA. Various material models like MAT_22, 54/55, 58/158, 59, 138, 261, 262, 161/162, are available to simulate intra and inter-laminar behavior of composite materials. Material model MAT_54/55 is the most commonly used which uses the Chang-Chang and Tsai-Wu failure criteria to model composite failure and it is only valid for thin shell elements. Failure can happens by any one of the following ways:

- If DFAIL (maximum strain for fibre tension) = 0, tensile fibre mode failure occurs if the Chang-Chang failure criterion satisfies.
- If DFAILT > 0, failure occurs when the tensile strain > DFAILT or strain < DFAILC (Maximum strain for fibre compression).
- If EFS (Effective failure strain) > 0, failure occurs in the laminate.
- If TFAIL (time step size criteria for element deletion) > 0, failure occurs based on the respective element's time step.

As soon as the failure happens in through-thickness integration points of a composite laminate, the element gets removed. And the elements which shares the nodes with abolished elements will start to lose the strength namely XT, XC, YT, YC in accordance to the SOFT parameter (constant). Where XT, YT are the tensile strength in longitudinal and transverse direction, XC and YC compressive strength in longitudinal and transverse directions respectively.

3. 2. FE Modelling of Glass/Epoxy Layers The method of modelling laminated composites depends on the scope of the simulation and the time required to run the analysis. Usually laminates can be modelled as a one shell element where all the layers can be defined using a single shell element and the second method is using layers of solid elements where the connection between layers can be node to node or using cohesive elements or TIEBREAK contact or by physically modelling adhesive. The last method is using layers of shell elements, in which the connection between layers can be done as the second method.

Here we have used one shell element modelling approach to assess performance of the composite laminates in terms of failure behavior, energy absorption and maximum displacement, so that the computational time can be reduced. [15] used this approach to minimize the complexity of analysis and to reduce the computational time. In this paper laminates of 5, 7 and 10mm thickness were modelled with a layer thickness of 0.25mm. The glass/epoxy finite element impact assembly model is shown in Figure 1. An impactor in the shape of a sphere was modelled as a solid part and solid brick elements were used for the mesh. The comparison parameters used in this study is given in the Table 1.

3. 3. Material and Contact Definition In LS-Dyna laminated composite shell elements material properties were defined using MAT 54/55 card and the MAT20 card was used for the impactor.

Since we have modelled only the tip of the impactor, its density has been intensified. The material properties this present study is given in Tables 2 and 3. The contact between the laminate and the impactor was defined by AUTOMATIC SURFACE TO SURFACE card in Ls-

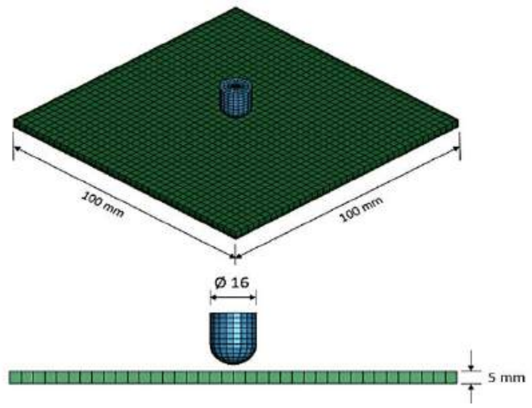

Figure 1. Finite element model of laminate and impactor

TABLE 1. Comparison parameters used in this study

Parameters	Units	Values
Thickness of the laminate	mm	5,7,10
Impact energy	J	50, 100, 150

TABLE 2. Material properties glass/epoxy lamina

Property description	Notation	Units	Value
Longitudinal elastic modulus	EA	MPa	32636.45
Transverse elastic modulus	EB	MPa	30326.93
Poisson's ratio	PRBA	--	0.22
In-plane shear modulus	GAB	MPa	2849.50
Tensile strength in longitudinal direction	XT	MPa	360.67
Tensile strength in transverse direction	YT	MPa	348.07
Compressive strength in longitudinal	XC	MPa	244.56
Compressive strength in transverse	YC	MPa	238.23
In-Plane shear strength	SC	MPa	64.00
Maximum strain for matrix failure	DFAILM	mm/mm	0.0115
Maximum in-plane shear strain	DFAILS	mm/mm	0.0225
Maximum strain for fibre tension	DFAILT	mm/mm	0.0111
Maximum strain for fibre compression	DFAILC	mm/mm	0.0221

TABLE 3. Material properties of the rigid solid impactor

Property description	Notation	Units	Value
Density	RO	Kg/m^3	7860
Young's Modulus	E	GPa	200
Poisson's ratio	PR	--	0.32

Prepost. Using this approach the impactor penetrates into the modelled shell elements considering the actual thickness of 5, 7, 10 mm, respectively in each case. It is assumed that the laminate exists in a dry form and a static friction coefficient of 0.2 is applied for the interaction between them.

3. 4. Mesh and Boundary Conditions The accuracy of the simulation results depends on the mesh quality and size. In order to find the optimum element size, a mesh sensitivity analysis is also performed since the mesh size is inversely proportional to the computational time. The impact performance of the laminate was analyzed by fixing the edges of the laminate using SPC card as shown in Figure 2 and a linear velocity is applied to the impactor corresponding to the impact energy. In this study three different energy values 50, 100 and 150J respectively were used and this can be achieved by dropping the impactor from a predefined height. However, to reduce the computational time here we have varied the impact velocity rather changing the height of the impactor. The impact test characteristics was based on the principle of energy conservation where the potential energy of the impactor head before impact is assumed equal to the kinetic energy after impact event [16]. The velocity can be calculated from the equation:

$$v = \sqrt{2gh}$$

where v, h and g are the impact velocity, height from which the impactor is dropped and g is the acceleration due to gravity.

4. RESULTS AND DISCUSSION

The acquired results of the low-velocity impact response analysis are presented in this section. The numerical results are divided into three main categories: contact force histories, the effect of laminate thickness and impact energy on damage behavior.

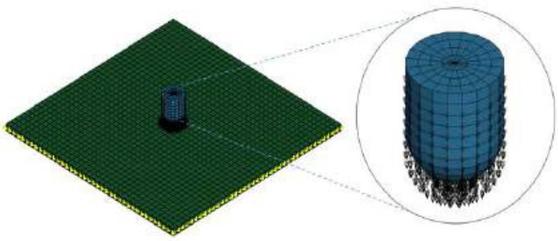

Figure 2. Boundary condition for the low velocity impact setup

4. 1. Force– Displacement Many researchers have studied the history of contact force during impact, since it can yield significant information about damage initiation and growth on composite laminates. Studies have recorded the occurrence of matrix cracking, matrix breakage and a minor delamination growth that happened as soon as the impactor hit the specimen. When the specimen gets impacted matrix cracking happened, so that there is a drop in the transverse stiffness as shown in Figures 3, 4 and 5. The curve continues to increase further and reaches the maximum peak force Fp. Fiber failure and delamination happens at the maximum peak force. The mass and velocity of the impactor, laminate thickness affect the critical failure load. The force-time, deflection-time and force-deflection plots shown in Figures 3, 4 and 5 reveal the characteristic behaviour of glass/epoxy laminates under low velocity. The maximum displacement and contact force at the time of impact are provided in the Table 4. Figure 6 reveals the typical contact force-deflection curve patterns of composites subjected to low velocity impact [17]. With the help of these curve patterns we can confirm whether the impact event is elastic, or impactor is penetrating or perforating into the laminate. In this study contact force increases with laminate deflection, so rebounding occurred. Moreover, the force-displacement curves can be categorized as three distinct zones A, B and C based on the behaviour of laminate during the time of impact. Zone A represents an elastic state, whereas in Zone B damage initiates and extends further to the peak where the deflection and contact forces are maximum. In general longer the zone B portion higher will be the energy absorption and damage tolerance of the laminates. Zone C is an unloading region where the deflection and contact force reach a minimum value.

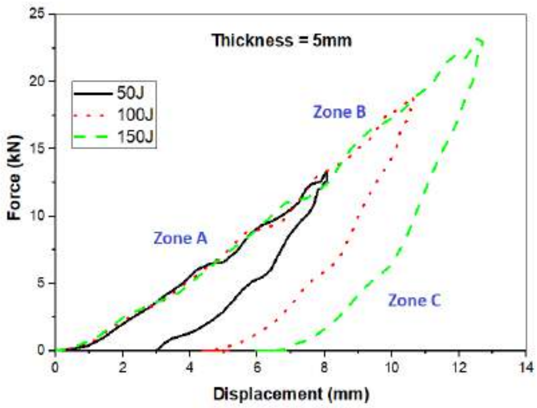

Figure 3. Force - displacement plot of 5 mm thick laminate at different energy

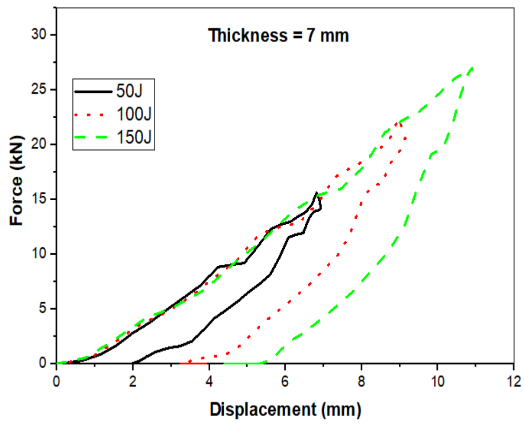

Figure 4. Force - displacement plot of 7 mm thick laminate at different energy

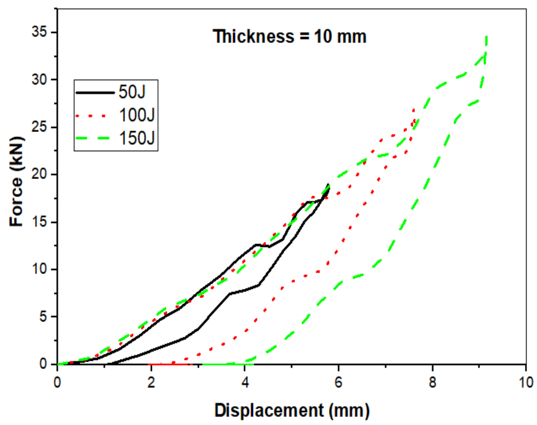

Figure 5. Force - displacement plot of 10 mm thick laminate at different energy

TABLE 4. Maximum deformation and contact force at the time of impact

Thickness (mm)	Max deformation (mm)			Contact Force (kN)		
	50J	**100J**	**150J**	**50J**	**100J**	**150J**
5	8.08	10.6	12.7	13.3	19	23.5
7	6.93	9.15	10.9	15.7	22.5	28.2
10	5.79	7.64	9.15	19.3	27.6	34.6

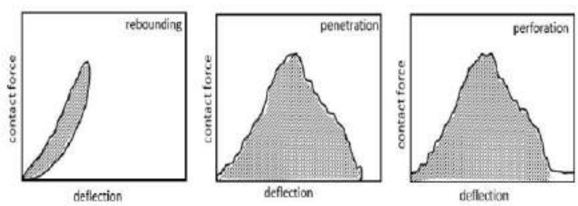

Figure 6. Typical contact force-deflection curves of composites subjected to low velocity impact

4. 2. Effect of Laminate Thickness on Damage Behaviour The results of numerical simulation as shown in Figures 7 (a-c) and 8 (a-c) reveals the behavior of glass/epoxy laminate at different ply thickness. It is identified that the prominent factors for damage mechanism are indentation, surface cracking, bending of laminates and fiber breakage [17]. The area of damage and the energy absorption for the different ply thickness and impact energy configuration are summarized in Table 5.

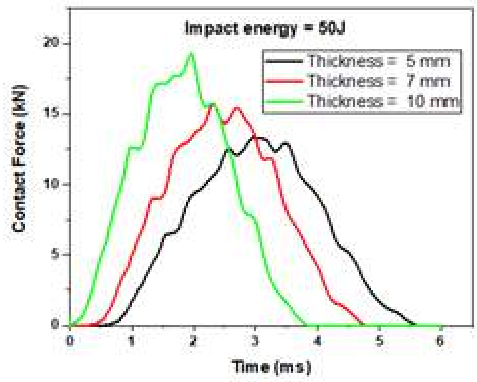

(a)

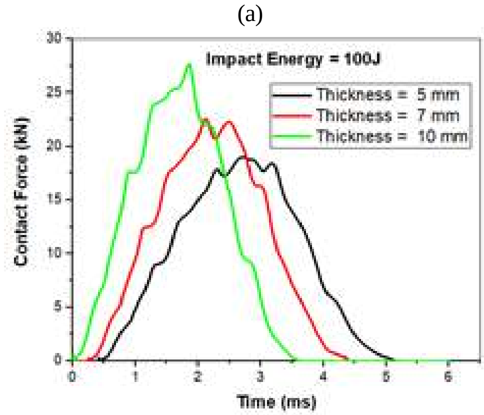

(b)

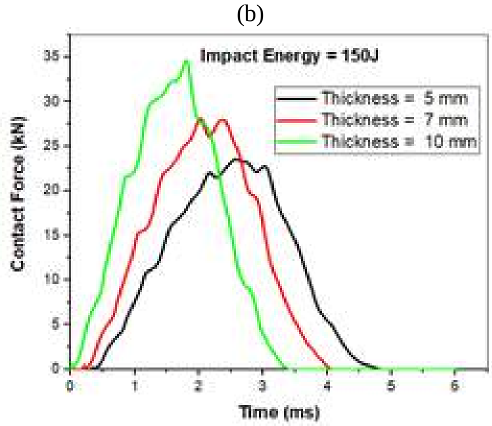

(c)

Figure 7. a, b, c Contact force history plots at impact energies 50, 100 and 150 J

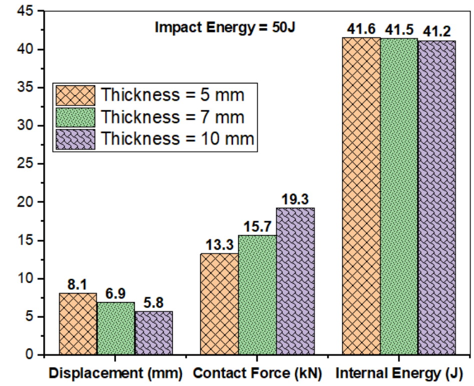

(a)

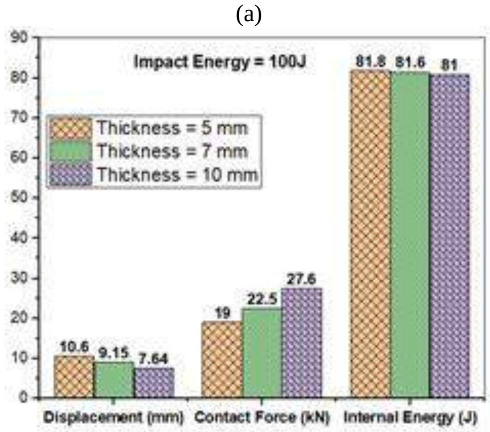

(b)

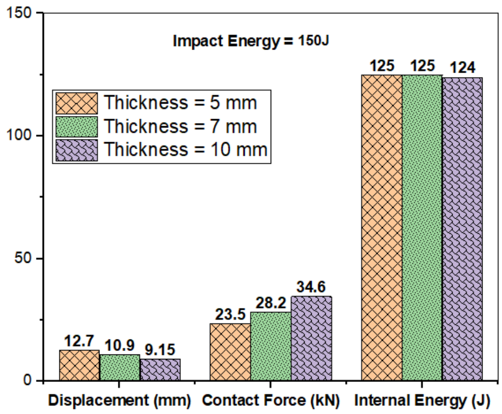

(c)

Figure 8. a, b, c Comparison of displacement, contact force and internal energy at 50, 100 and 150J

TABLE 5. Energy absorption and area of damage at the time of impact

Thick	Internal energy (J)			Damage area (kN)		
(mm)	50J	100J	150J	50J	100J	150J
5	41.6	81.8	125	2688.35	2850.52	3697.72
7	41.5	81.6	125	2679.71	2801.69	3240.50
10	41.2	81.0	124	2568.50	2768.34	2996.51

It is revealed that the area of damage is directly proportional to impact energy and inversely proportional to the laminate thickness. For instance, the area of fiber breakage for 5, 7 and 10 mm thick laminates were found to be 3697.72, 3240.50, 2996.51 mm^2 respectively, when impacted with 150 J energy. Whereas the contact force at the time of impact is keep on increasing with the ply thickness.

4. 3. Effect of Impact Energy on Damage Behaviour

The energy history curves of all the laminates impacted at 50J, 100 J and 150J are shown in Figure 9 (a-c). In genera,l the energy absorbed the specimen is the maximum value in internal energy history plot and the rebound energy or elastic energy is the difference between energy at flat portion and peak. The obtained results show that the rebound energy has increased at higher impact energies. Also whenever the absorbed energy is equal to the impact energy of the striker complete perforation occurs. In this study, there is no perforation but there is a slight traces of penetration occurred since around 75% of the impact energies were absorbed by the glass/epoxy laminates. Moreover, it is perceived the energy absorption rate has been decreased for thick laminates because of the stiffness and damage resistance increased.

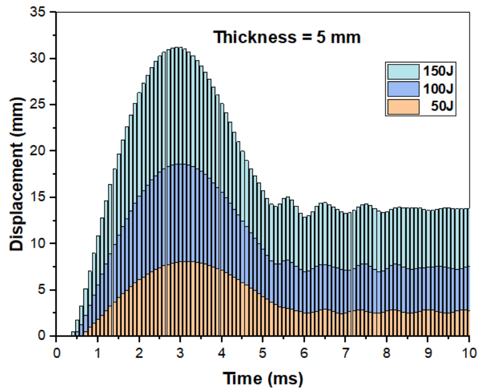

(a)

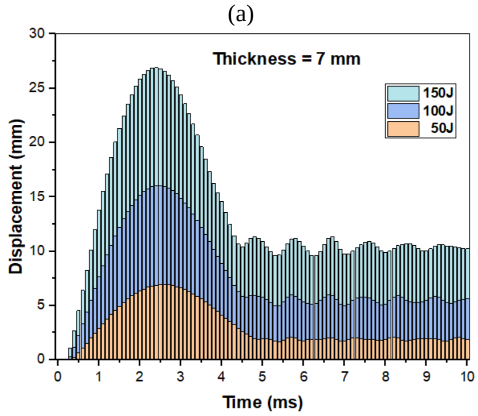

(b)

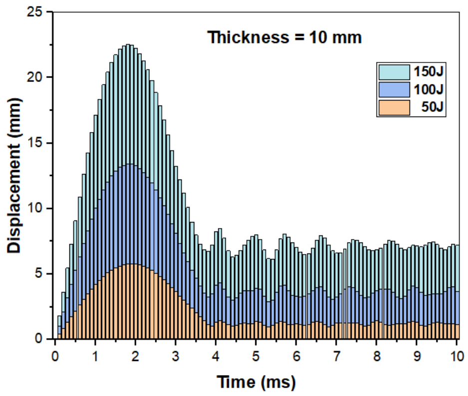

(c)

Figure 9. a, b, c Energy history plots of laminates of thickness 5, 7, 10 mm

4. 4. Correlation of Experimental and Numerical Results

The obtained results of this numerical study showed a higher compliance with the experimental results as shown in Tables 6 and 7. At higher thickness of the glass/epoxy laminates the numerical results are not correlated accurately because here the impact of laminated plates are modelled using thin shell element in order to reduce the computation time. But the model has shown better correlation at lower thickness in terms of deformation and contact force. In addition, if the setup was modelled using sold elements integrated cohesive zone elements or TIE_BREAK elements in LS-Prepost more accurate results would have obtained but the computational time should have increased. Usually Cohesive zone elements or TIE_BREAK elements are used to model the delamination or interlaminar interactions between plies, but here our intention is to study the impact response.

TABLE 6. Experimental versus numerical results for displacement

Laminate Thickness (mm)	Displacement (mm) at 100J		% Error
	Experimental	Numerical	
5	10.62	10.6	0.18
7	7.64	9.15	16.5
10	5.36	7.64	29.84

TABLE 7. Experimental versus numerical results for contact force

Laminate Thickness (mm)	Contact Force (kN) at 50J		% Error
	Experimental	Numerical	
5	14	13.3	5.26
7	16	15.7	1.91
10	21	19.3	8.81

5. CONCLUSIONS

Glass/epoxy laminated composite plates, which are subjected to low-velocity impact were numerically analyzed in this study. In-depth analyses were carried out in the aspect of assessing the damage initiation, energy absorption, rebounding or penetration of the impactor. A finite element impact analysis model was set up using a combination of shell and solid elements. The impact behavior was studied on the glass/epoxy laminate of different thicknesses 5, 7, 10 mm subject to impact energy of 50 J, 100 J and 150 J, respectively. The following decisions were attained from this study:

- The deformation of the glass/epoxy laminate was decreased at higher thickness because a large number of plies improved the stiffness and damage tolerance.
- Contact force generated at the event of impact is directly proportional to laminate thickness. And the energy absorption rate has slightly dropped for the increase in thickness.
- Moreover, for the selected set of impact parameters in this study the force-displacement curve behavior is completely rebounding with small traces of penetration and there is no perforation observed.

It is established that there is a decent agreement amongst experimental and numerical results even if the percentage of error is 29% at higher impact energy. This results can be improved by modeling the plies using solid elements integrated with cohesive elements and a good computational capacity.

6. REFERENCES

1. Ahmad. F, Hong, J. and Choi, H., “Hygro effects on the low-velocity impact behavior of unidirectional CFRP composite plates for aircraft applications” ***Composite Structures***, Vol. 135, (2016), 276-285.doi: 10.1016/j.compstruct.2015.09.040
2. Belingardi, G., and Vadori R., “Low velocity impact tests of laminate glass-fiber-epoxy matrix composite material plates” ***International Journal of Impact Engineering***, Vol. 27, (2002), 213-229, doi: 10.1016/S0734-743X(01)00040-9
3. Berk, B., Karakuzu, R., Murat Icten, B. and Arikan, V., “An experimental and numerical investigation on low velocity impact behavior of composite plates” ***Journal of Composite Materials***, Vol. 50, (2016), 3551-3559, doi: 10.1177/0021998315622805
4. Minak, G., and Ghelli, D., “Influence of diameter and boundary conditions on low velocity impact response of CFRP circular laminated plates” ***Composites Part B: Engineering***, Vol. 39, (2008), 962-972, doi: 10.1016/j.compositesb.2008.01.001.
5. Dogan, F., Hadavinia, H. and Donchev, T., “Delamination of impacted composite structures by cohesive zone interface elements and tiebreak contact” ***Central European Journal of Engineering***, Vol. 2, (2012), 612-626. doi: 10.2478/s13531-012-0018-0.
6. Phani, P., Sivaji, K. and Eswar, A., “Waviness Effect of Fiber on Buckling Behavior of Sisal/Carbon Nanotube Reinforced Composites Using Experimental Finite Element Method”

International Journal of Engineering Transactions C: Aspects, Vol. 34, No. 12, (2021), 2617-2623. doi: 10.5829/IJE.2021.34.12C.06

7. Hassan, M. A., Naderi, S. and Bushroa, A. R., "Low-velocity impact damage of woven fabric composites: Finite element simulation and experimental verification" ***Materials & Design***, Vol. 53, (2014), 706-718. doi: 10.1016/j.matdes.2013.07.068.
8. Karakuzu, R., Erbil, E. and Aktas, M., "Impact characterization of glass/epoxy composite plates: An experimental and numerical study" ***Composites Part B: Engineering***, Vol. 41, (2010), 388-395. doi: 10.1016/j.compositesb.2010.02.003
9. Ma, D., González-Jiménez, Á., Giglio, M., dos Santos Cougo, C. M., Amico, S. C. and Manes, A. "Multiscale modelling approach for simulating low velocity impact tests of aramid-epoxy composite with nanofillers" ***European Journal of Mechanics - A/Solids,*** (2021), 104286. doi: 10.1016/j.euromechsol.2021.104286
10. Zangana, S., Epaarachchi, J., Ferdous, W., Leng, J. and Schubel, P. "Behaviour of continuous fibre composite sandwich core under low-velocity impact" ***Thin-Walled Structures***, Vol. 158, (2021), 107157. doi: 10.1016/j.tws.2020.107157
11. Güneş, A. and Şahin, Ö. A., "Stiffness behavior of hybrid laminated composites with surface crack" ***Archives of Materials Science and Engineering***, Vol. 80, No. 2, (2016), 49-52. doi: 10.5604/18972764.1229632
12. Salehi-Khojin. A, Bashirzadeh R, Mahinfalah M, "The role of temperature on impact properties of Kevlar/fiberglass composite laminates" ***Composites Part B: Engineering***, Vol. 37, (2006), 593-602. doi: 10.1016/j.compositesb.2006.03.009
13. Al-Waily, M. and Jaafar, A. M., "Energy balance modelling of high velocity impact effect on composite plate structures" ***Archives of Materials Science and Engineering***. Vol. 111, No. 1, (2021), 14-33. doi: 10.5604/01.3001.0015.5562
14. Romano, M., Ehrlich, I., "Structural mechanic material damping in fabric reinforced composites: a review". ***Archives of Materials Science and Engineering***. Vol. 88, No. 1, (2017) 12-41. doi: 10.5604/01.3001.0010.7747
15. Gupta, N. K., Iqbal, M. A. and Sekhon, G. S., "Effect of projectile nose shape, impact velocity and target thickness on deformation behavior of aluminum plates" ***International Journal of Solids and Structures***, Vol. 44, No. 10, (2007), 3411-3439. doi: 10.1016/j.ijsolstr.2006.09.034
16. Seifoori, S. and Mahdian Parrany, A., "Impact damage detection in CFRP and GFRP curved composite laminates subjected to low-velocity impacts" ***Composite Structures***, Vol. 261, (2021), 113278. doi: 10.1016/j.compstruct.2020.113278.
17. Maio, L., Monaco, E. and Ricci, F., "Simulation of low velocity impact on composite laminates with progressive failure analysis" ***Composite Structures***, Vol. 103, (2013), 75-85. doi: 10.1016/j.compstruct.2013.02.027

Persian Abstract

چکیده

در مقاله ارائه شده، پدیده پاسخ ضربه لایه‌های شیشه/اپوکسی با ضخامت‌های ۵، ۷، ۱۰ میلی‌متر تحت تأثیر انرژی ضربه‌ای ۵۰، ۱۰۰، ۱۵۰ ژول با استفاده از نرم‌افزار اجزای محدود تجاری LS-DYNA مورد تجزیه و تحلیل عددی قرار گرفت. برای پیش‌بینی قابلیت جذب انرژی و پاسخ آسیب، یک مدل المان محدود توسعه داده شد. پاسخ ضربه از نظر حداکثر جابجایی، نیروی تماس در صورت ضربه و جذب انرژی ارزیابی شد. ورقه های با ضخامت بالاتر در مقایسه با ورقه های نازک نتایج بهتری در تغییر شکل و ایجاد نیروی تماسی نشان دادند. نتایج عددی بر حسب جابجایی و نیروی تماس با مطالعات تجربی در ادبیات تایید شده‌اند. علاوه بر این، تطابق خوبی بین نتایج عددی و مطالعات تجربی وجود دارد. در این مطالعه معیارهای شکست چانگ چانگ برای پیش‌بینی پاسخ ضربه در ضربه با سرعت پایین در نظر گرفته شد. بر اساس نتایج عددی مشاهده شده، قابلیت جذب انرژی و مقاومت سوراخی ساختار کامپوزیتی چند لایه نشان داده شد. این نتایج را می‌توان در طراحی و مدل‌سازی سازه چند لایه کامپوزیتی تحت بارهای ضربه‌ای اشاره کرد. یک مطالعه مستقل از شبکه در این مقاله انجام شده است که برای محققان در انتخاب اندازه عنصر بهینه برای کاهش زمان محاسباتی مفید خواهد بود. علاوه بر این، تجزیه و تحلیل اجزای محدود به طور منطقی پاسخ های بار-جابجایی ضربه و انرژی های سوراخ شدن صفحات چند لایه را پیش بینی کرد.

IJE TRANSACTIONS A: Basics Vol. 35, No. 05, (July 2022) 1291-1299

International Journal of Engineering

Journal Homepage: www.ije.ir

RESEARCH NOTE

Development of Work Breakdown Structure for Stadium Work as Project Guideline and Standard

A. Putro*, Y. Latief, A. Nursin, B. S. Soepandji

Department of Civil and Environmental Engineering, Faculty of Engineering, University of Indonesia, West Java, Indonesia

PAPER INFO

Paper history:
Received 23 February 2022
Received in revised form 26 March 2022
Accepted 30 March 2022

Keywords:
Stadium
Work Breakdown Structure
Standardization
Bill of Quantity

ABSTRACT

A Work Breakdown Structure (WBS) is a key visual project tool functioning as an obligation in managing construction projects, due to playing a crucial role from planning to execution. However, there are still several problems related to the implementation of WBS, such as miscommunication and poor development, where all involved execution parties do not accurately understand the scopes and objectives. This ultimately leads to project losses, based on cost, time, and quality, where standardization is not observed within the WBS preparation and development. Therefore, this study aims to develop a standard stadium WBS, for all involved execution parties to understand and achieve work information consistency. This was performed by mapping the Focus Group Discussions (FGDs) and Bill of Quantities (BQ) data of previous stadium projects with experts in their respective fields. The results showed the development of a standard WBS containing levels 1-6, including design alternatives, implementation requirements, and material specifications. During application, this tool helped to compile the entire scope of results-oriented projects as related guidelines and standards, with each hierarchical level from the top to the lower components. The obtained results also considered the consultants, contractors, and auditors at the planning, implementation, and monitoring stages, respectively.

doi: *10.5829/ije.2022.35.07a.08*

1. INTRODUCTION

The availability and adequacy of infrastructure are correlated to the economic growth of a country, due to being considered to have a positive and significant influence on environmental development and employment opportunities [1]. This is in line with the Indonesian government, which provides the efforts to intensify domestic development through the constructive elevation of state-owned buildings, whose classifications include stadiums. In this country, the construction of stadiums (new buildings or renovations) is found to be presently intensified. Therefore, this study aims to compile WBS standards, checklist and dictionary, which contains levels 1-6 including stadium alternative designs, implementation requirements, and material specifications. This is to indicate the needs of each Main Building, Field of Play, and Regional Works, respectively, where WBS shows materials and resources in level 6, as subsequent guidelines and standards for the performances of consultants, contractors, and auditors. Furthermore, Mangkuto et al. [2], Amelia and Yusuf [3] similarly argued that the stadiums were observed as architectural icons and benchmarks, which largely influenced the development of surrounding communities and infrastructures. In a construction project, a Work Breakdown Structure (WBS) plays an important role as the foundation for defining and establishing the framework for work management and completion, respectively [4]. This proves that creation of the tool is an obligation to be carried out from the planning to the execution stages. Despite being known as an important input in the management practice, many projects do not properly utilize the WBS, leading to the occurrence of errors in the work execution [5, 6]. In the construction industry, the key success factors are also being examined based on the perspectives of the owners, contractors, and consultants. These classified the identified indicators into

*Corresponding Author Email: jagadnegoro2002@gmail.com (A. Putro)

Please cite this article as: A. Putro, Y. Latief, A. Nursin, B. S. Soepandji, Development of Work Breakdown Structure for Stadium Work as Project Guideline and Standard, ***International Journal of Engineering, Transactions A: Basics***, Vol. 35, No. 07, (2022) 1291-1299

five main categories, including financial, interactive processes, human resources, contract agreements, and project specifications [7]. Despite this, the WBS implementation is found to still encounter many challenges for the involved parties, such as miscommunication and poor development, which leads to the incomprehensive and inaccurate knowledge of project scopes and objectives. Subsequently, this causes work errors and project losses, based on time, cost, and quality. This was in line with Suanda [6], which stated that many Indonesian projects did not accurately utilize WBS, leading to several problems such as delays, change orders, construction claims, and contractual disputes, whose main source is based on the form of alterations. This confirms that any alteration submitted and instructed by the contractor and engineer from the specified sequence or timing in a program is found to qualify as a major change [8].

WBS also plays a vital role after project execution, with different perspectives related to the auditors' results often observed to cause the return of a large amount of money to the government, through the contractors involved in the work package. These differences are commonly caused by the absence of standardization, guideline, and calculation methods, which provides quick and easy guidance [9, 10]. The process of standardization helps to achieve consistency in work management and indirectly reduce conflicts among project teams. In adopting this process, the aim is often based on the development of a specific level of conformity [11, 12]. Documentation standards and project notes also help in the development of a reference line, due to the provision of a communication channel among the project team. This explains that a standard stadium WBS is commonly used as a guideline to help achieve consistency and data standardization, which is often internally and externally utilized by project teams and auditors both in each project implementation stage.

2. STUDY SIGNIFICANCE

For the stadium projects, the results of the standard WBS development are expected to be used as a guideline towards the achievement of work consistency and standardization. These are to be used by various stakeholders in every project execution stage, especially for state-owned building construction. With a standardized definition, the effective and consistent distribution of crucial information is also expected to minimize the contractual disputes related to project scopes and activities.

3. LITERATURE REVIEW

3. 1. Definition of Work Breakdown Structure

A Work Breakdown Structure (WBS) is a deliverable-oriented hierarchical work decomposition carried out by the project team, to achieve objectives and produce appropriate results [13]. This explains that deliverables are unique products, results, or capabilities, used to display the services that should be produced in completing a process, phase, or project. It is often used narrowly based on external deliverables, which are the subject of approval by the project sponsor or customer. A deliverable is also defined as any measurable, tangible, and verifiable outcome or item that should be produced to fully or partially complete a project [4]. According to Schwalbe [14], the WBS was described as an oriented analysis of work, which defined the overall scope of the project. It was also observed as a basic document in project management, due to providing the basis for planning and managing schedules, costs, and changes. The study conducted by Project Management Institute [15] also defined the WBS as a hierarchical structure, which described and managed the total construction scope through deliverables, with each descending level in the hierarchy being an increasingly detailed definition of project work.

This indicates that a WBS organizes and defines the overall scope of the project to be completed, based on the relationship among work elements to the work objectives. The tool also provides an efficient format for defining, planning, and tracking the progress of the project work. Moreover, it organizes the required work by wrapping it into small manageable chunks, which are subsequently scheduled, estimated, monitored, and controlled. Descending from the top of the WBS hierarchy, each level is observed as an increasingly detailed definition of a project work [15]. The WBS is also a hierarchical list of the project tasks defining the scope, based on effort, timeline, and budget. Subsequently, the patience exhibited in the WBS saves a lot of effort in project execution, by helping to avoid rework and errors [16], due to being used to record and communicate project deliverables and achievements. The identification of these elements also relies on the experience of team members and the consultation with expert respondents. After deliverables and achievements are listed, resources are then assigned to each element and sub-element.

3. 2. Importance of Work Breakdown Structure

Despite ensuring project success, the WBS is still a key visual tool for management as follows [4]:

1. Clarifies the project scope by defining all the work.
2. Reflects the input from all team members.
3. Provides the baseline for subsequent change control.
4. Serves as a primary input to other project management processes.
5. Provides the framework for project control, performance monitoring, and communication.

6. Ensures that work appropriately correlates with the Responsibility Assignment Matrix (RAM) and the Organization Breakdown Structure (OBS).
7. Serves as an essential planning deliverable, supporting key project management functions.

3. 3. Creation of Work Breakdown Structure
The creation of WBS is a process that involves the decomposition of project deliverables and work into smaller parts, with more manageable components. This contains three stages, namely inputs, outputs, as well as tools and techniques [13]. In the preparation of the WBS, inputs include the scope management plan, project statement, requirement documentation, enterprise environmental factors, and organization process assets, which are subsequently analyzed using decomposition and expert judgment techniques, to produce outputs based on baseline and documents updates. The creation of WBS is also an iterative process considering the project objectives, design criteria, scope, technical requirements, and other attributes [4]. As a document, a WBS Dictionary is used to provide detailed information on each work package, regarding a summary description. This helps to identify and describe each work package (lowest level) in the WBS while minimizing the presence of scoop creep (additional scope or uncontrolled changes in project scope) through weak project scope definitions [17].

A WBS dictionary is also progressively described as a planning process, with most information being developed by other procedures and added to this document at a subsequent stage. This shows that the dictionary is the result of iterative techniques in the planning process [18]. Although not limited, the information in this document includes code of account identifier, work description, assumptions and constraints, responsible organization, schedule milestones, associated fixed activities, resources required, cost estimates, quality requirements, acceptance criteria, technical references, and agreement data [13]. Another element is the WBS checklists, which aims to evaluate all the tasks previously defined in tool, due to containing the questions related to functions. This is commonly a component-specific structured tool, aiming to verify that the required steps have been successfully performed. The form of this element also varies depending on the needs of the affected project, due to ranging from a simple to a complex checklist, based on project requirements and practices. In addition, many organizations reportedly have available standard checklists, to ensure consistency during task performances. When a checklist is used to support project completion, the results become part of the work record [13].

4. METHODOLOGY

This study used a systematic qualitative approach to develop a WBS standard, for the construction of a stadium project. This contained four steps, as shown in Figure 1.

4. 1. Identification of WBS Components for Stadium Work A documental review was employed to identify the work components within the WBS. This review used several related Ministerial documents, including the Minister of Public Works and Housing Regulation No. 22/28 of 2018/2016, concerning the Construction of State-Owned Buildings and the Guidelines for Work Unit Prices Analysis in the Public Works Sector, respectively. In the first regulation, the utilized data were specifically based on the information for the construction sector (Cipta Karya). In addition, the review also evaluated previous stadium project data, such as work plans and terms, bill of quantities, and owner's estimate price [5, 19, 20]. According to UEFA Guide [21] the design of football stadiums met several general requirements in the 21st Century, indicating that the identification process was also based on the criteria set by UEFA Guide and FIFA Standards [21].

Subsequently, the determination of the stadium-based WBS components was carried out through by mapping, as regards the Minister of Public Works and Housing Regulation No. 28 of 2016, which contains the coding and scope of building construction work, as well as the previous data to obtain the derivatives of the stadium's level 1-6 projects. This confirmed that the review used 56 stadiums' data, which contained 37 domestic and 19 overseas infrastructures, as summarized in Table 1.

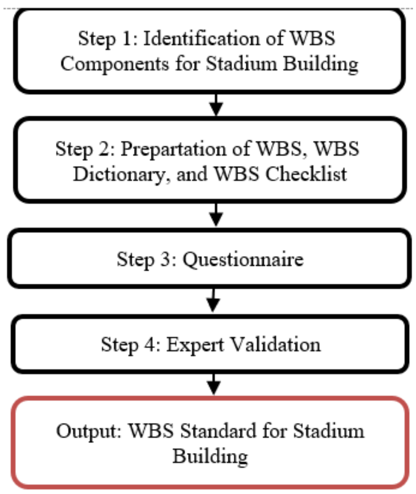

Figure 1. Study flow diagram

TABLE 1. Summary of stadium data

No	Name of Stadium	Location	Capacity	Status
1	Gelora Bung Karno Stadium	Jakarta	88,306	Domestic
2	Palaran Stadium	Samarinda	67,075	Domestic
3	Gelora Bung Utomo Stadium	Surabaya	50,000	Domestic
4	Utama Riau Stadium	Riau	45,000	Domestic
5	Jatidiri Stadium	Semarang	45,000	Domestic
6	Batakan Stadium	Balikpapan	40,000	Domestic
7	Gelora Sriwijaya Stadium	Palembang	40,000	Domestic
8	Jalak Harupat Stadium	Bandung	40,000	Domestic
9	Harapan Bangsa Stadium	Aceh	40,000	Domestic
10	Gelora Bandung Lautan Api Stadium	Bandung	38,000	Domestic
11	Wibawa Mukti Stadium	Bekasi	35,000	Domestic
12	Aji Imbut Stadium	Tenggarong	35,000	Domestic
13	Kanjuruhan Stadium	Malang	35,000	Domestic
14	Maguwoharjo Stadium	Sleman	30,000	Domestic
15	Gelora Delta Stadium	Sidoarjo	30,000	Domestic
16	Gelora 10 November Stadium	Surabaya	30,000	Domestic
17	Patriot Candrabhaga Stadium	Bekasi	28,000	Domestic
18	Manahan Stadium	Surakarta	25,000	Domestic
19	Sultan Agung Stadium	Bantul	25,000	Domestic
20	Gajayana Stadium	Malang	25,000	Domestic
21	Segiri Stadium	Samarinda	25,000	Domestic
22	Mandala Stadium	Papua	25,000	Domestic
23	Kaharudin Nasution Stadium	Pekanbaru	25,000	Domestic
24	Petrokimia Stadium	Gresik	20,000	Domestic
25	Papua Bangkit Stadium	Papua	40,263	Domestic
26	Kapten I Wayan Dipta Stadium	Bali	23,081	Domestic
27	Pakansari Stadium	Bogor	30,000	Domestic
28	Barombong Stadium	Makassar	40,000	Domestic
29	BMW (Jakarta International Stadium)	Jakarta	82,000	Domestic
30	Bekasi Stadium	Bekasi	25,000	Domestic
31	Istora PON Papua Construction	Papua	5,000	Domestic
32	Aquatic Stadium GBK Renovation	Jakarta	7,600	Domestic
33	Sport Center Manokwari Construction Planning	Papua	10,231	Domestic
34	Sports Facilities Improvement Project	Bogor	30,000	Domestic
35	DED Bekasi Stadium's Document	Bekasi	25,000	Domestic
36	Gedebage Football Stadium Construction	Bandung	38,000	Domestic
37	CSU - ON Campus Football Stadium	Colorado	41,000	International
38	The Washington Nationals Ballpark	Washington	41,313	International
39	Houston NFL Stadium	Texas, US	72,220	International
40	Hrvatskih Vitezova Stadium	Croatia	5,200	International

No	Name of Stadium	Location	Capacity	Status
41	SRC Stozice	Slovenia	16,000	International
42	Viking Stadion	Norway	16,000	International
43	Arena im Allerpark	Germany	30,000	International
44	Estadi Cornella El-Prat	Spain	40,000	International
45	NN Stadium in London	London	15,000	International
46	Washington State Stadium	Washington	72,000	International
47	Stade de France Stadium	France	80,000	International
48	Stadium of Australia	Australia	80,000	International
49	Munich New Stadium	Munich	66,000	International
50	Sapporo Dome	Japan	42,122	International
51	Murakata Barabai Stadium	Barabai	10,000	Domestic
52	Buck Shaw Stadium	California	10,000	International
53	Community America Ballpark	Kansas	8,461	International
54	Barnet Copthall	London	10,000	International
55	County Cricket Ground	Bristol	10,000	International
56	New Meadow	Shrewsbury	10,000	International

4. 2. Preparation of WBS, WBS Dictionary and WBS Checklist Based on the identification process, the WBS of this project was divided into three sections, namely the main stadium, field of play, and surrounding works. Each of these sections had its WBS, with the Dictionary and Checklist also arranged according to the breakdown structure.

4. 3. Expert Validation According to Hansen [22], expert interviews were used to validate the proposed WBS, dictionary, and checklists. These experts were required to have a minimum of 10 years of involvement in stadium projects, and also a Certificate of Intermediate Expertise. In this study, twelve experts with various specialties such as architecture and design development, civil works, as well as mechanical and electrical orientations, were observed, with their profiles and interview collection data listed in Table 2.

5. RESULTS AND DISCUSSION

The results showed that the WBS project was divided into three sections, namely the main stadium, field of play

TABLE 2. Expert profiles and interviewed data

No.	Expert	Expertise	Experience (Years)	Expertise Qualification	Interview Duration	Date of Interview
1	E1	Architecture & Design Development	42	Advanced	53 mins	4/18/2021
2	E2	Architecture & Design Development	20	Advanced	115 mins	3/20&27/2021
3	E3	Civil	26	Advanced	76 mins	3/30/2021
4	E4	Civil	26	Advanced	59 mins	3/24/2021
5	E5	Civil	17	Advanced	70 mins	3/20/2021
6	E6	Architecture	16	Advanced	70 mins	3/20/2021
7	E7	Mechanical & Electrical	17	Intermediate	107 mins	3/24/2021
8	E8	Mechanical & Electrical	10	Intermediate	67 mins	3/24/2021
9	E9	Mechanical & Electrical	13	Intermediate	52 mins	3/24/2021
10	E10	Mechanical & Electrical	24	Intermediate	100 mins	3/17/2021
11	E11	Mechanical & Electrical	34	Advanced	216 mins	3/20,21,27&28/2021

(FOP), and surrounding areas' works, respectively. This division was based on the zoning area, where the coverage of each scope is shown in Table 3.

TABLE 1. Scope of work for stadium projects

Main Stadium Work	1. Tribune Area 2. Athlete Facilities 3. Activity Management Facilities 4. Building Management Facilities 5. Media Facilities 6. Commercial Area
Field of Play (FOP)	1. Soccer Field 2. Athletic Track
Surrounding Areas	1. Parking Area 2. Landscape 3. Shuttle Bus 4. Railway Hub

Subsequently, each scope was degraded into work items, to form a WBS hierarchy from level 1 to 6. For instance, Table 4 presents a standard WBS for main stadium work, as validated by the experts. WBS level 1 is related to the scope of the stadium project, namely the main stadium (MS), FOP, and surrounding areas' works, respectively. Level 2 is also a division of work for each scope, with 3, 4, and 5 explaining and identifying the task type and packages, as well as describing the activity, respectively. Meanwhile, level 6 is related to the resources, including labor, tools, and materials. After being validated as a standard WBS, this structure was converted into a dictionary and checklist, which were subsequently confirmed by three experts with similar qualifications. This was to obtain feedback and comments on various elements, such as work components from level 1-6, person-in-charge, delivery, references, and other required dictionary aspects. Based on the results of validation and interviews, Tables 5 and 6 present an overview of the WBS dictionary and checklist, respectively.

According to Figures 2 and 3, the WBS dictionary was mainly used to describe each element of the project activities (level 5) and resources (level 6), respectively. This confirmed that the validated format described the main elements, such as the codes, responsibilities, resources, and results of each defined activity. Therefore, the WBS dictionary was needed to alleviate potential problems (see Table 5), due to being easier to read and understand by all involved parties. During the construction process, it was also used to effectively monitor and control each specified work package. Besides serving as a project management tool, the validation process subsequently proved that the development of the WBS Dictionary functioned as a very important primary document for the front-end planning phase. This was in line with the project sustainability, based on time, cost, and quality performance during the project lifecycle, e.g., the procurement of environmental-friendly materials for the stadium. The material specification was also thoroughly defined using the WBS dictionary, due to being the basis for determining activities, resources and quality requirements. In addition, the issues arising due to environmental or sustainability considerations were facilitated through a detailed WBS [13].

Based on Table 6, there was no significant changes recommended, although some descriptions were simplified. From the WBS checklist, architectural works had more detailed information and descriptions, due to the tasks being more complicated than others. This was in line with a previous study, where architectural and interior works had detailed and much simpler tasks, respectively [23]. Based on the interview results, the WBS dictionary and checklist were used as a guide to assist project managers with detailed information and descriptions for each work. This verified the importance of the elements as planning requirements, especially for the construction of complex projects such as stadiums.

TABLE 2. Validated standard WBS for main stadium work

WBS LEVEL 1		**WBS LEVEL 2**		**WBS LEVEL 3**	
CODE	Scope	CODE	Division	CODE	Work Package
1	Stadium Main Building	1.1	Design Development	1.1.1	Design Planning Work

WBS LEVEL 4		**WBS LEVEL 5**		**WBS LEVEL 6**		
CODE	Work Package	CODE	Activity	CODE	Type of Resource	Resource
1.1.1.1	Preparation	1.1.1.1.1.	Administrative and technical preparation	1.1.1.1.1.	Labor	Team Leader, Administrator

TABLE 5. Validated WBS dictionary

1.1	**Work Group/Division**	**:**	**Design Development**
1.1.1	Sub of Work/Section	:	Design Planning Work
1.1.1.1	Work Package	:	Preparation
	Person in Charge	:	-
	Description	:	This work involves administrative and technical preparations, formation of drafting teams, preparation of surveys and field observations, and preliminary reports planning, according to the existing regulations
	Deliverable	:	Project cost planning document
	References	:	**1.** Image Document **2.** RKS/Technical Specification Document **3.** Expert Validation

Code	**Activities**	**Resources**		
		Man	**Material**	**Equipment**
1.1.1.1.1	Administrative and Technical Preparation	**1.** Team Leader **2.** Administrator	…	…
1.1.1.1.2	Formation of the Drafting Team	**1.** Team Leader	…	…
1.1.1.1.3	Survey Preparation and Field Observation	**1.** Team Leader **2.** Structural/building experts **3.** Architects **4.** Planologists	…	…
1.1.1.1.4	Preparation of Preliminary Report	**1.** Team Leader **2.** Administrato	…	…

TABLE 6. Validated WBS Checklist

WBS Level	**Code**	**Details**	
1	1	Stadium Main Building Project	Name of the construction project being worked on
2	1.1	Design Development	There are several types of work in design development, namely planning, pre-design, the establishment of structures and drawings, construction implementation documents, procurement explanations & evaluations, periodic supervision, and insurance, according to the existing regulations.
3	1.1.1	Design Planning Work	Design planning work includes preparation, implementation, and submission of the final report, according to the existing provisions.
4	1.1.1.1	Preparation	This work involves administrative and technical preparations, formation of drafting teams, preparation of surveys and field observations, as well as preliminary reports planning, according to the existing regulations.

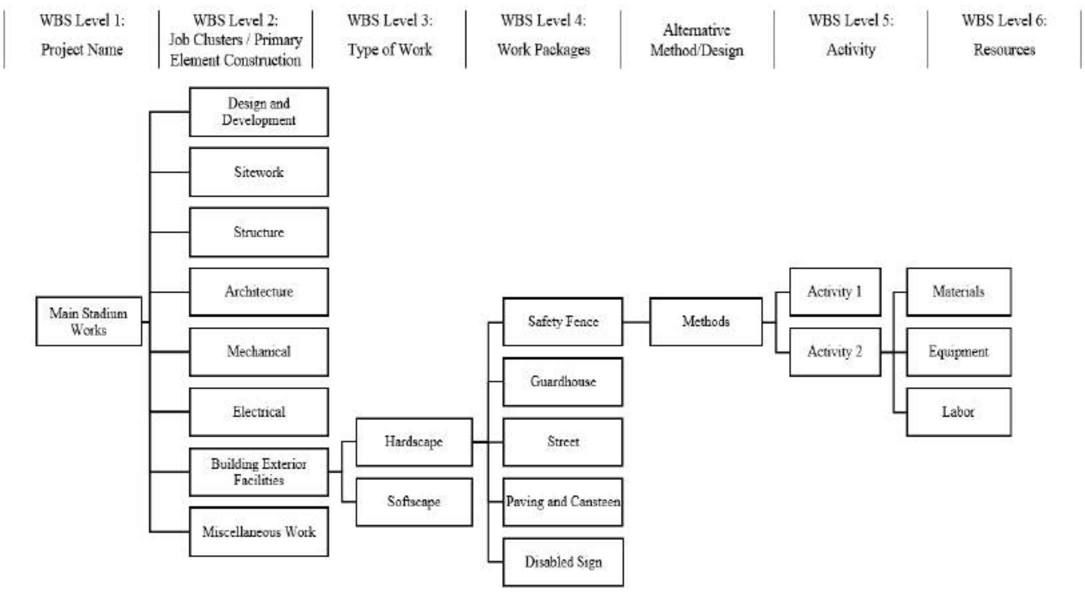

Figure 2. WBS Standard for main stadium works

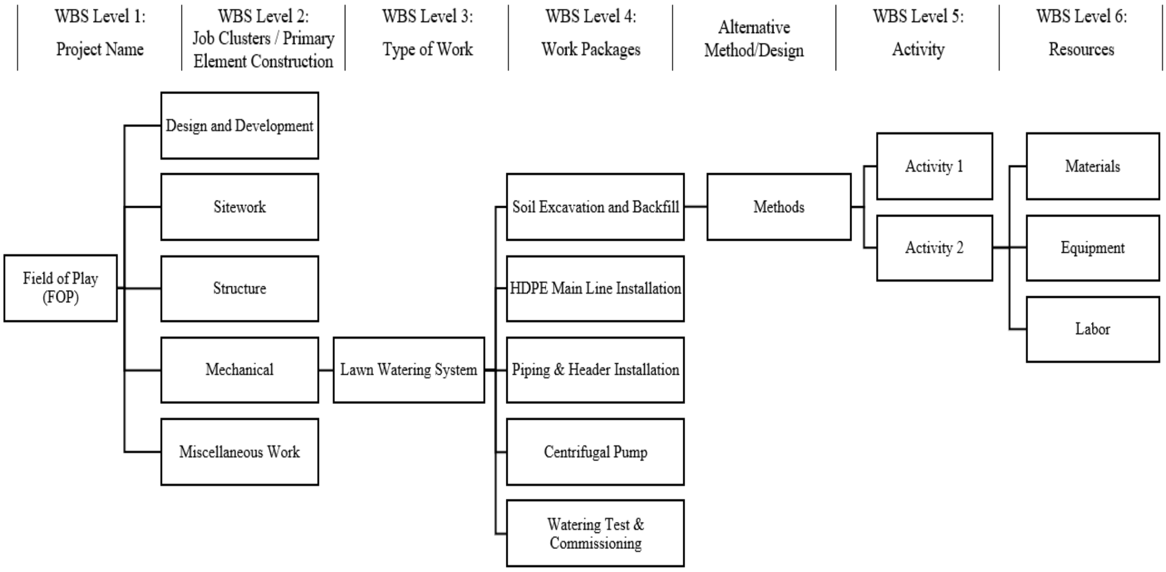

Figure 3. WBS standard for the field of play (FOP)

Despite being used to identify all required activities with detailed descriptions, these elements were often difficult to understand, due to the ambiguity of each job description. Therefore, word adjustments and modifications are essentially needed, especially when developing WBS dictionaries and checklists. The WBS Checklist also contributed to the easier evaluation of every required task, especially for stadium construction, which was divided into 3 categories, namely Main Stadium (MS), Field of Play (FOP), and surrounding areas' works, respectively.

6. CONCLUSION

This study aimed to create a WBS, which was to be used as a standard in the construction of stadium projects. From the results, the following conclusions were obtained,

1. The stadium-based WBS projects were grouped into 6 levels, namely scope (level 1), division (level 2), work type and packages (levels 3 and 4), activity (level 5), and resources (level 6).
2. There were also three WBS dictionaries and checklists each, for the main stadium, FOP, and surrounding areas' works, respectively.
3. Decomposing the components of WBS level 4 (work packages) was essentially necessary, based on the alternative or design methods to identify level 5 (list of activities).
4. WBS Level 6 was also identified after the definition of each activity implementation requirement.
5. A standard WBS document containing identification (level 1 to 6), dictionaries, and checklists, was successfully developed. These elements were related to each other and served as a guideline for stadium projects.
6. Using the proposed standard WBS, the consistency of work information was achieved.

Therefore, the preparation of a WBS standard for the construction of a stadium project was a guideline for all stakeholders, based on the achievement of accurate quality, cost, and time of implementation.

7. ACKNOWLEDGMENTS

The authors are grateful to the members of the SMM Team (Amelia Anggraini S.T., M.T., and Anna Wahidati S.T., M.T.), for supporting this study.

8. REFERENCES

1. Awandari, L.P.P. and Indrajaya, I.G.B., "Pengaruh infrastruktur, investasi, dan pertumbuhan ekonomi terhadap kesejahteraan masyarakat melalui kesempatan kerja", ***E-Jurnal Ekonomi Pembangunan Universitas Udayana***, Vol. 5, No. 12, (2016), 165388.
2. Mangkuto, R.A., Rachman, A.P., Aulia, A.G., Asri, A.D. and Rohmah, M., "Assessment of pitch floodlighting and glare condition in the main stadium of gelora bung karno, indonesia", ***Measurement***, Vol. 117, (2018), 186-199.
3. Anggraini, A. and Latief, Y., "Development of work breakdown structure standard for safety planning on stadium construction work based on risk", in Journal of Physics: Conference Series, IOP Publishing. Vol. 1858, No. 1, (2021), 012073.
4. Rose, K.H., *Book review: Practice standard for work breakdown structures—second edition: By project management institute*. 2006, SAGE Publications Sage CA: Los Angeles, CA.

5. Hidayah, D.N., Latief, Y. and Riantini, L.S., "Development of work breakdown structure standard based on risk for safety planning on dam construction work", in IOP Conference Series: Materials Science and Engineering, IOP Publishing. Vol. 420, No. 1, (2018), 012003.
6. Suanda, B., "Advanced & effective project management", Panduan Lengkap Bagi Praktisi Manajemen Proyek Profesional (Jakarta: PP Construction and Investment), (2016).
7. Asgari, M., Kheyroddin, A. and Naderpour, H., "Evaluation of project critical success factors for key construction players and objectives", ***International Journal of Engineering, Transactions B: Applications,*** Vol. 31, No. 2, (2018), 228-240.
8. Ansari, R., Banihashemi, S.A., Taherkhani, R. and Moradi., S., "Decision support systemn for analyzing key performance indicators in projects managemet", ***International Journal of Engineering, Transactions B: Applications***, Vol. 35, No. 5, (2022), 7-8, doi: 10.5829/ije.2022.35.05b.03.
9. Peli, M., "Standardisasi perhitungan volume (smm) untuk menghindari perbedaan persepsi dalam pembuatan rencana anggaran biaya pada proyek konstruksi di indonesia", ***Jurnal Rekayasa***, Vol. 7, No. 1, (2017), 88-103.
10. Jumas, D. and Tela, N., "Analisa kebutuhan standardisasi pengukuran kuantitas (standard method of measurement) pada industri konstruksi di indonesia", ***Jurnal Rekayasa***, Vol. 7, No. 1, (2017), 16-26.
11. Perumal, V.R. and Bakar, A.H.A., "The needs for standardization of document towards an efficient communication in the construction industry", ***Acta technica Corviniensis-Bulletin of Engineering***, Vol. 4, No. 1, (2011), 23.
12. Akbar, A.R.N., Mohammad, M.F., Ahmad, N. and Maisyam, M., "Adopting standardization in construction environment: Standard method of measurement (smms)", ***Procedia-Social and Behavioral Sciences***, Vol. 170, (2015), 37-48.
13. Farkas, E.B., "Review guide to the project management body of knowledge 6th edition", ***Podium***, Vol., No. 34, (2018), 85-88, doi.
14. Schwalbe, K., "Information technology project management, Cengage Learning, (2015).
15. Stackpole, C.S., "A user's manual to the pmbok guide, John Wiley & Sons, (2013).
16. Lee, J., Deng, W.-Y., Lee, W.-T., Lee, S.-J., Hsu, K.-H. and Ma, S.-P., "Integrating process and work breakdown structure with design structure matrix", ***Simulation***, Vol. 7, (2010), 8.
17. Postula, F.D., "Wbs criteria for effective project control", ***AACE International Transactions***, (1991), I6 (1).
18. Salsabila, F., Latief, Y., Riantini, L.S. and Muslim, F., "Development of dictionary and checklist based on wbs (work breakdown structure) of air side facilities in airport construction works for quality planning", in Proceedings of the International Conference on Industrial Engineering and Operations Management. No. August, (2020).
19. Lei, S., "Wbs-based risk identification for the whole process of real estate project and countermeasures", in National Conference on Information Technology and Computer Science, Citeseer. (2012).
20. Elsye, V., Latief, Y. and Sagita, L., "Development of work breakdown structure (wbs) standard for producing the risk based structural work safety plan of building", in MATEC Web of Conferences, EDP Sciences. Vol. 147, (2018), 06003.
21. UEFA, U., *Guide to quality stadiums*. 2011, UEFA Nyon, Switzerland.
22. Hansen, S., "Investigasi teknik wawancara dalam penelitian kualitatif manajemen konstruksi", ***Jurnal Teknik Sipil***, Vol. 27, No. 3, (2020), 283.
23. Amin, J., Sagita, L. and Latief, Y., "Work breakdown structure (wbs) dictionary and checklist development of stadium architectural and interior works for safety planning", in IOP Conference Series: Materials Science and Engineering, IOP Publishing. Vol. 930, No. 1, (2020), 012006.

Persian Abstract

چکیده

ساختار شکست کار (WBS)یک ابزار کلیدی پروژه بصری است که به عنوان یک تعهد در مدیریت پروژه‌های ساخت‌وساز عمل می‌کند، زیرا نقشی حیاتی از برنامه‌ریزی تا اجرا ایفا می‌کند .با این حال، هنوز مشکلات متعددی در ارتباط با اجرای WBS وجود دارد، مانند عدم ارتباط و توسعه ضعیف، که در آن همه طرف های اجرایی درگیر به طور دقیق دامنه و اهداف را درک نمی کنند .این در نهایت منجر به هدر رفت پروژه بر اساس هزینه، زمان و کیفیت می شود، جایی که استانداردسازی در آماده سازی و توسعه WBSرعایت نمی شود .بنابراین، این مطالعه با هدف توسعه یک استادیوم استاندارد WBS، برای همه طرف‌های اجرایی درگیر برای درک و دستیابی به سازگاری اطلاعات کاری انجام می‌شود .این کار با نقشه‌برداری از داده‌های بحث‌های گروهی متمرکز (FGDs)و (BQ)پروژه‌های قبلی استادیوم با متخصصان در زمینه مربوطه انجام شد .نتایج توسعه یک WBS استاندارد حاوی سطوح 1-6، از جمله جایگزین‌های طراحی، الزامات اجرا، و مشخصات مواد را نشان داد .در طول کاربرد، این ابزار به جمع‌آوری کل محدوده پروژه‌های نتیجه‌محور به عنوان دستورالعمل‌ها و استانداردهای مرتبط، با هر سطح سلسله مراتبی از اجزای بالا تا پایین‌تر کمک کرد .همچنین نتایج به‌دست‌آمده، مشاوران، پیمانکاران و حسابرسان را به ترتیب در مراحل برنامه‌ریزی، اجرا و نظارت مورد توجه قرار گرفت.

IJE TRANSACTIONS A: Basics Vol. 35, No. 05, (July 2022) 1300-1306

International Journal of Engineering

Journal Homepage: www.ije.ir

RESEARCH NOTE

Synthesis of Silica Nanoparticles from Silica Sand via Vibration Assisted Alkaline Solution Method

M. S. Hamzah[a,b], M. W. Wildan*[a], K. Kusmono[a], E. Suharyadi[c]

[a] Department of Mechanical and Industrial Engineering, Faculty of Engineering, Universitas Gadjah Mada, Yogyakarta, Indonesia
[b] Departement of Mechanical Engineering, Tadulako University, Palu, Indonesia
[c] Departement of Physics, Faculty of Mathematics and Natural Sciences, Universitas Gadjah Mada, Yogyakarta, Indonesia

PAPER INFO

Paper history:
Received 31 January 2022
Received in revised form 15 March 2022
Accepted 02 April 2022

Keywords:
Morphology
Dielectric Properties
Alkaline Fusion
Speaker Membrane

ABSTRACT

The effect of frequency of speaker membrane vibration on the grain size of the silica nanoparticles (SNP) was investigated. SNP was synthesized using the alkaline fusion method under the vibration of the membrane speaker. Variations of membrane vibration used in this research were 0, 50, 100, and 200 Hz. The material compositions, crystal structure, and morphology of the synthesized SNP were characterized using X-ray fluorescence (XRF), X-ray diffraction (XRD), and transmission electron microscopy (TEM), respectively. Meanwhile, its dielectric property was determined using impedance spectroscopy. The results showed that the SNP consisted of 99.35% silica and corresponded to the crystalline structure of quartz silica. The SNP size was decreased with increasing vibration frequencies. The smallest size of SNP (9.04±1.9 nm) was obtained at a frequency of 200 Hz. Moreover, the dielectric constant and dielectric losses were increased with an increase in membrane vibration frequency due to the decrease of SNP size.

doi: *10.5829/ije.2022.35.07a.09*

1. INTRODUCTION

Indonesia is a country that is rich in potential natural minerals, including oxide materials such as silica sand [1, 2]. There are many silica grains of sand in Indonesia, spread all over the country regions, such as in Poso Regency, Central Sulawesi. Silica sand obtained from Poso has a high SiO_2 content that can be utilized in industrial materials [3]. It can be processed into silica nano particles (SNP) through a top-down or bottom-up method [4]. For the last-mentioned method, SNP was obtained through chemical reactions using precursors. Particles in nanometer size provide advantages such as good electrical, optical, and magnetic properties [5]. SNP is widely used in industry because of its high productivity and low production costs [6]. Previous researchers have reported various methods in synthesizing the SNP, including hydrothermal [7, 8], sol-gel [9], sodium silicate solution [10, 11], alkaline fusion [12-14], and precipitation method [15]. These methods are generally carried out with stirring to inhibit grain growth; however, the resulting particles have still lacked. Other researchers have also developed several methods to obtain smaller sizes of particles. Indira and Malathi [16] reported the synthesis of hydroxyapatite nanoparticles for biomedical applications using ultrasonic and microwave methods. Rusianto et al. [17] reported the synthesizing of magnetite nanoparticles assisted by mechanical vibration. Yu et al. [18] reported the method of utilizing ultrasonic/mechanical vibrations in metallurgical processes such as welding and metal casting to control metal particle size. It was also reported that ultrasonic vibrations in the welding process can smooth particles and improve the mechanical properties of welds [18-20].

SNP can exist in three crystal structures, namely quartz, tridymite, and cristobalite. It has a large surface area, good heat resistance, high mechanical strength, and can be used as catalyst precursors, adsorbents, and composite filters, easy modification, good chemical stability, and low cytotoxicity [5, 21, 22]. SNP can be

*Corresponding Author Institutional Email: m_wildan@ugm.ac.id (M. W. Wildan)

Please cite this article as: M. S. Hamzah, M. W. Wildan, Kusmono, E. Suharyadi, Synthesis of Silica Nanoparticles from Silica Sand via Vibration Assisted Alkaline Solution Method, ***International Journal of Engineering, Transactions A: Basics***, Vol. 35, No. 07, (2022) 1300-1306

used to improve the cooling effect and efficiency of the vapor compression refrigeration cycle [23]. Nowdays, SNP is commonly used in various industries such as rubber, filler, catalyst carriers, [24-27], food, automobile, energy storage materials, piezoelectric materials, paints, medical, electronics, and others [28, 29]. A dielectric material is an insulator with high resistivity that can be polarized if there is an electrostatic dipole or under an external electric field [30]. Previous researchers have reported the impact of the nano-silica amount on its dielectric properties [31, 32]. The combination methods between alkaline fusion and membrane vibration can be used in synthesizing silica nanoparticles by heating the sample at a specific temperature, depositing it and then it followed by vibrating and stirring until the pH is neutral. This method is advantageous because it does not require a long time and does not require high energy [13]. As a result, the synthesis process takes place effectively and efficiently to produce nanoparticles. The SNP synthesis method that has been used so far has limitations, including the lack of nanoparticles produced, and the particle size is not controlled, so a new approach is needed.

This study reports the new method of SNP synthesizing by combining the alkaline fusion with membrane speaker vibration, which offers mass production of SNP with controllable size. This study aimed to investigate the effect of the frequency of speaker membrane vibration on the particle size and the dielectric properties.

2. MATERIALS AND METHODS

The raw material used to synthesize silica nanoparticles was obtained from silica sand on Poso Island, Central Sulawesi, Indonesia [33]. Sodium hydroxide and hydrochloric acid used in this work were bought from Merck (Germany).

Silica nanoparticles (SNP) was prepared by using a combination of alkaline fusion and speaker membrane methods as follows. Briefly, the raw silica sand was cleaned and dried in an oven. The metallic elements within the silica sand were removed using several permanent magnets to obtain non-metallic compounds with high concentrations. Silica sand was crushed using a ball mill to find smaller particle sizes. Then, the crushed silica sand was sieved into < 200 mesh using a sieve shaker. Silica sand concentrates were mixed with pro-analyst NaOH in a ratio of 1: 1 by weight fraction, then heated at 600℃ for 1 h. The heated mixture of silica sand and NaOH was put into a beaker glass which was filled with distilled water. The beaker glass was placed on a hot plate magnetic stirrer and heated at about 75℃ with a stirring speed of 500 rpm. Stirring was combined with the vibration of the speaker membrane with different frequencies of 0, 50, 100, and 200 Hz with a duration of 30 min, respectively. The solution was stirred for 16 h while the pre-analytical HCl solution was titrated with a concentration of 37% at 2 M. The solution would form a residue (silica gel) at the pH of 7-8. The silica precipitates were filtered using Whatman glass microfiber filter (grade 42, 2.5 μm) and then washed with distilled water until it turned white. The washed silica residues were dried in an oven at 100°C for 15 h and then characterized. Variations of membrane vibration used were 0, 50, 100, and 200 Hz, respectively, then referred to as SNP0, SNP50, SNP100, and SNP200. The schematic of the synthesis of SNP with the alkaline fusion method combined with a speaker membrane can be seen in Figure 1.

The chemical composition and microstructure of SNP were characterized using X-ray fluorescence (XRF) (RIGAKU-NEX-QC+QuanTES) and transmission electron microscope (TEM) (JEOL JEM-1400), respectively. Images of each SNP from the TEM image were analysed using Image J software to determine the grain size distribution. X-ray Diffraction analysis (Bruker D2 Phaser) was used to identify the crystalline phase of each SNP. Then, the synthesized SNPs at various frequencies of 0, 50, 100, and 200 Hz were compacted in a 15 mm diameter cylindrical die with pressure of 75 MPa to produce green bodies. The green bodies were sintered at 1360℃ for 2 h with a heating rate of 10℃/min. The dielectric properties of the sintered samples were tested using a computerized impedance spectroscopy device with a sine frequency generator that produced a modulating frequency in the range of 10 to 500 kHz.

3. RESULT AND DISCUSSION

3. 1. Synthesis of Silica Nanoparticles The main mineral in silica sand is quartz which has a tetrahedron

Figure 1. Schematic illustration of the synthesis method of SNP

structure, where at high temperatures, each tetrahedron will be separated from each other because the bonds between the anions and cations are not very strong [34], so that NaOH binds silica to form sodium metasilicate that was separated from other minerals. Consecutively, sodium metasilicate was titrated with HCl to produce hydrous silica and silicic acid. Then, the white residue in a gel was washed with distilled water to remove the remaining solution. The chemical reactions of this synthesis process are presented in Equations (1) and (2) [35].

$$SiO_2 + 2\,NaOH \rightarrow Na_2SiO_3 + H_2O \quad (1)$$

$$Na_2SiO_3 + HCl \rightarrow SiO_2 + 2NaCl + H_2O \quad (2)$$

3. 2. Composition Table 1 shows the chemical composition of the silica sand and SNP as revealed by XRF. It was found that both silica sand and SNP have the main component of SiO_2 around 99.35-99.64%. From Table 1, it can be also observed that the content of the same components is indicated by both silica sand and SNP. It can be concluded that the synthesis of SNP did not change the composition of silica sand.

3. 3. Crystal Structures The XRD diffractogram of the raw material (silica sand) and the obtained SNP are presented in Figure 2. As observed, 2θ of the peaks of raw material and SNP are not significantly different. As compared to JCPDS (33-1161 card number) for silica quartz, the appeared sharp peaks show that the raw material and SNP are in the quartz phase with the related 2θ are 20.90°, 26.70° 36.58°, 39.51°, 42.49°, 45.83°, 50.18°, 54.91°, 60.64°, 68.16°. In line with the literature, quartz is one of the crystalline phases of silicon oxide that formed at temperatures below 870°C [36]. From Figure 2, it can be seen that various vibration frequencies of the speaker membranes (0, 50, 100, and 200 Hz) did not affect the SNP crystal structure. The SNP synthesized with various frequencies exhibits a quartz phase. Furthermore, X-ray diffraction is not only used to identify the crystal structure but also is used to determine the crystal size by using the Scherer equation as shown in Equation (3) [17]:

TABLE 1. Chemical composition of silica sand and the SNP

Composition	Silica sand (wt%)	SNP (wt%)
SiO_2	99.64	99.35
TiO_2	0.20	0.18
Fe_2O_3	0.06	0.06
NiO	0.03	0.02
CuO	0.01	0.01
ZnO	0.01	0.01
Others	0.05	0.35

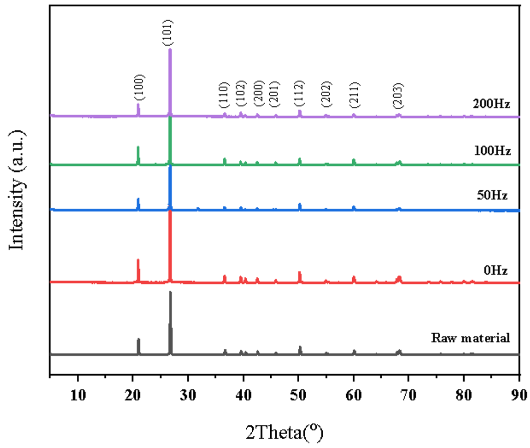

Figure 2. XRD diffractogram of synthesized SNP with various frequencies of speaker membrane vibration

$$D = (0.9\,\lambda)/(\beta \cos \theta) \quad (3)$$

where D is the size of the crystallite diameter (nm), λ is the wave length of the x-ray used, θ is the angle (1/2 peak angle), and β is the full width of half maximum (FWHM). The four peak at 2θ of 20.90°, 26.70°, 36.58°, and 50.18° are used as the basis for determining the size of the crystal diameter. It was found that the SNP crystal size obtained at different frequencies (0, 50, 100, and 200 Hz) are 10.8, 5.0, 1.04, and 0.9 nm, respectively. Based on the XRD results, it can be concluded that the synthesis of SNP by the alkaline fusion method combined with a speaker membrane did not change the crystal structure of silica sand. This finding is in consistent with XRF results as previously discussed. In addition, increasing the vibration frequency reduces the crystal size of the SNP. This is associated with an increase in frequency can increase the nucleation rate and then result in smaller crystal size [37].

3. 4. Morphology Studies Figure 3 shows the TEM images and the size distribution of SNP for various speaker membrane vibration frequencies. The size of silica particles is in the nanometer order, which depends on the frequency of the speaker membrane vibration. From Figure 3, it was found that the particle sizes of SNP at different frequencies of 0, 50, 100, and 200 Hz are 14±3.34, 12±2.54, 11±2.56, and 9±1.95 nm, respectively. The SNP size decreases with the imposition of speaker membrane vibrations. This indicates that the higher vibration frequency leads to a smaller size of produced SNP. Thus, the SNP size decreases with the application of speaker membrane vibrations. This is because the vibrational frequency of the membrane can inhibit crystal growth. After all, the arrangement of atoms becomes disturbed or unstable when speaker membrane vibration is applied. In comparison, the increase in frequency will increase the vibration energy, where the vibration energy

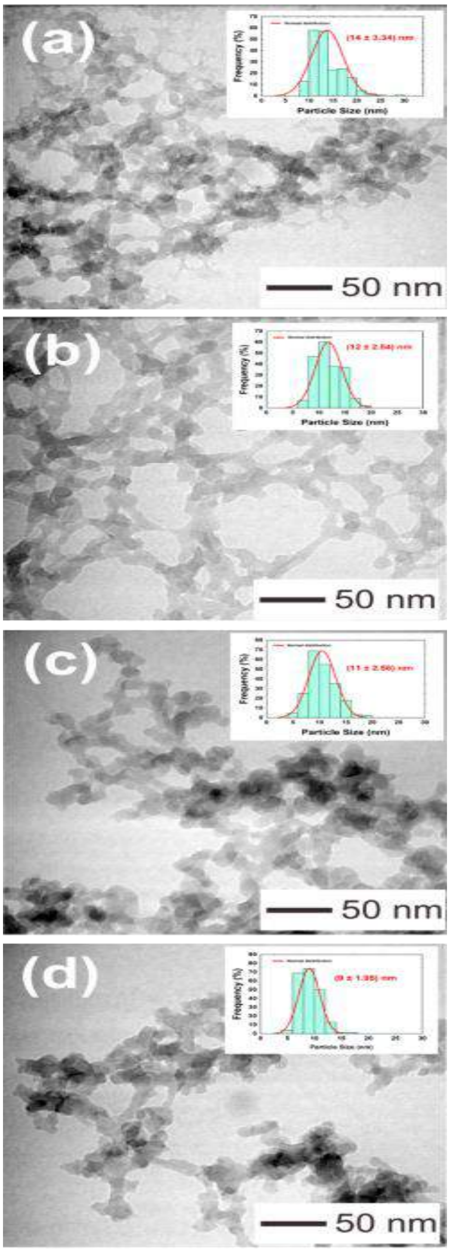

Figure 3. TEM images of SNP and its particle distributions with various speaker membrane vibration frequencies: a). 0 Hz, b). 50 Hz, c). 100 Hz, and d). 200 Hz

can inhibit the growth of crystals to form smaller particles [17]. The TEM results are consistent with the XRD results as mentioned before, where increasing the vibration frequency decreased the SNP crystal size.

3. 5. Dielectric Properties Figure 4 shows the frequency dependence of real dielectric permittivity (ε') and dielectric loss (ε''). The dielectric permittivity and dielectric loss of SNP0, SNP50, SNP100, and SNP200 are decreased with the increase of frequency. Meanwhile, the decrease in real dielectric permittivity and dielectric

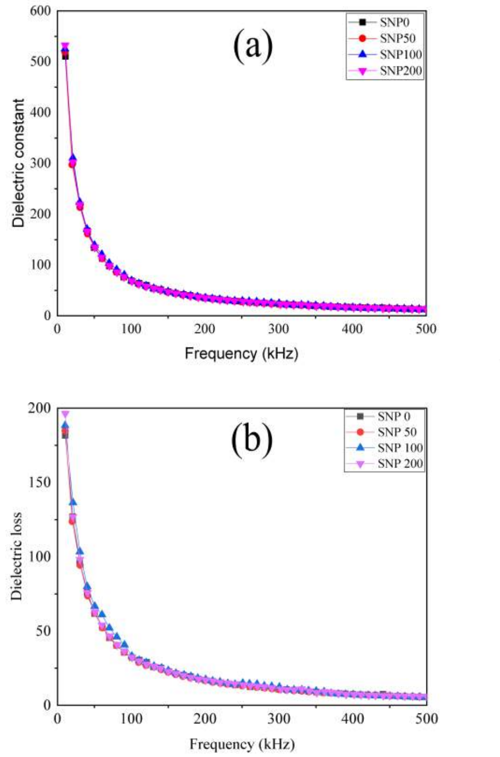

Figure 4. Frequency-dependent plot of permittivity for SNP0, SNP50, SNP100, and SNP200, (a) dielectric constant, and (b) dielectric loss

loss is significant in the range of 10 kHz to 200 kHz and be saturated over 200 kHz. The real dielectric constant and the imaginary dielectric constant are calculated by Equations (4), (5) and (6).

$$\Phi = \text{arc tan}\,(V_c/V_r) \quad (4)$$

$$\varepsilon' = (\text{d} \sin \theta)/(2\pi f\, \varepsilon_0\, A|Z|) \quad (5)$$

$$\varepsilon'' = \varepsilon' \tan \delta \quad (6)$$

where ϕ is the capacitance impedance which determined by |Z| = Vc max/Vr max × R, ε' is proportional to the energy stored and $\varepsilon r''$ is proportional to the energy lost or dissipated. While the loss tangent value is the ratio between the permittivity of the imaginary dielectric to the permittivity of the real dielectric. The two parts of the permittivity (real dielectric and dielectric loss) in the low-frequency region have strong dispersion. The real dielectric constant and dielectric loss show low values at high frequencies and increase with decreasing frequency. This phenomenon is comparable to that reported in the literature [37, 38].

The sample exhibits strong dielectric dispersion behavior at low frequencies due to the significant contribution of space charge polarization to dielectric properties, and the dielectric constant remains nearly constant at higher frequencies [39, 40]. Another thing that causes is the inability of electrons to align their position with a given electric field so that the polarization between grain decreases which affects the dielectric value.

The decrease in grain size causes an increase in the number of grains and grain boundaries, which directly reduces the number of dipole moments. The poling plane does not have many domains to exchange, so the poling process is inefficient in a particle. Similar types of results have been reported for oxide ceramics [41]. Furthermore, four types of polarization, i.e., dipolar, ionic, electronic, and interfacial polarization, contribute to the total polarization of the dielectric material [42]. The different magnitude of the real dielectric value in each sample is due to differences in grain size. Decreasing the grain size leads to a higher dielectric value [39, 43]. Moreover, the highest dielectric occurs in SNP200, which is in agreement with the TEM results. Other factors that affect the dielectric value are defects, residual stress at the interface, porosity, grain boundaries, and variations in crystal structure parameters [44].

4. CONCLUSIONS

Silica nanoparticles sourced from natural sand were successfully synthesized using the alkaline fusion method assisted by speaker membrane vibration. XRF analysis showed SiO_2 content of 99.36% by weight and a similar to the silica content of silica sand. XRD analysis indicated that the identified phase of SNP was quartz. TEM observations showed that the silica nanoparticle's size was decreased with an increase in speaker membrane vibration frequency. The dielectric constant and dielectric loss show high values at low frequencies and decrease at high frequencies, and this occurs in all samples. With an increasing frequency of the speaker membrane vibration during synthesis, the value of the dielectric constant was found to be higher, and this was the effect of decreasing the grain size of silica nanoparticles.

5. ACKNOWLEDGEMENTS

This work was supported by the Ministry of Education, Culture, Research and Technology of the Republic of Indonesia and Indonesia Endowment Fund for Education (LPDP) with contract number of KET-574/LPDP.4/2020.

6. REFERENCES

1. Hidayat, T. and Fitrianingrum, L., "Ecology and sociology analysis for mineral resources management in indonesia", in IOP Conference Series: Earth and Environmental Science, IOP Publishing. Vol. 483, No. 1, (2020), 012030.
2. Ismail, A., Saputri, L., Dwiatmoko, A., Susanto, B. and Nasikin, M., "A facile approach to synthesis of silica nanoparticles from silica sand and their application as superhydrophobic material", ***Journal of Asian Ceramic Societies***, Vol. 9, No. 2, (2021), 665-672, https://doi.org/10.1080/21870764.2021.1911057
3. Darwis, D., Khaeroni, R. and Iqbal, I., "Pemurnian dan karakterisasi silika menggunakan metode purifikasi (leaching) dengan variasi waktu milling pada pasir kuarsa desa pasir putih kecamatan pamona selatan kabupaten poso", ***Natural Science: Journal of Science and Technology***, Vol. 6, No. 2, (2017), https://doi.org/10.22487/25411969.2017.v6.i3.9201
4. Biswas, A., Bayer, I.S., Biris, A.S., Wang, T., Dervishi, E. and Faupel, F., "Advances in top–down and bottom–up surface nanofabrication: Techniques, applications & future prospects", ***Advances in Colloid and Interface Science***, Vol. 170, No. 1-2, (2012), 2-27, https://doi.org/10.1016/j.cis.2011.11.001
5. Khan, I., Saeed, K. and Khan, I., "Nanoparticles: Properties, applications and toxicities", ***Arabian Journal of Chemistry***, Vol. 12, No. 7, (2019), 908-931, https://doi.org/10.1016/j.arabjc.2017.05.011
6. Yu, K., Liang, Y., Ma, G., Yang, L. and Wang, T.-J., "Coupling of synthesis and modification to produce hydrophobic or functionalized nano-silica particles", ***Colloids and Surfaces A: Physicochemical and Engineering Aspects***, Vol. 574, No., (2019), 122-130.
7. Potapov, V., Efimenko, Y., Fediuk, R. and Gorev, D., "Effect of hydrothermal nanosilica on the performances of cement concrete", ***Construction and Building Materials***, Vol. 269, (2021), 121307, https://doi.org/10.1016/j.conbuildmat.2020.121307
8. Zainuri, M., "Synthesis of sio nanopowders containing quartz and cristobalite phases from silica sands", ***Materials Science-Poland***, Vol. 33, No. 1, (2015), 47-55, doi. https://doi.org/10.1515/msp-2015-0008
9. Owoeye, S.S., Abegunde, S.M. and Oji, B., "Effects of process variable on synthesis and characterization of amorphous silica nanoparticles using sodium silicate solutions as precursor by sol–gel method", ***Nano-Structures & Nano-Objects***, Vol. 25, No., (2021), 100625, doi. https://doi.org/10.1016/j.nanoso.2020.100625
10. El-Didamony, H., El-Fadaly, E., Amer, A.A. and Abazeed, I.H., "Synthesis and characterization of low cost nanosilica from sodium silicate solution and their applications in ceramic engobes", ***Boletín de la Sociedad Española de Cerámica y Vidrio***, Vol. 59, No. 1, (2020), 31-43, doi. https://doi.org/10.1016/j.bsecv.2019.06.004
11. Owoeye, S.S., Jegede, F.I. and Borisade, S.G., "Preparation and characterization of nano-sized silica xerogel particles using sodium silicate solution extracted from waste container glasses", ***Materials Chemistry and Physics***, Vol. 248, (2020), 122915, https://doi.org/10.1016/j.matchemphys.2020.122915
12. Wahyudi, A., Amalia, D. and Sariman, S., "Preparation of nano silica from silica sand through alkali fusion process", ***Indonesian Mining Journal***, Vol. 16, No. 3, (2013), 149-153.
13. Ayele, L., Pérez-Pariente, J., Chebude, Y. and Díaz, I., "Conventional versus alkali fusion synthesis of zeolite a from low grade kaolin", ***Applied Clay Science***, Vol. 132, (2016), 485-490, https://doi.org/10.1016/j.clay.2016.07.019
14. Shi, B. and Chang, Q., "Green synthesis of fly ash-based zeolite y by mixed alkali fusion method", ***Micro & Nano Letters***, Vol. 16, No. 11, (2021), 540-545, https://doi.org/10.1049/mna2.12083
15. Jyoti, A., Singh, R.K., Kumar, N., Aman, A.K. and Kar, M., "'Synthesis and properties of amorphous nanosilica from rice husk and its composites", ***Materials Science and Engineering:***

B, Vol. 263, (2021), 114871, https://doi.org/10.1016/j.mseb.2020.114871

16. Indira, J. and Malathi, K., "Comparison of template mediated ultrasonic and microwave irradiation method on the synthesis of hydroxyapatite nanoparticles for biomedical applications", ***Materials Today: Proceedings***, Vol. 51, (2022), 1765-1769, https://doi.org/10.1016/j.matpr.2021.03.028
17. Rusianto, T., Wildan, M.W. and Abraha, K., "Various sizes of the synthesized Fe_3O_4 nanoparticles assisted by mechanical vibrations", (2015).
18. Yu, M., Zhao, H., Xu, F., Chen, T., Zhou, L., Song, X. and Ma, N., "Influence of ultrasonic vibrations on the microstructure and mechanical properties of al/ti friction stir lap welds", ***Journal of Materials Processing Technology***, Vol. 282, (2020), 116676, https://doi.org/10.1016/j.jmatprotec.2020.116676
19. Lei, Z., Bi, J., Li, P., Li, Q., Chen, Y. and Zhang, D., "Melt flow and grain refining in ultrasonic vibration assisted laser welding process of az31b magnesium alloy", ***Optics & Laser Technology***, Vol. 108, (2018), 409-417, https://doi.org/10.1016/j.optlastec.2018.07.015
20. Zhou, S., Wang, B., Wu, D., Ma, G., Yang, G. and Wei, W., "Follow-up ultrasonic vibration assisted laser welding dissimilar metals for nuclear reactor pump can end sealing", ***Nuclear Materials and Energy***, Vol. 27, (2021), 100975, https://doi.org/10.1016/j.nme.2021.100975
21. Tolba, G.M., Bastaweesy, A., Ashour, E., Abdelmoez, W., Khalil, K.A. and Barakat, N.A., "Effective and highly recyclable ceramic membrane based on amorphous nanosilica for dye removal from the aqueous solutions", ***Arabian Journal of Chemistry***, Vol. 9, No. 2, (2016), 287-296, https://doi.org/10.1016/j.arabjc.2015.05.009
22. Ma, M., Li, H., Xiong, Y. and Dong, F., "Rational design, synthesis, and application of silica/graphene-based nanocomposite: A review", ***Materials & Design***, Vol. 198, (2021), 109367, https://doi.org/10.1016/j.matdes.2020.109367
23. Rahman, M.W.U., Rahman, M., Sarker, M., Rashid, F. and Al Mahmud, M.M., "Synthesis of nano silica particle from silica sand and characterization of nano silica based r134a refrigerant", ***Materials Today: Proceedings***, Vol. 46, (2021), 6816-6821, https://doi.org/10.1016/j.matpr.2021.04.368
24. Sattayanurak, S., Noordermeer, J.W., Sahakaro, K., Kaewsakul, W., Dierkes, W. and Blume, A., "Silica-reinforced natural rubber: Synergistic effects by addition of small amounts of secondary fillers to silica-reinforced natural rubber tire tread compounds", ***Advances in Materials Science and Engineering***, Vol. 2019, (2019), https://doi.org/10.1155/2019/5891051
25. Lee, S.Y., Kim, J.S., Lim, S.H., Jang, S.H., Kim, D.H., Park, N.-H., Jung, J.W. and Choi, J., "The investigation of the silica-reinforced rubber polymers with the methoxy type silane coupling agents", ***Polymers***, Vol. 12, No. 12, (2020), 3058, https://doi.org/10.3390/polym12123058
26. Torbati-Fard, N., Hosseini, S.M. and Razzaghi-Kashani, M., "Effect of the silica-rubber interface on the mechanical, viscoelastic, and tribological behaviors of filled styrene-butadiene rubber vulcanizates", ***Polymer Journal***, Vol. 52, No. 10, (2020), 1223-1234, https://doi.org/10.1038/s41428-020-0378-x
27. Borzouyi Kutenayi, S., Kiahosseini, S. and Talebpour, M., "The effect of caspian sea water on corrosion resistance and compressive strength of reinforced concrete containing different SiO_2 pozzolan", ***International Journal of Engineering, Transactions A: Basics*** Vol. 30, No. 10, (2017), 1464-1470, doi: 10.5829/ije.2017.30.10a.06
28. Jittabut, P., "Effect of nanosilica on mechanical and thermal properties of cement composites for thermal energy storage materials", ***Energy Procedia***, Vol. 79, (2015), 10-17, https://doi.org/10.4028/www.scientific.net/amr.1131.182
29. Hashemi, S. and MirzaeiMoghadamb, I., "Influence of nanosilica and polypropylene fibers on bond strength of reinforcement and structural lightweight concrete", ***Polymer***, Vol. 900, (2014), https://doi.org/10.5829/idosi.ije.2014.27.02b.10
30. Martinez-Vega, J., "Dielectric materials for electrical engineering, John Wiley & Sons, (2013).
31. Li, Y., Tian, M., Lei, Z., Xu, X. and Wang, S., "Effect of silicon dioxide nano-filler on dielectric and space charge properties of epoxy resin", ***High Voltage Engineering,*** Vol. 44, (2018), 1870-1877, https://doi.org/10.13336/j.1003-6520.hve.20180529019
32. Mentlík, V. and Michal, O., "Influence of SiO_2 nanoparticles and nanofibrous filler on the dielectric properties of epoxy-based composites", ***Materials Letters***, Vol. 223, (2018), 41-44, doi. https://doi.org/10.1016/j.matlet.2018.04.021
33. Ukhtiyani, I., Darwis, D. and Iqbal, I., "Purifikasi dan karakterisasi silika (SiO_2) berbasis pasir kuarsa dari desa pasir putih kecamatan pamona selatan kabupaten poso", ***Natural Science: Journal of Science and Technology***, Vol. 6, No. 3, (2017), https://doi.org/10.22487/25411969.2017.v6.i3.9201
34. Schweigert, I., Lehtinen, K., Carrier, M.J. and Zachariah, M.R., "Structure and properties of silica nanoclusters at high temperatures", ***Physical Review B***, Vol. 65, No. 23, (2002), 235410, doi: 10.1103/PhysRevB.65.235410.
35. Asadi, Z. and Norouzbeigi, R., "Synthesis of colloidal nanosilica from waste glass powder as a low cost precursor", ***Ceramics International***, Vol. 44, No. 18, (2018), 22692-22697, https://doi.org/10.1016/j.ceramint.2018.09.050
36. Vatalis, K.I., Charalambides, G. and Benetis, N.P., "Market of high purity quartz innovative applications", ***Procedia Economics and Finance***, Vol. 24, (2015), 734-742.
37. Jain, A., Panwar, A.K. and Jha, A., "Influence of milling duration on microstructural, electrical, ferroelectric and piezoelectric properties of ba0. 9sr0. 1zr0. 04ti0. 96o3 ceramic", ***Ceramics International***, Vol. 42, No. 16, (2016), 18771-18778.
38. Kumar, A., Kumarb, A. and Sharmaa, K., "Investigation of dielectric properties of Ni/N-TiO_2/P-Si/Al heterojunction in wide range of temperature and voltage", doi: 10.5829/ije.2022.35.04a.09.
39. El-Menshawy, O., El-Sissy, A., El-Wazery, M. and Elsad, R., "Electrical and mechanical performance of hybrid and non-hybrid composites", ***International Journal of Engineering***, Vol. 32, No. 4, (2019), 580-586, https://doi.org/10.5829/ije.2019.32.04a.16
40. Sari, K., Utomo, A.B.S., Abraha, K., Kartini, E., Yulianti, E. and Suharyadi, E., "Effect of milling time on the microstructure and dielectric properties of chitosan nanopowder", ***International Journal of Nanoelectronics & Materials***, Vol. 13, No. 1, (2020), doi: 10.1088/0022-3719/7/17/024
41. Martirena, H. and Burfoot, J., "Grain-size effects on properties of some ferroelectric ceramics", ***Journal of Physics C: Solid State Physics***, Vol. 7, No. 17, (1974), 3182, doi: 10.1088/0022-3719/7/17/024.
42. Kim, H.N. and Suslick, K.S., "The effects of ultrasound on crystals: Sonocrystallization and sonofragmentation", ***Crystals***, Vol. 8, No. 7, (2018), 280, https://doi.org/10.3390/cryst8070280
43. Hu, S., Luo, C., Li, P., Hu, J., Li, G., Jiang, H. and Zhang, W., "Effect of sintered temperature on structural and piezoelectric properties of barium titanate ceramic prepared by nano-scale precursors", ***Journal of Materials Science: Materials in Electronics***, Vol. 28, No. 13, (2017), 9322-9327, https://doi.org/10.1007/s10854-017-6670-7
44. Kumar, S., Supriya, S., Pradhan, L.K., Pandey, R. and Kar, M., "Grain size effect on magnetic and dielectric properties of barium hexaferrite (BHF)", ***Physica B: Condensed Matter***, Vol. 579, (2020), 411908, https://doi.org/10.1016/j.physb.2019.411908

Persian Abstract

چکیده

اثر فرکانس ارتعاش غشای بلندگو بر اندازه دانه نانوذرات سیلیس (SNP)مورد بررسی قرار گرفت. SNP با استفاده از روش همجوشی قلیایی تحت ارتعاش بلندگوی غشایی سنتز شد. تغییرات ارتعاش غشا در این تحقیق ۰، ۵۰، ۱۰۰ و ۲۰۰ هرتز بود. ترکیبات مواد، ساختار کریستالی و مورفولوژی SNP سنتز شده به ترتیب با استفاده از فلورسانس اشعه ایکس (XRF) ، پراش پرتو ایکس (XRD) و میکروسکوپ الکترونی عبوری (TEM) مشخص گردید. در همین حال، ویژگی دی الکتریک آن با استفاده از طیف سنجی امپدانس تعیین شد. نتایج نشان داد که SNP از ۹۹/۳۵ درصد سیلیس تشکیل شده و با ساختار کریستالی سیلیس کوارتز مطابقت دارد. اندازه SNP با افزایش فرکانس ارتعاش کاهش یافت. کوچکترین اندازه (9.04±1.9 SNP نانومتر در فرکانس ۲۰۰ هرتز به دست آمد. علاوه بر این، ثابت دی الکتریک و تلفات دی الکتریک با افزایش فرکانس ارتعاش غشا به دلیل کاهش اندازه SNP افزایش یافت.

IJE TRANSACTIONS A: Basics Vol. 35, No. 07, (July 2022) 1307-1316

International Journal of Engineering

Journal Homepage: www.ije.ir

Response of Rubcrete Continuous Deep Beams under Sinusoidal Loads

O. M. Makki*, H. M. K. Al-Mutairee

Department of Civil Engineering, College of Engineering, University of Babylon, Iraq

PAPER INFO

Paper history:
Received 24 February 2022
Received in revised form 26 March 2022
Accepted 29 March 2022

Keywords:
Harmonic Load
Sinusoidal Load
Continuous Deep Beams
Rubberized Concrete
Rubcrete

ABSTRACT

Continuous deep beams (CDBs) are the most used members in constructions with highly exposing to different types of dynamic loads. It is well known that; the concrete is a brittle material and has a weak resistance to energy absorption. Using scrapped tire rubber enhances the concrete energy absorption for sustainability purposes. Timoshenko beam theory has been used to solve CDBs subjected to sinusoidal load and has been adopted for verification of numerical results of ANSYS APDL V.15.0. Seven concrete mixes have been simulated with different types and amounts of aggregate – rubber replacements. Several parameters have been studied like replacing type, percentages, shear span of beam to depth ratio (a/h) and load intensity. It was found that Timoshenko beam theory can be used for harmonic loading CDBs. Furthermore, replacement in general provided more ductility due to rubber elasticity property. Gravel replacement by 45% has the larger displacement values among the other types. Also, it has been noted that, the sensitive of concrete deep beams towards a/h ratio stills considerable for harmonic loads, i.e. minimizing the ratio leads to decrementing the deflection wave amplitudes.

doi: *10.5829/ije.2022.35.07a.10*

NOMENCLATURE

a	Beam shear span	w_c	Concrete weight
b	beam width	Wn	Natural frequency
c	Damping factor	z	Studied point after pending (or depth of beam)
c^2	Correction factor	**Greek Symbols**	
E	Concrete elastic modulus	$\in_x$	Strain due to x-axis
F(t)	Applied harmonic load (point load)	γ_{zx}	Shear strain due to z-x axes
$f'c$	Concrete compressive strength	σ_x	Concrete stress towards x-axis
G	Shear modulus	τ_{zx}	Shear stress toward z-x axes
I	Moment of inertia of the section	ψ	Rotation angle
K	Beam stiffness	**Abbreviations**	
M	Moment of beam	ACI	American code institute
m	Beam mass (Kg)	CDBs	Continuous deep beams
Q	Beam shear	FR	Fine replacement
t	Applied load time.	GR	Gravel replacement

1. INTRODUCTION

Concrete continuous deep beams (CDBs) are widely used members as a load distributor (due to its high rigidity and stiffness) in many constructions like bridges, high rise buildings, girders and tanks (as shown in Figure 1) [1-5]. American Concrete Institute (ACI 318-19 code) specified two conditions for considering the concrete beam as a deep, which are, the clear span to total depth ratio does not exceed 4, or the concentrated load lies within the distance 2h from the supporting face [6]. Concrete deep beams largely exposed to dynamic loads in different intensities and since the concrete is a brittle material, then researches nowadays towards to enhance the concrete

*Corresponding Author Institutional Email: sth.ola.ali@student.uobabylon.edu.iq (O. M. Makki)

Please cite this article as: O. M. Makki, H. M. K. Al-Mutairee, Response of Rubcrete Continuous Deep Beams under Sinusoidal Loads, ***International Journal of Engineering, Transactions A: Basics,*** Vol. 35, No. 07, (2022) 1307-1316

energy absorption to dynamic loads. The published researches confirmed that, replacing scrapped tire rubber by a percentage of aggregate (or even adding it into the mix) provides an excellent energy absorption (but decreases the mechanical properties of concrete) [7-16]. The enhancement in impact energy of rubberized concrete (rubcrete) mixes reaches to (138-185-300-396%) for 5, 10, 15, 20% volumetric sand replacement, While (150-204-326-426%) for the same percentages of volumetric gravel replacement [17]. Too many types of dynamic loads may the CDBs exposed to, such as impact, seismic and moving vehicles load.

The simple form of harmonic load may occur by unbalanced rotating machines in building. Also, it may cause by hydrodynamic pressure which is generated due to propeller at the stern of a ship or by inertial effects in reciprocating machinery, and this types is more complex. It is worth to mention that the harmonic wave may come in different types which are: fundamental wave, 3rd harmonic wave and the distorted wave.

CDBs may exposed to harmonic loads at bridges due to vehicle movement and that will cause sin or cosine wave load on it. Adding rubber into concrete mix leads mainly to develop the concrete energy absorption of the bridges and enhance the overall dynamic properties. It can be noted from the next section that, there is no cutting-edge studying results gives us an indication about the CDBs response under harmonic loading. So, this paper consists of three parts, the first one is derived in a theoretical solution for analyzing the CDBs under harmonic loads. While the second part involved using the theoretical solution for checking the accuracy of numerical analysis. The third part studied the effect of adding rubber to concrete mix on the behavior of CDBs using ANSYS V.15.0 software program.

2. LITERATURE REVIEW

Generally, the response of continuous concrete deep beams has not investigated by the past researches especially for rubcrete mixes while it can be found some researches about an empirical equations to solve the seismic loads [18-21]. Numerical solutions by different software programs is interested with the reinforced concrete beams [22]. There are also some theoretical studies about concrete beams which exposed to harmonic loads [23-27] and plate foundation with regarding to Winkler model of subgrade reaction [28-30]. Through literature [25], the cracked and un-cracked concrete cantilever beam was investigated under the effect of harmonic load. It was found that, crack existing near to the fixed end support of the cantilever beam decreases the Eigen frequency compared with crack existing away from the fixed support. Also, displacement will be more for cracked beam compared to healthy beam, because of reduction in stiffness. Chen and Song [27] introduced a theoretical study for solving deep beams which were exposing to distributed harmonic load. Finite element (FE) method (By Mathlab software [31]) has been used for certificating the theoretical solution. It was noticed an excellent matching between the derived equation and the FE results. Continuous deep beams have been studied in many articles with static load [32-35], repeated and cyclic loads on simply supported deep beams [34, 36], rubberized continuous deep beams were statically tested [37, 38], and rubberized deep beams under static loads [39]; but, there was no investigation under the effect of harmonic loads. Therefore, solving the CDBs under the effect of harmonic loads has not been studied yet. Furthermore, the effect of using rubcrete instead of concrete at constructions with highly exposed to dynamic loads vibrations was investigated.

3. METHODS

The problem discussed in this research consists of three solutions. The first two are theoretical analyses which depend on deriving new equations for simulating the deflection of concrete continuous deep beams under sinusoidal loads. These two methods relenting on the dynamic general equation as well as the Timoshenko beam analysis. While the third solution involved a simulation of concrete beam by ANSYS APDL software and comparing the obtained results with the theoretical results then investigates some case studies to get the full description of parameter effect on the CDBs. Figure 2 shows a block diagram of the complete work and Figure 3 shows the selected CDBs model

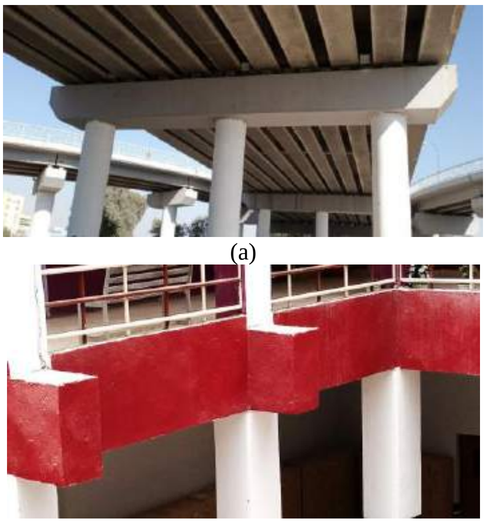

(a)

(b)

Figure 1. CDBs application at buildings

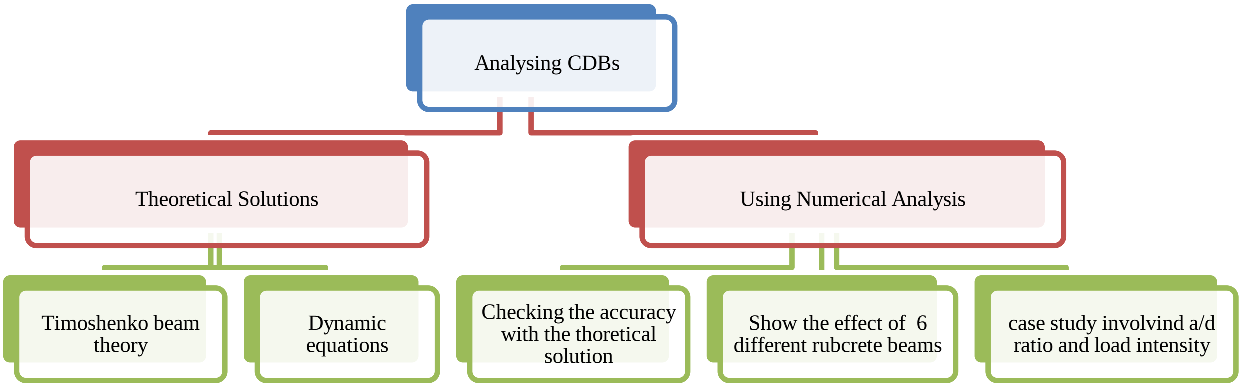

Figure 2. Overall study plane

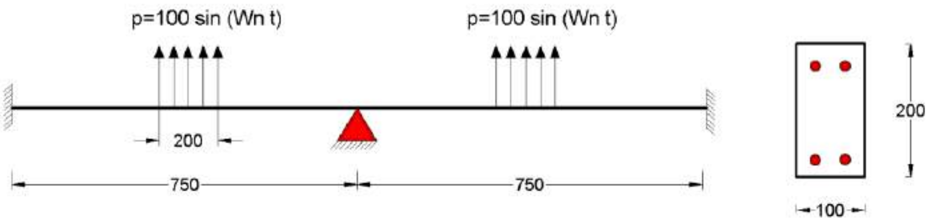

Figure 3. Beam details (all dimensions are in mm)

3. 1. Timoshenko Beam Solution It is difficult to get a plastic theoretical solution for continuous deep beams under the effect of harmonic load. So, an elastic solution has been derived and adopted for verification the analytical solution (by ANSYS V.15.0). Timoshenko beam theory [22] has been used which satisfied the requirement of deep beams, which are:

- The plane section does not remain plane after bending.
- The normal to the neutral plane after bending will not remain normal to the neutral but have an additional rotation due to high transverse shear deformation.
- Neglecting normal strain along the width.

The deriving equation of deep beam deflection is given in Equation (1).

$$\frac{d^4w}{dx^4} = \frac{q}{EI} - \frac{1}{c^2GA} \times \frac{d^2q}{dx^4} \quad (1)$$

Let $w(m) = \sum_{m=1}^{n} \sin(\frac{2m\pi x}{l})$ to satisfy the boundary conditions of continuous deep beam.

Substitute in Equation (1), to get the final equation of CDB deflection under harmonic load (Equation (2))

$$w_{at\ mid\ span} = 0.09752 \sin(w_n\ t) \quad (2)$$

3. 2. Dynamic Equation Solution In general, the structural members resist the dynamic load by its mass, stiffness and the magnitude of damping which depend on the material itself [31]. The damping ratio is ignored in most structural calculations for safety. For concrete, the damping factor does not exceed 6%. For solving the CDBs under sinusoidal loads, the dynamic equation response of structures is derived with ignoring the effect of deep beams, and as listed below (Equation (3))

$$m\ddot{y} + c\dot{y} + ky = F(t) \quad (3)$$

Applying the same details of beam at Figure 3, to get the time deflection equation for the given beam (Equation (4))

$$y = \frac{\frac{F(t)}{m}}{\frac{k}{m} - w_n^2} \quad (4)$$

3. 3. Numerical Simulation Beam 188 element has been used for simulating the CDB in ANSYS APDL software [39] (As shown in Figure 4). After trying some meshing sizes, it was found that , 20 mm meshing length gives a good agreement with the theoretical model in such fast rendering time. External supports were selected to fixed while the internal was of single vertical reaction.

Seven concrete mixes were simulated depending on Topcu's tested mixes [40], three percentages used which are (15, 30, 45) % for sand and gravel replacement besides the ordinary conventional mix. All concrete properties were extracted from literature [40]. Compressive strength, tensile strength, concrete unit weight and young's modulus for all mixes were summarized in Table 1. The input stress versus strain curve is shown in Figure 5. Young's modulus was

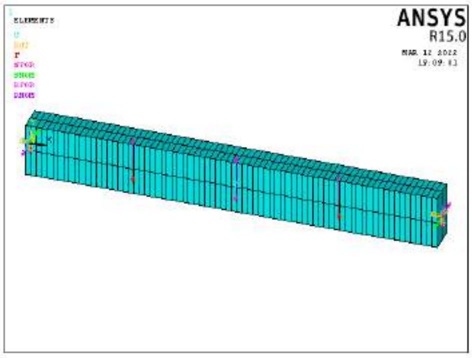

Figure 4. CDB modelling at ANSYS software

TABLE 1. Mechanical concrete properties

Mix	w_c (Kg/ m^3)	f'_c (MPa)	Ec (MPa)
NC	2300	23.48	22983
G15	2220	16.18	18092
G30	2140	12.62	15122
G45	2010	9.9	12192
S15	2220	24.22	22135
S30	2140	19.7	18894
S45	2010	14.77	14892

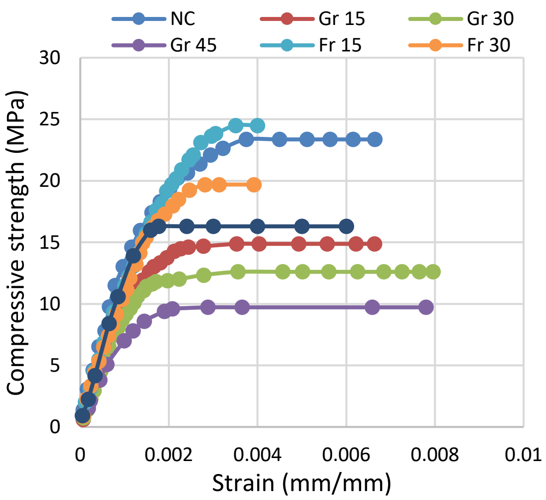

Figure 5. Inserted stress-strain curve into program

considered using ACI 318- 19 (Equation (5)) which is proportional to rubcrete weight (and as adopted for rubcrete mixes reported in literature [41]).

Table 1 shows the detains of elastic modulus values for all selected mixes. The analysis was displacement control with a tolerance factor equals 6%.

$$E_c = 0.043 * w_c^{1.5} * \sqrt{f_c'} \tag{5}$$

4. RESULTS

4. 1. Theoretical Results and Numerical Verification

The validation between numerical and theoretical beam solutions were investigated as illustrated in Figure 6. It can be noted that, a good match in beam response between the numerical and the Timoshenko beam solutions with slight differences in the amplitude between them caused due to that, the nonlinear simulation gives more accurate results. Because it simulates the problem as it is in the nature in a matter accurate than the theoretical solutions. This nonlinear model has been considered to use for simulating a parametric study for rubcrete beams. While, the solution using the general dynamic equation also gives the same response but with less accurate due to ignoring the effect of deep beam effect. It causes an error in deflection magnitudes but the good point, it also gives the same response.

4. 2. Rubberized CDBs Results

Nonlinear solution was investigated to study the effect of sinusoidal harmonic load for seven beams. One beam was simulated without any rubber replacement in order to be the reference model, the first group was of three beams with 15, 30, 45% of gravel replacement (GR) and the second group was of the same percentages of fine aggregate replacement (FR). The results for the seven beams as illustrated in Figures 6 to 9, the displacement, velocity and acceleration are discussed. From Figure 6, it can be noted that, the beam of normal concrete (NC) deflects in the less magnitude than the other beam due to its high compressive strength and low elasticity. Beam GR45 showed the maximum values of displacement due to the sinusoidal load because of its low compressive strength, elastic property, and large ability to absorb energy. Also, the negative values of deflection were higher than the positive, which is refers to that the beam approaches from cracking, in another word, if all-deflection points were in negative zone, then the beam is fully cracked. For all beams, the time period does not change in contract with the amplitude.

Velocity of beams data are also presented in Figure 7. It can be noted that, the velocity wave formed as distorted wave (the latter is a combination between fundamental and the third harmonic wave). The same arrangement of amplitude appears at both velocity and acceleration responses, as shown in Figures 7 and 8.

4. 3. Case Studies' Results

4. 3. 1. a/h Ratio Influence

The beam GR 45 showed the weakest model due to its low compressive strength and its high elasticity, so it has been considered for modelling the effect of changing a/h ratio because it represents the more dangerous case of rubcrete. Theoretically, the CDB behavior approaches to be flexural with a smaller a/h ratio, and its shear strength capacity increased linearly with a/h reduction [19]. The smaller a/h ratio shows minimum deformation capacity of CDB also ductility and beam load capacity [20, 21]. This fact was also noticed in the dynamic analysis of the rubcrete beams. The model of a/h=0.5 showed less displacement against the same load and rubcrete properties. The time durations of waves were still deposit but there was a visible difference in beams' amplitudes for all the given deep beams due to a/h difference, as shown in Figure 9.

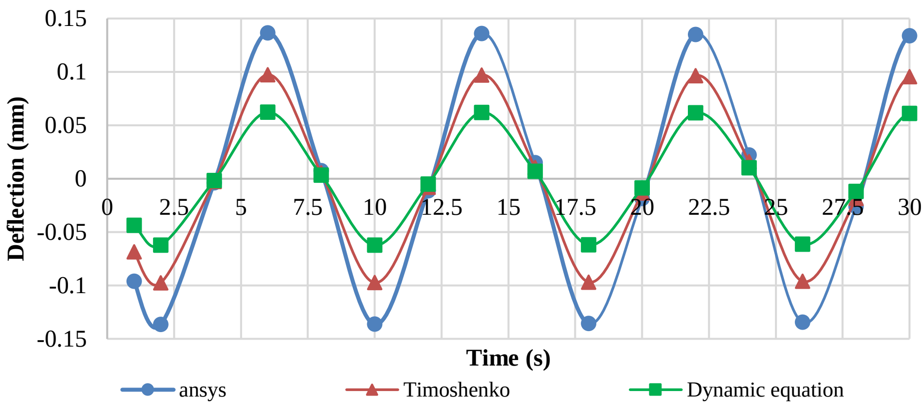

Figure 6. Verification of deflection by theoretical and analytical solutions

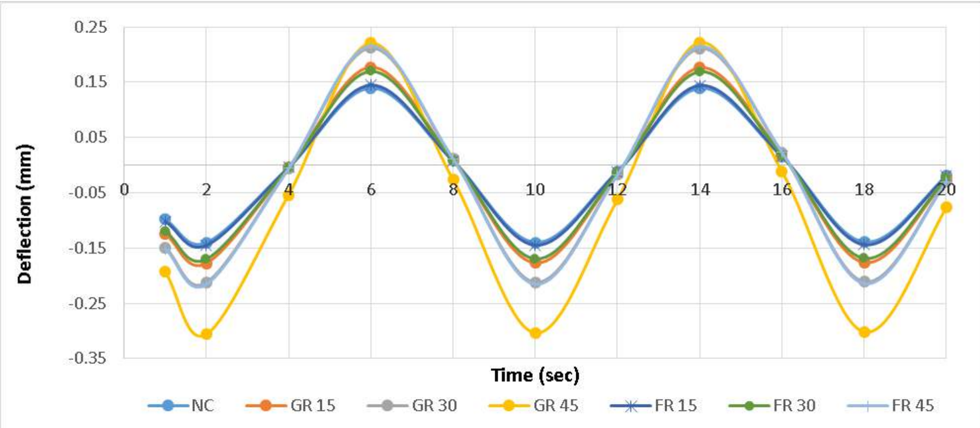

Figure 7. Rubcrete CDB deflections

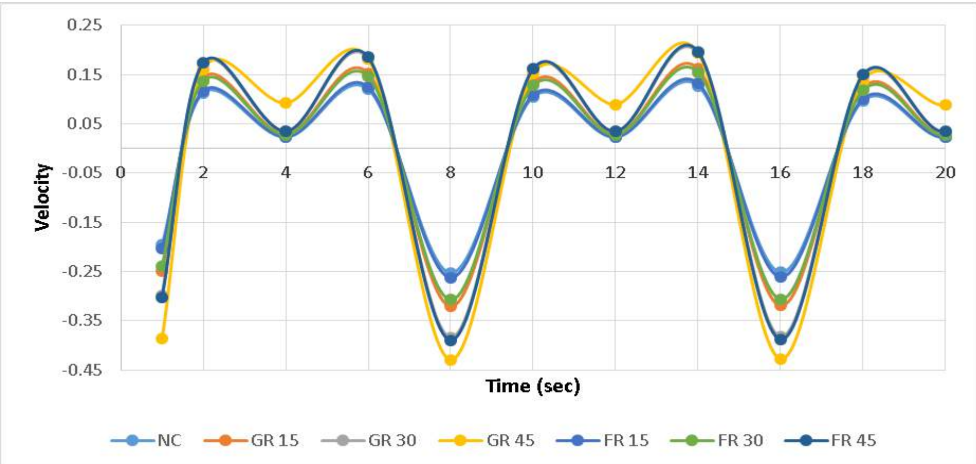

Figure 8. Velocity of beams under sinusoidal loading (mm/s)

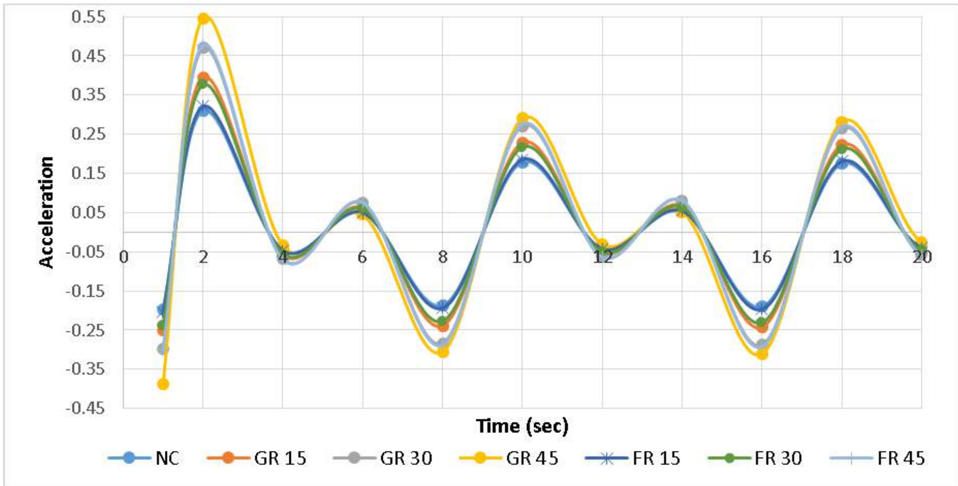

Figure 9. Beams acceleration (mm/s^2)

But in case of using a shallow beam (a/d=3), the velocity and acceleration amplitudes and periods changed (Figures 10 and 11). The time periods shift to the left with staying on the overall general wave shape. While the deflection (Figure 9) of shallow beam still keeps the periods and the overall general wave shape but with a significant large displacement comparing with the deep beams due to its higher bending capacity.

4. 3. 2. Load Intensity The specimen GR45 was selected to study the influence of incrementing load intensity. The original selected load was doubled, tripled, quadruple and quintuple. It can be seen that, the relatively low loads vibrate the beam about the original zero displacement axis but the higher ((300 and 400) × sin $W_n t$) the same wave shape occurred with high negative displacement only. Quintuple load forced the rubcrete model to a plastic flow. Also, from curves in Figure 12, it can be concluded that, the vibration amplitude of rubcrete CDBs depends in the first degree on a/h ratio, beams' natural frequency and the load intensity. The last conclusion also matched with literature discussions.

The higher displacement occurred when quadrupling the load, the beam deflects more by 80%, and 19.8% comparing with literature.

Figures (13-18) shows the stress versus time for CDBs. It can be noting that, the stress waves gets bigger when increasing harmonic load intensity on beams.

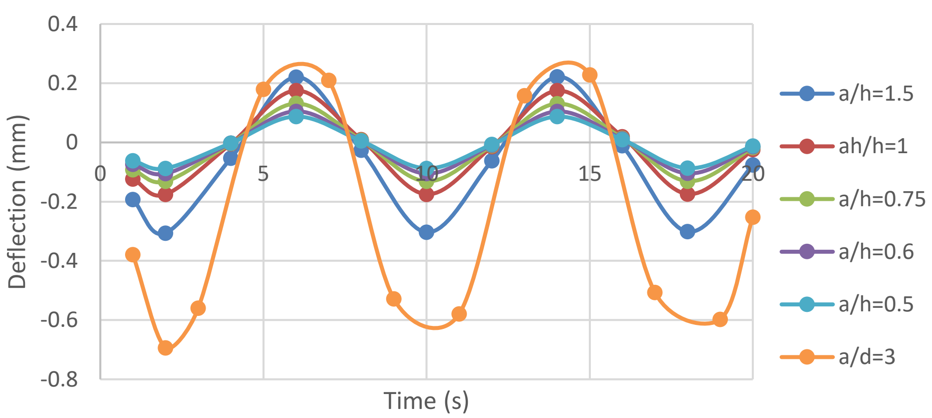

Figure 10. Influence of a/h ratio on rubcrete beams' deflection

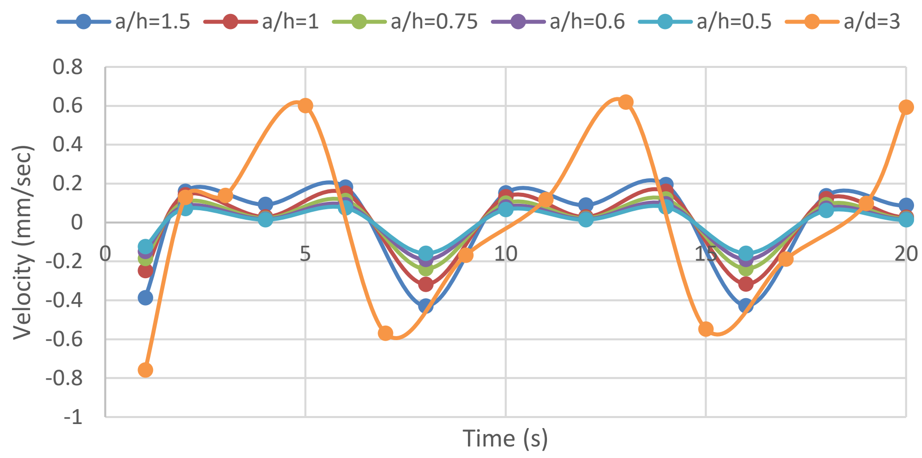

Figure 11. Velocity of CDBs of different beams depth

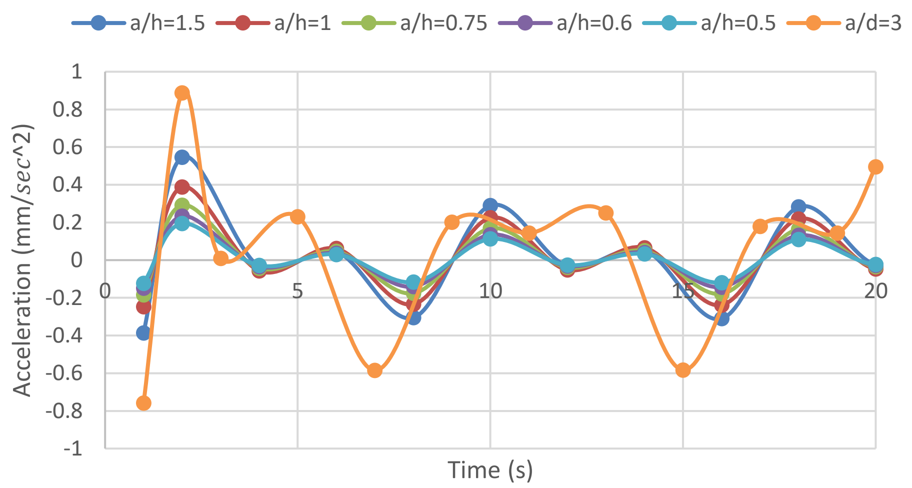

Figure 12. Acceleration of CDBs of different depths ((mm/s^2)

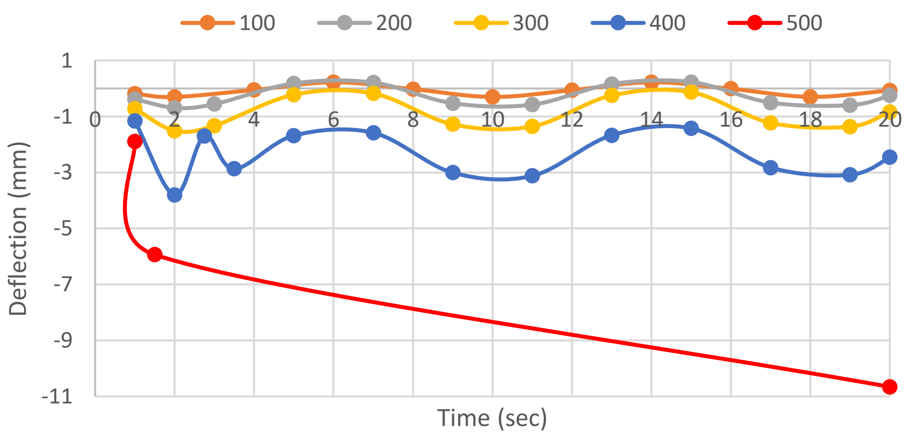

Figure 13. Effect of load increment on CDB deflection response

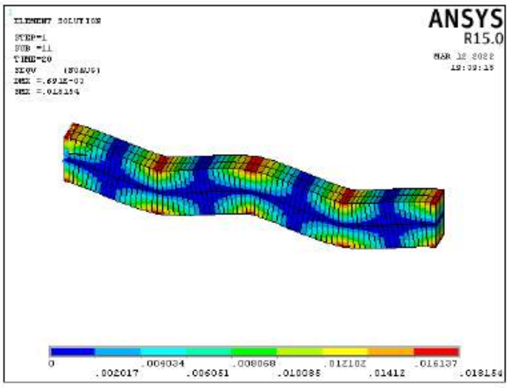

Figure 14. Von-Misses Stress for 100 sin $W_n t$ loading

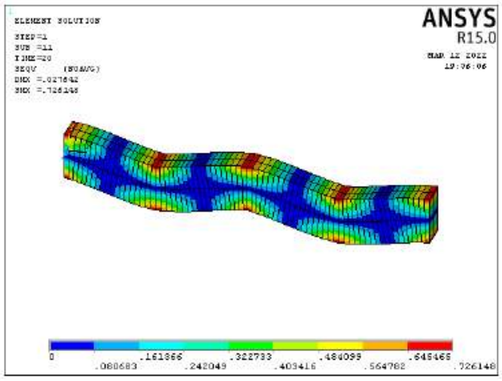

Figure 15. Von-Misses Stress for 200 sin $W_n t$ case

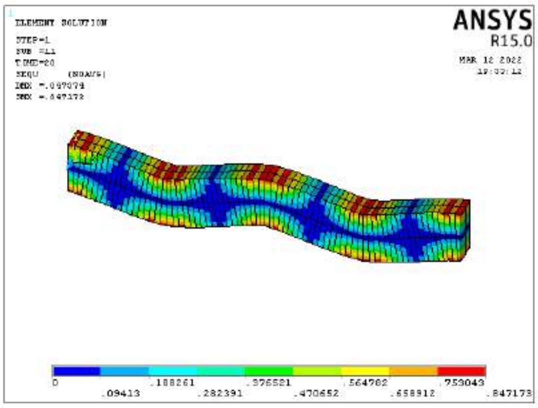

Figure 16. Von-Misses Stress for 300 sin $W_n t$ case

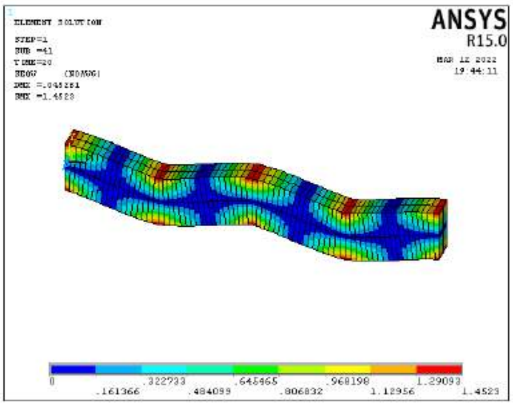

Figure 17. Von-Misses Stress for 400 sin $W_n t$

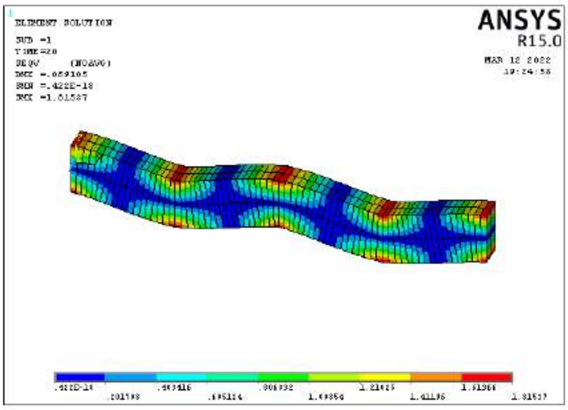

Figure 18. Stress for 500 sin $W_n t$ loading

5. DISCUSSION

CDBs may be exposed to harmonic loads due to many reasons like vehicle movement on bridges. The solution of CDBs under sinusoidal load and the behaviour of it has not been discovered yet. Timoshenko beam theory was used to discover the behaviour and finding the deflection response along beams. It provided the best match when comparing with the numerical solution. Concrete is a weak material against energy absorption. So, adding rubber for the mix enhances the dynamic properties. Timoshenko beam theory can be used for harmonic load with a significant degree of exact to the elastic response of CDBs. Also, solving the beam using the general dynamic equations gives a correct estimation for the beam response but an error value of displacement due to ignoring the deep beam effect so it is unfavourite to be used in CDBs analysis. From the numerical analysis, it was found that, Beam element 188 (in spite of its nonlinearity and it is a 2D model) offers a great degree of validation and the exactly same response with the theoretical method. It was found that, the replacement causes a large deflection capacity under the same load. That means the rubberized beam is more flexible against load. Generally, replacing rubber by aggregate leads to an increase in energy absorption and therefore enhanced the beam resistance for dynamic loading.

6. CONCLUSIONS AND FUTURE WORK

From the results, it can be concluded that, using rubber in concrete beams rises the beam deflection and enhances the ductility of beam against dynamic loads. Knowing that, replacing rubber of a coarse aggregate provides more energy absorption than that of the same percentage of fine aggregate replacement. The sensitivity of concrete deep beams towards a/h ratio is still considerable for harmonic loads, i.e., minimizing the ratio leads to decrementing the deflection wave amplitudes. It was also found that, higher load vibration intensity produces larger displacement amounts, and excessive loads may cause a plastic flow. Furthermore, the vibration amplitude of rubcrete CDBs depends mainly on a/h ratio, beams natural frequency and the load intensity. It is recommended in the future to study the nonlinear theoretical analysis of CDBs under the effect of dynamic loads to find the beam capacity under such conditions.

7. REFERENCES

1. Rogowsky, D.M., MacGregor, J.G. and Ong, S.Y., "Tests of reinforced concrete deep beams", (1983).
2. Salman, W.D., "Nonlinear behavior of reinforced concrete continuous deep beam", ***International Journal of Engineering Research & Technology***, Vol. 4, (2015), 2278-2281, doi: 10.17577/ijertv4is040460.
3. Abdul-Razzaq, K.S., Jalil, A.M. and Dawood, A.A., "Reinforced concrete continuous deep beams under the effect of different parameters", in AIP Conference Proceedings, AIP Publishing LLC. Vol. 2213, No. 1, (2020), 020127.
4. 426, J.A.-A.C., "Shear strength of reinforced concrete members (aci 426r-74)", in Proceedings ASCE. Vol. 99, No. ST6, (1973), 1148-1157.
5. Khatab, M.A., Ashour, A.F., Sheehan, T. and Lam, D., "Experimental investigation on continuous reinforced scc deep beams and comparisons with code provisions and models", ***Engineering Structures***, Vol. 131, (2017), 264-274, doi: 10.1016/j.engstruct.2016.11.005.
6. Qaedi, H., "Desain modifikasi struktur gedung kampus iii uin imam bonjol padang menggunakan metode beton pracetak dengan sambubungan basah berdasarkan aci 318m-19", Institut Teknologi Sepuluh Nopember, (2021),
7. Khan, S. and Singh, A., "Behavior of crumb rubber concrete", ***International Journal of Research in Engineering***, Vol. 8, (2018), 86-92, doi. https://www.researchgate.net/publication/333044437_Behavior_of_Crumb_Rubber_Concrete
8. Shah, S., Shrestha, S., Maharjan, S., Karki, N. and Shrestha, R., "Evaluation of performance of rubber concrete", in Proceedings of IOE Graduate Conference. Vol. 6, (2019), 599-603.
9. Raj, A., Nagarajan, P. and Shashikala, A., "Behaviour of fibre-reinforced rubcrete beams subjected to impact loading", ***Journal of the Institution of Engineers (India): Series A***, Vol. 101, No. 4, (2020), 597-617, doi: 10.1007/s40030-020-00470-4.
10. Najim, K.B. and Hall, M.R., "Mechanical and dynamic properties of self-compacting crumb rubber modified concrete", ***Construction and Building Materials***, Vol. 27, No. 1, (2012), 521-530, doi: 10.1016/j.conbuildmat.2011.07.013.
11. Sukontasukkul, P., "Use of crumb rubber to improve thermal and sound properties of pre-cast concrete panel", ***Construction and Building Materials***, Vol. 23, No. 2, (2009), 1084-1092, doi: 10.1016/j.conbuildmat.2008.05.021.
12. Elshazly, F.A., Mustafa, S.A. and Fawzy, H.M., "Rubberized concrete properties and its structural engineering applications–an overview", ***Egyptian Journal for Engineering Sciences and Technology***, Vol. 30, No. Civil and Architectural Engineering, (2020), 1-11, doi: 10.21608/eijest.2020.35823.1000.
13. Rahul, G.T., "Enhancing the properties of crumb rubber modified concrete with synthetic resin", (2020).
14. Grinys, A., Augonis, A., Daukšys, M. and Pupeikis, D., "Mechanical properties and durability of rubberized and sbr latex modified rubberized concrete", ***Construction and Building Materials***, Vol. 248, (2020), 118584, doi: 10.1016/j.conbuildmat.2020.118584.
15. Beiram, A. and Al-Mutairee, H., "Effect of using waste rubber as partial replacement of coarse aggregate on torsional strength of square reinforced concrete beam", doi: 10.5829/ije.2022.35.02b.16.
16. Al-Mutairee, H.M. and Makki, O.M., "Rubberized concrete mix–discussions for literature review", in Journal of Physics: Conference Series, IOP Publishing. Vol. 1895, No. 1, (2021), 012011.
17. Kadhim, A.A. and Kadhim, H.M., "Experimental investigation of rubberized reinforced concrete continuous deep beams", ***Journal of King Saud University-Engineering Sciences***, (2021).
18. LI, S., Yu, T. and Jia, J., "Empirical seismic vulnerability and damage of bottom frame seismic wall masonry structure: A case study in dujiangyan (china) region", ***International Journal of Engineering***, Vol. 32, No. 9, (2019), 1260-1268, doi: 10.5829/ije.2019.32.09c.05.
19. Siqi, L., Tianlai, Y. and Junfeng, J., "Investigation and analysis of empirical field seismic damage to bottom frame seismic wall masonry structure", ***International Journal of Engineering***, Vol. 32, No. 8, (2019), 1082-1089, doi: 10.5829/ije.2019.32.08b.04.
20. Li, S.-Q. and Chen, Y.-S., "Analysis of the probability matrix model for the seismic damage vulnerability of empirical structures", ***Natural Hazards***, Vol. 104, No. 1, (2020), 705-730, doi: 10.1007/s11069-020-04187-2.
21. Gautam, D., Adhikari, R., Rupakhety, R. and Koirala, P., "An empirical method for seismic vulnerability assessment of nepali school buildings", ***Bulletin of Earthquake Engineering***, Vol. 18, No. 13, (2020), 5965-5982, doi: 10.1007/s10518-020-00922-z.
22. Stoynova, I., "Vibration analysis of the simply supported r/c beam", in IOP Conference Series: Materials Science and Engineering, IOP Publishing. Vol. 1141, No. 1, (2021), 012036.
23. Chen, G., Mu, H. and Yang, X., "Dynamic responses of rc beams under slowly swept harmonic loads", (2000).
24. Şimşek, M. and Kocatürk, T., "Dynamic analysis of eccentrically prestressed damped beam under moving harmonic force using higher order shear deformation theory", ***Journal of Structural Engineering***, Vol. 133, No. 12, (2007), 1733-1741.
25. Sushmitha, N. and Hegde, M.N., "Harmonic analysis of cantilever beam with and without cracks", ***International Research Journal of Engineering and Technology***, Vol. 6, No. 9, (2019), 692-695, doi.
26. Mohammadzadeh, S., Esmaeili, M. and Mehrali, M., "Dynamic response of double beam rested on stochastic foundation under harmonic moving load", ***International Journal for Numerical and Analytical Methods in Geomechanics***, Vol. 38, No. 6, (2014), 572-592, doi: 10.1002/nag.
27. Chen, Y., Song, Y., Yang, J. and Teng, T., "A new method of forced vibration problem of deep beams under distributed harmonic load", ***International Journal of Materials and Structural Integrity***, Vol. 12, No. 1-3, (2018), 179-193.
28. Civalek, Ö., Özturk, B. and Yavas, A., "Nonlinear transient dynamic response of clamped rectangular plates on two-parameter foundations by the algorithm of the singular convolution", ***International Journal of Science and Technology***, Vol. 2, No. 2, (2007), 165-177.

29. Aydin, E., Dutkiewicz, M., Öztürk, B. and Sonmez, M., "Optimization of elastic spring supports for cantilever beams", ***Structural and Multidisciplinary Optimization***, Vol. 62, No. 1, (2020), 55-81.
30. Civalek, O. and Ozturk, B., "Free vibration analysis of tapered beam-column with pinned ends embedded in winkler-pasternak elastic foundation", ***Geomechanics and Engineering***, Vol. 2, No. 1, (2010), 45-56,.
31. Toolbox, S.M., "Matlab", ***Mathworks Inc***, (1993).
32. Mohamed, A.M., Mahmoud, K. and El-Salakawy, E.F., "Behavior of simply supported and continuous concrete deep beams reinforced with gfrp bars", ***Journal of Composites for Construction***, Vol. 24, No. 4, (2020), 04020032, doi: 10.1061/(asce)cc.1943-5614.0001039.
33. Zargarian, M. and Rahai, A., "Theoretical and experimental studies of two-span reinforced concrete deep beams and comparisons with strut-and-tie method", ***Advances in Civil Engineering***, Vol. 2021, (2021), doi: 10.1155/2021/8880067.
34. Khalaf, M.R. and Al-Ahmed, A.H.A., "Effect of large openings on the behavior of reinforced concrete continuous deep beams under static and repeated load", in E3S Web of Conferences, EDP Sciences. Vol. 318, (2021), 03012.
35. Makki, O.M. and Al-Mutairee, H.M., "Continuous deep beams behavior under static loads: A review study", in IOP Conference Series: Earth and Environmental Science, IOP Publishing. Vol. 961, No. 1, (2022), 012034.
36. Hassan, S.A. and Faroun, G.A., "Behavior of hybrid reinforced concrete deep beams under repeated loading", ***Civil and Environmental Research***, Vol. 8, No. 10, (2016), 14-37.
37. Kadhim, A.A. and Kadhim, H.M., "Loading capacity prediction of rubberized reinforced concrete continuous deep beams", in IOP Conference Series: Materials Science and Engineering, IOP Publishing. Vol. 1090, No. 1, (2021), 012031.
38. Sandeep, M., Nagarajan, P. and Shashikala, A., "Behaviour of steel fibre reinforced rubberized continuous deep beams", in IOP Conference Series: Materials Science and Engineering, IOP Publishing. Vol. 330, No. 1, (2018), 012125.
39. Clough, R. and Penzien, J., *Dynamics of structures third edit., berkeley, ca 94704 USA: Computers & structures*. 1995, Inc.
40. Topcu, I.B., "The properties of rubberized concretes", ***Cement and Concrete Research***, Vol. 25, No. 2, (1995), 304-310, doi: 10.1016/0008-8846(95)00014-3.
41. Bisht, K. and Ramana, P., "Evaluation of mechanical and durability properties of crumb rubber concrete", ***Construction and Building Materials***, Vol. 155, (2017), 811-817, doi: 10.1016/j.conbuildmat.2017.08.131.

Persian Abstract

چکیده

تیرهای عمیق پیوسته (CDB) پرکاربردترین اعضا در ساخت و سازها هستند و به شدت در معرض انواع مختلف بارهای دینامیکی هستند. معروف است که؛ بتن ماده ای شکننده است و مقاومت ضعیفی در برابر جذب انرژی دارد. استفاده از لاستیک تایرهای ضایع شده، جذب انرژی بتن و همچنین برای اهداف پایداری را افزایش می دهد. تئوری تیر تیموشنکو برای حل CDBهای تحت بار سینوسی استفاده شده است و برای تأیید نتایج عددی ANSYS APDL V.15.0 به کار گرفته شده است. هفت مخلوط بتن با نوع و مقادیر متفاوت سنگدانه – جایگزینی لاستیک شبیه سازی شده است. پارامترهای مختلفی مانند نوع جایگزینی، درصد جایگزینی، نسبت برشی تیر به عمق (a/h) و شدت بار مورد مطالعه قرار گرفته است. مشخص شده است که تئوری پرتو تیموشنکو را می توان برای پرتو پیوسته بارگذاری شده هارمونیک به میزان قابل توجهی از پاسخ الاستیک CDBها استفاده کرد. علاوه بر این، جایگزینی به طور کلی به دلیل خاصیت ارتجاعی لاستیک، انعطاف پذیری بیشتری را ارائه می دهد. جایگزینی شن به میزان ٤٥ درصد، مقادیر جابجایی بیشتری را در میان انواع دیگر دارد. همچنین توجه شده است که حساس بودن تیرهای عمیق بتنی به نسبت (a/h) نسبت به بارهای هارمونیک قابل توجه است، یعنی به حداقل رساندن این نسبت منجر به کاهش دامنه موج انحراف می شود.

International Journal of Engineering

Journal Homepage: www.ije.ir

A Compositional Adaptation-based Approach for Recommending Learning Resources in Software Development

M. Tayefeh Mahmoudi*[a], K. Badie[b], M. H. Moosaee[c], A. Souri[d]

[a] *Data Analysis & Processing Research Group, IT Research Faculty, ICT Research Institute, Iran*
[b] *E-Content & E-Services Research Group, IT Research Faculty, ICT Research Institute, Iran*
[c] *Computer Engineering Group, Science & Culture University, Iran*
[d] *Electrical Engineering Group, Islamic Azad University South Tehran Branch, Iran*

PAPER INFO

Paper history:
Received 01 March 2022
Received in revised form 15 March 2022
Accepted 02 April 2022

Keywords:
Recommender System
Learning Resource
Case–based Reasoning
Compositional Adaptation
Semantic Similarity
Domain-specific Ontology

ABSTRACT

In this paper, we discussed the application of a compositional adaptation approach to recommend learning resources to users in the area of software development. This approach makes use of a domain-specific ontology in this area to find those words, which are used in the technical description of the stored cases. A point peculiar with representing cases in the proposed approach is to take into account the characteristics of included learning resources, which justify the way they support the essential operations in the case of solution. In this way, only those components that comply with user's request would be considered in the final solution. In the paper, the performance of the proposed approach for recommending learning resources together with the status of user experience in his/ her interaction with the resulted recommending system, have been evaluated. Results demonstrate the fact that the learning resources through this approach are sufficiently beneficial for the users. Although the proposed approach has been applied for recommending learning resources in the area of software development, it can be equally applied to any technological area through developing domain-specific ontology for that area. This is mainly because any technological area has its own specific objects/ entities holding their own semantic similarities that finally lead to forming a domain-specific ontology for that area.

***doi**: 10.5829/ije.2022.35.07a.11*

1. INTRODUCTION

In recent years, there has been a significant increase in the number of learning resources in various areas, especially in areas related to design, implementation and development of a software product. This huge amount of learning resources in the internet has been created due to the growing need of developers and the rapid growth of technology in this area. The question is which parts of these resources are essential for the developers, which of them yield a better education in practice while more functional, and finally which resource is more suitable for starting or continuing the learning process according to the level of the learner's knowledge. Therefore, choice selection turns to be difficult for the learners in general, and this causes difficulties on going from one resource to other resources. Previously, traditional systems used to provide static and non-intelligent or semi-intelligent algorithms. But modern systems namely intelligent tutoring systems, make use of information such as behavior, feedback or model of users, try to increase the quality of their suggestions and promote users' knowledge, skills and engagement as well [1, 2]. Taking the above-mentioned points into account, in this paper a compositional adaptation approach to case-based reasoning is proposed to upgrade recommendation of learning resources within the scope of project development as a significant scope of activity. To retrieve appropriate cases, a sort of ontology is employed which helps find cases that are semantically similar to what users express in terms of technical requirements for implementing a particular software application. Since a

*Corresponding Author Email: mahmodi@itrc.ac.ir (M. T. Mahmoudi)

Please cite this article as: M. Tayefeh Mahmoudi, K. Badie, M. H. Moosaee, A. Souri, A Compositional Adaptation-based Approach for Recommending Learning Resources in Software Development, ***International Journal of Engineering, Transactions A: Basics,*** Vol. 35, No. 07, (2022) 1317-1329

problem situation may be complex, educational resources for software development projects need to be combined in order to yield potential solutions. Compositional adaptation is therefore believed to be a helpful means in this regard.

2. RELATED WORK

Nowadays, recommender systems have received remarkable attention in social networks [3] educational institutions, with particular emphasis on e-learning and online learning, especially in the area of computer science [4]. These systems have been developed to directly help learners and also instructors choose useful and relevant learning resources such as courses or exercises based on deep reinforcement learning [5]. Some systems have also been developed to meet educational requirements among the massive number of educational resources [6]. Moreover, recommender systems useful for technology enhanced learning may support and enhance learning practices in design, development and test of socio-technical innovations [7]. These systems are able to intensify teaching and practicing based on a variety of reasoning methods [8]. There also exist some hybrid recommender systems, which are adaptive to learner's preferences and are able to generate recommendations by some hybrid approaches such as content-based filtering, collaborative selection and opinion mining as well [9-11]. Another kind of hybrid recommender system also exists, which makes use of ontology and sequential pattern mining (SPM) to evaluate the domain knowledge of the learner and learning resources, and determine the learners' consecutive learning patterns [12]. Moreover, there are some adaptive/intelligent web-based educational systems, which, not only focus on adaptive presentation and navigation, but also provide intelligent solutions for problem analysis and solving as well as curriculum sequencing [13]. In this respect, a ITS named Fuse has been developed based on both fuzzy and semantic reasoning to provide learning recommendations adaptively [14]. In this way, the user-centered design has shown to be a suitable basis for developing various kinds of learning recommenders. Regarding that, supporting adaptive feedback based on students' offline information and online resources, should also be regarded [15]. These studies demonstrate that making personalized environments in learning recommendation systems is the process that must consider learners' requirements respecting the learning contexts.

Most of the aforementioned systems employ rule-based or filtering methods to recommend personalizing the contents/learning resources [16] whereas situations exist that pre-experienced cases can also help recommendations come true more effectively. In this regard, various algorithms of case-based reasoning seem to be helpful [17-19].

A brief review on employment of CBR in educational systems shows that it is, not only applicable for suggesting suitable courses of massive open online courses (MOOCs) [20], but also is useful for planning towards personalization [21], contextualization [22] as well as recommendation [23, 24] and intelligent assistance [25]. Here, case adaptation is believed to have a promising role in providing reasonable solutions. Accordingly, utilizing an appropriate compositional adaptation method may play a significant role, especially in the situations where the components of a solution are capable of being adapted separately [26], or vice versa, where a solution is not dividable into some independent components and is therefore to be combined with other solutions. Although a variety of compositional adaptation algorithms have been proposed [19, 23]. However, they seem not to be adequate in the situations where a kind of semantic similarity exists between a problem and the stored cases. Considering this point, we propose a new approach for recommending the educational resources that has the ability to consider this semantic similarity in some way.

3. THE PROPOSED APPROACH TO DEVELOPING CBR-BASED RECOMMENDER SYSTEM

3. 1. Basic Idea By a CBR-based system, we mean any system, which functions on the ground of case-based reasoning, which has the ability to provide solutions for new problems based on the similarity which does exist between the current problem situation and the problem situations experienced in the past. The peculiarity of case-based reasoning in general, is to provide additional facts for a problem situation based on the cases experienced in the past. In many cases, the components of the problem situation and those in the stored cases are entities with at- one- glance different meanings thus making the issue of case adaptation rather problematic. However, the possibility exists in such a situation that the components chosen from different cases may be incompatible with each other thus increasing the risk of obtaining a non – reasonable solution. To overcome such a problem, in our approach certain constraints are to be included in the cases to assure the validity of a solution at different stages of composition. Solution in a case comprises a set of components as well as the functionality, which is to be exhibited by it. It should be noted that each component in a case itself holds a characteristic with respect to another component in the case whose information can increase the assurance of a solution's validity in some way. In this way, the higher number of such characteristics, a higher expectation would exist for the validity of a case solution.

Taking the above discussion into account, status of similarity between a problem situation and the existing case may be assessed from both aspects of "functionality" and "components". "Functionality" is to figure out which cases are to be taken into account as cases, and "components" to find out due to which shared properties the components in a case can be linked to those in the other cases [27]. Once cases with high priority were figured out, it would then be necessary to find out first how their components can be regarded similar to those in the problem situation and then take into account the very relations, which are considered between the components in these cases. To provide such types of information, ontology-type structures developed for specific problem domains are of particular significance. With regard to an ontology-type structure, entities in terms of classes and individuals (instances or objects) are connected to each other through considering some relations which are of particular significance to the corresponding domain (Software Development in our case). These relations are basically derived from the nature of Software Development, which in turn calls for concepts such as "implementation", "target for", "kind of", "tool for", …, which are of high significance to it. Let us say incorporating such concepts as relations (between classes and individuals) provides a suitable medium for us to arrange the popular items of interest in such a way that their similarity can be found out in a reasonable manner. Obviously, greater the number of relations as well as the depth of this ontology, a higher expectation would exist for the possibility of justifying similarity between a component in the current problem and some component in a stored case. It is to be noted that, despite the fact that the complexity emerged in such a way may at one look be an obstacle to finding similarity, there are however some cases (though not so frequent) where the status of similarity between the components may not be so clear. Thus in order not to miss the chance of retrieving a relevant case, we naturally would need an ontology with higher complexity.Regarding this we should keep in mind having an ontology with high complexity doesn't necessirily mean to afford high computational cost for finding similarity for all the problem situations. What we intend to do is to provide a medium wherein alternative component in a stored case can be found for a component in the current problem through figuring out the connection which does exist between them within this ontology-type structure. Once such a connection was found, we may conclude that the two components are semantically similar to each other. Having found those components in the stored cases, they would then be worth being transferred to the problem situation as the complementary components, and in the meantime those irrelevant components that are not compatible with the requirements of the problem situation can be deleted. To keep the final solution as suitable as possible, only one component from each retrieved case ought to be added to the problem situation. It should be noted that, to validate the considered ontology and its impact on the soundness of the final results, the meaningful relations discussed above would with no doubt be of high significance, which are defined by specialists who make the ontology based on the basic knowledge of domain specific ontology and the semantic labels defining the relations between the existing nodes. The pseudo-code of the proposed algorithm is also presented in Figure 1.

3. 2. An Example Suppose that a user wants to develop "A Social Network Application on Mobile Platform for Consulting on Type of Restaurants in Specific Map Location". Here, situation in a case comprises a "title" with technical content, and a "technical description" with regard to the utility of this title. In the meantime, solution of a case comprises a number of components standing for appropriate learning resources, which can support the operations that are essential to realizing the case situation. Such a support is in fact a characteristic of a learning resource (as a component) which justifies how it can help a certain operation be performed in a favourable manner.

```
Procedure SEMANTIC_CBR
Input: pre-stored cases, problem situation
Set significant categories, properties or characteristics of
ongoing problem situation
for each combinations of significant categories, properties or
characteristics, P
  for each pre-stored case, C
 Determine semantic similarity between the components of C
and P
      for each constraints S in constraint list
        if any component of C satisfy constraint S then
          if any component of P does not satisfy constraint S
then
              Add the complementary component to the list of P
          end if
              Delete constraint S from the list of constraints
          end if
        end for
  end for
end for
print possible alternatives of the final solution
end procedure
```

Figure 1. The pseudo code of proposed algorithm for recommendation based on semantic compositional adaptation

With regard to the case retrieval process, we have to see, which cases out of those stored in the library, can support this request in some way. In our approach, in order to retrieve a case, there should exist at least one item in its "technical description" which can be identical to a keyword in the user's request. Suppose that, none of the cases has such an ability. It would now be important to check whether some words exist in the domain – specific ontology developed for this purpose, which can be semantically similar to the user's request keywords in some way. It should be noted that a domain-specific ontology has the ability to replace the keywords of the user's request with those words in the "technical description" of a case, which, though not exacly the same are semantically similar to them. To construct a domain-specific ontology, significant aspects of the related technology covering issues related to "infrastructure", "methods", "tools" as well as "applications & services" can be taken into account. Considering this point a part of the domain-specific ontology used for this example is shown in Figure 2. A domain specific ontology can generally be made based on the consensus obtained among the specialists of that domain on the one side and the basic knowledge of that domain on the other side. In our research we followed this procedure.

Coming back to the above example, and supposing that the request keywords ("mobile platform", "consulting" and "map location") have not been directly used in the "technical description" of any stored case, the ontology of Figure 2 would tell us that there exist the words"android", "chatting" and "location", which respectively correspond to these keywords and are able to justify retrieval of the cases of Figures 3(a), 3(b), 3(c), since these terms ("android", "chatting", and "location") have been fairly used in their descriptions. Having retrieved these cases, it would now be important to check which parts in the corresponding solutions can be considered as the alternative parts for the final solution on the related request. With regard to the case of Figure 3(a), learning resources on "Java Language", "Java

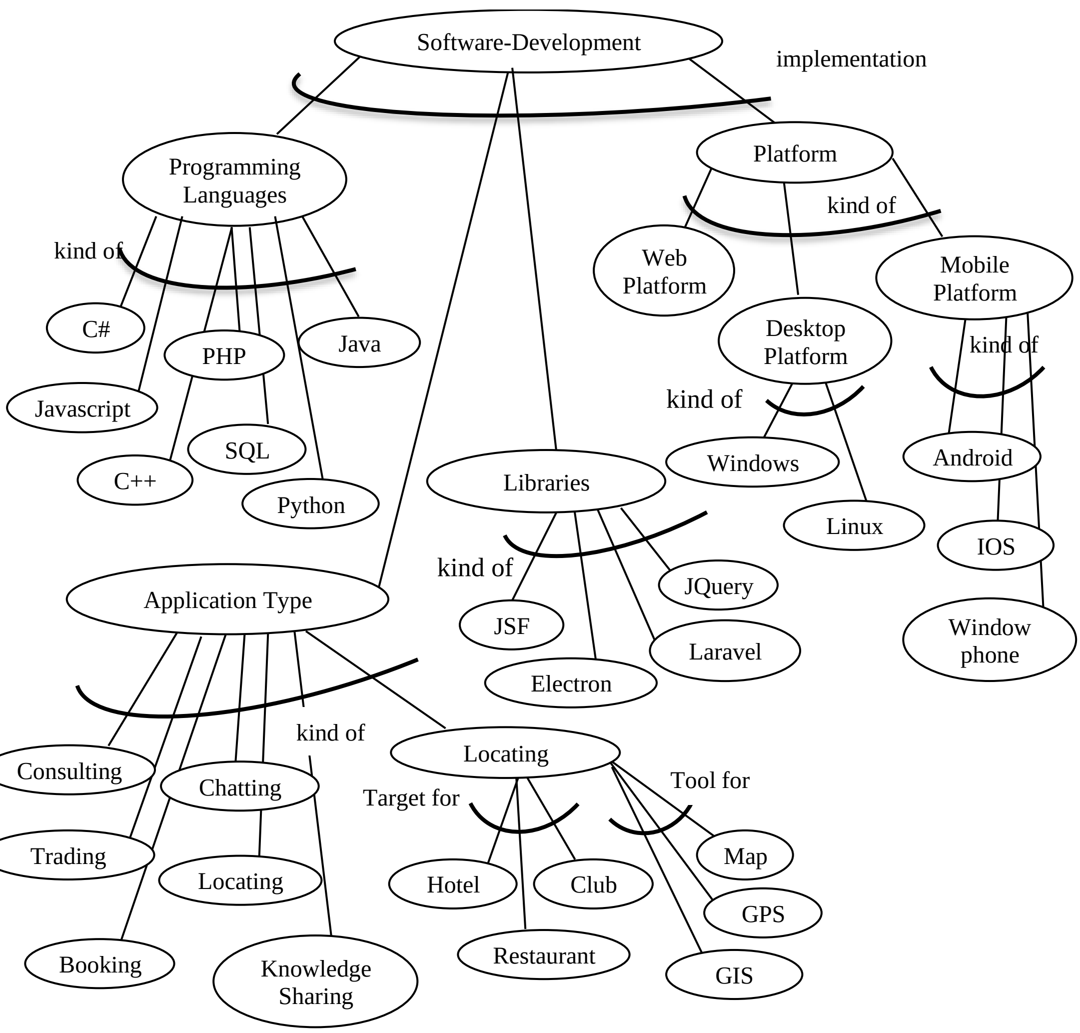

Figure 2. A part of domain –specific ontology used in the example

Language", "SQLite Database Manager", "XML Markup Language" and again "Java Language" can take such a responsibility, since they serve "Implementing Business Logic for Android", " Implementing Database for Android" and " Implementing User Interface for Android" which comply with the user's request. Our basis for reasoning is to take into account the very similarity which does exist between the keywords in the "user's request" on the one side, and the keywords existing in the situation of the corresponding case on the other side, which is actually realized by means of "domain specific ontology" discussed here.

However there exists no need for learning resources on "Soap Protocol", "Magneto Framework" and "MySQL Database Manager", since they have got nothing to do with the requirements in the request of Figure 3(a). In our approach, the so-called requirements are with regard to the main keyword in the user's query; "Mobile platform" in this case which comprises entities such as "Java Language", "Java Language", "SQLite Database Manager", "XML Markup Language" and again "Java Language". These entities can be used as active resources for learning "Implementing Business Logic for Android","Implementing Database for Android" and "Implementing User Interface for Android" as illustrated in Figure 3(a). In the same manner, some parts in the cases of Figures 3(b) and 3(c), as highlighted, are considered as the parts for the final solution. As the result, set of "learning resources" for the related request would be "Java language" , "SQLite

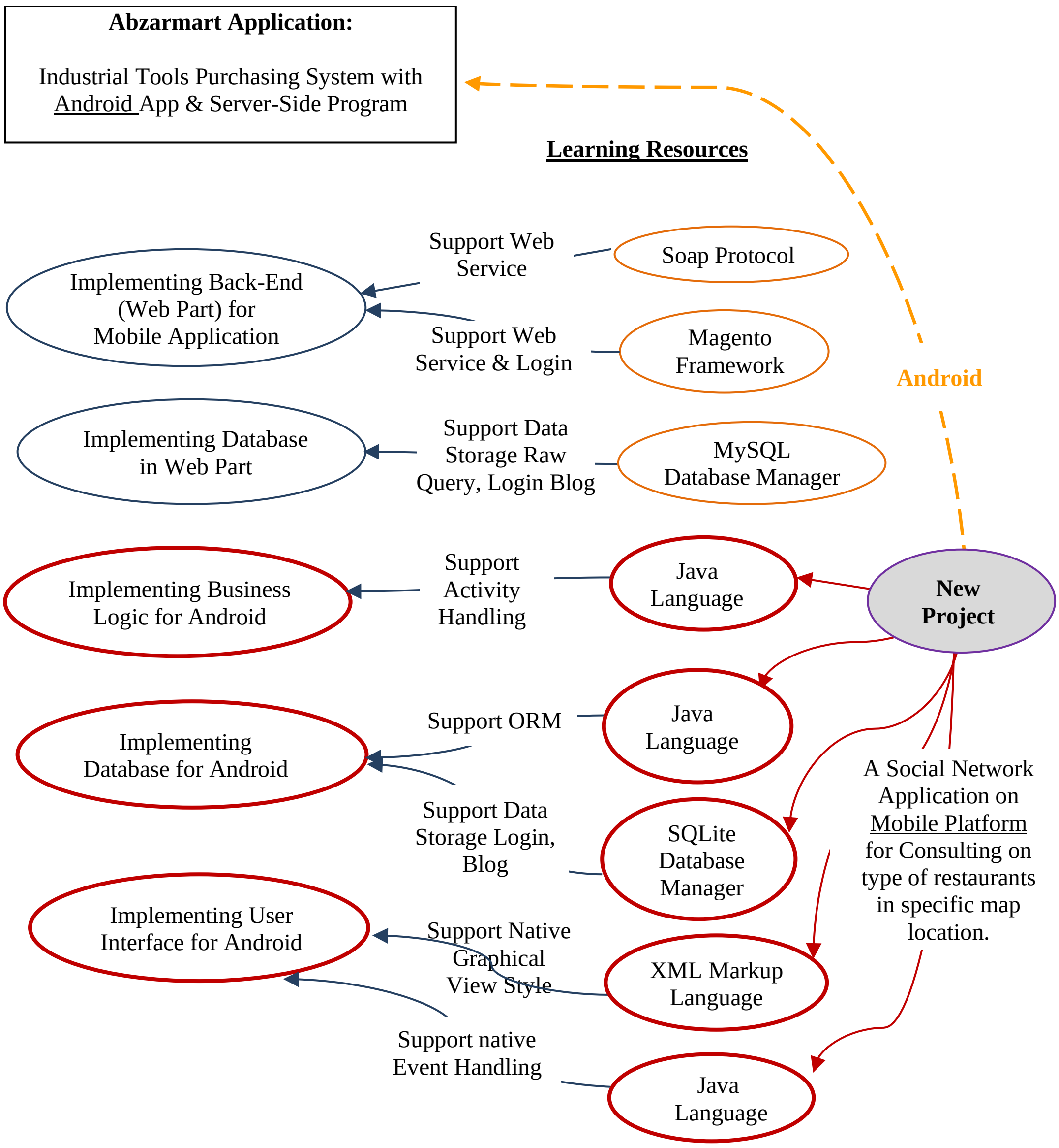

Figure 3(a). An example on compositional adaptation about implementing Android Application

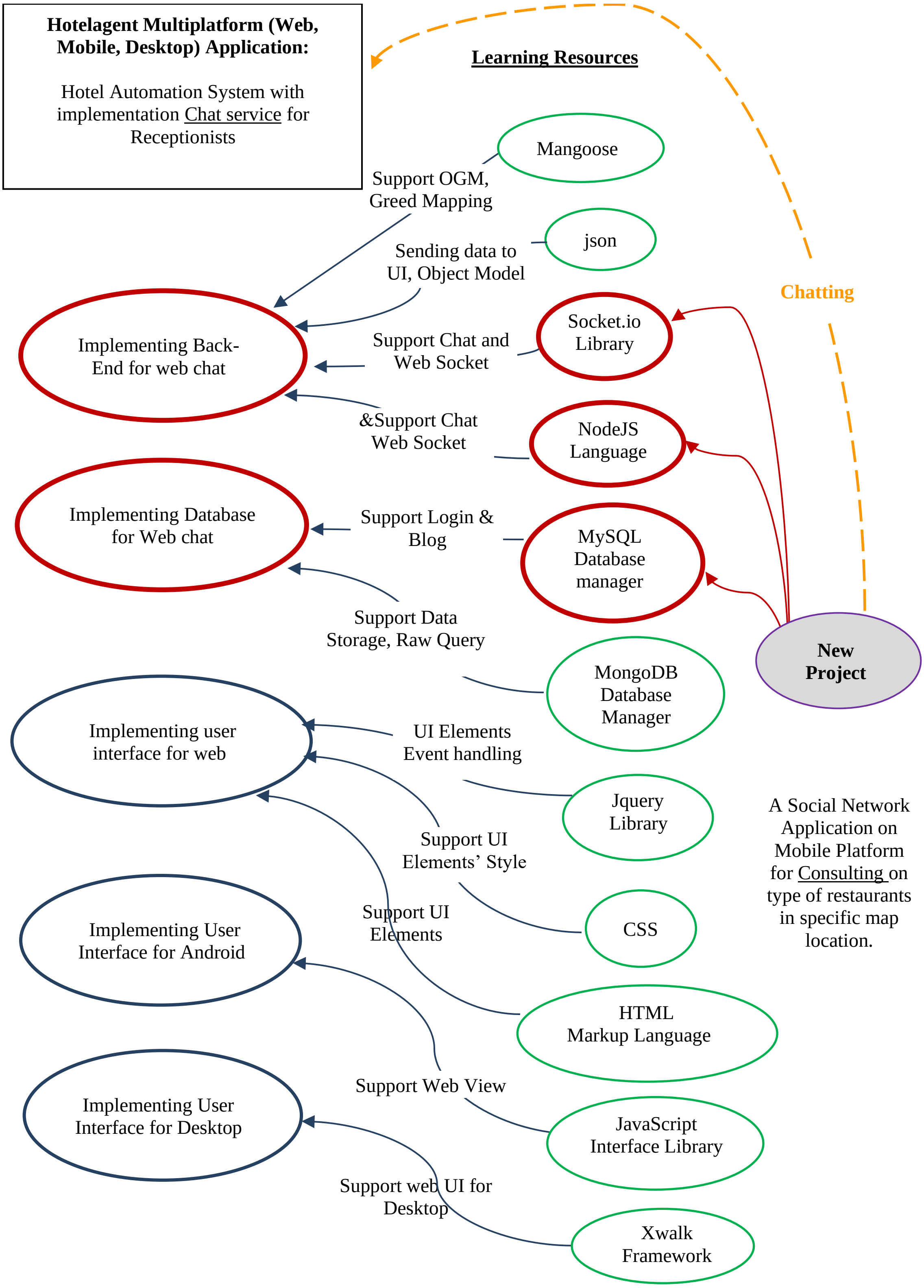

Figure 3(b). An example on compositional adaptation about implementing Communicating by Chat Services

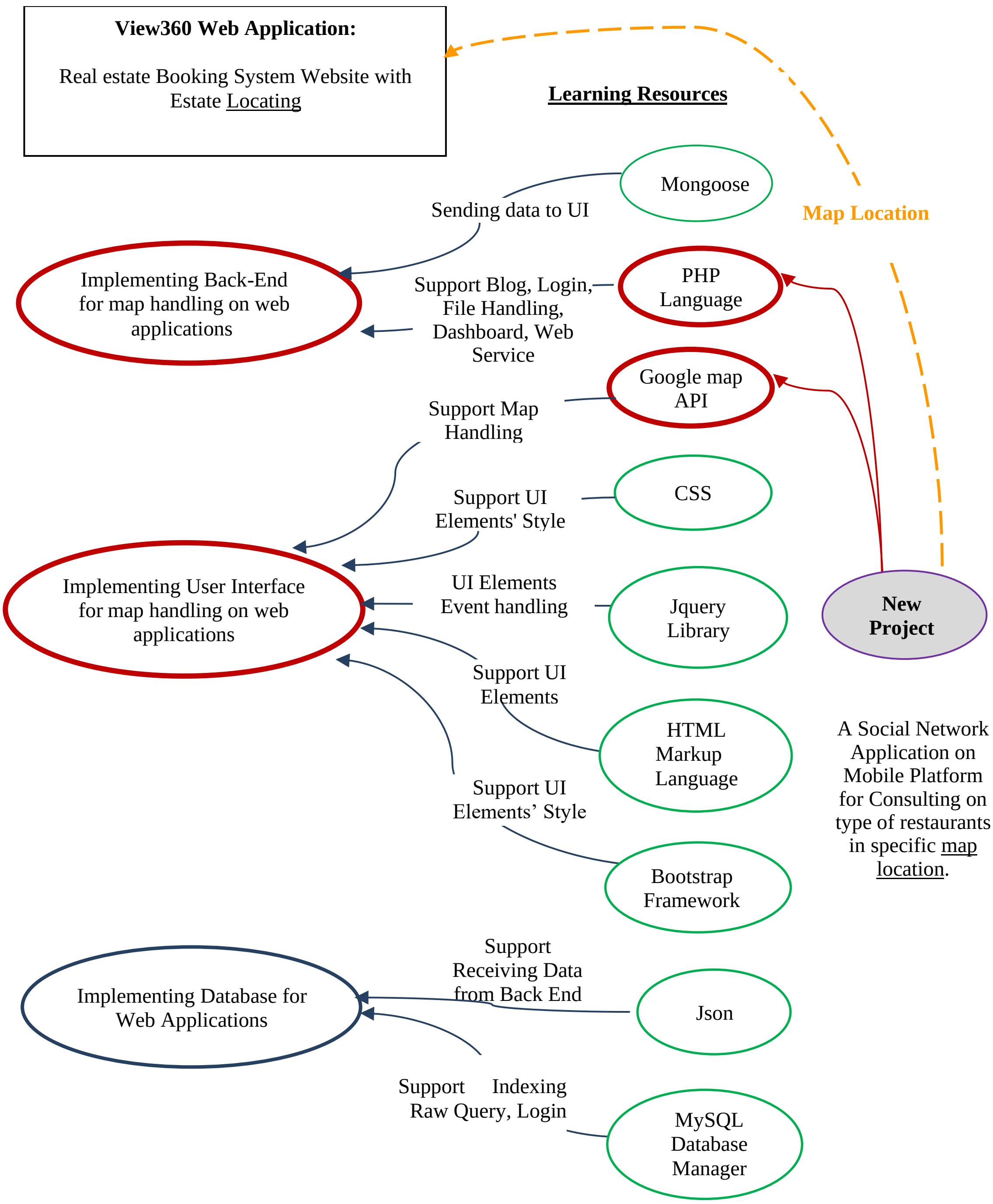

Figure 3(c). An example on compositional adaptation about implementing Map Location

Database Manager", "XML Markup Languge", "NodeJS Language", "My SQL Database Manager", "PHP Language" and "Google Map API". For instance, "Java Language" can be applied for supporting activity handling towards implementing business logic for android or for supporting ORM towards implementing database for android or for supporting native event handling towards implementing user interface for android.

4. EXPERIMENTAL EVALUATION AND RESULTS

To evaluate the impact of the system on the recommendation of different learning sources, the system has experimented on real users with academic education in the field of computer science. In particular, more than 100 computer science graduated students, junior developers in the field of software programming, took part in this experiment. After a short training, each participant worked with the system at least 15 minutes, and then filled in the UEQ questionnaire which was designed by Laugwitz, et al. [28] and has been known as a standard tool for assessing various scales of user experience in different research works.

As Manouselis et al. [7] mentioned the qualitative comparison of e-learning recommender systems is very difficult due to their strong dependence on context. Therefore, the main purpose of our experiment is to determine the accuracy of the diagnosis and prediction of resources required by the user. Users' satisfaction measured by the corresponding section designed in the system is also evaluated. Each set of the experiments is calculated by grouping the users, ten by ten, based on their time order. The average value taken for each of these groups is presented in Figures 4 and 5.

4. 1. Performance Measure To evaluate the performance of the proposed recommender system, precision, recall, and f-measure were considered. The reason for using such factors goes back to the retrieval nature of the proposed CBR-based recommender system which calls for selecting those factors which can be responsible for validating a retrieval process. In this regrad, two ways usually exist for identifying the relevancy of the items in a recommender system: 1) applying pre-tagged datasets, 2) receiving the feedback of the user, which in our case, the second way was examined.

Precision is, in fact, is a measure to evaluate the accuracy of data retrieval, which in this experiment results in a ratio of the number of learning materials resources regarded as relevant (by the user) to the total number of learning materials recommended by the system. Figure 4 reveals the slight slope of the precision by increasing the number of tests. As the numbers of system users and appropriate stored cases increase, the precision is also increased. When there are more stored cases in the system, more possibility would exist to have similar cases with the problem situation, and as a result, more comprehensive solutions for the problem's constraints. So, due to the existence of more similar cases, components causing errors would hold lower priority, and would therefore have less effect on the formation of the final solution. In this way, the accuracy of the system will ultimately be increased. On the other hand, the recall is a measure to evaluate the number of related items that are properly retrieved, and the result would therefore be equal to the ratio of the number of correct learning materials resources retrieved to all the related learning materials resources. Regarding Figure 5, due to the fact that the number of recommended references highly depends on the problem posed by the user, unlike the usual situations wherein the recall index is used to evaluate the comprehensiveness of the retrieved results, the total number of related resources in the system is expected to be limited. Therefore, the recall

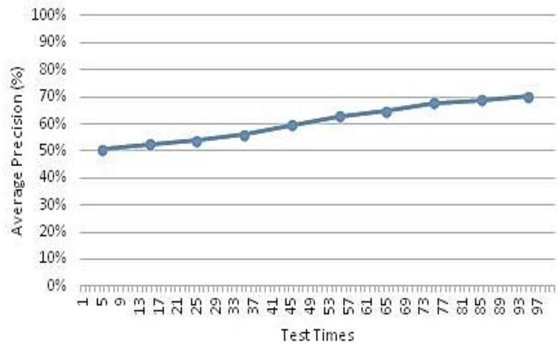

Figure 4. Average precision change over test times

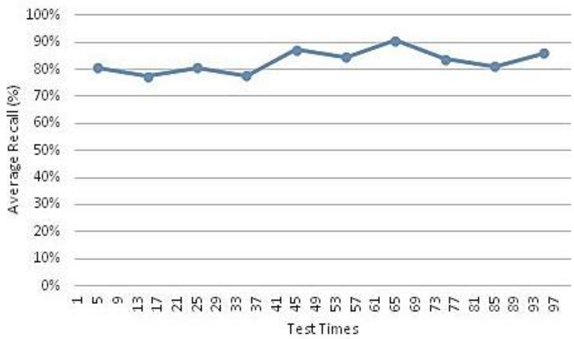

Figure 5. Average precision change over test times

measure would have no significant changes, and would always be in a range of 0.75 to 0.90.

In such a case where these two criteria are close to each other, in order to better assess the system, another criterion called F-measure, is considered to take care of the harmonic mean of precision and recall (Figure 6). According to Figures 4-6, through increasing the precision and stability of the recall criterion, F-measure increased as the combination of these two.

Another measurable and essential criterion in such systems is the time, or in other words, the accessibility to various resources and presenting them as the final solution. There are several factors in determining the retrieval time in this system: the number of resources received per user or per problem situation's constraint, the number of keywords in the user's request or words that are semantically related to the resources in the system, and total number of stored cases in the database which are generally reflected during the retrieval and representing of the final solution (Figures 7-9).

Figure 7 shows the increase of retrieval time when the number of retrieved sources for each keyword or each constraint in the problem situation is increased. For example, if the system recommends two different learning resources for one semantically meaningful element in the problem situation, it takes 151 milliseconds to find and retrieve these resources. It is obvious that the number of semantically connected

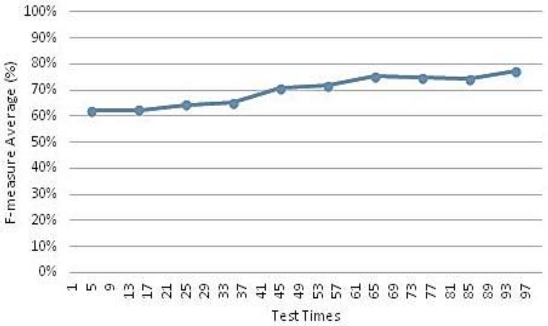

Figure 6. F-measure average change over test times

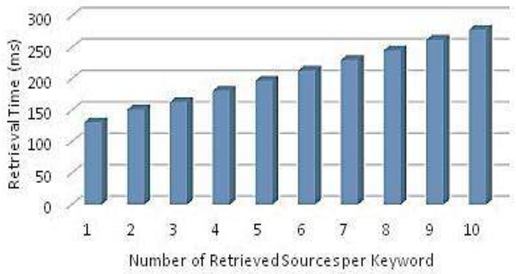

Figure 7. Average precision change over test times

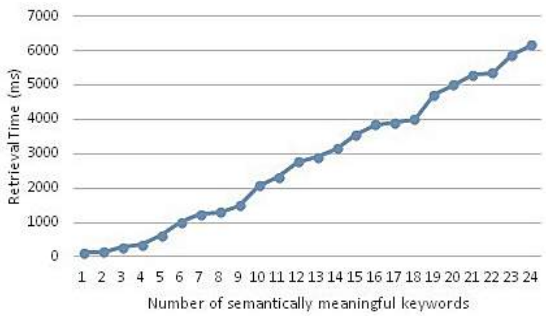

Figure 8. Retrieval time by keywords count

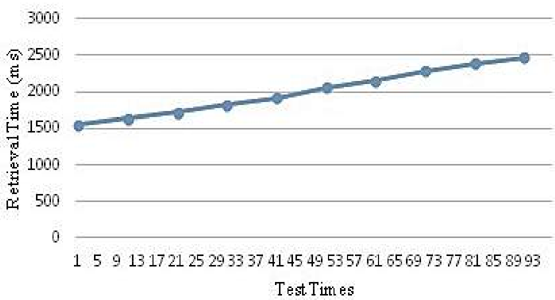

Figure 9. Total retrieval time over test times

keywords in the problem situation would affect directly the retrieval time.

According to Figure 8, when the number of semantically meaningful keywords in the problem situation is increased, it would take much more time in order to represent connected resources to these keywords as a solution. For example, when the problem situation contains 13 keywords, which are semantically connected to different sources, it takes about 3000 milliseconds for retrieving the connected resources and representing them to the user as a final solution.

Regarding Figure 9, and assuming that the other factors in this title are normalized, we notice that the total retrieval time has been increased over the test times mainly because of an increase in the stored cases as the basis for search. It is seen that this increase occurs linearly, because of using an ontology for finding similar cases. Let say, within-ontology search for this purpose causes the system to check each pre-stored case in order to find the most similar cases to the problem situation.

4. 2. User Satisfaction Measure There is a specific element in the user interface of the system that announces user's satisfaction degree towards the presented solutions. In this regard, users are grouped ten by ten based on the corresponding time orders. The average of satisfaction in each group is shown in Figure 10. According to Figure 10, user satisfaction seems to have increased due to an increase in the number accurate recommended resources.

In the meantime, it has to be noticed that when the number of resources tremendously increases, the user confronts a sort of conflict in finding the most appropriate resources for his purpose. Taking this point into consideration, and based on the results shown in Figure 11, the suitable number of recommended resources to be presented to the user is 2 to 3. It is obvious that, a threshold bigger than this may cause confusion and resultantly dissatisfaction, while the one less than this may similarly be not satisfactory either.

4. 3. User Experience Measure User experience is considered as one of the most important issues in the field of human-computer interaction, which in fact examines the users' perceptions and sentiments toward the system or application they interact with. Developers usually count on their achievements on users'

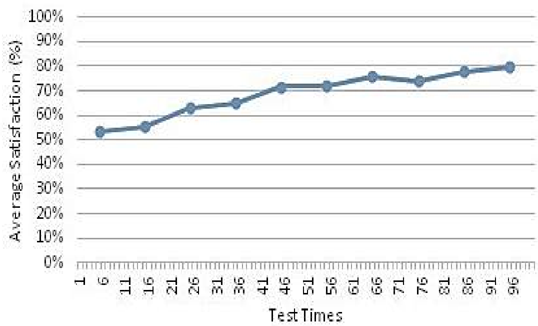

Figure 10. Average satisfaction change over test times

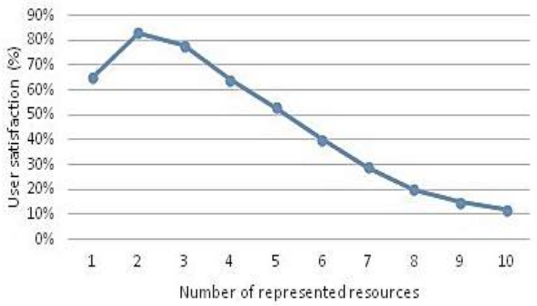

Figure 11. User satisfaction percentage by the number of represented resources for each constraint

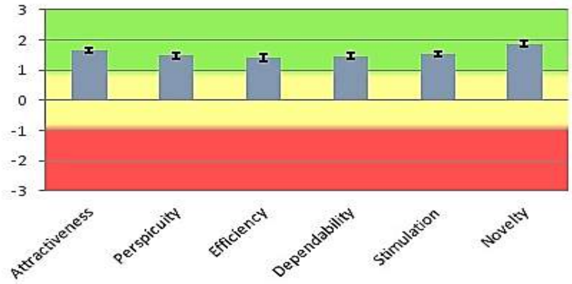

Figure 12. UEQ test result on six scales with confidence intervals

experiences, which result in improving the usability and friendliness of their system application [29]. Moreover, in complex projects where the number of requirements is high, for choosing customers' priorities during the product development, an intelligent algorithm such as Binary Artificial Algae Algorithm seems to be useful [30].

Considering the above points into account, in this paper, we decided to evaluate our recommender system from the user experience perspective, too. In this respect, a kind of user experience questionnaire (UEQ) designed by [30] was applied. The related test includes six scales of "attractiveness", "perspicuity", "efficiency", "dependability", "stimulation" and "novelty". It is to be noted that these scales, were measured according to some specific items which are considered in this questionnaire exactly for this purpose. The user's general feeling is calculated by the "attractiveness" scale, and ought to be affected by the other five scales. Thus, these scales are not independent of each other. The reason for using such a questionnaire is that it has been known as a standard tool for assessing various scales of user experience, and has functioned successfully in a variety of research works [31-33].

To evaluate the proposed system based on user experience perspective, in this experiment, 100 B.Sc. graduated engineers in computer science and computer-engineering fields voluntary accepted to have cooperation. After a short training, each participant worked with the system at least 15 minutes, and then filled in the user experience questionnaire (UEQ questionnaire). As illustrated in Figure 12, all UEQ's quality scales show a positive evaluation. Among them, "novelty" seems to be the highest. That is because no compositional adaptation with the specifications of the suggested approach has functioned for proposing appropriate resources for software development projects such as the one we proposed in this paper. Next to that "attraction" scale has turned to be highly acceptable, as the user interface of the system has been designed well and user-friendly. The other task-related scales (such as "assortment", "perspicuity", "efficiency", and "dependability"), are a little bit lower, because the system is in the pilot state and for the moment, the case library may not cover all resources for software development projects; a fact which in turn may cause weak outcome in facing complex or obscure requests.

More investigation on the mean value of UEQ reveals that "novelty" and "efficiency" are the two extremes of the spectrum. With respect to the standard deviation, it is noticeable that the highest value belongs to "perspicuity". That means there has been no consensus among participants on "perspicuity", while the most common belief has been on "attractiveness" among the participants. That is why the second highest average is allocated to "attractiveness". Table 1 shows the mean values, standard deviation and confidence interval of each UEQ's scale by 5% confidence intervals.

To evaluate the UEQ scales of our proposed system (compared to the other existing systems), the UEQ test dataset containing data from 9905 users in 246 studies concerning different products (like social networks, business software, web shops and etc.) has been considered. Figure 13 illustrates the status of each scale compared to the others.

As it is seen from the figure, "novelty" exists in the excellent area that means the proposed recommender system is in the range of 10% of the most successful systems. This outcome is achieved because of its semantic potential in finding and offering several appropriate solutions to the users. Respectively, the second place is allocated by "attractiveness" which reflects the good impression of users through working with this system. Next to "attraction", "stimulation" holds the third mean value. Results of test demonstrate that the proposed system has the ability to motivate users for further usage. The reason is the very accuracy and completeness of the previous suggestions already provided by the system. In this scale, the proposed system is placed in a position better than 75% of the other systems in the dataset. This comes true whereas just 10% of other products provide a better "stimulation" a fact that is quite remarkable for such a prototype system.

TABLE 1. UEQ's scales mean, standard deviation and confidence intervals (p=0.05)

Scale	Mean	Std. Dev.	N	Confidence	Confidence interval	
Attractiveness	1.643	0.425	100	0.083	1.560	1.727
Perspicuity	1.475	0.609	100	0.119	1.356	1.594
Efficiency	1.418	0.546	100	0.107	1.310	1.525
Dependability	1.463	0.515	100	0.101	1.361	1.564
Stimulation	1.535	0.437	100	0.086	1.449	1.621
Novelty	1.875	0.556	100	0.109	1.766	1.984

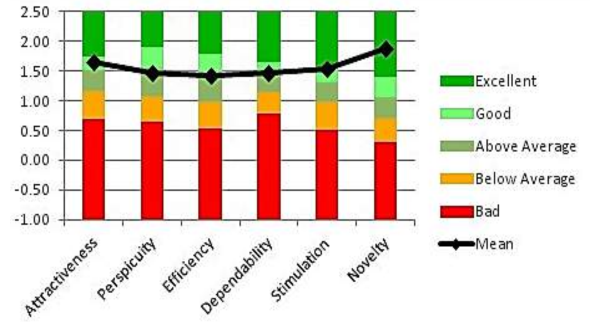

Figure 13. UEQ test result in comparison with the other systems/ products

On the other side, "Perspicuity" and "dependability" behave almost in a similar manner, and both are superior to 50% of the similar systems in the dataset. The very convenience in getting familiar with the system from the perspective of "perspicuity", and the safe control on interactions and complying the users' expectations from the "dependability" viewpoint, make the proposed system as successful as possible. However, by increasing the number of cases in the case library, and characterizing more significant semantic similarity (either between the cases or between the problem situation and the cases), more reliable and comprehensive solutions are expected to be provided, and "efficiency" of the system will thus increase. Moreover, by upgrading the hardware of the system, higher performance in general, and less retrieval time in particular, will be resulted.

5. CONCLUSION AND FUTURE PROSPECTS

In this paper, a compositional adaptation approach was presented for tailoring different types of learning resources in the area of software development with the purpose of recommending them to the users. The main point in this approach is the ability to produce a solution in the situations where the keywords in the user's request might not have necessarily been used in the technical descriptions of the stored cases. A domain-specific ontology, which comprises significant aspects of a technological area such as "infrastructure", "methods & tools", "applications & services", has been shown to be helpful in this regard. A salient point in our approach to compositional adaptation is that, the components in a case solution may hold some characteristics, which would justify the way the essential operations in the case solution are supported. This, as shown in the paper, gives us the chance to consider only those components that comply with the requirements of the user's request. In this way, the components gathered from the corresponding retrieved cases can be joined together to shape the final solution for the user's request. Although the approach emphasized in this paper has been proposed for recommending learning resources in the area of software development, it however can be equally applied to other technological areas as well through developing domain-specific ontology for that area. Therefore, the proposed approach can be regarded as a helpful means for recommending learning resources in any technological area in general. As a future research work, developing highly efficient domain-specific ontology as well as considering fuzzy logic for assessing semantic similarity, is suggested.

6. REFERENCES

1. Holstein, K., Yu, Z., Sewall, J., Popescu, O., McLaren, B.M. and Aleven, V., "Opening up an intelligent tutoring system development environment for extensible student modeling", in International Conference on Artificial Intelligence in Education, Springer. (2018), 169-183.
2. Dwivedi, A., Dwivedi, P., Bobek, S. and Zabukovšek, S.S., "Factors affecting students' engagement with online content in blended learning", ***Kybernetes***, (2019), https://doi.org/10.1108/K-10-2018-0559
3. Jaderyan, M. and Khotanlou, H., "Automatic hashtag recommendation in social networking and microblogging platforms using a knowledge-intensive content-based approach", ***International Journal of Engineering***, ***Transactions B: Applications***, Vol. 32, No. 8, (2019), 1101-1116, doi: 10.5829/ije.2019.32.08b.06.
4. Lu, J., Wu, D., Mao, M., Wang, W. and Zhang, G., "Recommender system application developments: A survey", ***Decision Support Systems***, Vol. 74, (2015), 12-32, https://doi.org/10.1016/j.dss.2015.03.008
5. Ai, F., Chen, Y., Guo, Y., Zhao, Y., Wang, Z., Fu, G. and Wang, G., "Concept-aware deep knowledge tracing and exercise recommendation in an online learning system", ***International Educational Data Mining Society***, (2019).
6. Ahn, J.-w., Tejwani, R., Sundararajan, S., Sipolins, A., O'Hara, S., Paul, A., Kokku, R., Kjallstrom, J., Dang, N.H. and Huang, Y., "Intelligent virtual reality tutoring system supporting open educational resource access", in International Conference on Intelligent Tutoring Systems, Springer. (2018), 280-286.
7. Manouselis, N., Drachsler, H., Vuorikari, R., Hummel, H. and Koper, R., Recommender systems in technology enhanced learning, in Recommender systems handbook. 2011, Springer.387-415.

8. Huang, M.J., Chiang, H.K., Wu, P.F. and Hsieh, Y.J., "A multi-strategy machine learning student modeling for intelligent tutoring systems: Based on blackboard approach", ***Library Hi Tech***, (2013), https://doi.org/10.1108/07378831311329059

9. Barzegar Nozari, R., Koohi, H. and Mahmodi, E., "A novel trust computation method based on user ratings to improve the recommendation", ***International Journal of Engineering***, Vol. 33, No. 3, (2020), 377-386, doi: 10.5829/IJE.2020.33.03C.02.

10. Lops, P., Jannach, D., Musto, C., Bogers, T. and Koolen, M., "Trends in content-based recommendation", ***User Modeling and User-Adapted Interaction***, Vol. 29, No. 2, (2019), 239-249, https://doi.org/10.1007/s11257-019-09231-w

11. Cheng, L.C. and Lin, M.-C., "A hybrid recommender system for the mining of consumer preferences from their reviews", ***Journal of Information Science***, Vol. 46, No. 5, (2020), 664-682, https://doi.org/10.1177/0165551519849510

12. Tarus, J.K., Niu, Z. and Yousif, A., "A hybrid knowledge-based recommender system for e-learning based on ontology and sequential pattern mining", ***Future Generation Computer Systems***, Vol. 72, (2017), 37-48, https://doi.org/10.1016/j.future.2017.02.049

13. Lin, F., Graf, S. and McGreal, R., "Adaptive and intelligent web-based educational systems", (2009).

14. Cuong, N.D.H., Arch-Int, N. and Arch-Int, S., "Fuse: A fuzzy-semantic framework for personalizing learning recommendations", ***International Journal of Information Technology & Decision Making***, Vol. 17, No. 04, (2018), 1173-1201, https://doi.org/10.1142/S0219622018500220

15. Azcona, D., Hsiao, I.-H. and Smeaton, A.F., "Detecting students-at-risk in computer programming classes with learning analytics from students' digital footprints", ***User Modeling and User-Adapted Interaction***, Vol. 29, No. 4, (2019), 759-788, doi: 10.1007/s11257-019-09234-7.

16. Kolodner, J.L., Cox, M.T. and González-Calero, P.A., "Case-based reasoning-inspired approaches to education", ***The Knowledge Engineering Review***, Vol. 20, No. 3, (2005), 299-303, doi. https://doi.org/10.1017/S0269888906000634

17. Dixit, P., Nagar, H. and Dixit, S., "Student performance prediction using case based reasoning knowledge base system (cbr-kbs) based data mining", ***International Journal of Information and Education Technology***, Vol. 12, No. 1, (2022), doi: 10.18178/ijiet.2022.12.1.1583.

18. Reyhani, N., Badie, K. and Kharrat, M., "A new approach to compositional adaptation based on optimizing the global distance function and its application in an intelligent tutoring system", in Proceedings Fifth IEEE Workshop on Mobile Computing Systems and Applications, IEEE. (2003), 285-290.

19. Arshadi, N. and Badie, K., "A compositional approach to solution adaptation in case-based reasoning and its application to tutoring library", in Proceedings of 8th German Workshop on Case-Based Reasoning. Lammerbuckel, Citeseer. Vol. 11, (2000).

20. Bousbahi, F. and Chorfi, H., "Mooc-rec: A case based recommender system for moocs", ***Procedia-Social and Behavioral Sciences***, Vol. 195, (2015), 1813-1822, doi. https://doi.org/10.1016/j.sbspro.2015.06.395

21. Garrido, A., Morales, L. and Serina, I., "On the use of case-based planning for e-learning personalization", ***Expert Systems with Applications***, Vol. 60, (2016), 1-15, doi. https://doi.org/10.1016/j.eswa.2016.04.030

22. Guessoum, D., Miraoui, M. and Tadj, C., "Contextual case-based reasoning applied to a mobile device", ***International Journal of Pervasive Computing and Communications***, (2017), doi. https://doi.org/10.1108/IJPCC-11-2016-0056

23. Nasiri, S., Zenkert, J. and Fathi, M., "Improving cbr adaptation for recommendation of associated references in a knowledge-based learning assistant system", ***Neurocomputing***, Vol. 250, (2017), 5-17, https://doi.org/10.1016/j.neucom.2016.10.078

24. Salam, A. and Fathurrahmad, F., "Student final project recommendation system model using case-based reasoning (cbr) method", ***Jurnal Mantik***, Vol. 5, No. 3, (2021), 1535-1542, https://iocscience.org/ejournal/index.php/mantik/article/view/1641

25. Dhiman, H., Wächter, C., Fellmann, M. and Röcker, C., "Intelligent assistants", ***Business & Information Systems Engineering***, (2022), 1-21, doi: 10.1007/s12599-022-00743-1.

26. Wilke, W. and Bergmann, R., "Techniques and knowledge used for adaptation during case-based problem solving", in International Conference on Industrial, Engineering and Other Applications of Applied Intelligent Systems, Springer. (1998), 497-506.

27. Badie, K. and Mahmoudi, M.T., "Compositional adaptation in case-based reasoning based on the semantic relations between the components in the cases", in 2017 IEEE International Conference on INnovations in Intelligent SysTems and Applications (INISTA), IEEE. (2017), 449-454.

28. Laugwitz, B., Held, T. and Schrepp, M., "Construction and evaluation of a user experience questionnaire", in Symposium of the Austrian HCI and usability engineering group, Springer. (2008), 63-76.

29. Laumer, S., Maier, C. and Weitzel, T., "Information quality, user satisfaction, and the manifestation of workarounds: A qualitative and quantitative study of enterprise content management system users", ***European Journal of Information Systems***, Vol. 26, No. 4, (2017), 333-360, https://doi.org/10.1057/s41303-016-0029-7

30. Pirozmand, P., Ebrahimnejad, A., Alrezaamiri, H. and Motameni, H., "A novel approach for the next software release using a binary artificial algae algorithm", ***Journal of Intelligent & Fuzzy Systems***, Vol. 40, No. 3, (2021), 5027-5041, doi: 10.3233/JIFS-201759.

31. Hinderks, A., Meiners, A.-L., Domínguez Mayo, F.J. and Thomaschewski, J., "Interpreting the results from the user experience questionnaire (UEQ) using importance-performance analysis (IPA)", in WEBIST 2019: 15th International Conference on Web Information Systems and Technologies (2019), pp. 388-395., ScitePress Digital Library. (2019).

32. Rauschenberger, M., Schrepp, M., Pérez Cota, M., Olschner, S. and Thomaschewski, J., "Efficient measurement of the user experience of interactive products. How to use the user experience questionnaire (UEQ). Example: Spanish language version", (2013), doi: 10.9781/ijimai.2013.215.

33. Schrepp, M., Hinderks, A., Thomaschewski, J. and Marcus, A., "Design, user experience, and usability. Theories, methods, and tools for designing the user experience", ***Lecture Notes in Computer Science***, Vol. 8517, (2014), 383-392, doi. https://doi.org/10.1007/978-3-319-07668-3_37

Persian Abstract

چکیده

در این مقاله در خصوص کاربرد رویکرد سازگارسازی ترکیبی جهت پیشنهاد منابع یادگیری به کاربران درحوزه توسعه نرم افزار بحث می شود. بدین منظور از یک هستان نگار پیشنهادی وابسته به دامنه جهت جستجوی کلماتی که در توصیف فنی مورد های ذخیره شده بکار رفته اند استفاده می شود. آنچه در بازنمایی موردهای رویکرد پیشنهادی حائز اهمیت است، ارائه دقیق مشخصات منابع یادگیری در بخش راه حل های موردهاست. بدین ترتیب تنها راه حل هایی که با درخواست کاربر متناسب باشد، بازگردانده خواهد شد. دراین مقاله کارایی رویکرد پیشنهادی جهت پیشنهاد منابع یادگیری همراه با وضعیت تجربه کاربر در تعامل با سیستم پیسنهاد دهنده نیز مورد ارزیابی قرار گرفته است. نتایج حاصل نشان می دهد که منابه یادگیری پیشنهادی توسط این رویکرد برای کاربران با درجه رضایت بالایی مفید فایده بوده است. لازم به ذکر است که هرچند رویکرد پیشنهادی بکار گرفته شده جهت پیشنهاد منابع یادگیری در حوزه توسعه نرم افزاراستفاده شده است ولیکن قابل استفاده در حوزه های فنی دیگر به شرط طراحی هستان نگار دامنه آن موضوع نیز می باشد.

IJE TRANSACTIONS A: Basics Vol. 35, No. 07, (July 2022) 1330-1342

International Journal of Engineering

Journal Homepage: www.ije.ir

Jensen-Shannon Divergence of Two Eddy Current Distributions Induced by Circular and Fractal Koch Excitation Coils

C. Guolong*, C. Zheng, J. Wuyin

School of Mechanical and Electrical Engineering, Lanzhou university of technology, Lanzhou, China

PAPER INFO

Paper history:
Received 08 March 2022
Received in revised form 28 March 202
Accepted 09 April 2022

Keywords:
Jensen-Shannon Divergence
Fractal Geometry
Excitation Coil
Eddy Current Testing
Differential Pickup Probes
Entropy

ABSTRACT

Eddy current distribution is important to the performance of planar eddy current probes. In this paper, the Jensen-Shannon divergences of tangential intersection angle spectrum and radial direction energy spectrum were proposed to evaluate the difference between eddy current distributions generated by circular and fractal Koch excitation coils. By the simulation for the circular and Koch shape excitation coils, it works out that the difference of the eddy current distributions between the two kinds of coils becomes larger and larger with an increase in the values of the two Jensen-Shannon divergences. At the same time, the correlation between the change of Jensen-Shannon divergence and the detectability of the short crack in the special direction was discussed through simulation and experiment results. It is found that, relative to the crack in 0° direction, the detectability of the Koch and circular differential pickup probes to the crack in 90° direction has a correlation with the Jensen-Shannon divergence of tangential intersection angle spectrum. The width of each signal generated by the two probes has a correlation with the Jensen-Shannon divergence of radial direction energy spectrum.

***doi**: 10.5829/ije.2022.35.07a.12*

1. INTRODUCTION

As one of the common nondestructive methods, eddy current (EC) testing (ECT) based on the principle of electromagnetic induction has the advantages of non-contact, using without coupling agent and fast testing speed [1]. According to these advantages, it is widely used to detect defects on the surface or subsurface of conductors. In the process of ECT, EC probes are taken as the source of information to obtain some physical properties of tested objects. When detecting the defects in components, EC probes determine the performance of the whole ECT system. Furthermore, they have an impact on the accuracy of subsequent quantitative evaluation to defects.

Recently, the research of EC probes focuses on improving the structure. Traditional three-dimensional rigid EC probes can test metal parts with simple geometry structure of the surface, but they are not able to reach some tested portion thoroughly for the components with complex structure [2,3]. In view of this, two-dimensional planar flexible EC probes have been proposed. This category of probe can be manufactured easily, folded and touch the tested surface furthest [4,5]. Therefore, it overcomes the disadvantage of three-dimensional probe. Aimed at the design of flexible or planar EC probe, various coil structures have been proposed like meandering winding magnetometer structure [6], rosette structure [7,8], rectangular structures [9,10], circular spiral structure [11,12], floral-shape structure [13], butterfly-shape structure [14], Koch-shape structure [15,16]. In addition, some special structures and configuration methods were put forward for the inspection of flaws. Xie et al. [17] used a novel flexible EC probe to detect small cracks of materials with complex geometry. Zhang et al. [18] designed a flexible EC probe whose coils are arranged as a parallel and stagger method for the inspection of last stage blades of a steam turbine. Aouf et al. [19] proposed a multi-probe system composed of three differential probes which are arranged within a specific configuration. This kind of configuration has efficiency and robustness in the

*Corresponding Author Institutional Email: cgl20061273@126.com
(C. Guolong)

Please cite this article as: C. Guolong, C. Zheng, J. Wuyin, Jensen-Shannon Divergence of Two Eddy Current Distributions Induced by Circular and Fractal Koch Excitation Coils, ***International Journal of Engineering, Transactions A: Basics,*** Vol. 35, No. 07, (2022) 1330-1342

detection of cracks. Chen et al. [20] designed a double-layer differential planar coil to detect surface defects, and has high sensitivity even under large lift-off affection. Fan et al. [21] proposed a flexible EC probe based on a TMR probe, this kind of probe can quantitatively monitor the cracks below 3-5mm of material surface. Zhang et al. [22] presented a planar EC probe whose excitation coils were energized by three-phase currents. This excitation method is sensitive to defects of any orientations.

Nevertheless, flexible EC probes have fewer coil turns than those of three-dimensional rigid probes. Also, EC distributions induced by coils determine the interaction effect between ECs and cracks. Therefore, the suitable coil structure and configuration play key roles in flexible EC probes [23], and it is necessary to evaluate the EC distributions for the sake of designing coil structure reasonably. Zhang et al. [24] firstly analyzed EC distributions of line, circle and fractal Koch coils through information entropy. Subsequently, Chen et al. [25, 26] put forward information entropy based on tangential intersection angle spectrum (TIAS) and radial direction energy spectrum (RDES). In Chen's method, the TIAS can evaluate EC distributions from their diversity in directions, and the RDES can reflect the concentration degree of EC distributions under excitation coils. However, the information entropy cannot evaluate the difference between EC distributions induced by two different coils. To solve this problem, the relative entropy and cross entropy were proposed for the evaluation of EC distributions induced by two different coils [23]. Whereas, the relative entropy and cross entropy are asymmetric for two probability distributions, and cannot evaluate the difference of them accurately. Hence, in this study, Jensen-Shannon (JS) divergences of TIAS and RDES are proposed to evaluate the EC distributions between two kinds of coils. Taken as an example, the EC distributions induced by a circular coil and a Koch coil are studied. In addition, simulations and experiments of circular and Koch differential pickup probes are carried out respectively to research the correlation between the performance of the two probes and the JS divergences.

2. METHODOLOGY

2. 1. Basic Principle of JS Divergence

According to Jensen inequation and Shannon entropy, Lin proposed a new measure, JS divergence, to evaluate several probability distributions [27]. As the increment of entropy, JS divergence is commonly used to evaluate the similarity between two probability distributions. It can be formulated as Equation (1):

$$\mathrm{JS}(\mathrm{P}\,||\,\mathrm{Q})=\frac{1}{2}\mathrm{KL}(\mathrm{P}\,||\,\frac{\mathrm{P+Q}}{2})+\frac{1}{2}\mathrm{KL}(\mathrm{Q}\,||\,\frac{\mathrm{P+Q}}{2}) \tag{1}$$

where P and Q are two different probability distributions, respectively. $\mathrm{KL}(\mathrm{P}\,||\,\mathrm{Q})$ represents Kullback-Leibler (KL) divergence namely the relative entropy, and it can be expressed as Equation (2):

$$\mathrm{KL}(\mathrm{P}\,||\,\mathrm{Q})=\mathrm{E_P}\,\log\frac{\mathrm{P}}{\mathrm{Q}} \tag{2}$$

The range of JS divergence is [0,1]. When its value increases from 0 to 1, it means that the similarity of P and Q will decrease. Otherwise, JS divergence overcomes the asymmetry of KL divergence for the evaluation between two probability distributions.

2. 2. JS Divergence of TIAS In order to evaluate the difference of EC distributions induced by two kinds of excitation coils from the view of the richness of TIA, the JS divergences of TIASs are worked out via four steps as shown in Figure 1.

(1) As is shown in Figure 1(a), sample points are distributed uniformly and with the same interval. The energy of the EC at every point is $J^2(\mathrm{x,y}) = J_\mathrm{x}^2(\mathrm{x,y}) + J_\mathrm{y}^2(\mathrm{x,y})$.

(2) The intersection angle θ of every point is the angle between AB line and EC vector J in Figure 1(b). Thereinto, AB line is perpendicular to AO line. Thus, the intersection angle can be expressed as Equation (3):

$$\theta = <\overrightarrow{\mathrm{AB}}, \vec{J}> = \arccos\frac{\mathrm{y}J_\mathrm{x} - \mathrm{x}J_\mathrm{y}}{\sqrt{\mathrm{x}^2+\mathrm{y}^2}\sqrt{J_\mathrm{x}^2+J_\mathrm{y}^2}},\ \mathrm{for}\ \mathrm{x}^2+\mathrm{y}^2\neq 0 \tag{3}$$

In the expression, $\theta=\begin{cases}\theta & \text{if } \theta\leq 90° \\ 180°\text{-}\theta & \text{else}\end{cases}$.

(3) The range $[0°, 90°]$ is equally divided into m parts. The size of every angle interval is $\frac{90°}{\mathrm{m}}$. Therefore, the energy of EC in every angle interval can be calculated by Equation (4):

$$J_\mathrm{p}^2(\mathrm{k})=\sum J^2_{90°(\mathrm{k}-1)/\mathrm{m}\leq\theta_\mathrm{k}\leq 90°\mathrm{k/m}}(\mathrm{x,y}) \tag{4}$$

where θ_k is the intersection angle belonging to k-th angle interval. Hence, the TIAS is calculated by Equation (5):

$$\mathrm{P(k)} = \frac{J_\mathrm{p}^2(\mathrm{k})}{\sum_{\mathrm{k}=1}^{\mathrm{m}} J_\mathrm{p}^2(\mathrm{k})} \tag{5}$$

It is known from the above that can characterize the TIAS under a specific EC distribution. Via the same approach, $\mathrm{Q(k)} = \frac{J_\mathrm{q}^2(\mathrm{k})}{\sum_{\mathrm{k}=1}^{\mathrm{m}} J_\mathrm{q}^2(\mathrm{k})}$ is used to characterize the TIAS under another kind of EC distribution. In Figure 1c, there are schematic diagrams of TIASs under two different kinds of EC distributions.

(4) Based on the TIASs, the JS divergence is further calculated by Equation (6).

$$JS(P(k)\,||\,Q(k))=\frac{1}{2}KL(P(k)\,||\,\frac{P(k)+Q(k)}{2})+\frac{1}{2}KL(Q(k)\quad\frac{P(k)+Q(k)}{2}) \tag{6}$$

2. 3. JS Divergence of RDES In order to evaluate the difference of EC distributions induced by two kinds of excitation coils from the view of distribution proportion of RDE in annuluses, the JS divergences of RDESs are worked out via four steps as follows.

(1) The method to set sample points is the same as section 2.2.

(2) As can be seen from Figures 2(a) and 2(b), the sample space includes annuluses whose widths are same as each other. The radius of the circle located in the center has the same width h for every annulus.

(3) The EC energy in every annulus can be expressed as Equation (7):

$$J_s^2(j)=\sum J^2_{h(j-1)\le r_j\le hj}(x,y) \tag{7}$$

where r_j denotes the distance between the sample point in the j-th (i=1,2,3···n) annulus and origin.

The total EC energy in all annuluses is $J_s^2=\sum_{j=1}^{n} J^2_{0\le r_j\le hn}(x,y)$.

Thus, the RDES can be calculated by Equation (8):

$$S(j)=\frac{J_s^2(j)}{\sum_{j=1}^{n}J_s^2(j)} \tag{8}$$

S(j) can characterize the RDES under one EC distribution. Correspondingly, $T(j)=\frac{J_t^2(j)}{\sum_{j=1}^{n}J_t^2(j)}$ can be used to describe the RDES under another EC distribution in the same way. Figure 2(c) displays the RDESs about two different EC distributions.

(4) Then, by Equation (9), the JS divergence based on RDES can be obtained to evaluate the difference between two EC distributions.

$$JS(S(j)\,||\,T(j))=\frac{1}{2}KL(S(j)\,||\,\frac{S(j)+T(j)}{2})+\frac{1}{2}KL(T(j)\,|\,\frac{S(j)+T(j)}{2}) \tag{9}$$

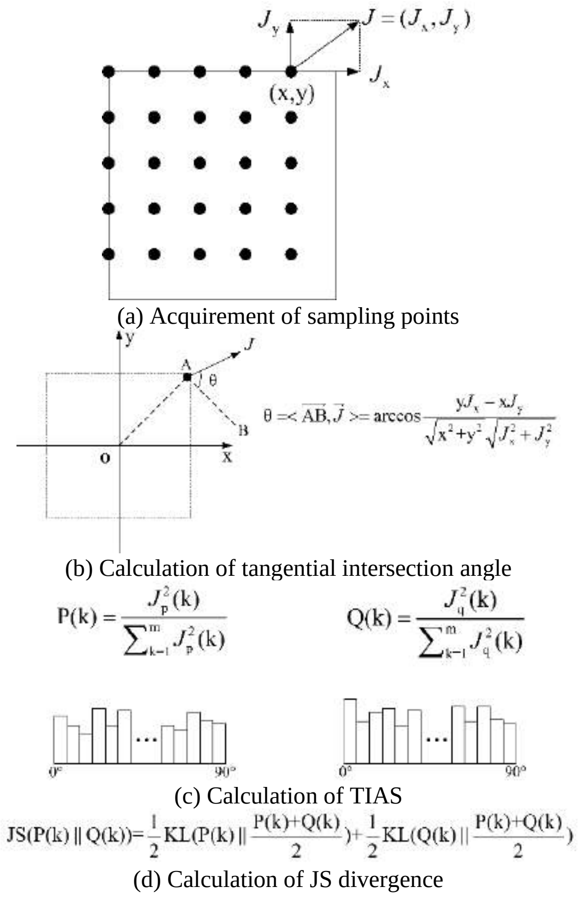

Figure 1. The steps to calculate JS divergence of TIAS

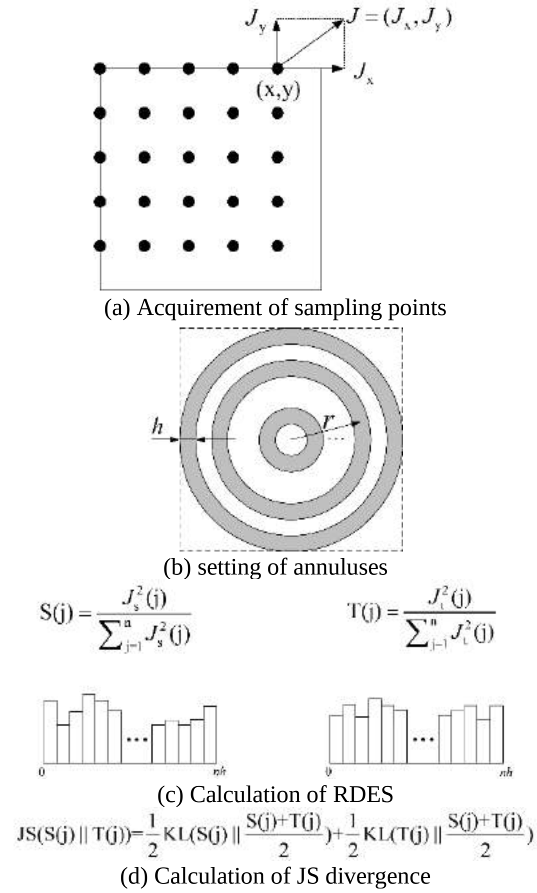

Figure 2. The steps to calculate JS divergence of RDES.

3. FINITE ELEMENT MODELING

In order to extract the EC vectors, the FEMs in allusion to excitation coils were established by COMSOL Multiphysics 5.5. The FEM is composed of three parts: air domain, excitation coil and specimen. Table 1 summarized their main parameters. As is shown in Figure 3(a), there is the FEM of Koch excitation coil under 0.1mm lift-off distance. The element type of the air domain is free tetrahedron mesh. The specimen has two element types. There is a circular area with 10 mm radius on the surface of the specimen, and this field is divided into smaller free triangle mesh. Then, the free triangle mesh is permeated in 1.6 mm far away from the specimen surface by sweeping. Consequently, a column with 1.6 mm high and 10 mm radius is full of the free triangle mesh. The rest element type of the specimen is free tetrahedron mesh. Also, the rest element type of the whole model is free tetrahedron mesh.The mesh of element is shown in Figure 3(b). All of the FEMs are calculated in frequency domain, the set frequencies are 1 kHz, 10 kHz, 20 kHz, 50 kHz, 100 kHz, 200 kHz, 500 kHz, 1000 kHz, 2000 kHz, 5000 kHz and 10000 kHz. In addition, the physics control equations of the FEMs are listed in Equation (10):

$$\begin{cases} \nabla \times \mathbf{H} = \mathbf{J} \\ \mathbf{B} = \nabla \times \mathbf{A} \\ \mathbf{E} = -\mathrm{j}\omega\mathbf{A} \\ \mathbf{J} = \sigma\mathbf{E} + \mathrm{j}\omega\mathbf{D} \end{cases} \tag{10}$$

where $\mathbf{H}$, $\mathbf{J}$, $\mathbf{B}$, $\mathbf{A}$, $\mathbf{E}$ and $\mathbf{D}$ stand for magnetic field, current density, magnetic flux density, magnetic vector potential, electric field, and displacement density, respectively.

TABLE 1. The parameters of FEM

Parameters	Set
Air domain	Dimension: 50 mm ×50 mm×30 mm Relative permeability: 1 Relative permittivity: 1 Conductivity :10 S/m
Koch excitation coil	Diameter of circumcircle: 10 mm (Ideal coil) Edge current: 1 A
Circular excitation coil	Diameter: 10 mm (Ideal coil) Edge current: 1A
Specimen	Aluminum Dimension: 35 mm ×35 mm×6 mm Relative permeability: 1 Relative permittivity: 1 Conductivity :3.774×10^7 S/m

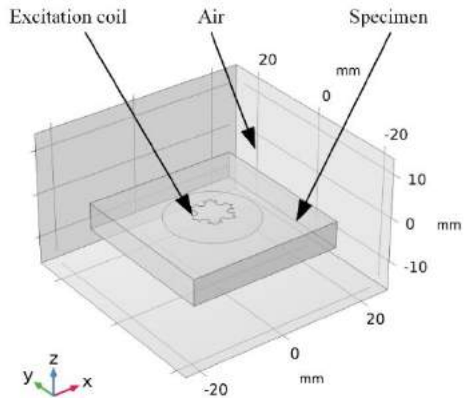

(a) FEM

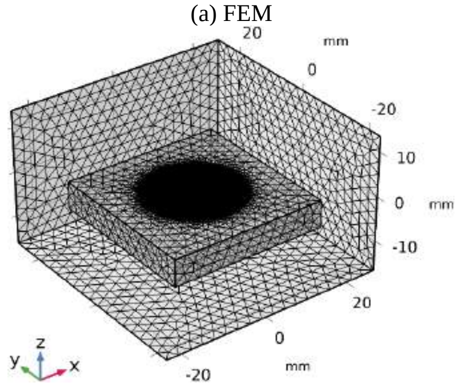

(b) Meshing

Figure 3. FEM of Koch excitation coil

The boundary condition of the FEMs is magnetic insulation, which is presented as Equation (11):

$$\mathbf{n} \times \mathbf{A} = \mathbf{0} \tag{11}$$

where $\mathbf{n}$ is the vector which is perpendicular to the surface of the air domain.

In addition, to research the correlation between the detectability of the differential pickup probes and the change of EC distributions reflected by JS divergence, the circular differential pickup probe and Koch differential pickup probe were simulated under different lift-off distances. Figure 4 is the FEM of the Koch differential pickup probe for the inspection of the crack. This kind of probe consists of an excitation coil and two pickup coils, and every pickup coil is composed of half of the Koch coil. In addition, the pickup coils are under the excitation coil, and the distance between the pickup coils and the excitation coil is 0.4mm. The tested crack is 3mm in length, 0.25mm in width and 1.6mm in depth. The scanning direction to the crack is 0° and 90°. Compared with Table 1, some parameters are adjusted: the size of air domain is $60\ \mathrm{mm} \times 60\ \mathrm{mm} \times 30\ \mathrm{mm}$, and the size of specimen is $50\mathrm{mm} \times 50\mathrm{mm} \times 6\mathrm{mm}$. The element types and meshing method is similar to that of the FEM in Figure 3.

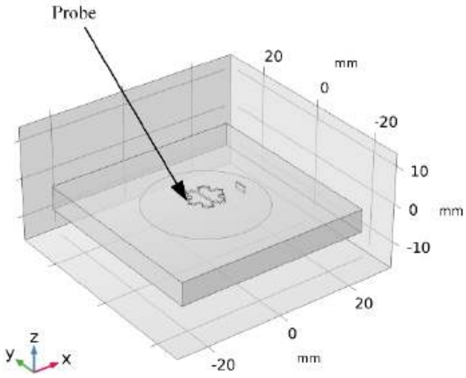

Figure 4. FEM when Koch differential pickup probe inspects crack.

4. EXPERIMENTAL SYSTEM

For the sake of validating the correlation between JS divergence and simulation results of probes relative to crack, the experiment concerned with Koch and circular differential pickup EC probes was carried out. In Figure 5, there is the schematic of the experimental system.

The progress of the experiment can be regarded as two parts: the excitation to signals and the pickup to signals.

The excitation part: firstly, a function generator was used to output signals from two channels. Thereinto, the signal output from channel 1 is a sinusoidal signal whose frequency is 100KHz (excitation frequency) and peak-to-peak value (Vpp) of voltage is 400mV; the signal output from channel 2 is a cosine signal, and its frequency and Vpp are the same as those of channel 1. After that, the signal output from channel 1 flowed into two directions: one passed through a power amplifier and entered into the excitation coil of the probe, the other entered the input end of signal conditioning circuit. In addition, the signal output from channel 2 of the function generator was connected with the input end of the signal conditioning circuit.

The pickup part: this experiment took advantage of the pickup coil on probes to obtain the crack signal detected from a specimen. Then, the signal was demodulated into real part and imaginary part signals. Eventually, the real part and imaginary part signals were gotten via data acquisition card and computer.

To realize the above process, the experimental system was built as shown in Figure 6. The probe was installed on the 3-D scanner and the tested specimen was fixed under the probe. The 3-D scanner was controlled by the computer, which made the probe inspect the pre-crack on the specimen in definite directions. In the experiment, the crack with 3mm in length, 0.25mm in width and 1.6mm in depth was scanned under different lift-off distances (the lift-off distance is set from 0.1mm to 2mm, and the interval is 0.1mm). The directions of scanned crack were set as 0° and 90° which are defined as the angle between scanning direction and crack direction in length, as can be seen in Figure 7.

5. RESULT and DISCUSSION

5. 1. JS Divergence

To evaluate the difference of EC distributions between Koch excitation coil and circular excitation coil quantitatively, under different excitation frequencies, the values of JS divergence were calculated at the lift-off distances from 0.1mm and 10.0mm (The interval is 0.1mm from 0.1mm to 2.0mm and 0.5mm from 2.0mm to 10.0mm.)

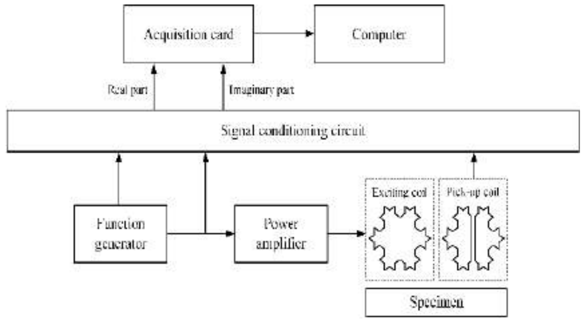

Figure 5. The schematic of experimental system

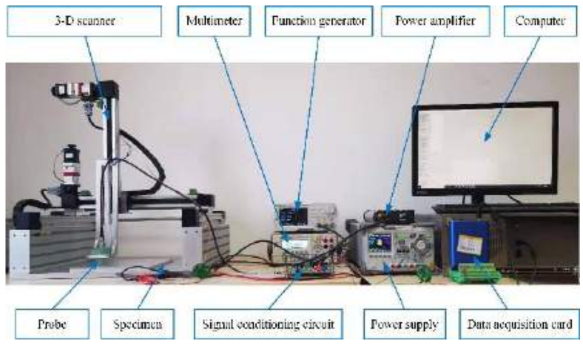

Figure 6. The experimental system

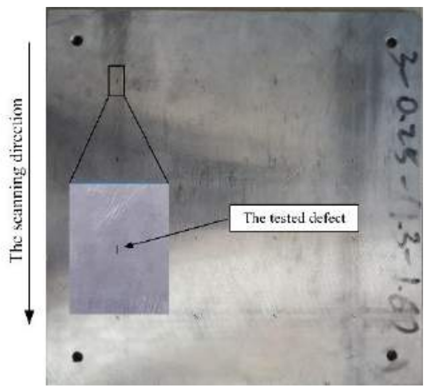

Figure 7. The crack and scanning direction

5. 1. 1. JS Divergence of TIAS Figure 8 shows the values of JS divergence of TIAS. From the perspective of the diversity of EC directions, the result characterizes the difference of EC distributions induced by Koch excitation coil and circular excitation coil under different lift-off distances and excitation frequencies. In general, for each excitation frequency, the value of JS divergence decreases with the increase of the lift-off distance and is close to 0 bit ultimately. In other words, the richness of TIA of EC distribution between the two kinds of coils is getting close. Eventually, the richness is almost identical. When the lift-off distance increases from 0.3 mm to 3.0 mm, the value of JS divergence increases with the increase of the excitation frequency. Therefore, the EC induced by the Koch coil distributes in more directions than the circular coil. When the lift-off distance increases to more than 3 mm, the change of JS divergence is inapparent and close to 0. At this time, the EC distributions between the two kinds of coils are almost identical, and their directions become single. What should be noticed is that the values of JS divergence under 0.1mm, 0.2mm, 0.3mm lift-off distance grows when the excitation frequencies are 500 kHz, 1000 kHz, 2000 kHz, 5000 kHz and 10000 kHz. In addition, there is the maximum value of JS divergence when the excitation frequency is 5000 kHz and the lift-off distance is 0.3 mm. It is illustrated that the EC distributions of Koch excitation coil and circular excitation coil have the biggest difference in the richness of TIA on this occasion.

5. 1. 2. JS Divergence of RDES In Figure 9, there are values of JS divergence based on RDES. Under different lift-off distances and excitation frequencies, the result characterized the difference of EC distributions between Koch excitation coil and circular excitation coil from the view of the EC distribution proportion in each annulus. For each frequency, the value of JS divergence reduces with the increase of the lift-off distance and tends to a horizontal line ultimately. It is illustrated that the ECs induced by Koch coil and circular coil distribute on more and more annuluses. Meanwhile, the EC distribution proportion of the Koch coil in each annulus becomes more and more identical to the EC distribution proportion of the circular coil. When the JS divergence is almost 0 bit, the number of annuluses occupied by the EC induced by the two coils is extremely close to each other. When the lift-off distance is definite, the value of JS divergence increases with the increase of the excitation frequency. It can be inferred that the difference of the number of annuluses occupied by the EC distributions between Koch excitation coil and the circular excitation coil becomes bigger and bigger. In the whole picture, the maximum value of JS divergence exists under 0.1mm lift-off distance and 10000 kHz. At this time, the number of annuluses occupied by the EC distribution induced by the circular coil has the largest difference relative to the number of annuluses occupied by the EC distribution induced by the Koch coil.

5. 2. FEM Simulation Result

5. 2. 1. EC Distributions of Excitation Coil In this section, the difference of EC distributions induced by Koch and circular coils are conveyed intuitively with the increase of the lift-off distance.

As is shown in Figure 10, there are EC distributions induced by Koch excitation coil and circular excitation coil. An obvious Koch-shape EC distribution can be seen in Figure 10(a) when the lift-off distance is 0.1mm. With the increase of lift-off distance, it is increasingly close to a circular EC distribution. Figure 10(b) is the EC distribution under 2.0mm lift-off distance where the Koch shape fades apparently. Figures 10(c) and 10(d) are EC distributions generated by the circular excitation coil when the lift-off distances are 0.1mm and 2.0mm, respectively. The difference of the EC distributions between Figures 10(a) and 10(c) is larger than it between Figures 10(b) and 10(d). The results of JS divergence can illustrate this phenomenon quantitatively.

As can be seen in Figure 11, it shows that the EC distributions when the crack in 0° and 90° directions is

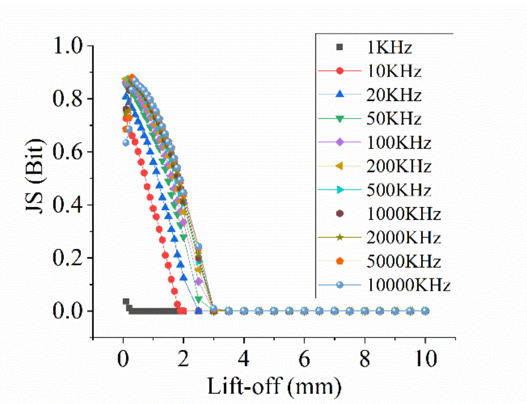

Figure 8. JS of TIAS

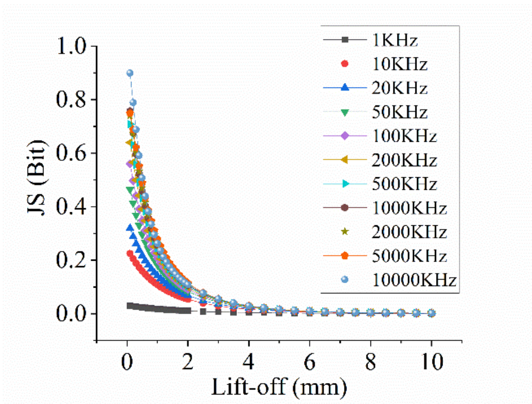

Figure 9. JS of RDES

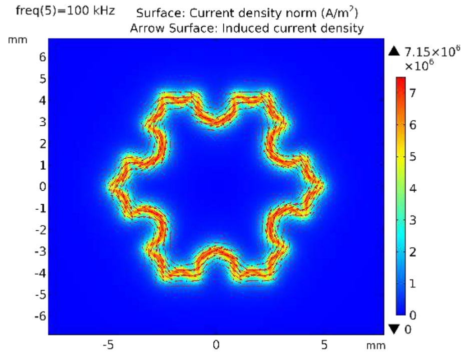

(a) EC distribution of Koch excitation coil under 0.1mm lift-off distance

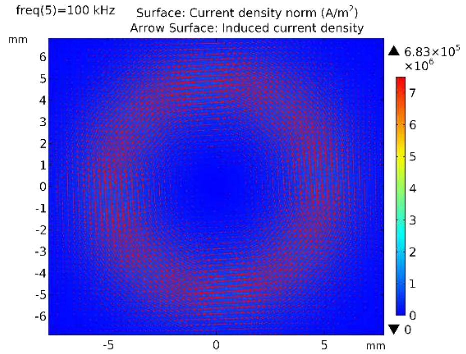

(b) EC distribution of Koch excitation coil under 2.0mm lift-off distance

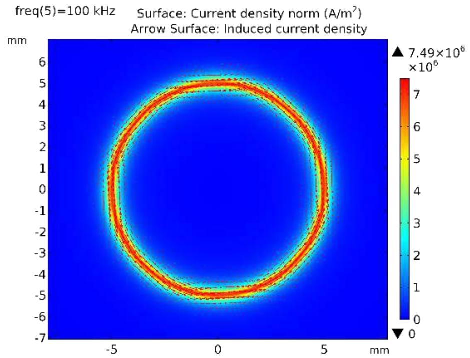

(c) EC distribution of circular excitation coil under 0.1mm lift-off distance

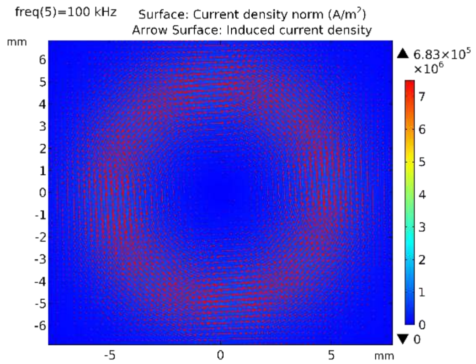

(d) EC distribution of circular excitation coil under 2.0mm lift-off distance

Figure 10. EC distributions of Koch excitation coil and circular excitation coil under 100 kHz

inspected via Koch differential pickup probe. For Koch probe, when the lift-off distance is 0.1mm, the EC induced by its excitation coil distributes in more orientations. Furthermore, the angle between EC vectors and the crack is diverse as shown in Figures 11(a) and 11(b). Conversely, when the lift-off is 2.0mm, the angle between EC vectors and the crack is relatively single as shown in Figures 11(c) and 11(d).

5. 2. 2. Correlation Between the Crack Signals in Two Directions and JS Divergence of TIAS

In order to study the detectability of Koch and circular

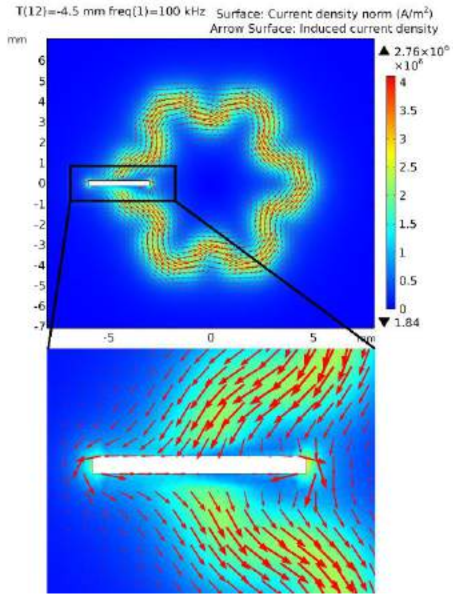

(a) Detection of crack in 0° direction under 0.1 mm lift-off distance

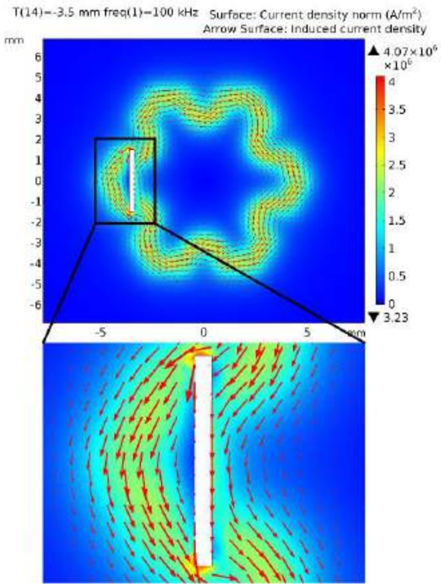

(b) Detection of crack in 90° direction under 0.1 mm lift-off distance

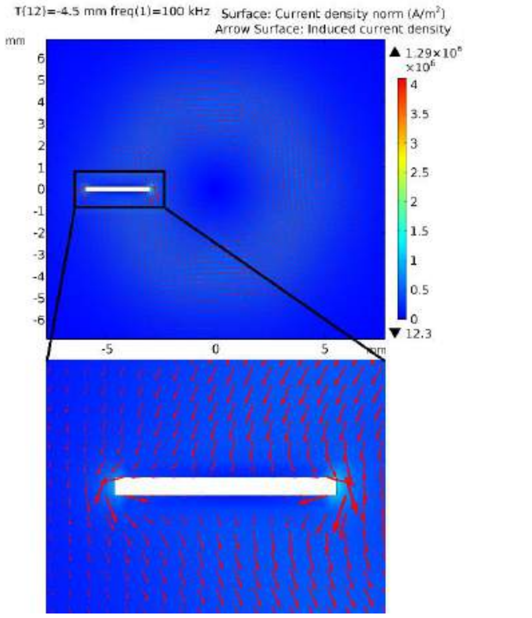

(c) Detection of crack in 0° direction under 2.0 mm lift-off distance

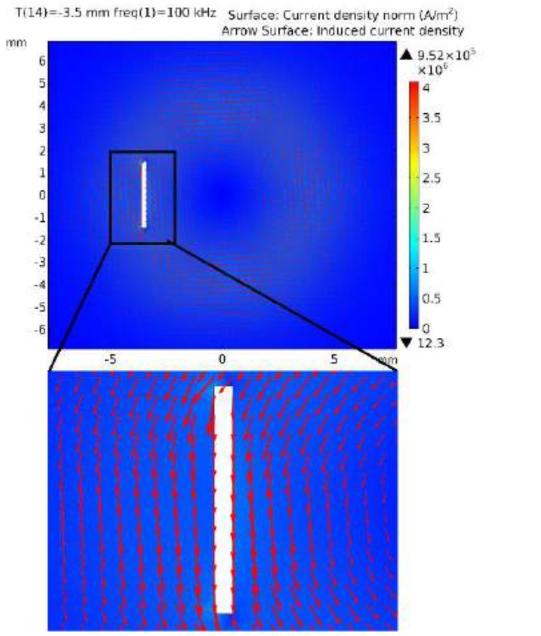

(d) Detection of crack in 90° direction under 2.0 mm lift-off distance

Figure 11. EC distributions of Koch differential pickup probe for the crack detection

pickup probes to the crack in two directions (0° and 90°) and the correlation between the detectability to 90° crack and JS divergence of TIAS, the EC distributions with crack and the rate of relative change of 90° crack to 0° crack are obtained.

Through the same approach to analyze, the inspection of the crack in 0° and 90° directions was carried out by the circular differential pickup probe. As can be seen in Figure 12, there are EC distributions of the circular differential pickup probe for the detection of crack when the lift-off distances are 0.1 mm and 2.0 mm. Although the geometry of circular EC distribution changes not obviously, the angle between the crack and EC vectors becomes more and more monotonous.

In order to research the correlation between the difference of signal in 0° direction and the JS divergence of TIAS, the V_{pp} of signals in 0° and 90° directions were extracted via simulation results with regard to Koch and circular differential pickup probes firstly. Then, the rate

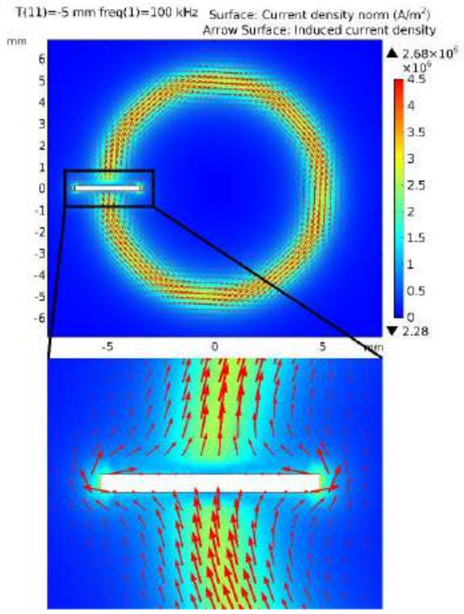

(a) Detection of crack in 0° direction under 0.1 mm lift-off distance

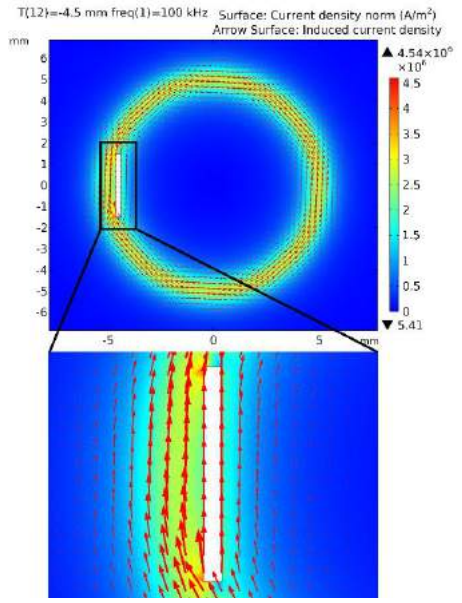

(b) Detection of crack in 90° direction under 0.1 mm lift-off distance

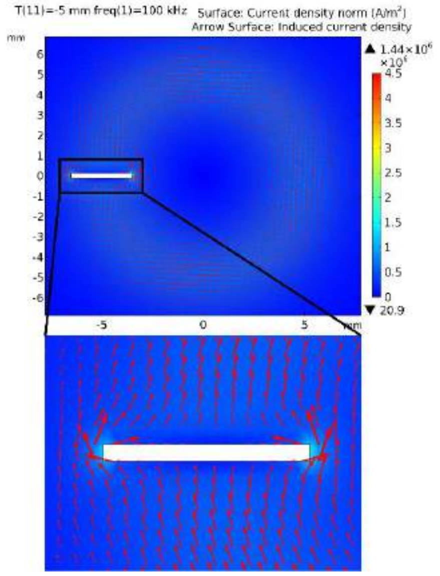

(c) Detection of crack in 0° direction under 2.0 mm lift-off distance

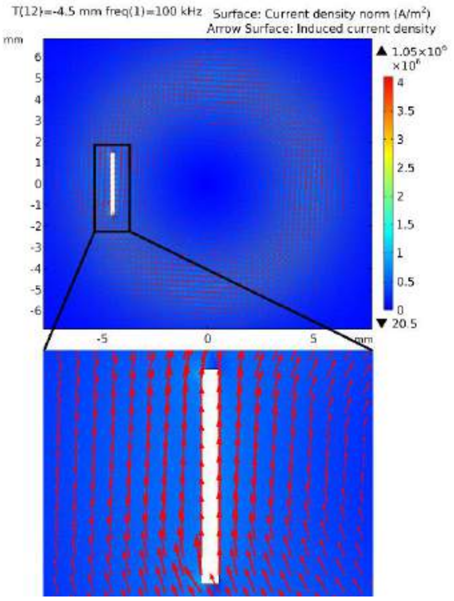

(d) Detection of crack in 90° direction under 2.0 mm lift-off distance

Figure 12. EC distributions of circular differential pickup probe for the crack detection

of relative change of the signal V_{pp} in 90° to the V_{pp} in 0° is calculated by Equation (12):

$$\text{Rate of relative change} = \frac{V_{pp}\ \text{of}\ 0° - V_{pp}\ \text{of}\ 90°}{V_{pp}\ \text{of}\ 0°} \tag{12}$$

By the way, the signals output from the two probes mainly denote the real part signals. As is shown in Figure 13, for the Vpp of signals output from both Koch and circular probes, the rate of relative change increases with the increase of the lift-off distance. It means that the two probes become less and less sensitive for the inspection of the crack in 90° direction relative to the crack in 0° direction. In addition, due to the intrinsic insensitivity of circular probe to the crack in 90° direction, the rates of relative change of circular probe are commonly higher than those of Koch probe. Furthermore, the difference of the rates of relative change of the two probes is smaller and smaller with the increase of the lift-off distance. The reason could be that the EC distributions induced by the two probes get close to each other. Meanwhile, the detectability of both probes to the crack in 90° direction becomes weak with the increase of the lift-off distance.

According to the result of JS divergence of TIAS, with the increase of the lift-off distance, the value of JS divergence is smaller and smaller when the excitation frequency is 100KHz. The TIA of EC distributions generated by Koch and circular probes is more and more monotonous, which contributes rarely to the inspection of the crack in 90° direction. Consequently, the detectability of the two probes is getting closer and closer aimed at the crack in 90° direction, which conforms to the discussion of the previous paragraph.

5. 2. 3. Correlation Between the Width of Crack Signals and JS Divergence of RDES In order to research the correlation between the width of 90° crack signals and JS divergence of RDES, the EC distributions and the output voltages (the voltage of real part signals) of crack detection were obtained by simulation.

Figure 14 shows the EC distributions concerned with the crack detected by Koch and circular differential pickup probes under 0.1mm and 2.0mm lift-off distances. In Figures 14 (a) and 14(b), when the crack passes the edge of EC distributions induced by Koch and circular probes under 0.1mm lift-off distance, due to the different number of annuluses occupied by EC distributions, the signals output from the two probes also have discrimination. At this time, the width of EC distribution determines the area range of interaction between crack

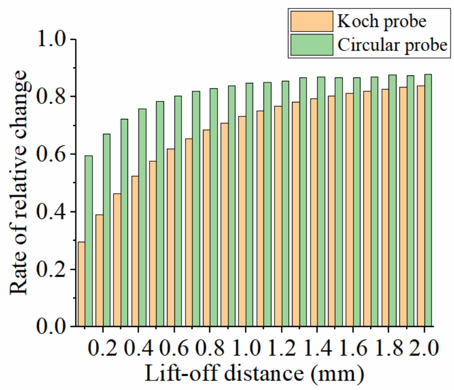

Figure 13. The rate of relative change of the V_{pp} in 90° to the V_{pp} in 0°.

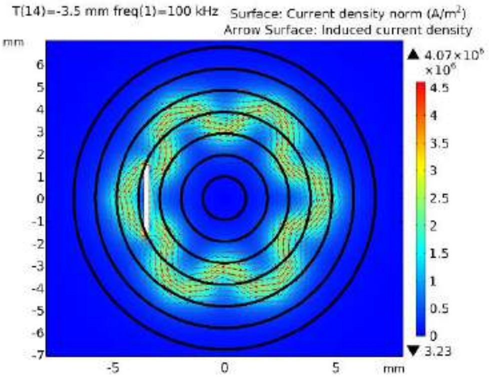

(a) Detection of crack using Koch probe under 0.1 mm lift-off distance

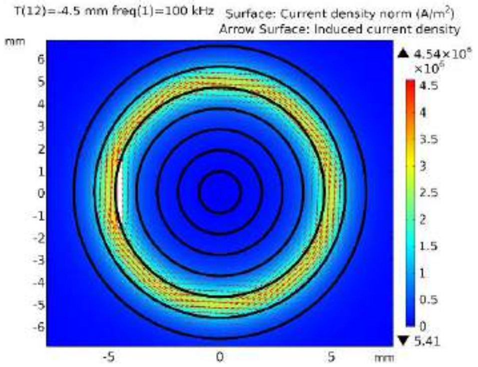

(b) Detection of crack using circular probe under 0.1 mm lift-off distance

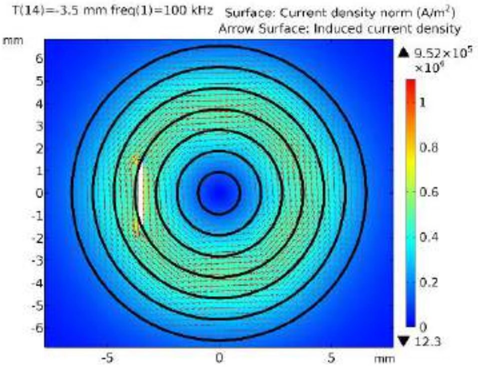

(c) Detection of crack using Koch probe under 2.0 mm lift-off distance

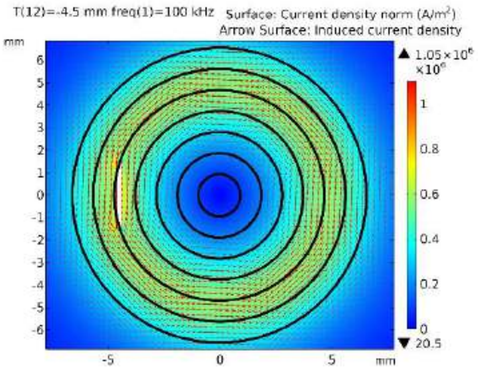

(d) Detection of crack using circular probe under 2.0 mm lift-off distance

Figure 14. EC distributions for the crack detection

and EC. Then, the full width at half maxima (FWHM) of signal namely the width of the signal as shown in Figure 15 was reflected by that. When the lift-off distance increase to 2.0mm as shown in Figures 14 (c) and 14(d), the two EC distributions take up more annuluses correspondingly. Moreover, the area of interaction between crack and EC increases as well.

In order to convey the width of every signal output from the two probes more obviously, the normalization and Gaussian fitting are conducted after getting the signals. In Figure 16, it displays the signals under 0.2mm to 2.0mm lift-off (the step is 0.2mm) distance after normalization and Gaussian fitting. Then, the left FWHM of every signal under every lift-off distance is calculated as the width of the signal. As can be seen in Figure 17, with the increase of lift-off distance, the width of the signal of Koch probe increases at a slow speed, but that of circular probe increases at a relatively fast speed. At the same time, the widths of signals from the two probes are getting close to each other. When the lift-off distance is 2.0mm, the widths of signals of the two probes have little difference.

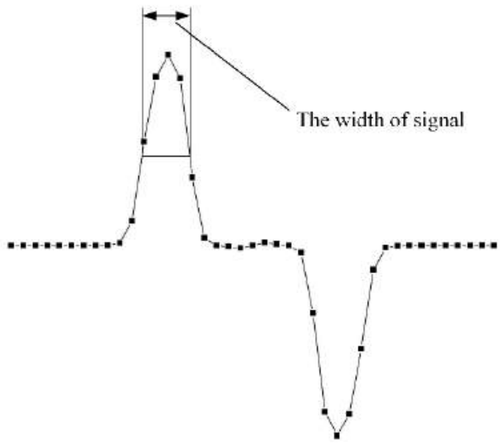

Figure 15. The schematic of the width of signal

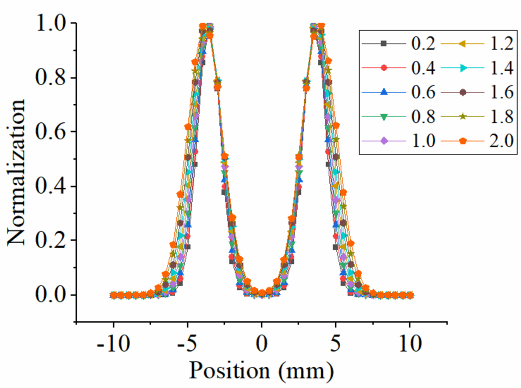

(a) Koch probe

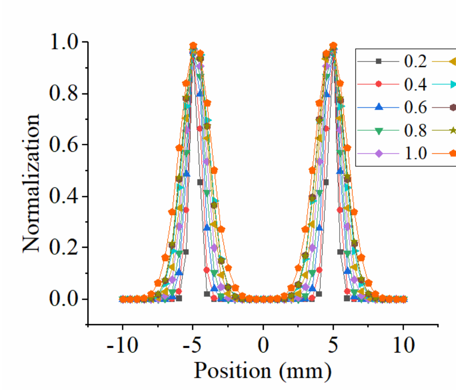

(b) circular probe

Figure 16. The signals after normalization and Gaussian fitting

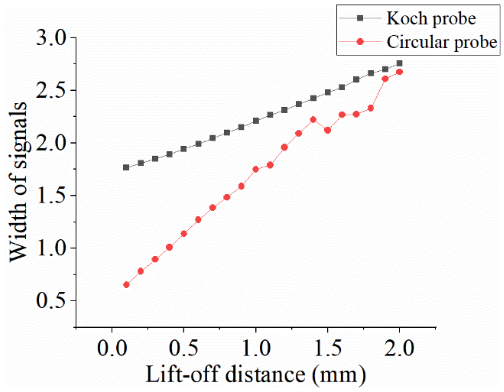

Figure 17. The schematic of the width of signal

The result can be explicated by the JS divergence of RDES. Because the EC distribution proportion of Koch coil in each annulus becomes more and more identical to the EC distribution proportion of circular coil, the ranges of interaction between the EC induced by the two probes and crack approach to each other. Therefore, it is consistent with the discussion about the widths of signals.

5. 3. Experiment Result In order to validate the simulation result, the experiment about circular and Koch differential pickup probes was carried out.

Figure 18 presents the rates of relative change calculated by Equation (12). Generally speaking, for the Koch probe, although there is fluctuation from 0.1mm to 0.4mm lift-off distance and 1.7mm to 2.0mm distance, the rate of relative change maintains an upward trend when the lift-off distance increases from 0.5mm to 1.6mm. Therefore, it is consistent with the simulation result to some extent. For the circular probe, the tendency of the rates of relative change is consistent with the simulation result under low lift-off distance.

Figure 19 shows the output voltage obtained from the Koch probe and circular probe in the experiment.

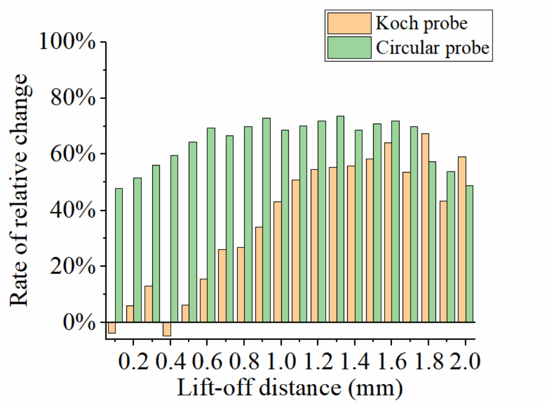

Figure 18. The rate of relative change of the V_{pp} in 90° to the V_{pp} in 0°

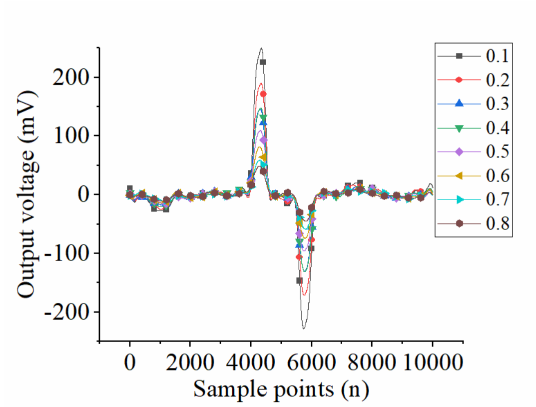

(a) The signals output from Koch probe

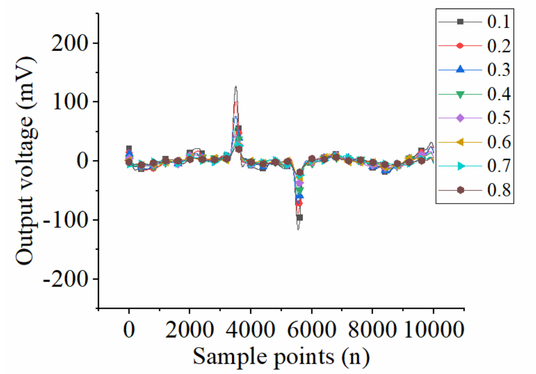

(b) The signals output from circular probe

Figure 19. The values of voltage of signals output from two probes

Similarly, each signal was processed by normalization and Gaussian fitting. In order to see the width of each signal clearly, the single peak of each signal from the two probes was set in the same range length of sample points (the range of sample points of Koch probe is from 2800 to 4400, and the range of sample points of the circular probe is from 3400 to 5000) as shown in Figure 20. Then, the left FWHM of every signal is calculated. It can be seen from Figure 21 that the width of signals from the Koch probe is larger than the width from the circular probe when the lift-off distance is small. Meanwhile, with the increase of the lift-off distance, the width of each signal of the circular probe is close to the width of the Koch probe gradually. Therefore, the experiment result is identical to the simulation result.

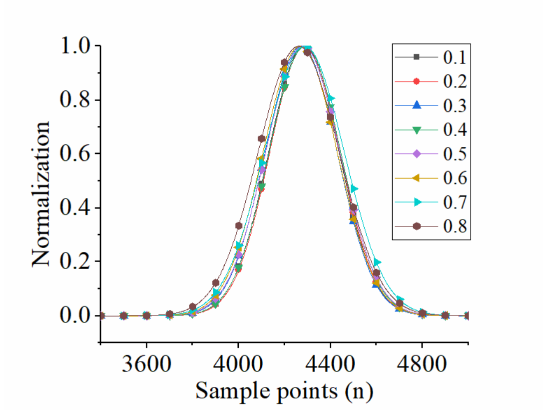

(a) Koch probe

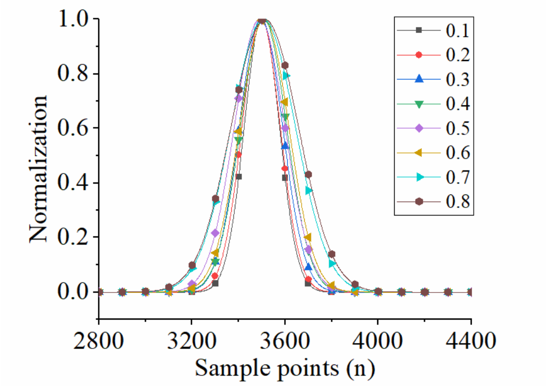

(b) circular probe

Figure 20. The signals after normalization and Gaussian fitting

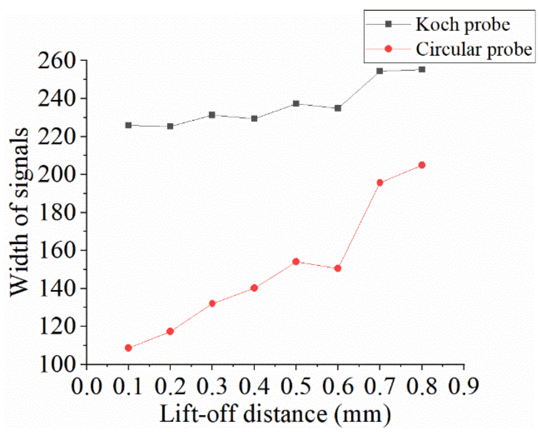

Figure 21. The left FWHM of signals after normalization and Gaussian fitting

6. CONCLUSIONS

In this paper, from the perspective of the diversity of EC orientations and the concentration degree of EC distributions, the JS divergence was applied to evaluate the difference of EC distributions between two different excitation coils. Then, in allusion to the Koch and circular differential pickup probes, the simulation result was conducted to study the correlation between the crack signals and JS divergence. Finally, the experiment was realized to verify the simulation result. It can be concluded that:

(1) In general, with the increase of the lift-off distance and decrease of the excitation frequency, the richness of TIA between Koch coil and circular coil gets close gradually based on the JS divergence of TIAS.

(2) Based on the JS divergence of RDES, with the increase of the lift-off distance and decrease of the excitation frequency, the number of annuluses occupied by the EC distributions induced by Koch and circular coils get close to each other increasingly.

(3) The detectability of Koch and circular differential pickup probes to the crack in 90° direction has a strong correlation with the JS divergence of TIAS to some extent.

(4) The width of crack signals has a relatively strong correlation with the JS divergence of RDES.

7. ACKNOWLEDGE

This work was financially supported by the National Nature Science Foundation of China (Grant No. 51807086 and 12162021), Department of Education of Gansu Province of China (Grant No. 2021QB-047) and the Hongliu youth found of Lanzhou University of Technology.

8. REFERENCES

1. Garcia-Martin, J., Gomez-Gil, J., and Vazquez-Sanchez, E., “Non-destructive techniques based on eddy current testing”, ***Sensors***, Vol. 11, (2011), 2525-2565. DOI: 10.3390/s110302525

2. Gilles-Pascaud, C., Decitre, J.M., Vacher, F., Fermon, C., Pannetier, M., and Cattiaux, G., “Eddy current flexible probes for complex geometries”, AIP Conference Proceedings, (2006), 399-406. DOI: 10.1063/1.2184556

3. Martinos, J., and Martinos, T., “Experimental development flexible eddy current planar probe”, ***Non-Destructive Testing***, (2015), 1-3.

4. Ding, T.H., Chen, X.L., and Huang, Y.P., "Ultra-Thin flexible eddy current sensor array for gap measurements", ***Tsinghua Science and Technology***, Vol. 9, No. 6, (2004), 667-671.
5. Meyendorf, N., Grundy, D., Baaklini, G.Y., Washabaugh, A., Schlicker, D., Michel, B., Shay, I., and Goldfine, N., "Health monitoring using MWM-array and IDED-array sensor networks", ***Advanced Sensor Technologies for Nondestructive Evaluation and Structural Health Monitoring***, Vol. 5770, (2005), 14-23. DOI: 10.1117/12.606069
6. Zilberstein, V., Walrath, K., Grundy, D., Schlicker, D., Goldfine, N., Abramovici, E., and Yentzer, T., "MWM eddy-current arrays for crack initiation and growth monitoring", ***International Journal of Fatigue,*** Vol. 25, (2003), 1147-1155. DOI: 10.1016/j.ijfatigue.2003.08.010
7. Ding, H., He, Y.T., and Jiao, S.B., "Rosette eddy current sensor for structural health monitoring", ***Applied Mechanics and Materials***, Vol. 330, (2013), 430-436. DOI: 10.4028/www.scientific.net/AMM.330.430
8. Fan, X.H., Chen, T., He, Y.T., Du, J.Q., Ma, B.L., and Song, Y.J., "An excitation coil layout method for improving the sensitivity of a rosette flexible eddy current array sensor", ***Smart Materials and Structures***, Vol. 29, (2020), 1-16. DOI: 10.1088/1361-665X/ab5455
9. Sun, Z.G., Cai, D., Zou, C., Zhang, W.Z., and Chen, Q., "A flexible arrayed eddy current sensor for inspection of hollow axle inner surfaces", ***Sensors***, Vol. 16, (2016), 1-9. DOI: 10.3390/s16070952
10. Zhang, H.Y., Ma, L.Y., and Xie, F.Q., "A method of steel ball surface quality inspection based on flexible arrayed eddy current sensor", ***Measurement***, Vol. 144, (2019), 192-202. DOI: 10.1016/j.measurement.2019.05.056
11. Xiao, M., Ju, F., Ning, P., He, Z.Q., Li, K.Y., Zhou, C., and Zhang, Y.Z., "Effects of filler type and aging on self-sensing capacity of cement paste using eddy current-based nondestructive detection", ***Measurement***, Vol. 182, (2021), 1-9. DOI: 10.1016/j.measurement.2021.109708
12. Yin, X.K., Zhang, X.R., Li, Y.Y., Zhu, T., Hutchins, D., Li, W., Chen, G.M., "A combined inductive and capacitive non-destructive evaluation technique using a single spiral coil sensor", ***IEEE Sensors Journal***, Vol. 21, No. 16, (2021), 18187-18195. DOI: 10.1109/JSEN.2021.3084204
13. She, S.B., He, Y.Z., Chen, Y.F., and Chady, T., "Flexible floral eddy current probe for detecting flaws in metal plate", ***IEEE Sensors Journal***, Vol. 20, No. 18, (2020), 10521-10529. DOI: 10.1109/JSEN.2020.2995472
14. She, S.B., Liu, Y.Z., Zhang, S.J., Wen, Z.Z., Zhou, Z.J., Liu, X.K., Sui, Z.H., Ren, D.T., Zhang, F., and He, Y.Z., "Flexible differential butterfly-shape eddy current array sensor for defect detection of screw thread", ***IEEE Sensors Journal***, DOI: 10.1109/JSEN.2021.3093550.
15. Chen, G.L., Cao, Z., and Zhang, W.M., "A novel planar differential Koch fractal eddy current probe with parallel wound topological structure", ***Journal of Sensors***, (2021), 1-13. DOI: 10.1155/2021/6671189
16. Chen, G.L., Zhang, W.M., and Pang, W.H., "Koch curve fractal geometry excitation probe for EC non-destructive testing", ***Measurement***, Vol. 124, (2018), 470-478. DOI: 10.1016/j.measurement.2018.04.031
17. Xie, R.F., Chen, D.X., Pan, M.C., Tian, W.G., Wu, X.Z., Zhou, W.H., and Tang, Y., "Fatigue crack length sizing using a novel flexible eddy current sensor array", ***Sensors***, Vol. 15, (2015) 32138-32151. DOI: 10.3390/s151229911
18. Zhang, W.P., Wang, C.L., Xie, F.Q., and Zhang, H.Y., "Defect imaging curved surface based on flexible eddy current array sensor", ***Measurement***, Vol. 151, (2020), 1-10. DOI: 10.1016/j.measurement.2019.107280
19. Aouf, A., Bouchala, T., Abdou, A., and Abdelhadi, B., "Eddy current probe configuration for full rail top surface inspection", ***Instrumentation Mesure Métrologie***, Vol. 20, No. 2, (2021), 65-72. DOI: 10.18280/i2m.200201
20. Chen, K.F., Gao, B., Tian, G.Y., Yang, Y.P., Yang, C.R., and Ma, Q.P., "Differential coupling double-layer coil for EC testing with high lift-off", ***IEEE Sensors Journal***, Vol. 21, No. 16, (2021), 18146-18155. DOI: 10.1109/JSEN.2021.3076880
21. Fan, X.H., Chen, T., He, Y.T., and Du, J.Q., "Influence of spatial winding distribution of flexible eddy current sensor on quantitative monitoring of subsurface cracks", ***Measurement***, Vol. 178, (2021), 1-15. DOI: 10.1016/j.measurement.2021.109382
22. Zhang, N., Ye, C.F., Peng, L., and Tao, Y., "Eddy current probe with three-phase excitation and integrated array tunnel magnetoresistance sensors", ***IEEE Transactions on Industrial Electronics***, Vol. 68, No. 6, (2021), 5325-5336. DOI: 10.1109/TIE.2020.2989704
23. Chen, G.L., and Cao, Z., "Quantitative evaluation of eddy current distribution by relative entropy and cross entropy", ***Measurement and Control***, Vol. 54, (2021), 1-6. DOI: 10.1177/0020294020984201
24. Zhang, W.M., Chen, G.L., and Pang, W.H., "Shannon information entropy of eddy current density distribution", ***Nondestructive Testing and Evaluation***, Vol. 32, (2016), 152-165. DOI: 10.1080/10589759.2016.1184266
25. Chen, G.L., "Two novel information entropy indices for analysis of the eddy current distribution", ***Entropy***, Vol. 20, (2018), 1-8. DOI: 10.3390/e20090699
26. Chen, G.L., and Zhang, W.M., "Angular spectral density and information entropy for eddy current distribution", ***Entropy***, Vol. 18, (2016), 1-11. DOI: 10.3390/e18110392
27. Lin, J.H., "Divergence measures based on the Shannon entropy", ***IEEE Transactions on Information Theory***, Vol. 37, No. 1, (1991), 145-151. DOI: 10.1109/18.61115

Persian Abstract

چکیده

توزیع جریان گردابی برای عملکرد پروب های جریان گردابی مسطح مهم است. در این مقاله، واگرایی جنسن-شانون طیف زاویه تقاطع مماسی و طیف انرژی جهت شعاعی برای ارزیابی تفاوت بین توزیع‌های جریان گردابی تولید شده توسط کویل‌های محرک دایره‌ای و فراکتالی کوخ پیشنهاد شد. با شبیه سازی برای کویل های محرک دایره ای و کوخ، مشخص می شود که تفاوت توزیع جریان گردابی بین دو نوع کویل با افزایش مقادیر دو واگرایی جنسن-شانون بزرگتر و بزرگتر می شود. در همان زمان، همبستگی بین تغییر واگرایی جنسن-شانون و قابلیت تشخیص ترک کوتاه در جهت خاص از طریق نتایج شبیه‌سازی و آزمایش مورد بحث قرار گرفت. مشخص شد که، نسبت به ترک در جهت ۰ درجه، قابلیت تشخیص پروب‌های پیکاپ دیفرانسیل کوخ و دایره‌ای به ترک در جهت ۹۰ درجه با واگرایی جنسن-شانون طیف زاویه تقاطع مماسی همبستگی دارد. عرض هر سیگنال تولید شده توسط دو پروب با واگرایی جنسن-شانون طیف انرژی جهت شعاعی همبستگی دارد.

IJE TRANSACTIONS A: Basics Vol. 35, No. 07, (July 2022) 1343-1354

International Journal of Engineering

Journal Homepage: www.ije.ir

Collision-free Inverse Kinematics of Redundant Manipulator for Agricultural Applications through Optimization Techniques

A. Sridhar Reddy*[a], V. V. M. J. Satish Chembuly[b], V. V. S. Kesava Rao[a]

[a] *Department of Mechanical Engineering, College of Engineering (A), Andhra University, Visakhapatnam, India*
[b] *Department of Mechanical Engineering, Aditya College of Engineering and Technology, Surampalem, India*

PAPER INFO

Paper history:
Received 29 January 2022
Received in revised form 16 March 2022
Accepted 12 April 2022

Keywords:
Agricultural Robot
Redundant Manipulator
Inverse Kinematics
Optimization
Obstacle Avoidance
Simscape Multibody

ABSTRACT

This article presents an optimization-based technique for solving the *inverse kinematics* (IK) of spatially redundant manipulators in agricultural environments (workspaces). A kinematic configuration of 9 *degrees of freedom* (DOF) manipulator with eight revolute and one prismatic joint has been modelled to improve the accessibility in complex workspaces. The proposed manipulator has been simulated for harvesting fruits and vegetables. To perform the desired task in the working environment, the IK solution of the robot needs to be determined. The IK problem has been formulated as a constrained optimization problem with the objective of minimizing the positional and orientational errors by avoiding obstacles. A 3D CAD environment with different fruits and vegetable plants has been modelled in Solidworks. A target location in this environment has been chosen to pluck the fruit/vegetables. The trunk, branches, and leaves are considered as obstructions. The collision avoidance technique was implemented using a bounding box approach by including a collision detection algorithm. IK simulations of the spatial redundant manipulator in a cluttered environment were performed and results are reported. The joint trajectories of the robot while reaching desired task-space location has been depicted using Simscape Multibody. The results demonstrate that the end-effector of the robot has been reached desired task location successfully with an accurate IK solution. The approach is adaptable in a wide range of working environments based on the simulation results of the IK solution of robots.

doi: *10.5829/ije.2022.35.07a.13*

NOMENCLATURE

IK	Inverse kinematics	URDF	Unified Robotic Description Format
DOF	Degrees of freedom	P_{error}	Positional error
CAD	Computer aided design	O_{error}	Orientational error
2D, 3D	Two, Three dimensional	f	Minimization function
a	Link length	**Greek Symbols**	
d	Join offset	α	Link twist
l_i	Length of the i^{th} link	θ	Joint angle
C_i	Penalty for i^{th} iteration	$(\alpha_d, \beta_d, \gamma_d)$	Desired orientation of end effector in Euler angles
q_i	Joint variable for i^{th} joint	$(\alpha_a, \beta_a, \gamma_a)$	Actual orientation of end effector in Euler angles
SQP	Sequential Quadratic Programming	**Subscripts**	
R^2	Correlation coefficient	i	Link number
D–H	Denavit– Hartenberg	l	Lower bound
slx	Simulink model data format	u	Upper bound

*Corresponding Author Institutional Email: asridhareddy@andhrauniversity.edu.in (A. Sridhar Reddy)

Please cite this article as: A. Sridhar Reddy, V. V. M. J. Satish Chembuly, V. V. S. Kesava Rao, Collision-free Inverse Kinematics of Redundant Manipulator for Agricultural Applications through Optimization Techniques, ***International Journal of Engineering, Transactions A: Basics***, Vol. 35, No. 07, (2022) 1343-1354

1. INTRODUCTION

During the cultivation of bulk commodity crops like wheat, rice, and sugarcane, the tractor and combine harvester has virtually replaced the need for manual labor. Despite recent advances in agricultural automation, high-value specialty crops such as fruits and vegetables, horticulture, and nursery crops still rely mostly on labour. A large seasonal workforce is needed to produce a fresh market of fruits like guava and apples. Harvesting is a time-sensitive activity, with unpredictable weather patterns producing uncertainty when organizing employment [1]. When harvesting individual fruits and vegetables in horticulture and greenhouses, robots are required to identify the task space location. For these applications, reaching the desired task location by avoiding tree trunks, branches, and leaves remains challenging with respect to robot manipulation. Agricultural robots need to be perceptive and intelligent that are programmed to conduct a wide range of operations such as transplanting, cultivating, spraying, pruning, and harvesting [2] in a complex environment. Pedersen et al. [3] focused on the economic feasibility for applying autonomous robotic systems compared to conventional systems in different applications of cultivation. The use of robotic systems in agricultural applications seems more economically feasible than conventional harvesting equipment based on the conclusions drawn. By considering the profitable usage of robots in agriculture, Belforte et al. [4] designed and built a 3 DOF robot for spraying and precision fertilization applications.

Because of high crop harvesting expenses, researchers are concerned about the utilization of robots in the agricultural environment. In the twentieth century, technical developments in agricultural mechanization profoundly altered the structure of modern agriculture [5]. Bechar and Vigneault [6] presented a review on the design and development of agricultural robots along with associated principles and limitations. Selective harvesting is a challenging task for robots due to high levels of variation in objects, environmental, cultivation system, and task variation as well as incomplete information of the environment, noisy data from sensors. Kootstra et al. [7] discussed the current state of selective harvesting of apple, tomatoes, and broccoli in greenhouse, orchard, and open-field conditions. Perception, the complexity of the environment, task variation, operational speed, and safety are some of the critical components for harvesting robots.

From the literature, it has been noted that robots have been widely used in different harvesting applications. In such cases, the robot manipulator should be flexible enough to access the desired location. Because of its greater flexibility and maneuverability within a complex environment, it requires more DOF than is needed to accomplish the given task. These robots are kinematically redundant in nature. The excess DOF of the robot manipulator enables to reach the desired task location by avoiding the obstacles in the workspace [8].

In *Inverse Kinematics* (IK) [9], all possible sets of joint angles can be calculated, which could be used to attain the given position and orientation of the end-effector. This problem can be solved either analytically or numerically [10]. In an analytical approach, the solution can be obtained as a closed-form, and these solutions are desirable because they are faster than numerical solutions; however, such a solution is inherently dependent on the DOF of a manipulator. In the numerical approach, the solution can be obtained by iterative methods and these solutions are computationally effective even with an increase in the number of DOF. Aristidou and Lasenby [11] reviewed Jacobian Inverse methods (Pseudo-inverse, transpose, singular value decomposition, Damped least square, pseudo-inverse Damped least squares, and so on), Newton Methods, Sequential Monte Carlo methods, and Heuristic IK algorithms for solving IK problems numerically. A new heuristic IK methodology *'Forward and Backward Reaching Inverse Kinematics'* (FABRIK) was proposed by Aristidou and Lasenby [11].

In the literature, some of the researchers conducted several studies on IK methods using optimization techniques. Goldenberg and Lawrence [12] proposed a constrained optimization technique-based algorithm for redundant axes manipulators to obtain restrictive motion and to select a solution when multiple solutions exist. Kumar et al. [13] considered a 7 DOF (PA-10) manipulator for the IK solution and formulated it as a nonlinear optimization problem with the objective of energy minimization, for smooth tracking of the desired path. Bagheri et al. [14] acquired the IK solutions for 6 DOF robot by applying neural networks.

Many researchers solved the IK problem by considering joint level velocities by calculating the pseudo inverse of Jacobian [15]. These are sensitive at the singular configuration, also increasing the computational cost. An optimization-based approach for solving the IK problem of a planar redundant manipulator to avoid obstacles and singularities was implemented at a joint position level by avoiding the use of inverse of Jacobian, which is computationally effective [16].

In agricultural environments, the robot must be able to identify the task-space and obstacles in the environment in order to move around for harvesting purposes. As a result, obstacle detection becomes a major issue when harvesting robots are involved. To capture workspace coordinates vision sensors are needed. Vision sensors can be *two-dimensional* (2D) visual sensors or *three-dimensional* (3D) visual sensors. A monocular vision system is a 2D visual sensor type, that contains a single camera. It is used to detect fruit/vegetable in the field. These sensors can be *Charge Coupled Device* (CCD) or *Complementary Metal Oxide Semiconductor* (CMOS). A binocular stereo-vision system is a 3D visual sensor, consisting of two cameras separated with some distance. The 3D map of fruit/vegetable can be obtained by the triangulation method [17]. Hartley and Sturm [18] developed an algorithm for the Triangulation problem to get the optimal global solution used to find the location of an object. van Henten et al. [19] used CCD as a vision sensor during the harvesting of cucumbers. A binocular stereo-vision system is mounted on Agrobot to identify the ripe tomato by Buemi et al. [20]. By capturing the images of the real-time environment, the coordinates of the workspace have been determined in the present work.

A virtual workspace with fruits and vegetables has been modelled, which resembles a real-time environment, and the dimensions are similar to the images that are taken. After creating the 3D map of the environment, the robot manipulator needs to reach the task-space (for fruit picking) location by avoiding the collision with obstacles (tree trunk, stems, etc.). Collision avoidance plays a pivotal role in motion planning and the IK of robot manipulators. A wide variety of techniques have been adopted for collision avoidance. Potential field methods are widely used obstacle avoidance techniques for mobile robots and manipulators. Khatib [21] proposed an artificial potential field method for obstacle avoidance. In this approach, obstacles exert repulsive forces, and the goal exerts an attractive force on the robot end-effector, from these, resultant force determines the direction of travel. Korayem et al. [22] presented a methodology for collision-free trajectory planning of mobile manipulators in cluttered environments based on potential field functions. Here, the mobile manipulator parts and environmental obstacles are modeled as ellipsoidal bodies. Based on the dynamic distance between colliding objects, Korayem et al. [23] formulated a dynamic potential function for tracking moving targets in dynamic environments for mobile manipulators. Potential field functions are also employed for collision avoidance during the motion planning of non-holonomic mobile robots in a cluttered environment [24]. Tang et al. [25] proposed an improved mathematical model of the APF (artificial potential field) method for the motion planning algorithm of citrus-picking robots. While the potential field principle is attractive due to its elegance and simplicity, however, it has significant problems of trapping at local minima, no passage between closely spaced obstacles, causing unstable motion in the presence of obstacles, and oscillations in narrow passages [26]. Gottschalk et al. [27] proposed an algorithm by placing a tight-fitting *oriented bounding box* (OBB) around a collection of polygons and grouping them into a tree hierarchy. This algorithm traverses two such trees and tests for overlaps based on the separating axis theorem. This algorithm takes a long time for parallel close proximity scenarios. Barequet and Har-Peled [28] discussed an algorithm for approximating the minimum-volume bounding box for 3-dimensional point sets, but this was not suitable for ellipsoidal point sets. Held et al. [29] used tetrahedron geometric primitive for generating bounding volume. But it does not fit tightly for many of the objects. This algorithm has to be recomputed if the orientation of the object is changed. Chembuly and Voruganti [30] implemented a classical constrained optimization technique to perform inverse kinematics of hyper redundant manipulator along with collision avoidance algorithm. Here, the boundaries of obstacles are enveloped by a 3D bounding box. A set of points are taken on the manipulator, when these point coordinates are inside the bounding box, a collision was detected.

Bac et al. [31] conducted a study on harversting robots, and reported that the algorithms available for obstacle localization, task planning, and motion planning are very limited. Tinoco et al. [32] pointed out the need for path planning and collision avoidance algorithms for agricultural applications. From the literature, it is observed that most of the IK solution and Collision avoidance techniques implemented for agricultural applications are computationally expensive and difficult for solving. Hence, there is a need for robots in agricultural applications, which can travel through narrow regions to spray the pesticides and/or to pick the fruits/vegetables by avoiding the collision with surrounding tree branches, which motivates study on agricultural robots. This paper proposed a redundant manipulator to access the task-space location in any direction. IK for the redundant manipulator was computed by considering it as an optimization problem to reduce the computational burden. Incorporating a collision detection algorithm into the bounding box approach can help to eliminate robot collisions with surrounding objects.

This paper is structured as follows. In section 2 discussion on harvesting robot. Section 3 describes the collision detection technique. Section 4 describes the optimization and problem formulation; then the results and discussion in section 5 and finally with conclusions.

2. HARVESTING ROBOT

2. 1. Manipulator Requirements In the present study, the trellis for agricultural plantations is positioned at 1000 mm from the ground. Fruits of guava trees grow 500 mm to 1200 mm above the ground. A 9DOF manipulator with 1P8R configuration was selected based on the requirements. A prismatic joint is selected for accessing large displacement in the vertical direction. The last 3 DOF of the manipulator constitutes wrist, which allows a roll-pitch-yaw motion for the end-effector.

2. 2. Kinematic Model Kinematic modeling is the basis for trajectory planning and control. The Denavit–Hartenberg approach is used to analyze forward kinematics the robot Parameters can be specified to build the coordinate relationship between adjacent joints.

The assignment of coordinate frames at the robot joints is the first step in the forward kinematic analysis, and these frames are used to determine the location and orientation of one frame relative to another frame. Redundant manipulator frame assignment is depicted in Figure 1(a), the robot configuration for the proposed work is modeled using Solidworks, shown in Figure 1(b). Conventional D–H parameters are provided for the frames and listed in Table 1.

The transformation of the frame (i) relative to the previous frame $(i-1)$ is derived from a generalized homogeneous transformation matrix, given in Equation (1)

$$ {}^{i-1}_{i}T = \begin{bmatrix} \cos\theta_i & -\sin\theta_i\cos\alpha_i & \sin\theta_i\sin\alpha_i & a_i\cos\theta_i \\ \sin\theta_i & \cos\theta_i\cos\alpha_i & -\cos\theta_i\sin\alpha_i & a_i\sin\theta_i \\ 0 & \sin\alpha_i & \cos\alpha_i & d_i \\ 0 & 0 & 0 & 1 \end{bmatrix} \quad (1) $$

For the serial manipulator shown in Figure 1(b), the end-effector's final location relative to the base frame is given by:

$$ {}^{0}_{9}T = {}^{0}_{1}T\,{}^{1}_{2}T\,{}^{2}_{3}T\,{}^{3}_{4}T\,{}^{4}_{5}T\,{}^{5}_{6}T\,{}^{6}_{7}T\,{}^{7}_{8}T\,{}^{8}_{9}T \quad (2) $$

Using the homogeneous transformation matrix Equation (2), the end-effector position and orientation can be determined.

2. 3. Object Identification in the Environment In the agricultural field, images are taken in different directions of views for locating the object (fruit/vegetables). The coordinates of the object can be

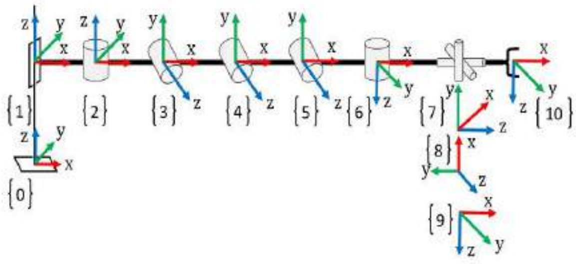

(a) frame assignment

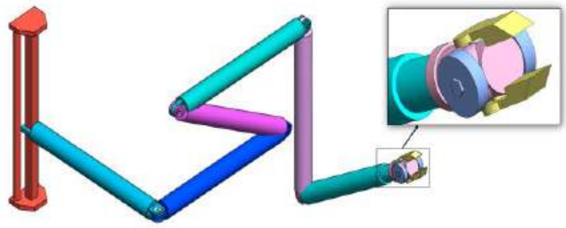

(b) Solidworks 3D model

Figure 1. Redundant Manipulator

determined by using the 'mapping technique' [33]. This technique requires some data points from the image to map with real-world coordinates.

For this purpose, four random locations are identified in the field and their distance is measured from the reference point. Then the images were taken, the pixels at target locations can be mapped with actual distances using Matlab image processing toolbox.

Actual measured distances vs. image pixels are summarized in Table 2, and a quadratic polynomial curve was fitted as shown Figure 2 and Equation (3) which has a correlation coefficient (R^2) equal to 0.9995. The correlation coefficient near one represents the best-fitted curve. So, this regression equation is further used to find the real-world coordinates from the image data.

$$ y = 0.0667x^2 - 24.664x + 2546.5 \quad (3) $$

where x is data from the image, y is the location of the object in the real-world coordinate system.

Figure 3 shows the distance measurement in the Bitter gourd field using the *Image processing toolbox*.

TABLE 1. D-H parameters

link	α	a	θ	d
1	0	l_1	0	d_1
2	90	L_2	0	0
3	0	L_3	0	0
4	0	L_4	0	0
5	90	L_5	0	0
6	-90	l_6	-90	0
7	-90	0	90	0
8	90	0	-90	0
9	0	0	0	0

TABLE 2. Image vs. field measured data

S. No.	**Measurement**	
	Image (pixel)	**Field (mm)**
1	202	280
2	214	330
3	253	570
4	280	870

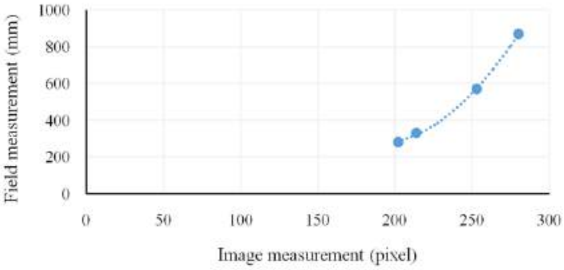

Figure 2. Polynomial curve fitting for image mapping

(a) Image from front

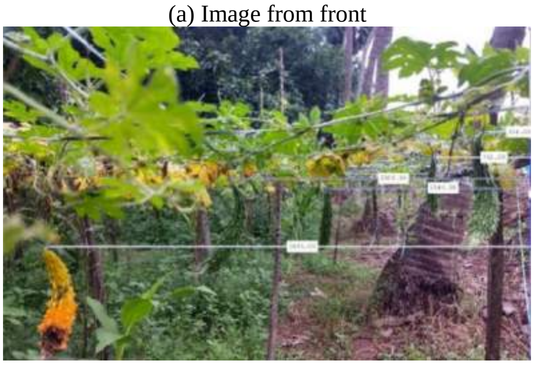

(b) Image from side

Figure 3. Field images of Bitter gourd

3. COLLISION DETECTION TECHNIQUE

To perform agricultural operations, the redundant manipulator must avoid collisions with the surroundings. Collisions can be detected by the bounding box technique [30]. In the present study, different vegetables and guava fruits are considered as task-space locations for picking/plucking operations. Trellis, tree trunks, and branches are considered as the obstacles. These obstacles need to be bound by the 3D bounding box. The solid boundaries of each object are represented by a set of points. From this set of points, the extremum coordinates of points are found. These extremum coordinates are used to find the vertices of the bounding box using a convex hull algorithm, the facet information (i.e., the vertices which are used to form a particular face) is calculated. Finally, a 3D bounding box is modelled around each obstacle using facets and their corresponding vertices as shown in Figure 4. Whenever a particular configuration of manipulator links lies within this bounding box, a collision can be detected. The collision detection algorithm is stated in Table 3. To implement the algorithm for convex and concave-shaped obstacles, the obstacle can be enveloped by using several small bounding boxes. So this algorithm can be effectively implemented to different complex-shaped obstacles.

TABLE 3. Collision detection algorithm

Algorithm: Collision detection
1. Input: bounding box extremum coordinates.
$x_{min}, y_{min}, z_{min}, x_{max}, y_{max}, z_{max}$ and point $p_i(p_{ix}, p_{iy}, p_{iz})$
2. Collision condition:
for $i = 1:n$
if $x_{min} <= p_{ix} <= x_{max}$ && $y_{min} <= p_{iy} <= y_{max}$
&& $z_{min} <= p_{iz} <= z_{max}$
collision with obstacle
else
no collision with the obstacle
end
end

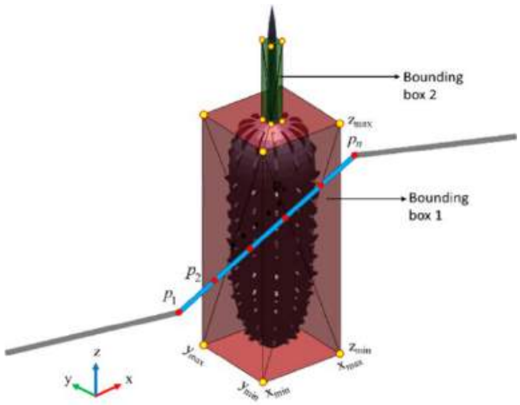

(a) 3D view

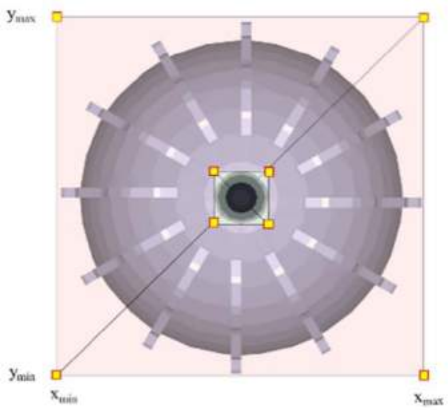

(b) top view

Figure 4. Object encompassed by a bounding box

For detecting a collision with obstacles, a set of uniformly distributed points $p_1, p_2, \ldots, p_n$ on each link of the manipulator, and extremum points of the bounding boxes are considered. Each point on the manipulator is taken as a query point 'q' and a check will be performed with bounding box extremum points. Whenever the query point lies within the bounding box, a collision is detected between the manipulator and the obstacle. The configuration that leads to collisions has been determined using the aforesaid approach and these configurations should be avoided.

To eliminate the configuration that causes a collision with the environment, a penalty approach has been implemented during the calculation of IK for robot manipulator.

4. OPTIMIZATION AND PROBLEM FORMULATION

To obtain the joint variables, the IK problem of the redundant manipulator is formulated using classical optimization technique at the joint position level. this approach was easily applied to any redundant manipulators with a different configuration.

4. 1 Objective Function The objective function is the manipulator's reachability. This is can be measured as the total cumulative error in Euclidean distances and Euler angles, that is, the error in the position and orientation of the manipulator's end-effector to reach the intended task space locations. A schematic diagram of a general serial redundant manipulator is shown in Figure 5. In cartesian coordinates, the position error can be expressed as:

$$P_{error} = (x_d - x_a)^2 + (y_d - y_a)^2 + (z_d - z_a)^2 \tag{4}$$

In Equation (4), (x_d, y_d, z_d) and (x_a, y_a, z_a) are vectors that correspond to desired (r_d) and actual (r_a) positions respectively.

Similarly, orientation error can be expressed as:

$$O_{error} = (\alpha_d - \alpha_a)^2 + (\beta_d - \beta_a)^2 + (\gamma_d - \gamma_a)^2 \tag{5}$$

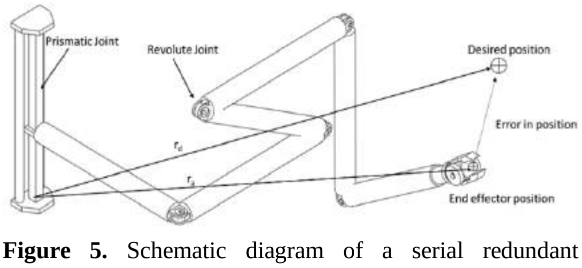

Figure 5. Schematic diagram of a serial redundant manipulator

In the above, Equation (5), $(\alpha_d, \beta_d, \gamma_d)$ and $(\alpha_a, \beta_a, \gamma_a)$ are Euler angles corresponding to desired and actual orientations respectively in relation with base frame.

To compute the cartesian coordinates of the end-effector's position in terms of the D-H parameters, $[a, \alpha, d, \theta]$, the conventional forward kinematics method is utilized.

As a result, the objective function can be defined as the sum of the cumulative errors of position and orientations. Finally, the objective function can be expressed in Equation (6):

Minimize:

$$f = [(x_{id} - x_{ia})^2 + (y_{id} - y_{ia})^2 + (z_{id} - z_{ia})^2 + (\alpha_{id} - \alpha_{ia})^2 + (\beta_{id} - \beta_{ia})^2 + (\gamma_{id} - \gamma_{ia})^2] \tag{6}$$

From the above equation, a suitable configuration for the manipulator was obtained. But to get a collision-free configuration for the manipulator, penalties are imposed in the objective function. The modified objective function for the IK problem is given in Equation 6. Due to this penalty, the objective function is again run (search) for minimization.

$$\text{Minimize: } f = [(x_{id} - x_{ia})^2 + (y_{id} - y_{ia})^2 + (z_{id} - z_{ia})^2 + (\alpha_{id} - \alpha_{ia})^2 + (\beta_{id} - \beta_{ia})^2 + (\gamma_{id} - \gamma_{ia})^2] + \sum_{i=1}^{m} C_i \tag{7}$$

where C_i is the i^{th} penalty when there is a collision and m is the number of collisions.

4. 2 Constraints due to Limiting Values of D-H Parameters The DH parameters of the linkages are constrained. These are imposed as limitations on the optimization technique.

In this study, one of the joints is prismatic and the remaining are revolute. As a corollary, the joint variable for each link, say q, would be either d (for prismatic) or θ (for revolute). Constraints on the DH parameters for the i^{th} link can be expressed in the following manner given in Equation (8):

$$\begin{cases} a_{il} \le a_i \le a_{iu}, \\ \alpha_{il} \le \alpha_i \le \alpha_{iu}, \\ d_{il} \le d_i \le d_{iu} & \text{if the joint is prismatic,} \\ \theta_{il} \le \theta_i \le \theta_{iu} & \text{if the joint is revolute,} \\ q_{il} \le q_i \le q_{iu} & \forall j \end{cases} \tag{8}$$

where $i = 1, 2, ..., n$; l in suffix represents lower bound while u represents the upper bound.

In the present study, joint variable limits are presented in Equation (9).

$$\begin{cases} 0 \le d_1 \le 20cm & \text{for Prismatic joint,} \\ -180 \le \theta_i \le 180 & \text{if the joint is revolute for i=2,3,..6.,} \\ -90 \le \theta_i \le 90 & \text{if the joint is revolute for i=7,8,9} \end{cases} \quad (9)$$

4. 3. Optimization Technique To solve the objective function with constraints we used one of the classical optimization methods i.e., 'Sequential Quadratic Programming (SQP) technique'**. SQP method is the most advanced nonlinear programming technique. SQP is a quadratic approximation of the Lagrangian function with constraints linearization. To get the search direction, a quadratic subproblem is formulated and solved. A modified BFGS formula is used to update the Hessian matrix during the line search, which can be done with two alternative merit functions. By using this approach, simulations are carried out in the present study. This algorithm gives the optimum values at local minima. The problem of trapping at local minima can be overcome by considering multiple initial guesses from different start points, which can be known as the "multi-start technique", and it can be easily extended to a global minimum problem.

5. RESULTS AND DISCUSSION

In this section, results of IK simulations for robot operating in different agricultural environments are presented. Three different virtual environments are modelled which depicts the real-time environment in the agricultural field. Simulations of the robot are carried out in this modelled environment. For fruit/ vegetable picking operations, a redundant robot with nine links and 9-DOF is considered. The first six links are of uniform length, with 20 cm each in a cylindrical shape with 2cm diameter. The last 3 links constitute the wrist, which allows the end-effector to place in the desired orientation. The IK solutions for the redundant robot manipulator are computed using optimization technique as discussed in section 4. The collision detection technique was implemented and extended to cylindrical links for avoiding obstacles like tree trunks and branches, as discussed in section 3 using Equation (6). To determine the collision between the cylindrical links and obstacles, the surface of the link is considered as a series of circles. If any coordinates of these circles are lies within the bounding box, a collision can be detected by using the algorithm discussed in section 3. A constant value of penalty is added to the objective function for all cases of simulations. The penalty value can be determined based on the merit function which was used as the objective of the optimization. The penalty value is taken as 100 for the simulation of a redundant manipulator in the agricultural environment.

Configuration of robot manipulator during the simulation was plotted in Matlab. However, it is not possible to show the orientation of the manipulator in a Matlab environment. So, here the orientation was presented using Simscape Multibody in the Simulink environment. To represent in Simulink environment, the robot is modelled in Solidworks and saved in Unified Robotic Description Format (URDF) file format, by describing the robot's physical contacts and joint locations. In the Simulink environment, the model was shown as a number of blocks as depicted in Figure 6. To show the agricultural environment, different virtual 3D models were added using the *'file solid'* block. For identifying the position of the end-effector a *'transformation sensor'* was added at wrist and same data is exported to Matlab workspace through *'PS- Simulink Converter'*. This environment was saved in.*slx* file. format.

In the present work, we considered three different agricultural fields namely: Bitter gourd, Tindora, and Guava garden. These fields are modelled in Solidworks which resembles real environments. Task-space locations are identified from the image, using mapping technique as mentioned in section 2.3, coordinates of the task-space location in real-world were determined.

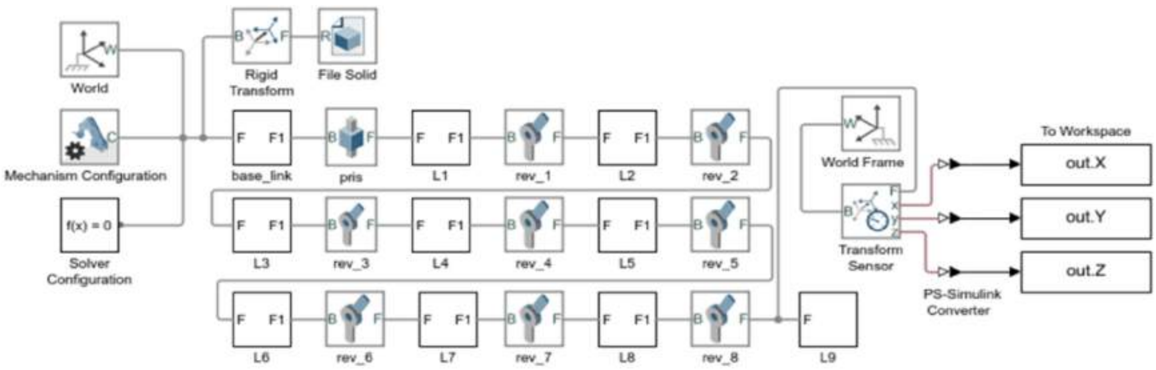

Figure 6. Simulink environment of 9 DOF robot

5. 1. Case Studies

Application 1: Bitter Gourd:

Figure 7 shows the virtual environment of Bitter gourd plants. Here Bitter gourd is to be harvested and several obstacles such as leaves, stems, and trellis could be avoided for collision-free travel (configuration) of the manipulator. In the cluttered environment, the robot is directed to move from one task space location to another task space location by avoiding obstacles. Collisions with obstacles can be avoided by bounding box criteria as mentioned in section 3. Using the numerical method, IK for redundant manipulator determined as discussed in section 4, and configuration was plotted to reach (42,36,60) mm location in the environment, as shown in Figure 8. Figure 9 shows the robot manipulator moving from one task space location (38, 34, 60) to another task space location (59, -15, 60) by avoiding obstacles in between them. The IK solutions at different locations are presented in Table 4.

The computational time for attaining an IK solution of the redundant manipulator in a cluttered environment is about 54 seconds, which is less when compared to evolutionary algorithms [34]. For all cases, the positional error is very small. The configuration and orientation of the manipulator for one task-space location are shown in Figure 10 using Simscape Multibody. The error values during simulations were compared with existing

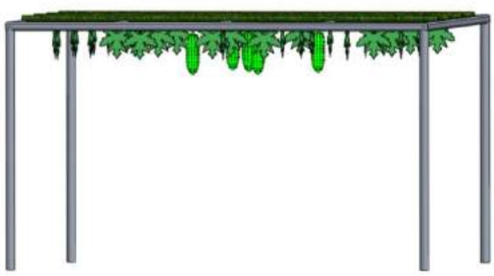

Figure 7. Solidworks model of Bitter gourd environment

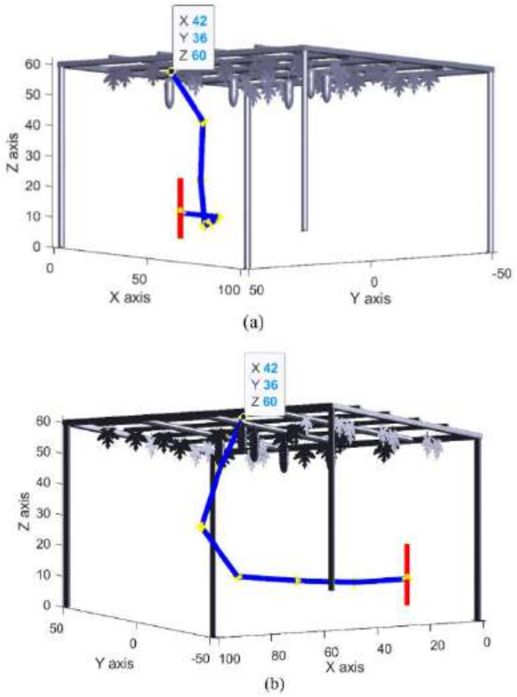

Figure 8. Robot configuration in different views at task location (42,36,60)

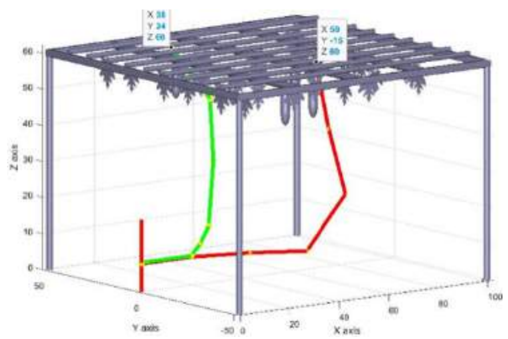

Figure 9. Manipulator configuration for different task space locations: (38,34,60) and (59,- 15,60)

TABLE 4. Joint variables for different task space locations

S. No	Task space locations		Joint variables									Error
	Position (cm)	Orientation (degrees)	(cm)	(degrees)								
			q_1	θ_1	θ_2	θ_3	θ_4	θ_5	θ_6	θ_7	θ_8	
1	(38,34,60)	(-26,12,34)	8.16	44.57	5.33	50.95	56.99	-35.41	6.34	221.30	50.87	1.13e-07
2	(43.25,29.25,55)	(-10,5,23)	8.12	35.38	-4.73	55.25	66.34	-31.29	1.50	-131.07	43.13	6.79e-08
3	(48.5,24.5,50)	(-30,-40,20)	8.14	27.85	-16.29	58.61	74.69	-24.68	1.50	30.30	21.22	2.11e-07
4	(53.75,19.75,55)	(-22,14,33)	8.15	21.76	-9.88	55.08	67.54	-16.94	1.50	-29.89	-33.31	1.38e-07
5	(59,15,60)	(30,16,22)	7.91	15.60	-2.06	50.47	58.72	-11.41	13.43	13.45	34.23	1.50e-07
6	(59,-15,60)	(23,43,17)	7.84	-15.58	-1.90	50.38	58.62	11.46	11.76	33.71	23.54	1.49e-07

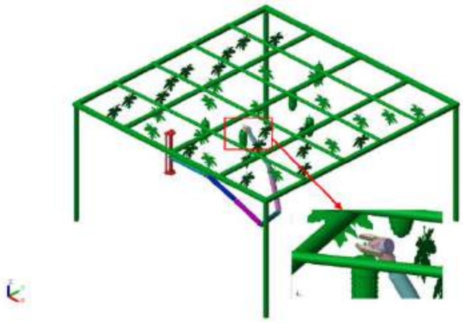

Figure 10. Configuration and orientation of manipulator for given task space location in Bitter gourd environment

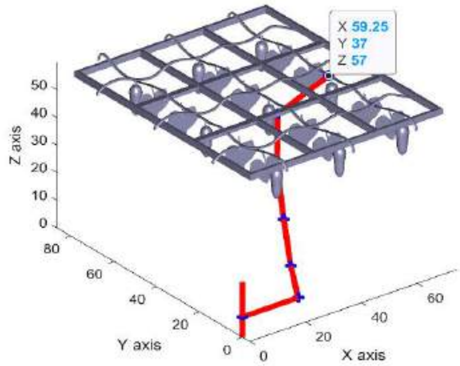

Figure 12. Manipulator configuration at task location of (59.25,37,57)

literature. It is observed that for ten link manipulators optimized function value (error value) is 0.0036 [35]. In present studies, the error values are negligible (10^{-7} to 10^{-8} times) compared to the positional error in literature, which is almost zero and ensures that the end-effector reaches the desired target precisely.

Application 2: Tindora: The virtual environment of Tindora plants is shown in Figure 11. Configuration of robot for reaching the location of (59.25,37,57) is plotted in Figure 12. Error during the IK solution is in order of 10^{-8}, which shows a minimal positional error of the manipulator. For better visibility of orientation, 3D model of robot in the virtual environment using Simscape shown in Figure 13 along with the orientation of end-effector.

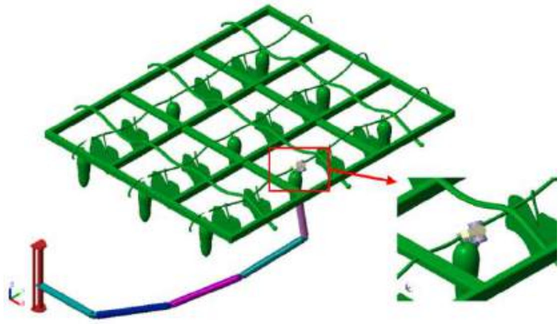

Figure 13. Configuration and orientation of manipulator for given task space location in Bitter gourd environment

Application 3: Guava: A 3D environment of guava plants is modeled and presented in Figure 14. The robot is directed to move from (49,69,62) task-space location to (57, -67, 60) via some intermediate task-space locations. All these configurations are plotted as shown in Figure 15. 3D model of the robot along with orientation is depicted in Figure 16.

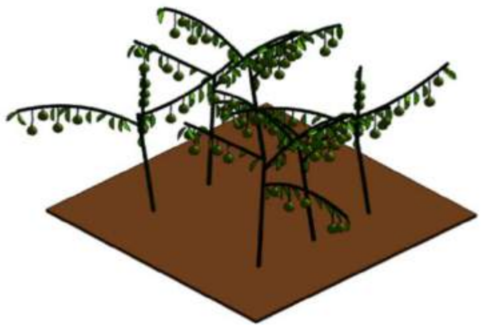

Figure 14. 3D model of Guava environment

5. 2. Joint Trajectory with Simulation Study

Joint variables are calculated for particular task-space locations as discussed in section 4. In this section, a simulation study is performed to identify the position, velocity, and acceleration of joints with respect to time period, during robot motion. To perform the simulation study in a *Simscape* environment, it is required to add step input for each joint by specifying targeted values. The position, velocity, and acceleration of each joint are

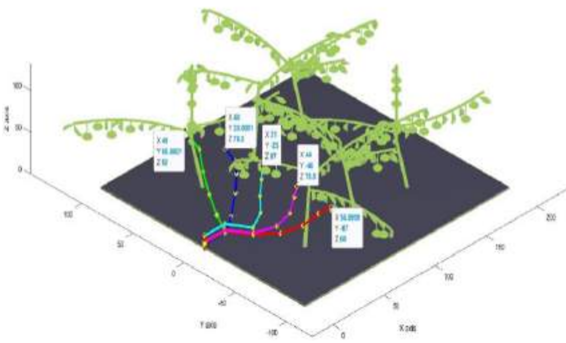

Figure 15. Different configurations of manipulator in Matlab environment

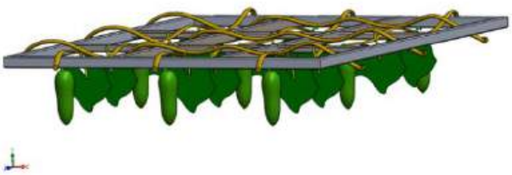

Figure 11. 3D model of Tindora environment in Solidworks

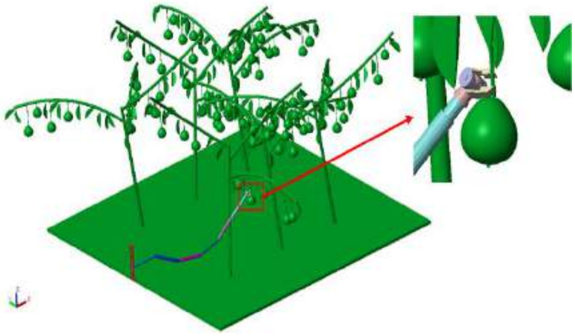

Figure 16. Configuration and orientation of manipulator for given task space location in guava environment

sensed and viewed in the scope box. Also, the location of end-effector is sensed by the *transform sensor*. For understanding of the Simulink model, a block diagram of the last joint is presented in Figure 17.

A simulation study is performed for 0.01 second. During the simulation of the manipulator, each joint variable with respect to time is presented in Figure 18. During simulations, all joints are directed to move from zero position to targeted position. Figure 18(a) shows the change in positions of all 9 joints. From the figure, it is observed that all joints are beginning at zero position, when time proceeds, joint positional values are uniformly increasing to reach the final position. Figure 18(b) shows the variation of velocities. Initially, there is an increase in velocities up to some period of time and then reaches the maximum value. Constant velocity profile was followed after reaching maximum values. Figure 18(c) shows the variations in accelerations. Accelerations of each joint is started at zero and there is a raise in up to some time period, after that there is a smooth decrement to reach zero without jerks during the simulation.

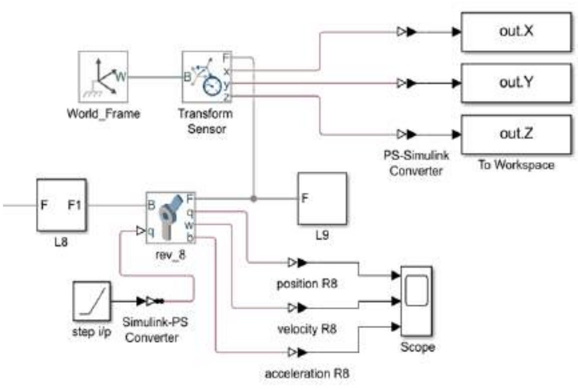

Figure 17. Block diagram for wrist location in Simulink environment

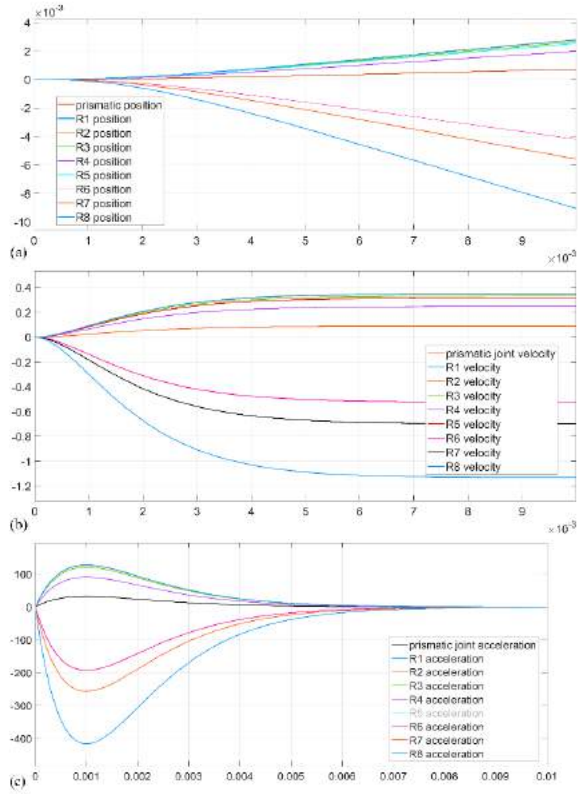

Figure 18. Variation of Joint variables at different time period (a) position (b) velocity (c) acceleration profiles

6. CONCLUSIONS

This article presented the kinematic design of a redundant agricultural harvesting manipulator. This redundant manipulator is intended to be used for different agricultural tasks in the harvesting of crops like Bitter gourd, tindora, and guava. The manipulator has to access the plant from any direction by avoiding collision with obstacles. To access the plant, a configuration of the robot was obtained by inverse kinematics. IK problem was formulated as a nonlinear optimization problem. A classical nonlinear optimization SQP method was used to find the joint variables along with the obstacle avoiding technique. The collision avoidance technique was implemented using a bounding box approach by including a collision detection algorithm. The results demonstrate that the IK solution was accurate. The joint trajectories of the robot while reaching desired task-space location has been depicted using Simscape Multibody. Smooth joint trajectories corresponding to motion were attained during the simulation. The study can be extended to optimal design of manipulator along with an increased number of degrees of freedom at joints and dynamic control of the robot manipulator.

7. REFERENCES

1. Silwal, A., Davidson, J.R., Karkee, M., Mo, C., Zhang, Q. and Lewis, K., "Design, integration, and field evaluation of a robotic apple harvester", ***Journal of Field Robotics***, Vol. 34, No. 6, (2017), 1140-1159, doi: 10.1002/rob.21715
2. Edan, Y., Han, S. and Kondo, N., "Automation in agriculture", Springer handbook of automation, (2009), 1095-1128, doi: 10.1007/978-3-540-78831-7_63
3. Pedersen, S.M., Fountas, S., Have, H. and Blackmore, B., "Agricultural robots—system analysis and economic feasibility", ***Precision Agriculture,*** Vol. 7, No. 4, (2006), 295-308, doi: 10.1007/s11119-006-9014-9
4. Belforte, G., Deboli, R., Gay, P., Piccarolo, P. and Aimonino, D.R., "Robot design and testing for greenhouse applications", ***Biosystems Engineering***, Vol. 95, No. 3, (2006), 309-321, doi: 10.1016/j.biosystemseng.2006.07.004
5. Hayashi, S., Shigematsu, K., Yamamoto, S., Kobayashi, K., Kohno, Y., Kamata, J. and Kurita, M., "Evaluation of a strawberry-harvesting robot in a field test", ***Biosystems Engineering***, Vol. 105, No. 2, (2010), 160-171, doi: 10.1016/j.biosystemseng.2009.09.011
6. Bechar, A. and Vigneault, C., "Agricultural robots for field operations: Concepts and components", ***Biosystems Engineering***, Vol. 149, (2016), 94-111, doi: 10.1016/j.biosystemseng.2016.06.014
7. Kootstra, G., Wang, X., Blok, P.M., Hemming, J. and Van Henten, E., "Selective harvesting robotics: Current research, trends, and future directions", ***Current Robotics Reports***, Vol. 2, No. 1, (2021), 95-104, doi: 10.1007/s43154-020-00034-1
8. Maciejewski, A.A. and Klein, C.A., "Obstacle avoidance for kinematically redundant manipulators in dynamically varying environments", ***The International Journal of Robotics Research***, Vol. 4, No. 3, (1985), 109-117, doi: 10.1177/027836498500400308
9. Korayem, M.H., Ahmadi, R., Jafari, N., Jamali, Y., Kioumarsi, M. And Habibnezhad, A., "Design, modeling, implementation and experimental analysis of 6r robot (technical note)", ***International Journal of Engineering, Transactions A: Basics,*** Vol. 21, No. 1, (2008), 71-84.
10. Craig, J.J., "Introduction to robotics: Mechanics and control, Pearson Educacion, (2005), ISBN-13: 9781292040042
11. Aristidou, A. and Lasenby, J., "Inverse kinematics: A review of existing techniques and introduction of a new fast iterative solver", University of Cambridge Technical Report, (2009) CUED/F-INFENG/TR-632.
12. Goldenberg, A.A. and Lawrence, D.L., "A generalized solution to the inverse kinematics of robotic manipulators", ***Journal of Dynamic Systems, Measurement, and Control***, Vol. 107, No. 1, (1985), 103-106, doi: 10.1115/1.3140699
13. Kumar, S., Sukavanam, N. and Balasubramanian, R., "An optimization approach to solve the inverse kinematics of redundant manipulator", ***International Journal of Information and System Sciences (Institute for Scientific Computing and Information)***, Vol. 6, No. 4, (2010), 414-423.
14. Bagheri, A., Narimanzadeh, N., Siavash, A.S. And Khoobkar, A.R., "Gmdh type neural networks and their application to the identification of the inverse kinematics equations of robotic manipulators (research note)", ***International Journal of Engineering***, Vol. 18, No. 2, (2005), 135-143.
15. Whitney, D.E., "Resolved motion rate control of manipulators and human prostheses", ***IEEE Transactions on man-machine systems***, Vol. 10, No. 2, (1969), 47-53, doi: 10.1109/TMMS.1969.299896
16. Chembuly, V.S. and Voruganti, H.K., "An optimization based inverse kinematics of redundant robots avoiding obstacles and singularities", in Proceedings of the Advances in Robotics. (2017), 1-6, doi: 10.1145/3132446.3134888
17. Zhao, Y., Gong, L., Huang, Y. and Liu, C., "A review of key techniques of vision-based control for harvesting robot", ***Computers and Electronics in Agriculture***, Vol. 127, (2016), 311-323, doi: 10.1016/j.compag.2016.06.022
18. Hartley, R.I. and Sturm, P., "Triangulation", ***Computer Vision and Image Understanding***, Vol. 68, No. 2, (1997), 146-157, doi: 10.1006/cviu.1997.0547
19. Van Henten, E., Schenk, E., Van Willigenburg, L., Meuleman, J. and Barreiro, P., "Collision-free inverse kinematics of the redundant seven-link manipulator used in a cucumber picking robot", ***Biosystems Engineering***, Vol. 106, No. 2, (2010), 112-124, doi: 10.1016/j.biosystemseng.2010.01.007
20. Buemi, F., Massa, M., Sandini, G. and Costi, G., "The agrobot project", ***Advances in Space Research***, Vol. 18, No. 1-2, (1996), 185-189, doi: 10.1016/0273-1177(95)00807-Q
21. Khatib, O., Real-time obstacle avoidance for manipulators and mobile robots, in Autonomous robot vehicles. 1986, Springer.396-404, doi: 10.1007/978-1-4613-8997-2_29
22. Korayem, M., Nazemizadeh, M. and Azimirad, V., "Optimal trajectory planning of wheeled mobile manipulators in cluttered environments using potential functions", ***Scientia Iranica***, Vol. 18, No. 5, (2011), 1138-1147, doi: 10.1016/j.scient.2011.08.026
23. Korayem, M., Nazemizadeh, M. and Rahimi, H., "Trajectory optimization of nonholonomic mobile manipulators departing to a moving target amidst moving obstacles", ***Acta Mechanica***, Vol. 224, No. 5, (2013), 995-1008, doi: 10.1007/s00707-012-0799-5
24. Korayem, M.H., Nazemizadeh, M. and Nohooji, H.R., "Optimal point-to-point motion planning of non-holonomic mobile robots in the presence of multiple obstacles", ***Journal of the Brazilian Society of Mechanical Sciences and Engineering***, Vol. 36, No. 1, (2014), 221-232, doi: 10.1007/s40430-013-0063-5
25. Tang, Z., Xu, L., Wang, Y., Kang, Z. and Xie, H., "Collision-free motion planning of a six-link manipulator used in a citrus picking robot", ***Applied Sciences***, Vol. 11, No. 23, (2021), 11336, doi: 10.3390/app112311336
26. Koren, Y. and Borenstein, J., "Potential field methods and their inherent limitations for mobile robot navigation", in ICRA. Vol. 2, (1991), 1398-1404, doi: 10.1109/ROBOT.1991.131810
27. Gottschalk, S., Lin, M.C. and Manocha, D., "Obbtree: A hierarchical structure for rapid interference detection", in Proceedings of the 23rd annual conference on Computer graphics and interactive techniques. (1996), 171-180, doi: 10.1145/237170.237244
28. Barequet, G. and Har-Peled, S., "Efficiently approximating the minimum-volume bounding box of a point set in three dimensions", ***Journal of Algorithms***, Vol. 38, No. 1, (2001), 91-109, doi: 10.1006/jagm.2000.1127
29. Held, M., Klosowski, J.T. and Mitchell, J.S., "Evaluation of collision detection methods for virtual reality fly-throughs", in Canadian Conference on Computational Geometry, Citeseer. (1995), 205-210.
30. Chembuly, V. and Voruganti, H.K., "An efficient approach for inverse kinematics and redundancy resolution of spatial redundant robots for cluttered environment", ***SN Applied Sciences***, Vol. 2, No. 6, (2020), 1-20, doi: 10.1007/s42452-020-2825-x
31. Bac, C.W., Van Henten, E.J., Hemming, J. and Edan, Y., "Harvesting robots for high-value crops: State-of-the-art review and challenges ahead", ***Journal of Field Robotics***, Vol. 31, No. 6, (2014), 888-911, doi: 10.1002/rob.21525
32. Tinoco, V., Silva, M.F., Santos, F.N., Rocha, L.F., Magalhães, S. and Santos, L.C., "A review of pruning and harvesting

manipulators", in 2021 IEEE International Conference on Autonomous Robot Systems and Competitions (ICARSC), IEEE. (2021), 155-160, doi: 10.1109/ICARSC52212.2021.9429806

33. Wu, Y., Tang, F. and Li, H., "Image-based camera localization: An overview", ***Visual Computing for Industry, Biomedicine, and Art,*** Vol. 1, No. 1, (2018), 1-13, doi: 10.1186/s42492-018-0008-z

34. Tabandeh, S., Melek, W.W. and Clark, C.M., "An adaptive niching genetic algorithm approach for generating multiple solutions of serial manipulator inverse kinematics with applications to modular robots", ***Robotica***, Vol. 28, No. 4, (2010), 493-507, doi: 10.1017/S0263574709005803

35. Singla, E., Tripathi, S., Rakesh, V. and Dasgupta, B., "Dimensional synthesis of kinematically redundant serial manipulators for cluttered environments", ***Robotics and Autonomous Systems***, Vol. 58, No. 5, (2010), 585-595, doi: 10.1016/j.robot.2009.12.005

Persian Abstract

چکیده

این مقاله یک تکنیک مبتنی بر بهینه‌سازی را برای حل سینماتیک معکوس (IK)دستکاری‌کننده‌های اضافی فضایی در محیط‌های کشاورزی (فضاهای کاری) ارائه می‌کند. یک پیکربندی سینماتیکی با ۹ درجه آزادی (DOF)با هشت چرخش و یک مفصل منشوری برای بهبود دسترسی در فضاهای کاری پیچیده مدل‌سازی شده است. دستکاری کننده پیشنهادی برای برداشت میوه ها و سبزیجات شبیه سازی شده است. برای انجام کار مورد نظر در محیط کاری نیاز است که راه حل IK ربات مشخص شود. مسئله IK به عنوان یک مسئله بهینه سازی محدود با هدف به حداقل رساندن خطاهای موقعیتی و جهت گیری با اجتناب از موانع فرموله شده است. یک محیط CAD سه بعدی با گیاهان مختلف میوه و سبزیجات در Solidworks مدل سازی شده است. یک مکان هدف در این محیط برای چیدن میوه/سبزیجات انتخاب شده است. تنه، شاخه ها و برگ ها به عنوان انسداد در نظر گرفته می شوند. تکنیک اجتناب از برخورد با استفاده از رویکرد جعبه مرزی با گنجاندن یک الگوریتم تشخیص برخورد اجرا شد. شبیه‌سازی‌های IK از دستکاری‌کننده اضافی فضایی در یک محیط بهم ریخته انجام شد و نتایج گزارش شد. مسیرهای مشترک ربات در حین رسیدن به مکان فضای کاری مورد نظر با استفاده از Simscape Multibody به تصویر کشیده شده است. نتایج نشان می‌دهد که عامل پایانی ربات با یک راه‌حل دقیق IK با موفقیت به محل کار مورد نظر رسیده است. این رویکرد در طیف گسترده ای از محیط های کاری بر اساس نتایج شبیه سازی راه حل IK ربات ها سازگار است.

IJE TRANSACTIONS A: Basics Vol. 35, No. 07, (July 2022) 1355-1364

International Journal of Engineering

Journal Homepage: www.ije.ir

Surface Roughness in Abrasive Mixed Rotary Electrical Discharge Machining: Experimental Approach

A. Lamba*[a], V. Vipin[b]

[a] Department of Mechanical and Automation Engineering, G. B. Pant Okhla-I Campus, DSEU, Delhi, India
[b] Department of Mechanical Engineering, Delhi Technological University, Delhi, India

PAPER INFO

Paper history:
Received 22 January 2022
Received in revised form 19 March 2022
Accepted 30 March 2022

Keywords:
Electrical Discharge Machining
D3 Steel
Full Factorial Experimentation
Surface Roughness
Analysis of Variance

ABSTRACT

This research study focused on the alliance of blending silicon carbide powder of size 60 μm into dielectric oil (kerosene) with electrode revolution in electrical discharge machining of D3 steel using electrode made of copper. Peak current, pulse on-time, and electrode revolution were picked as machining variables to check their influence on the surface roughness of the workpiece. The full factorial experimentation was performed with 27 experimental runs. The analysis of variance result indicated electrode revolution as the most influential variable with a percentage aid of 32.75%, followed by peak current and pulse on-time, which accounted for 28.98 and 6.09%, respectively. The decrement in surface roughness was recorded at higher electrode rotational speed. The field emission scanning electron microscopy of machined samples was performed and results showed significant improvement on surface characteristics. The surface finish improved from 12.36 μm to 10.32 μm in silicon carbide powder blended rotational electrical discharge machining over traditional electrical discharge machining. The minimum surface roughness achieved was 4.81 μm at optimal conditions.

doi: *10.5829/ije.2022.35.07a.14*

NOMENCLATURE

EDM	Electrical discharge machining	SR	Surface roughness
Pc	Peak current (A)	SiC	Silicon carbide
Pot	Pulse on-time (μs)	ANOVA	Analysis of variance
Erpm	Electrode revolution (rpm)	FESEM	Field emission scanning electron microscopy

1. INTRODUCTION

The ever increasing demand for highly accurate cutting methods has led to the origination of electrical discharge machining (EDM). The material removal in EDM happens with electrical sparks enabling the ejection of tiny debris particles from the workpiece surrounded by EDM fluid. As the sparks generate beneath the electrode's surface, the impression generated on the workpiece's surface replicates the shape of the electrode. The temperature generated by the sparks is of the order of 8000-20000 °C which evaporates the material [1]. The debris thus generated are removed with the help of circulating oil. This cutting style has completely revolutionized the traditional approach with its extraordinary features like contact-less machining, the ability to cut intricate shapes of material of high hardness including composites with a softer tool material. This method has found a concrete place in almost all machining industries throughout the world. Apart from its many advantages, the process also suffers from disadvantages. The disadvantages include limited material removal capability, difficulty in producing sharp corners in complex shapes, rough surfaces, etc. [2]. In the quest for improvements over these limitations, the researchers initially focused on optimal combinations of input process parameters, and thereafter, as time passed, the focus was shifted to the development of different

*Corresponding author emial: *ajay.lamba@dseu.ac.in* (A. Lamba)

Please cite this article as: A. Lamba, V. Vipin, Surface Roughness in Abrasive Mixed Rotary Electrical Discharge Machining: Experimental Approach, ***International Journal of Engineering, Transactions A: Basics***, Vol. 35, No. 07, (2022) 1355-1364

EDM variants. In the past two decades, researchers [3-10] all over the world tailored various successful attempts by their profound search in the domain of electrical discharge machining. These successful attempts by researchers led to the development of different variants resulting in near dry EDM, powder blended EDM, EDM with electrode revolution, vibration-assisted EDM, ultrasonic vibration-assisted EDM, ultrasonic vibration-assisted EDM with a cryogenically cooled electrode, magnetic field-assisted EDM, rotating magnetic field and ultrasonic-assisted EDM, etc. Out of the various research fields, two areas namely, EDM with electrode revolution and powder blended EDM were focused for deeper analysis.

2. LITERATURE SURVEY

The literature review is summarized in Table 1. The presented literature [11-13] showed that surface roughness is improved by electrode revolution [4, 14-17]. It can be seen that the blending of suitable powder type into main dielectric media improved the surface roughness during machining with EDM. In light of these observations [4, 11-17], it was seen that the individual studies are available that improved the same output characteristic i.e. surface roughness. Hence, a research gap was identified by clubbing these two approaches intending to improve the surface roughness even more. Hence, a study involving both electrode revolution and powder blending in the same setup was planned to assess the surface roughness for a work-tool combo of D3 steel

TABLE 1. Summary of literature review

Author	EDM type	W/p material	Tool material	Process parameters	Output responses	Methodology	Findings	Ref.
Chattopadhyay et al.	Rotary EDM	EN8 steel	Cu	peak current, pulse on-time, tool rotation	SR, MRR, EWR	TRD	The study revealed peak current and electrode revolution as highly influential factors affecting SR.	[5]
Shih and Shu	Rotary EDM	AISI D2 tool steel	Cu	discharge depth, electrode rotational speed, discharge direction, polarity, pulse duration, flushing direction, dielectric fluid	SR, MRR, EWR	TRD	1. They claimed minimum surface roughness of 2 µm (R_t) with a negative polarity electrode. 2. Pulse duration and peak current were reported to be the most influential parameters.	[11]
Aliakbari and Baseri	Rotary EDM	X210Cr12 tool steel	Cu	pulse on time, peak current, electrode rotation	SR, MRR, EWR, overcut	TRD	1. They achieved a decreasing trend in the value of SR with the increase in electrode rpm. 2. The minimum surface roughness recorded with a solid electrode, one-eccentric hole electrode, and two-eccentric holes electrode were 5.755 µm, 6.209 µm and 6.68 µm, respectively.	[12]
Dwivedi and Choudhury	Rotary EDM	AISI D3 tool steel	Cu	tool rotation, current	SR	–	1. Electrode revolution caused fewer overall micro-cracks and resulted in a better surface. 2. The improvements in surface characteristics were 10% higher in comparison to stationary EDM i.e. without electrode revolution.	[13]
Kansal et al.	Silicon powder blended EDM	EN31 tool steel	Cu	powder concentration, duty cycle, pulse on-time, peak current	SR, MRR	RSM	1. The apparent improvement in surface characteristics was seen with the use of silicon powder in dielectric oil. 2. SR was mainly affected by peak current and concentration of powder. 3. The lowest SR value was reported at high peak current and powder concentration.	[4]

Bhattacharya et al.	Gr and Al powder blended EDM	EN 31, H 11, HCHCr die steel;	Cu, W-Cu	pulse on-time, pulse off-time, current, powder, electrode, dielectric, w/p material	SR, MRR, TWR	TRD	1. Powder along with other factors such as pulse on-time and peak current significantly affected SR. 2. The surface quality with graphite powder blended oil was found better.	[14]
Bhattacharya et al.	Si, Gr, and W powder blended EDM	HCHCr steel, H 11 hot die steel, AISI 1045 steel;	Gr, Br, W-Cu	pulse on-time, current, type of powder, powder concentration	SR, microhardness	TRD	1. The results indicated the improvement in the surface finish of the processed parts. 2. The surface finish was mostly affected by pulse on-time, peak current, and powder concentration.	[15]
Singh et al.	Gr powder blended EDM	Super Co 605;	Gr	pulse on-time, pulse off-time, current, polarity, discharge voltage, flushing pressure	microhardness	TRD	The improvement in the surface finish was noted significantly.	[16]
Kumar et al.	Alumina powder blended EDM	Inconel 825; copper electrode		pulse on-time, current, gap voltage	SR, MRR, RLT	RSM	1. The average surface roughness obtained with powder blended EDM and conventional EDM was 2.8912 µm and 2.4169 µm, respectively. Furthermore, an average improvement of 0.4743 µm surface roughness was obtained by the proposed PMEDM. 2. At the centre values of parameters (peak current 5A, pulse on-time 7 µs, gap voltage 30V), the improvement claimed was 0.758 µm. 3. The improvement was recorded as a result of a larger inter-electrode gap due to the presence of powder particles, which facilitated better debris removal	[17]

Gr –Graphite; Al – Aluminium; HCHCr – High carbon high chromium; Si – Silicon; W – Tungsten; Cu – Copper; W-Cu – Tungsten copper; Br – Brass; RLT – Recast layer thickness; TRD – Taguchi's robust design; RSM– Response surface methodology

and copper. This research work also presents a comparison of surface roughness values obtained with the proposed method to those with conventional EDM for centre values of parameters along with analysis of machined surface through SEM micrographs.

3. MATERIALS AND METHODS

The experiments were performed on a Sparkonix EDM 35A machine. This traditional EDM machine was modified for electrode revolution. For this, a rotary die was fabricated and installed on the EDM head. This rotary die was integrated with the HMC AC servo motor through the chain and sprocket. After this, a separate tank of size (510 mm × 285 mm × 160 mm) was also fabricated to add silicon carbide powder of 60-micron particle size with EDM oil (kerosene). The powder concentration was fixed at 6g/l which yielded the finest surface during trial experiments. A small plastic impeller coupled with a stirrer motor shaft was used for continuously stirring the dielectric oil to ensure proper powder circulation in the tank. The stirrer rotational speed in a tank of 17 liters of oil (auxiliary tank) was measured using a digital tachometer (DT-2234B). The tachometer showed 565 rpm of the shaft. The machining of D3 steel was accomplished using a copper electrode. The size of the workpiece and electrode diameter were (47 mm × 31 mm × 7.5 mm) and 20 mm, respectively. Figure 1 illustrates the actual machining setup along with the fabricated rotary die and copper electrode. A comprehensive schematic diagram of the investigational setup is also presented in Figure 2. The elemental constitution of the work material is listed in Table 2. The randomization of run order was performed before conducting the experiments to distribute randomly the variance due to uncontrollable factors. The full factorial experimentation was done by taking three parameters, namely, peak current (Pc), pulse on-time (Pot), and electrode revolution (Erpm) to observe surface roughness as the output characteristic. The pulse-off time value was 30 µs during experiments. The total sparking time was kept fixed at 2 minutes for experimental runs. Table 3 displays the machining variables and their levels. The trials were done in triplicate before the surface roughness measurements were recorded. These values were also evaluated at three different sites on the workpiece's cavity. The average of these readings was noted as a

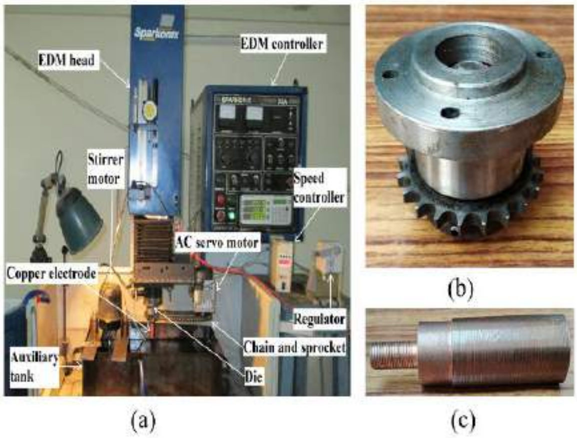

Figure 1. (a) Setup for experimental runs; (b) electrode revolution die; (c) copper electrode

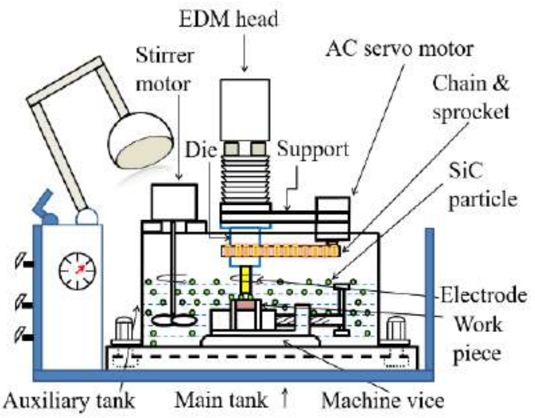

Figure 2. Schematic diagram of the investigational setup

TABLE 2. Elemental constitution of D3 steel

Cr	C	O	Si	Mn	S	P	W	V	Fe
13.40	2.23	2.0	0.41	0.40	0.03	0.05	0.15	0.08	81.25

TABLE 3. Machining variables

Parameter	Unit	Abbreviation	Level		
			1	2	3
Peak current	Ampere (A)	Pc	12	18	24
Pulse on-time	micro-seconds (μs)	Pot	100	400	1000
Electrode revolution	rpm	Erpm	1200	1500	1800

result of each experiment. For measuring SR, Tesa Rugosurf 10G tester was used by fixing a stylus traverse span of 0.8 mm each for 5 cut-offs. The results of surface roughness are presented in Table 4 along with their input factor level settings**.**

4. STATISTICAL MODELING OF THE RESPONSE CHARACTERISTIC

To set up a linkage between machining variables and SR of D3 steel, regression analysis of roughness data was done and consequently, a regression equation of 2nd order was developed. Analysis of variance (ANOVA) was done to discover the important terms and interactions between them along with their percentage contributions in surface roughness of D3 steel. The outcomes of ANOVA of SR after removing insignificant terms and interactions will be presented in the next section. Only terms conforming to a P-value (< 0.05) were considered as per 95% confidence interval [18]. During machining, noise due to uncontrollable factors affects the machining results. As a consequence, variation is likely to occur in data. Therefore, an assessment of the range for the predicted model was done encompassing the deviation due to noise. This deviation range [8] was computed by Equation (1). Therefore, prediction by the statistical model can be given by $Y \pm \Delta Y$, where ΔY is given as follows:

$$\Delta Y = t_{\alpha/2,DF} \times \sqrt{V_e} \tag{1}$$

where Y represents response characteristic, t represents the value of t-distribution corresponding to the specified significance level ($\alpha/2 = 0.05$, at 95% confidence interval) and degree of freedom of residual error (DF). V_e represents the residual error of the adjusted mean square. The surface roughness prediction model and the range equation for D3 steel are represented by Equations (2) and (3), respectively.

$$\begin{aligned} \mathrm{SR} &= 12.976 + (0.2112 \times \mathrm{Pc}) + (0.00489 \times \\ &\mathrm{Pot}) - (0.006702 \times \mathrm{Erpm}) - (0.000011 \times \mathrm{Pot} \times \\ &\mathrm{Pot}) + (0.000004 \times \mathrm{Pot} \times \mathrm{Erpm}) \end{aligned} \tag{2}$$

$$\mathrm{SR}_{\mathrm{range}} = \mathrm{SR} \pm 0.92 \text{ microns} \tag{3}$$

Table 4 summarized 27 experimental runs with machining variables and outcome characteristics.

5. STATISTICAL MODEL VALIDATION

The validation of the statistical model was done by calculating the prediction value supplemented by range with the help of Equations (2) and (3) and thereafter, validating the values thus obtained with experimental results. The results of predicted and experimental findings for arbitrarily chosen run orders 20, 16, 11, and 25 are presented in Table 5. Furthermore, all other values were also checked and found well within the range. Figure 3 shows the surface roughness versus run order plot for experiment and predicted values. The fitness of the regression predictor can also be ascertained from the distribution of residuals. Figure 4(a-d) depicts the surface roughness residual distribution diagrams illustrating normal probability chart, residual versus fitted value, vertical bar chart, and residual versus observation chart. From Figure 4(a, c), it is evident that all the residuals adhere to a straight line indicating normal distribution. The regression model is thus validated.

TABLE 4. Experimental runs

Run order	Machining variables			Output characteristics			
	Pc (A)	Pot (μs)	Erpm (rpm)	SR			Mean SR (μm)
				1	2	3	
1	12	1000	1500	5.73	6.41	5.59	5.91
2	18	100	1200	10.21	9.6	9.44	9.75
3	18	100	1500	8.86	7.35	7.82	8.01
4	12	100	1500	7.21	7.23	6.83	7.09
5	24	400	1800	9.64	9.89	9.93	9.82
6	12	400	1800	6.13	6.89	6.9	6.64
7	18	100	1800	5.6	6.2	5.42	5.74
8	18	400	1200	10.7	10.31	11.6	10.87
9	18	1000	1800	5.52	5.36	6.07	5.65
10	24	1000	1500	7.71	8.76	8.49	8.32
11	18	400	1500	9.87	11	10.09	10.32
12	24	100	1500	9.3	8.54	8.53	8.79
13	12	1000	1200	6.9	6.97	6.71	6.86
14	12	1000	1800	4.88	5.39	5.36	5.21
15	18	400	1800	7.63	8.71	7.51	7.95
16	12	100	1800	4.83	4.84	4.76	4.81
17	18	1000	1200	7.59	8.26	8.09	7.98
18	24	1000	1200	9.24	8.37	7.86	8.49
19	24	100	1800	6.19	6.7	6.43	6.44
20	12	100	1200	7.6	7.54	8.41	7.85
21	24	400	1500	11.46	10.86	11.04	11.12
22	24	400	1200	12.81	11.79	11.37	11.99
23	24	100	1200	11.36	11.74	11.13	11.41
24	12	400	1500	7.71	7.53	8.43	7.89
25	24	1000	1800	8.7	8.18	7.09	7.99
26	18	1000	1500	6.7	6.84	7.76	7.1
27	12	400	1200	9.11	9.42	9.37	9.3

TABLE 5. Statistical model validation

Run order	Machining variables			SR (microns)	
	Pc (A)	Pot (μs)	Erpm (rpm)	Predicted	Experiment
20	12	100	1200	8.38 ± 0.92	7.85
16	12	100	1800	4.54 ± 0.92	4.81
11	18	400	1500	9.54 ± 0.92	10.32
25	24	1000	1800	7.64 ± 0.92	7.99

6. RESULTS AND DISCUSSION

The effects of peak current (Pc), pulse on-time (Pot), and electrode revolution (Erpm) on SR of D3 steel along with their percentage share are portrayed in Figure 5. This was drawn by taking the mean value of SR at each level of Pc,

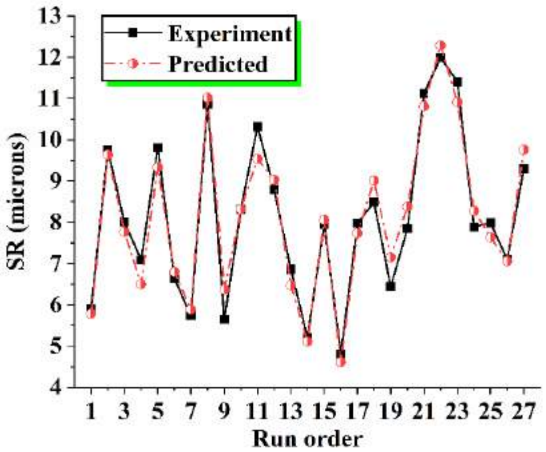

Figure 3. A comparative plot of surface roughness of experiment and predicted values

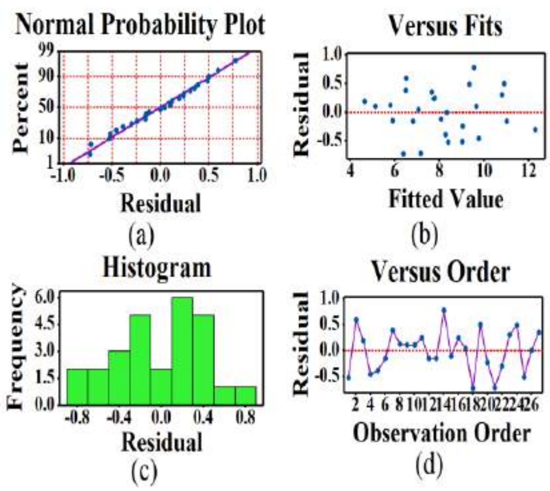

Figure 4. Residual plots of surface roughness (a) normal probability chart; (b) residual versus fitted value; (c) vertical bar chart; (d) residual versus observation order

Pot, and Erpm. Hence, three different mean values are shown for each variable. These mean response values are depicted in Table 6. Furthermore, Figure 6(a-c) depicts the plots of surface roughness versus electrode revolution at different peak currents of 12 A, 18A, and 24 A. From ANOVA outcomes in Table 7, it was found that the highest contribution was made by Erpm followed by Pc and Pot with 32.75, 28.98 and 6.09%, respectively.

6. 1. Effect of Peak Current Figure 5(a) illustrates the upshot of peak current on SR. It is observed that the rise in peak current results in an increase in SR. The reason may be assigned to the supply of higher energy at a high peak current which leads to deeper craters on the workpiece [19, 20]. These deep craters make the surface rougher, and hence, higher SR was observed [21].

6. 2. Effect of Pulse On-Time The effect of pulse on-time (Pot) on SR may be witnessed from Figure 5(a). The increase of Pot from 100 µs to 400 µs has been found to increase SR whereas, SR decreased with a further increase in Pot from 400 µs to 1000 µs. The reason may be credited to the widening of the plasma channel at a high Pot. This decreases the spark intensity, ultimately, leading to less energy impact on the work piece, and hence, less crater size [9, 22]. This smoothed the surface for large pulse on-time values such as 1000 µs.

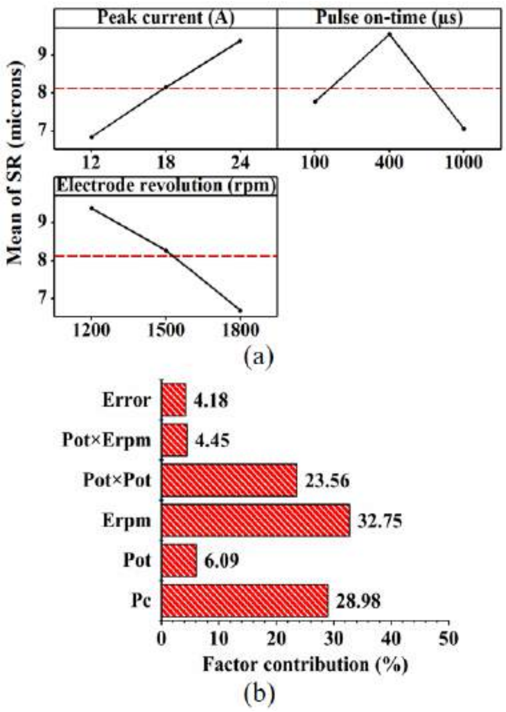

Figure 5. (a) Main effect plot and (b) percentage aid of machining variables on SR

TABLE 6. Response table of means

Level	Pc (A)	Pot (µs)	Erpm (rpm)
1	6.84	7.766	9.389
2	8.152	9.544	8.283
3	9.374	7.057	6.694
Delta	2.534	2.488	2.694
Rank	2	3	1

6. 3. Effect of Electrode Revolution It may be elucidated from Figure 5(a) and Figure 6(a-c) that the rise in electrode revolution resulted in improvement of rendered surface quality. The rationale of this achievement may be contributed to the efficient cleaning

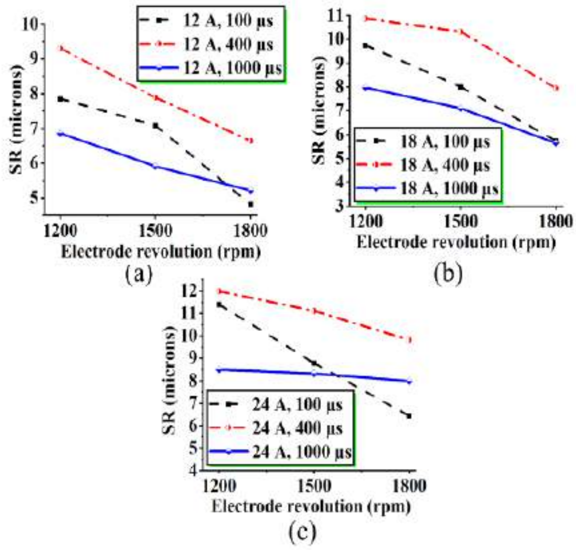

Figure 6. Effect of electrode revolution on surface roughness at peak current (a) 12 A; (b) 18 A; (c) 24 A

TABLE 7. Analysis of variance table for SR

Source	DF	Seq. SS	Share	Adj. SS	Adj. MS	F-Value	P-Value
Regression	5	95.57	95.82%	95.57	19.11	96.29	0.000
Pc	1	28.90	28.98%	28.90	28.90	145.61	0.000
Pot	1	6.07	6.09%	1.39	1.39	7.04	0.015
Erpm	1	32.67	32.75%	26.11	26.11	131.57	0.000
Pot × Pot	1	23.49	23.56%	23.49	23.49	118.36	0.000
Pot × Erpm	1	4.43	4.45%	4.43	4.43	22.34	0.000
Error	21	4.16	4.18%	4.16	0.19		
Total	26	99.74	100.00%				

DF: degree of freedom; Seq. SS: sequential sum of squares; Adj. SS: adjusted sum of squares; Adj. MS: adjusted mean square; F: Fisher's value.

of debris from the machining area. With the increase in electrode revolution, centrifugal force increases, and as the fluid also has abrasive silicon carbide powder, better abrasion, as well as fast cleaning, have benefited the surface, and hence, less surface roughness was obtained [13].

7. INTERACTION EFFECT

Analysis of variance has shown the interaction between pulse on-time and electrode revolution to be inevitable due to a lower P-value than 0.05. Figure 7 depicts the interaction and surface plot of pulse on-time and electrode revolution. The surface roughness of D3 steel was found to increase from 100 to 400 µs and then, decreased from 400 to 1000 µs for all values of electrode revolution. The lower electrode revolution has resulted in a rough surface than the higher rotational values. The minimum surface roughness was recorded at the lowest setting of pulse on-time (100 µs) and the highest setting of electrode revolution (1800 rpm), respectively. The rationale for this particular combination is once again reiterated to the better circulation of dielectric oil facilitated by higher centrifugal force at 1800 rpm of electrode revolution along with abrasive effects of the powder. Simultaneously, the surface finish was augmented by shallow craters due to low-intensity sparks at 100 µs of pulse on-time.

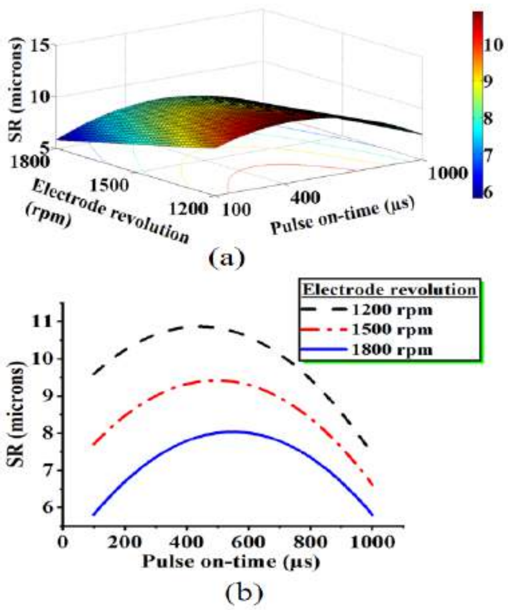

Figure 7. (a) Surface plot; (b) interaction plot of pulse on-time and electrode revolution on SR

8. SURFACE ROUGHNESS PARAMETRIC ANALYSIS

The parametric analysis of surface roughness profiles was executed at Pc-18A, Pot-400 µs and Erpm-1500 rpm with traditional EDM and SiC powder blended rotational EDM. Surface roughness profiles with details of parameters are depicted in Figure 8 for both processes. Three parameters total profile height (Rt), root mean square roughness (Rq), and roughness average (Ra) were measured. The reason for selecting these specific parameters was their capability to explain the entire profile at a glance and acceptance throughout the industries. These parameters in traditional EDM and SiC powder blended rotational EDM were found to be Rt-86.63 µm, Rq-15.85 µm, Ra-12.36 µm, and Rt-70.30 µm, Rq-12.45 µm, Ra-10.32 µm, respectively (refer Figure 8). With these results, the integration of SiC powder blending into EDM oil along with electrode revolution has outperformed the traditional method of EDM machining. The credit of this improvement goes to the efficient dispersal of debris from the inter-electrode gap and formation of shallow craters, facilitated by blending of powder and electrode revolution.

9. SURFACE MORPHOLOGY

Figure 9 shows the result of field emission scanning electron microscopy performed on machined surfaces by traditional EDM and SiC powder blended rotational EDM. The surface images were captured at a magnification of (500×) for both the processes and further, images at a magnification of (2000×) show the in-depth analysis of crater dimensions. The traditional EDM process resulted in a rough surface and had a lot of cracks and craters (refer Figure 9(a)). An addition of powder and electrode revolution have resulted in a fine surface with fewer cracks (refer Figure 9(b)). Furthermore, the in-depth crater dimension analysis revealed good results with silicon carbide powder blended rotational EDM. The maximum crater depth measured was 18.6 µm in traditional EDM whereas, it was 8.51 µm in SiC powder blended rotational EDM (refer Figure 9(c, d)). These results are a clear reflection of a better surface in SiC powder blended rotational EDM. The reason for the improved surface may be assigned to the efficacious expelling of debris by electrode rotation [13, 23] and higher gap owing to the existence of powder particles blended with EDM oil, which also facilitates effective flushing of debris[17, 24]. Along with this, the intensity of the sparks decreases because of a higher gap between the work piece and electrode leading to the shallow craters, and hence surface finish increases.

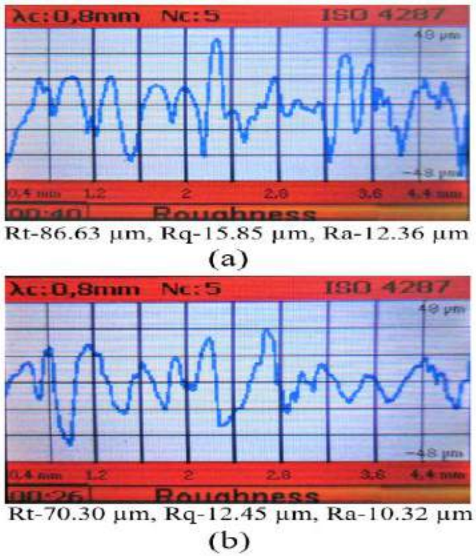

Figure 8. Surface roughness profiles (a) traditional EDM; (b) SiC powder blended rotational EDM. (Pc-18A, Pot-400 µs, Erpm-1500 rpm). (Rt- total profile height, Rq- root mean square roughness, Ra- roughness average)

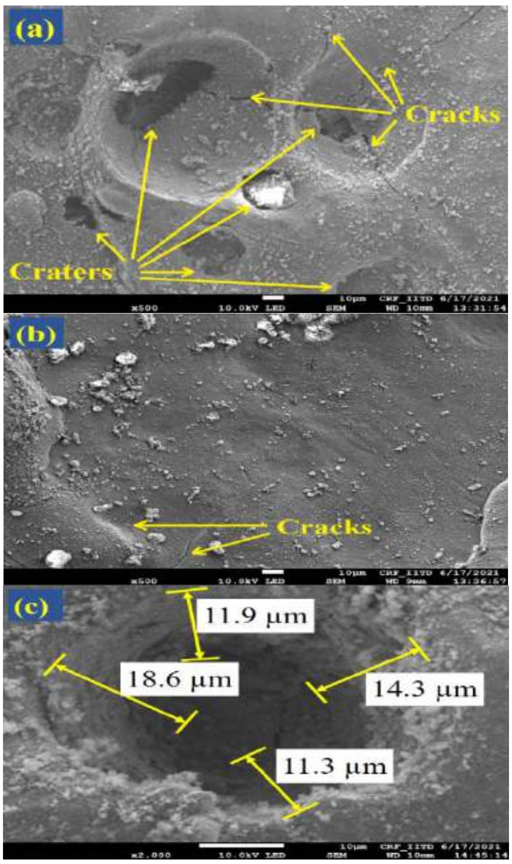

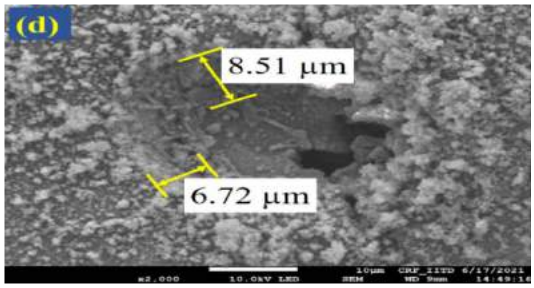

Figure 9. FESEM images of machined samples (a) traditional EDM (500×); (b) SiC powder blended rotational EDM (500×); (c) traditional EDM (2000×) (d) SiC powder blended rotational EDM (2000×). (peak current 18A, pulse on-time 400 µs, electrode revolution 1500 rpm)

10. CONCLUSIONS AND FUTURE SCOPE

The study on surface roughness of D3 steel with the copper electrode in SiC powder blended rotational EDM resulted in the following conclusions:

1. The surface roughness increased with peak current. An increase in SR with pulse on-time was also observed up to 400 µs and a decrease in thereafter.
2. SR reduced with an increase in electrode revolution. An improvement of 28.67% was achieved in the experimented range.
3. The statistical analysis to study the effect of EDM parameters on surface roughness was successfully done.
4. The parametric settings that favoured the highest surface quality were Pc-12A, Pot-100 µs, and Erpm-1800 rpm. At these optimal settings, surface roughness was 4.81 µm.
5. The surface morphology results justified the applicability of SiC powder blended rotational EDM in comparison to the traditional EDM as it led to the creation of fewer cracks and shallow craters on the surface of the work piece. The maximum crater depths were 8.51 µm and 18.6 µm in SiC powder blended rotational EDM and traditional EDM, respectively.
6. The surface roughness profiles recorded with SiC powder blended rotational EDM and traditional EDM have also shown an appreciable decrease in surface roughness (Ra) from 12.36 µm to 10.32 µm.

The future scope of work in the proposed area may be extended with analysis of inter-electrode gap. With exact estimation of gap distance, flushing of debris can be further improved. The spark travel can also be analysed under the influence of electrode rotation as its transverse and inclined travel might affect the discharge crater dimensions.

11. LIMITATIONS

The application of the proposed process is limited to only circular cavity either blind or through-hole as the electrode is under rotation while machining. So, it cannot be used for random cavity/impression generation like for die making.

12. DECLARATION

This research study was conducted without any funding from any agency.

13. REFERENCES

1. Ho, K. H., Newman, S. T. "State of the art electrical discharge machining (EDM)", ***International Journal of Machine Tools and Manufacture***, Vol. 43, No. 13, (2003), 1287-1300. DOI:10.1016/S0890-6955(03)00162-7
2. Qosim, N., Supriadi, S., Puspitasari, P., Kreshanti, P. "Mechanical surface treatments of Ti-6Al-4V Miniplate implant manufactured by electrical discharge machining", ***International Journal of Engineering, Transactions A: Basics***, Vol. 31, No. 7, (2018), 1103-1108. DOI:10.5829/ije.2018.31.07a.14
3. Puthumana, G., Joshi, S. S. "Investigations into performance of dry EDM using slotted electrodes", ***International Journal of Precision Engineering and Manufacturing***, Vol. 12, No. 6, (2011), 957-963. DOI:10.1007/s12541-011-0128-2
4. Kansal, H. K., Singh, S., Kumar, P. "Parametric optimization of powder mixed electrical discharge machining by response surface methodology", ***Journal of Materials Processing Technology***, Vol. 169, No. 3, (2005), 427-436. DOI:10.1016/j.jmatprotec.2005.03.028
5. Chattopadhyay, K. D., Verma, S., Satsangi, P. S., Sharma, P. C. "Development of empirical model for different process parameters during rotary electrical discharge machining of copper-steel (EN-8) system", ***Journal of Materials Processing Technology***, Vol. 209, No. 3, (2009), 1454-1465. DOI:10.1016/j.jmatprotec.2008.03.068
6. Tong, H., Li, Y., Wang, Y. "Experimental research on vibration assisted EDM of micro-structures with non-circular cross-section", ***Journal of Materials Processing Technology***, Vol. 208, No. 1-3, (2008), 289-298. DOI:10.1016/j.jmatprotec.2007.12.126
7. Abdullah, A., Shabgard, M. R. "Effect of ultrasonic vibration of tool on electrical discharge machining of cemented tungsten carbide (WC-Co)", ***International Journal of Advanced Manufacturing Technology***, Vol. 38, No. 11-12, (2008), 1137-1147. DOI:10.1007/s00170-007-1168-8
8. Srivastava, V., Pandey, P. M. "Experimental investigation on electrical discharge machining process with ultrasonic-assisted cryogenically cooled electrode", ***Proceedings of the Institution of Mechanical Engineers, Part B: Journal of Engineering Manufacture***, Vol. 227, No. 2, (2013), 301-314. DOI:10.1177/0954405412469487
9. Beravala, H., Pandey, P. M. "Experimental investigations to evaluate the effect of magnetic field on the performance of air and argon gas assisted EDM processes", ***Journal of Manufacturing Processes***, Vol. 34, (2018), 356-373. DOI:10.1016/j.jmapro.2018.06.026
10. Singh, G., Satsangi, P. S., Prajapati, D. R. "Effect of Rotating Magnetic Field and Ultrasonic Vibration on Micro-EDM Process", ***Arabian Journal for Science and Engineering***, Vol. 45, No. 2, (2020), 1059-1070. DOI:10.1007/s13369-019-04229-3
11. Shih, H. R., Shu, K. M. "A study of electrical discharge grinding using a rotary disk electrode", ***International Journal of Advanced Manufacturing Technology***, Vol. 38, No. 1-2, (2008), 59-67. DOI:10.1007/s00170-007-1068-y
12. Aliakbari, E., Baseri, H. "Optimization of machining parameters in rotary EDM process by using the Taguchi method", ***International Journal of Advanced Manufacturing Technology***, Vol. 62, No. 9-12, (2012), 1041-1053. DOI:10.1007/s00170-011-3862-9
13. Dwivedi, A. P., Choudhury, S. K. "Improvement in the Surface Integrity of AISI D3 Tool Steel Using Rotary Tool Electric Discharge Machining Process", ***Procedia Technology***, Vol. 23, (2016), 280-287. DOI:10.1016/j.protcy.2016.03.028
14. Bhattacharya, A., Batish, A., Singh, G., Singla, V. K. "Optimal parameter settings for rough and finish machining of die steels in powder-mixed EDM", ***International Journal of Advanced Manufacturing Technology***, Vol. 61, No. 5-8, (2012), 537-548. DOI:10.1007/s00170-011-3716-5
15. Bhattacharya, A., Batish, A., Kumar, N. "Surface characterization and material migration during surface modification of die steels with silicon, graphite and tungsten powder in EDM process", ***Journal of Mechanical Science and Technology***, Vol. 27, No. 1, (2013), 133-140. DOI:10.1007/s12206-012-0883-8
16. Singh, A. K., Kumar, S., Singh, V. P. "Effect of the addition of conductive powder in dielectric on the surface properties of superalloy Super Co 605 by EDM process", ***International Journal of Advanced Manufacturing Technology***, Vol. 77, No. 1-4, (2015), 99-106. DOI:10.1007/s00170-014-6433-z
17. Kumar, A., Mandal, A., Dixit, A. R., Das, A. K., Kumar, S., Ranjan, R. "Comparison in the performance of EDM and NPMEDM using Al 2 O 3 nanopowder as an impurity in DI water dielectric", ***International Journal of Advanced Manufacturing Technology***, Vol. 100, No. 5-8, (2019), 1327-1339. DOI:10.1007/s00170-018-3126-z
18. Moghaddam, M. A., Kolahan, F. "Improvement of Surface Finish when EDM AISI 2312 Hot Worked Steel using Taguchi Approach and Genetic Algorithm", ***International Journal of Engineering, Transactions C: Aspects***, Vol. 27, No. 3(C), (2014), 417-424. DOI:10.5829/idosi.ije.2014.27.03c.09
19. Prakash, K. S., Gopal, P. M., Rahul, R. N. "Effect of material and machining features in electric discharge machining of 6061Al/rock dust composites", ***Indian Journal of Engineering and Materials Sciences***, Vol. 27, No. 2, (2020), 471-480
20. Singh, S., Maheshwari, S., Pandey, P. C. "Some investigations into the electric discharge machining of hardened tool steel using different electrode materials", ***Journal of Materials Processing Technology***, Vol. 149, No. 1-3, (2004), 272-277. DOI:10.1016/j.jmatprotec.2003.11.046
21. Phan, N. H., Donga, P. V., Muthuramalingamb, T., Thiena, N. V., Dunga, H. T., Hunga, T. Q., Duca, N. V., Lya, N. T. "Experimental investigation of uncoated electrode and PVD AlCrNi coating on surface roughness in electrical discharge machining of Ti-6Al-4V", ***International Journal of Engineering, Transactions A: Basics***, Vol. 34, No. 4, (2021), 928-934. DOI:10.5829/ije.2021.34.04a.19
22. Beravala, H., Pandey, P. M. "Experimental investigations to evaluate the surface integrity in the magnetic field and air/gas-assisted EDM", ***Journal of the Brazilian Society of Mechanical Sciences and Engineering***, Vol. 43, No. 4, (2021), 213. DOI:10.1007/s40430-021-02929-2
23. Bajaj, R., Dixit, A. R., Tiwari, A. K., Chauhan, N. K. "Machining performance enhancement of en-31 diesteel using mwcnt mixed rotary edm", ***Indian Journal of Engineering and Materials Sciences***, Vol. 27, No. 2, (2020), 309-319.

24. Joshi, A. Y., Joshi, A. Y. "A systematic review on powder mixed electrical discharge machining", ***Heliyon***, Vol. 5, No. 12, (2019), e02963. DOI:10.1016/j.heliyon.2019.e02963

Persian Abstract

چکیده

این مطالعه تحقیقاتی بر روی اتحاد پودر کاربید سیلیکون به اندازه ٦٠ میکرومتر به روغن دی الکتریک (نفت سفید) با چرخش الکترود در ماشینکاری تخلیه الکتریکی فولاد D3 با استفاده از الکترود ساخته شده از مس متمرکز گردید. جریان پیک، زمان پالس و چرخش الکترود به عنوان متغیرهای ماشینکاری برای بررسی تأثیر آنها بر زبری سطح قطعه کار انتخاب شدند. آزمایش فاکتوریل کامل با ٢٧ اجرای آزمایشی انجام شد. نتایج تحلیل واریانس نشان داد که چرخش الکترود به‌عنوان تأثیرگذارترین متغیر با درصد کمک ٣٢/٧٥ درصد، پس از پیک جریان و پالس به‌موقع به‌ترتیب ٢٨/٩٨ و ٦/٠٩ درصد است. کاهش زبری سطح در سرعت چرخش الکترود بالاتر ثبت گردید. میکروسکوپ الکترونی روبشی گسیل میدانی نمونه های ماشین کاری شده انجام شد و نتایج بهبود قابل توجهی را در ویژگی های سطح نشان داد. پرداخت سطح از ١٢/٣٦ میکرومتر به ١٠/٣٢ میکرومتر در ماشینکاری تخلیه الکتریکی چرخشی مخلوط پودر کاربید سیلیکون نسبت به ماشینکاری تخلیه الکتریکی سنتی بهبود یافته است. حداقل زبری سطح به دست آمده ٤/٨١ میکرومتر در شرایط بهینه بود.

IJE TRANSACTIONS A: Basics Vol. 35, No. 07, (July 2022) 1365-1374

International Journal of Engineering

Journal Homepage: www.ije.ir

Effect of Steel Fiber Volume Fraction on the Mechanical Behavior of Ultra-high Performance Concrete Composites

G. Gautham Kishore Reddy*, P. Ramadoss

Department of Civil Engineering, Pondicherry Engineering College, Puducherry, India

PAPER INFO

Paper history:
Received 06 March 2022
Received in revised form 19 April 2022
Accepted 22 April 2022

Keywords:
Alccofine
Crimped Steel Fiber
Ultra-high Performance Concrete Composites
Ultra-high Performance Fiber Reinforced Concrete
Stress-Strain Behavior
Empirical Expression

ABSTRACT

In order to investigate the effect of fiber volume fraction on the mechanical behavior of ultra-high performance concrete composites (UHPCC), five different volume fractions of macro steel fibers (V_f = 0.5, 1, 1.5, 2 and 2.5%) are used within identical mortar matrix. Ultra-high performance fiber reinforced concrete (UHPFRC) mix was designed to achieve a compressive strength of 155 MPa based on the particle packing method. For 12 series of UHPCC mixes, compressive strength, splitting tensile strength, flexural strength, and modulus of elasticity at 28 days are determined. Test results showed a significant improvement in splitting tensile and flexural strengths of UHPFRC with the addition of steel fibers. The maximum values of compressive, splitting tensile and flexural strengths were 155.39, 17.76, and 32.50 MPa, respectively. Stress-strain behavior of fiber-reinforced concrete composites is studied and elastic modulus values evaluated are in the range of 39.52-47.99 GPa. Empirical expressions are developed based on the test results in terms of fiber volume fraction to predict the 28-day strengths of UHPFRC. Comparing the experimental values of earlier researchers to the ones predicted by empirical equations, the average absolute error (AAE) value obtained is within 5%. The proposed model's predictions are in good agreement with the experimental values. Relationship between compressive and flexure strengths of UHPFRC isdeveloped with R^2=0.99 and validated.

doi: *10.5829/ije.2022.35.07a.15*

NOMENCLATURE

UHPCC	Ultra-high performance concrete composites	f_c	Compressive strength of UHPCC
UHPFRC	Ultra-high performance fiber reinforced concrete	f_{cf}	Compressive strength of UHPFRC
QP	Quartz powder	f_{sp}	splitting tensile strength of UHPCC
GGBS	Ground grannulated blast furnace slag	f_{spf}	splitting tensile strength of UHPFRC
kN	Kilo Newton	f_r	flexural strength of UHPCC
MPa	Megapascal	f_{rf}	flexural strength of UHPFRC
GPa	Gigapascal	E_c	modulus of elasticity of UHPCC
V_f	Fiber volume-fraction	E_{cf}	modulus of elasticity of UHPFRC

1. INTRODUCTION

Ultra-high performance concrete (UHPC) is a brittle material. In order to overcome this property micro/macro steel fibers are incorporated in to the concrete matrix [1-3]. Since many years researchers have been studying and trying to improve the tensile properties of UHPFRC in terms of flexural strength and bending capacity [4-5]. Steel fibers in the concrete matrix improve the mechanical properties, ductility, toughness and impact strength [6-8]. Mostly, fiber parameters like quantity, shape, and orientation determine the tensile performance of UHPFRC [9-11]. UHPFRC is commonly developed using steel fibers having a diameter of 0.20 mm and a length of 13 mm [12-14]. A steel fiber volume fraction of 2 % is often used to develop an economical and workable UHPFRC [15-16].

The effect of steel fiber-volume fraction (V_f = 1, 2, 3 and 4%) in UHPFRC was studied by Yoo et al. [17] and found that the best results were observed in the concrete

*Corresponding Author Institutional Email: gauthamkishorereddy@pec.edu (G. Gautham Kishore Reddy)

Please cite this article as: G. Gautham Kishore Reddy, P. Ramadoss, Effect of Steel Fiber Volume Fraction on the Mechanical Behavior of Ultra-high Performance Concrete Composites, ***International Journal of Engineering, Transactions A: Basics***, Vol. 35, No. 07, (2022) 1365-1374

mixture with V_f = 3% in terms of interfacial bond strength, mechanical and shrinkage behaviors. Three different steel fiber lengths (8, 12 and 16mm) and volume fractions (V_f = 1, 3 and 6%) were used by Abbas et al. [18] for his investigations on UHPFRC mixtures. The results showed an improvement in the mechanical properties of the UHPFRC mixtures with increment in steel fiber volume fraction. It was also observed that UHPFRC mixtures having short steel fibers had better flexural performance when compared with concrete mixtures having a similar volume of long steel fibers. Yu et al. [19] found that the inclusion of steel fibers controlled flexural toughness when the mechanical properties and flexural toughness were investigated for the UHPFRC which was developed with a low binder content. A 5% enhancement in compressive strength was observed by Tsioulou et al. [20] in a UHPFRC mixture containing a 3% steel fiber-volume fraction when compared to plain UHPC as he investigated the addition of different steel fiber volume fractions (V_f = 0, 1, and 3%) in UHPFRC.

To achieve the needed strengths and material properties, variable steel fiber volume fractions, widely ranging from (V_f = 0-6%) were used in different studies to develop UHPFRC. The most convincing technique to improve the tensile performance of UHPCC is by increasing the steel fiber volume fraction [21-23]. Moreover, the literature showslimited use of macro steel fibers when compared to micro and short steel fibers in the development of UHPFRC [29-31]. In this context, the present study gains prominence as macro and long steel fibers are used to develop UHPFRC and therefore to study their effect on mechanical properties and elastic modulus.

2. EXPERIMENTAL PROGRAM

2. 1. Materials and Mix Proportions

The mix proportion of UHPFRC with w/c ratio of 0.25, used in this study is presented in Table 1. The chemical compositions of Ordinary Portland cement (OPC) of 53-Grade, Alccofine 1203, Quartz powder, and Ground granulated blast furnace slag (GGBS) are listed in Table 2 and these were used as cementitious materials. Locally available river sand confirming to IS 383 (1970) was used as fine aggregate.. For adequate workability of UHPFRC, poly carboxylate ether (PCE) based super plasticizer (SP) was added. For investigating the effect of fiber volume fraction on mechanical properties of UHPFRC, the crimped macro steel fibers with an aspect ratio of 70 and having dimensions of 35 mm length and a diameter of 0.5 mm were used with UHPCC at V_f = 0.5, 1, 1.5, 2 and 2.5%. In this study, two mixes of UHPFRC were developed with varying fiber volume fraction. Mix designations from UHPCC-AQ to UHPFRC-AQ 2.5, UHPFRC is designed with alccofine and quartz powder and mix designations from UHPCC-AG to UHPFRC-AG 2.5, UHPFRC is designed with alccofine and GGBS [24-25]. The number denotes fiber volume fraction in percentage. All the cast specimens were cured at room temperature and tested at 28 days.

2. 2. Test setup and Procedure

2. 2. 1. Compression Test Compressive strength tests were conducted on 100 x 100 x 100 mm^3 cube specimens according to IS 516-2004. The tests were carried out on a servo-controlled compression testing machine (CTM) having a maximum load capacity of 2000 kN, and the load was applied at a rate of 14 MPa/min. To calculate the average compressive strength, a minimum of three specimens were tested.

2. 2. 2. Splitting Tensile Test On a 2000 kN capacity CTM, a cylindrical specimen with dimensions 100 mm dia. and 200 mm height was used for splitting tensile strength testing according to ASTM C 496-1996.

2. 2. 3. Flexure Test According to ASTM C78-1994 [26], flexural strength tests were performed on 100

TABLE 1. Mix Proportion of UHPCC

Material	UHPFRC-AQ	UHPFRC-AG
Cement	1	1
Alccofine	0.25	0.25
Quartz Powder	0.3	-
GGBS	-	0.3
Fine Aggregate	1.2	1.2
w/c	0.25	0.25
SP (%)	2	2
Steel fiber, V_f (%)	0-2.5	0-2.5

TABLE 2. Chemical Composition of Cementitious Materials

Compound (%)	Cement	Alccofine	Quartz Powder	GGBS
SiO_2	18.91	34.83	99.5	33.45
Al_2O_3	4.51	21.44	0.08	13.46
Fe_2O_3	4.94	1.39	0.04	0.31
CaO	66.67	33.91	0.01	41.7
MgO	0.87	6.81	0.01	5.99
SO_3	2.5	0.010	0.01	2.74
K_2O	0.43	-	0.01	0.29
Na_2O	0.12	-	0.01	0.16
LOI	1.7	1.42	0.28	0.26

x 100 x 500 mm^3 prismsunder third point loading with a simply supported span of 400 mm on a hydraulically controlled closed loop universal testing machine (UTM) of capacity 1000 kN.

The tests were carried out at a rate of 0.1 mm/min of deformation.

2. 2. 4. Modulus of Elasticity A cylindrical specimen having dimensions of 150 mm dia. and 300 mm height isused for the uniaxial compression test according to ASTM C 39-1992 [27] in a CTM with a maximum load capacity of 3000 kN.

3. RESULTS AND DISCUSSIONS

3. 1. Compressive Strength Compressive strength (f_{cf}) values of 12 UHPFRC mixtures are listed in Table 3 according to their fiber volume fractions. Figure 1 illustrates the graphical representation of compressive strength values. To calculate the compressive strength, an average of at least three tested specimens was taken. From both Figure 1 and Table 3, it can be observed that the addition of steel fibers to UHPCC improved the compressive strength of concrete mixes. A gradual increase in compressive strength was observed with the increment in steel fiber volume fraction of up to 2%. However, the UHPFRC mixtures containing 2.5% steel fibers had a minimum impact with a negligible increment in compressive strength. The improvement of compressive strength with steel fiber addition can be attributed to the ability of fibers to hold the concrete matrix together and delay the micro-crack formation. And beyond 2%, higher fiber content resulted in negligible improvement due to the inhomogeneous distribution of fibers in the concrete mixture.

A maximum compressive strength of 155.39 MPa was attained by the UHPFRC-AG 2.5 mixture, which is around 13.7% higher than the unreinforced UHPCC-AG. In a comparison of the two UHPFRC mixtures, UHPFRC-AG yielded higher compressive strength values than UHPFRC-AQ at all fiber volume fractions. The addition of long macro steel fibers to UHPCC has an overall moderate improvement in compressive strength, as the literature suggests an increment of around 30% with the addition of short, micro steel fibers [18]. The other reason for moderate improvement could be due to the fact that the improvement in compressive strength is high when the UHPFRC mixtures containing a high volume of steel fibers are temperature cured. All the tested cube specimens exhibited brittle failure. The unreinforced UHPCC specimens collapsed with rapid and explosive failures, whereas the fiber reinforced UHPFRC specimens collapsed gradually without considerable fragmentation. The failure pattern of UHPFRC cube specimen under compressive loading is shown in Figure 2(a).

The compressive strength values of UHPFRC mixtures can be expressed as a function of fiber volume fraction (V_f) using the linear regression analysis on experimental results presented in Table 3, and the expressions are as follows:

$$f_{cf} = f_c + 6.58\ (v_f) \quad \text{for UHPFRC-AQ} \tag{1}$$

$$f_{cf} = f_c + 7.52\ (v_f) \quad \text{for UHPFRC-AG} \tag{2}$$

TABLE 3. 28-Day Compressive, Splitting tensile and Flexural Strength Properties of UHPFRC and their Improvements

Mix ID	Fiber Volume Fraction (v_f) (%)	28 days Compressive strength (MPa)	Improvement in Strength (%)	28 days Splitting tensile strength (MPa)	Improvement in Strength (%)	28 days Flexural Strength (MPa)	Improvement in Strength (%)
UHPCC-AQ	0	132.57	0.00	10.35	0.00	17.46	0.00
UHPFRC-AQ 0.5	0.5	137.61	3.80	11.85	14.50	20.62	18.10
UHPFRC-AQ 1	1	141.32	6.60	13.07	26.30	23.69	35.70
UHPFRC-AQ 1.5	1.5	144.50	9.00	13.95	34.80	26.09	49.40
UHPFRC-AQ 2	2	147.55	11.30	14.70	42.00	27.64	58.30
UHPFRC-AQ 2.5	2.5	149.01	12.40	15.08	45.70	28.44	62.90
UHPCC-AG	0	136.67	0.00	11.73	0.00	19.24	0.00
UHPFRC-AG 0.5	0.5	142.00	3.90	13.56	15.60	22.93	19.20
UHPFRC-AG 1	1	146.24	7.00	15.19	29.50	26.19	36.10
UHPFRC-AG 1.5	1.5	149.93	9.70	16.29	38.90	28.98	50.60
UHPFRC-AG 2	2	153.48	12.30	17.25	47.10	31.30	62.70
UHPFRC-AG 2.5	2.5	155.39	13.70	17.76	51.40	32.50	68.90

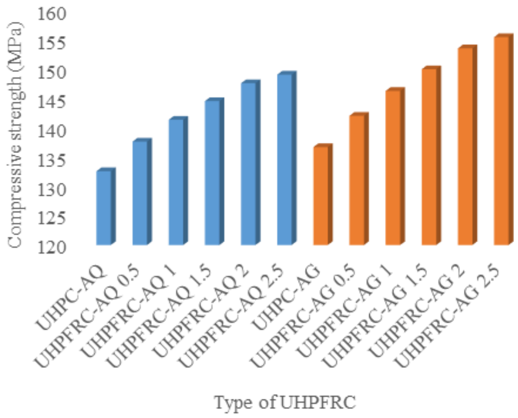

Figure 1. Compressive strength development of various UHPFRC mixes with varying fiber volume fraction (V_f)

The empirical equations developed by using linear regression analysis on experimental values is used to predict the compressive strength values of UHPFRC mixtures and are presented in Table 4. The experimental values of earlier researchers were compared with the values predicted by developed empirical equations, and the average absolute error (AAE) obtained was within 5%. Figure 3 shows the comparison of experimental values of compressive strength (MPa) of UHPFRC with the predicted values by the model. It isfound that the predictions obtained by the proposed model arein good agreement with experimental values.

3. 2. Splitting-tensile Strength The addition of steel fibers resulted in a significant improvement in the tensile properties of UHPFRC. Table 3 presents the splitting tensile strength values of UHPFRC mixtures along with the percentage improvement with the addition of steel fibers. A splitting tensile strength of 10.35 MPa was obtained by the UHPCC-AQ mixture having zero fiber content, which increased by 45.7% to 15.08 MPa. This shows the significance of steel fiber incorporation in UHPFRC to obtain the desired tensile performance. Figure 4 shows the increment of splitting tensile strength (f_{spf}) as a function of fiber volume fraction (V_f). 17.76 MPa is the highest splitting tensile strength value obtained by the UHPFRC-AG 2.5 mixture, and the maximum improvement observed is 51.4% when compared to its unreinforced counterpart. Plain UHPCC displayed high splitting tensile strength with rapid brittle failure, but UHPFRC with fiber reinforcement exhibited greater splitting tensile strength due to the combined

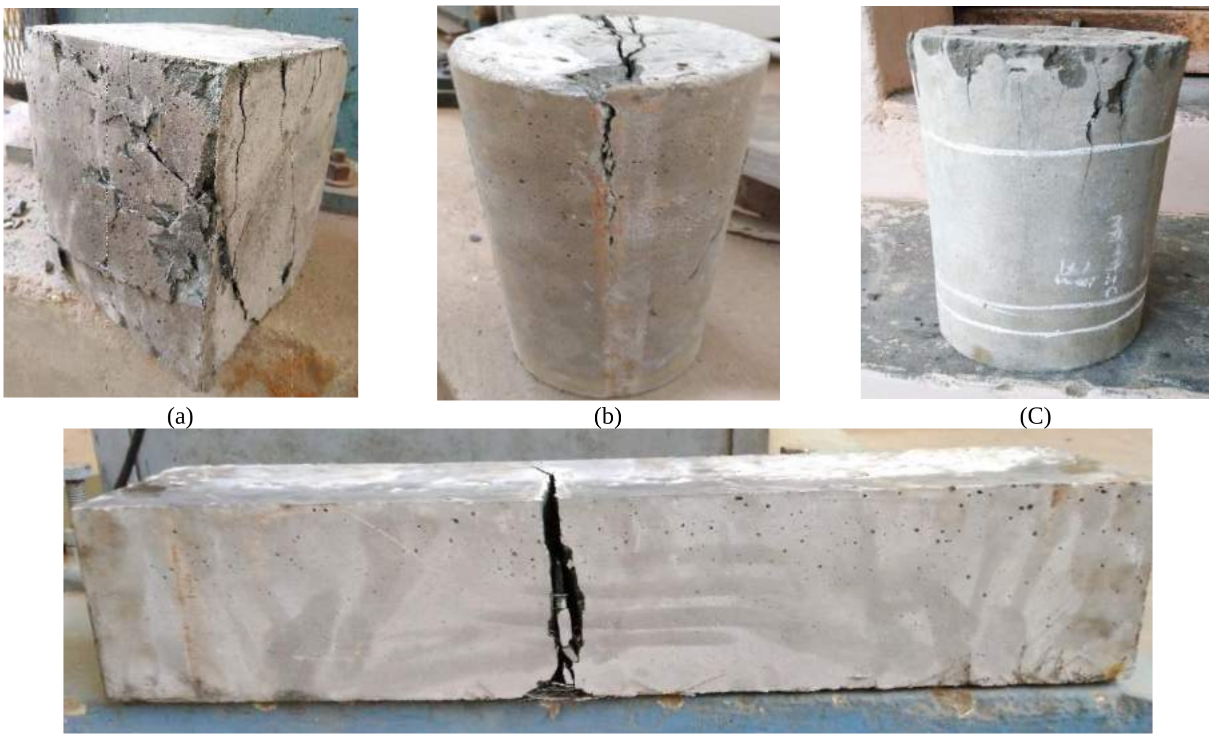

(a) (b) (C)

(d)

Figure 2. Failure patterns of UHPFRC specimens under (a) Compressive load, (b) Splitting tensile load, (c) Uni-axial compression load, and (d) Flexural load

TABLE 4. Predicted Compressive Strength of UHPFRC

Mix ID	Fiber Volume Fraction (v_f) (%)	28 days Compressive strength (MPa)		Absolute Error (%)
		Experimental values	Predicted values	
UHPCC-AQ	0	132.57	132.57	0.00
UHPFRC-AQ 0.5	0.5	137.61	135.86	1.27
UHPFRC-AQ 1	1	141.32	139.15	1.53
UHPFRC-AQ 1.5	1.5	144.50	142.44	1.42
UHPFRC-AQ 2	2	147.55	145.74	1.23
UHPFRC-AQ 2.5	2.5	149.01	149.03	0.01
UHPCC-AG	0	136.67	136.67	0.00
UHPFRC-AG 0.5	0.5	142.00	140.43	1.10
UHPFRC-AG 1	1	146.24	144.20	1.39
UHPFRC-AG 1.5	1.5	149.93	147.96	1.31
UHPFRC-AG 2	2	153.48	151.73	1.14
UHPFRC-AG 2.5	2.5	155.39	155.49	0.06

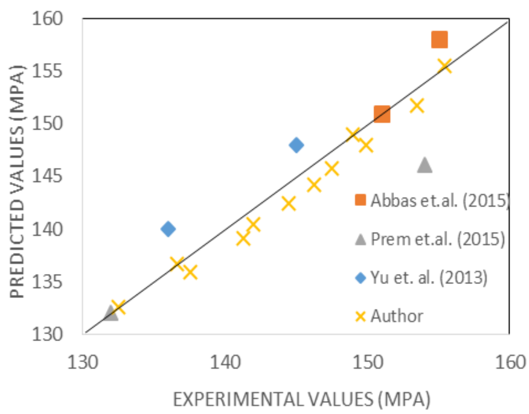

Figure 3. Comparison of experimental values of compressive strength (MPa) of UHPFRC with the predicted values by model

contribution of the UHPFRC matrix and steel fibers to the splitting tensile force. The failure pattern of UHPFRC cylinder specimen under splitting tensile load is shown in Figure 2(b).

The splitting tensile strength values of UHPFRC mixtures can be expressed as a function of fiber volume fraction (V_f) using the linear regression analysis on experimental results presented in Table 3. The splitting tensile strength with respect to steel fiber volume frsaction is shown in Figure 4.

The expressions are stated as follows:

$f_{spf} = f_{sp} + 1.88\ (v_f)$ for UHPFRC-AQ (3)

$f_{spf} = f_{sp} + 2.41\ (v_f)$ for UHPFRC-AG (4)

The empirical equations developed by using linear regression analysis on experimental values is used to predict the splitting tensile strength values of UHPFRC mixtures and are presented in Table 5.

3. 3. Flexure Strength

The flexural strength values of UHPFRC mixtures with five different steel fiber volume fractions (V_f = 0.5, 1, 1.5, 2, and 2.5%) are presented in Table 3 and subsequently shown in Figure 5. Flexural strength increased with fiber content, reaching a maximum at 2.5% by volume of steel fibers. Out of all the mechanical properties, flexural strength was the most improved parameter with the addition of steel fibers, and a minimum percentage increment of 18.10% for UHPFRC-AQ 0.5. All the test specimens displayed deflection-hardening behavior once steel fibers were added, resulting in greater load-carrying capability after the first crack. The maximum flexural strength obtained was 32.50 MPa for the UHPFRC-AG specimen with 2.5% by volume of steel fibers; this value is 68.9, 49.70, 32.80, 18.30% and 6.20% higher than those of the specimens with 0, 0.5, 1, 1.5 and 2% by volume of steel fibers respectively. These findings suggest that the fiber volume fraction has a significant impact on the post-cracking behavior of UHPFRC, such as strength, deflection, and crack width. The fiber content had a considerable influence on the fracture surface roughness; the roughness increased as the fiber concentration increased. This is because more fibers are randomly dispersed and orientated at the crack surface when the fiber content is higher. The failure pattern of UHPFRC prism specimen under flexural load is shown in Figure 2(d).

The flexural strength values of UHPFRC mixtures can be expressed as a function of fiber volume fraction (Vf) using the linear regression analysis on experimental results presented in Table 3, and the expressions are as follows:

$f_{rf} = f_r + 4.47\ (v_f)$ for UHPFRC-AQ (7)

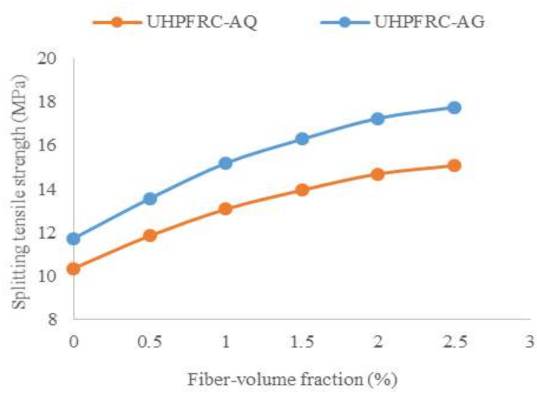

Figure 4. Splitting Tensile strength vs. Steel Fiber Volume Fraction (%)

TABLE 5. Predicted Splitting Tensile Strength of UHPFRC

Mix ID	Fiber Volume Fraction (v_f) (%)	28 days Splitting tensile strength (MPa)		Absolute Error (%)
		Experimental values	Predicted values	
UHPCC-AQ	0	10.35	10.35	0.00
UHPFRC-AQ 0.5	0.5	11.85	11.29	4.69
UHPFRC-AQ 1	1	13.07	12.24	6.37
UHPFRC-AQ 1.5	1.5	13.95	13.18	5.50
UHPFRC-AQ 2	2	14.70	14.13	3.86
UHPFRC-AQ 2.5	2.5	15.08	15.07	0.04
UHPCC-AG	0	11.73	11.73	0.00
UHPFRC-AG 0.5	0.5	13.56	12.94	4.57
UHPFRC-AG 1	1	15.19	14.15	6.85
UHPFRC-AG 1.5	1.5	16.29	15.36	5.73
UHPFRC-AG 2	2	17.25	16.57	3.98
UHPFRC-AG 2.5	2.5	17.76	17.78	0.10

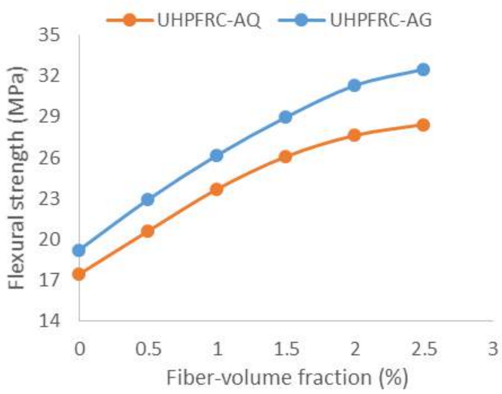

Figure 5. Flexural strength vs. Steel Fiber Volume Fraction (%)

$f_{rf} = f_r + 5.38\ (v_f)$ for UHPFRC-AG (8)

The empirical equations developed by using linear regression analysis on experimental values is used to predict the flexural strength values of UHPFRC mixtures and are presented in Table 6.

3. 4. Relationship between Flexural Strength and Compressive Strength

The relationship between flexural strength and compressive strength of UHPFRC has been obtained using statistical analysis on experimental data and is displayed in Figure 6. The empirical equation for flexural strength of UHPFRC with a correlation coefficient of $R^2 = 0.99$ is as follows:

$$f_{rf} = 0.679 f_{cf} - 72.88 \quad (10)$$

TABLE 6. Predicted Flexural Strength of UHPFRC

Mix ID	Fiber Volume Fraction (v_f) (%)	28 days Flexural tensile strength (MPa)		Absolute Error (%)
		Experimental values	Predicted values	
UHPCC-AQ	0	17.46	17.46	0.00
UHPFRC-AQ 0.5	0.5	20.62	19.70	4.47
UHPFRC-AQ 1	1	23.69	21.94	7.41
UHPFRC-AQ 1.5	1.5	26.09	24.18	7.32
UHPFRC-AQ 2	2	27.64	26.42	4.43
UHPFRC-AQ 2.5	2.5	28.44	28.65	0.75
UHPCC-AG	0	19.24	19.24	0.00
UHPFRC-AG 0.5	0.5	22.93	21.93	4.37
UHPFRC-AG 1	1	26.19	24.62	5.97
UHPFRC-AG 1.5	1.5	28.98	27.31	5.74
UHPFRC-AG 2	2	31.30	30.00	4.15
UHPFRC-AG 2.5	2.5	32.50	32.69	0.61

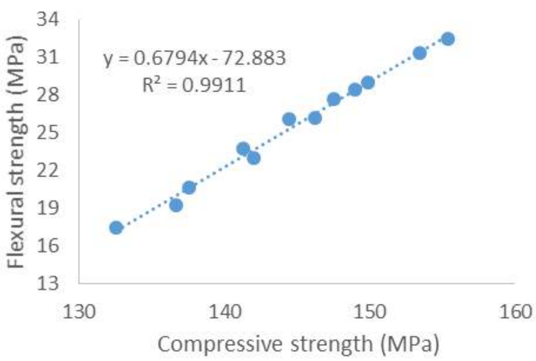

Figure 6. Relation between Flexural Strength and Compressive Strength (MPa) of UHPFRC

3. 5. Modulus of Elasticity

The variation of elastic modulus, (E_{cf}) values for the UHPFRC mixtures with the effect of fiber volume fraction (V_f) is presented in Table 7 and Figure 7. Steel fiber addition to UHPCC increased corresponding strain at peak stress, and in turn improved its toughness. The fiber volume fraction has a direct relationship with this behavior. A UHPFRC mixture containing alccofine and quartz powder obtained an elastic modulus value of 39.52 GPa for the unreinforced specimen and 46.32 GPa for the UHPFRC-AQ 2.5, which has a 2.5% steel fiber volume fraction. Similarly, an UHPFRC mixture containing alccofine and GGBS obtained a higher elastic modulus value of 40.74 GPa for an unreinforced specimen and 47.99 GPa for UHPFRC-AG 2.5, having a 2.5% steel fiber-volume fraction. The explosive failure demonstrated by unreinforced UHPCC specimens posed risks and reading measurement

TABLE 7. Modulus of Elasticity of UHPFRC

Mix ID	Fiber Volume Fraction (v_f) (%)	Modulus of elasticity (GPa)
UHPC-AQ	0	39.52
UHPFRC-AQ 0.5	0.5	41.54
UHPFRC-AQ 1	1	43.43
UHPFRC-AQ 1.5	1.5	45.01
UHPFRC-AQ 2	2	45.96
UHPFRC-AQ 2.5	2.5	46.32
UHPC-AG	0	40.74
UHPFRC-AG 0.5	0.5	42.94
UHPFRC-AG 1	1	44.98
UHPFRC-AG 1.5	1.5	46.53
UHPFRC-AG 2	2	47.54
UHPFRC-AG 2.5	2.5	47.99

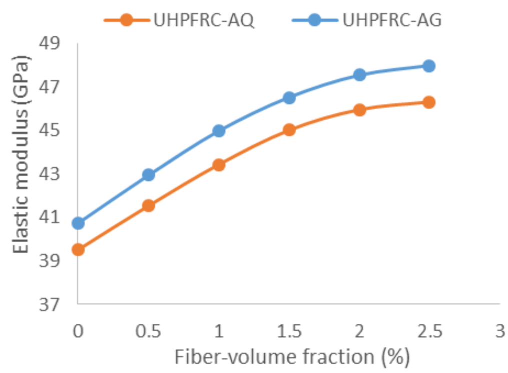

Figure 7. Modulus of elasticity vs. Steel Fiber Volume Fraction (%)

challenges, which are observed in normal concrete but UHPFRC displayed higher compressive strain. According to the crack pattern on tested cylindrical specimens, it was observed that vertical cracks were formed on specimens with lower steel fiber volume fractions and diagonal cracks were formed on specimens with higher steel fiber volume fractions. The failure pattern of UHPFRC cylinder specimen under uni-axial compressive load is shown in Figure 2(c).

The elastic modulus values of UHPFRC mixtures can be expressed as a function of fiber volume fraction (V_f) using the linear regression analysis on experimental results presented in Table 7, and the expressions are as follows:

$$E_{cf} = E_c + 2.79\,(v_f) \quad \text{for UHPFRC-AQ} \tag{11}$$

$$E_{cf} = E_c + 2.94\,(v_f) \quad \text{for UHPFRC-AG} \tag{12}$$

The empirical equation developed by using linear regression analysis on experimental values is used to predict the elastic modulus values of UHPFRC mixtures and are presented in Table 8.

3. 6. Stress-strain Behavior Under stresses developed roughly below the 70% strength of UHPFRC, linear elastic behavior is observed. Figures 8 and 9 show the stress-strain behavior of UHPFRC-AQ and UHPFRC-AG, respectively. From stress-strain curves, it can be observed that a linear ascent is exhibited up to the peak stress. It is also observed that the strain at corresponding peak stresses increases as the fiber volume fraction and strength of UHPFRC mixtures increase. The stress-strain behavior of unreinforced UHPCC specimens showed a sudden dip in stress values and a negligible increment in strain values beyond the peak stress. UHPFRC mixtures displayed a nonlinear strain-hardening phase after the elastic phase, owing to the formation of micro cracks in the concrete matrix. The interlocking of interfacial bonds carried the load instead of the concrete matrix. The higher steel fiber volume fractions of UHPFRC displayed greater interlocking, resulting in higher stress values. Steel fiber volume fraction (V_f) greatly influences the post-peak curve.For the UHPFRC mixtures with lower fiber volume fractions, the post peak curve is nearly as steep as the ascending curve in pre-peak stage, whereas for the UHPFRC mixtures with higher fiber volume fractions, the post peak curve slopes more gradually. There was a minimum influence of V_f on initial stiffness, but in the softening region, higher V_f resulted in greater peak load. A peak stress of 109 MPa was obsereved for UHPCC-AG mixture and a peak stress of 124 MPa was observed for UHPFRC-AG 2.5 mixture.

TABLE 8. Predicted Modulus of Elasticity of UHPFRC

Mix ID	Fiber Volume Fraction (v_f) (%)	Modulus of elasticity (GPa)		Absolute Error (%)
		Experimental values	Predicted values	
UHPCC-AQ	0	39.52	39.52	0.00
UHPFRC-AQ 0.5	0.5	41.54	40.92	1.49
UHPFRC-AQ 1	1	43.43	42.31	2.58
UHPFRC-AQ 1.5	1.5	45.01	43.71	2.90
UHPFRC-AQ 2	2	45.96	45.10	1.87
UHPFRC-AQ 2.5	2.5	46.32	46.50	0.39
UHPCC-AG	0	40.74	40.74	0.00
UHPFRC-AG 0.5	0.5	42.94	42.21	1.69
UHPFRC-AG 1	1	44.98	43.69	2.86
UHPFRC-AG 1.5	1.5	46.53	45.16	2.92
UHPFRC-AG 2	2	47.54	46.64	1.90
UHPFRC-AG 2.5	2.5	47.99	48.11	0.25

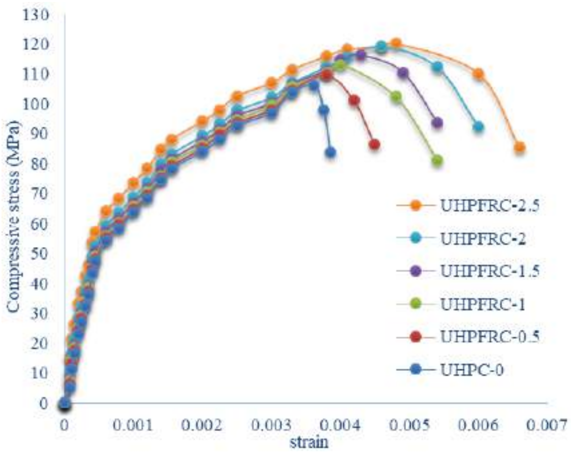

Figure 8. Stress-Strain behavior of UHPFRC-AQ

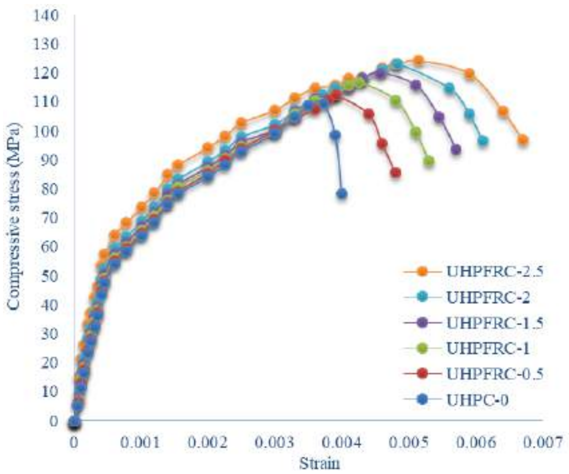

Figure 9. Stress-Strain behavior of UHPFRC-AG

4. CONCLUSIONS

The effect of steel fiber volume fraction on the mechanical performance of UHPCC was investigated, and the following conclusions can be drawn:

- Addition of steel fibers to UHPCC resulted moderate improvement in compressive strength and significant improvement in splitting tensile and flexure strengths. Improvement in strengths observed is 13.7, 51.4, and 68.9% for compressive, splitting tensile, and flexural strengths, respectively for UHPFRC at V_f = 2.5% compared to UHPCC.
- Addition of steel fibres up to 2% by volume improved the compressive strength and elastic modulus significantly and above 2% of volume fraction, negligible improvement was observed.
- The maximum splitting tensile strength obtained for UHPFRC-AG is 17.76 MPa for UHPFRC with V_f = 2.5%, which is 51.4% higher than the corresponding UHPCC mixture.
- The maximum flexural strength obtained is 32.50 MPa for UHPFRC-AG with V_f = 2.5%, which is 68.9% higher than the corresponding UHPCC mixture.
- For all fiber volume fractions, UHPFRC-AG exhibited superior performance compared to UHPFRC-AQ.
- Empirical equations developed for the prediction of strength properties as a function of steel fiber volume fraction and the predicted values were compared with the experimental data of earlier researchers. It was found that the equations developed, evaluated the strength values with high efficacy.
- Relation between compressive and flexural strengths of UHPFRC has been developed and reliability of the model in predicting the strength is very good.

6. ACKNOWLEDGEMENT

This research is financially supported by Council of Scientific and Industrial Research (CSIR), New Delhi, India. (Acknowledgement no. 141082/2K19/1; File no. 08/0518(11175)/2021- EMR-I.

7. REFERENCES

1. Bayard, O., and Ple, O. "Fracture mechanics of reactive powder concrete: Material modeling and experimental investigations", ***Engineering Fracture Mechanics,*** Vol. 70, No. 7-8, (2003), 839-851. DOI: 10.1016/S0013-7944(02)00153-4
2. Graybeal, B. "Material property characterization of ultrahigh performance concrete", in FHWA-HRT-06-103, U.S. Department of Transportation (2006), 176.
3. Wang, D., Shi, C., Wu, Z., Xiao, J., Huang, Z., and Fang, Z. "A review on ultra-high performance concrete: Part II. Hydration, microstructure and properties", ***Construction and Building Materials,*** Vol. 96, (2015), 368-377. DOI: 10.1016/j.conbuildmat.2015.08.095
4. Kim, D. J., Naaman, A. E., and El-Tawil, S. "Comparative flexural behavior of four fiber reinforced cementitious composites", ***Cement and Concrete Composites,*** Vol. 30, No. 10, (2013), 917-928. DOI: 10.1016/j.cemconcomp.2008.08.002
5. Nguyen, D. L., Kim D. J., Ryu, G. S., and Koh, K. T. "Size effect on flexural behavior of ultrahigh- performance hybrid fiber-reinforced concrete", ***Composites Part B: Engineering,*** Vol. 45, No. 1, (2012), 1104-1116. DOI: 10.1016/j.compositesb.2012.07.012
6. Ramadoss, P., and Nagamani, K. "Tensile strength and durability characteristics of high performance fiber reinforced concrete", ***the Arabian Journal for Science and Engineering,*** Vol. 33, No. 2, (2008), 307-319.
7. Ramadoss, P. "Modelling for the evaluation of strength and toughness of high performance fiber reinforced concrete", ***Journal of Engineering Science and Technology,*** Vol. 7, No. 3, (2012), 280-291.

8. Hannawi, K., Bian, H., Agbodjan, W. P., and Raghavan, B. “Effect of different types of fibers on the microstructure and the mechanical behavior of ultra-high performance fiber reinforced concretes”, ***Composites Part B: Engineering,*** Vol. 86, (2016), 214-220. DOI: 10.1016/j.compositesb.2015.09.059

9. Wille, K., Kim, D. J., and Naaman, A. E. “Strain-hardening UHP-FRC with low fiber contents”, ***Material Structures,*** Vol. 44, No. 3, (2011), 583-98. DOI: 10.1617/s11527-010-9650-4

10. Kim, D. J., Park, S. H., Ryu, G. S., and Koh, K. T. “Comparative flexural behavior of hybrid ultra-high performance fiber reinforced concrete with different macro fibers”, ***Construction and Building Materials,*** Vol. 25, No. 11, (2011), 4144-4155. DOI: 10.1016/j.conbuildmat.2011.04.051

11. Yoo, D. Y., Kang, S. T., Lee, J. H., and Yoon, Y. S. “Effect of shrinkage reducing admixture on tensile and flexural behaviors of UHPFRC considering fiber distribution characteristics”, ***Cement and Concrete Research,*** Vol. 54, (2013), 180-190. DOI: 10.1016/j.cemconres.2013.09.006

12. Schmidt, M., Fehling, E., and Geisenhanslueke, C. (Eds.). In International Symposium on Ultra High Performance Concrete, Kassel, Germany, (2004), 868.

13. Schmidt, M., Fehling, E., Glotzbach, C., Frohlich, S., and Piotrowski, S. (Eds.). In Third International Symposium on UHPC and Nanotechnology for High Performance Construction Materials, Kassel, Germany, (2012), 1036.

14. Fehling, E., Schmidt, M., and Stuerwald, S. (Eds.). In Second International Symposium on Ultra-high Performance Concrete, Kassel, Germany, (2008), 902.

15. Richard, P., and Cheyrezy, M. “Composition of reactive powder concretes”, ***Cement and Concrete Research,*** Vol. 25, (1995), 1501-1511. DOI: 10.1016/0008-8846(95)00144-2

16. Prem P. R., Murthy, R., and Bharatkumar, B. “Influence of curing regime and steel fibers on the mechanical properties of UHPC”, ***Magazine of Concrete Research,*** Vol. 67, No. 18, (2015), 988-1002. DOI: 10.1680/macr.14.00333

17. Yoo, D. Y., Shin, H. O., Yang, J. M., and Yoon, Y. S. “Material and bond properties of ultra-high performance fiber reinforced concrete with micro steel fibers”, ***Composites Part B: Engineering,*** Vol. 58, (2014), 122-133. DOI: 10.1016/j.compositesb.2013.10.081

18. Abbas, S., Ahmed, M., Soliman, Moncef, L., and Nehdi. “Exploring mechanical and durability properties of ultra-high performance concrete incorporating various steel fiber lengths and dosages”, ***Construction and Building Materials,*** Vol. 75, (2015), 429-441. DOI: 10.1016/j.conbuildmat.2014.11.017

19. Yu, R., Spiesz, P., and Brouwers, H. J. H “Mix design and properties assessment of ultra-high performance fiber reinforced concrete (UHPFRC)”, ***Cement and Concrete Research,*** Vol. 56, (2014), 29-39. DOI: 10.1016/j.cemconres.2013.11.002

20. Tsioulou, O., Lampropoulos, A., and Paschalis, S. “Combined Non-Destructive Testing (NDT) method for the evaluation of the mechanical characteristics of ultra-high performance fibre reinforced concrete (UHPFRC)”, ***Construction and Building Materials,*** Vol. 131, (2017), 66-77. DOI: 10.1016/j.conbuildmat.2016.11.068

21. Kang, S. T., and Kim, J. K. “Investigation on the flexural behavior of UHPCC considering the effect of fiber orientation distribution”, ***Construction and Building Materials,*** Vol. 28, No. 1, (2012), 57-65. DOI: 10.1016/j.conbuildmat.2011.07.003

22. Aydin, S., and Baradan, B. “The effect of fiber properties on high performance alkali activated slag/silica fume mortars”, ***Composites Part B: Engineering,*** Vol. 45, No. 1, (2013), 63-69. DOI: 10.1016/j.compositesb.2012.09.080

23. Wuest, J., Denarié, E., and Brühwiler, E. “Model for predicting the UHPFRC tensile hardening response”, in Proceedings of the second international symposium on ultra-high performance concrete, Kassel, Germany, (2008), 153-60.

24. Reddy, G. G. K., and Ramadoss, P. “Influence of alccofine incorporation on the mechanical behaviour of ultra-high performance concrete (UHPC)”, ***Materials Today: Proceedings,*** Vol. 33, (2020), 789-797. DOI: 10.1016/j.matpr.2020.06.180

25. Reddy, G. G. K., and Ramadoss, P. “Performance evaluation of ultra-high performance concrete designed with alccofine”, ***Innovative Infrastructure Solutions,*** Vol. 6, (2021), 6. DOI: 10.1007/s41062-020-00375-y

26. ASTM C 78-1994, “Standard test method for flexural strength of concrete specimens”, American Society for Testing and Materials, 2004.

27. ASTM C 39-1992, “Standard test method for compressive strength of fiber reinforced concrete”, American Society for Testing and Materials, 2004.

28. Ramadoss, P., and Prabath, N. V. N. “Engineering properties and prediction of strength of high performance fiber reinforced concrete***”, Electronics Journal of Structural Engineering,*** Vol. 21, No. 1, (2021), 76-90.

29. Madhkhan, M., and Saeidian, P. “Mechanical properties of ultra-high performance concrete reinforced by glass fibers under accelerated aging”, ***International Journal of Engineering, Transactions B: Applications,*** Vol. 34, No. 5, (2021), 1074-1084. DOI: 10.5829/IJE.2021.34.05B.01

30. Dhundasi, A. A., Khadiranaikar, R. B., and Momin, A. I. A. “Stress-strain characteristics of reactive powder concrete under cyclic loading”, ***International Journal of Engineering, Transactions A: Basics,*** Vol. 35, No. 1, (2022), 172-183. DOI: 10.5829/10.5829/ije.2022.35.01a.16

31. Hajsadeghi, M., Jalali, M., Chin, C. S., Zirakian, T., and Bahrebar, M. “Flexural characteristics of fibre reinforced concrete with an optimised spirally deformed steel fiber”, ***International Journal of Engineering, Transactions C: Aspects***, Vol. 34, No. 6, (2021), 1390-1397. DOI: 10.1016/j.engstruct.2020.110863

Persian Abstract

چکیده

به منظور بررسی اثر کسر حجمی الیاف بر رفتار مکانیکی کامپوزیت های بتن با عملکرد فوق العاده بالا (UHPCC)، پنج کسر حجمی مختلف از الیاف ماکرو فولادی (Vf = 0.5، ۱، ۱.۵، ۲ و ۲.۵٪) در داخل استفاده می شود. ماتریس ملات یکسان مخلوط بتن مسلح با الیاف با کارایی فوق العاده بالا (UHPFRC)برای دستیابی به مقاومت فشاری ۱۵۵ مگاپاسکال بر اساس روش بسته بندی ذرات طراحی شده است. برای ۱۲ سری مخلوط UHPCC، استحکام فشاری، مقاومت کششی شکافی، مقاومت خمشی و مدول الاستیسیته در ۲۸ روز تعیین می‌شود. نتایج آزمایش بهبود قابل توجهی را در استحکام کششی و خمشی UHPFRC با افزودن الیاف فولادی نشان داد. حداکثر مقاومت های فشاری، کششی شکافی و خمشی به ترتیب ۱۵۵.۳۹، ۱۷.۷٦ و ۳۲.۵۰ مگاپاسکال بود. رفتار تنش-کرنش کامپوزیت های بتن تقویت شده با الیاف مورد مطالعه قرار گرفته و مقادیر مدول الاستیک ارزیابی شده در محدوده ۳۹.۵۲-٤٧.۹۹ GPa می باشد. عبارات تجربی بر اساس نتایج آزمایش بر حسب کسر حجمی فیبر برای پیش‌بینی نقاط قوت ۲۸ روزه UHPFRC ایجاد شده‌اند. با مقایسه مقادیر تجربی محققان قبلی با مقادیر پیش‌بینی‌شده توسط معادلات تجربی، میانگین خطای مطلق (AAE)مقدار به‌دست‌آمده در ۵٪ است. پیش‌بینی‌های مدل پیشنهادی مطابقت خوبی با مقادیر تجربی دارد. رابطه بین مقاومت فشاری و خمشی UHPFRC با R^2=0.99 توسعه یافته و تایید شده است.

IJE TRANSACTIONS A: Basics Vol. 35, No. 07, (July 2022) 1375-1387

International Journal of Engineering

Journal Homepage: www.ije.ir

Graph Centrality Algorithms for Hardware Trojan Detection at Gate-Level Netlists

M. Hashemi[+a], A. Momeni[+a], A. Pashrashid[b], S. Mohammadi[*a]

[a] *School of Electrical and Computer Engineering, College of Engineering, University of Tehran, Tehran, Iran*
[b] *Department of Computer Engineering, Sharif University of Technology, Tehran, Iran*

PAPER INFO

Paper history:
Received 12 January 2022
Received in revised form 24 April 2022
Accepted 25 April 2022

Keywords:
Hardware Trojan Detection
Structural Gate-Level Analysis
Graph Centrality Algorithms
Feature Extraction
Feature Selection

ABSTRACT

The rapid growth in the supply chain of electronic devices has led companies to purchase Intellectual Property or Integrated Circuits from unreliable sources. This dispersion in the design to fabrication stages of IP/IC has led to new attacks called hardware Trojans. Hardware Trojans can bargain information, reduce performance, or cause failure. Various methods have been introduced to detect or prevent hardware Trojans. Machine learning methods are one of these. Selecting the type and number of input variables in the learning algorithm has an important role in the performance of the learning model. Some previous hardware Trojan detection studies have used structural gate-level features to create data sets for machine learning models. In this paper, a method based on directed graphs for extracting features is proposed. The proposed method use Graph Centrality Algorithm and structural gate-level features. To examine the importance and the impact of the extracted features with the proposed method, three types of data sets are created as input to the learning model made with XGBoost. The trained learning models based on these three data sets show that extracting graph-based features has improved the F1-score by 10% and the ROC by 22%. The combination of these features with the structural gate-level features improved the F1-score by 17.5% and the ROC by 38.5%.

***doi**: 10.5829/ije.2022.35.07a.16*

1. INTRODUCTION

Hardware Trojan (HT) can be defined as an action meant to change the circuit or cause intentional damage to the circuit in order to change the circuit's functionality or reduce circuit reliability or reveal the circuit information. A simple block diagram of a HT is depicted in Figure , which contains two main parts, including Trigger and payload. The Trojans can be added to the circuit in all producing stages (descriptive IC, design, manufacturing, and test) by the attacker. Hence, the HT detection and confrontation with them are more complicated than fault detection during manufacturing. In the design stage, the Trojan can be inserted easily by changing the hardware description. Therefore, it is critical to identify Trojans in the design stage.

*Corresponding Author Institutional Email: smohamadi@ut.ac.ir (S. Mohammadi)
+M. Hashemi and A. Momeni equally contributed in this work

According to the literature, machine learning can be used as one of the effective methods in identifying the HTs. The detection of HTs can be considered as a classification process. Also, gate-level netlists can be used to create features that distinguish between Trojan and normal nets. Therefore, machine learning algorithms and efficient mathematical calculations can make a more accurate classification between Trojan and normal nets.

The distinguishing features of Trojan nets and the normal nets is the key point in this paper in order to

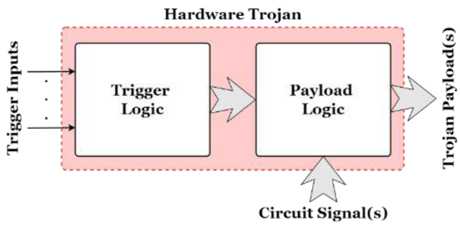

Figure 1. General structure of a HT [1]

Please cite this article as: M. Hashemi, A. Momeni, A. Pashrashid, S. Mohammadi, Graph Centrality Algorithms for Hardware Trojan Detection at Gate-Level Netlists, ***International Journal of Engineering, Transactions A: Basics***, Vol. 35, No. 07, (2022) 1375-1387

identify HTs using the supervised learning method. If the extracted feature sets are too small, the machine learning cannot cluster and identify the Trojans. In addition, if the feature sets are too large, the Curse of Dimensionality event occurs, and the clustering will not be done in a correct manner. Therefore, it is essential to extract the features of Trojan nets and then, reduce the number of the features so that the model be efficient. Several approaches can be employed to extract the features of the HTs as follows:

- The structural features of the circuit: for instance, the number of fan-ins, the number of the flip-flops, the distance of each net from the primary input or primary output, etc.;
- The test features of the circuit: these features include Sandia Controllability/Observability Analysis Program (SCOAP) parameters [2], like the level of controllability and observability of the circuit nets;
- The Register Transfer Level (RTL)-code features of the circuit: the structure of the RTL code is investigated, and the features like the number of the existing modules in the code, the number of existing signal types in each module, the number of "always" statements in each module, the number of primary input or output variables, and the number of register-type variables, etc. are extracted.

The idea of graph-level features in detecting HTs using machine learning methods can be a starting point for future work and development. While using machine learning to detect HTs, selecting the type and number of input variables of the learning method has a significant role in the performance of the learning model. In previous studies, the structural features of the gate-level netlists have been used to create data sets for the machine learning model used to detect HTs. Extracting some of these features at the gate-level is difficult and requires creating complex data structures from the circuit netlist and then implementing specific algorithms to extract each feature [3]. In this research, two methods based on directed graphs for extracting gate-level features are proposed. The proposed tool does converting a gate-level netlist to a directed graph easily. We use available optimal graph algorithms to work on graphs or extract graph-level features. The contributions of this paper are summarized as follows: 1) as the size of the circuits increases, analyzing the structure of the gate-level netlist and extracting its features becomes more complex. In this research, in order to simplify and increase the efficiency of HT analysis, we used a gate-level netlist mapped to directed graphs; 2) the information of graph is maintained by an efficient data structure to be analyzed. In addition, directed graphs can express more information about the behavior of the circuit, thereby helping detect Trojans; 3) in this study, new approaches have been proposed in order to simplify the extraction of appropriate features, so that the accuracy of the trained model is improved; 4) the proposed method uses Graph Centrality Algorithm and structural gate-level features; 5) to examine the importance and the impact of the extracted features with the proposed method, three types of data sets are created as input to the learning model made with XGBoost [4].

The rest of the paper is organized as follows. Section II provides some background regarding the gate-level features of HT(s) and the issues of the existing approaches. Section III introduces the methodology of the proposed methods as well as the metrics that can help evaluate the quality of detection. Section IV discusses the results in terms of accuracy of detection. Finally, section V concludes this study and suggest some points that can improve the quality of HT detection.

2. BACKGROUND AND RELATED WORK

HT detection at the gate-level is essential in identifying Trojans in the design stage. The identifying methods in the gate-level enable the developers and the System-On-Chip (SOC) designers to test the IPs provided from insecure resources [5]. Using machine learning is one of these approaches that can be utilized to identify HTs. This approach is based on extracting appropriate feature sets for training the model in order to identify Trojans. Extraction or calculation of appropriate features that can increase the accuracy of trained models is complicated and challenging in large gate-level netlists. In this section, the conducted studies in the field of identifying HTs for gate-level netlists will be reviewed.

HT detection methods usually include two stages as follows:

- First, the circuit features are extracted;
- Then, the extracted features are investigated and analyzed using different methods.

According to the analysis methods of the extracted features, the Trojan identification approaches can be divided into three main classes as follows:

- Search-based methods;
- Threshold-based methods;
- Machine-learning-based methods.

In the following subsection, the conducted works in these fields are reviewed briefly.

2. 1. Search-based Identification Methods

In this methods, the netlist of the circuit is processed to find the nets with the Trojan feature. Unused Circuitry Identification (UCI) [6] is a method that is applied to code coverage. However, UCI has also been used to identify HT at the gate-level [7]. It is designed to identify the parts of the circuit that are inactive during the execution or when they are inactive most of the time. UCI algorithm makes a Data-flow graph, in which the nodes are the circuit nets, and the edges indicate the current between the circuit nets. In the next step, it is investigated whether during the simulation the current flows between every two nodes of the corresponding graph. Therefore, the unused nets can be identified in this way. The disadvantage of this method is that it cannot be applied to large circuits because the exhaustive simulation of these circuits is very time-consuming, and sometimes impossible.

VeriTrust is another work in this field [7] that includes a tracer and a checker. The checker identifies the activation history of the SOP and POS sections of the circuit. These inputs are investigated using the checker in three aspects: additional inputs, non-additional inputs, and logic synthesis so that the circuit function is simplified again. This solution requires a white-box accessibility of the hardware IP since it uses static analysis of the code and is based on functional verification. Besides, this method is time-consuming.

2. 2. Threshold Value-based Methods In these approaches, a threshold value is defined for each of the circuit features, and if any net exceeds this threshold limit, the net is recognized as a Trojan. A method called FANCI is presented by Waksman et al. [8] which is based on functional analysis. This method distinguishes the parts of the circuit that are inactive. For this purpose, they proposed a metric called control value(CV) to identify nearly-unused logic. This metric measures the degree of control that an input has on the operation and outputs of a digital circuit. Next, the Trojan nets and the normal nets are identified according to CV and a threshold value. The complexity of CV calculation increases exponentially with the circuit's size. Therefore, the authors have approximated the CV value using innovative techniques. Hence, this method is still time-consuming, and the statistics show that it is not accurate, as it identifies many healthy nets as Trojan nets. Another disadvantage of this method is that it only can be applied to hybrid circuits., Other approaches have also been proposed by Fyrbiak et al. [9] and Sullivan et al. [10] in order to employ this method in hybrid circuits. Nevertheless, this method does not have proper performance in hybrid circuits with high clock levels.

2. 3. Machine Learning-based Methods As machine learning technology grows rapidly, more researchers have become interested in this method to identify the HTs. Machine learning methods have been utilized for identifying HTs at the gate-level for the first time [11]. The gate-level hardware features have been employed to accomplish this as follows:

- $LGFi$ (Logic-gate fan-in): The number of inputs of two previous levels of the gate;
- FFi, FFo: The least distance (level) of each net from the input and output of a flip-flop, respectively;
- PI, PO: The least distance of a net to the primary inputs and outputs of the circuit, respectively.

Figure 2 shows an example of calculating the structural gate-level features, and the values of these five features have been demonstrated for net n. The fan-in value of net n at the second level is four. Since the distance of flip-flop A distance from net n is two, FFi is equal 2.

These features are employed as input in Support Vector Machine (SVM) clustering. The main problem in this method is the long distance between the number of normal nets and the Trojan nets. In order to address this issue and data balancing, the repeated-feature vectors for the healthy nets are eliminated so that the number of the normal nets and the Trojan nets are equaled.

Hasegawa et al. [12] and Ye et al. [13] extracted 51 features of the Trojan nets have been from the netlists of Trust-Hub benchmarks. Salmani et al. [14] and Shakya, 15] applied machine learning in the first stage in order to perform an effective clustering of HTs. In the next step, 11 features (logic gate fan-in, the number of input/output-side net flip-flops, the number of input/output-side net multiplexers, the number of input/output-side net loops, the constant values, and the distance of net from the primary inputs or outputs) have been selected among 51 features in order to reduce the dimensions and prevent dimension congestion event. Random forest classifier has been used to select more essential features.

Ye et al. [13] and Hoque et al. [16] have balanced first the data set by generating new HT data. In this approach, the benchmarks are produced by using Trojan-insertion tools in IP so that the inserted Trojans are difficult to distinguish. Second, the related data to Trojan features are extracted from them, and a trained model is made based on the extracted data set. This trained model is used for identifying HTs.

Salmani [17] utilized combinational testability measured as HT features. By this purpose, the testability indices is calculated using SCOAP. They include controllability and observability of zero and one values of circuit nets. In tsalmani's work [17], an unsupervised method has been used for clustering the Trojans. Some

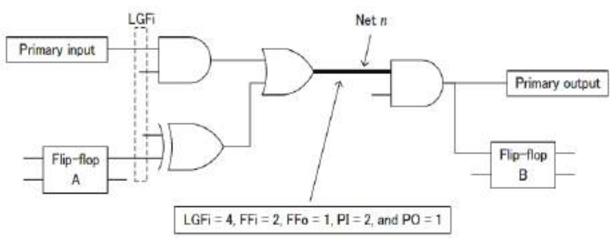

Figure 2. An example of structural gate-level features calculation [11]

Trojans change the sequential nets and signals as well as the circuit hybrid signals. Xie et al. [18] utilized the sequential testability indices as the features of the HTs.

An ensemble learning based method has been proposed by Wang et al. [19] to identify HT features in which the trigger part of Trojans has been used. In this approach, as shown in Figure , two different learning models have been made to identify hybrid and sequential triggers. These two models have been combined using hybrid learning.

Kurihara and Togawa [20] have proposed a 25 hardware-Trojan features based on the structure of trigger circuits for machine-learning-based HT detection. Their experimental results show that the average true positive rate (TPR) and the average true negative rate (TNR) are 63.6% and 100.0%, respectively. However, compared to our proposed method, the average TPR is 15.46% lower.

3. METHODOLOGY AND PROPOSED METHOD

Security analysis for Trojan detection in IP cores have been explored mostly in gate-level netlists. In these types of analysis, structural features are extracted to find the hidden structure of Trojans. Considering the size of real circuits, structural analysis to extract features is too complex to be done easily. In this paper, we have used a simple mapping to convert gate-level netlist to a directed graph. This method not only helps to present an efficient analysis, but also provides more information about the functionality of the circuit. Thus, this would be helpful for Trojan detection.

3. 1. Preliminaries

3. 1. 1. Gate-level Netlist to Directed Graph Mapping

The construction of a directed graph of a gate-level netlist is done as follows: we consider the inputs and outputs of each gate as nodes and the gate as an edge, and then the graph based on the relations between the gates in the list. Figure 4 shows directed graph representations for some gate examples.

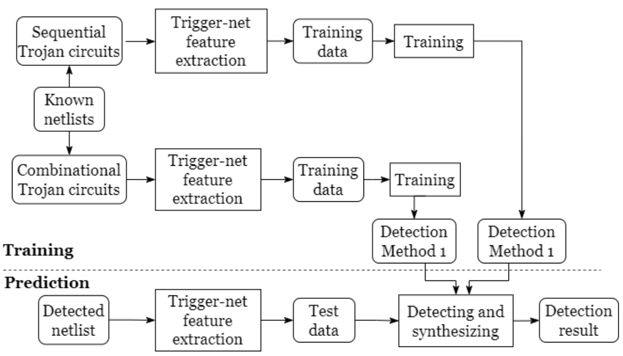

Figure 3. Overall stages of identifying Trojans based on hybrid/sequential triggers [19]

Figure 5 shows the directed graph of the RS232-T1000 Trojan circuit of the Trust-Hub benchmarks [14, 15]. To construct a digraph, using a tool implemented in Python, the netlist is processed to read the individual gates (nets) of the circuit and, depending on the input and output of each gate, it extracts an edge-list file containing all the pairs (input-output) of the gates. It means this is a file containing edges of the directed graph. Then, with this file we can create a graph and display it by graph tools and Python libraries. For example, with a graph library like networkx this edge-list is read and the graph is displayed. Consider an AND gate with a, b as its inputs and c as its output. The developed tool adds edges a-c and b-c to the edge-list file.

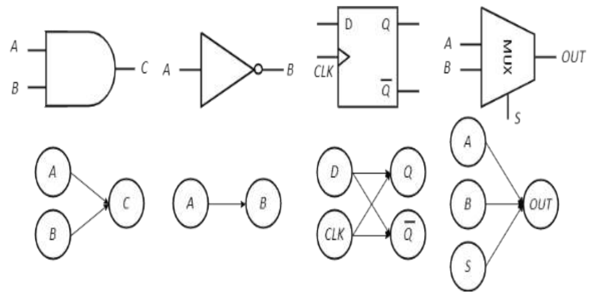

Figure 4. Directed graph representations for some gates

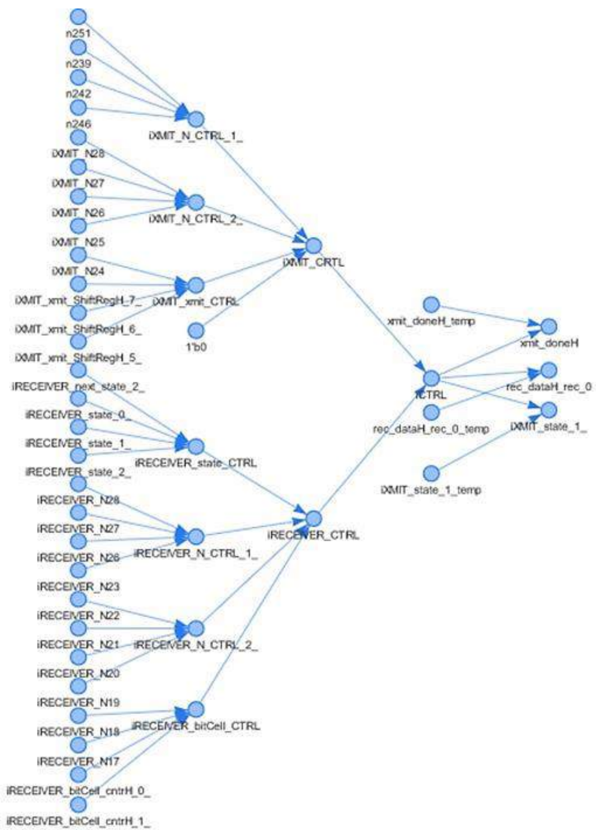

Figure 5. Directed graph of RS232-T1000

3. 1. 2. Graph Centrality Algorithms In graphs or graphs, centrality measures are used to determine the importance of nodes. A centrality measure is a function that assigns a number to each node according to the importance of that vertex in the graph. Extensive research has been done to calculate centrality measures in order to reduce its calculation as much as possible or to be able to perform these calculations in parallel by distributing them on different computers. The most important centrality measures are:

Degree centrality: It is defined as the number of links incident upon a node (i.e., the number of ties that a node has). The most important node has higher degree.

Betweenness centrality: It measures the number of times a node lies on the shortest path between other nodes. In fact, it calculates how many nodes need this node to communicate faster (with less intermediaries). The higher betweenness of a node means more information passes through this node. The betweenness of node *v* in a graph is calculated as follows [22]:

$$C_B(v) = \sum_{s \neq v \neq t \in V} \frac{\sigma_{st}(v)}{\sigma_{st}} \quad (1)$$

where σ_{st} is total number of shortest paths between node s and node t, and $\sigma_{st}(v)$ is the number of paths between s and t that pass through node v.

Closeness centrality: A node is considered as a close node if it requires a small number of interfaces to communicate with other nodes [23].

Eigen vector centrality: The importance of a node is calculated based on adjacent nodes. If a node is connected to important nodes, its importance also increases under their influence. This method repeatedly considers the importance of neighbors to calculate eigenvector centrality. All nodes are first given an initial score and then, continued in a chain until they reach stability. Scoring in this method is based on the concept that nodes with high connections help the nodes that follow them in terms of eigenvector centrality [24].

PageRank: The rank of a page depends on the rank of the pages that are linked to it. Since we do not initially know the rank of pages, in this algorithm, all pages are first given the same rank as the initial rank. Then, the algorithm is run repetitively until the rank of each page converges to a number. Only nodes that have a neighbor and a link from others to themselves will be ranked, otherwise their rank will be zero [25, 26].

Hub centrality: It is the ability of a node to form a relation with other nodes in a graph.

Authority centrality: It is calculated based on the number of relations that other nodes have with a node.

Clustering coefficient: This criterion calculates the tendency of a node to create a cluster with other nodes. For example, 0.5 for a node means that there is 50% chance of communication between neighboring nodes.

Modularity class: It calculates the effect of a node on other nodes in the community in which it is located and on the nodes in other communities.

3. 2. Preparing Data Set This is the most important step in the supervised machine learning process. The input data set in a learning model must be carefully prepared both in terms of size and quality of its features so that the learning model can be well trained and be used for a high-precision prediction model. In this study, in the first step to prepare a data set for detecting HTs using machine learning, the benchmarks of Table 1 have been collected [14, 15]. The used benchmarks are Verilog-HDL gate-level netlists and we know beforehand which net is a Trojan net and which net is a normal net. Then, the data sets shown in Table 2 have been created.

3. 2. 1. First Data Set: Specified by Graph Centrality Algorithm In the first step, we collect the gate-level benchmarks mentioned in the previous section. In the second step, using our tool written in Python, we start to process each benchmark and generate a .csv file containing the edges of the graph. In the third step, using Gephi tool [29], we read each of these files to calculate the centrality criteria of each graph and generate their report as output. In the last step, we read these generated reports using a tool written in Python to produce a data set containing the

TABLE 1. Properties of used benchmarks [14, 15]

Benchmark	No. of nets		Benchmark	No. of nets	
	Normal	Trojan		Normal	Trojan
RS232-T1000	297	13	s38584-T100	7342	19
RS232-T1100	297	12	s15850-T100	2417	28
RS232-T1200	297	14	s35932-T100	6405	15
RS232-T1300	297	9	s35932-T200	6382	17
RS232-T1400	297	13	s35932-T300	6405	36
RS232-T1500	297	15	s38417-T100	5798	12
RS232-T1600	297	13	s38417-T200	5798	15
			s38417-T300	5827	15

TABLE 2. Data sets used in this work

Data Set	Description
Proposed 1	Based on graph centrality features of directed graphs extracted from benchmarks
SGL	**S**tructural **G**ate-**L**evel features [12, 27, 28]
Proposed 2	Merge features extracted from Prop.1 and SGL

nets of all circuits along with 18 centrality features for each net. Given that in the first step we identify the Trojan sections of each circuit, in this step the labeling of each net would be also done for the data set. We label Trojan nets as “1” and other nets as “0”.

3. 2. 2. Second Data Set: Specified by Structural Gate-Level Features The use of structural features of gate-level netlist in detection of HTs by machine learning has been studied in several studies. Here, we use the structural gate-level features published [12, 27, 28] to construct the data set. Because we do not have a database based on this type of features, we have written a tool in Python to extract these types of features from the gate-level netlist. Then the information of each net (including input/output to net, type of gate, and a gate-level structural feature vector) has been calculated and stored in the dictionary. After completing dictionary, we store its information as a data set file in the output.

3. 2. 3. Third Data Set: Specified by Structural Gate-Level Features and Graph Centrality Algorithm In order to add more accuracy to the extracted features of the proposed method with the structural features of the gat-level netlist, we have created a new data set based on the integration of these two types of data sets, which are mentioned in Table 3. Some structural features that are introduced in [12, 27, 28], are:

- Fan_in_x: In case of combinational circuits, trigger circuits require multiple logic gates since they have to implement complex trigger conditions. If the trigger is a rare condition, the number of fan-ins tends to become large. Since hts tend to have rare trigger conditions, the number of fan-ins in Trojan nets must be large compared to normal nets. Hence, fan_in_x that is defined as the number of fan-ins up to x-level away from the net n is an important feature to detect hts.
- In_ff_x (out_ff_x), in_nearestff (out_nearestff): Since the hts circuits are too small and placed locally, the level of flip-flops for sequential-trigger circuits must be small enough. So, in_ff_x that is designed as the number of flip-flops up to x-level away from the input (output) side of the net n, plays an important role to detect hts. Also, the levels of the nearest flip-flops from the input (output) side of the net n are defined as in_nearest flip-flop and out nearest flip-flop, respectively and are extracted as Trojan features.
- In_mux_x (out_mux_x), in_nearestmux (out_ nearestmux): Some hts have multiplexers which receive trigger signals from trigger circuits and switch output signals to activate malfunctions. Therefore, the number of multiplexers up to x-level away from the input side and output side of the net n (in multiplexer x and out multiplexer x, respectively), and the level of the nearest multiplexers from the input side and output side of the net n (in nearest multiplexer and out nearest multiplexer respectively) are extracted as Trojan features.
- In_nearestpi (out_nearestpi): Primary inputs (PI) are often selected as triggers of hts. Primary outputs (PO) are often used as output ports of internal signals for malfunctions. It means Trojan nets are likely to be placed close to pis and pos. So, in_nearestpi (out_nearestpi) that equals the minimum levels from net n to any PI (PO) is extracted as Trojan feature.

Graph centrality features that are used by Gephi tool are introduced by Tarjan [30], hence, we skip detailed introduction. As a brief review:

- Strong component: a strongly connected component of a digraph is a maximal set of vertices that there is a path from any one vertex to any other vertex in the set.

3. 3. Use of Machine Learning XGBoost is a decision-tree-based ensemble Machine Learning algorithm that uses a gradient boosting framework. The implementation of the algorithm was engineered for efficiency of compute time and memory resources. A design goal was to make the best use of available resources to train the model. Some key algorithm implementation features include:

- Sparse aware implementation with automatic handling of missing data values;
- Block structure to support the parallelization of tree construction;

TABLE 3. Merging extracted features from Prop.1 and SGL

Graph Centrality Features		**Structural Features ($1 \le x \le 5$) [12, 27, 28]**
Strong Component no.	PageRank	fan_in_x
Component no.	Authority	in_ff_x
weighted degree	degree	out_ff_x
Weighted in Degree	In degree	in_mux_x
Weighted out Degree	Out degree	out_mux_x
Eigen Centrality	Hub	in_nearestFF
Closeness Centrality	Eccentricity	out_nearestFF
Betweenness Centrality		in_nearestPI
Harmonic Closeness Centrality		out_nearestPO
Clustering Coefficient		in_nearestMux
Modularity Class		out_nearestMux

- Continued training to further boost an already fitted model on new data.

In this research, XGBoost learning model is used for classification. The inputs to the model are the data sets with their related set of features and the learning parameters. Default parameters are used in this learning model, some of them are listed in Table 4. The output is the trained model that we use for HT detection. Also, We have used three different methods, XGBoost, Scikit-learn, and SHAP libraries, to analyze the importance and impact of the proposed extracted features of three data sets on the accuracy of HT detection:

- Method 1: Use XGBoost function to determine the importance of features. In XGBoost algorithm, the relative importance of features is measured by several criteria. One of these criteria is the split weight, which is the number of times a feature has been used to separate data in a tree in all boosted trees. More important features are more involved in the construction of trees, and the other features are used to reduce errors;
- Method 2: Use Scikit-learn library for computing permutation importance of features. In fact, we used the feature permutation method that is available in Scikit-learn library to calculate the importance of features. In this method, the increasing rate of the learning model prediction error is measured for each change in features (until the relation between the feature and the correct output is lost). Permuting the feature that has lower importance will not greatly affect the accuracy of the output of model;
- Method 3: Determine the importance of the features based on the calculated Shapley additive explanation (SHAP) values. SHAP is a library that provides a mechanism to calculate Shapley values. In this method that is based on the concept of Shapley values in game theory, the effect of each feature on the output of the learning model is measured using co-operative game theory. Each feature is considered as a player in the game and the output of the predicted model is the final reward of the game. Shapley values determine the role of each player (feature) in the final reward (predicted model).

TABLE 3. Used learning model parameters

Paremeter	Value
base score	0.5
booster	gbtree
Learning rate	0.1
Max depth	3

TABLE 4. Statistical features of the first data set

Feature	mean	std	min	0.25	0.5	0.75	max
in degree	3.0352	1.33	0	2	4	4	6
out degree	3.0352	37.69	0	1	2	3	2553
degree	6.0704	37.65	1	4	5	7	2553
weighted in degree	3.0352	1.33	0	2	4	4	6
weighted out degree	3.0352	37.695	0	1	2	3	2553
weighted degree	6.0704	37.65	1	4	5	7	2553
eccentricity	62.16	37.245	0	37	49	97	171
ClosnessCentrality	0.0528	0.072	0	0.03	0.037	0.06	1
HarmonicClosenessCentrality	0.0623	0.076	0	0.039	0.046	0.071	1
BetweennessCentrality	0.0044	0.014	0	0.001	0.001	0.003	0.37
authority	0.0085	0.015	0	0	0	0.019	0.114
hub	0.0008	0.018	0	0	0	0	0.72
ModularityClass	9.1958	8.79	0	2	7	15	38
ClusteringCoefficient	0.9583	2.75	0	0	0.1	0.3	15
PageRank	0.0003	0.001	0	0	0	0	0.022
component no.	0.0164	0.478	0	0	0	0	22
StrongComponent no.	104.63	149.05	0	37	59	85	1010
EigenCentrality	0.277	0.202	0	0.14	0.24	0.363	1

4. RESULTS AND ANALYSIS

Based on the two proposed methods and the structural features of the gate-level netlist, three data sets on 15 benchmarks have been created in total. Using XGBoost learning model, we have evaluated and compared these data sets and their features. We used Jupyter to develop our Python tool on a Core(TM) i5-4200M CPU machine.

4. 1. Statistical Results of the First Data Set

Table 5 summarizes the statistical characteristics of the first data set with 48,722 rows and 18 columns. The rows of this data set contain all 15 netlists of the Trust-Hub benchmarks [14, 15]. Its columns contain 18 features of graph centrality extracted from directed graphs of benchmarks and one column for the label. Statistical characteristics include mean, standard deviation, minimum, maximum and quartile values of each feature.

As shown in Figure 6, there is a significant difference between the mean features of the normal nets and Trojan nets in this data set. The value distribution of different features for Trojan and normal nets has a significant difference in Figure 7. So, these features can be used to detect Trojan nets using a machine learning model.

4.2 Importance of the First Data Set Features and the Accuracy of the Learning Model

Figure shows the importance of the features using the XGBoost

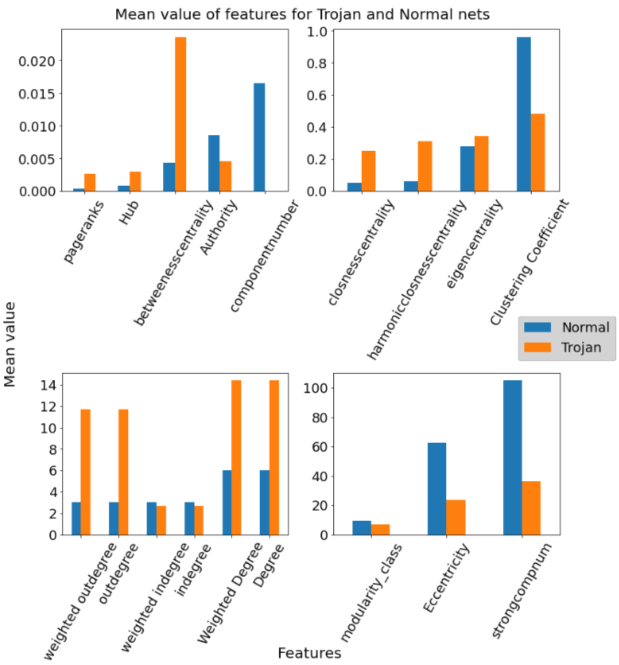

Figure 6. Mean value of features for normal and Trojan nets

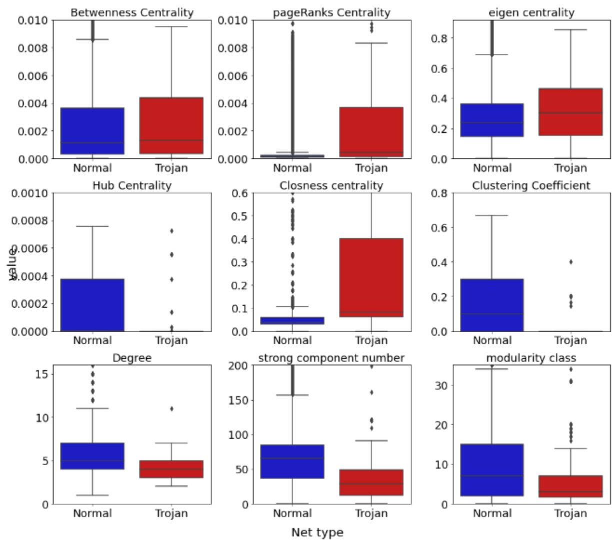

Figure 7. Value distribution of some features in normal and Trojan nets

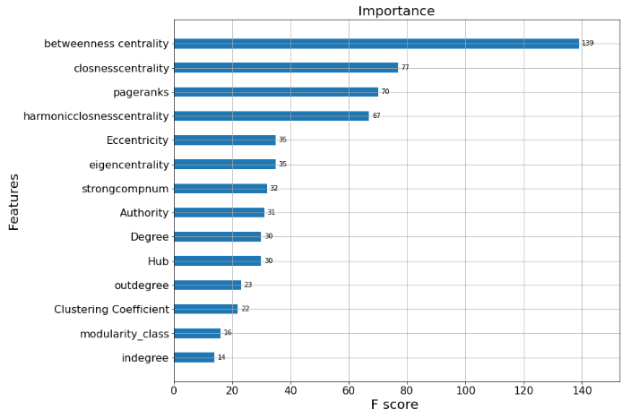

Figure 8. High importance features of the first data set in XGBoost

functions. Sorting these types of features is based on the effectiveness of each feature in improving the F-score value. Figure 9 shows the importance of the features by permutation method using Scikit-learn library. High importance features in XGBoost method are also ranked higher with a slight difference.

Figure 10 shows the importance of the features of this data set. It also shows how each features affects the output, using Shapley values method. Shapley is a unified framework for interpreting predictions that assigns each feature an important value for a particular prediction. According to Shapley values chart, the Hub has the highest importance. The lower value of the Hub per net increases the probability of being a Trojan net. The betweenness centrality feature ranks second and higher value for that means high probability to be Trojan. The betweenness centrality determines how

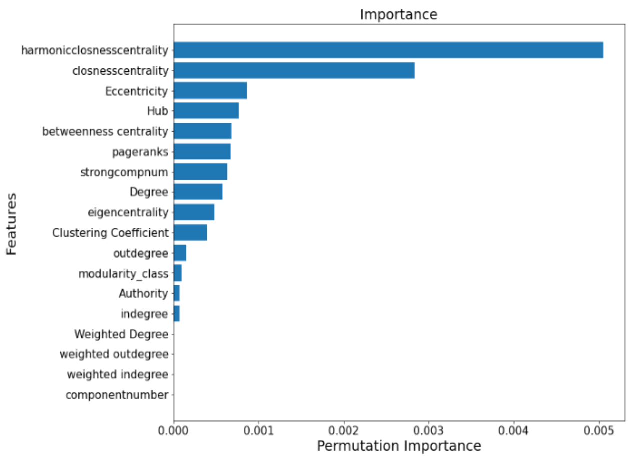

Figure 9. Features of the first data set with permutation and Scikit-learn library

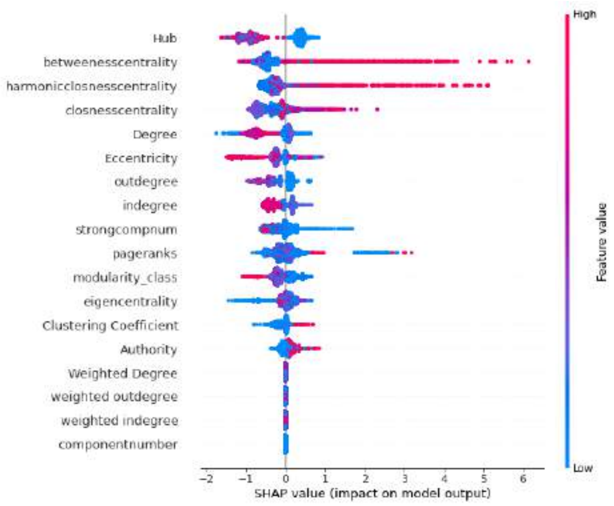

Figure 10. Importance of the features of the first data set by Shapley values

many times a node is in the shortest paths in a graph. Because there is a complex circuit with many inputs before a Trojan net, these nets have higher betweenness centrality in the directed graph. The harmonic closeness centrality is the next important feature. It can be seen that nets with higher centrality features have greater probability of being Trojan nets. This is because Trojan nets are placed farther away from other nets, as a result, their average distance from other nets is greater in directed graph Table 6 and Table 7. show the accuracy of XGBoost learning model trained with the first data set. The experimental results show that the average true positive rate (TPR), and the average true negative rate (TNR) are 66.66 and 99.99%, respectively.

4. 3. Statistical Results of the Second Data Set Table 8 summarizes the statistical characteristics of the second data set. There are 48,321 rows and 32 columns

TABLE 5. Accuracy of classifying the trained learning model with first data set

Class	Precision	Recall	F1-score	Support
Normal nets	1.00	1.00	1.00	14542
Trojan nets	0.96	0.67	0.79	75

TABLE 6. Confusion matrix based on first data set

Actual \ Predicted	Normal	Trojan
Normal nets	14540	2
Trojan nets	25	50

in this data set. The rows of this data set contain all 15 netlists of the benchmarks. Its columns contain 31 gate-level structural features and 1 column for label. Statistical characteristics include mean, standard deviation, minimum, maximum, and quartile values of each feature.

While calculating features such as out-nearestMUX, which indicates the distance of the nearest multiplexer to a net, if there is no multiplexer after a net to the main outputs of the circuit, the value of that feature is set to a constant value (approximately equivalent to the longest path of the circuit).

4. 4. Analysis of the Third Data Set In previous sections, the importance of structural gate-level features and features based on the graph centrality algorithm were discussed. In addition, the effect of each of these features on the accuracy of the learning model was considered. In this section, the third data set that is a combination of these two data sets is examined in terms of the importance of features and the accuracy of the trained learning model.

Figure 11 shows the features of this data set obtained with the XGBoost functions. As shown in this figure, the centrality features of the graph are mostly in higher order than the structural features of the gate-level. Only out-ff-5 that is a gate-level feature is among the top 10 features. The three most important features in this data set are the graph centrality features (PageRank, harmonic closeness centrality, and betweenness centrality) which are far from the others.

As **Error! Reference source not found.** shows, the centrality features of the graph are mostly in higher order compared to others in the third data set with permutation and Scikit-learn library. In this method, out-ff-5, out-nearestMUX, in-nearestPI, and in-nearestFF features, which are structural gate-level features, have been able to be among the top features.

The importance of the features of the third data set with Shapley values is shown in Figure . In this method, graph centrality features are still in higher

TABLE 8. Statistical features of the second data set

Feature	Count	mean	std	min	0.25	0.5	0.75	max
fan-in-1	48321	3.07	1.37	0	2	4	4	6
fan-in-2	48321	6.31	3.12	0	5	6	8	23
fan-in-3	48321	11.55	6.6	0	7	10	16	58
fan-in-4	48321	20.39	13.21	0	11	19	30	129
fan-in-5	48321	34.86	25.18	0	15	31	52	258
in-mux-1	48321	0	0.026	0	0	0	0	2
in-mux-2	48321	0	0.039	0	0	0	0	2
in-mux-3	48321	0	0.053	0	0	0	0	2
in-mux-4	48321	0	0.073	0	0	0	0	2
in-mux-5	48321	0	0.098	0	0	0	0	2
out-mux-1	48321	0	0.035	0	0	0	0	3
out-mux-2	48321	0	0.059	0	0	0	0	3
out-mux-3	48321		0.08	0	0	0	0	3
out-mux-4	48321	0.1	0.12	0	0	0	0	3
out-mux-5	48321	0.01	0.16	0	0	0	0	3
out-ff-1	48321	1.7	37.81	0	0	1	2	2552
out-ff-2	48321	3.24	37.9	0	0	2	4	2552
out-ff-3	48321	5.9	38.2	0	2	4	7	2553
out-ff-4	48321	10.13	39.13	0	4	7	11	2553
out-ff-5	48321	16.54	41.77	0	7	12	18	2553
in-ff-1	48321	0	0.03	0	0	0	0	2
in-ff-2	48321	3.13	2.05	0	2	3	4	15
in-ff-3	48321	6.26	3.887	0	4	6	8	33
in-ff-4	48321	11.17	7.14	0	7	10	15	69
in-ff-5	48321	18.4	12.52	0	11	16	25	139
out-nearestMUX	48321	58.91	42.4	0	14	99	99	99
out-nearestPO	48321	4.76	5.88	0	3	4	6	99
out-nearestDFF	48321	3.15	12.6	0	0	1	3	99
in-nearestMUX	48321	79.37	35.02	0	99	99	99	99
in-nearestPI	48321	2.27	4.05	0	1	2	3	99
in-nearestDFF	48321	10.24	28.8	0	0	1	2	99
net_type	48321	0.01	0.07	0	0	0	0	1

ranks compared to the structural gate-level features. Positive and negative impact of each feature on the output of the learning model can also be seen in this figure.

Table 9 shows the accuracy of XGBoost learning model trained with third data set, which shows better results than all previous methods. Confusion matrix of this learning model is shown in Table 10. The experimental results demonstrate that the average true positive rate (TPR), and the average true negative rate (TNR) become 79.06 and 100.0%, respectively. It shows this trained learning model improves the average TPR, while keeping the average TNR comparable to the existing state-of-the-art methods.

4. 5. Accuracy of Trained Learning Models with Different Data Sets Figure 14 compares the accuracy of the trained learning models based on

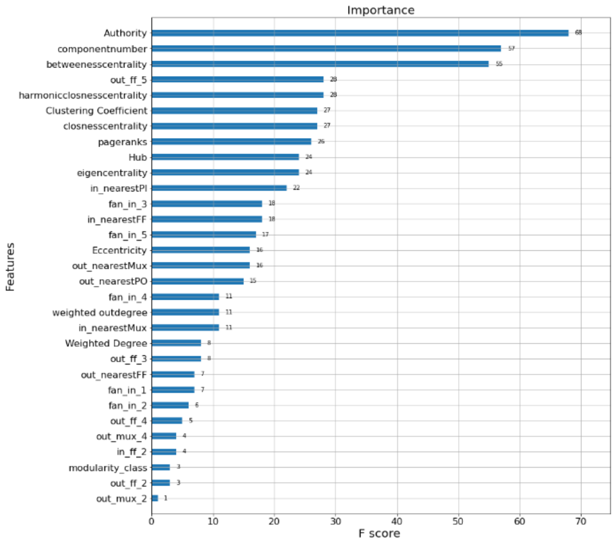

Figure 11. High importance features of the third data set in XGBoost

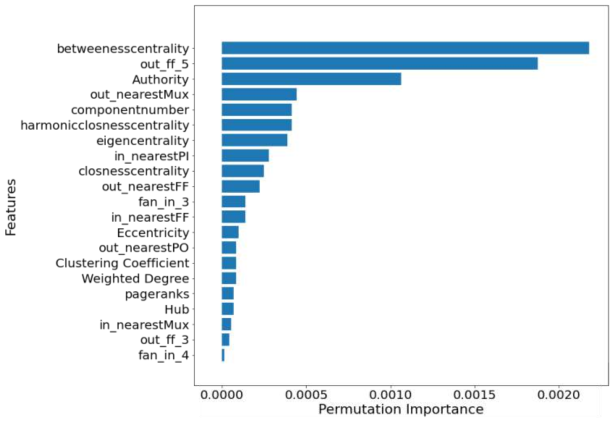

Figure 12. Features of the third data set with permutation and Scikit-learn library

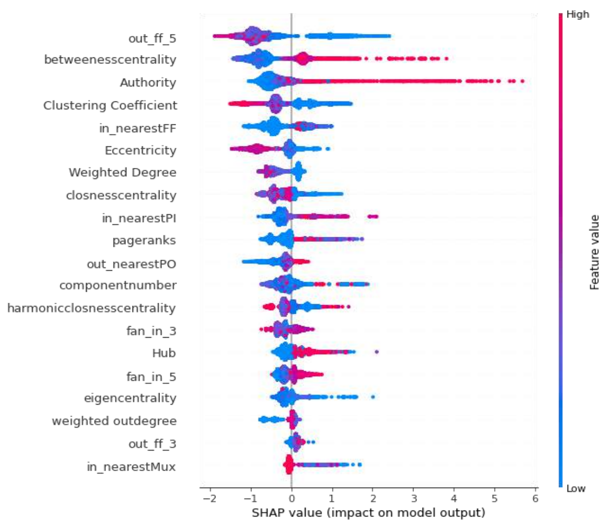

Figure 13. Importance of the features of the third data set by Shapley values

TABLE 9. Accuracy of classifying the trained learning model with third data set

Class	Precision	Recall	F1-score	Support
Normal nets	1.00	1.00	1.00	14400
Trojan nets	1	0.79	0.88	86

TABLE 10. Confusion matrix based on third data set

Predicted / Actual	Normal	Trojan
Normal nets	14400	0
Trojan nets	18	68

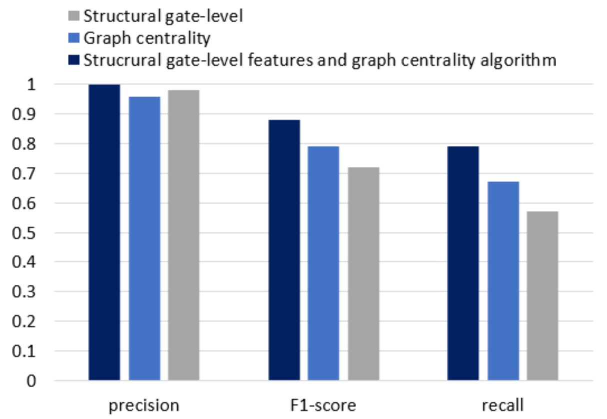

Figure 14. Accuracy of trained learning models with different feature extraction methods

different feature sets. As seen in the figure, the trained learning model has the highest accuracy with a combination of graph centrality and structural gate-level features.

Another method for evaluating performance of binary classification is the Receiver Operating Characteristic (ROC) curve. The performance of binary classifier algorithms is usually measured by parameters called sensitivity or recall. Both of these parameters are combined and displayed as a curve in the ROC diagram. Figure shows ROC diagram of three proposed data sets. As it turns out, the learning model based on combining graph centrality features and structural gate-level features has better ROC with $AUC = 1$.

4. 6. Runtime Overhead Since Hasegawa et al. [12], liu et al. [27] and Kurihara et al. [28] did not report the execution time of each feature for the benchmarks and we did not have access to those functions, we wrote the calculation functions of those features based on the description presented by et al. [12], liu et al. [27] and Kurihara et al. [28] to be able to provide comparison. Some of the functions were too complex with long

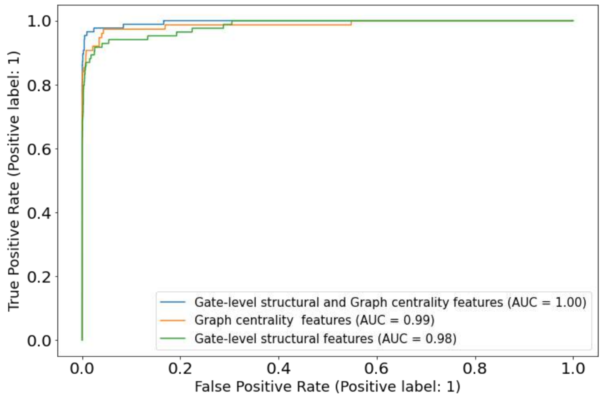

Figure 15. ROC diagrams of trained learning models with three data sets

execution time and motivated us to present graph centrality features to be able to use optimal graph algorithms available in Gephi tool with a very convenient time complexity.

Time complexity of the training phase is directly related to the size of the data set. In all used data sets, the number of rows is the same. Our proposed data set (based on graph centrality features) has a smaller number of features, and as a result, the step of calculating the importance of features and selecting them is done in less time.

5. CONCLUSION AND FUTURE WORKS

In this paper, a method based on directed graphs for extracting features is proposed. The proposed method use Graph Centrality Algorithm and structural gate-level features. To examine the importance and the impact of the extracted features with the proposed method, three types of data sets are created as input to the learning model made with XGBoost. The trained learning models based on these three data sets shows that extracting graph-based features has improved the F1-score by 10% and the ROC by 22%. The combination of these features with the structural gate-level features improved the F1-score by 17.5% and the ROC by 38.5%.

In the proposed method, Gephi tool is used to extract the graph-level features. To integrate the steps of creating a data set and training the learning model and then HT detection, a suitable library in Python can be used to calculate these features. Also, an API can be designed to communicate with Gephi tool.

To improve the accuracy of HT detection, graph embedding methods or graph node classification can be used. In this way, first the directed graph should be extracted. Then, a set of features would be assigned to each nodes in the graph. This set of features can be obtained in the following ways for each node in graph:

- Using the Node2vec method;
- Calculate the structural features of the gate-level and assign these features to graph nodes.

After performing the above steps, we will have a multigraph where a feature vector is assigned to each its node. Thereby, it is possible to use different methods of node classification such as GCN and GraphSAG to classify Trojan nodes.

6. REFERENCES

1. Bhunia, S., Hsiao, M.S., Banga, M. and Narasimhan, S., "Hardware trojan attacks: Threat analysis and countermeasures", ***Proceedings of the IEEE***, Vol. 102, No. 8, (2014), 1229-1247, doi: 10.1109/JPROC.2014.2334493.
2. Goldstein, L.H. and Thigpen, E.L., "Scoap: Sandia controllability/observability analysis program", in Proceedings of the 17th Design Automation Conference., (1980), 190-196, doi: 10.1145/800139.804528.
3. Esfandian, N. and Hosseinpour, K., "A clustering-based approach for features extraction in spectro-temporal domain using artificial neural network", ***International Journal of Engineering,Transactions B: Applications***, Vol. 34, No. 2, (2021), 452-457, doi: 10.5829/IJE.2021.34.02B.17.
4. Chen, T. and Guestrin, C., "Xgboost: A scalable tree boosting system", in Proceedings of the 22nd acm sigkdd international conference on knowledge discovery anionsd data mining. Vol., No. Issue, (2016), 785-794, doi: 10.1145/2939672.2939785.
5. Yang, Y., Ye, J., Cao, Y., Zhang, J., Li, X., Li, H. and Hu, Y., "Survey: Hardware trojan detection for netlist", in 2020 IEEE 29th Asian Test Symposium (ATS), IEEE. , (2020), 1-6, doi: 10.1109/ATS49688.2020.9301614.
6. Hicks, M., Finnicum, M., King, S.T., Martin, M.M. and Smith, J.M., "Overcoming an untrusted computing base: Detecting and removing malicious hardware automatically", in 2010 IEEE symposium on security and privacy, IEEE., (2010), 159-172, doi: 10.1109/SP.2010.18.
7. Zhang, J., Yuan, F., Wei, L., Liu, Y. and Xu, Q., "Veritrust: Verification for hardware trust", ***IEEE Transactions on Computer-Aided Design of Integrated Circuits and Systems***, Vol. 34, No. 7, (2015), 1148-1161, doi: 10.1109/TCAD.2015.2422836.
8. Waksman, A., Suozzo, M. and Sethumadhavan, S., "FANCI: Identification of stealthy malicious logic using boolean functional analysis", in Proceedings of the 2013 ACM SIGSAC conference on Computer & communications security., (2013), 697-708, doi: 10.1145/2508859.2516654.
9. Fyrbiak, M., Wallat, S., Swierczynski, P., Hoffmann, M., Hoppach, S., Wilhelm, M., Weidlich, T., Tessier, R. and Paar, C., "Hal—the missing piece of the puzzle for hardware reverse engineering, trojan detection and insertion", ***IEEE Transactions on Dependable and Secure Computing***, Vol. 16, No. 3, (2018), 498-510, doi: 10.1109/TDSC.2018.2812183.
10. Sullivan, D., Biggers, J., Zhu, G., Zhang, S. and Jin, Y., "Fight-metric: Functional identification of gate-level hardware trustworthiness", in Proceedings of the 51st Annual Design Automation Conference., (2014), 1-4, doi: 10.1145/2593069.2596681.
11. Hasegawa, K., Oya, M., Yanagisawa, M. and Togawa, N., "Hardware trojans classification for gate-level netlists based on machine learning", in 2016 IEEE 22nd International Symposium on On-Line Testing and Robust System Design (IOLTS), IEEE., (2016), 203-206, doi: 10.1109/IOLTS.2016.7604700.

12. Hasegawa, K., Yanagisawa, M. and Togawa, N., "Trojan-feature extraction at gate-level netlists and its application to hardware-trojan detection using random forest classifier", in 2017 IEEE International Symposium on Circuits and Systems (ISCAS), IEEE., (2017), 1-4, doi: 10.1109/ISCAS.2017.8050827.

13. Ye, J., Yang, Y., Gong, Y., Hu, Y. and Li, X., "Grey zone in pre-silicon hardware trojan detection", in 2018 IEEE International Test Conference in Asia (ITC-Asia), IEEE., (2018), 79-84, doi: 10.1109/ITC-Asia.2018.00024.

14. Salmani, H., Tehranipoor, M. and Karri, R., "On design vulnerability analysis and trust benchmarks development", in 2013 IEEE 31st international conference on computer design (ICCD), IEEE., (2013), 471-474, doi: 10.1109/ICCD.2013.6657085.

15. Shakya, B., He, T., Salmani, H., Forte, D., Bhunia, S. and Tehranipoor, M., "Benchmarking of hardware trojans and maliciously affected circuits", ***Journal of Hardware and Systems Security***, Vol. 1, No. 1, (2017), 85-102, doi: 10.1007/s41635-017-0001-6.

16. Hoque, T., Cruz, J., Chakraborty, P. and Bhunia, S., "Hardware ip trust validation: Learn (the untrustworthy), and verify", in 2018 IEEE International Test Conference (ITC), IEEE., (2018), 1-10, doi: 10.1109/TEST.2018.8624727.

17. Salmani, H., "COTD: Reference-free hardware trojan detection and recovery based on controllability and observability in gate-level netlist", ***IEEE Transactions on Information Forensics and Security***, Vol. 12, No. 2, (2016), 338-350, doi: 10.1109/TIFS.2016.2613842.

18. Xie, X., Sun, Y., Chen, H. and Ding, Y., "Hardware trojans classification based on controllability and observability in gate-level netlist", ***IEICE Electronics Express***, Vol. 14, No. 18, (2017), 20170682-20170682, doi: 10.1587/elex.14.20170682.

19. Wang, Y., Han, T., Han, X. and Liu, P., "Ensemble-learning-based hardware trojans detection method by detecting the trigger nets", in 2019 IEEE International Symposium on Circuits and Systems (ISCAS), IEEE., (2019), 1-5, doi: 10.1109/ISCAS.2019.8702539.

20. Kurihara, T. and Togawa, N., "Hardware-trojan classification based on the structure of trigger circuits utilizing random forests", in 2021 IEEE 27th International Symposium on On-Line Testing and Robust System Design (IOLTS), IEEE., (2021), 1-4, doi: 10.1109/IOLTS52814.2021.9486700.

21. Hagberg, A., Swart, P. and S Chult, D., *Exploring network structure, dynamics, and function using networkx*. 2008, Los Alamos National Lab.(LANL), Los Alamos, NM (United States).

22. Brandes, U., "A faster algorithm for betweenness centrality", ***Journal of Mathematical Sociology***, Vol. 25, No. 2, (2001), 163-177, doi: 10.1080/0022250X.2001.9990249.

23. Chen, D., Lü, L., Shang, M.-S., Zhang, Y.-C. and Zhou, T., "Identifying influential nodes in complex networks", ***Physica a: Statistical mechanics and its applications***, Vol. 391, No. 4, (2012), 1777-1787, doi: 10.1016/j.physa.2011.09.017.

24. Rodrigues, F.A., "Network centrality: An introduction", in A mathematical modeling approach from nonlinear dynamics to complex systems. 2019, Springer. 177-196, doi: 10.48550/arXiv.1901.07901.

25. Upstill, T., Craswell, N. and Hawking, D., "Predicting fame and fortune: Pagerank or indegree?", (2003).

26. Jaderyan, M. and Khotanlou, H., "Automatic hashtag recommendation in social networking and microblogging platforms using a knowledge-intensive content-based approach", ***International Journal of Engineering, Transactions B: Applications***, Vol. 32, No. 8, (2019), 1101-1116, doi: 10.5829/IJE.2019.32.08B.06.

27. Liu, Q., Zhao, P. and Chen, F., "A hardware trojan detection method based on structural features of trojan and host circuits", ***IEEE Access***, Vol. 7, (2019), 44632-44644, doi: 10.1109/ACCESS.2019.2908088.

28. Kurihara, T., Hasegawa, K. and Togawa, N., "Evaluation on hardware-trojan detection at gate-level ip cores utilizing machine learning methods", in 2020 IEEE 26th International Symposium on On-Line Testing and Robust System Design (IOLTS), IEEE., (2020), 1-4, doi: 10.1109/IOLTS50870.2020.9159740.

29. Bastian, M., Heymann, S. and Jacomy, M., "Gephi: An open source software for exploring and manipulating networks", in Third international AAAI conference on weblogs and social media., (2009) , doi: 10.13140/2.1.1341.1520.

30. Tarjan, R., "Depth-first search and linear graph algorithms", ***SIAM Journal on Computing***, Vol. 1, No. 2, (1972), 146-160, doi: 10.1137/0201010.

31. Pedregosa, F., Varoquaux, G., Gramfort, A., Michel, V., Thirion, B., Grisel, O., Blondel, M., Prettenhofer, P., Weiss, R. and Dubourg, V., "Scikit-learn: Machine learning in python", ***the Journal of Machine Learning Research***, Vol. 12, (2011), 2825-2830, doi: 10.5555/1953048.2078195.

32. Lundberg, S.M. and Lee, S.-I., "A unified approach to interpreting model predictions", in Proceedings of the 31st international conference on neural information processing systems., (2017), 4768-4777, doi: 10.48550/arXiv.1705.07874.

Persian Abstract

چکیده

پراکندگی موجود در مراحل طراحی تا ساخت مدارهای مجتمع، به حمله‌های جدیدی به نام تروجان سخت‌فزاری در زنجیره تولید مدارهای مجتمع منجر شده است. این حمله‌ها می‌توانند اطلاعات رمزنگاری شده را سرقت کنند، عملکرد مدار را کاهش دهند یا موجب خرابی کلی تراشه شوند. روش‌های مختلفی برای تشخیص یا جلوگیری از تروجان‌های سخت‌افزاری معرفی شده که استفاده از یادگیری ماشین یکی از این روش‌ها بوده که اخیرا مورد توجه بسیار قرار گرفته است. در پژوهش‌های قبلی از ویژگی‌های ساختاری سطح گیت برای ایجاد مجموعه داده در مدل یادگیری ماشین و تشخیص تروجان‌های سخت‌افزاری استفاده شده است. در این مقاله دو روش مبتنی بر گراف‌های جهت‌دار برای استخراج ویژگی‌ها پیشنهاد شده است: روش اول استفاده از معیارهای مرکزیت گراف و روش دوم ترکیب این معیارها با ویژگی‌های ساختاری سطح گیت است. بر اساس این دو روش پیشنهادی و روش استخراج ویژگی‌های ساختاری سطح گیت، در مجموع سه مجموعه داده متفاوت ایجاد شده است. برای بررسی میزان اهمیت و تاثیر ویژگی‌های استخراج شده با روش‌های پیشنهادی و مقایسه آنها با روش استخراج ویژگی‌های سطح گیت، سه نوع مجموعه داده ایجاد شده به عنوان ورودی به مدل یادگیری ساخته شده با XGBoost داده شد. بررسی دقت مدل‌های یادگیری آموزش دیده براساس این سه مجموعه داده نشان داد که روش استخراج ویژگی‌های مبتنی بر مرکزیت گراف، معیار F1-score را به میزان ۱۰ درصد و معیار ROC را به میزان ۲۲ درصد بهبود داده است. ترکیب این ویژگی‌ها با ویژگی‌های ساختاری سطح گیت، معیار F1-score را به میزان ۱۷.۵ درصد و معیار ROC را به میزان ۳۸.۵ درصد بهبود داده است.

IJE TRANSACTIONS A: Basics Vol. 35, No. 07, (July 2022) 1388-1397

International Journal of Engineering

Journal Homepage: www.ije.ir

Effects of KCC-1/Ag Nanoparticles on the Mechanical Properties of Concrete

S. M. Ahmadi[a], A. Honarbakhsh*[b,c], R. Zhiani[d,e], D. Tavakoli[f]

[a] *Department of Civil Engineering, Toos Institute of Higher Education, Mashhad, Iran*
[b] *Department of Civil Engineering, Neyshabur Branch, Islamic Azad University, Neyshabur, Iran*
[c] *New Materials Technology and Processing Research Center, Department of Civil Engineering, Neyshabur Branch, Islamic Azad University, Neyshabur, Iran*
[d] *Department of Chemistry, Neyshabur Branch, Islamic Azad University, Neyshabur, Razavi-Khorasan, Iran*
[e] *New Materials Technology and Processing Research Center, Department of Chemistry, Neyshabur Branch, Islamic Azad University, Neyshabur, Iran*
[f] *Department of Civil Engineering, Shahrekord Branch, Islamic Azad University, Shahrekord, Iran*

PAPER INFO

Paper history:
Received 22 January 2022
Received in revised form 15 April 2022
Accepted 24 April 2022

Keywords:
Concrete
Nano KCC-1/Ag
Nano-SiO2
Mechanical Properties

ABSTRACT

The effect of nano KCC-1/Ag and nano SiO_2 in concrete have been investigated in this study. Nano KCC-1/Ag and nano SiO_2 are synthesized and their characterization was investigated by FTIR, SEM, and TEM analysis. After that, these materials use as cement replacement in 1, 2, and 3 percent amounts. SEM images illustrate the denser structure of KCC-1/Ag nanoparticles. Furthermore, in the FTIR spectra 3640 cm^{-1} is related to C-S-H, which is sharper and more severe in samples with nano KCC-1/Ag and nano SiO_2. The results revealed that nano SiO_2 and nano KCC-1/Ag both improved the microstructure of cement paste and increased the concrete compressive and splitting tensile strength. For comparison the performance of nano KCC-1/Ag and nano SiO_2, the results indicated that nano KCC-1/Ag improved the microstructure of concrete better than nano SiO_2. Hence, it has a better performance in enhancing the strength of concrete. The study showed that the optimal percentage of using nano KCC-1/Ag was 2%.

doi: *10.5829/ije.2022.35.07a.17*

1. INTRUDUCTION

Improving the quality of concrete, as one of the most important building materials, has always been a concern. In recent years, it has been shown that using different pozzolanic materials has improved the quality of concrete [1-4]. After the advent of nanotechnology, their use in building industry was taken into consideration as it was thought that they can assist with the improvement of concrete quality. Building industry will be one of the main consumers of nanoproducts [5]. The impacts of nanomaterials on building materials have been specifically taken into account. Nano metal oxide such as Fe_2O_3, Al_2O_3, TiO_2 and etc were added to concrete separately. The authors nociced that addition of a small dosage of nanoparticles to the mix contributes not only to enhancing mechanical properties of SCC, but this also leads to significant improvements in the durability properties of SCC, in spite of the mprovement of concrete with w/c=0.4 was quite negligible [6]. They noticed tha although nanomaterials such as Au, Pd, Ag and etc. are rarely used in building materials (generally due to their high prices); while, they have strong potentials to remove concrete weaknesses such as high permeability, low compressive strength, cracking, weak ability, and low abrasion resistance. To reach this, SiO_2 is the most important material, which are used in concrete. It gained better compressive and tensile strength, to be more exact it could improve those features by 17% and nearly 15%, respectively [7]. Further, one of the most effective pozzolanic materials used extensively in concrete has been silica fume as it can improve most of concrete properties and also the micro structure of concrete [8]. Given this point, after imtroducing of nano-technology to building industry, attentions were drawn to nano SiO_2.

*Corresponding Author Email Address: amin_honarbakhsh@yahoo.com (A. Honarbakhsh)

Please cite this article as: S. M. Ahmadi, A. Honarbakhsh, R. Zhiani, D. Tavakoli, Effects of KCC-1/Ag Nanoparticles on the Mechanical Properties of Concrete, ***International Journal of Engineering, Transactions A: Basics***, Vol. 35, No. 07, (2022) 1388-1397

Studies on the effect of nano SiO_2 on concrete have remarkably increased and their results are being implemented in building industry. In fact, many researchers have produced new materials based on nano SiO_2. Most of these studies have reported beneficial results such as better setting time, slump, shrinkage and durability [7]. It has also been shown that adding nano SiO_2 might enhance the strength of concrete more than silica fume [9]. This improvement emerges from the pozzolanic activity of nano SiO_2 and improvement of the concrete micro structure. In fact, the pozzolanic activity of nano SiO_2 consumes CH and produces secondary CSH,which increases the quality of concrete [10]. In 2020, Alhawat et al. [11] conducted studies on concrete with different amount of nano SiO_2, diverse surface area and various w/b ratio, which revealed that the optimum amount of these factors could improved performance of concrete. Tavakoli et al. [12] also examined the properties of concrete produced with waste clay brick, as substitute of sand, in combination with nano SiO_2. Their results showed that, although the samples including just waste clay brick cause decreasing the mechanical properties of concrete, the sample containing 25% clay brick with only 1% nano SiO_2 could improve the compressive strength of concrete to around at 16%. Furthermore, Qing et al. [13] investigated the use of nano SiO_2 in cement mortar and compared it with Silica fume. They reported that, while the effectiveness of nano SiO_2 starts from early age, that of Silica fume is in the long term. Thus, to enhance the short-term strength, nano SiO_2 was recommended. It has also been reported that the pozzolanic activity of nano SiO_2 is more than that of Silica fume. Nazari and Riahi [14] examined the mechanical, microstructural and thermal behavior of self compacting concrete, which contains SiO_2 nanoparticles. They concluded that an increase in the ratio of nanoparticles led to increase of resistance against abrasion for the cured samples, which are saturated in water or lime-saturated water. They also argued that this situation was not observed for compressive strength in curing bath. In another study by Heidari and Tavakoli [15], the simultaneous effect of ceramic waste pozzolan and nano SiO_2 was investigated. They revealed that concrete, which was mixed with various percent of waste ceramic alone caused a considerable decrease. As a result, the beneficial mixture was the one with optimum amount of nano SiO_2 and ceramic waste, which improved the concrete features. In their study, the rate of improvement in compressive strength was nearly 12% at 28-days aged, which is lower than our article. Moreover,the results of this study supported the improvement of compressive strength and also water absorption of concrete containing nano SiO_2. Additionally, in other study, they compared impact of nano SiO_2 and Silica fume. It was shown that the effectiveness of nano SiO_2 on strength properties was more than that of silica fume [9]. Gunasekara et al. [16] investigated the effect of nano SiO_2 on high volume fly ash (HVFA) hydrated lime blended concrete. They noticed that utilizing of HVFA with appropriate percent of nano SiO_2 can improved mechanical properties of the mixtures in compared with the control sample. Said et al. [17] examined the effect of colloid nano SiO_2 on concrete incorporating ordinary cement and fly ash. They noticed that nano SiO_2 expedite the hydration process which, in turn, played an important role in achievement of strength at early ages. However, the mixture containing 3 to 6% nano SiO_2 along with 30% fly ash improved mechanical proprties of concrete only a negligible amount compared to control sample. Long et al. [18] showed that suitable or unsuitable dispersion of nano SiO_2 in cement paste plays an important role in its performance. Excessive substitution of nano SiO_2 can cause the agglomeration of particles in cement paste and creates a weak point in concrete, which in turn, reduces the concrete strength. They also revealed that 1% substitution of nano SiO_2 can lead to the maximum compressive strength. They observed that any substitution more than 1% decreases the compressive strength. Serag [19] studied the mechanical properties of high performance concrete with the presence of macro polymer fiber and nano SiO_2. Their result showed that nano SiO_2 increased the splitting tensile strength due to the improvement of the bond between cement paste and aggregates. In another study by Heidari et al. [20] the influence of nano SiO_2 and metakaolin on concrete containing ceramic waste materials was examined. This study revealed that nano metakaolin has a better effect in comparison with SiO_2, wchich could improve the compressive strength of concrete. Also, another research regarded the simultaneous effect of waste materials and nano SiO_2 on roller compactor concrete. This study also indicated that nano SiO_2 improved the compressive strength, splitting tensile strength, water absorption, and abrasion resistance of the concrete [21]. Ltifi et al. [22] also investigated the effect of nano silica on early age and durability properties of cement mortars. The study uncovered that mechanical properties of all the samples had increased compared with the controlvsample. Nazari and Riahi [14] studied the substitution effect of 0 to 5% nano SiO_2 on compressive strength of high performance concrete. They reported that adding nano SiO_2 up to 4% lead to an increase of compressive strength and adding nano SiO_2 more than 4% led to a decrease of compressive strength, which was due to inappropriate dispersion of nano SiO_2 and lack of enough CH for pozzolanic activity. Amin and el-Hassan [23] compared the compressive strength of high performance concrete by using nano Ferrite and SiO_2 with different aggregates including crushed dolomite and granite instead of natural ones. The study unveiled that resistance improved by adding nano ferrite 17% and SiO_2.

Zhang et al. [24] found that concrete mixture containing 15% coal fly ash and 3% NS improved compressive strength nearly15.5%.

Moreover, many researchers have improved the structure of nanomaterials specially nano SiO_2 for using in industries. These studies have also made it possible to obtain new properties in these materials by synthesizing nanomaterial with different shapes, textures, and structures [7].

A new type of nanoparticles Silica (KCC-1), which has a large number of positive aspects, has found by previous researches. The substance has nummerous sinalon groups on the surface of KCC-1, which can carry surface molecules well [25]. On the other hand, nanosilver is widely utilized due to its distinguish features. Including being antibacterial and having several surface active points. Some these materials such as nano KCC-1/Ag have pores in wrinkled forms and special center-radial pore structures with their pore sizes gradually increasing from the center to the surface [26]. These walls, which have been dispersed steadily in three dimensions. This unique structure not only increases the specific surface, but also increases the possibility of access to active sites and pores. Nano KCC-1/Ag was developed by Ouyang et al. [26]. The porous walls of it has expanded in wrinkled form from the center of particles toward outside along with radius. This has created a unique and dandelion-like shape for it. These walls, which have been distributed steadily in three dimensions, have created open pores on the structure. This peerless shape not only increases the specific surface area but also increases the possibility of access to the pores and active sites of it that, in turn, improves the efficiency of it in various applications. Given these points, the use of this nanomaterial in concrete has been under scrutiny.

Nano KCC-1/Ag has been employed in different industries [27]. It has been investigated that KCC-1 is definitely functional substance for producing new materials. For instance, it has high surface area, which could establish numerous connection with other particles, like Ag. In addition to this with regard to economy, the cost of Ag is relatively economic compare to other pricey metals, Such as Au and Pd [28].

Different studies have confirmed the high activity and performance of this material in comparison with nano SiO_2 [26]. However, no study has ever dealt with its application in construction materials such as cement and concrete. This study, aims to address such a gap by studying on the effect of nano KCC-1/Ag on concrete and comparing its effect with that of nano SiO_2. To do this, first, nano KCC-1/Ag and nano SiO_2 were synthesized and then replaced the cement of concrete in 1 to 3% of cement weight. Next, the identification tests such as compressive and splitting tensile strengths were implemented and obtained results were reported.

2. MATREIALS AND METHOD

2. 1. Materials

2. 1. 1. Cement ASTM type II cement was used in this study (Zaveh Torbat Company). Physical and chemical properties of this cement is summarized in Table 1.

2. 1. 2. Aggregates Aggregates were obtained from rock limestone aggregates from Neyshabur mine. All aggregate properties were in accordance with ASTM C33 standard. The physical properties of the aggregate are listed in Table 2.

2. 1. 3. Water In this study, Neyshabur drinking water has been used. The values of chloride, sulfate and pH of the solution are 25 mg/l, 17 m /l and 7, respectively.

2. 1. 4. Superplasticizer Due to the high water absorption of nanomaterials in this study, a suitable superplasticizer was used to maintain the workability of concrete. The superplasticizer is branded Glenium 55p and is based on polycarboxylate. The specifications of this superplasticizer are stated in Table 3.

2. 1. 5. Synthesis of Nano SiO_2 Nano SiO_2 used in this study was extracted via synthesis operation. To synthesize it, 2 ml of tetraethyl orthosilicate was mixed

TABLE 1. Properties of cement

Chemical Properties		Physical Properties	
% SiO_2	20.92	Specific surface area (cm^2/g)	3425
% Al_2O_3	4.61	Sieve Residue 90 μm	0.28
% Fe_2O_3	4.16	Sieve Residue 45 μm	9.24
% CaO	62.10	% Autoclave Expansion	0.10
% MgO	2.75	Initial Setting Time (min)	155
% Na_2O	0.30	Final Setting Time (min)	205
% K_2O	0.59	Specific Gravity (g/cm^3)	3.18
% SO_3	2.20	Free CaO	1.04
% LSF	94.24	3-day Compressive Strength	315
% CL	0.017	7-day Compressive Strength	386
% LOI	1.50	28-day Compressive Strength	520

TABLE 2. Physical properties of aggregate

Property	Sand	Gravel
Density (kg/m^3)	2.58	2.64
Water Absorption (%)	2.12	1.01
Bulk Density (kg/m^3)	1710	1530
Los Angeles (%)	-	21.34

TABLE 3. Properties of the superplasticizer admixture

Aspect	Relative Density	pH	Chloride Ion Content
Dark brown free-flowing liquid	1.20±0.02 at 25 °C	6-7	< 0.2%

with 5 ml ethanol. Then, it was put on the Stirrer and was exposed at 60 °C for reflux operation.

After half an hour, 2 ml ammonium was added to the solution and the reflux process restarted for two hours. Finally, after separation of sediments from the liquid by centrifuge machine and drying particles at 60 centigrade degrees in the oven, nano SiO_2 was obtained. To examine the synthesized nano particles, FTIR was utilized.

2. 1. 6. Synthesis of Nano KCC-1/Ag To synthesize Nano-Kcc-1/Ag, first, 0.3 g of Urea along with 30 ml deionized water was poured in a balloon and then was placed in the ultrasonic device for one hour so that the two materials would be mixed thoroughly. The ultrasonic device makes magnetic impacts in the nano scale and can mix the two particles completely. In the next stage, 0.5 g trimethyl hexadecyl ammonium bromide was combined with 0.75 ml 1-pentanol and 30 ml cyclohexane. Then, this mixture was added to the previous solution after one hour (solution 1). Then, 1.35 ml tetraethyl orthosilicate was added to the mixture of urea and deionized water and this new mixture was placed in the ultrasonic device once more (solution 2). Altogether , the mixture(solutions 1 and 2) was put into the stirrer device for reflux operation for two hours. The rotation speed of reflux was on 5 mod and the operation started at 120 °C for 5 hours. After 5 hours, the sedimentation was obtained. The precipitates washed and centrifuged several times. At the end, The sediments was put into the oven at 60 °C to dry to obtain KCC-1 nanoparticle. For increasing the density of dandelion branches and the specific surface of nano-KCC-1, silver cover was used. After preparation of nano-KCC-1, some experiment was done to place silver nitrate nanoparticles on it. For that, $AgNO_3$ was used. In this substance, nitrate was removed through a chemical process and only silver remains. To put silver on nano-KCC-1, 0.5 g nano-KCC-1 was mixed with 0.14 ml (3- aminopropyl) trimethoxysilane and 100 ml toluene and 0.1 g $AgNO_3$. Then, the mixture was stirrered at 45 °C for the reflux operation. The reflux was done in an environment incorporating nitrogen gas so that intended activities would be done ideally. After 12 hours, the sedimentation was obtained completely. In the next stage, the sedimentation separated from the solution by centrifugation. It should be pointed out that KCC-1 nanoparticles were in suspension and were changed to finer particles in the reflux process. After the separation stage, the sedimentation were put into an oven to dry at 60 °C. Finally, KCC-1/Ag nanoparticle was resulted.

2. 1. 7. Tests Compressive strength of samples based on BS 1881 standard and their splitting tensile strength based on ASTM C496 standard at 7, 28, and 90 days were estimated. Perkin-Elmer FTIR with resolution of 4 cm^{-1} in 64 scan mode was used to check the bending bands vibrational stretching. Moreover, to examine the nanomaterials structure with TEM, Philips CM10 at 100 KV was utilized. Finally, SEM was employed to study the microstructure of concrete and nanomaterials. The SEM image was given to confirm the formation of nano SiO_2 and KCC-1/Ag nanoparticles. Figure 1 represents the SEM image of synthesized nano SiO_2. As we can see, the produced nano SiO_2 has a steady and consistent structure with particles diameter of almost 40 nm. In Figure 2, apparently reveal the formation of the KCC-1/Ag nano material. As it is clear, the particles have a steady distribution and a dandelion sophere-shape. To compare, the KCC-1/Ag nanoparticles have steadier and denser structure than SiO_2 nanopaticles. Moreover, for higher resolution TEM image was taken as is shown in Figure 3. TEM image illustrates the Dandelion-shaped structure, which could provide a high amount of bonds because of so many branches. To know better about the performance of nano KCC-1/Ag, some tests were implemented on concrete microstructure. Since the

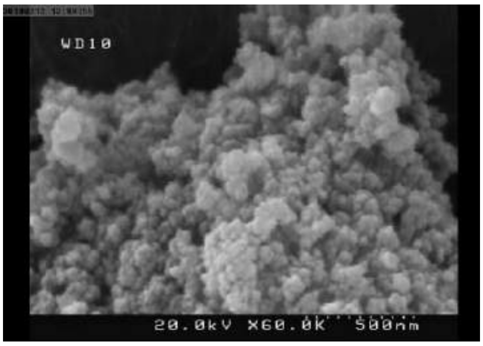

Figure 1. SEM image of nano SiO_2 ,at 500nm resolution

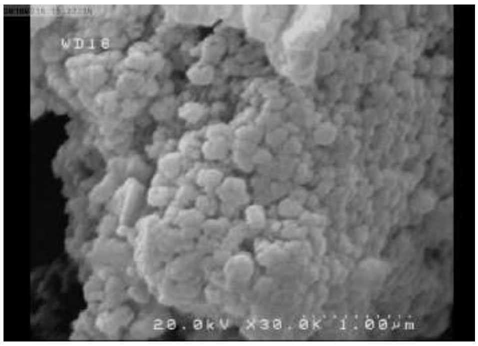

Figure 2. SEM image of nano KCC-1/Ag, at 1 µm resolution

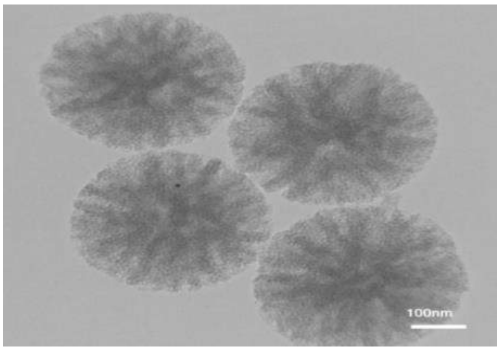

Figure 3. TEM image of nano KCC-1/Ag, at 100 nm resolution

optimal percentage was determined to be 2%, the identification tests of microstructure were done on the samples incorporating 2% nanomaterials at 28 days of age.

2. 2. Method In this study, nanomaterials replaced cement in 1, 2, and 3 percent. Moreover, seven mix designs with nano SiO_2 (CN), 3 ones with replacement of nano KCC-1A/g (CK), and one mix as the control sample (C) were prepared. Table 4 presents the mix designs.

For each mix design, 18 samples including 9 cylinder ones (30×15) and 9 cubic ones (10cm×10cm×10cm) were made. All the three ones were used to determine strength at one of the ages of 7, 28, and 90 days. Samples were created based on ASTMC42 standard and they were then cured in lime saturated water pool at 23±2 °C. It should be pointed out that given the high specific surface area of nanomaterials, the selected nanomaterial was mixed with part of the mix water using a stirrer at 120 RPM so that the agglomeration of materials in concrete would be hindered. In addition, in light of the high water absorption of nanomaterials and slump reduction of concrete, a superplasticizer was added to mixes.

3. RESULTS AND DISCUSSION

3. 1. Comperessive and Splitting Tensile Strengths Figure 4 represents compressive strength results at 7, 28, and 90 days. The compressive strength obtained in this study for 7 days was between

TABLE 4. Mix designs

Mix Name	Constituents (kg/m³)						
	Gravel	Sand	Water	Cement	Nano KCC-1/Ag	Nano SiO_2	Water reducer
C	525	1226	195	425	-	-	-
CN1	525	1226	195	420.75	-	4.25	2.5
CN2	525	1226	195	417	-	8.5	3.3
CN3	525	1226	195	412.25	-	12.75	4.3
CK1	525	1226	195	420.75	4.25	-	2.5
CK2	525	1226	195	417	8.5	-	3.3
CK3	525	1226	195	412.25	12.75	-	4.3

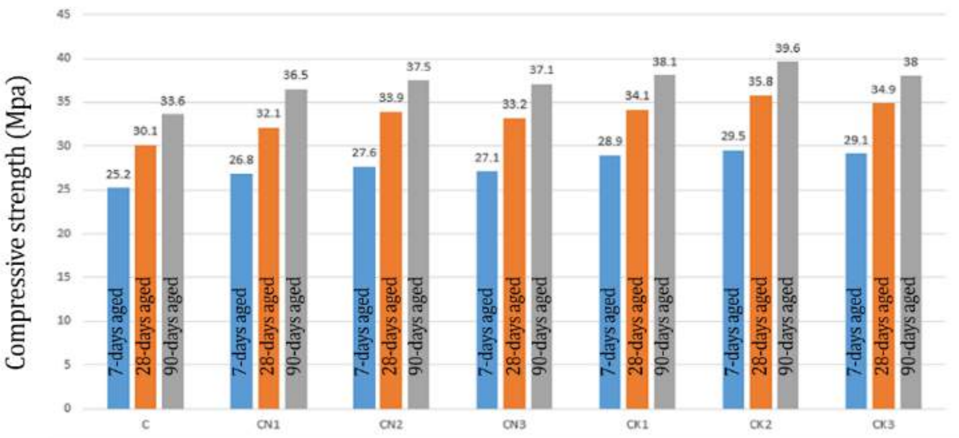

Figure 4. Compressive strength of mixes C: control sample, CN: (samples containing 1,2 and 3% nano SiO_2), CK: (samples containing1,2 and 3% nano KCC-1/Ag)

25.2MPa and 29.5MPa; for 28 days was between 30.1MPa and 35.8MPa; and for the 90 days was between 33.6MPa and 39.6MPa.

These results indicate that adding nano SiO_2 and nano KCC-1/Ag increased the compressive strength of concrete in all ages. However, this increase was more for nano KCC-1/Ag. Thus, this material had a better performance in comparison with nano SiO_2.

The highest increase of strength was observed in the sample incorporating 2% of nano KCC-1/Ag at 90 days (39.6 MP). The strength increased at 90 days for CN1, CN2, CN3, CK1, CK2, and CK3 in comparison with the control sample was 8.63%, 11.60%, 10.41%, 13.39%, 17.85%, and 13.09%, respectively. The same increase in nano SiO_2 samples was also reported in the previous studies. The reason for this increase is related to the pozzolanic activity of these materials as well as their filling effects. They can improve the microstructure of cement paste through their reaction with CH and production of secondary CSH. Because the compressive strength of samples containing 3% of nano SiO_2 and nano KCC-1/Ag showed a little reduction of strength compared with the ones with 2%, it can be concluded that the optimal percentage is 2%. This can be attributed to some reasons. First, adding high amount of nanomaterial causes CH to be used completely in hydration products. Thus, the extra nanomaterial remains in concrete as an inactive substance which, in turn, triggers defects and inconsistency in concrete. On the other hand, the high amount of nano material cannot be mixed in concrete very well (due to its high specific surface area) and some of the material may remain as agglomerate. This can damage the consistency of concrete.

Furthermore, the high water absorption of nanomaterial can create small cracks in concrete and negatively affect its strength. In samples with 2% of nano SiO_2, the increase rate of strength at 7, 28, and 90 days of age, in comparison with the control sample, was 6.34, 12.62%, and 11.60% respectively. This shows the suitable performance of nano SiO_2 at 28 days of age. In some previous studies, the suitable performance of nano SiO_2 was reported to be at 7 days of age. This might be due to the smaller size of nano SiO_2 and its higher specific surface area in those studies.

In addition, for the sample with 2% of nano KCC-1/Ag, the increase of strength at 7, 28, and 90 days of age was 17.06%, 18.93%, and 17.85%, respectively. In these samples, the best performance was also related to the age of 28 days. In comparison with Tavakoli et al. [12] paper,which investigated in the effect of adding waste clay brick and nano SiO_2 to concrete mixtures, our result is higher. In fact, they figured out that the sample containing 25% waste clay brick and only 1% nano SiO_2 could correct the compressive strength of concrete approximately 16%. In other works, Heidari et al. [15] studied the properties of concrete, which included ground ceramic powder and nano SiO_2. Their study indicated that, the samples containing only waste ceramic decreased the mechanical properties, while the sample including 10% waste ceramic and 1% nanoSiO_2 could increase the strength around 12% in comparison with control sample, which is fewer than our result.

Moreover, Heidari et al. [20] in another paper found that the concrete sample containing nano metakaolin have better influene on concrete strengths rather than the one containing nano SiO_2. However, the improvemen of ratio in comparison with our study is quite negligible.

Zhang et al. [24] showed that the concrete mixture containing 15% coal fly ash and only 3% nano SiO_2 improved compressive strength at around 15.5%.

The compressive strength of the 90 days sample containing 2% nano KCC-1/Ag in comparison with the same sample containing 2% of nano SiO_2 showed an almost 5.6% increase of strength.

In general, the samples with nano KCC-1/Ag performed better than those with nano SiO_2 and this was due to their higher contact surface because of their dandelion structure. Higher contact level leads to more activity and better dispersion of the cement paste microstructure. This can affect all properties of concrete positively.

Figure 5 shows the results pertaining to splitting tensile strength. This strength in samples of 7 days was from 2.21MPa to 2.58MPa; for those of 28 days was from 3.13MPa to 3.67MPa; and for those of 90 days was 3.52MPa to 4.12MPa. The highest splitting tensile strength was observed in the sample with CK2.

This increase of splitting tensile strength at 90 days for CN1, CN2, CN3, CK1, CK2, and CK3 in comparison with the control sample was 9.37%, 12.21%, 11.07%, 10.51%, 17.04%, and 13.92%, respectively. The trend of splitting tensile strength is the same of that for compressive strength. Moreover, Fallah et al. [29] tested the splitting tensile strength of nano-SiO_2 concrete. When 3% nano-SiO_2 replaced cement, the tensile strength of Nanosilica modified concrete was improved by 16% than that of ordinary concrete. While in our study the strengthening effect of adding nano KCC-1/Ag on the splitting tensile strength of concrete was 17.04%. Therefore, it proves that KCC-1/Ag is more effective than nano SiO_2. Moreover, Tavakoli et al. [21] investigated in effect of waste concrete and glass along with nano SiO_2 in roller-compacted concrete. They noticed that splitting tensile strength of the concrete, which contains 40% glass and 0.7% nano silica, increased around 12.67%. while the mixture, containing 40% waste concrete and 0.7% nano silica was approximately equal to that of control sample.

In the samples with nanomaterials, an increase of splitting tensile strength was observed compared with

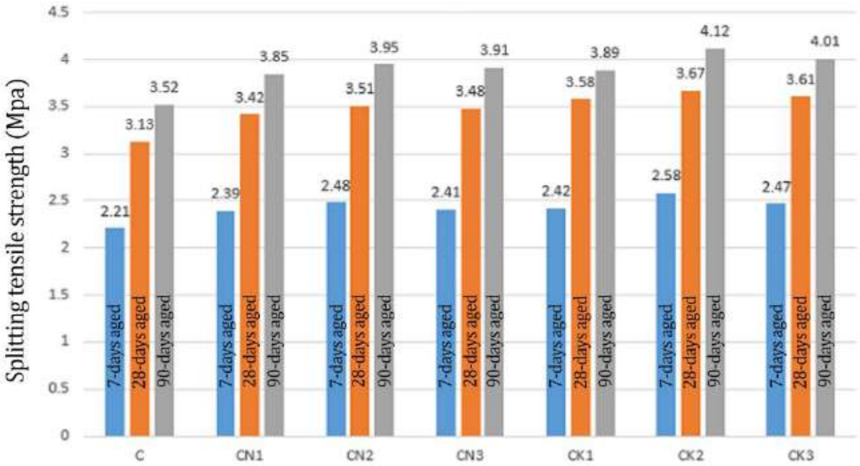

Figure 5. Splitting tensile strength of mixes C: control sample, CN: (samples containing 1,2 and 3% nano SiO_2), CK: (samples containing 1,2 and 3% nano KCC-1/Ag)

3. 2. SEM Image Analysis To examine the effect of nanomaterials on concrete, SEM was used. Figure 6 shows the images prepared from control samples with 2% of nano SiO_2 and 2% of nano KCC-1/Ag. As the photos show, in the control sample, porosity is easily observable.

Adding nanomaterials to concrete and implementation of pozzolanic activity leads to the production of secondary C-S-H and also more reduction in concrete pores. These, in turn, make the concrete structure denser, more steady, and with a higher quality. Comparing the samples with nano SiO_2 and nano KCC-1/Ag, it is noticed that the sample with nano KCC-1/Ag could produce a denser cement paste largely due to its higher activity. As Ouyang et al. [26] obtained the same structure in their research.

Consistency in concrete structure and reduction in pores in comparison with the sample containing nano SiO_2 is clearly observable in this sample. Using nano KCC-1/Ag made the concrete structure denser and as a result, pores, CH, and ettringite are not visible in the photo. In the figure, in fact, we can clearly observe the high activity of nano KCC-1/Ag and the reason for strength increase in samples incorporating nano KCC-1/Ag.

3. 3. FTIR Image Analysis Figure 7 shows a comparison of the three spectra of samples (a) of the control sample without nanoparticles (b) of the sample with SiO_2 nanoparticles and (c) of the sample with nanoparticles of KCC1 / Ag**.**

Figure 7(a, b and c) shows similar indexes for cement matrices as well. The pertinent peak is at 1425cm^{-1} limit and small ones between 800 and 790cm^{-1} are related to carbonate bonds. Bands related to the spectrum between 3434- 3430cm^{-1} are also connected with the hydrogen bond of OH in molecular and chemical water. Furthermore, the peak at 1090cm^{-1} limit belongs to the sulfate bonds in cement paste. But the most important peak that is related to hydrated silicate happens at almost 1000cm^{-1}.

As the Figure 7 indicate, the peak at 3640cm^{-1} related to C-S-H is sharper and more severe in samples with nano KCC-1/Ag and nano SiO_2.

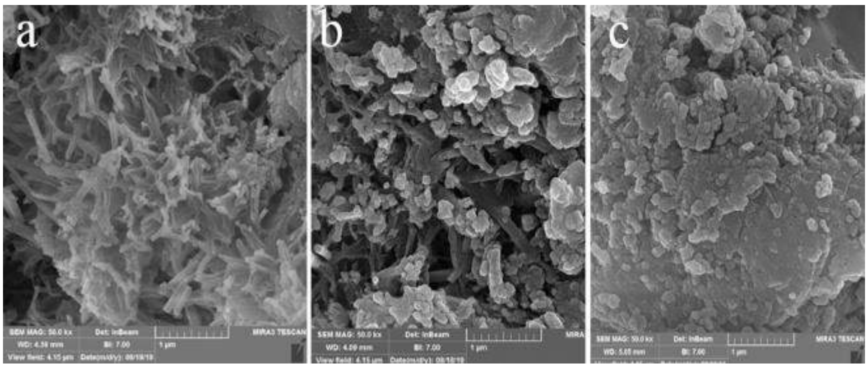

Figure 6. SEM: (a) Control concrete sample (b) nano SiO_2 concrete sample (c) nano KCC-1/Ag concrete sample

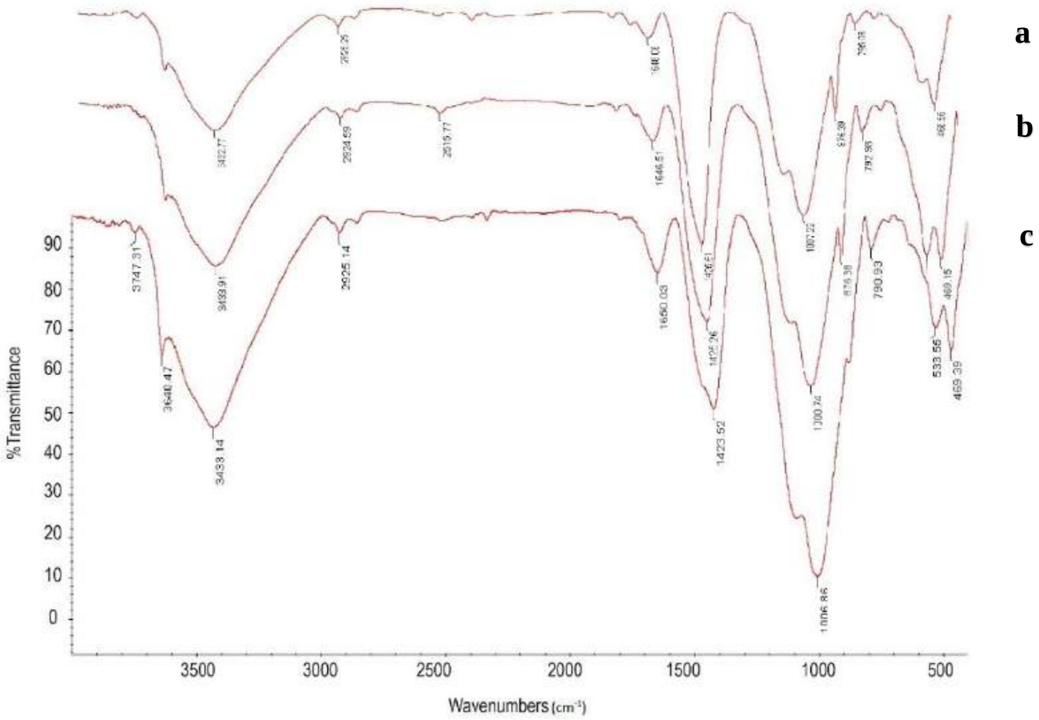

Figure 7. FTIR analysis: (a) Control concrete sample (b) nano SiO_2 concrete sample (c) nano KCC-1/Ag concrete sample

Additionally, the peak in the sample containing nano KCC-1/Ag is sharper than the peak in the sample containing nano SiO_2. This is related to the use of $Ca(OH)_2$ and its turn into C-S-H gel through the pozzolanic activity of nanomaterials in concrete. As it also observed, the C-S-H rate in samples with nano KCC-1/Ag is more than that in the samples with nano SiO_2 and also the control sample.

As it was already mentioned, more production of secondary C-S-H leads to the creation of a denser concrete and an increase of strength and other properties of concrete. This confirms the high activity of nano KCC-1/Ag and its desirable performance in concrete. No significant difference was observed in other peaks.

Additionally, the peak between 790-793cm^{-1} indicates the formation of Si-O-Si bond and the peak at 469cm^{-1} is related to the splitting tensile vibration of Si-O. The resulted spectrum is in line with that the previously conducted studies. This, in fact, confirms the accuracy and correctness of synthesis process [20].

4. CONCLUSION

While there are various researches about nano SiO_2 and KCC-1/Ag, this article has investigated the effects of them in concrete and compared them. To achieve this, nano KCC-1/Ag and nano SiO_2 were used as a cement replacement with 1 to 3 percent, then the compressive strength, splitting tensile strength, and the microstructure of concrete were examined.

The results uncovered that:

- Both Nano SiO_2 and nano KCC-1/Ag enhanced the microstructure of concrete as they can reduce the porosity and defects of concrete. However, the performance of nano KCC-1/Ag was better than that of nano SiO_2 largely due to its high activity and also its dandelion-like structure.
- In general, the Pozzolanic activity of nano KCC-1/Ag was more than that of nano SiO_2. The KCC-1/Ag nanoparticles increased the concrete compressive and splitting tensile strengths at 7 and 90-day of age. Also, an increase of compressive strength by 19% compared to the control sample was reported. This amount of increase was more than that of nano SiO_2. Hence, this material has a better performance in concrete compared with nano SiO_2.
- Observations of SEM images indicate the high activity of nano KCC-1/Ag. Denser and more steady structure of the samples containing nano KCC-1/Ag is apparent when compared with the control sample and the one containing nano SiO_2.
- The obtained optimal percentage for using nano KCC-1/Ag in concrete was 2% of replacement. Higher percentages showed weaker performance.

- Since one of the main positive aspects of KCC-1/Ag nanoparticles is being antibacterial, it could use mostly in medical buildings.
- In compare with other pricey metals, Ag is nearly economic to use in construction industry.
- Due to having dandelion-shape, KCC-1/Ag nanoparticles are able to establish numerous connection, wchich result better density in mixtures.

Given these findings related to nano KCC-1/Ag and its high activity in concrete, it may be contended that the use of this material in concrete is desirable and further studies need to be conducted in this regard.

5. REFRENCES

1. Hossain, M., Karim, M., Hasan, M., Hossain, M. and Zain, M., "Durability of mortar and concrete made up of pozzolans as a partial replacement of cement: A review", ***Construction and Building Materials***, Vol. 116, (2016), 128-140, doi: 10.1016/j.conbuildmat.2016.04.147.
2. Borzouyi Kutenayi, S., Kiahosseini, S.R. and Talebpour, M.H., "The effect of caspian sea water on corrosion resistance and compressive strength of reinforced concrete containing different SiO_2 pozzolan", ***International Journal of Engineering***, ***Transactions A: Basics,*** Vol. 30, No. 10, (2017), 1464-1470, doi: 10.5829/ije.2017.30.10a.06
3. Heidarzad Moghaddam, H., Maleki, A. and Lotfollahi-Yaghin, M., "Durability and mechanical properties of self-compacting concretes with combined use of aluminium oxide nanoparticles and glass fiber", ***International Journal of Engineering***, ***Transactions A: Basics***, Vol. 34, No. 1, (2021), 26-38, doi: 10.5829/ije.2021.34.01a.04.
4. Delaram, F., Mohammadi, Y. and Adlparvar, M., "Evaluation of the combined use of waste paper sludge ash and nanomaterials on mechanical properties and durability of high strength concretes", ***International Journal of Engineering***, ***Transactions A: Basics***, Vol. 34, No. 7, (2021), 1653-1666, doi: 10.5829/IJE.2021.34.07A.10.
5. Bartos, P.J., Nanotechnology in construction: A roadmap for development, in Nanotechnology in construction 3. 2009, Springer.15-26. doi: 10.1007/978-3-642-00980-8_2
6. Joshaghani, A., Balapour, M., Mashhadian, M. and Ozbakkaloglu, T., "Effects of nano-TiO_2, nano-Al_2O_3, and nano-fe2o3 on rheology, mechanical and durability properties of self-consolidating concrete (scc): An experimental study", ***Construction and Building Materials***, Vol. 245, (2020), 118444, doi: 10.1016/j.conbuildmat.2020.118444.
7. Zhuang, C. and Chen, Y., "The effect of nano- SiO_2 on concrete properties: A review", ***Nanotechnology Reviews***, Vol. 8, No. 1, (2019), 562-572, doi: 10.1515/ntrev-2019-0050.
8. Siddique, R., "Utilization of silica fume in concrete: Review of hardened properties", ***Resources, Conservation and Recycling***, Vol. 55, No. 11, (2011), 923-932, doi: 10.1016/j.resconrec.2011.06.012.
9. Tavakoli, D. and Heidari, A., "Properties of concrete incorporating silica fume and nano- SiO_2", ***Indian Journal of Science and Technology***, Vol. 6, No. 1, (2013), 3946-3950, doi: 10.17485/ijst/2013/v6i1/30569.
10. Norhasri, M.M., Hamidah, M. and Fadzil, A.M., "Applications of using nano material in concrete: A review", ***Construction and Building Materials***, Vol. 133, (2017), 91-97, doi: 10.1016/j.conbuildmat.2016.12.005.
11. Alhawat, M., Ashour, A. and El-Khoja, A., "Properties of concrete incorporating different nano silica particles", ***Materials Research Innovations***, Vol. 24, No. 3, (2020), 133-144, doi: 10.1080/14328917.2019.1616140.
12. Tavakoli, D., Heidari, A. and Pilehrood, S.H., "Properties of concrete made with waste clay brick as sand incorporating nano sio^ sub 2", ***Indian Journal of Science and Technology***, Vol. 7, No. 12, (2014), 1899, doi: 10.17485/ijst/2014/v7i12.1.
13. Qing, Y., Zenan, Z., Deyu, K. and Rongshen, C., "Influence of nano-SiO_2 addition on properties of hardened cement paste as compared with silica fume", ***Construction and Building Materials***, Vol. 21, No. 3, (2007), 539-545, doi: 10.1016/j.conbuildmat.2005.09.001.
14. Nazari, A. and Riahi, S., "Microstructural, thermal, physical and mechanical behavior of the self compacting concrete containing SiO_2 nanoparticles", ***Materials Science and Engineering: A***, Vol. 527, No. 29-30, (2010), 7663-7672, doi: 10.1016/j.msea.2010.08.095.
15. Heidari, A. and Tavakoli, D., "A study of the mechanical properties of ground ceramic powder concrete incorporating nano-SiO_2 particles", ***Construction and Building Materials***, Vol. 38, (2013), 255-264, doi: 10.1016/j.conbuildmat.2012.07.110.
16. Gunasekara, C., Sandanayake, M., Zhou, Z., Law, D.W. and Setunge, S., "Effect of nano-silica addition into high volume fly ash–hydrated lime blended concrete", ***Construction and Building Materials***, Vol. 253, (2020), 119205, doi: 10.1016/j.conbuildmat.2020.119205.
17. Said, A.M., Zeidan, M.S., Bassuoni, M. and Tian, Y., "Properties of concrete incorporating nano-silica", ***Construction and Building Materials***, Vol. 36, (2012), 838-844, doi: 10.1016/j.conbuildmat.2012.06.044.
18. Long, W.-J., Xiao, B.-X., Gu, Y.-C. and Xing, F., "Micro-and macro-scale characterization of nano-SiO_2 reinforced alkali activated slag composites", ***Materials Characterization***, Vol. 136, (2018), 111-121, doi: 10.1016/j.matchar.2017.12.013.
19. Serag, M.I., Yasien, A.M., El-Feky, M.S. and Elkady, H., "Effect of nano silica on concrete bond strength modes of failure", ***International Journal of GEOMATE,*** Vol. 12, (2017), 2892-2899, https://geomatejournal.com/geomate/article/view/738.
20. Heidari, A., Tavakoli, S. and Tavakoli, D., "Reusing waste ceramic and waste sanitary ware in concrete as pozzolans with nano-silica and metakaolin", ***International Journal of Sustainable Construction Engineering and Technology***, Vol. 10, No. 1, (2019), doi: 10.30880/ijscet.2019.10.01.006.
21. Tavakoli, D., Dehkordi, R.S., Divandari, H. and de Brito, J., "Properties of roller-compacted concrete pavement containing waste aggregates and nano SiO_2", ***Construction and Building Materials***, Vol. 249, (2020), 118747, doi: 10.1016/j.conbuildmat.2020.118747.
22. Ltifi, M. and Zafar, I., "Influence of nano-silica on early age and durability properties of cement mortars", ***Advances in Cement Research***, Vol. 33, No. 9, (2021), 386-397, doi: 10.1680/jadcr.19.00157
23. Amin, M. and Abu el-Hassan, K., "Effect of using different types of nano materials on mechanical properties of high strength concrete", ***Construction and Building Materials***, Vol. 80, (2015), 116-124, doi: 10.1016/j.conbuildmat.2014.12.075.
24. Zhang, P., Sha, D., Li, Q., Zhao, S. and Ling, Y., "Effect of nano silica particles on impact resistance and durability of concrete containing coal fly ash", ***Nanomaterials***, Vol. 11, No. 5, (2021), 1296, doi: 10.3390/nano11051296.
25. Hongtao, C., Jiaqi, C., Dong, Y., Miao, Y., Qing, L. and Jingru, Z., "Preparation and application of methimazole molecularly imprinted polymer based on silver-loaded dendritic fiber-type silica", ***RSC Advances***, Vol. 11, No. 22, (2021), 13446-13457, doi: 10.1039/D1RA00958C.

26. Ouyang, M., Wang, Y., Zhang, J., Zhao, Y., Wang, S. and Ma, X., "Three dimensional ag/kcc-1 catalyst with a hierarchical fibrous framework for the hydrogenation of dimethyl oxalate", ***RSC Advances***, Vol. 6, No. 16, (2016), 12788-12791, doi: 10.1039/C5RA26602E.

27. Shabir, J., Rani, S., Sharma, M., Garkoti, C. and Mozumdar, S., "Synthesis of dendritic fibrous nanosilica over a cubic core (csio 2@ dfns) with catalytically efficient silver nanoparticles for reduction of nitroarenes and degradation of organic dyes", ***RSC Advances***, Vol. 10, No. 14, (2020), 8140-8151, doi: 10.1039/D0RA00402B.

28. Sadeghzadeh, S.M., Zhiani, R. and Emrani, S., "A versatile supported silver for heterogeneously catalysed processes: Synthesis of 3-acyloxylindolines solvent-free conditions", ***Applied Organometallic Chemistry***, Vol. 32, No. 3, (2018), e4130, doi: 10.1002/aoc.4130.

29. Fallah, S. and Nematzadeh, M., "Mechanical properties and durability of high-strength concrete containing macro-polymeric and polypropylene fibers with nano-silica and silica fume", ***Construction and Building Materials***, Vol. 132, (2017), 170-187, doi: 10.1016/j.conbuildmat.2016.11.100.

Persian Abstract

چکیده

اثر نانو KCC-1/Ag و مقایسه آن با نانو SiO_2 در بتن در این مطالعه بررسی شده است. برای این منظور ابتدا نانو KCC-1/Ag و نانو SiO_2 در آزمایشگاه سنتز شده و سپس تست‌های شناسایی مانند FTIR، SEM و TEM بر روی نمونه‌های سنتز شده اجرا شده اند. پس از آن، این مواد به عنوان جایگزین سیمان در مقادیر ۱، ۲ و ۳ درصد استفاده گردیده است. مقاومت فشاری، مقاومت کششی شکست، FTIR و SEM بر روی نمونه‌ها انجام شده تا اثربخشی نانو KCC-1/Ag و نانو SiO_2 بر خواص بتن بررسی شود. نتایج نشان داد که نانو SiO_2 و نانو KCC-1/Ag هر دو ریزساختار خمیر سیمان را بهبود بخشیدند و مقاومت کششی فشاری و کششی بتن را افزایش دادند. با مقایسه عملکرد نانو KCC-1/Ag و نانو SiO_2، نتایج به‌دست‌آمده نشان داد که نانو KCC-1/Ag ریزساختار بتن را بهتر از نانو SiO_2 بهبود می‌بخشد. از این رو عملکرد بهتری در افزایش مقاومت بتن دارد. این مطالعه نشان داد که درصد بهینه استفاده از نانو KCC-1/Ag ۲درصد است.

IJE TRANSACTIONS A: Basics Vol. 35, No. 07, (July 2022) 1398-1415

International Journal of Engineering

Journal Homepage: www.ije.ir

Vibration Analysis of Double Deck Floating Roof of Storage Tank in Cases of Tube, Ordinary and Thickened Foam Seals

H. Ahmadi*[a], M. H. Kadivar[b]

[a] *International College, Shiraz University, Shiraz, Iran*

[b] *School of Mechanical Engineering, Shiraz University, Shiraz, Iran*

PAPER INFO

Paper history:
Received 23 January 2022
Received in revised form 11 April 2022
Accepted 01 May 2022

Keywords:
Slosh
Finite Element
Vibration Mitigation
Fluid-structure Interaction
Earthquake

ABSTRACT

Vibration of a floating roof in cases of tube and foam seals has been analyzed by ANSYS. Fluid-Structure Interaction (FSI) and sloshing phenomenon have been considered. Modal responses, time waves and frequency spectrums of the roof vibrations in the two sealing cases were evaluated during horizontal seismic excitation of the tank base. Then, the effects of the main mechanical factors of the seal on the roof vibration were investigated. The roof vibration amplitude in the foam sealing case was considerably lower than that in the tube sealing case due to more damping of the foam seal. Also, the foam sealing case had higher natural frequency than the tube sealing case due to more tank-axial (vertical) shear modulus of the foam seal in relative to the tube seal. Regarding this result, the foam seal was vertically added by 50% and the tank base was seismically excited again. It was seen that this improvement in thickness has more contribution to the floating roof vibration mitigation.

***doi**: 10.5829/ije.2022.35.07a.18*

NOMENCLATURE

b	Initial gap between the roof and shell	σ_t	Tube shell stress
$[C]$	Proportional damping matrix	δ	Kronecker delta
E	Instantanious modulus of elasticity	ζ	Damping ratio
F	Force	ρ	Density of the tank liquid (kg/m^3)
$[F]$	Seismic forces matrix	λ	Sloshing height
g	Gravity (m/s^2)	τ	Tube shell thickness
h	Height the liquid inside the tube seal	μ	Friction coefficient
$[M]$	Mass matrix	η	Loss factor
K	Stiffness	ε	Strain
$[K]$	Stiffness matrix	ω	Rotational frequency
p	Pressure	**Subscripts**	
$[P]$	Pressure matrix	f	Tank liquid
$[R]$	Fluid-structure coupling matrix	j	Annular sector number
Δu	Gap size change	i	Principle axis
$[U]$	Structure displacement matrix	l	Liquid inside the tube
ΔW	Energy loss	n	Normal direction
W_0	Input energy	s	Solid
Δx	Roof horizontal displacement	sy	Tangential tank-axial direction
Greek Symbols		sz	Tangential circumferential direction
σ	Stress tensor	t	Tube shell

1. INTRODUCTION

In oil industries, hydrocarbon storage tanks must have floating roof in order to prevent vaporization and loss of the products that may also be flammable or hazardous to the environment. There are two types of floating roof: Single Deck Floating Roof (SDFR) and Double Deck Floating Roof (DDFR). A SDFR is made up of a single-

*Corresponding Author Email: *ahmadihs1354@gmail.com* (H. Ahmadi)

Please cite this article as: H. Ahmadi, M. H. Kadivar, Vibration Analysis of the Double Deck Floating Roof of a Storage Tank in the Cases of the Tube, Ordinary and Thickened Foam Seals, ***International Journal of Engineering, Transactions A: Basics***, Vol. 35, No. 07, (2022) 1398-1415

layer deck plate at the roof center and an annular bulk named pontoon around the deck plate. A DDFR consists essentially of a lower deck, an upper deck and some stiffeners between them. In Figure 1, the lower deck and stiffeners are demonstrated. In addition, a segment of a DDFR and an overall view of some roofed tanks can be seen in Figures 2 and 3. Refer to the descriptions represented by Ahmadi and Kadivar [1] and also by Kuan [2] about the storage tanks and floating roofs.

On the other hand, there is a gap between the floating roof and the tank shell in order to facilitate tank-axial (vertical) movement of the roof when the liquid rises up and falls down. However, this gap should be filled with a seal to prevent the liquid escape through this area. Arrangement of a roof seal relative to the tank shell and floating roof has been demonstrated in Figure 2.

Earthquakes produce long-period oscillations on the liquid surface of storage tanks, which is called sloshing phenomenon [3]. Slosh induces vibration to the floating roof through Fluid-Structure Interaction (FSI). Such seismic oscillation may result in consequences such as sinking of the roof, destructive fire of the products or splash of the toxic liquid to the environment. Some events due to the roof slosh have been mentioned in the studies provided by Chang and Lin [4], in other studies by Hatayama [5] and Ahmadi and Kadivar [1]. Figure 3 shows some floating roofed tanks in Tomakomai during 2003 Tokachi-oki earthquake. In this Figure, open-top fire happened in tank 'b', i.e. the fire spread to all parts of the roof. Usually in such events, the tanks catch fire due to the sparks generated by up down movement of the roof against the seal and shell.

Hence, seismic vibration of the floating roof of the storage tank has been taken into consideration as an important problem in many studies. In this way, several attempts were made toward vibration mitigation of the floating roof vibration and risk assessment of petroleum storage tanks [6-9]. However, so far, the floating roof outer rim was modeled as a free or fixed boundary condition or with radial only-compression springs. Salarieh et al. [10] modeled deck plate as a flexural element rather than membrane. Shabani investigated the induced stresses in SDFR of some seismically-excited storage tanks [11]. Yoshida et al. [12, 13] considered a free peripheral boundary for a floating roof to investigate sloshing characteristics of a storage tank. Golzar et al. [14] analyzed the slosh of a storage tank floating roof under different earthquakes. In these investigations, the moments and shear modulus of the floating roof edges have been taken equal to zero. Shabani and Golzar [15] assumed zero axial traction for computation of the seismic deflection of a floating roof. Goudarzi [16] studied the second seismic vibration mode of a floating roof by considering free-edge boundary for the roof. Goudarzi [17] studied the attenuation effect of a SDFR by assuming free-edge boundary for the roof. He [18] also proposed a practical seismic procedure for evaluating the sloshing response and the dynamic stresses inside a DDFR subjected to seismic excitation. The roof edge was also assumed free in this study. Meera and Reshmi [19] studied the SDFR vibration regarding different patterns for the SDFR stiffeners. They assumed

Figure 1. Lower deck and floating roof stiffeners configuration (courtesy of Kavan Sadid Sanaat Koosha)

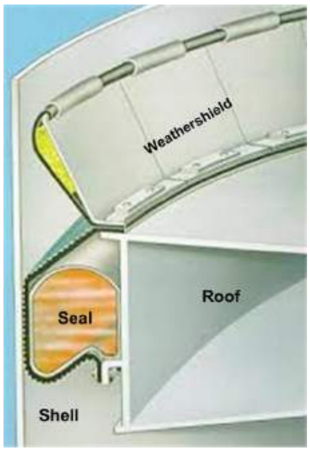

Figure 2. Arrangement of a roof seal relative to the tank shell and the floating roof

Figure 3. Open top fire in a crude oil tank [5]

fixed boundary for the roof. The stress pattern of a circular SDFR and a DDFR with free edges under a seismic excitation was illustrated by Golzar et al. [20]. Belostotsky et al. [21] considered all the essential parts of the storage tank in their analysis. The roof seal was modeled as radial only-compression springs. However, the numerical results of such research have not been represented. Hosseini et al. [22] studied the seismic vibration of the storage tank assuming a rigid disk as the floating roof and some radial only-compression springs as the seal.

The aforementioned studies were only devoted to the analysis of the roof vibration. In some other researches, several vibration suppression approaches were also applied to the roof and were evaluated by conventional analytical or numerical procedures. Sakai and Inoue [23] proposed some isolating rubbers between the layers of the pontoons of a SDFR in order to reduce seismic vibration. Utsumi [6] studied the effect of a vibration absorber including mass, damper and spring on a SDFR vibration. Kobayashi and Sato [7] designed a vibration absorber which have a U-shaped tube in addition to mass, damper and spring for passive vibration control of the roof. Hasheminejad and Mohammadi [8] discussed an active control method for vibration mitigation of a floating roof. Hosseini et al. [24] conducted an experimental study using a Suspended Annular Baffle hanging from the floating-roof to reduce the maximum sloshing height. Ruiz et al. [25] proposed a new type of liquid mass damper, called tuned liquid damper for vibration attenuation of the roof. However, the above analysis was conducted with no seal existence. In this work, the seal parameters will be taken into account for vibration suppression of the floating roof.

As described above, in most of the studies in the literature, vibration of the floating roofs have been investigated regarding free or fixed edge for the roof. In other words, the seal was neglected in the analysis. It is obvious that the boundary condition is an essential parameter for solution of a structural dynamic system. Therefore, considering free-edge boundary condition, as was assumed in most of the aforementioned works, makes a substantial deviation from the actual sloshing condition of the floating roof.

In some other scarce studies, the seal was modeled as radial only-compression springs ignoring the seal stiffness in the other directions. The main contribution of the seal radial forces is to improve the sticking condition by increasing the friction forces at the seal-shell contact. However, friction forces of the seal must be limited such that it does not prevent the roof slipping during the liquid level change. In the present work, the effect of slipping to the roof sloshing will be discussed in addition to the radial elastic modulus effect.

Sloshing occurs in the vertical direction. Therefore, the vertical forces will have some contribution to the sloshing. In addition, the tangential vertical forces can rapture the sticking condition of the seal changing the roof deformation pattern. Therefore, the stiffness of the seal in the vertical direction can be revised in order to suppress the floating roof sloshing. On the other hand, the radial space between the roof edge and the wall is small relative to the roof radius. Therefore, the seal shear stress can also be effective in the sloshing of the roof. Ahmadi and Kadivar [1] investigated seismic vibration of a floating roof by considering the main mechanical properties of the seal including shear and elastic modulus in all directions. However, the contribution of the seal stiffness in each Degrees of Freedom (DoF) was not clarified. Therefore, in the present work, the contribution of the modulus of the seal to the DDFR vibration will be discussed in the all DoFs including vertical shear modulus .

Damping is another essential factor in the vibration suppression of the dynamic systems. As the seal incorporates in the roof vibration through the roof peripheral boundary, the seal damping can affect the roof vibration. Hence, an attempt will be made to use the seal damping to reduce the roof vibration .

Mass is another factor that contribute to the vibration of a flexible system through the effective and modal masses. The attachment of the seal to the roof periphery incorporates the seal mass in the roof mass configuration. As the seal volume is constant in the default design, the effect of the seal density on the roof slosh will also be investigated in the present study.

Several types of seals are used in the oil industries. Tube and foam seals are the two conventional ones, which are used in this study. Fundamental characteristics of the other seals can be extracted through analysis of these two seals. A tube seal, as its name suggests, is a tube containing liquid which is used for sealing the roof peripheral gap. A foam seal is a cover with suitable foam inside it that is used for the same purpose. Figure 4 shows overall configuration of these two types of seal.

Regarding the above descriptions, the following parameters of the foam and tube seal are more impressive.

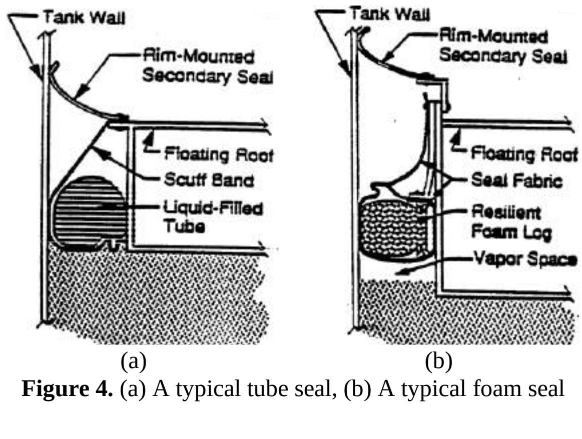

(a) (b)

Figure 4. (a) A typical tube seal, (b) A typical foam seal

1. Foam has more shear modulus than water. Therefore, generally, a foam seal has more shear modulus than a tube seal in a similar sealing mechanism.
2. Radial modulus of the foam seal will be extracted from the properties of the conventional foams. Radial modulus of the tube seal will be computed numerically. However, regardless of the seal type, the seal radial forces must be limited in a range in order to facilitate vertical movement of the roof during water level change.
3. Damping of the foam seal is more than tube seal due to the hysteresis damping present in the foam during vibration.
4. The tube seal mass is more than the foam seal mass as water has more density than foam.
5. The slipping condition depends on the radial forces and is independent of the seal type as described so far. Hence, the slipping effect on the roof sloshing will be investigated regardless of the seal type.

As described so far, free boundary condition was assumed in about 90% of the previous works for floating roof vibration analysis, and in some other studies radial springs has been considered, while slosh movement is in the vertical direction and peripheral friction can resist such movement. Hence, the novelty of the present work is to analyze and optimize the contribution of a boundary condition including the damping and vertial shear modulus of the seal and slipping or sticking condition at this area. For this purpose, vibration of a DDFR will be evaluated in the two cases of tube and foam seal considering the main mechanical parameters of the seal which was described so far. Furthermore, according to the achieved results, a new method for DDFR vibration mitigation will be recommended and discussed.

2. THEORIES OF THE ROOF VIBRATION WITH CONTACT SEALS

In ANSYS Parametric Design Language (APDL), numerical simulation of the fluid in terms of the dynamic pressures and Fluid-Structure Interaction (FSI) in a fully coupled manner as well as sloshing phenomenon is possible [26]. Fully coupled method facilitates the solution of the problem by one equation. However, it spends more solution time than loosely coupled approach, although the result of the former approach is more exact. The fundamental of FSI is the structure deformation and the fluid forces. Refer to the descriptions provided by Sigrist [27] for more detail about the type of fluid-structure coupling methods. In a storage tank with a floating roof, sloshing phenomenon exists at the roof-liquid interface in addition to FSI according to the following relation.

$$p_{slosh} = -\rho_f g \lambda \tag{1}$$

Therefore, in the sloshing surface, the displacement-based stiffness matrix due to gravity can be added to the coupled system of elemental equations as:

$$\begin{bmatrix} [\mathrm{M}_s] & 0 \\ \rho_f\left[R^T\right] & \left[\mathrm{M}_f\right] \end{bmatrix} \begin{Bmatrix} [\ddot{\mathrm{U}}] \\ [\ddot{\mathrm{P}}] \end{Bmatrix} + \begin{bmatrix} [\mathrm{C}_s] & 0 \\ 0 & \left[\mathrm{C}_f\right] \end{bmatrix} \begin{Bmatrix} [\dot{\mathrm{U}}] \\ [\dot{\mathrm{P}}] \end{Bmatrix} + \begin{bmatrix} [\mathrm{K}_s]+[\mathrm{K}_{slosh}] & \text{-R} \\ 0 & \left[\mathrm{K}_f\right] \end{bmatrix} \begin{Bmatrix} [\mathrm{U}] \\ [\mathrm{P}] \end{Bmatrix} = \begin{Bmatrix} [\mathrm{F}] \\ 0 \end{Bmatrix} \tag{2}$$

However, boundary condition around the roof must also be considered in this regard. As stated before, floating roof edges are connected to the seals.

One of the distinct mechanical characteristic of the tube seal is its normal pressure behavior versus displacement that can be considered as the seal elasticity according to the following relation.

$$\sigma_{ii} = -p_t \delta_{ii} \tag{3}$$

It will be shown that this property is not so effective in the roof vibration. Therefore, a simple model has been used for it as follows. The tube seal around the roof is divided into some annular sectors. Location and nomenclature of a typical sector has been demonstrated in Figure 5. Then, the average total pressure of the tube in each discretized time step is estimated as the sum of the average static pressures due to the liquid weight in the tube and the hoop stress of the tube shell. The idea behind the hoop stress calculation is the relation represented by Beer et al. [28] for thin-walled circular pressure vessels. However, in this subject, tube seal cross section will expand in the form of a right triangle due to the limitations provided by scuff band as demonstrated in Figure 6. Therefore, a direction correction is applied to the relation derived by these authors as follows.

$$p_j = \rho_l g\left(\frac{h}{2}+\Delta h\right)+\frac{\sigma_t \tau}{(b-\Delta x)}\left(1+\frac{\Delta h}{\sqrt{(b-\Delta x)^2+(\Delta h)^2}}\right) \tag{4}$$

As can be seen in Figure 6, the maximum variation of the tube seal height ‘Δh’ due to ‘Δx’ roof progression is on the right of the triangle. Assuming constant volume of water in the tube sector during the roof progression, this value can be calculated by the following equation.

$$h\Delta x = \frac{(b-\Delta x)\Delta h}{2} \tag{5}$$

which leads to

$$\Delta h = \frac{2h\Delta x}{b-\Delta x} \tag{6}$$

The left hand side of Equation (5) is the water regression in the tube, and the right hand side is water rise through the scuff band triangular hollow space. Note that the bottom side of the scuff band is under the liquid or vapor

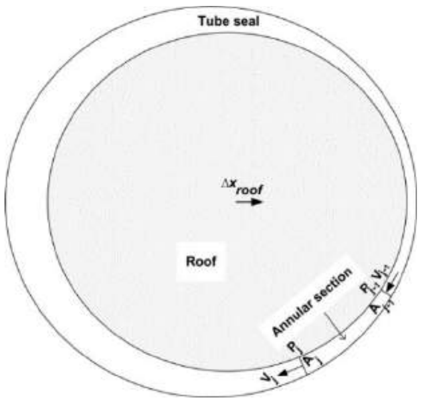

Figure 5. Location and fluid nomenclature of an annular sector of a tube seal

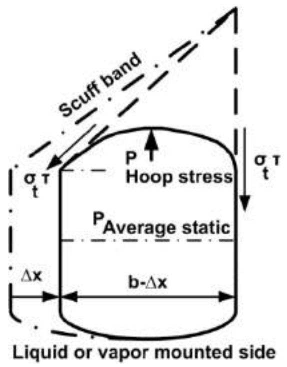

Figure 6. Tube seal behavior during deformation

However, Equation (4) does not comply with the laboratory condition of the stress-strain test, as the water escape from the sectors in the circumferential direction 'sz' is considered zero. This flow blocking assumption must be compensated in the form of Poisson's ratio. In this regard, the Poisson's ratio is involved in the non-linear stress-strain relation according to Hook's law for multiaxial loading of the homogeneous materials [28].

$$\varepsilon = \frac{\sigma_n}{E} - \nu \frac{\sigma_{sz}}{E} \tag{7}$$

Assuming uniform hydrostatic pressure in the tube sector 'j' and using equations (3) and (7), the strain can be represented in terms of the hydrostatic pressure as

$$\varepsilon_j = \frac{p_j\left(1-\upsilon\right)}{E_j} \tag{8}$$

Having Poisson's ratio, strain and pressure, the instantaneous elastic modulus can be derived from the above equation.

In Equations (4-8), non-linear relations between the stress and strain of the tube seal were established. Foam seals also have non-linear stress-strain relationship, i.e. elasticity of the foam seal depends on the regions in which the stress applied to it. In this regard, the elasticity behavior of the foams can be classified into three regions: linear elastic, plateau and densification as indicated in Figure 7 [29]. Generally, polyurethane foams are used for floating roof sealing.

The seal foam is installed in the roof-shell gap with an initial pre-compression. This pre-compression moves the stress-strain operating condition to the plateau region. Therefore, the foam seals generally work in the plateau region.

Another distinct property of the foam is vibration absorption. Foam behaves differently in loading and unloading. As Figure 8 shows, the area between the loading and unloading curve is the energy loss due to the hysteresis loop. This property makes the foam to be a type of viscoelastic material. Viscoelasticity of the foam can reduce the roof vibration through hysteresis energy loss. Hence, damping effect of the foam seal to the roof vibration has been discussed. The loss factor due to the foam hysteresis can be computed from the following equation.

$$\eta = \frac{\Delta W}{2\pi W_0} \tag{9}$$

According to the loss factor, damping ratio can be calculated as

$$\zeta = \frac{\eta}{2} \tag{10}$$

However, the seal participates in the roof vibration only if it is in the closed contact with the tank shell. Closed and open contact depends on the following relations.

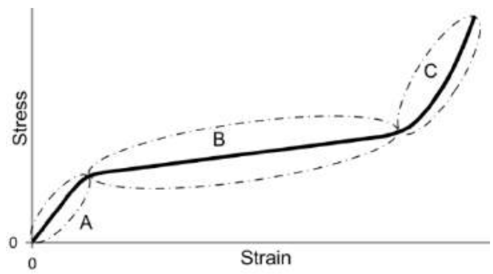

Figure 7. Stress-strain curve of a polyurethane foam in (a) linear elastic, (b) plateau, (c) densification regions

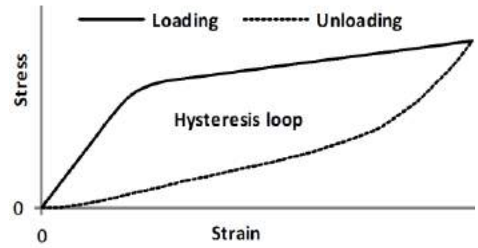

Figure 8. Representation of the hysteresis damping in the foam seals

$$F_n = \begin{cases} 0 & \text{if } \Delta u_n > 0 \text{ (Open Contact)} \\ K_n \Delta u_n & \text{if } \Delta u_n \leq 0 \text{ (Closed Contact)} \end{cases} \quad (11)$$

There are two cases of the closed contact: sticking or slipping. In sticking, the tangential movement is only due to the flexibility of the contact materials. On the other hand, slipping occurs if the vertical forces on the contact area exceed tangential friction forces [26]. This principle can be represented by:

$$F_{sy} = \begin{cases} K_{sy} \Delta u_y & \text{if } \sqrt{F_{sy}^2 + F_{sz}^2} - \mu F_n < 0 \\ & \text{(Sticking)} \\ \mu K_n \Delta u_n & \text{if } \sqrt{F_{sy}^2 + F_{sz}^2} - \mu F_n = 0 \\ & \text{(Slipping)} \end{cases} \quad (12)$$

3. TANK AND FLOATING ROOF SPECIFICATIONS

A cylindrical storage tank with a DDFR is considered for analysis. Tank body and DDFR specifications are selected according to Siraf storage tank located in south of Iran. The content of the storage tank is natural gas condensate. The general specifications of the storage tank and shell are summarized in Table 1.

Floating roof dimensions are also given in Table 2. Lower and upper decks of the roof are stiffened by bulkheads, trusses and rafters. Bulkheads are dividing walls for separation of the radial and annular compartments.

So far, all the essential parts of the roof, liquid and tank shell have been introduced. The objective is to study and compare the vibration of the roof in the two sealing cases of the tube and foam seal. Therefore, dimensions and mechanical characteristics of these two types of seal are required, which will be introduced in the next section.

TABLE 1. Storage tank general and shell specifications

Parameter	Value
Tank height	14 m
Tank diameter	60 m
Liquid density	648 kg/m^3
Liquid Viscosity	8.9e-4 Pa.s
Rated wall thickness	0.02 m
Liquid height considering sufficient freeboard	12 m
Metal density	7850 kg/m^3
Metal Young's modulus	2e11 N/m^2
Metal Poisson's ratio	0.3

TABLE 2. Floating roof dimension

Parameter	Value
Height	0.672 m
Upper deck thickness	0.00477 m
Lower deck thickness	0.00637 m
Height in contact with seal	0.40 m
Gap between roof rim and shell	0.20 m

4. MECHANICAL SPECIFICATIONS OF THE TUBE AND FOAM SEAL

The internal envelope of the tube seal is the shell that holds the water. The outer envelope is the scuff band, which supports the tube against rubbing and collapsing. The thickness of the tube shell has been taken 2mm while the scuff band has been considered as a fixture that will be described later.

The behavior of the tube seal during a horizontal simulating motion of the roof has been modeled as follows:

1. The tube is filled with water after installation. The hydrostatic pressure produced in this step is considered as the initial stress of the seal. This value was 1970 Pa.
2. The total length of the tube, which is equal to the roof circumference, has been divided into 16 annular sectors.
3. The horizontal movement of the roof relative to the tank shell during an earthquake has been modeled as small displacements applied to the roof in very short time segments.
4. These small movements change the liquid level of the tube. This increases the hydrostatic pressure. In addition, a static pressure will be generated due to the tensions produced in the tube shell. The total stress of the seal is equal to the sum of these two values that is computed by Equation (4).
5. Lateral scape of the water from the sectors has also been considered as Poisson's ratio involvement according to Equation (8).

Different time segments have different displacements, as mentioned in Table 3 for the first quadrant. Such sequence of pressure variation is repeated in the other quadrants. In each sector, horizontal motion the roof is different as can be distinguished from Figure 5. Thus, each sector will have distinct stress-strain relationship. Table 3 expresses the pressures of each sector resulted from the horizontal displacements applied to the roof.

Poisson's ratio has been taken equal to 0.5 which is Poisson's ratio of water as the main part of the tube. Using Table 3, non-linear relations between the stress and strain of the tube seal were established for each sector. The strains were calculated by non-dimensional

TABLE 3. Tube seal pressure in the first quadrant in pascal

Horizontal displacement of the roof		0.006	0.0048	0.0036	0.0024	0.0012
Sectors in the first quadrant	1	27087	20861	15285	10307	5881
	2	22382	17448	12970	8916	5255
	3	14615	11700	8988	6468	4129
	4	6108	5197	4329	3501	2712

quantities of the displacements in Table 3. Using the strains and the pressures summarized in this table, instantaneous stresses were derived from Equation (8). The above values were introduced to the macro in table format. Damping ratio of the tube seal was considered 0.05 that is approximately equal to the natural rubber damping affected by the fluid friction inside the tube.

For tube and foam seal comparison, the stress-strain curve of the selected foam seal is shown in Figure 9. The governing stress-strain relationship has been estimated considering reasonable stiffness of the foams provided by some manufacturers [30].

Damping of the seal was estimated according to the usual hysteresis loops present in polyurethane (PU) foams [29] and using Equations (9-10). Based on these considerations, damping ratio of the foam was estimated 0.15.

The foam seal is also installed by an initial compression. An initial compressive stress of 17.9KPa has been considered for the foam seal. Having the stress value, the initial compressive strains can be obtained from Figure 9 as:

$$\varepsilon_0 = 0.43\, mm / mm \qquad (10)$$

In addition, some retainers are used to install the seal, as demonstrated in Figure 4. Tube and foam seals both have weather shield and envelope. Weather shield protects the seal against harsh environment. Tube shell in the tube seal and foam envelope in the foam seal affect

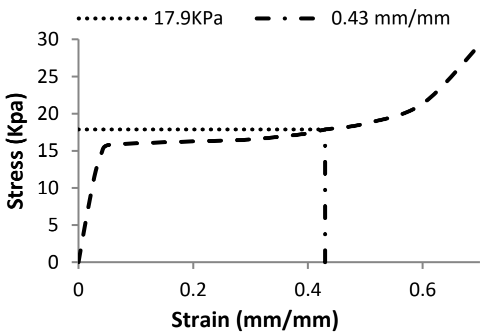

Figure 9. Stress-strain diagram of the foam seal with initial stress and strain

the mechanical characteristics of the seal in the same way. In addition, scuff band holds the tube seal to protect it from wear and tear. For foam seal, similar apparatus is used instead of the scuff band. According to the aforementioned descriptions, the fixtures used for holding the tube and foam seals have approximately the same mechanical properties. Hence, equal elastic and shear modulus have been added to the tube and foam seals due to the presence of the fixtures.

5. MODELING AND MESHING

A macro using APDL has been provided to perform finite element analysis of the fluid and structures of the tank. 99618 elements have been used in the model. The basic of this work is similar to the study that was performed by Ahmadi and Kadivar [1]. In addition, slosh and seal-shell contact models have been improved. Also, some details about the floating roof and slosh modeling have been introduced. In Figures 10 and 11, exploded views of the finite element model of the tank system are illustrated. Figure 10 includes the main roof parts and a layer of the liquid elements. In Figure 11, shell, liquid, seal and contact elements have been demonstrated.

For liquid meshing, three dimensional (3-D), 8-node wave elements have been used. In the elements inside the fluid, the pressure-based wave equation are established. FSI was applied at the shell-liquid and the roof-liquid interfaces. At such areas, displacement DoFs are also activated. All nodes of the upper surface of the liquid are located so that they coincide with the corresponding roof nodes in the radial and angular directions. This condition facilitates FSI for the roof-liquid common boundary. In Figure 11c, a sector of the lower deck has been added to the upper surface of the liquid to show the node coincidence. Then, meshing coincidence was extended to the lower liquid levels to produce liquid elements, and to the stiffeners and upper deck as illustrated in Figure 12. In addition to FSI, slosh condition must also be provided at the nodes of the upper surface of the liquid. Note that only dynamic pressure is involved in the liquid modeling.

The seals are fixed to the floating roof perimeter while it can move relative to the tank shell that is in contact with it. 4-node 3-D interface elements have been used to model the seal. This type of element is generally suitable for modeling the washers and gaskets such as the current application. Both the tube and foam seals are approximately equal in dimension. For this reason, the same element shape has been selected for both of them.

Contact element is another factor that involves in the roof vibration. There are several methods for modeling the contact elements, from which 3-D node-to-node contact elements have been used. Penalty method has been taken into account for solution of the contact parameters. The method of calculating the normal, i.e.

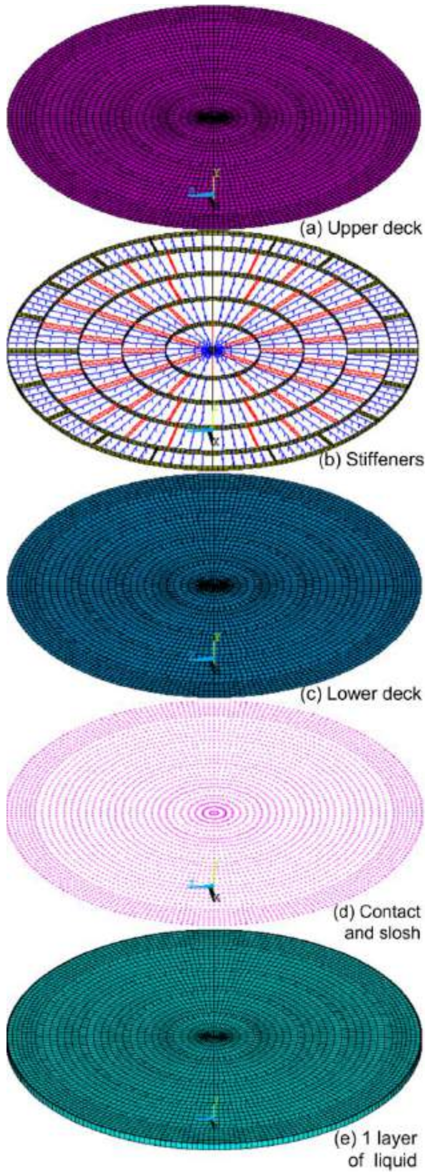

Figure 10. Exploded finite element model of the roof and its adjacent liquid

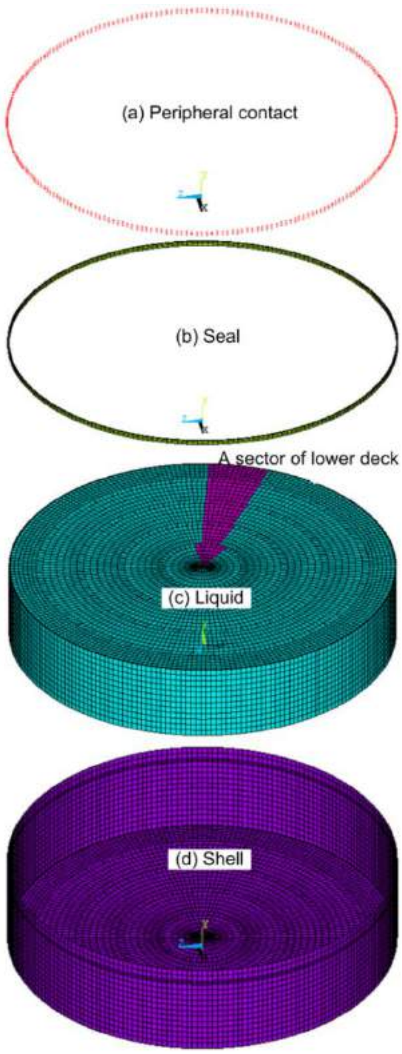

Figure 11. Exploded finite element model of the shell, liquid and seal

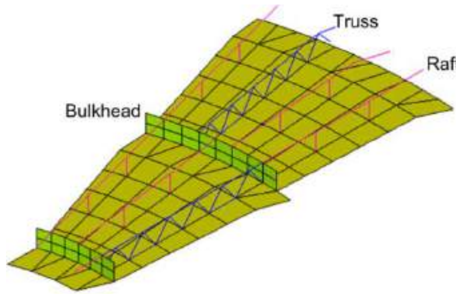

Figure 12. Meshing coincidence of the lower deck and stiffeners

tank radial direction, and tangential forces was depicted in Equations (11-12). Contact forces including normal and friction forces will be transferred only in the case of closed contact. On the other hand, opening of the contact element may lead to divergence. Open or closed contact is determined based on the gap size. The gap size is automatically calculated from the node locations of the gap element during simulation or from the real constant applied before simulation. In the present analysis, the gap real constant was set to zero ignoring the node locations. Also, some weak springs with 1e-6N/m stiffness have been applied to prevent such divergence.

Tangential movement of the seal in the contact area along the vertical direction is possible. This may happen in the two ways that was explained with Equation (12). In sticking condition, the seal can move relative to the shell in the vertical direction depending on the tangential stiffness of the seal. However, slippage occurs when the applied tangential force on the node exceeds the friction force. If during the excitation, the tangential force reduces to less than the friction force, the contact element will return to the sticking state. The amount of the force required for complete slippage of the seal is set to 1000N. In this estimation, the coefficient of friction between nylon and steel (0.6) [31], initial compression of the seals, friction between the weather shield and the shell has been considered. The major challenge in this regard is the seal crumpling due to non-homogeneous slippage of the seal in the circumferential and vertical direction; some nodes of the seal may slip while the adjacent nodes are in the sticking state. This condition leads to the seal crumpling and divergence of the calculation results. To overcome this problem, gradual slippage has been implemented by distributing the tangential contact force to several spring-sliders [26].

Two important conditions must be provided at the roof-liquid interface: the first condition is the roof-liquid FSI, and the other is the sloshing that is transferred to roof. In this regard, there are two kinds of pressure in the liquid adjacent to the roof. The first one is the impulsive pressure, which depends on the speed of sound and appears in the roof-fluid FSI. The other is the convective pressure, which is due to gravity, and appears in the slosh phenomenon.

For FSI establishment, contact elements has been generated between the lower deck and liquid, and then FSI was introduced. For slosh generation, the gravity condition must be satisfied on the liquid upper surface. Presence of gravity acceleration is essential especially for the upper elements of the liquid. Therefore, gravity acceleration was applied to the liquid. Then, sloshing was considered according to Equation (1). For simulation of this phenomenon, displacement-based stiffness elements were generated by adding some vertical springs to the upper surface of the liquid. The other end of each spring must be connected to a node with the same radial position with the upper end and zero vertical displacement. Therefore, the lower ends were connected to the tank bottom nodes. Finally, these springs were omitted in the post-processing. The upper ends of the springs are shown with contact elements in Figure 10d.

So far, finite element model of all the essential components of the tank has been presented. It is intended to discuss the vibration characteristics of the roof in the two cases of seals. For this purpose, modal and time history analysis has been performed to obtain the seismic behavior of the roof, which will be discussed in the next sections.

6. MODAL ANALYSIS AND RESPONSE SPECTRUM METHOD

Modal analysis has been conducted in the two sealing cases of the tube and foam seal using the model introduced so far. The first two dominant natural frequencies resulted from the modal analysis have been summarized in Table 4. In modal analysis, mass and stiffness matrix of the roof is calculated based on its initial stable position. Therefore, the result of the modal analysis is linear with respect to the mass and stiffness matrices. However, time history analysis is non-linear in this respect, which will be discussed later. Hence, the frequency values indicated in Table 4 were revised according to the time history results to achieve the values that are more realistic. For convenience, the first two dominant natural frequencies are indexed as fn1 and fn2. Comparison of the natural frequencies in the two sealing cases indicates that the amount of the seals participation in the roof vibration is significant. Hence, ignoring them, as in many references, will lead to unrealistic results.

In another row of Table 4, response displacement is mentioned that depends on the magnitude of the earthquake response spectrum at the intended natural frequency. Response spectrum is a function of the frequency spectrum of the earthquake and the damping ratio of the studied system at its natural frequency. Refer to the descriptions provided by Shelke [32, 33] and Versluis [34] for more information about the response displacement and frequency response. Different earthquakes have different frequency spectra. On the other hand, comparison must be accomplished in equal excitation amplitude. In this section, equalization has been done by taking equal spectrum displacements. For this purpose, for each natural frequency, a harmonic excitation was applied with a frequency equal to the considered natural frequency during 20s. The amplitude was considered to be 0.01m for the first natural frequency and 0.001m for the second one. Such amplitudes were equal in both sealing cases. For determination of the roof vibration, modal response was calculated using response spectrum method described above. Modal response represents the maximum amplitude of the system at the intended natural frequency. These values are listed in the last row of Table 4.

Table 4 exhibits that the natural frequency of the roof in the foam sealing case is higher than that in tube sealing case. fn1 frequency for the foam sealing case was 9% higher than that in the tube sealing case. This value was 0.9% for fn2. This difference is due to the higher shear modulus of the foam seal than the tube seal. Modal responses show that in similar excitation the vibration of the roof in the foam sealing case is lower than that in the tube sealing case. In this regard, modal response of fn1 in the foam sealing case was 18% less than that in the tube sealing case. This value was 20% for fn2. This difference is due to the more damping ratio of the foam seal in relative to the tube seal.

In response spectrum method, only maximum displacement of the roof was determined at the dominant natural frequencies. In order to know the overall

TABLE 4. Dominant natural frequencies of the storage tank in the tube and foam sealing cases and their modal characteristics under horizontal excitation

Sealing case	Tube seal		Foam seal	
Natural frequency index	fn1	fn2	fn1	fn2
Frequency value (in Hz)	0.175	0.725	0.191	0.735
γ (Participation factor)	1.116e5	1.128e5	1.242e5	1.276e5
$=\theta_{\max}$ (High spot displacement of the mass normalized mode shape)	0.883e-5	0.849e-5	0.828e-5	0.857e-5
Damping ratio	0.0228	0.0435	0.0484	0.0678
S_a (Response displacement (in m))	0.848	0.108	0.665	0.073
Modal response $=\theta_{\max}\times\gamma\times S_a$	0.836	0.103	0.684	0.080

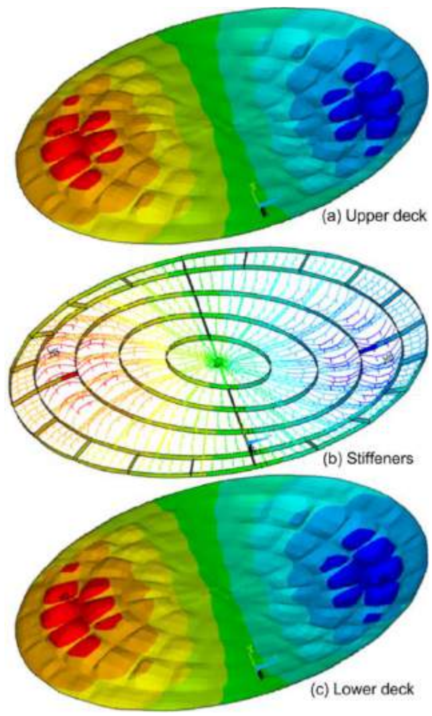

Figure 13. First mode shape of the roof

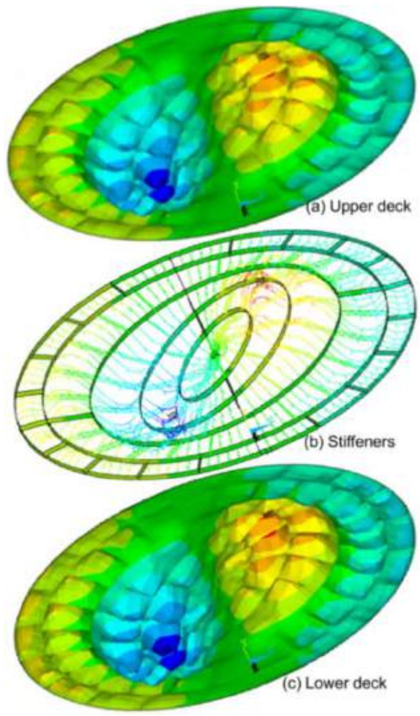

Figure 14. Second mode shape of the roof

vibration pattern of roof in modal analysis, mode shape analysis is required.

7. MODE SHAPES

Modal analysis exhibited similar mode shapes for the two sealing cases in the first and second dominant natural frequencies. Therefore, only the roof mode shapes in the foam sealing case have been demonstrated. In Figures 13 and 14, the first and second mode shapes of the roof have been shown respectively. In these figures, maximum absolute displacements are indicated by 'MX' and 'MN'. Hereafter, this area will be referred to as 'high spot' so as not to be mistaken with the time wave peak. These figures showed that the high spots of the mode shapes are located on the upper deck. The lower deck has lower vibration as it is limited on the both sides, and it is thicker than the upper deck. Therefore, high spot of the upper deck will be used hereafter for vibration comparison. 'MX' or 'MN' spot whichever has more vibration will be selected.

8. TIME HISTORY ANALYSIS

In this analysis, time step increments have been used during the application of some excitation time waves. The system specifications and FSI characteristics are similar to the modal analysis. Newmark time integration with Newton-Raphson numerical approach has been taken into account for solution.

The base of the storage tank was excited horizontally by 1999 Izmit earthquake in Sakaria of Turkey taken from SeismoSignal software accelerograms [35]. Izmit earthquake has been selected as an earthquake near Iran, i.e. the country where the tank is located. This earthquake caused 30 to 45 floating roofed tanks to catch fire due to excessive sloshing [5]. The stated earthquake has a great effect on the first natural frequency of the floating roofs.

Time analysis has been accomplished by ANSYS. 0.03s time steps have been selected for the time history analysis. In Figure 15, time wave of Sakaria earthquake in the horizontal direction is demonstrated. As can be seen, Peak Ground Acceleration (PGA) of the time wave has been scaled to 0.2g.

Maximum vibrations due to the earthquake were occurred in the high spot as mentioned in the modal analysis. Therefore, vibration of this spot was selected for demonstration of the time waves. Figure 16 shows the time domain vibration of the roof at high spot for the tube and foam sealing cases. As the figure shows, the analysis has been performed in 20s for forced vibration simulation and 20s during free vibration. In this figure, more vibration in the tube sealing case than the foam sealing case is evident.

In Figure 17, Fast Fourier Transformation (FFT) of the roof vibration at high spot has been illustrated, which verifies higher vibration of the roof in tube sealing case than the foam sealing case. In this figure, FFT of Sakaria earthquake is also demonstrated. As shown, the vibration in the foam sealing case is lower than that in the tube sealing case despite its excitation value. In this regard, vibration/excitation in the tube sealing case was 0.84, while this value was 0.59 in the foam sealing case during such time duration.

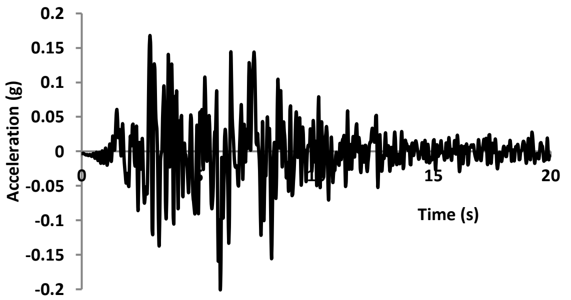

Figure 15. Time wave demonstration of the Sakaria earthquake in the horizontal direction

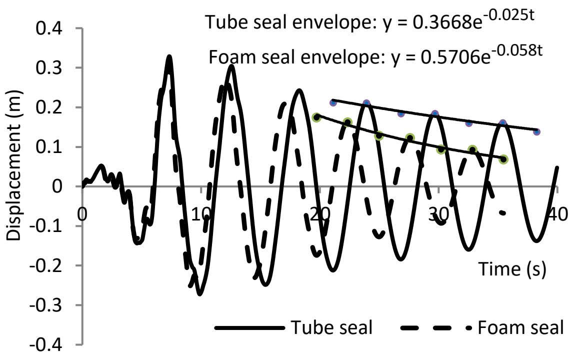

Figure 16. Time domain vibration of the roof high spot in the tube and foam sealing cases due to the horizontal component of the Sakaria earthquake

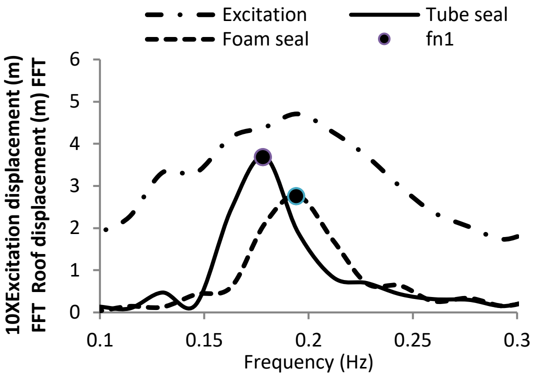

Figure 17. FFT of the roof vibration in the tube and foam sealing cases due to the horizontal component of the Sakaria earthquake

So far, vibration displacements of the roof in the tube and foam sealing cases were compared. However, simulation time is also involved in the comparison. Therefore, some manipulation is needed in order to cancel out the involvement of the time in the vibration comparison. In Figures 16 and 17, this was conducted by performing the analysis in equal number of cycles and by continuing the analysis to the free vibration as possible. Lower vibration in the foam sealing case is obvious in this analysis. However, in similar cases where the vibration amplitudes are close to each other, more simulation time is needed. More precise approach is the steady-state method. The governing relationships in the steady-state vibration were developed by Ahmadi and Kadivar [1]. Based on these relationships, the tank was excited with equal harmonic amplitude at a frequency equal to the natural frequency of each sealing case. Simulation time was extended to the steady-state condition to have time-independent evaluation. Vibrations of the roof in the two sealing cases were compared in Figure 18 using this approach. In this vibration simulation, a low equal value of damping has been added to both sealing cases to reach the steady state sooner. It clearly shows that the floating roof has less vulnerability to the seismic vibrations in the foam sealing case.

So far, seismic vibration of the roof showed less vibration vulnerability in the foam sealing case. However, it is required to identify the main factors of the seal, which are effective to the roof vibration. In this regard, parametric study of the seal will be discussed.

9. INVESTIGATION OF THE EFFECTS OF THE MECHANICAL PARAMETERS OF THE SEAL ON THE FLOATING ROOF VIBRATION

The main mechanical parameters of the seal are surface slipping, damping, density and elastic and shear modulus.

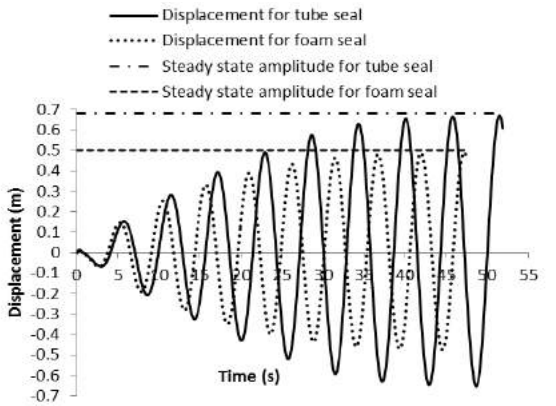

Figure 18. Comparison of the steady-state vibration of the roof in the tube and foam sealing cases under harmonic horizontal excitation

The stiffness of the contact in the sticking state has been taken approximately equal to the seal stiffness. Sakaria PGA has been set to 0.2g so far. In this condition, the contact mechanism was not in the slipping state. Although, there was some vertical movement of the roof periphery with respect to the tank shell. In order to observe the effect of slipping, the PGA was increased to 0.5g. In Figure 19, the difference between these two PGA cases is shown by demonstrating the friction force versus time on the high spot of the foam seal. The slip of the seal at 1000N for the PGA=0.5g is evident in this figure. The phenomenon has been appeared in several peaks when the roof went up and down.

Figure 20 shows friction force distribution of the contact spring-slider at 14.01s during the Sakaria earthquake in the foam sealing case. Several slips can be observed in the red and blue zones as their contact forces reach 1000N.

In the spite the slips shown in Figures 19 and 20, the seal and tank at the contact area had approximately the same radial displacement at most compressive contact area. Figure 21 shows the radial displacement of the seal and the tank shell at such point. In other words, the seal did not have interference with the tank shell, which is desirable for this calculation.

Considering the contact slip present in the 0.5g-scaled excitation, vibration behavior of the roof was analyzed for the two sealing cases in such slipping condition. In Figure 22, the result of such analysis has been demonstrated, and vibration of the roof was compared in the two sealing cases. As can be seen, the vibration amplitudes have been increased by a ratio approximately equal to the PGA ratio, i.e. 0.5g/0.2g. Also, the time periods have not changed. On the other hand, the roof vibration in the foam sealing case is still less than that in the tube sealing case. This investigation shows that the limited slip of the roof does not have significant effect on the roof vibration criteria and the comparison that has been done so far.

Damping ratios were derived from the exponent of the envelope curves in the free vibration part of Figures 16 and 23 that is '$-\varsigma\omega t$'.

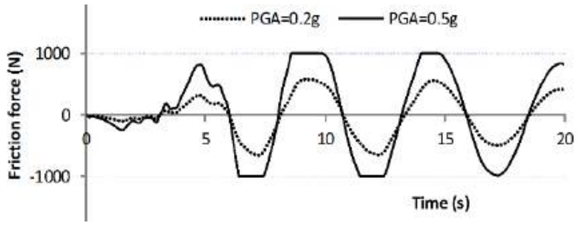

Figure 19. Friction force on the high spot of the foam seal for PGA=0.2g and PGA=0.5g

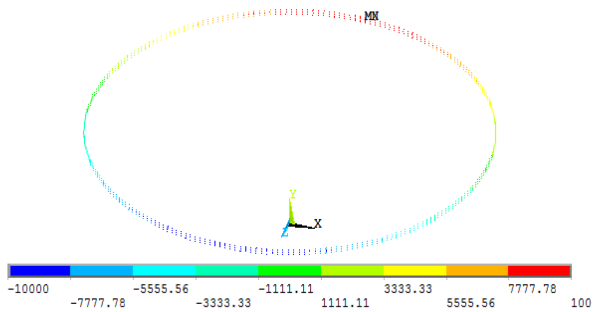

Figure 20. Force distribution of the contact spring-slider at 14.01s during Sakaria earthquake in the foam sealing case

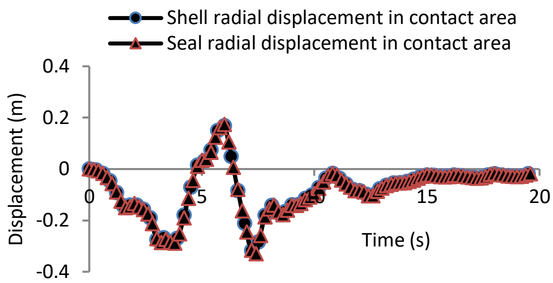

Figure 21. Radial displacement of the seal and tank shell at the most compressive contact area

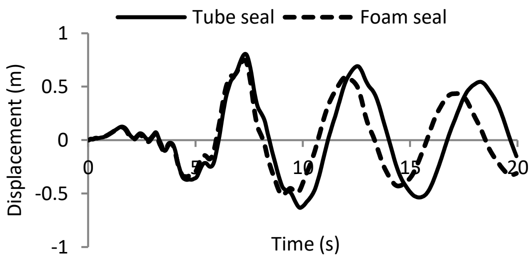

Figure 22. Time wave vibration of the roof high spot due to 0.5g-scaled Sakaria earthquake in the tube and foam sealing case

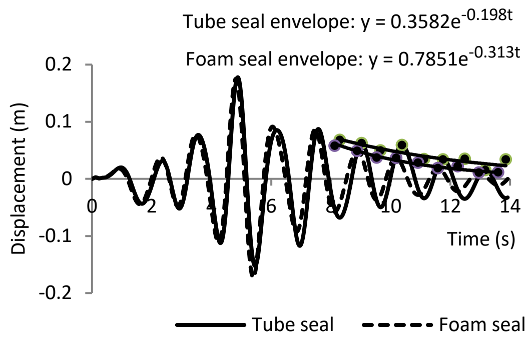

Figure 23. Calculation of the logarithmic decrement of the roof at the second natural frequencies in the tube and foam sealing cases

The damping ratios summarized in Table 5 show that they have been increased from the tube sealing case to foam sealing case. This fact exhibits the effect of the foam hysteresis damping on the roof vibration.

Then, the foam density was increased from 34 kg/m^3, i.e. the foam seal density, to 1000 kg/m^3, i.e. the tube seal density. The vibration of the roof was approximately the same in the two cases as was expected. This is because the seal mass is negligible in comparison to the roof mass.

In the next step, modulus of elasticity of the seal has been increases 10 times without changing shear modulus. This assumption is to observe the effect of the elastic modulus regardless of the shear modulus variation. Although in fact, these two factors are interdependent. The result showed that the roof vibration was approximately equal in the two cases.

After that, assuming anisotropic seal, the shear modulus was increased without elastic modulus change. The vibration of the roof did not change due to the circumferential shear modulus variation. However, the shear modulus change in the vertical (tank-axial) direction resulted in the variation of the natural frequency and participation factor .

The aforementioned studies showed that the seal damping and vertical shear modulus have the most contributions to the roof vibration. Damping ratio of the seal suppresses the roof vibration, and shear modulus increases the natural frequency of the roof. Higher damping ratio of the foam seal with respect to the tube seal leads to more vibration damping of the roof as were observed in Figures 16 and 23. As in many oil industries, water is selected as the liquid inside the tube. The shear modulus in the tube seal is low as the shear modulus of water is negligible. On the other hand, foam has higher shear modulus than water, which leads to higher shear modulus of the foam seal in comparison to the tube seal.

TABLE 5. Equivalent damping ratios (ζ) of the first and second natural frequencies for the tube and foam sealing cases

Seal type	ζ for fn1	ζ for fn2
Tube	0.0228	0.0435
Foam	0.0484	0.0678

Based on the above-mentioned results, foam seal is preferred for the roof vibration suppression due to more damping. In addition, it is recommended to add some extra-foam vertically in order to have more damping which leads to a thickend foam seal. Figure 5 shows that the empty space in this region allows the installation of the additional foam. Inclusion of more damping to the seal fixtures or weather shield will also contribute to such vibration suppression. In this regard, damping of the foam seal was assumed to have 50% increment. Note that the total radial initial forces exerted by the foam seal on the tank shell must be kept constant during foam addition. This strategy lets the roof to have smooth vertical movement when the tank liquid level changes. Such foam addition is desirable regarding the cheap price of the foams relative to the other materials used in the storage tank industries and the possibility of the execution. The amount of vibration mitigation has been studied by application of 2017 Sarpol-e Zahab earthquake [36]. Sarpol-e Zahab earthquake is a recent earthquake in the east of Iran, which occurred in the same seismotechtonic province of the studied storage tank, i.e. Zagros. The studies conducted by Yazdani and Kowsari [37] predicted high probability density of earthquake occurrence in this province. Earthquake prediction in this province can also be studied using the method presented by Sadeghian and Emamgholi Babadi [38].

Time wave of the horizontal component of this earthquake is demonstrated in Figure 24. This earthquake has been frequency-modulated in order to have equal excitation at the natural frequencies of the ordinary and extra-foam sealing cases. Hence, displacement of the excitation is approximately equal in the two sealing cases. Therefore, in order to have dimensionless comparison, vibration displacement has been analyzed. The result has been demonstrated in Figure 25. This figure compares the time wave displacement of the roof high spot in the ordinary foam and extra-foam sealing cases. Vibration peak has been decreased about 12% due to the extra-foam seal application. However, the natural frequency has been increased. Furthermore, in the thickened foam seal, the third cycle has about 62% decrement with respect to the maximum peak while this value is about 52% in the ordinary foam seal. This fact shows more decay rate of the roof vibration in the thichened foam sealing case.

Note that velocity comparison will also yield the same result, because both the excitation and vibration output must be multiplied by their respective rotational natural frequency, which in turn will lead to the same ‘output/input’ values.

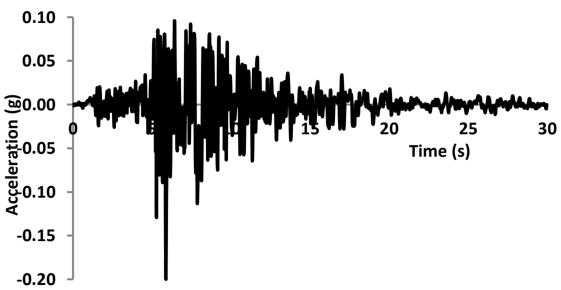

Figure 24. Time wave demonstration of the SarPol-e Zahab earthquake in the horizontal direction

The roof horizontal stress was also compared in the two cases of ordinary and extra-foam seal. The most intensive times were selected for the analysis according to Figure 25 time wave. In this figure, vibration peak has been occurred at 10.92s in the ordinary seal and 9.44s for extra-foam seal. These times were selected for stress demonstration of the upper deck. The result is shown in Figures 26 and 27. As it can be seen, the most intensive stress has been occurred at the spot of the seal and tank shell collision in the earthquake direction. This spot is indexed by 'MX' in Figures 26 and 27, and is selected for time simulation of the roof stress in Figure 28. The stress was calculated in the earthquake action direction. This figure also verifies the less severity of the roof in the extra-foam sealing case with respect to the ordinary foam sealing case.

10. ANALYSIS OF THE LIQUID BEHAVIOR

To analyze the liquid effect on the roof vibration, the dynamic pressure on the elements adjacent to the liquid surface was investigated. For this purpose, the dynamic pressure at 10.92s under SarPol-e Zahab earthquake for ordinary foam sealing case has been illustrated in Figure 29. Furthermore, vertical displacement of the liquid and some adjacent structures in cutaway views have been demonstrated in Figure 30. Figure 29 shows that the

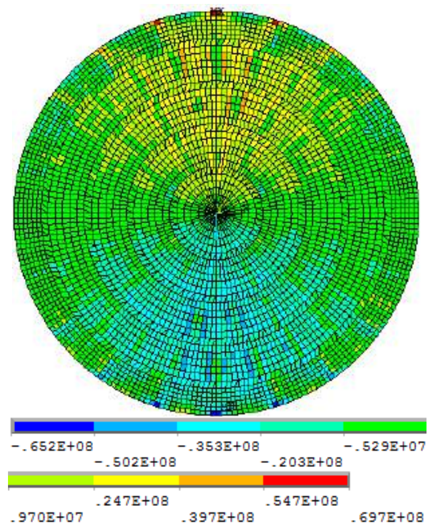

Figure 26. Stress pattern of the upper deck at the time of the peak stress (10.92s) due to the SarPol-e Zahab earthquake in the excitation direction in the ordinary foam sealing case

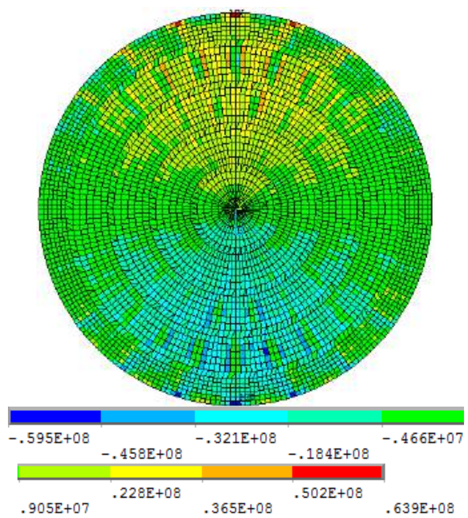

Figure 27. Stress pattern of the upper deck at the time of the peak stress (9.44s) due to the SarPol-e Zahab earthquake in the excitation direction in the extra- foam sealing case

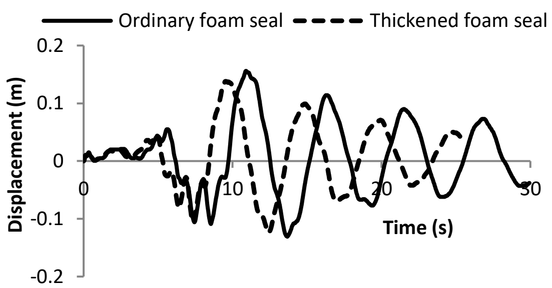

Figure 25. Time wave vibration of the roof high spot in the ordinary and thickened (extra) foam sealing cases due to the SarPol-e Zahab earthquake

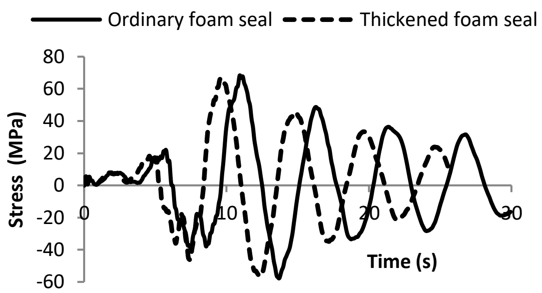

Figure 28. Time simulation of the stress of the roof high spot in the ordinary and thickened (extra) foam sealing cases due to the SarPol-e Zahab earthquake

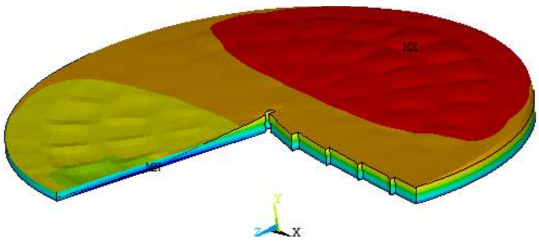

Figure 29. Dynamic pressure at 10.92s under SarPol-e Zahab earthquake in the ordinary foam sealing case

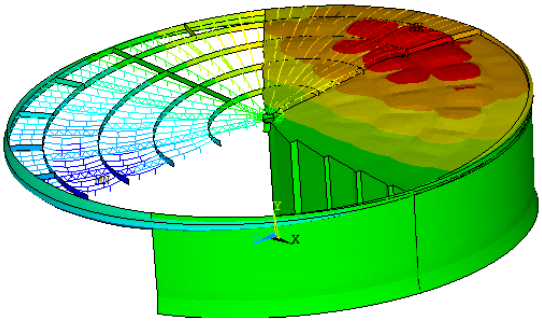

Figure 30. Vertical displacement of the liquid and the roof parts under SarPol-e Zahab earthquake at 10.92s in the ordinary foam sealing case

liquid dynamic pressure pattern is consistent with the displacements depicted in Figure 30. In addition, the two latest figures coincide with the first mode shape shown in Figure 13.

11. VALIDATION OF THE NUMERICAL MODEL

An attempt was made to validate the results obtained from the modal and time history analysis. However, the present model is significantly different from the previous models of the literature. Such complicated structure of the roof in addition to the contact and slipping behavior have not been proposed in the previous studies. These differences make it difficult to find similar models to verify the results. Hence, the only way is to simplify the present model. In this way, the upper deck and stiffeners have been omitted in the verification, and the natural frequencies were compared with the results obtained from the analytical method recommended in Eurocode 8 part 4 standard [39]. The considered tank was assumed to have fixed conditions at the base as in the present work. However, this analytical approach was recommended for bare tanks. In this work, the equivalent condition for bare tank has been provided by using low-modulus lower deck. In this condition, the first natural frequency of the storage tank was compared with the Eurocode 8 part 4 standard. The result of such comparison has been summarized in Table 6. In this table, the natural frequencies are converged to the values close to the natural frequency computed by Eurocode 8 along with the reduction of the elastic modulus of the lower deck.

As described before, two methods have been used for vibration severity calculation: response spectrum and time history methods. In the response spectrum approach, the maximum vibration peak is calculated at the considered natural frequency. In the time history analysis, this quantity can also be derived from the time wave vibration data. Time wave vibration curves showed that the first natural frequency is the dominant part of the maximum vibration peak. Hence, comparison of the vibration peak obtained by these two approaches is possible. In Table 7, these two results are summarized for the foam sealing case under the excitation of Sakaria and SarPol-e Zahab earthquakes. As can be seen, the right and left columns have good compatibility.

For time history validation, it is difficult to find a similar seismic wave rather than finding the same model with the one used in the references, as the earthquake records used in the literature do not have accurate addressing of the station. Small frequency deviation from the first natural frequency may lead to a significant vibration difference of the roof. However, the present time history analysis was compared with the model studied by Moslemi and Kianoush [40] under the 1940 El Centro earthquake. The available data from this earthquake was found to be similar with the one used in the reference as possible. Refer to the aforementioned analysis to find the specifications of the model studied by the authors. As can be seen, the storage tank was a concrete shell containing water without floating roof. The present model was changed to the studied model. However, the lower deck has also been added to the

TABLE 6. Comparison of the natural frequencies calculated by Eurocode 8 and the present method in the absence of the upper deck and stiffeners

Frequency Index	fn1 (in Hz)	fn2 (in Hz)
Eurocode 8 method	0.0978	0.2072
$E_{lower\ deck} = 2e11$Pa	0.1036	0.2235
$E_{lower\ deck} = 2e8$ Pa	0.1016	0.2197
$E_{lower\ deck} = 2e5$ Pa	0.1016	0.2195

TABLE 7. Comparison of the maximum vibration peak obtained by response spectrum and time history methods

Excitation type	Modal response by response spectrum method	Vibration peak by time history analysis
Sakaria earthquake	0.302	0.304
SarPol-e Zahab earthquake	0.150	0.156

system to check the validity of FSI and the dynamic behavior of the selected part of the roof. As Figures 31 and 32 show, high spot vibration of the lower deck conforms approximately with the high spot vibration of the liquid surface calculated by Moslemi and Kianoush.

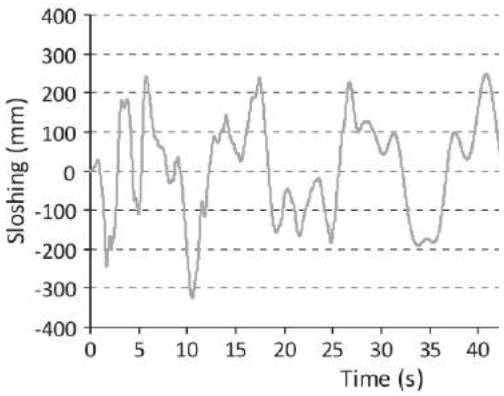

Figure 31. Time wave vibration of the liquid surface high spot due to 1940-El Centro earthquake with 0.4g scaling calculated by Moslemi and Kianoush

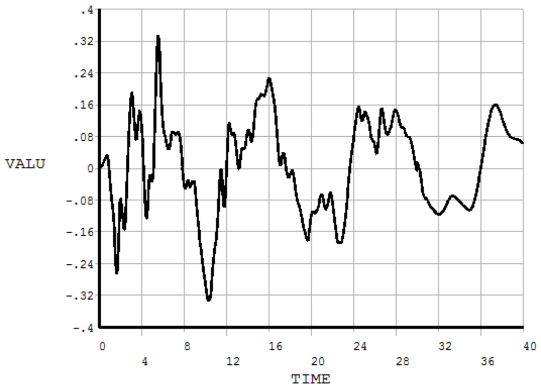

Figure 32. Time wave vibration of the lower deck high spot due to 1940-El Centro earthquake with 0.4g scaling calculated in the present study (This figure is the ANSYS output in which 'VALU' is displacement in meter, and 'TIME' is in second.)

12. CONCLUSION

To study and compare the seismic behavior of the floating roof in the tube and foam sealing cases, modal and time history analysis have been performed .

In modal analysis, hydroelastic natural frequencies of the floating roof, mode shapes and modal responses were obtained, which led to the following results.

1. The first and second natural frequencies in the foam sealing case were higher than that in tube sealing case.

2. The mode shapes of the dominant natural frequencies were similar in the two sealing cases.

3. In equal harmonic excitation, modal response of the first and second natural frequencies in the foam sealing case was less than that in the tube sealing case.

In time history analysis, the storage tank was excited by the horizontal component of Sakaria earthquake and two harmonics with equal amplitude at the first natural frequency of each sealing case through which the following results were achieved.

1. Vibration/excitation of the first and second natural frequencies in the foam sealing case was lower than than in the tube sealing case.

2. Steady state amplitude due to the harmonic excitation in the foam sealing case was lower than than in the tube sealing case.

It was concluded from the above modal and time history analysis that the floating roof is less vulnerable to seismic vibration in the foam sealing case than in tube sealing case. To identify the contribution of the seal factors to this phenomenon, mechanical parameters of the seal including elastic and shear modulus, density, damping and slipping has been investigated. In this regard, it was concluded that

1. The hysteresis damping in the foam seal is the cause of the vibration mitigation of the roof in this sealing case.

2. More vertical shear modulus of the foam seal than the tube seal is the main factor in increment of the natural frequency.

3. Slip of the seal periphery does not change the aforementioned conclusion.

4. The effect of the other factors of the seal on the roof vibration is negligible.

Regarding the above achievements, the foam damping was assumed to be increased by 50% by addition of some foam in the vertical direction. Time history analysis of the roof vibration has been carried out with the new revised foam seal by excitation of the tank with the horizontal component of the SarPol-e Zahab earthquake. Numerical results shows that the vibration of the roof in the thickened foam sealing case is considerably lower than that in the ordinary foam sealing case. The above extra-foam addition has been recommended as an approach for more vibration mitigation of the roof.

13. REFERENCES

1. Ahmadi, H. and Kadivar, M.H., "Seismic analysis of double deck floating roofs of siraf storage tanks with condensate, light and heavy crude oils", ***International Journal of Engineering, Transactions A: Basics***, Vol. 34, No. 10, (2021), 2319-2331, doi: 10.5829/ije.2021.34.10a.13

2. Kuan, S.Y., "Design, construction and operation of the floating roof tank", University of Southern Queensland, Mechanical and Mechatronic Engineering, Australia, Bachelor of Engineering, (2009); Available from:https://eprints.usq.edu.au/8503

3. Trimulyono, A., Chrismianto, D., Samuel, S. and Aslami, M.H., "Single-phase and two-phase smoothed particle hydrodynamics

for sloshing in the low filling ratio of the prismatic tank", ***International Journal of Engineering, Transactions B: Applications,*** Vol. 34, No. 5, (2021), 1345-1351, doi: 10.5829/IJE.2021.34.05B.30

4. Chang, J.I. and Lin, C.-C., "A study of storage tank accidents", ***Journal of Loss Prevention in the Process Industries***, Vol. 19, No. 1, (2006), 51-59, doi: 10.1016/j.jlp.2005.05.015

5. Hatayama, K., "Lessons from the 2003 tokachi-oki, japan, earthquake for prediction of long-period strong ground motions and sloshing damage to oil storage tanks", ***Journal of Seismology***, Vol. 12, No. 2, (2008), 255-263, doi: 10.1007/s10950-007-9066-y

6. Utsumi, M., "Vibration reduction of a floating roof by dynamic vibration absorbers", ***Journal of Pressure Vessel Technology***, Vol. 133, No. 4, (2011), doi: 10.1115/1.4002923

7. Kobayashi, N., Sato, T. and Torisaka, A., "Passive control of liquid sloshing in floating roof tank with multi dynamic absorber", in ASME 2013 Pressure Vessels and Piping Conference. Vol. 8: Seismic Engineering, (2013), doi: 10.1115/pvp2013-97229

8. Hasheminejad, S.M. and Mohammadi, M.M., "Active sloshing control in a smart flexible cylindrical floating roof tank", ***Journal of Fluids and Structures***, Vol. 66, (2016), 350-381, doi: 10.1016/j.jfluidstructs.2016.07.022

9. Esfandian, H., Goodarzian Urimi, M. and Shokoohi Rad, A., "Risk assessment of gasoline storage unit of national iranian oil product distribution company using phast software", ***International Journal of Engineering***, ***Transactions A: Basics***, Vol. 34, No. 4, (2021), 763-768, doi: 10.5829/IJE.2021.34.04A.02

10. Salarieh, H., shabani, r. and tariverdilo, s., "Effect of flexural and membrane stiffness on the analysis of floating roofs", ***International Journal of Engineering, Transactions A: Basics***, Vol. 23, No. 1, (2010), 57-64; Available from: https://www.ije.ir/article_71832.html

11. Shabani, R., "Stress patterns in single deck floating roofs subjected to ground motion accelerations", ***International Journal of Engineering***, ***Transactions C: Aspects***, Vol. 26, No. 12, (2013), 1495-1504, doi: 10.5829/idosi.ije.2013.26.12c.10

12. Yoshida, S., Sekine, K. and Mitsuta, T., "Axisymmetric finite element analysis for sloshing response of floating roofs in cylindrical storage tanks", ***Journal of Environment and Engineering***, Vol. 5, No. 1, (2010), 27-38, doi: 10.1299/jee.5.27

13. Yoshida, S., Sekine, K. and Iwata, K., "Sloshing characteristics of single deck floating roofs in aboveground storage tanks: Natural periods and vibration modes", in ASME 2009 Pressure Vessels and Piping Conference. Vol. Volume 7: Operations, Applications and Components, (2009), 191-199, doi: 10.1115/pvp2009-77187

14. Golzar, F.G., Shabani, R., Tariverdilo, S. and Rezazadeh, G., "Sloshing response of floating roofed liquid storage tanks subjected to earthquakes of different types", ***Journal of Pressure Vessel Technology***, Vol. 134, No. 5, (2012), doi: 10.1115/1.4006858

15. Shabani, R. and Golzar, F.G., "Large deflection analysis of floating roofs subjected to earthquake ground motions", ***Nonlinear Analysis: Real World Applications***, Vol. 13, No. 5, (2012), 2034-2048, doi: 10.1016/j.nonrwa.2011.12.026

16. Goudarzi, M.A., "Seismic behavior of a single deck floating roof due to second sloshing mode", ***Journal of Pressure Vessel Technology***, Vol. 135, No. 1, (2012), doi: 10.1115/1.4007291

17. Ali Goudarzi, M., "Attenuation effects of a single deck floating roof in a liquid storage tank", ***Journal of Pressure Vessel Technology***, Vol. 136, No. 1, (2013), doi: 10.1115/1.4025344

18. Goudarzi, M.A., "Seismic design of a double deck floating roof type used for liquid storage tanks", ***Journal of Pressure Vessel Technology***, Vol. 137, No. 4, (2015)., DOI: 10.1115/1.4029111

19. Meera, U.S. and Reshmi, P.R., "Dynamic analysis of single deck floating roof with deck stiffeners", ***International Research Journal of Engineering and Technology (IRJET)***, Vol. 04, No. 04, (2017), 3522-3526; Available from: https://www.irjet.net/archives/V4/i4/IRJET-V4I4844.pdf

20. Golzar, F.G., Shabani, R. and Tariverdilo, S., "Stress analyses in single deck and double deck floating roofs subjected to earthquake ground motions", ***Scientia Iranica***, Vol. 24, No. 2, (2017), 727-739, doi: 10.24200/sci.2017.4057

21. Belostotsky, A.M., Akimov, P.A. and Afansyeva, I.N., "Multilevel methodology of numerical seismic analysis of coupled systems “foundation – shell – pontoon (floating roof) – column(s) – fluid”", ***Procedia Engineering***, Vol. 153, (2016), 89-94., doi: 10.1016/j.proeng.2016.08.085

22. Hosseini, M., Soroor, A., Sardar, A. and Jafarieh, F., "A simplified method for seismic analysis of tanks with floating roof by using finite element method: Case study of kharg (southern iran) island tanks", ***Procedia Engineering***, Vol. 14, (2011), 2884-2890, doi: 10.1016/j.proeng.2011.07.363

23. Sakai F., I.R., "Some considerations on seismic design and controls of sloshing in floating-roofed oil tanks", in The 14th World Conference on Earthquake Engineering, Beijing, China., (2008)

24. Hosseini, M., Goudarzi, M.A. and Soroor, A., "Reduction of seismic sloshing in floating roof liquid storage tanks by using a suspended annular baffle (SAB)", ***Journal of Fluids and Structures***, Vol. 71, (2017), 40-55, doi: 10.1016/j.jfluidstructs.2017.02.008

25. Ruiz, R., "A new type of tuned liquid damper and its effectiveness in enhancing seismic performance: Numerical characterization, experimental validation, parametric analysis and life-cycle based design. (2015); Available from: https://repositorio.uc.cl/handle/11534/21185

26. ANSYS.Inc. *Customer support | ansys*. [cited 04 May 2022]; Available from: https://www.ansys.com/support

27. Sigrist, J.-F., "Fluid-structure interaction: An introduction to finite element coupling, John Wiley & Sons, (2015)

28. Beer, F., Jr. Johnston, E.R., DeWolf, J. and Mazurek, D., "Mechanics of materials, McGraw-Hill Education, (2011)

29. Alzoubi, M., Al-Waked, R. and Tanbour, E., "Compression and hysteresis curves of nonlinear polyurethane foams under different densities, strain rates and different environmental conditions", ***Journal of Mechanical Engineering***, Vol. Volume 9, No., (2011), 101-109, doi: 10.1115/IMECE2011-62290

30. Tanks, G. *External floating roof tanks*. [cited 04 May 2022]; Available from: https://www.gsctanks.com

31. Watanabe, M. and Yamaguchi, H., "The friction and wear properties of nylon", ***Wear***, Vol. 110, No. 3, (1986), 379-388, doi: 10.1016/0043-1648(86)90111-0

32. Shelke, S., Vankudre, H. and Patil, V., "Comparative evaluation of mode combination methods in seismic analysis using response spectrum method for tank structure using fea-seismic fea", in Applied Mechanics and Materials, Trans Tech Publ. Vol. 110, (2012), 5240-5248, doi: 10.4028/www.scientific.net/AMM.110-116.5240

33. Norouzi, A.H., Gerami, M., Vahdani, R. and Sivandi-Pour, A., "Effects of multiple structure-soil-structure interactions considering the earthquake waveform and structures elevation effects", ***International Journal of Engineering***, ***Transactions B: Applications***, Vol. 33, No. 5, (2020), 744-752, doi: 10.5829/ije.2020.33.05b.05

34. Versluis, M., "Hydrodynamic pressures on large lock structures", Delft University of Technology, Civil Engineering and Geosciences, Netherlands, Master of Science, (2010)

35. Seismosoft.Co. *Seismosignal support*. cited 04 May 2022]; Available from: https://seismosoft.com/support/seismosignal-support

36. *Iran road, housing & urban development research center: Iran strong motion network*. [cited 04 May 2022]; Available from: https://smd.bhrc.ac.ir/Portal/en/Search/BigQuakes

37. Yazdani, A.-. and Kowsari, M., "Statistical prediction of the sequence of large earthquakes in iran", ***International Journal of Engineering***, ***Transactions B: Applications***, Vol. 24, No. 4, (2011), 325-336., doi: 10.5829/idosi.ije.2011.24.04b.03

38. Sadeghian, T. and E. Babadi, M., "Earthquake prediction modeling using dynamic changes (case study: Alborz region)", ***International Journal of Engineering, Transactions B: Applications***, Vol. 34, No. 2, (2021), 355-366, doi: 10.5829/ije.2021.34.02b.07

39. Committee, E., *Eurocode 8- design of structures for earthquake resistance- part 4: Silos, tanks and pipelines*, in *Specific principles and application rules for tanks*. 2006, European Committee for Standardization: Brussels.81; Available from: https://www.phd.eng.br/wp-content/uploads/2014/12/en.1998.4.2006.pdf

40. Moslemi, M. and Kianoush, M.R., "Parametric study on dynamic behavior of cylindrical ground-supported tanks", ***Engineering Structures***, Vol. 42, (2012), 214-230, doi: 10.1016/j.engstruct.2012.04.026.

Persian Abstract

چکیده

ارتعاش سقف شناور در دو حالت آب‌بند تیوبی و فومی بوسیله نرم‌افزار انسیس تحلیل شده است. اندرکنش سیال و سازه و پدیده اسلاش لحاظ گردیده است. پاسخ‌های مودال، موج‌های زمانی و طیف‌های فرکانسی ارتعاش سقف در دو حالت آب‌بندی طی تحریک لرزه‌ای افقی کف مخزن ارزیابی شد. سپس، تأثیر عوامل مکانیکی اصلی آب‌بند بر لرزش سقف بررسی گردید. ارتعاش سقف در حالت آب‌بند فومی به طور قابل توجه از حالت آب‌بند تیوبی کمتر بود که ناشی از میرایی بیشتر آب‌بند فومی نسبت به آب‌بند فومی می‌باشد. همچنین، فرکانس طبیعی حالت آب‌بند فومی از فرکانس طبیعی حالت آب‌بند تیوبی بیشتر بود که به علت مدول برشی بیشتر آب‌بند فومی در راستای عمودی (محور مخزن) می‌باشد. با توجه به این نتیجه، آب‌بند فومی در راستای عمودی خلاصی موجود افزایش داده شد و کف مخزن دوباره تحت تحریک لرزه‌ای قرار گرفت. ملاحظه شد این ارتقاء به لرزه‌گیری بیشتر سقف کمک می‌نماید.

IJE TRANSACTIONS A: Basics Vol. 35, No. 07, (July 2022) 1416-1427

International Journal of Engineering

Journal Homepage: www.ije.ir

High Temperature Corrosion Behavior of High Velocity Oxy Fuel Sprayed NiCrMoFeCoAl-30%SiO_2 and NiCrMoFeCoAl-30%Cr_2O_3 Composite Coatings on ASTM SA213-T22 Steel in a Coal-fired Boiler Environment

V. G. Patil*[a], B. Somasundaram[a], S. Kandaiah[b], M. R. Ramesh[c], S. kumar[a]

[a] *School of Mechanical Engineering, REVA University Bengaluru, India*
[b] *Department of Chemistry, School of Applied Sciences, REVA University Bengaluru, India*
[c] *National Institute of Technology Karnataka, Surathkal, Mangalore, India*

PAPER INFO

Paper history:
Received 06 February 2022
Received in revised form 23 April 2022
Accepted 24 April 2022

Keywords:
Hot Corrosion
High-velocity Oxy Fuel
Thermogravimetric Analysis
Thermal Spraying
Oxide Scale

ABSTRACT

High-velocity oxy fuel (HVOF) sprayed coatings can improve the corrosion resistance of bare ASTM SA213-T22 boiler steel. In this report, we have investigated the NiCrMoFeCoAl-30%SiO_2 and NiCrMoFeCoAl-30%Cr_2O_3 composite coatings were deposited on bare ASTM SA213-T22 boiler steel for corrosion protection. High-temperature corrosion studies were conducted in a molten salt (Na_2SO_4-60%V_2O_5) environment at 700ºC under thermo-cyclic conditions. The as-sprayed composite coatings are characterized for microstructure and mechanical properties. The thermo-gravimetric method was utilized to understand the kinetics of corrosion. Characterization of the corrosion products was examined by using scanning electron microscope (SEM)/ Energy dispersive spectroscopy (EDS) and X-ray diffraction (XRD) techniques. The obtained results suggest both the composite coatings are favorable to corrosion resistance over the bare ASTM SA213-T22 boiler steel. The NiCrMoFeCoAl-30%Cr_2O_3 composite coating was concluded to present a superior corrosion resistance in the high-temperature corrosion environment because of the uniform distribution of the composite coating matrix and the development of protective protection Cr_2O_3 in the scale. The molten salt heat-treated chromium oxide containing coating shows good corrosion stability than the silica composite. This could be attributed to the high temperature assisted formation metal chromates, chromites and oxide layers.

***doi**: 10.5829/ije.2022.35.07a.19*

1. INTRODUCTION

High-performance coatings formulated on the surface of materials by thermal spraying technology are among the most efficient methods to enhance corrosion, wear, and oxidation resistance properties and extend their lifespan [1-5]. Generally, the boiler steel materials were subjected to high-temperature environment and corrosive conditions in industries. Several coating methods were used to protect the boiler steel alloy [1-5]. Singh et al. [6] had investigated the performance of uncoated T-91 steel and HVOF coated Ni-20Cr & (Cr_3C_2–25 (Ni–20Cr) steels which were subjected to 40%Na_2SO_4–V_2O_5 environment at 900°C. The Cr_3C_2–25(Ni–20Cr) coated steel was superior towards corrosion resistant than the Ni-20Cr coated steel. The uncoated T-91 steel was found to gain higher weight. AK et al. [7] reported that the HVOF method can be used to fabricate better carbide-metal coating along with good bond strength, high density, low decarburization, and high hardness. Sidhu et al. [8] had examined the behavior of bare and HVOF coated samples after high-temperature treatment in Na_2SO_4–60%V_2O_5 environment at 900°C. The NiCr coated steel was ascertained to be very effective for corrosion resistance than the bare steel. The bare sample shows the spalling of oxide scales during high-temperature corrosion. Thermal spray technology is a rapidly developing surface engineering area and is

*Corresponding Author Email: patilviresh751@gmail.com (V. G. Patil)

Please cite this article as: V. G. Patil, B. Somasundaram, S. Kandaiah, M. R. Ramesh, S. kumar, High Temperature Corrosion Behavior of High Velocity Oxy Fuel Sprayed NiCrMoFeCoAl-30%SiO_2 and NiCrMoFeCoAl-30%Cr_2O_3 Composite Coatings on ASTM SA213-T22 Steel in a Coal-fired Boiler Environment, ***International Journal of Engineering, Transactions A: Basics***, Vol. 35, No. 07, (2022) 1416-1427

extensively employed to protect metallic surfaces against high-temperature corrosion [9, 10]. The HVOF coated samples are advantageous to corrosion resistance. Degradation occurs especially within the hot sections of boilers due to hot corrosion [11]. Goyal et al. [12] had studied the performance of uncoated and HVOF coated T22 specimens were subjected to the molten salt environment at 700°C. The results exposed that bare ASTM-SA213- T22 steel suffered spallation of the Fe_2O_3 scale. The HVOF coated T22 steel specimens showed lower weight gain with corrosion resistance. Mahesh et al. [13] examined the high-temperature corrosion behavior of uncoated Superfer 800 and HVOF coated samples in an actual coal-fired boiler environment at 700°C for 1000 h. NiCrAl coated Superfer 800 sample exhibits superior corrosion resistance to hot corrosion than Ni–5Al coated Superfer 800 sample in an actual coal-fired boiler environment. Wang et al. [14] remarked in their research studies on the oil-fired power generators that the formulation of sulfate salts and ashes are the distinctive high-temperature corrosion origins. Sidhu et al. [15] had investigated the high-temperature corrosion behavior of uncoated (ASME SA213-T22 and T91) and HVOF coated 93WC-Cr_3C_2-7Ni, WC-17Co specimens which were exposed to an actual coal-fired boiler environment. The high-temperature corrosion resistance of 93(WC-Cr_3C_2)-7Ni-coated steel sample was better among all coated samples. Sreenivasulu and Manikandan [16] had studied the high-temperature corrosion behavior of uncoated alloy 80A, HVOF coated Cr3C2-25NiCr, and NiCrMoNb samples were subjected to the molten salt environment at 900°C. The Cr_3C_2-25NiCr coating had shown good corrosion resistance compared to bare alloy 80A. Chatha et al. [17] studied the hot corrosion behavior of uncoated and coated steels subjected to the molten salt environment at 750°C. The T91 boiler tube steel shows superior mass gain, because of the development of oxide scales (Fe_2O_3). The 80Ni–Cr coating was noticed to be very effective in corrosion resistance than the Cr_3C_2–25(Ni–20Cr) coating. The high-temperature corrosion reduces the corrosion-resistant properties of the boiler tube steels, conclusively resulting in the premature breakdown of boiler parts [18, 19]. Somasundaram et al. [20] were investigated the hot corrosion behavior of HVOF sprayed (60%Cr_3C_2–NiCr) +5 % Si coatings on Superfer 800 H, SA213-T22, and MDN-310 substrate alloys. The coated and uncoated samples were exposed to a molten salt environment at 700°C. It was observed that the HVOF coated samples presented more beneficial corrosion resistance than the bare samples. Mangla et al. [21] had explored the high-temperature corrosion behavior of HVOF and Plasma sprayed 80%Ni20%Cr coated SA-213-T22 steel exposed to the molten salt environment at 900°C. It concludes that HVOF sprayed coating exhibits a superior corrosion resistance than the PS method. Kaur et al. [22] were studied the behavior of uncoated T22 boiler steel and HVOF sprayed 75%Cr_3C_2-25%NiCr coated samples were subjected to the molten salt, air, and actual boiler environments for 50 cycles. The HVOF coated steel was noticed to be complete and spallation-free, while the uncoated T22 boiler steel was endured. Kaur et al. [22] explored the hot corrosion behavior of T22 bare steel utilized in boilers. The contaminations present in fuel employed such as Na, S, and V cause material corrosion. Reactions between these impurities in the presence of oxygen lead to ash deposits, like $NaVO_3$, Na_2SO_4, and V_2O_5, which cause harsh corrosion [23, 24]. Kaushal et al. [25] had explored the high-temperature corrosion performance of uncoated ASTM A213 347H boiler steel and HVOF coated Ni-20Cr samples in a Na_2SO_4-60%V_2O_5 environment at 900°C. The bare T22 steel endured a higher rate of deprivation and wide spallation. The 80Ni-Cr coating was effective in less weight gain and corrosion resistance. The coating enhances the lifespan of structural parts by protecting the surface against wear and corrosion [26-28]. Zhang et al. [29] were studied the high-temperature corrosion conflict of HVOF sprayed CoCrAlSiY coated steel with different Si (0wt%, 2wt%, and 5wt %) concentrations are exposed to 75% Na_2SO_4-25% NaCl at 900 º C. An increase in Si concentration reduces the average corrosion diffusion depth of the HVOF coating. Thus, it helps to improve the corrosion resistance of the HVOF coating in the given environment. Saricimen et al. [30] were studied the high-temperature corrosion performance of HVOF and plasma sprayed Ni & Co-based metallic coated 310 stainless steel specimens are exposed to NaCl, Na_2SO_4, and V_2O_5 salt mixtures at 900°C. Experimental results indicate that Cobalt-based coatings perform better than Nickel-based coating. Sidhu et al. [31] were explored the high-temperature corrosion behavior of bare ASTM SA213-T11 steel and HVOF coated specimens are subjected to a Na_2SO_4-60%V_2O_5 environment at 900ºC. NiCr Coating presented a better corrosive resistance than uncoated steel and WC-Co & Cr_3C_2-NiCr coatings. Shi et al. [32] were investigated the high-temperature corrosion behavior of HVOF Cr_3C_2-NiCr/NiCrAlY coated UMCo50 alloy samples are subjected to the Na_2SO_4 environment at different temperatures. The results explored that the Cr_3C_2-NiCr coating was relatively dense and mainly compiled of Cr_3C_2, NiCr, and a minor quantity of Cr_7C_3 three phases. Table 1 illustrates the summary of the literature review.

In the current study, the composite coatings were formulated on ASTM SA213-T22 steel by using the HVOF technique. To the best of our knowledge, there is no reported literature on high-temperature corrosion behavior of HVOF sprayed NiCrMoFeCoAl-30%SiO_2 and NiCrMoFeCoAl-30%Cr_2O_3 composite coatings.

The degradation of T22 boiler steel is progressive when subjected to high-temperature industrial conditions.

TABLE 1. Summary of the literature review

S. No.	Year	Authors	Coating material	Substrate	Process	Remarks
1	2022	Ebrahimi et al. [1]	Bi-layered Hydroxyapatite /Al_2O_3-SiO_2 (with 10, 20, 30 %wt SiO_2) were deposited on Ti	Commercial pure Ti (ASTM grade #2)	Plasma spray	The composition of Al_2O_3-20% wt SiO_2 shows excellent protection which is attributed to their particular compositions, properties and microstructures.
2	2021	Spandana et al. [2]	YSZ/TiO_2 over NiCr bond coat	TV1 alloy of aluminium	Plasma spray HVOF	TBC coated piston shows the increase in brake thermal efficiency and decrease in brake specific fuel consumption compared to the uncoated piston.
3	2017	Rahnavard [3]	CYSZ/NiCrAlY	Inconel 738	Plasma spray	Functional grade material with thermal barrier - Very promising potential as a novel TBC material.
4	2013	Mhdipoor and Rahimipour [4]	Yttria stabilized zirconia (YSZ) and ceria stabilized zirconia (ZrO_2 25CeO_2 2.5Y_2O_3)	Ni-Based superalloy (Inconel738) and 1020 steel	Plasma spray	CSZ TBCs had better resistant to high temperature corrosion than YSZ TBCs.
5	2017	Naeimi and Tahari [5]	MCrAlY/ CoNiCrAlY	Inconel 738 Superalloy	HVOF	The increase of surface roughness as a result of the other oxides including Cr_2O_3, NiO, and spinel, inhomogeneous and non-uniform thermal oxide layer created and oxidation was constantly increased.
6	2016	Singh et al. [6]	Ni-20Cr & (Cr_3C_2–25 (Ni–20Cr)	T-91 steel	HVOF	The Cr_3C_2–25(Ni–20Cr) coated steel was good corrosion resistant to the Ni-20Cr coated steel.
7	2003	AK et al. [7]	80Ni-20Cr	Stainless steel	HVOF	HVOF with carbide-metal coating, exhibit good bond strength, low decarburization, high density and high hardness.
8	2006	Sidhu et al. [8]	Ni–20Cr	ASTM-SA-210 GrA1, ASTM-SA213 (T-11) and ASTM-SA213 (T-22)	HVOF	NiCr coated steel was ascertained to be good corrosion resistance than the substrate steel.
9	2003	Uusitalo et al. [9]	Ni50Cr Ni57Cr Ni21Cr9Mo	Ferritic steel Austenitic steel	HVOF	Ni-based coatings was good corrosion resistance than the ferritic steel.
10	1992	Wang et al. [10]	Chromized-siliconized	1018 carbon steel and 2.25 Cr-[Mo steel	Plasma spray	The chromized-siliconized coatings had lower material wastage in both the static and the dynamic oxidation tests than did the chromized-aluminized and straight chromized coatings
11	2002	Rapp [11]	-	-	-	An evolution of a negative solubility gradient as a criterion for continuing hot corrosion is made
12	2019	Goyal et al. [12]	Cr_2O_3–1wt%CNT Cr_2O_3–2wt%CNT Cr_2O_3–4wt%CNT Cr_2O_3–6wt%CNT Cr_2O_3–8wt%CNT	ASTM-SA213-T22 steel	HVOF	The T22 substrate steel suffered spallation of the Fe_2O_3 scale. The HVOF coated T22 substrate steel samples showed lower weight gains with corrosion resistance.
13	2010	Mahesh et al. [13]	NiCrAl and Ni–5Al	Superfer 800	HVOF	NiCrAl coated Superfer 800 sample exhibits good corrosion resistance to hot corrosion than Ni–5Al coated Superfer 800 sample in an actual coal-fired boiler environment.

14	2002	Wang et al. [14]	Na_2SO_4 coating	The tungsten-bearing and Al2O3-forming superalloy, MARM247,	-	The oil-fired power generators show that the formulation of sulfate salts and ashes are the distinctive hot corrosion origins.
15	2019	Sidhu et al. [15]	93WC-Cr_3C_2-7Ni WC-17Co	ASME SA213-T22 and T91	HVOF	The high-temperature corrosion resistance of 93(WC-Cr_3C_2)-7Ni-coated steel sample was better among all coated samples.
16	2018	Manikandan [16]	Cr_3C_2-25NiCr and NiCrMoNb	Alloy 80A	HVOF	The Cr_3C_2-25NiCr coating had shown good corrosion resistance as equated to substrate alloy 80A.
17	2012	Chatha et al. [17]	80Ni–Cr and Cr_3C_2–25(Ni–20Cr)	T91 boiler tube steel	HVOF	The 80Ni–Cr coating was noticed to be very effective in corrosion resistance than the Cr_3C_2–25(Ni–20Cr) coating.
18	2016	Loghman-Estarki et al. [18]	YSZ, ScYSZ, NiCrAlY	Ni-based supperalloy	Plasma spray	ScYSZ coating has more hot corrosion resistance than YSZ coatings
19	2018	Aadhavan et al. [19]	Ceria coating	AISI 304, AISI 410, Inconel 600	electron beam physical vapor deposition	The high-temperature corrosion reduces the properties of the boiler tube steels, conclusively resulting in the premature breakdown of boiler parts
20	2015	Somasundaram et al. [20]	(60%Cr_3C_2–NiCr) + 5 % Si	Superfer 800 H, SA213-T22, and MDN-310	HVOF	HVOF coated specimens displays more beneficial corrosion resistance than the bare samples.
21	2017	Mangla et al. [21]	80%Ni20%Cr	SA-213-T22	HVOF and Plasma spray	HVOF sprayed coating shows superior corrosion resistance than the PS method
22	2012	Kaur et al. [22]	75%Cr_3C_2-25%NiCr	SA-213-T22	HVOF	The HVOF coated steel was remarked to be complete and spallation-free, while the uncoated T22 boiler steel was endured.
23	2007	Sidhu et al. [23]	SiO_2 (60.27%), Al_2O_3 (25.46%), Fe_2O_3(6.02%), CaO (3.68%), MgO (1.06%) and SO_3 (0.12%)	Carbon steel	Plasma spray	The coating was effective to decrease the oxidation and salt corrosion resistance of the carbon steel.
24	1987	Rapp [24]	-	-	-	In-situ electrochemical analysis on hot corrosion, kinetics, morphologies and the mechanisms.
25	2011	Kaushal et al. [25]	Ni-20Cr, 80Ni-Cr	ASTM A213 347H boiler steel	HVOF	The 80Ni-Cr coating was effective in less weight gain and corrosion resistance.
26	2013	Paul et al. [26]	NiCrBSiFe, alloy 718, alloy 625, and alloy C-276	P91	HVOF	The performance of the coatings dependent on its composition and the test conditions. Corrosion stability : alloy 625 > NiCrBSiFe > alloy 718 alloy C-276.
27	2013	Hong et al. [27]	NiCrBSiWFeCoC alloy	AISI 1045 steel	HVOF	The HVOF sprayed NiCrBSiWFeCoC alloy coating - presence of amorphous phase and low porosity and good corrosion resistant.
28	2012	Zhang et al. [28]	CoCrAlSiY coated steel with different Si (0wt%, 2wt%, and 5wt %)	SA-213-T22	HVOF	The increase of Si concentration reduces the average corrosion diffusion depth of the HVOF coating.
29	2017	Shuting et al. [29]	CoCrAlSiY coating with different Si concentrations (0wt%, 2wt% and 5wt%)	GH907	HVOF	Corrosion penetration depth of the coating increases with the rising of temperature, while the increasing of Si concentration decreases the average corrosion penetration depth of the coating
30	2014	Saricimen et al. [30]	Coating, Co_01 Coating, Co_02 Coating, Ni_03	310 stainless steel	HVOF and Plasma spray	Cobalt-based coatings perform better than Nickel-based coating.

31	2007	Sidhu et al. [31]	Cr3C2-NiCr, NiCr, WC-Co and Stellite-6 alloy	ASTM SA213-T11 steel	HVOF	NiCr Coating presented a better corrosive resistance than uncoated steel and WC-Co & Cr_3C_2-NiCr coatings.
32	2020	Shi et al. [32]	Cr_3C_2-NiCr/NiCrAlY	UMCo50 alloy	HVOF	Cr_3C_2-NiCr coating was relatively dense and mainly composed of Cr_3C_2, NiCr, and a minor quantity of Cr_7C_3 three peaks.

To simulate these conditions, we have performed experiments at molten salt (Na_2SO_4–60%V_2O_5) conditions and tested the bare T22 and the above coatings performance. Here the attempt was made to compare the corrosion effect of chromium oxide or silicon dioxide in metal composite HVOF coatings under heat treatment in molten salt conditions. Furthermore, the efforts were made towards the systematic analysis using microscopic, structural and gravimetric changes of bare and HVOF coated at high-temperature molten salt corrosive conditions. Here the oxidative effect of the molten salt mixture at high temperature could aggravate the T22 steel corrosion. Furthermore, investigations were performed to understand the comparative effect of silica and chromium oxides in the HVOF composite coatings. The coated and uncoated samples were exposed to the molten salt environment at 700°C under thermocyclic environments. Corrosion damage was evaluated by using the weight gain method. XRD and SEM/EDS methods to characterize the corroded samples. The high temperature assisted formation of surface metal chromites, chromates and oxide is shown to improve the corrosion stability with chromium oxide coatings. Hence this study is to identify a suitable coating for protecting uncoated T22 steel and to characterize the high-temperature corrosion effect of HVOF-sprayed composite coatings on T22 substrate steel. To develop a reliable laboratory simulation test method for assessing hot corrosion damage, the following methodology is used in this research work, shown in Figure 1.

2. EXPERIMENTAL SECTION

2. 1. Substrate Material

T22 steel has been designated as the bare material in the current investigation. For exposure tests, specimens were sectioned from ASTM SA213-T22 steel in square (25 mm × 25 mm × 5 mm) shapes. Sectioned specimens were grit blasted with aluminum oxide before HVOF formulation. The drum jigs were rotated on a turntable during spraying to ensure the application of uniform coatings with a limited edge effect. Table 2 illustrates the nominal chemical composition for T22 substrate steel.

2. 2. Formulation of the Coatings

HVOF method was employed to deposit NiCrMoFeCoAl-30%SiO_2 and NiCrMoFeCoAl-30%Cr_2O_3 composite coatings on the T22 substrate steel. The coating powders having particle size in the range of 45 - 60 μm range. The steel tubes utilized in fabrication of boilers face high temperatures [33]. HVOF coating parameters are listed in Table 3. The compositions of the powders utilized in the present examination are tabulated in Table 4. All the standard spray parameters and the spray distance were reserved constant all over the coating procedure. The average coating thickness obtained was 197 μm. The coatings were accumulated on all six edges of the base metal. The grit blasting was executed to get a fine surface roughness and stimulate the best possible adhesion between substrate and coating. SEM coupled with EDAX is used to study the microstructure and the compositions of the specimens. XRD technique was used to analyze the phases of coatings.

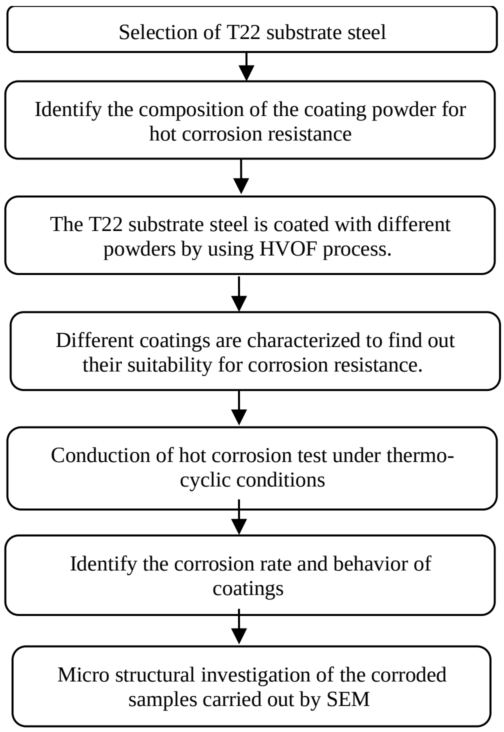

Figure 1. Scheme of coating process and characterization

TABLE 2. Chemical composition (wt%) of T22 substrate steel

Fe	Ni	Cr	Ti	Al	Mo	Mn	Si	C
Bal.	-	2.55	-	-	1.10	0.52	0.43	0.14

TABLE 3. Coating parameters used for HVOF spray process

HVOF process parameter	Quantity units
Oxygen flow rate	250 l/min
Fuel (LPG) flow rate	65-70 l/min
Air-flow rate	550 l/min
Spray distance	178 mm
Powder feed rate	28 g/min
Fuel (LPG) pressure	681 kPa
Oxygen pressure	981 kPa
Air pressure	588 kPa

TABLE 4. Chemical composition of the composite coatings (wt %) used in this study

HVOF coatings	Ni	Cr	Mo	Fe	Co	Al	SiO_2	Cr_2O_3
NiCrMoFeCoAl-30%SiO_2	39.9	15.4	2.1	4.9	4.2	3.5	30	-
NiCrMoFeCoAl-30%Cr_2O_3	39.9	15.4	2.1	4.9	4.2	3.5	-	30

2. 3. Coatings Characterization Techniques An image analyzer (Metaplus software) helps to compute the composite coatings' porosity based on ASTM B276. The mean value of the eight readings was computed for each specimen to evaluate coated steel's porosity. The SEM helped to obtain a cross-sectional micrograph of composite coatings. An inverted metallurgical microscope (OLYMPUS BX53M UPRIGHT METALLURGICAL MICROSCOPE) helps to evaluate the coating thickness. The composite coatings microhardness was evaluated using the Micro Vickers Hardness tester (VH1102, Reva University Bangalore) at a load of 300g at eight different locations on the cross-section a coated specimen. After the surface characterization techniques, the specimens were sectioned, mounted in transoptic powder, and exposed to polishing. The diamond paste (0.3 μm) helped to obtain a mirror finishing. The X-ray diffractometer did an XRD analysis on the coated and uncoated surface. It is operated by using CuKα as radiation at 40 kV and 30 mA. The samples were scanned within the 2θ range of 10° to 80°. SEM/EDAX analysis technique helps to characterize the surface, cross-sectional composition, & morphologies of the coated and uncoated specimens.

2. 4. Cyclic High Temperature Corrosion Test High temperature corrosion studies were performed in a (Na_2SO_4–60%V_2O_5) molten salt solution for 50 cycles under thermocyclic conditions, with each cycle comprised of 1 h of heating in the furnace at 700^0C, followed by 20 min cooling at ambient temperature [34]. The silicon carbide tube furnace is shown in Figure 2. The experimental conditions were selected to replicate the environment in energy-producing units such as furnaces and boilers [35-38]. The silicon carbide tube heater was standardized to the precision of ±5°C utilizing a Pt/Pt–13% Rh thermocouple. Before testing, the physical measurements of the samples were noted carefully with a vernier caliper to measure their dimensions. For comparison, the hot corrosion testing was performed on HVOF coated & bare specimens. The bare and coated specimens were mirror-polished with 1 μm by Al_2O_3 wheel-cloth polishing earlier than the corrosion test. A molten salt of Na_2SO_4–60%V_2O_5 is systematically blended with distilled water. The molten salt was applied uniformly and the coating distribution varies in the range of 3-5 mg/cm^2 on preheated specimens at 250^0C. The salt-coated sample was dehydrated at 100 °C for 3–4 h in the oven. Subsequently, the dehydrated salt-coated sample preserved in the alumina boat was balanced before the high-temperature corrosion test. Each specimen was positioned in the crucible and the weight was evaluated along with the boat and variance in weight data had been remarked. Weight-change data were determined at the end of each cycle. The surfaces of the corroded samples were visually examined to record the color, luster, peeling, and spalling of the scale. After the corrosion studies, the corroded surfaces were investigated by XRD and SEM/EDS techniques.

3. RESULTS

3. 1. Characterization for As-deposited Coatings The coating thickness has been measured from the optical microscope is around 200 μm. The microhardness of HVOF composite coatings is exhibited in Figure 3. Microhardness tests were performed using the model VH1102 auto to determine the microhardness of coated specimens along the cross-section with a load of 300g and a dwell period of 10s. The microhardness of the T22 substrate steel is measured to be around 270 $HV_{0.3}$. The average microhardness values of the NiCrMoFeCoAl-30%SiO_2 and NiCrMoFeCoAl-30%Cr_2O_3 composite

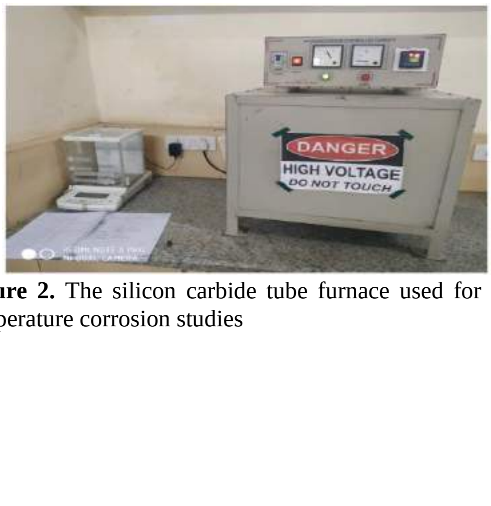

Figure 2. The silicon carbide tube furnace used for high temperature corrosion studies

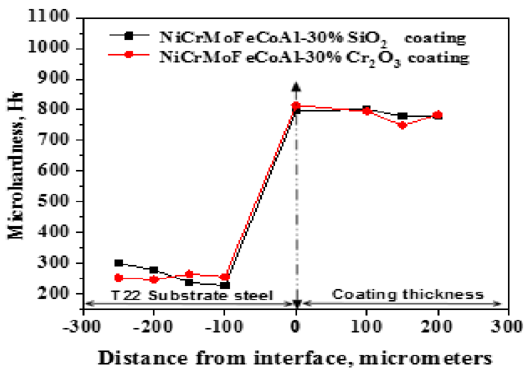

Figure 3. Cross-sectional microhardness profile for HVOF coatings across the cross-section

coatings have been determined to be around 801.9 $HV_{0.3}$ and 814.3 $HV_{0.3}$, respectively. The porosity of these coatings is less than 1.6%. The characterizations of coatings are tabulated in Table 5.

3. 2. Visual Examination Figures 4 (a)-4(c) demonstrates the macrographs of the uncoated T22 steel, NiCrMoFeCoAl-30%SiO_2, and NiCrMoFeCoAl-30%Cr_2O_3 composite coatings are exposed to hot corrosion. The uncoated T22 steel (Figure 4a) appears to dark grey colored oxide scale during the 1st cycle and turned to blackish gray color in the 10th cycle, and the color remains similar up to the end of the cycle. The formation of scales on the T22 substrate steel was determined to be friable and revealed the rupture on a surface. Throughout the early hot corrosion cycles, the formation of the spalling of the oxide scale on the T22 substrate steel was remarked. The NiCrMoFeCoAl-30%SiO_2 coated (Figure 4b) specimen appeared as a faded brown color in the 10th cycle and remains the same until the 50th cycle. The dark gray color of the NiCrMoFeCoAl-30%Cr_2O_3 coated (Figure 4c) specimen changes to grey color in the 10th cycle and remains identical till the end of the corrosion study. Until the end of the high-temperature corrosion study, these composite coatings have not shown any severe spalling of scale, no peeling-off, and no visible cracks on coating layers.

TABLE 5. Variation of porosity, microhardness, and coating thickness of HVOF coated samples

HVOF coatings	Porosity (%)	Vickers Microhardness, VHN (GPa)	Coating thickness (μm)
NiCrMoFeCoAl-30%SiO_2	1.69	801.9 HV 0.3	197
NiCrMoFeCoAl-30%Cr_2O_3	1.66	814.3 HV 0.3	197

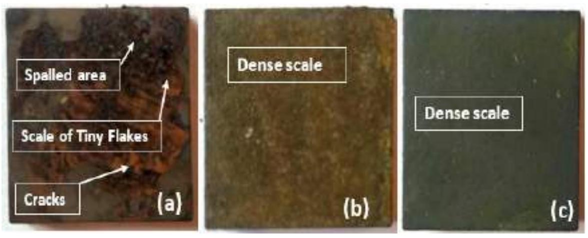

Figure 4. Macro images of the uncoated (a) T22 substrate steel and HVOF coated (b) NiCrMoFeCoAl-30%SiO_2 (c) NiCrMoFeCoAl-30%Cr2O3 specimens are subjected to Na_2SO_4–60%V_2O_5 environment at 700°C

3. 3. Corrosion Kinetics in Molten Salt The weight change per unit area to the no. of cycles is plotted for the T22 steel, NiCrMoFeCoAl-30%SiO_2, and NiCrMoFeCoAl-30%Cr_2O_3 composite coatings are subjected to hot corrosion under thermocyclic conditions are shown in Figure 5(a). The weight gain expeditiously rises up to the 10th cycle in T22 substrate steel. After continuing rise in weight gain is remarked until the 50 cycles. The net weight change of the samples in the molten salt environment signifies the combined effects of the weight loss due to the oxide scales of suspected fluxing and spalling and the weight gain owing to the oxide scale formations. The T22 substrate steel exhibited more differences in the weight change as compared to that of composite coatings. The plot of (weight change/area)^2 vs. no. of cycles for coated and uncoated specimens are presented in Figure 5(b). It can be noted from the graph that T22 steel exhibited some deviations from the parabolic rate law, while composite coatings followed the parabolic rate law. The formation of a thick oxide scale due to the chemical reaction of the composite coatings, T22 substrate steel showed higher weight gain than the NiCrMoFeCoAl-30%SiO_2 and NiCrMoFeCoAl-30%Cr_2O_3 composite coatings. Figure 5(b) clarifies that coated and uncoated specimens in a hot corrosion environment obey the parabolic rate law. *kp* is resulting from the experimental correlation of parabolic rate law Equation (1):

$$(\Delta W/A)^2 = kp \times t \quad (1)$$

where ΔW is the change in weight of T22 steel for initial weight, *A* signifies per unit area and *t* signifies the duration for oxidation in sec. The plot of cumulative weight gain is shown in Figure 6. The hot corrosion resistance of coated and uncoated samples, based on cumulative weight gain, remarked as follows:

Uncoated T22 substrate steel ≥ NiCrMoFeCoAl-30%SiO_2 Coated Steel ≥ NiCrMoFeCoAl-30%Cr_2O_3 Coated Steel.

Table 6 illustrates the cumulative weight gain and k_p values of uncoated and coated specimens.

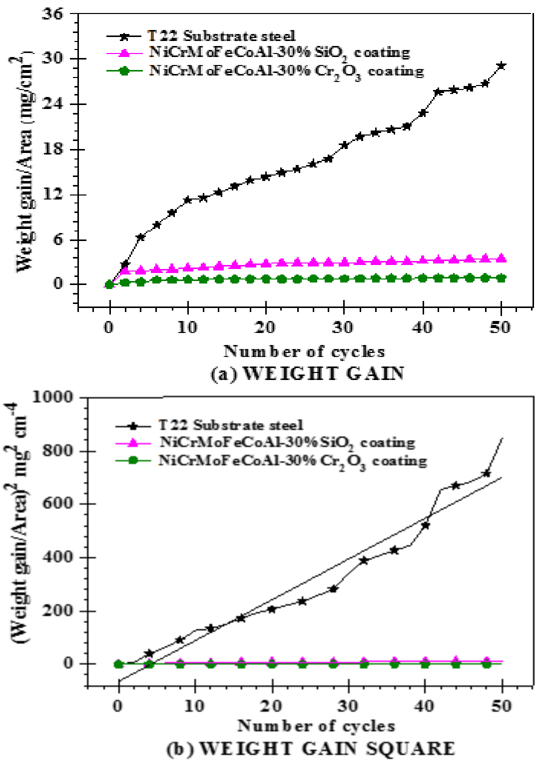

Figure 5. Hot corrosion plots of (weight gain/area) and (weight gain/area)^2 vs. time (h) for bare and composite coated steels subjected to the hot corrosion at 700^{0}C

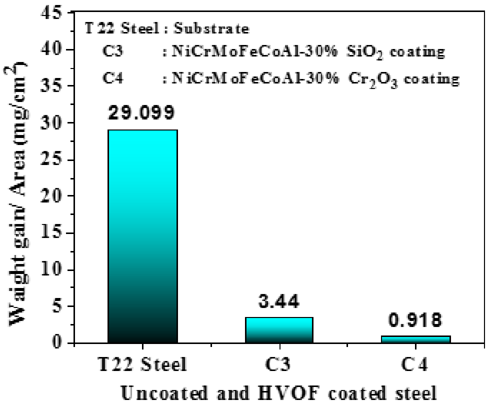

Figure 6. Total weight gain of uncoated T22 steel and composite coated steels subjected to the hot corrosion at 700^{0}C

TABLE 6. Calculated values of the total weight gain and kp

Specimens	Cumulative Weight gain (mg/ cm^2)	k_p g^2/cm^4/s^1
T22 substrate steel	29.099	4.2486×10^{-9}
NiCrMoFeCoAl-30%SiO$_2$ coating	3.4408	5.2869×10^{-11}
NiCrMoFeCoAl-30%Cr$_2$O$_3$ coating	0.9186	3.7972×10^{-11}

3. 4. XRD Analysis of the Oxide Phase Constituents

The XRD profiles for phase ID of the scales composed on corroded T22 substrate steel and composite coatings are depicted in Figures 7(a-c). Fe_2O_3 has been recognized as the major constituent in the scale of the T22 substrate steel along with the minor phases of Cr_2S_3, $NaVO_3$, and NaV_2O_5 on their surface are demonstrated in Figure 7(a). In the case of NiCrMoFeCoAl-30%SiO_2 composite coating is found to have a presence of major phases as SiO_2, Al_2SiO_5, $CoSi_2$, Al_2O_3, and $Cr_2(SO_4)_3$ along with some minor phases of Fe_2SiO_4, $FeVO_4$ & Cr_3Si are compiled in Figure 7(b). In the case of NiCrMoFeCoAl-30%Cr_2O_3 composite coating is found to have a presence of major phases as Cr_2O_3, $NaVO_3$, & $NiCr_2O_4$ together with minor phases of $AlFeO_3$ and Co_3Fe_7 were detected in Figure 7(c). The high temperature assisted formation of metal chromites and chromates could further enhance the corrosion stability.

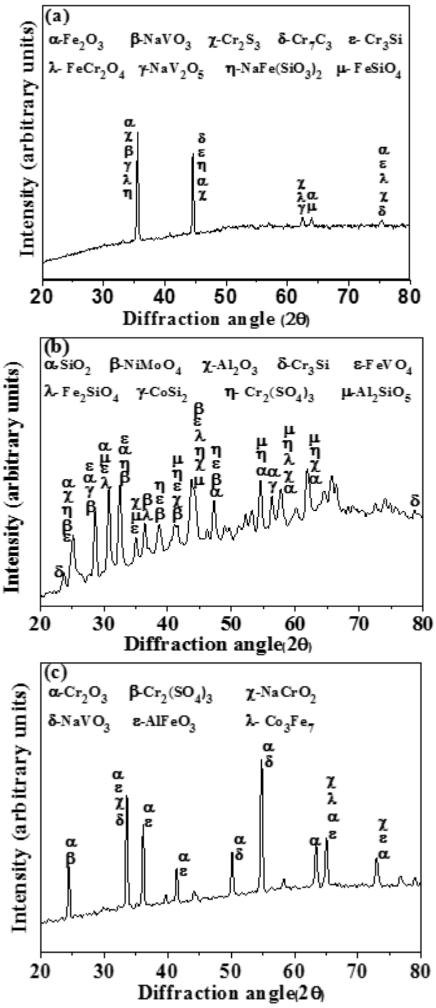

Figure 7. XRD patterns for uncoated (a) T22 substrate steel and HVOF coated (b) NiCrMoFeCoAl-30%SiO_2 (c) NiCrMoFeCoAl-30%Cr_2O_3 specimens exposed to hot corrosion at 700 °C

3. 5. SEM/EDS Analysis of the Oxide Scales The SEM/ EDS micrographs depicting the surface morphology of T22 substrate steel and composite coatings which are subjected to hot corrosion is shown in Figure 8(a-c). The EDS analysis is specified in some selected areas and EDS spots on the surface of the exposed specimens. The formation of oxide scales on the uncoated T22 steel had a rough surface. Black spots, suspected swelling, and scale spallation were observed on the surface. The EDS analysis of T22 substrate steel mainly consists of Fe_2O_3 in a major quantity, and a minor quantity of NiO, V_2O_5, Cr_2O_3, and SiO_2 scales were detected at EDS spot 1. The formation of Fe_2O_3, Al_2O_3, and MnO_x scales are identified at selected area 1 (Figure 8a). The oxide scale of hot corroded T22 boiler tube steel is principally comprised of a hematite (Fe_2O_3) oxide scale as supported by EDS, XRD, and cross-sectional analysis. The formation of the hematite (Fe_2O_3) oxide scale has been analyzed and reported as a non-protective scale, during the failure study of superheater tubes due to fireside corrosion [39, 40]. The SEM/EDS depicting the surface morphology of NiCrMoFeCoAl-30%SiO_2 composite coated specimen demonstrated in Figure 8(b), the formation of SiO_2, Cr_2O_3, and Al_2O_3 at EDS spot 1. Al_2O_3, SiO_2, Mo_2O_3, and Fe_2O_3 scales were observed at selected area 1. The oxide scale on the NiCrMoFeCoAl-30%Cr_2O_3 composite coated specimen (Figure 8c) has a massive structure. The formation of scales mainly consists of Cr_2O_3, V_2O_5. NiO and Na_2O at selected area1. Cr_2O_3, Na_2O, V_2O_5, and Al_2O_3 scales were detected at EDS spot 1. The overall surface scale formed on coated specimens to be dense clusters, continuous and uniform structure and there is no spallation and crack free. The formation of Cr_2O_3, Na_2O, SiO_2, and Al_2O_3 presence of noted phases are observed in both XRD and EDS analysis and it has been proved.

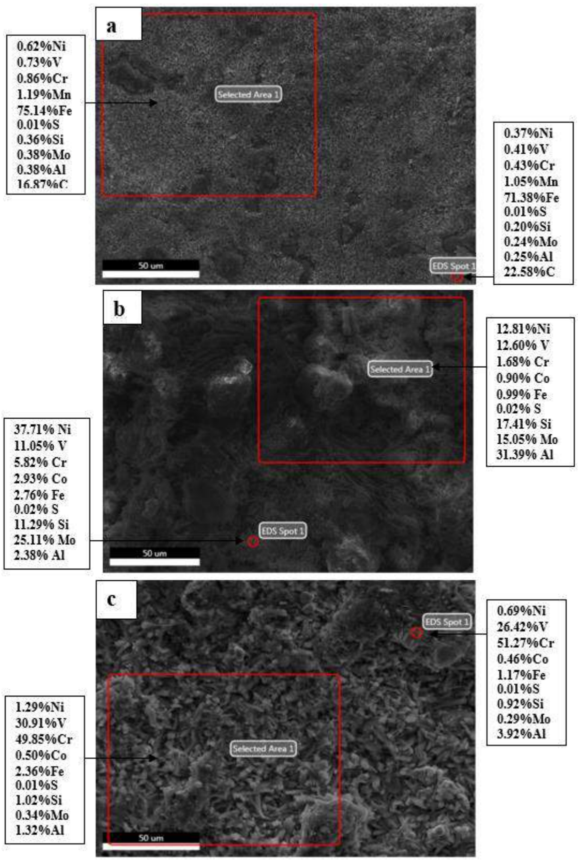

Figure 8. SEM / EDS surface analysis for the bare and coated specimens after hot corrosion test at 700°C

3. 6. Cross-sectional SEM/EDS Analysis of the Oxide Scales SEM/EDS and BSEI cross-sectional investigation of hot corroded specimens are presented in Figures 9(a) and 9(b). EDS has been taken at different points throughout the scale, coating, and substrate. The oxide scale formed was non-porous and dense in the composite coatings. The formation of oxide scales on the cross-section of NiCrMoFeCoAl-30%SiO_2 coated steel can be remarked from Figure 9(a). The scale's top layer (point 1) comprises Fe, C, Cr, & Ni with oxygen. Point 2 indicates the presence of Ni, Cr, Mo, & Co oxide scales. Further, in point 3, the interface between substrate and coating consists of Ni, Cr, Co, and Mo oxide scales are identified. Elemental variation through the cross-section of NiCrMoFeCoAl-30%Cr_2O_3 coated steel exhibited in Figure 9(b), the presence of Cr, O, & V are in a rich amount, along with the fair amount of Ni and a lower amount of Al, Mo, Na, and Co oxide scales are identified at point 1. Point 2, specifies the presence of Ni, Cr, and Co oxides scales. Point 3 depicts the existence of Fe, Al, & Cr, together with oxygen at the interface between the coating and substrate. A crack-free, continuous, lamellar, dense, and uniform oxide scales are formed on the coated specimen.

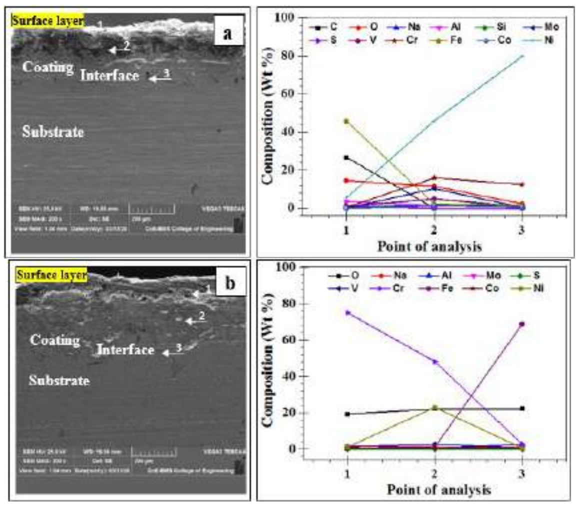

Figure 9. BSEI & EDS point analysis (wt %) across the c/s of the composite coated (a) NiCrMoFeCoAl-30%SiO_2 (b) NiCrMoFeCoAl-30%Cr_2O_3 samples after hot corrosion test

4. DISCUSSIONS

The cumulative observations of the above microscopic, structural and gravimetric analysis evident the progressive corrosion of uncoated T22 steel and the severe corrosion under molten salt conditions. The porous nature of the hot corroded products could further allow the propagation of corrosion. The high weight gain was observed with uncoated T22 while the lowest was with 30% Cr_2O_3 containing coatings. The high-temperature effects along with Na_2SO_4-60%V_2O_5 further enhance the oxidative process of the uncoated T22. However, both the HVOF coatings show improved stability in term of weight gain kinetic analysis. The significance of gravimetric data analysis is to determine the augmented kinetics induced by the Na_2SO_4-60%V_2O_5 eutectic mixture. The thick oxide scale formed on bare T22 steel predominantly comprises of iron oxide on hot corroded T22 steel, suggest the higher hot corrosion rate. This is further enhanced by the existence of other metal oxides which is observed in SEM/EDS and XRD analysis. As the consequence of the presence of higher valent metal ions, there could be an increase in the local acidic nature along with molten salt mixture on the T22 surface. This could result in the acidic fluxing of the protective oxides and impart more porous oxide scale which progressively allows the aggressive gaseous mixture to reach the base metal surface at high temperature. The hot corrosion kinetics of the NiCrMoFeCoAl-30%SiO_2 coated steel showed parabolic behavior. The oxides of SiO_2, Mo_2O_3, and V_2O_5 formed on the surface have minimal solubility in the highly acidic and oxidative salt environment. Also coefficient of thermal expansion of these oxides are in close range and hence the thermal stresses are minimized. The oxide scales formed on the coated steel are adherent and dense without any scale spalling and cracking. The oxide scales formed effectively protect the substrate alloy, as the cyclic oxidation behavior of all the coatings is dictated mainly by the scale spallation resistance. The superior hot corrosion resistance of NiCrMoFeCoAl-30%Cr_2O_3 can be attributed to the thick protective oxide scale developed on the surface. The uppermost layer of the oxide scale mainly contains oxides and spinel oxides of Cr and Ni and O which have minimal solubility in highly acidic Na_2SO_4-60%V_2O_5 melt. These oxides act as a barrier to the diffusion of O_2 and corrosive species of molten salt into the inside of the coating, hence the coating region beneath this oxide scale remains unoxidized. Slow oxidation kinetics and parabolic behavior observed during the gravimetric studies show a diffusion-limited reaction rate. During the initial stages of hot corrosion, the formation of Cr_2O_3 from the chromium oxide prevents the preferential oxidation of Ni and Cr. The refractory Ni and Cr are a strengthener to maintain the mechanical properties of the coating. The hot corroded HVOF coating containing Cr_2O_3 forms metal chromites, chromates and oxides which could further enhance the protection against the progressive corrosion. Also, the cross-sectional view of the heat-treated Cr_2O_3 containing coating shows less porous and high dense compared to SiO_2. This protects the base T22 from the access of corroding species at high temperature. This further supports the enhanced corrosion resistance of NiCrMoFeCoAl-30%Cr_2O_3 than the SiO_2 based composite coating.

5. CONCLUSIONS

In the current investigation, the composite coatings were deposited on uncoated T22 steel and the behavior of high-temperature corrosion was studied. From the analysis, the following conclusions are drawn:

1. The NiCrMoFeCoAl-30%SiO_2 and NiCrMoFeCoAl-30%Cr_2O_3 composite coatings are effectively deposited by the HVOF process on T22 substrate steel. The coating thickness was around 200 μm.
2. The uncoated T22 steel has suffered peeling of scale, intense spelling, and tremendous weight gain. The weight gain of the NiCrMoFeCoAl-30%SiO_2 and NiCrMoFeCoAl-30%Cr_2O_3 coated specimens were 88.17% and 96.84% respectively, lower than that of the uncoated T22 steel in the molten salt environment at 700^0C under thermocyclic conditions
3. NiCrMoFeCoAl-30%Cr_2O_3 coated T22 steel shows the existence of Cr_2O_3 was encountered as a principal phase and NiCrMoFeCoAl-30%SiO_2 coated T22 steel shows the presence of Al_2O_3 and SiO_2 were encountered as principal phases in the molten salt environment at 700^0C by SEM/EDS and XRD analysis.
4. The corrosion resistance of composite coatings are improved as compared to the substrate specimen. The corrosion resistance of coated and uncoated specimens presented in the following order:

NiCrMoFeCoAl-30%Cr_2O_3 coating> NiCrMoFeCoAl-30%SiO_2 coating> T22 substrate steel. The HVOF composite coating containing chromium oxides shows enhanced high-temperature heating stability compared to silica composite.

6. ACKNOWLEDGMENT

Authors thanks REVA University and BMSCE for surface and structural characterization facilities.

7. REFERENCES

1. Ebrahimi, N., Sedaghat Ahangari Hosseinzadeh, A., Vaezi, M. and Mozafari, M., "Evaluation of corrosion resistance of bi-

layered plasma-sprayed coating on titanium implants", ***International Journal of Engineering***, ***Transactions A: Basics,*** Vol. 35, No. 4, (2022), 635-643, doi: 10.5829/ije.2022.35.04A.03.

2. Veda Spandana, V., Jamuna Rani, G., Venkateswarlu, K. and Venu Madhav, V., "Experimental study on yttria stabilized and titanium oxide thermal barrier coated piston effect on engine performance and emission characteristics", ***International Journal of Engineering***, ***Transactions C: Basics,*** Vol. 34, No. 12, (2021), 2611-2616, doi: 10.5829/ije.2021.34.12c.05.

3. Rahnavard, M., "Hot corrosion behavior of functional graded material thermal barrier coating (research note)", ***International Journal of Engineering***, ***Transactions A: Basics,*** Vol. 30, No. 1, (2017), 101-108, doi: 10.5829/idosi.ije.2017.30.01a.13.

4. Mahdipoor, M.S. and Rahimipour, M.R., "Comparative study of plasma sprayed yittria and ceria stabilized zirconia properties", ***International Journal of Engineering***, ***Transactions A: Basics,*** Vol. 26, No. 1, (2013), 13-18, doi: 10.5829/idosi.ije.2013.26.01a.02.

5. NAEIMI, F. and Tahari, M., "Effect of surface morphologies on the isothermal oxidation behavior of mcraly coatings fabricated by high-velocity oxyfuel processes", ***International Journal of Engineering***, ***Transactions C: Basics,*** Vol. 30, No. 3, (2017), 432-438, doi: 10.5829/idosi.ije.2017.30.03c.13.

6. Singh, S., Goyal, K. and Goyal, R., "Performance of cr3c2-25 (ni-20cr) and ni-20cr coatings on t91 boiler tube steel in simulated boiler environment at 900° c", ***Chemical and Materials Engineering***, Vol. 4, No. 4, (2016), 57-64, doi: 10.13189/cme.2016.040401.

7. Ak, N., Tekmen, C., Ozdemir, I., Soykan, H. and Celik, E., "Nicr coatings on stainless steel by hvof technique", ***Surface and Coatings Technology***, Vol. 174, (2003), 1070-1073, doi: 10.1016/S0257-8972(03)00367-0.

8. Sidhu, H.S., Sidhu, B.S. and Prakash, S., "Evaluation of the hot corrosion behavior of lpg assisted hvof nicr wire sprayed boiler tube steels in molten salt environments", ***ISIJ International***, Vol. 46, No. 7, (2006), 1067-1074, doi: 10.2355/isijinternational.46.1067.

9. Uusitalo, M., Vuoristo, P. and Mäntylä, T., "High temperature corrosion of coatings and boiler steels in oxidizing chlorine-containing atmosphere", ***Materials Science and Engineering: A***, Vol. 346, No. 1-2, (2003), 168-177, doi: 10.1016/S0921-5093(02)00537-3.

10. Wang, B., Geng, G. and Levy, A., "Erosion and erosion-corrosion behavior of chromized-siliconized steel", ***Surface and Coatings Technology***, Vol. 54, (1992), 529-535, doi: 10.1016/S0257-8972(07)80077-6.

11. Rapp, R.A., "Hot corrosion of materials: A fluxing mechanism?", ***Corrosion science***, Vol. 44, No. 2, (2002), 209-221, doi: 10.1016/S0010-938X(01)00057-9.

12. Goyal, K., Singh, H. and Bhatia, R., "Hot-corrosion behavior of cr2o3-cnt-coated astm-sa213-t22 steel in a molten salt environment at 700° c", ***International Journal of Minerals, Metallurgy, and Materials***, Vol. 26, No. 3, (2019), 337-344, doi: 10.1007/s12613-019-1742-8.

13. Mahesh, R., Jayaganthan, R. and Prakash, S., "Evaluation of hot corrosion behaviour of hvof sprayed ni–5al and nicral coatings in coal fired boiler environment", ***Surface engineering***, Vol. 26, No. 6, (2010), 413-421, doi: 10.1179/174329409X451164.

14. Wang, C.-J. and Lin, J.-S., "The oxidation of mar m247 superalloy with na2so4 coating", ***Materials Chemistry and Physics***, Vol. 76, No. 2, (2002), 123-129, doi: 10.1016/S0254-0584(01)00527-2.

15. Sidhu, V.P.S., Goyal, K. and Goyal, R., "Hot corrosion behaviour of hvof-sprayed 93 (wc-cr3c2)-7ni and 83wc-17co coatings on boiler tube steel in coal fired boiler", ***Australian Journal of Mechanical Engineering***, Vol. 17, No. 2, (2019), 127-132, doi: 10.1080/14484846.2017.1364834.

16. Sreenivasulu, V. and Manikandan, M., "Hot corrosion studies of hvof sprayed carbide and metallic powder coatings on alloy 80a at 900° c", ***Materials Research Express***, Vol. 6, No. 3, (2018), 036519, doi: 10.1088/2053-1591/aaf65d.

17. Chatha, S.S., Sidhu, H.S. and Sidhu, B.S., "High temperature hot corrosion behaviour of nicr and Cr_3C_2–nicr coatings on t91 boiler steel in an aggressive environment at 750 c", ***Surface and Coatings Technology***, Vol. 206, No. 19-20, (2012), 3839-3850, doi: 10.1016/j.surfcoat.2012.01.060.

18. Loghman-Estarki, M., Razavi, R.S., Edris, H., Bakhshi, S., Nejati, M. and Jamali, H., "Comparison of hot corrosion behavior of nanostructured scysz and ysz thermal barrier coatings", ***Ceramics International***, Vol. 42, No. 6, (2016), 7432-7439, doi: 10.1016/j.ceramint.2016.01.147.

19. Aadhavan, R., Bhanuchandar, S. and Babu, K.S., "Surface coating of ceria nanostructures for high-temperature oxidation protection", ***Materials Research Express***, Vol. 5, No. 4, (2018), 045025, doi: 10.1088/2053-1591/aaba46.

20. Somasundaram, B., Kadoli, R. and Ramesh, M., "Hot corrosion behaviour of hvof sprayed (Cr_3C_2–35% nicr)+ 5% si coatings in the presence of na2so4–60% v2o5 at 700° c", ***Transactions of the Indian Institute of Metals***, Vol. 68, No. 2, (2015), 257-268, doi: 10.1007/s12666-014-0453-0.

21. Mangla, A., Chawla, V. and Singh, G., "Comparative study of hot corrosion behavior of hvof and plasma sprayed Ni20Cr coating on sa213 (t22) boiler steel in Na_2SO_4-60% v2o5 environment", ***International Journal of Engineering Sciences & Research Technology***, Vol. 4, No. 11, (2017), 2348-8034, doi: 10.5281/zenodo.1037655.

22. Kaur, M., Singh, H. and Prakash, S., "High-temperature behavior of a high-velocity oxy-fuel sprayed Cr_3C_2-nicr coating", ***Metallurgical and Materials Transactions A***, Vol. 43, No. 8, (2012), 2979-2993, doi: 10.1007/s11661-012-1118-4.

23. Sidhu, B.S., Singh, H., Puri, D. and Prakash, S., "Wear and oxidation behaviour of shrouded plasma sprayed fly ash coatings", ***Tribology International***, Vol. 40, No. 5, (2007), 800-808, doi: 10.1016/j.triboint.2006.07.006.

24. Rapp, R.A., "Chemistry and electrochemistry of hot corrosion of metals", ***Materials Science and Engineering***, Vol. 87, (1987), 319-327, doi: 10.1016/0025-5416(87)90394-6.

25. Kaushal, G., Singh, H. and Prakash, S., "High temperature corrosion behaviour of hvof-sprayed Ni-20Cr coating on boiler steel in molten salt environment at 900° c", ***International Journal of Surface Science and Engineering***, Vol. 5, No. 5-6, (2011), 415-433, doi: 10.1504/IJSURFSE.2011.044388.

26. Paul, S. and Harvey, M., "Corrosion testing of ni alloy hvof coatings in high temperature environments for biomass applications", ***Journal of Thermal Spray Technology***, Vol. 22, No. 2, (2013), 316-327, doi: 10.1007/s11666-012-9820-8.

27. Hong, S., Wu, Y., Li, G., Wang, B., Gao, W. and Ying, G., "Microstructural characteristics of high-velocity oxygen-fuel (hvof) sprayed nickel-based alloy coating", ***Journal of Alloys and Compounds***, Vol. 581, (2013), 398-403, doi: 10.1016/j.jallcom.2013.07.109.

28. Bala, N., Singh, H., Prakash, S. and Karthikeyan, J., "Investigations on the behavior of hvof and cold sprayed ni-20cr coating on t22 boiler steel in actual boiler environment", ***Journal of Thermal Spray Technology***, Vol. 21, No. 1, (2012), 144-158, doi: 10.1007/s11666-011-9698-x.

29. Shuting, Z., Kaiping, D., Xianjing, R. and Ji, S., "Effect of si on hot corrosion resistance of cocraly coating", ***Rare Metal Materials and Engineering***, Vol. 46, No. 10, (2017), 2807-2811, doi: 10.1016/S1875-5372 (18)30011-0.

30. Saricimen, H., Quddus, A. and Ul-Hamid, A., "Hot corrosion behavior of plasma and hvof sprayed co-and ni-based coatings at 900 c", ***Protection of Metals and Physical Chemistry of Surfaces***, Vol. 50, No. 3, (2014), 391-399, doi: 10.1134/S2070205114030162.

31. Sidhu, H., Sidhu, B. and Prakash, S., "Hot corrosion behavior of hvof sprayed coatings on astm sa213-t11 steel", ***Journal of Thermal Spray Technology***, Vol. 16, No. 3, (2007), 349-354, doi: 10.1007/s11666-007-9029-4.

32. Shi, M., Xue, Z., Liang, H., Yan, Z., Liu, X. and Zhang, S., "High velocity oxygen fuel sprayed cr3c2-nicr coatings against na2so4 hot corrosion at different temperatures", ***Ceramics International***, Vol. 46, No. 15, (2020), 23629-23635, doi: 10.1016/j.ceramint.2020.06.135.

33. Sidhu, B.S. and Prakash, S., "Evaluation of the corrosion behaviour of plasma-sprayed ni3al coatings on steel in oxidation and molten salt environments at 900 c", ***Surface and Coatings Technology***, Vol. 166, No. 1, (2003), 89-100, doi: 10.1016/S0257-8972(02)00772-7.

34. Rani, A., Bala, N. and Gupta, C., "Characterization and hot corrosion behavior of d-gun sprayed Cr_3C_2-75% Al_2O_3 coated astm-sa210-a1 boiler steel in molten salt environment", ***Anti-Corrosion Methods and Materials***, (2017), doi: 10.1108/ACMM-09-2016-1712.

35. Deb, D., Iyer, S.R. and Radhakrishnan, V., "A comparative study of oxidation and hot corrosion of a cast nickel base superalloy in different corrosive environments", ***Materials Letters***, Vol. 29, No. 1-3, (1996), 19-23, doi: 10.1016/S0167-577X (96)00109-7.

36. Wang, C.-J., Chang, Y.-C. and Su, Y.-H., "The hot corrosion of fe-mn-al–c alloy with NaCl/Na_2SO_4 coating mixtures at 750° c", ***Oxidation of Metals***, Vol. 59, No. 1, (2003), 115-133, doi: 10.1023/A: 1023022100300.

37. Zheng, L., Maicang, Z. and Jianxin, D., "Hot corrosion behavior of powder metallurgy rene95 nickel-based superalloy in molten nacl– Na_2SO_4 salts", ***Materials & Design***, Vol. 32, No. 4, (2011), 1981-1989, doi: 10.1016/j.matdes.2010.11.067.

38. Tsaur, C.-C., Rock, J.C., Wang, C.-J. and Su, Y.-H., "The hot corrosion of 310 stainless steel with pre-coated NaCl/ Na_2SO_4 mixtures at 750 c", ***Materials Chemistry and Physics***, Vol. 89, No. 2-3, (2005), 445-453, doi: 10.1016/j.matchemphys.2004.10.002.

39. Bala, N., Singh, H. and Prakash, S., "Accelerated hot corrosion studies of cold spray ni–50cr coating on boiler steels", ***Materials & Design***, Vol. 31, No. 1, (2010), 244-253, doi: 10.1016/j.matdes.2009.06.033.

40. Sidhu, T., Prakash, S. and Agrawal, R., "Characterisations of hvof sprayed nicrbsi coatings on Ni-and Fe-based superalloys and evaluation of cyclic oxidation behaviour of some ni-based superalloys in molten salt environment", ***Thin Solid Films***, Vol. 515, No. 1, (2006), 95-105, doi: 10.1016/j.tsf.2005.12.041.

Persian Abstract

چکیده

پوشش‌های پاشیده شده با سوخت اکسی با سرعت بالا (HVOF) می‌توانند مقاومت در برابر خوردگی فولاد لخت دیگ بخار ASTM SA213-T22 را بهبود بخشند. در این گزارش، ما پوشش‌های کامپوزیت NiCrMoFeCoAl-30% SiO2 و NiCrMoFeCoAl-30% Cr2O3 را بررسی کرده‌ایم که برای محافظت در برابر خوردگی روی فولاد بویلر لخت ASTM SA213-T22 قرار گرفته‌اند. مطالعات خوردگی در دمای بالا در محیط نمک مذاب (Na2SO4-60% V2O5)در دمای ۷۰۰ درجه سانتیگراد تحت شرایط ترمو سیکلیک انجام شد. پوشش های کامپوزیت اسپری شده برای ریزساختار و خواص مکانیکی مشخص می شوند. روش گرما وزنی برای درک سینتیک خوردگی استفاده شد. ویژگی‌های محصولات خوردگی با استفاده از تکنیک‌های میکروسکوپ الکترونی روبشی (SEM)طیف‌سنجی پراکنده انرژی (EDS)و پراش اشعه ایکس (XRD)مورد بررسی قرار گرفت. نتایج به‌دست‌آمده نشان می‌دهد که هر دو پوشش کامپوزیت نسبت به فولاد بویلر لخت ASTM SA213-T22 نسبت به مقاومت در برابر خوردگی مطلوب هستند. پوشش کامپوزیت NiCrMoFeCoAl-30% Cr2O3 به دلیل توزیع یکنواخت ماتریس پوشش کامپوزیت و توسعه حفاظت محافظ Cr2O3 در مقیاس، به این نتیجه رسید که مقاومت در برابر خوردگی برتر را در محیط خوردگی با دمای بالا ارائه دهد. نمک مذاب دارای پوشش حاوی اکسید کروم عملیات حرارتی شده، پایداری خوردگی خوبی نسبت به کامپوزیت سیلیس نشان می دهد. این را می توان به کرومات های فلزی، کرومیت ها و لایه های اکسید به کمک دمای بالا نسبت داد.

IJE TRANSACTIONS A: Basics Vol. 35, No. 07, (July 2022) 1428-1439

International Journal of Engineering

Journal Homepage: www.ije.ir

3D Finite Element Model for Recycled Asphalt Mixtures with High Percentages of Reclaimed Asphalt Pavement Rutting Simulation

M. M. Majidi Shad[a], M. M. Khabiri[a*], M. Arabani[b], H. Bahmani[a]

[a] *Department of Civil Engineering, Yazd University, Yazd, Iran*
[b] *Department of Civil Engineering, University of Guilan, Guilan, Iran*

PAPER INFO

Paper history:
Received 11 February 2022
Received in revised form 01 May 2022
Accepted 08 May 2022

Keywords:
Hot Mix Asphalt
Reclaimed Asphalt Pavement
Rejuvenator Agents
Rutting
Finite Element Method

ABSTRACT

The rising cost of asphalt pavements reconstruction, the discussion of non-renewable resources maintenance and reducing the harmful impacts caused by reclaimed asphalt pavement (RAP) disposal have led to reusing RAP material and studying its effects on asphalt mixture performance. In this paper, recycled asphalt mixtures with higher contents of RAP were investigated, and a method was defined for evaluating the rutting behavior of conventional and recycled asphalt mixtures. Rutting is one of the major distresses in flexible pavements, commonly caused by the accumulation of permanent deformation in the asphalt layer of the pavement structure during its service life. For study purpose, conventional and recycled asphalt samples (containing 50% and 80% RAP + rejuvenator agents) were prepared. Then indirect tensile and uniaxial repeated loading tests were conducted to obtain elastic and creep properties of the studied mixtures. The available creep power-law model in ABAQUS finite element program was used to simulate rutting. After developing models, fairly acceptable outputs have been achieved regarding wheel track test results. Moreover, results showed that the addition of 50% and 80% RAP decreased rut depth by 33% and 47%, respectively.

***doi**: 10.5829/ije.2022.35.07a.20*

1. INTRODUCTION

Over the years, pavement engineers have been developing various performance prediction methods and software programs, which some are simple and others more complex. A significant amount of effort in researches focused on predicting different distresses appearing in asphalt pavements, such as rutting, fatigue, moisture susceptibility, and thermal cracking [1-3]. The deterioration of pavements is affected by the properties of the used materials, mixing condition, pavements structure, applied traffic, and climate situation to account as the key factors [3, 4]. Models that predict different pavement deteriorations with accuracy help decision-makers for adequate and timely fund allocations for maintenance of the roads and mixture design experts to approach a better asphalt mixture that will resist longer [5-7]. Rutting is regarded as a major distress, which can even be a reason for initiating other distresses in flexible pavements. Rutting is caused by the accumulation of permanent deformation in any of the layers in the pavement structure, which occurs due to tire pressure and axial load repetition. It typically appears as longitudinal depressions in the wheel paths, sometimes accompanied by small upheavals to the sides [8, 9]. The accumulation of permanent deformation in the asphaltic layers, mostly in warm weather conditions, is a significant component of rutting in flexible pavements. Deformation growth leads to safety performance concerns in pavements and the excessive cost of repairs [9, 10]. This is why pavement designers should keep asphalt rutting performance in mind, when designing asphalt pavements. By researching on improvements of hot-mix asphalt (HMA) materials, mix designs, and pavement assessment methods, including laboratory and field testing, an increase in pavement lifespan and considerable cost savings in pavement maintenance and rehabilitation can be achieved [11, 12].

*Corresponding Author Institutional Email: mkhabiri@yazd.ac.ir (M. M. Khabirib)

Please cite this article as: M. M. Majidi Shad, M. M. Khabiri, M. Arabani, H. Bahmani, 3D Finite Element Model for Recycled Asphalt Mixtures with High Percentages of Reclaimed Asphalt Pavement Rutting Simulation, ***International Journal of Engineering, Transactions A: Basics***, Vol. 35, No. 07, (2022) 1428-1439

Since hot asphalt mixtures' performance depends on factors like time, stress and temperature, it is somehow sophisticated to predict their rutting performance; therefore, it is important to utilize a suitable constitutive model when modeling the permanent deformation of asphalt mixtures. Different models such as elasticity, viscoelasticity, viscoelastoplasticity, plasticity, and creep have been used in researches to characterize asphalt behavior [13-15].

The finite element method (FEM) is now one of the most widely applied methods for solving mathematical models of many engineering problems. It is based on the idea of building a complicated object with simple blocks or dividing a complicated object into smaller and manageable pieces [16, 17]. Two types of finite element programs are available to determine the stress, strain, and deformation in flexible pavement systems, including programs developed specifically for pavement systems analysis and general-purpose finite element programs .

While EverStressFE and MICHPAVE are examples of the first type of programs, ANSYS and ABAQUS belong to the second type. The first type programs are more user-friendly and can be used by even non-professionals. However, they have some disadvantages, like MICHPAVE only gives 2D outputs. Also, both programs are designed based on local pavement specifications, making them less capable of studying varied cases. Having a strong library to simulate complex behavioral models in materials including linear, nonlinear and viscoelastic, has made ABAQUS a powerful tool allowing to consider almost all controlling parameters (cracks, damping, static or dynamic loading) has made it popular between researchers to develop 2D or 3D models because of higher accuracy than other programs and also to utilize different constitutive models and geometries in order to evaluate any structured performance [18, 19].

The construction and maintenance of pavements require large amounts of aggregates, which typically account for more than 90% of asphalt mixtures by weight [20, 21]. This is while both bitumen and aggregates used in asphalt mixtures are supplied from non-renewable resources. With the continuously increasing costs of construction materials and concern over environmental issues, the pavement industry is attracted to the use of reclaimed asphalt pavement (RAP) materials in the construction of asphalt pavement [22, 23]. Based on the mixture type, between 10 and 40% RAP materials are currently used in HMA [23, 24]. One way to promote sustainability in road construction is the feasibility of increasing RAP content in asphalt mixtures and having mixtures with similar performance characteristics as HMA. So far, different studies have been conducted on various additives, rejuvenator agents, and mixing processes to improve the rheological properties of RAP aged binder for having more recycled mixtures resistant against common pavement distresses [25, 26]. However, many countries do not take up the opportunities because of uncertainty in performance prediction [27]. Therefore, several researchers have tried to obtain a clear and more reliable understanding of RAP asphalt mixtures' performance by using methodological and theoretical models alongside laboratory outputs [28, 29]. As mentioned earlier, rutting is one significant distress that occurs due to the repetition of external load on the pavement during its service life, so the ability to predict rutting can be used as a component in sustainable models and help increase pavements lifespan. Although, studies have shown that RAP mixtures are less vulnerable to rutting than other distress. But still, in many mechanical studies, the impact of different factors on increasing or decreasing rut depth in such mixtures is being evaluated [30-32].

In this study, two different recycled mixtures, respectively containing 50 and 80% RAP material, rejuvenated with a petroleum-based rejuvenating agent and also conventional asphalt mixture (containing 0% RAP) were assessed then an analytical method was provided to characterize the rutting behavior of studied mixtures, under the simulation of wheels repeated loading. Indirect tensile stiffness modulus (ITSM) and repeated load axial (RLA) tests were performed on the studied samples in order to assess mixtures' behavior and obtain creep power-law parameters required for modeling. Afterward, a 3D finite element model in ABAQUS software was developed. Finally, the models were evaluated and calibrated with wheel track test results .

2. MATERIALS AND SAMPLE PREPARATION

RAP materials were collected from a hot in-place asphalt rehabilitation project, which was in process on one of the highways in Guilan Province, Iran (see Figure 1). RAP asphalt binder was extracted with centrifuge extraction, using toluene as a solvent according to ASTM D2172. Both new and RAP original aggregates were siliceous type aggregates. The gradation of new (virgin) aggregates, RAP aggregates and design gradation used in

Figure 1. The RAP used in this study

this study are presented in Table 1. The design gradation is the dense gradation within upper and lower limits of the proposed gradation No. 4 of Iran Highway Asphalt Paving (IHAP) Code No.234 for surface courses (AASHTO Type IV gradation) [33]. After long-term field use, the gradation of the aged asphalt mixture usually tends to get finer. Thus, the gradation of new aggregates was set to compensate this problem in reaching the specified design gradation.

The virgin asphalt binder applied in this study was a 60/70 penetration grade base bitumen (AC 60/70) produced by Pasargad oil company. The properties of the virgin and extracted RAP asphalt binders are listed in Table 2, where the RAP binder is observed to be stiffer than the virgin binder due to aging.

Using rejuvenator agents is an effective way to restore aged binder properties. Rejuvenators are suitable for mixtures with high contents of RAP [34]. A petroleum-based rejuvenator agent with low viscosity and asphaltene contents was selected for this project. Its properties are shown in Table 3.

Three types of HMA samples were prepared in this study; accordingly, one conventional HMA mixture without RAP as a control mix and two recycled asphalt mixtures, respectively containing 50% (HMA-50%RAP) and 80% (HMA-80%RAP) RAP, were designed.

Several methods can be used to prepare recycled mixtures in laboratories, and most of them are usually different from what really occurs in industrial mixing methods. Here it was tried to simulate the hot in-place recycling process for producing the recycled mixtures. When producing the recycled mixtures, firstly, the rejuvenator was added into 160ºC RAP and blended for 3 minutes to make the rejuvenator diffuse properly in RAP. In order to have a positive effect on the RAP binder, the optimal quantity of the rejuvenator was determined to be 7% by weight of the RAP asphalt binder. The mixing process of the computed rejuvenator agents with RAP binder is the most important part of producing recycled mixtures. Secondly, after blending the rejuvenator with RAP, the pre-prepared fresh HMA (new aggregates + virgin binder) with the right portions for each mix was added into the blend and mixed. The mixing temperature was 155ºC, and the compaction temperature was 140ºC for all types of mixtures. Marshall mix design according to ASTM D1559 was employed to design the mixtures. The optimum binder content was determined related to 4% air voids content in the whole mix compacted under 75 blows on each side of cylindrical samples. The optimum binder content for the conventional HMA-50%RAP and HMA-80%RAP mixtures was 5.1%, 4.8% and 4.6%, respectively.

TABLE 1. Gradations (% passing) of RAP materials, new aggregates and design gradation

Sieve size (mm)	RAP	New aggregates added into		Design gradation (Target gradation for recycled mixtures)	Lower–upper limits
		recycled mixture containing 80% RAP	recycled mixture containing 50% RAP		
19	100	100	100	100	100
12.5	94	100	96.4	95.2	90-100
4.75	50	70	58	54	44-74
2.36	31	50	38.6	34.8	28-58
0.3	8	15	10.8	9.4	5-21
0.075	4	6	4.8	4.4	2-10

TABLE 2. Properties of virgin (60/70 penetration grade type) and RAP asphalt binder

Test	Virgin	RAP
Penetration (100 g, 5 s, 25◦C), 0.1 mm	64	31
Ductility (25◦C, 5 cm/min), cm	112	-
Softening point (◦C)	51	55
Flash point (◦C)	262	-

TABLE 3. Properties of the rejuvenator used in this study

Indices	Values
Viscosity (60°C, cSt)	119
Specific gravity (25 °C)	0.973
Flash point (°C)	219
TFOT aged	
Residual viscosity ratio	1.1
Mass loss percent (%)	2.7

3. LABORATORY TESTS

3. 1. Indirect Tensile Stiffness Modulus (ITSM) Test

One of the standard tests for determining the stiffness of bituminous materials is the ITSM test. In this study, the Nottingham Asphalt Tester (NAT) was used to conduct the test, which is a non-destructive method .

Asphalt mixture stiffness modulus is one of the essential mechanical properties for the analysis and design of flexible pavements. That is directly associated with the capacity of the material to distribute load [35, 36]. The stiffness of a material is also represented by the ratio between stress and strain, which is called Young's modulus of elasticity [35].

The laboratory test procedure adopted in this research was in accordance with British standard DD213. The test was held at 40ºC inside the temperature-controlled cabinet, and cylindrical asphalt samples with a diameter of 101.6 mm and 63.5 ± 1.0 mm height were used.

Repeated load pulses with a given rise time of 124 ms out of a 0.1 s loading time was applied in the test. After each loading, the specimen was left to rest for 0.9 s. Based on the ITSM test, bituminous mixtures stiffness modulus can be determined using Equation (1) below:

$$S_m = \frac{L\,(v + 0.27)}{D \times t} \quad (1)$$

where, S_m is the stiffness modulus (MPa), L is the peak value of the applied vertical load (N), D is the mean amplitude of the horizontal deformation obtained from two or more applications of the load pulse (mm), t is the mean thickness of the test specimen (mm), and v is the Poisson's ratio (a value of 0.35 is assumed in HMA).

3. 2. Repeated Load Axial (RLA) Test The RLA test can simulate actual condition better than static tests. A repeated load is a simple test for assessing the resistance to permanent deformation. The most significant result of this test is the accumulated permanent strain curve against loading cycles. Analogous to most visco-elasto-plastic materials, the creep curve of asphalt mastic can be generally divided into three stages: decelerated creep, equi-velocity creep, and accelerated creep [18, 37]. Figure 2 represents the typical three-stage permanent deformation behavior of asphalt mixture in the dynamic creep test. The strain rate shows the strain slop value in graphics to help determination of each stage. The slope of strain in the second zone is constant.

The NAT was used to conduct the test on cylindrical asphalt samples with a diameter of 101.6 mm and height of 63.5 ± 1.0 mm, following British standard DD 226: 1996. In order to determine the required parameters for finite element modeling, repeated load axial magnitude was fixed on 100 and 200 kPa at a temperature of 40ºC in a temperature control cabinet. In each test, 2000 cycles were applied, including a 1.0 s loading period and a 1.0 s resting period for each cycle (4000s). Two LVDTs measured the vertical deformation of the specimens.

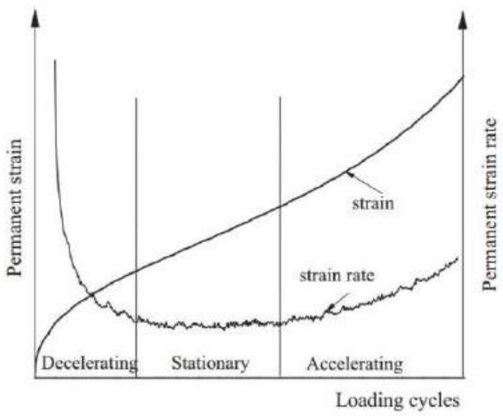

Figure 2. Typical creep curve [18]

3. 3. Wheel Track Test The wheel track test is a routine test used for characterizing the rutting resistance potential of HMA mixtures in the laboratory. In wheel track test, a wheel is rolled across the surface of an asphalt sample. The wheel can also be steel or solid rubber. As the wheel tracking test is considered a simulator of in-situ pavement performance, it is a popular tool for identifying rutting potential [38, 39].

The Hamburg wheel tracking device (HWTD) was used in this study. In order to evaluate asphalt mixtures rut depth, a total wheel load of 710 N with a pace of 53 ± 2 passes per minute was applied to 30×30×5 cm slab specimens with a target air void of 4%. A slab specimen under the test is shown in Figure 3. The test was conducted inside the environmental chamber at the temperature of 40ºC, in which the samples were placed 4 h before testing.

4. WHEEL TRACK TEST FINITE ELEMENT MODELLING

The finite element model was developed in ABAQUS software to simulate the wheel track test and asphalt permanent deformation growth under the rolling wheel. ABAQUS is a powerful FEM program that solves different problems, using linear analyses for simple problems as well as nonlinear analyses for complicated ones [40]. Because of the large longitudinal dimension, the stress state in pavement structures can be defined as a plane stress condition. Although using a 2D model instead of a 3D model decreases the total computation time, in this study 3D models were adopted for more accuracy and better visualization. Considering the wheel track test condition, the middle section of the asphalt samples was modeled under several numbers of wheel passes to predict rut depth. The schematic diagram of the wheel track test adopted for modeling in ABAQUS is exposed in Figure 4.

Dimensions of the model were 300×300×50 mm according to asphalt sample dimensions in the wheel track test. But because of the symmetry in model geometry, just half the width of the sample was modeled

Figure 3. Wheel track test

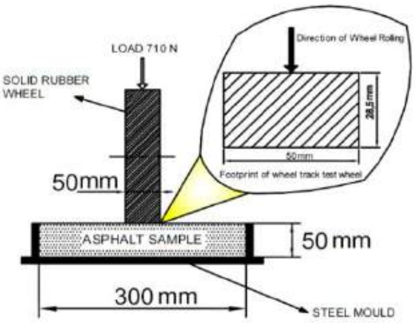

Figure 4. 2D schematic diagram of wheel track test model and wheel footprint

to show results clearly. The 3D model of the asphalt sample in ABAQUS is illustrated in Figure 5. It presented a general view of the adopted finite element meshing and boundary conditions of the model. The model consisted of 10800 elements and 12749 nodes. The vertical movements were only allowed along the edges of the model under the wheels longitudinal rolling pass, and no vertical or even horizontal movement was allowed along the other edges. A coarse or fine mesh can have negative effects on overall modeling results [41, 42]. Because of mesh size effect on models stress level the stress approach was used for mesh convergence study. Therefore the area we wanted to simulate and the stress we needed to evaluate was in the area under the wheel pass, so after several modifications and checking in mesh size we reached a constant pick stress level within the optimum size of 5*5 mm cubical elements and away from the loading area, larger elements were used that can easily be seen in Figure 5.

Considering the model requirements an 8-node Linear Brick Element (C3D8R) with the classical integration was selected in ABAQUS. The node numbering pattern is shown in Figure 6. The 8-node brick element is an equally spaced and sized element, which is one of the consistent and accurate types of elements for almost all kinds of simulations.

The footprint of the solid rubber wheel on the surface of the asphalt sample in the wheel track test is illustrated in Figure 4. The tire print can be measured using carbon paper or paint [43]. The solid rubber wheel creates

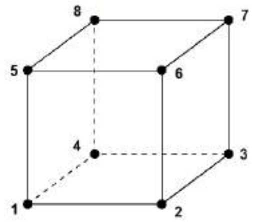

Figure 6. 8-node brick element

uniform pressures therefore the contact area between the wheel and the pavement, unlike the imprint of pneumatic tires, is exactly rectangular. The simulated footprint with the average length of 28.5 mm was used to calculate the loading time and the contact pressure. In the model, a loading pressure of 500 kPa was put along 25 mm of the middle of the sample (half the width of the wheel footprint), as presented in Figure 5.

It is somehow complex to model the wheel track test real loading mechanism with all of its details. Therefore a simple method was used to simulate the test accurately. In this modeling process, the load is instantly and statically applied to the section, and the cumulative time is considered upon the wheel passes number. This approach significantly reduces the computational time [44]. So the asphalt surface is the only node set (or true surface) in this simulation. Therefore the properties for general contact were set by ABAQUS default values [40].

The time of wheel loading in one pass is calculated according to the wheel's pace and the effective length, which the wheel and specimen are in contact [45]. Then the length of the wheel footprint is divided by the wheel speed to determine the load time. With the average wheel footprint length of 28.5 mm the loading time for each pass was calculated to be about 0.14 s. The step loading and load duration conversion described by Hua [44], as shown in Figures 7 and 8, was used in this study. In Figure 7, the movement of wheel load in the wheel track test on surface element No.1 is simulated with a step loading sequence, where the load is at its maximum from T1 to T2. While from time T0 to T1 and from time T2 to T3, the total load applied on the surface of element No.l is not at its maximum and changes linearly from zero to

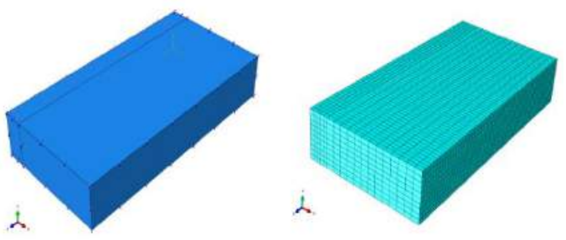

Figure 5. Asphalt sample 3D model boundary conditions and element meshes

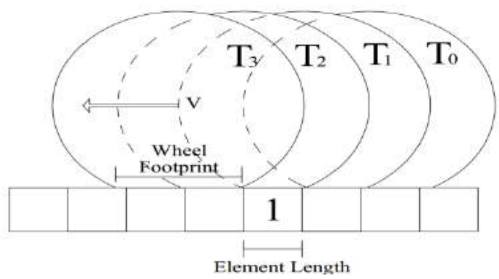

Figure 7. Wheel step by step movement and load application on element number one

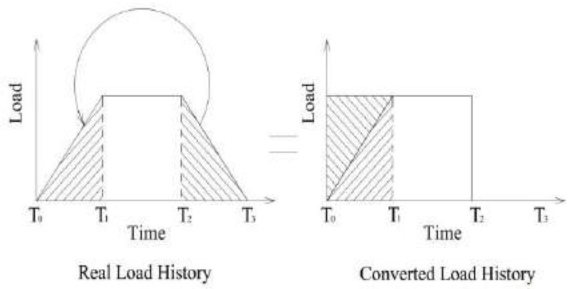

Figure 8. Load duration conversion

maximum and vice versa, respectively, which is presented in Figure 8. Based on the conversion, the T1–T2 time is 0.14 s, and the T0–T1 and T2–T3 time periods (the beginning and end length loading time) will be 0.07 s. Then, the transformed time of loading for each pass is 0.21 s; thus, the transformed time of loading for 4000 wheel pass will be 840 s.

5. CREEP POWER-LAW

Creep models can be used to characterize asphalt mixtures. The creep power-law available in the ABAQUS library is practical and suitable for problems related to the rutting of flexible pavements [11]. ABAQUS finite element program provides two versions of the creep power-law model, one time-hardening version and the other is strain-hardening version [40]. Since asphalt behavior depends on the term of time, the nonlinear time-hardening model formulated as shown in Equation (2) was utilized.

$$\dot{\varepsilon} = A\,\sigma^{n} t^{m} \tag{2}$$

where $\dot{\varepsilon}$ is the axial creep strain rate, σ is the uniaxial equivalent deviatoric stress, t is the total loading time, and A, n, m are material related parameters. Equation (3) is the integral expression of Equation (2), where ε is the creep strain.

$$\varepsilon = \frac{A}{m+1}\sigma^{n} t^{m+1} \tag{3}$$

6. RESULTS AND DISCUSSION

6. 1. Indirect Tensile Stiffness Modulus (ITSM) Test Results

For both the HMA-50%RAP and HMA-80%RAP samples, stiffness modulus was higher as compared to that in conventional samples without RAP, which can be a result of RAP asphalt binder and aggregates addition. The ITSM test results for all mixtures are shown in Table 4. The obtained values are the average of three tested specimens.

6. 2. Repeated Load Axial (RLA) Test Results

The RLA test revealed the visco-elasto-plastic behavior of asphalt mixtures. According to Figure 9, test results under the axial repeated stress of 100 and 200 kPa, at temperature 40ºC, show that creep curves are smooth and just have the first two stages at 100 kPa; but, at the stress of 200 kPa, the creep curve turns steeper, and the third stage of creep strain gets to start. As can be seen in Figure 9, recycled samples have lower strain values at a certain temperature and level of stress. It is generally accepted that lower strain values indicate higher rutting resistance. Samples creep rate graph is presented with CR prefix in Figure 9.

TABLE 4. ITSM values of the conventional and recycled asphalt mixtures

Mixture type	Young's modulus of elasticity (MPa)	Poisson's ratio
Conventional	1045	0.35
HMA-50% RAP	1447	0.35
HMA-80% RAP	1510	0.35

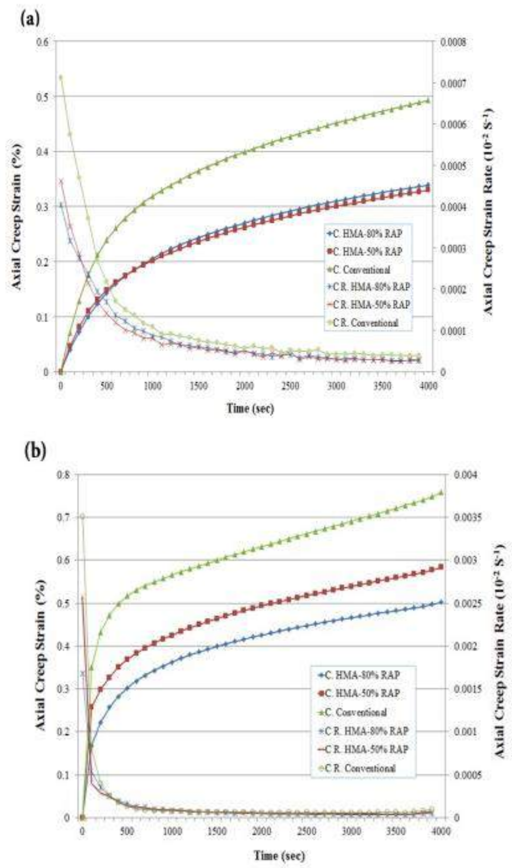

Figure 9. Creep curves and creep rate for conventional, HMA-50%RAP and HMA-80%RAP mixtures. (a) at stress of 100 kPa; (b) at stress of 200 kPa

6. 3. Wheel Track Test Results According to test results, with an increase in the number of load passes, rut depth slightly increased for all the specimens, and the HMA-80%RAP sample had the least increase in value. As presented in Table 5, the addition of RAP decreased rutting by 33 and 47% in HMA-50%RAP and the HMA-80%RAP samples, respectively, compared to the conventional sample.

6. 4. Determination of Modeling Parameters An analysis of the visco-elasto-plastic behavior of the conventional HMA-50%RAP and HMA-80%RAP asphalt mixtures is necessary for developing the required parameters of the time-hardening version of the creep model used in ABAQUS software according to Equation 2. Equation 4 and Figure 10 show different types of strain that occur in materials with visco-elasto-plastic behavior under load applications .

$$\varepsilon(t) = \varepsilon_e + \varepsilon_p + \varepsilon_{ve}(t) + \varepsilon_{vp}(t) \tag{4}$$

where $\varepsilon(t)$ is total strain after elapses of time (t), ε_e is the elastic strain, ε_p is the plastic strain, ε_{ve} is the visco-elastic strain, ε_{vp} is the visco-plastic strain. In some other studies, thermal strain component (ε_T) is also included in total strain [46].

As presented in Figure 10, after the first loading phase, the mixture will recover some of the deflection during the rest period, and the remained deflection that accumulates with each progressive loading cycle afterward makes the permanent strain. The non-recoverable strain value in asphalt is the sum of plastic and visco-plastic strain components [47].

TABLE 5. Asphalt mixtures wheel track test results at 500 kPa stress and 40ºC

Mixture type	Rut depth (mm)				
	Number of passes				
	400	**1000**	**2000**	**3000**	**4000**
Conventional	0.32	0.51	0.67	0.73	0.78
HMA-50% RAP	0.23	0.32	0.415	0.47	0.52
HMA-80% RAP	0.22	0.31	0.37	0.395	0.415

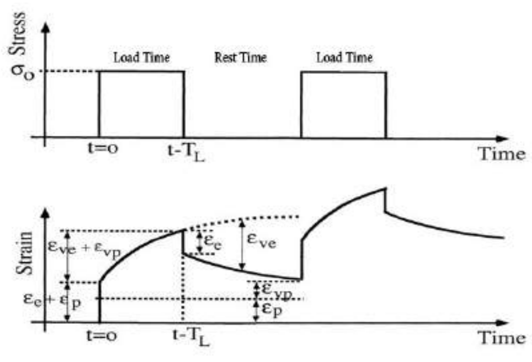

Figure 10. Asphalt stress and strain components under repeated loading

Studies have shown that visco-plastic strain is the main contributor to permanent deformation, and at large numbers of loading cycles, plastic strain value can be considered insignificant [48, 49]. In this study, in order to model pavement behavior, the plastic strain was not separated and instead, it was considered to be a part of the visco-plastic strain; therefore, the accumulated permanent strain values obtained from RLA test were used as visco-plastic strain for determining asphalt mixtures required creep power law parameters. Besides, the permanent strain in the decelerating creep zone is mainly due to the initial air void consolidation which is not related to the asphalt mixture rutting resistance over the service life, therefore it was not considered.

The visco-plastic strain of the secondary and tertiary zones was drawn versus time for all the mixtures at the two stress levels of 100 and 200 kPa, as shown in Figure 11 on a log–log scale. The secondary zone starts from where the strain rate gets constant. The asphalt strain trend, reflected in Figure 11, shows that the samples tend to have larger strains and steeper slopes with the increase in stress level. Also, Figure 11 demonstrates that the addition of RAP in the asphalt samples can reduce strain rate.

Parameter (m) of the creep power-law model relates with parameter (β), as shown in Equation (5). According to many researches, parameter (m) has a value between -1 and 0 [50]. Average slopes of tangents in corresponding trend lines shown in Figure 11 for each mixture at 40ºC, are estimated as parameter (β) value.

$$m = \beta - 1 \tag{5}$$

Parameter (β) is also used to set up a quadratic regression equation, where the ($\frac{\varepsilon_{vp}}{t^{\beta}}$) versus stress level relationship presented in Figure 12 for each mixture, gives a creep model as defined in Equation (6).

$$B(\sigma) = \varepsilon_{vp}(\sigma, t, N) / t^{\beta} \tag{6}$$

According to Figure 12, by determining the coefficients (b1 and b2), $B(\sigma)$ can be explained as a second order polynomial function presented by Equation (7). Therefore, the visco-plastic strain can be articulated as Equation (8) [50].

$$B(\sigma) = b_1\sigma + b_2\sigma^2 \tag{7}$$

$$\varepsilon_{vp}(\sigma, t, N) = (b_1\sigma + b_2\sigma^2) \times t^{\beta} \tag{8}$$

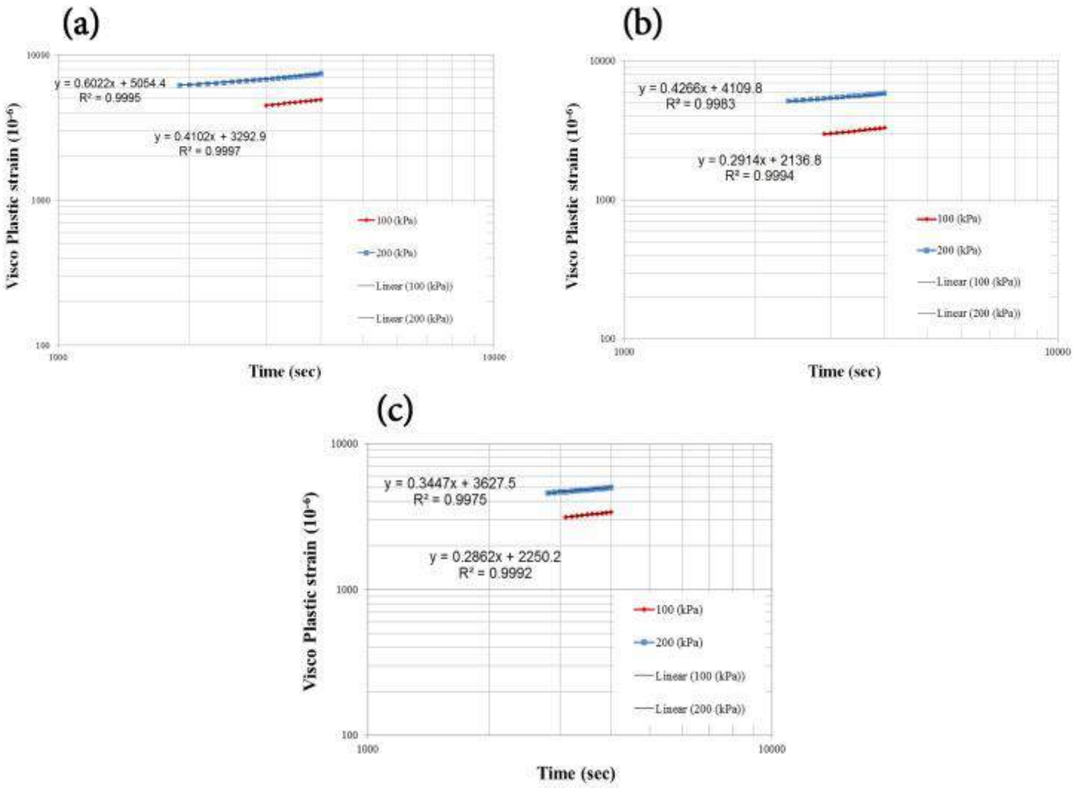

Figure 11. Visco plastic strain versus time at 40ºC for (a) conventional mixtures; (b) HMA-50% RAP mixtures and (c) HMA-80% RAP mixtures

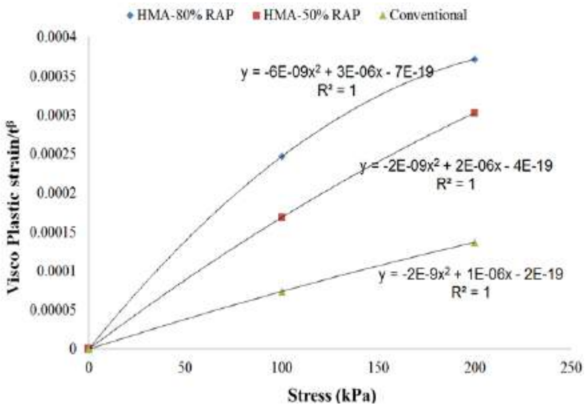

Figure 12. Visco plastic strain/t^{β} versus stress relationship at 40ºC for conventional mixtures; HMA-50% RAP mixtures and HMA-80% RAP mixtures

Except for parameter (m), which was directly derived from creep strain curves, other parameters of creep power-law (A) and (n) were developed by regression analysis. To do so, the solver tool in the Microsoft Excel program was used to fit Equations (3) and (8). The obtained values for creep power-law parameters are represented in Table 6. According to the parameters determination procedure, each asphalt sample has its own set of creep parameters.

TABLE 6. Asphalt mixtures creep power-law parameters

Mixture type	A ($\times10^{-6}$)	n	m
Conventional	1.87	0.67	-0.4938
HMA-50% RAP	2.34	0.72	-0.641
HMA-80% RAP	2.65	0.72	-0.6846

Finally, the creep law parameters and elastic properties for each mix were respectively entered in the plasticity and elasticity groups inside ABAQUS finite element program to model the asphalt wheel track test.

6. 5. Finite Element Modeling Results ABAQUS contour plots showing the predicted deformation for all types of the studied mixtures after 4000 wheel passes at 40ºC and stress level of 500 kPa are shown in Figure 13. The contour plots deformation scale factor is 30. It is shown in Figure 13 that under and near the wheels loading area, the deformation value is more than in other areas. The finite element model was also capable to predict the upward deformation of the asphalt samples, which was not managed to be recorded during the wheel

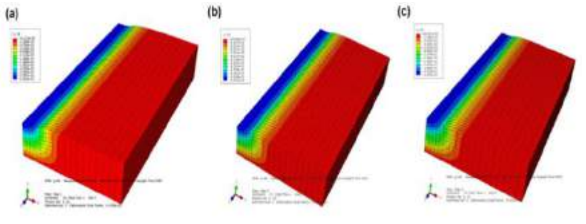

Figure 13. Predicted deformed shape of (a) conventional; (b) HMA-50% RAP and (c) HMA-80% RAP, samples after 4000 passes

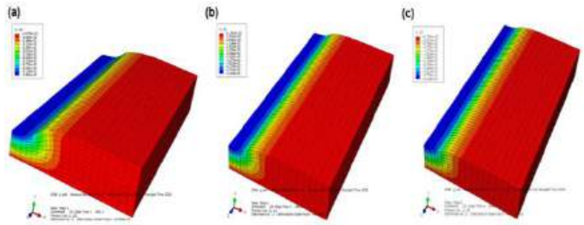

Figure 14. (a) conventional; (b) HMA-50% RAP and (c) HMA-80% RAP, samples deformation prediction shape after calibration

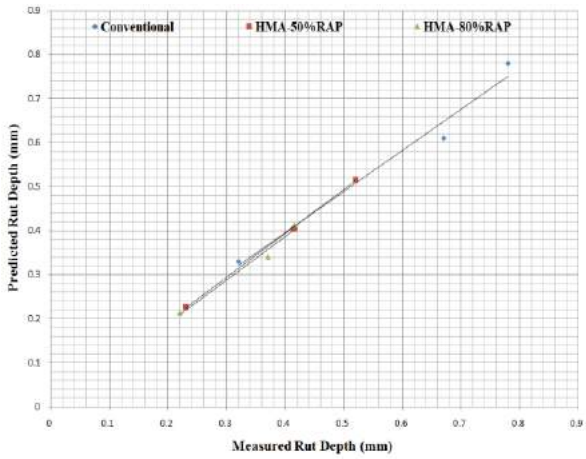

Figure 15. Relationship between Measured and Predicted rutting of asphalt samples

track test. Maximum values of the predicted rutting for the conventional, 50 and 80% RAP asphalt samples are 0.283, 0.237 and 0.223 mm, respectively. The predicted asphalt rut depth ranking complies with the overall rank based on the wheel track test results, where HMA-80%RAP has the lowest rutting rank. One reason for the difference between the predicted and measured values is because of the mixtures mass decrease in the primary rutting stage which is not considered in the analytical creep model and the difference in asphalt samples confinement situations under the RLA compared to the wheel track test. Another probable cause for this is the axial repeated stress of 100 kPa, at temperature 40ºC, having a creep rate partially interring the second zone in studied samples, maybe not suitable enough to gain proper visco-elasto-plastic properties.

The model has the capability to be calibrated. For this purpose, some modification was applied to the initial obtained creep law parameters. The (n) parameter is stress related. As rutting evaluation in the wheel track test was executed at steady loading stress, the (n) parameter did not vary and is fixed at the original level for each sample. Parameter (A) is the value of the y-axis intercept while parameter (m) is related to the slope of the strain–time relationship curve in a log–log scale [11]. Parameters (A) and (m) were adjusted to match the rutting depth measured for the first 400 wheel passes. To reach an acceptable adjustment, new creep parameters were estimated by means of trial and error. Each time the value of (A) and (m) in the models was adjusted, and predictions were compared with measured rut depths. The adjusted parameters are presented in Table 7.

Figure 14 shows samples deformed shape by 4000 passes after calibration. Figure 15 presents the models prediction versus rutting measured at the number of wheel passes 400, 2000 and 4000. As can be seen after calibrations against measured values till the first 400 passes, comparisons between the predicted rut depth in modeling and the measured rut depth in wheel track at 2000 and 4000 passes showed a difference less than 8%. It shows that the presented model can capture pavements rutting behavior for different numbers of loading cycles. Figure 15 also shows that the conventional sample had the highest rate of rutting accumulation in the early stages of loading .

TABLE 7. Modified creep parameters values after calibration

Mixture type	A	n	m
Conventional	1.09×10^{-5}	0.67	-0.6441
HMA-50% RAP	5.68×10^{-6}	0.72	-0.6577
HMA-80% RAP	6.64×10^{-6}	0.72	-0.7515

7. CONCLUSIONS

In this paper, rutting performance of conventional and recycled asphalt mixtures containing high portions of RAP mixed with rejuvenator agent was investigated and simulated based on the introduced approach and laboratory performance test outputs. According to the obtained data, some conclusions are summarized as follows:

- The optimum binder content for mixes containing RAP reduced as the amount of RAP increased. The optimum binder contents were 5.1%, 4.8% and 4.6%

for conventional, 50 and 80%RAP mixtures, respectively .

- The presence of RAP in the asphalt mixtures tended to increase their stiffness and decrease their creep strain, as compared to the conventional asphalt mixtures .
- Incorporating RAP material and increasing its portion in recycled asphalt mixtures improved the rutting resistance in comparison with conventional asphalt mixture.
- RAP reduced rut depth regarding both experimental and simulation results.
- Rutting predictions of the developed finite element model were consistent with the wheel track test results.
- Regarding simulation results for both the conventional and recycled asphalt mixtures, with some tuning on the modeling parameters, the proposed method and finite element model showed to be a feasible tool for predicting asphalt mixtures rutting behavior.

It is recommended that further research can be done on profiling the RAP mixtures behavior against other prevailing distresses under different combinations of variables as a technique to produce more reliable mixtures with higher RAP percent and similar performance characteristics as HMA.

8. REFERENCES

1. Du, Y., Chen, J., Han, Z. and Liu, W., "A review on solutions for improving rutting resistance of asphalt pavement and test methods", ***Construction and Building Materials***, Vol. 168, (2018), 893-905. https://doi.org/10.1016/j.conbuildmat.2018.02.151
2. Foroutan Mirhosseini, A., Kavussi, A., Jalal Kamali, M.H., Khabiri, M.M. and Hassani, A., "Evaluating fatigue behavior of asphalt binders and mixes containing date seed ash", ***Journal of Civil Engineering and Management***, Vol. 23, No. 8, (2017), 1164-1175. https://doi.org/10.3846/13923730.2017.1396560
3. Han, J. and Shiwakoti, H., "Wheel tracking methods to evaluate moisture sensitivity of hot-mix asphalt mixtures", ***Frontiers of Structural And Civil Engineering***, Vol. 10, No. 1, (2016), 30-43. doi: 10.1007/s11709-016-0318-1
4. Bahmani, H., Khani Sanij, H., Roshani, R., Majidi Shad, M.M., Hosseini, S.H., Edalati, M., Olazar, M. and Almasi, S., "Influence of mixing conditions of modified bitumen on the moisture sensitivity of asphalt compounds", ***International Journal of Engineering,*** (2022). https://dx.doi.org/10.5829/ije.2022.35.05b.02
5. Wang, Z., Guo, N., Wang, S. and Xu, Y., "Prediction of highway asphalt pavement performance based on markov chain and artificial neural network approach", ***Journal of Supercomputing,*** (2020). https://doi.org/10.1007/s11227-020-03329-4
6. Dave, E.V., Leon, S. and Park, K., "Thermal cracking prediction model and software for asphalt pavements", in Transportation and Development Institute Congress 2011: Integrated Transportation and Development for a Better Tomorrow., (2011), 667-676. doi: 10.1061/41167(398)64
7. Chopra, T., Parida, M., Kwatra, N. and Chopra, P., "Development of pavement distress deterioration prediction models for urban road network using genetic programming", ***Advances in Civil Engineering***, Vol. 2018, (2018). https://doi.org/10.1155/2018/1253108
8. Khodadadi, M., Moghadas Nejad, F. and Khodaii, A., "Comparison of rut susceptibility parameters in modified bitumen with ppa", ***AUT Journal of Civil Engineering***, Vol. 1, No. 2, (2017), 129-134. doi: 10.22060/ceej.2017.12383.5198
9. Xu, T. and Huang, X., "Investigation into causes of in-place rutting in asphalt pavement", ***Construction and Building Materials***, Vol. 28, No. 1, (2012), 525-530. https://doi.org/10.1016/j.conbuildmat.2011.09.007
10. Abukhettala, M.E., "The relationship between marshall stability, flow and rutting of the new malaysian hot-mix asphalt mixtures", Universiti Teknologi Malaysia, master, (2006).
11. White, T., Haddock, J., Hand, A. and Fang, H., Contributions of pavement structural layers to rutting of hot mix asphalt pavements. Transportation research board, nchrp report 468, washington, .Dc. (2002).
12. Al-Haydari, I.S., Al-Haidari, H.S., Mohammed-Noor Khudhur, H., Waleed Jummah, N. and Abd Al-Hamza, M., "Durability and aging characteristics of sustainable paving mixture", ***International Journal of Engineering***, ***Transactions B: Applications,*** Vol. 34, No. 8, (2021), 1865-1873. https://dx.doi.org/10.5829/ije.2021.34.08b.07
13. Behbahani, H., Ziari, H. and Kamboozia, N., "Evaluation of the visco-elasto-plastic behavior of glasphalt mixtures through generalized and classic burger's models modification", ***Construction and Building Materials***, Vol. 118, (2016), 36-42. https://doi.org/10.1016/j.conbuildmat.2016.04.157
14. Pei, J., Fan, Z., Liu, H., Zhang, J., Li, R. and Li, Y., "Nonlinear viscoelastic model for asphalt mixture subjected to repeated loading", ***Road Materials and Pavement Design***, Vol. 17, No. 4, (2016), 892-905. https://doi.org/10.1080/14680629.2015.1137781
15. Mirabdolazimi, S.M. and Shafabakhsh, G.A., "New model for visco-elastic behavior of asphalt mixture with combined effect of stress and temperature", ***International Journal of Engineering***, ***Transactions C: Aspects,*** Vol. 31, No. 6, (2018), 894-902. https://dx.doi.org/10.5829/ije.2018.31.06c.05
16. Chen, X. and Liu, Y., "Finite element modeling and simulation with ansys workbench, CRC Press, (2014).
17. You, L., Yan, K. and Liu, N., "Assessing artificial neural network performance for predicting interlayer conditions and layer modulus of multi-layered flexible pavement", ***Frontiers of Structural and Civil Engineering***, (2020), 1-14. https://doi.org/10.1007/s11709-020-0609-4
18. Zhang, J., Zhu, C., Li, X., Pei, J. and Chen, J., "Characterizing the three-stage rutting behavior of asphalt pavement with semi-rigid base by using umat in abaqus", ***Construction and Building Materials***, Vol. 140, (2017), 496-507. https://doi.org/10.1016/j.conbuildmat.2017.02.152
19. Elseifi, M.A., Al-Qadi, I.L. and Yoo, P.J., "Viscoelastic modeling and field validation of flexible pavements", ***Journal of Engineering Mechanics***, Vol. 132, No. 2, (2006), 172-178. https://doi.org/10.1061/(ASCE)0733-9399(2006)132:2(172)
20. Huang, Y., Bird, R.N. and Heidrich, O., "A review of the use of recycled solid waste materials in asphalt pavements", ***Resources, Conservation and Recycling***, Vol. 52, No. 1, (2007), 58-73. https://doi.org/10.1016/j.resconrec.2007.02.002
21. Khabiri, M.M., "The effect of stabilized subbase containing waste construction materials on reduction of pavement rutting depth", ***Electronic Journal of Geotechnical Engineering***, Vol. 15, (2010), 1211-1219.

22. Valdés, G., Pérez-Jiménez, F., Miró, R., Martínez, A. and Botella, R., "Experimental study of recycled asphalt mixtures with high percentages of reclaimed asphalt pavement (RAP)", ***Construction and Building Materials***, Vol. 25, No. 3, (2011), 1289-1297. https://doi.org/10.1016/j.conbuildmat.2010.09.016

23. Padula, F.R., Nicodemos, S., Mendes, J.C., Willis, R. and Taylor, A., "Evaluation of fatigue performance of high rap-wma mixtures", ***International Journal of Pavement Research and Technology***, Vol. 12, No. 4, (2019), 430-434. https://doi.org/10.1007/s42947-019-0051-y

24. Hussain, A. and Yanjun, Q., "Effect of reclaimed asphalt pavement on the properties of asphalt binders", ***Procedia Engineering,*** Vol. 54, (2013), 840-850. https://doi.org/10.1016/j.proeng.2013.03.077

25. Pradhan, S.K. and Sahoo, U.C., "Evaluation of recycled asphalt mixtures rejuvenated with madhuca longifolia (mahua) oil", ***International Journal of Pavement Research and Technology***, (2020), 1-11. https://doi.org/10.1007/s42947-020-0279-6

26. Saleh, M., "Laboratory evaluation of warm mix asphalt incorporating high rap proportion by using evotherm and sylvaroad additives", ***Construction and Building Materials***, Vol. 114, (2016), 580-587. https://doi.org/10.1016/j.conbuildmat.2016.03.200

27. Thom, N. and Dawson, A., "Sustainable road design: Promoting recycling and non-conventional materials", ***Sustainability***, Vol. 11, No. 21, (2019), 6106. https://doi.org/10.3390/su11216106

28. Zaumanis, M. and Mallick, R.B., "Finite element modeling of rejuvenator diffusion in rap binder film–simulation of plant mixing process", in Multi-scale modeling and characterization of infrastructure materials. (2013), 407-419. doi: 10.1007/978-94-007-6878-9_30

29. Yan, J., Zhu, H., Zhang, Z., Gao, L. and Charmot, S., "The theoretical analysis of the rap aged asphalt influence on the performance of asphalt emulsion cold recycled mixes", ***Construction and Building Materials***, Vol. 71, (2014), 444-450. https://doi.org/10.1016/j.conbuildmat.2014.09.002

30. Syed, I.A., Mannan, U.A. and Tarefder, R.A., "Comparison of rut performance of asphalt concrete and binder containing warm mix additives", ***International Journal of Pavement Research and Technology***, Vol. 12, No. 2, (2019), 162-169. https://doi.org/10.1007/s42947-019-0021-4

31. Moghadas Nejad, F., Azarhoosh, A., Hamedi, G.H. and Roshani, H., "Rutting performance prediction of warm mix asphalt containing reclaimed asphalt pavements", ***Road Materials and Pavement Design***, Vol. 15, No. 1, (2014), 207-219. https://doi.org/10.1080/14680629.2013.868820

32. Zhu, X., Sun, Y., Du, C., Wang, W., Liu, J. and Chen, J., "Rutting and fatigue performance evaluation of warm mix asphalt mastic containing high percentage of artificial rap binder", ***Construction and Building Materials***, Vol. 240, (2020), 117860. https://doi.org/10.1016/j.conbuildmat.2019.117860

33. Code, Iran Highway Asphalt Paving. "Ministry of Road and Transportation Research and Education Center." (2003).

34. Shen, J., Amirkhanian, S. and Tang, B., "Effects of rejuvenator on performance-based properties of rejuvenated asphalt binder and mixtures", ***Construction and Building Materials***, Vol. 21, No. 5, (2007), 958-964. https://doi.org/10.1016/j.conbuildmat.2006.03.006

35. Arabani, M. and Kamboozia, N., "New achievements in visco-elastoplastic constitutive model and temperature sensitivity of glasphalt", ***International Journal of Pavement Engineering***, Vol. 15, No. 9, (2014), 810-830. https://doi.org/10.1080/10298436.2014.893317

36. Pasetto, M. and Baldo, N., "Experimental evaluation of high performance base course and road base asphalt concrete with electric arc furnace steel slags", ***Journal of Hazardous Materials***, Vol. 181, No. 1, (2010), 938-948. https://doi.org/10.1016/j.jhazmat.2010.05.104

37. Arabani, M. and Kamboozia, N., "The linear visco-elastic behaviour of glasphalt mixture under dynamic loading conditions", ***Construction and Building Materials***, Vol. 41, (2013), 594-601 https://doi.org/10.1016/j.conbuildmat.2012.12.023

38. Taherkhani, H., "Experimental characterisation of the compressive permanent deformation behaviour in asphaltic mixtures", University of Nottingham, (2006).

39. Radhakrishnan, V., Chowdari, G.S., Reddy, K.S. and Chattaraj, R., "Evaluation of wheel tracking and field rutting susceptibility of dense bituminous mixes", ***Road Materials and Pavement Design***, (2017), 1-20. https://doi.org/10.1080/14680629.2017.1374998

40. Hibbit, K., "Sorensen, Inc. (2005). ABAQUS/standard User's Manual, Version 6.5. Hibbit, Karlsson & Sorensen." Inc., Pawtucket, *RI*.

41. Bigdeli, M. and Monfared, V., "The prediction of stress and strain behaviors in composite gears using fem", ***International Journal of Engineering***, ***Transactions B: Applications,*** Vol. 34, No. 2, (2021), 556-563. https://dx.doi.org/10.5829/ije.2021.34.02b.29

42. Al-Tememy, M., Al-Neami, M. and Asswad, M., "Finite element analysis on behavior of single battered pile in sandy soil under pullout loading", ***International Journal of Engineering***, ***Transactions C: Aspects,*** Vol. 35, No. 06, (2022) 1127-1134. https://dx.doi.org/10.5829/ije.2022.35.06c.04

43. Moazami, D., Muni, R., Hamid, H. and Yusoff, Z.M., "Effect of tire footprint area in pavement response studies", ***International Journal of Physical Sciences***, Vol. 6, No. 21, (2011), 5040-5047. doi: 10.5897/IJPS11.1085

44. Hua, J. "Finite element modeling and analysis of accelerated pavement testing devices and rutting phenomenon", Doctoral dissertation, Purdue University, (2000).

45. ARA, Inc., ERES Consultants Division. "Guide for Mechanistic–Empirical Design of New and Rehabilitated Pavement Structures." Final Rep., NCHRP Project 1-37A, (2004).

46. Shahbodagh, B., Habte, M., Khoshghalb, A. and Khalili, N., "A bounding surface elasto-viscoplastic constitutive model for non-isothermal cyclic analysis of asphaltic materials", ***International Journal for Numerical and Analytical Methods in Geomechanics***, (2016). https://doi.org/10.1002/nag.2574

47. Von Quintus, H. L., "Performance prediction models in the superpave mix design system, Strategic Highway Research Program, National Research Council Washington, DC, USA, Vol. 699, (1994).

48. Uzarowski, L., "The development of asphalt mix creep parameters and finite element modeling of asphalt rutting (doctoral dissertation)", University of Waterloo, (2006).

49. Zhang, Y., Luo, R. and Lytton, R.L., "Characterizing permanent deformation and fracture of asphalt mixtures by using compressive dynamic modulus tests", ***Journal of Materials in Civil Engineering***, Vol. 24, No. 7, (2011), 898-906. https://doi.org/10.1061/(ASCE)MT.1943-5533.0000471

50. Perl, M., Uzan, J. and Sides, A., "Visco-elasto-plastic constitutive law for a bituminous mixture under repeated loading", ***Transportation Research Record***, Vol. 911, (1983), 20-26.

Persian Abstract

چکیده

روند صعودی هزینه‌های مرمت و بازسازی خرابی‌ها در روسازی‌های آسفالتی بعلاوه بحث حفظ منابع تجدیدناپذیر و کاهش اثرات نامطلوب زیست‌محیطی دپوی مصالح خرده آسفالتی، سازمان‌ها و نهادهای مرتبط را به استفاده از مصالح آسفالت بازیافتی در مخلوط‌های آسفالتی ترغیب نموده است. در این مطالعه نمونه‌های حاوی درصدهای بالایی از مصالح آسفالت بازیافتی مورد بررسی قرار گرفتند و روندی برای ارزیابی رفتار شیارشدگی آسفالت‌های گرم معمول و بازیافتی ارائه گردید. شیارشدگی به عنوان یکی از خرابی‌های مطرح در روسازی‌های انعطاف‌پذیر، معمولا به واسطه تجمع تغییر شکل ماندگار در لایه رویه آسفالتی در طول عمر خدمت‌دهی روسازی پدید می‌آید. از این رو در این مطالعه نمونه‌های معمول و بازیافتی (حاوی ۵۰ و ۸۰ درصد مصالح بازیافتی بعلاوه مواد جوان‌کننده) تهیه گشت. سپس تست‌های مقاومت کششی غیرمستقیم و بار محوری تکرار شونده جهت بدست آوردن خصوصیات الاستیک و خزشی نمونه‌ها انجام گردید. همچنین از رابطه توانی خزش در کتابخانه نرم افزار المان محدود آباکوس برای شبیه‌سازی شیارشدگی استفاده شد. با توجه به نتایج تست ویل‌تراک، مدل‌های توسعه یافته شبیه‌سازی رفتار شیارشدگی توانستند خروجی‌های مناسبی ارائه نمایند. بعلاوه نتایج آزمایشگاهی نشان داد که افزودن ۵۰٪ و ۸۰٪ خرده مصالح آسفالت بازیافتی به ترتیب سبب ۳۳٪ و ٤۷٪ کاهش در شیارشدگی نمونه‌ها گردید.

IJE TRANSACTIONS A: Basics Vol. 35, No. 07, (July 2022) 1440-1456

International Journal of Engineering

Journal Homepage: www.ije.ir

Efficient Metaheuristic Algorithms for a Robust and Sustainable Water Supply and Wastewater Collection System

S. Vazifeh-Shenas, M. Ghorbani*, A. Firozzarea

Department of Agricultural Economics, Ferdowsi University of Mashhad, Mashhad, Iran

PAPER INFO

Paper history:
Received 11 April 2022
Received in revised form 29 April 2022
Accepted 07 May 2022

Keywords:
Water Supply and Wastewater Collection
Sustainable Development
Robust Optimization
Red Deer Algorithm
Keshtel Algorithm

ABSTRACT

An efficient design of a water supply and wastewater collection system is significantly important to tackle the natural uncertainty of this system and the sustainable development goals in developing countries like Iran. To address the natural uncertainty in the water supply and the challenge of global warming, this design must be robust and this motivates a robust optimization. To consider the sustainability criteria, this design should cover all economic, environmental and social impacts. Hence, this study develops innovative solutions based on recent and traditional metaheuristic algorithms for a robust and sustainable water supply and wastewater collection system. Red deer algorithm (RDA) and Keshtel algorithm (KA) as the recent algorithms, are employed. These recent algorithms are compared with the state-of-the-art methods like genetic algorithm (GA) and particle swarm optimization (PSO). An application of our model and algorithms, is tested on a case study in North Khorasan province. After performing some analyses on the performance of our algorithms and sensitivities on the model, a discussion is provided to conclude managerial insights and findings for practitioners in the applied system.

***doi**: 10.5829/ije.2022.35.07a.21*

1. INTRODUCTION

The global warming and water threat are two of main concerns which motivate an efficient design for the water supply and wastewater collection system [1]. It goes without saying that the demand of drinking water is highly increased nowadays as the level of community health and population growth, are increased [2]. To integrate the direct flows of water supply from rivers to demand zones with the reverse flows from collecting and recycling of the wastewater, the water resources management is combined by the theory of supply chain management [3, 4]. This paper uses a sustainable supply chain management with the robust optimization to model an efficient design of water supply and wastewater collection system in North Khorasan province in Iran.

Sustainable supply chain management theory is a combination of three legislative requirements in organizations to reduce risks related to environmental pollution (ISO 14000) and to increase the social responsibility corporation (ISO 26000) as well as the economic performance [5, 6]. Given the instability of water resources management from an economic, environmental and social perspectives, the use of sustainable supply chain management for water resources management can be a major challenge from a management perspective for all organizations involved in this field [7, 8]. The use of triple bottom lines of sustainable development with conflicting economic, environmental and social goals, is an issue that is difficult to model and the model of sustainable development for water supply and wastewater network, is rarely contributed in the literature [9].

One of the most important challenges in the logistics management of water supply and wastewater collection is to handle the uncertainty in the supply and demand of water resources and its optimal allocation between facilities to refine, recycle and create the drinking water [9, 10]. Due to the dry and fragile climate of Iran and the variety of recent droughts, the importance of water as a

*Corresponding Author Institutional Email: ghorbani@um.ac.ir (M. Ghorbani)

Please cite this article as: S. Vazifeh-Shenas, M. Ghorbani, A. Firozzarea, Efficient Metaheuristic Algorithms for a Robust and Sustainable Water Supply and Wastewater Collection System, ***International Journal of Engineering, Transactions A: Basics***, Vol. 35, No. 07, (2022) 1440-1456

vital input is becoming more apparent than ever before. A recent study in water resources management in Iran [1] shows that this country is geographically one of the arid regions of the world. In this regard, the water scarcity is one of the most important concerns for the development of this country. An efficient water network design must be able to control the uncertainty in the water network such as the situation of rainfall, uncontrolled exploitation on the other hand as well as water wasted from the side, increasing consumption, whether urban, industrial and, most importantly, agricultural applications [9]. This is the reason of a poor management of water resources and the water crisis in Iran. This great uncertainty emphasizes the needs to develop a robust optimization technique. Therefore, this study proposes a robust optimization model for the sustainable water network design problem in North Khorasan province in Iran.

One of the most cited and oldest articles in this field can be attributed to Goulter and Morgan [11]. They used a complex integer linear programming to model an inverse water distribution network. In the reverse water distribution network, we collect wastewater and its household uses. They sought to reduce the cost of the water distribution network piping system. Goldman and Saykally [12] in 2003 used a linear programming model to allocate water from the Tigris and Euphrates rivers to the agricultural, urban, and hydroelectric sectors in the Middle East. In this regard, they used a cooperative game theory to identify sustainable allocations that all stakeholders are willing to accept. Ultimately, the output of their model is the allocation of revenue from cooperation between players for different amounts of energy prices as well as economic efficiency.

In 2006, Samani and Mottaghi [13] used a branch-and-bound-based method for solving a linear programming model to analyze the water distribution network design problem. In 2008, Wang et al. [14] considered a collaborative water allocation model in the form of a general mathematical programming approach to model efficient and equitable water allocation among competitive consumers, and addressed it on the issue of large-scale water allocation in the South Saskatchewan River Basin in the province of Alberta in Canada. This optimization model includes two stages. First, the allocation of water rights and second, the reallocation of water and their net benefits, they used methods such as cooperative play to examine how net benefits could be fairly reallocated. In another study, Samani and Zanganeh [15] developed a mixed integer linear programming for a water resource allocation network. Fattahi and Fayyaz [16] developed a multi-objective linear programming for the first time to allocate water resources. The objectives of the proposed problem including economic costs, wastewater reduction and demand level optimization were optimized. In another definitively optimization model in 2011, Verleye and Aghezzaf [17] developed a nonlinear mixed integer programming model to cover all economic dimensions of the problem of allocating water resources in direct and inverse water distribution network.

Due to severe uncertainty in water resources and its consumption and lack of sufficient knowledge in climate forecasting to decide on the allocation of water resources in the long time period, the existing uncertainty at all levels of the water network was modeled by many researchers. In this regard, the use of probabilistic, fuzzy, and robust planning has been widely used in the literature review. For example, in 2012, Eum et al. [18] developed an integrated reservoir management system to change the existing reservoir operation to adapt the climate changes conditions. The reservoir management system included three methods, i.e., the nearest neighbor climate generating model, hydrological model, and the differential evolutionary optimization model. In their research, six probabilistic scenarios were used. Their results have shown that the integrated management system provides optimal control curves for reservoir operation that reflect the hydrological characteristics for future climate scenarios and can be useful for the development of adaptive reservoir operation solutions. In 2013, a model was developed by Kang, and Lansey, [19] based on probabilistic scenarios in the multi-objective optimization platform. The conflicting goals were driven by demand uncertainty and the risk of population growth in the water consumption.

Zhang et al. [20] developed a nonlinear hydraulic model by optimizing system economic costs and demand uncertainty. Steinbrueckh [21] focused on international conflict to find the effects of increasing water scarcity and the use of game theory to model. In 2015, a scenario-based model for measuring water pressure in pipes and its relationship with water consumption demand and its uncertainty was presented by Pérez et al. [22]. In another study, Mortazavi-Naeini, et al. [23] developed a multi-objective scenario-based model with nonlinear programming and pursuit of three goals. Objectives were included minimizing all structural and operational costs of the water distribution system and the expected value of the system and climate change scenarios. Mo et al. [24] analyzed the number of water scenarios in rivers and groundwater resources with distance parameters using a probabilistic programming approach.

In 2016, using this bargaining method, Degefu et al. [25] solved the problem of water sharing in the Nile Basin under critical water conditions and compared the results with the results of using the classical bankruptcy allocation rules. Subsequently, Schwartz et al. [26] developed a robust optimization model to minimize water supply chain costs with hydraulic uncertainty of water fluctuations according to industrial and domestic water demand prediction scenarios. Naderi and Pishvaee [27] developed a bi-objective model for the water network design with the possibility of redesigning and reconstructing after the worst possible scenarios. The objectives of the model were to optimize the expected costs and wastewater network considering the number of uncertain parameters such as demand, water vapor and water loss rate from rivers and groundwater sources. In another similar study, Naderi and Pishvaee [28] proposed an integrated network to consider the water distribution network and the wastewater network using a feasibility planning based on a possible two-stage scenario.

Recently, Ghelichi et al., [29] developed another integrated model to simultaneously consider the forward and backward flows of the water network. A solid planning as a solution for the case study of the city of Mashhad was implemented as their main contribution. Sahebjamnia and Fathollahi-Fard [30] performed a closed-loop supply chain method for the integrated network of water resources allocation using linear mixed integer modeling under fuzzy uncertainty. They used Lagrangian relaxation algorithm as their problem-solving method. In 2020, Fathollahi-Fard et al. [1] implemented an enhanced Lagrangian algorithm using an adaptive strategy for solving the integrated problem of water supply and wastewater collection for a case study in West Azerbaijan province in Iran. Fathollahi-Fard et al. [9] developed a multi-objective optimization model for an integrated water network design based on the goals of sustainability. They used an improved social engineering optimization algorithm as their problem-solving method. Yang et al. [5] introduced an iterative approach to design a water network considering regeneration units. Their method firstly estimates the initial concentrations of regenerated streams and identifies the regenerated streams for reusing and finally allocates the water sources and regenerated streams to industrial, agricultural and urban demands. In 2021, Sakib et al. [10] proposed Bayesian network model to predict and evaluated disasters in the water network based on legal, environmental, safety, political, social, economic, and technical factors. At last but not least, Abdul-Ghani et al., [31] analyzed the environmental impacts of the seawater and wastewater collection in a case study in Malaysia. Their simulation model was run using machine learning algorithms.

One important research gap is to develop an innovative solution for the water supply and wastewater collection models. These models are academically classified as a combinatorial optimization problem and they are naturally NP-hard [9]. The theory of no free lunch [32] confirms that the traditional algorithms may not be efficient for solving the NP-hard optimization problems when they are compared with new algorithms. This motivates our attempts to propose the red deer algorithm (RDA) [33] and Keshtel algorithm (KA) [34] for the first time in the literature in this research area. One goal of our paper is to compare these recent algorithms with two traditional ones including the genetic algorithm (GA) [35] and particle swarm optimization (PSO) [36].

Having a conclusion about our contributions in the proposed problem, although Fathollahi-Fard et al. [9] proposed the concept of sustainable closed-loop supply chain management for the water supply and wastewater collection system, they did not use a robust optimization model and this study for the first time considers environmental emissions, job opportunities and lost working days as the constraints in addition to the logistical constraints for the proposed sustainable water network design problem. It goes without saying that although many real cases were applied to the literature review, this study for the first time evaluates a sustainable water supply and wastewater collection network design in North Khorasan province in Iran as one of water threats in the center of Asia.

Based on aforementioned contributions in comparison with the literature review, the main contributions are twofold. First, a robust optimization is contributed to the address a sustainable water supply chain network with an application a case study in North Khorasan province in Iran. The second contribution is the development of new metaheuristics like RDA and KA for the first time in this research area. Other parts are organized as follows: Section 2 studies the problem description and establishes the proposed robust optimization model. Section 3 is the development of encoding plan for the proposed model and the description of our metaheuristic algorithms. Section 4 is the description of the case study as an application of our study. Section 5 creates a comparison among algorithms and some sensitivity analyses on the proposed model. Finally, Section 6 provides a summary of this research with findings and future works.

2. PROBLEM DESCRIPTION

Here, we illustrate the description of our optimization model and then introduce the concept of robust optimization and finally, the proposed model is developed. A graphical presentation of the proposed water network is given in Figure 1.

In our water system, different water types are existed, i.e., recycled water, wastewater, surface water, sludge water, drinking water, and groundwater. Water resources in the earth are surface water from dams and groundwater from ground water resources. The surface water can be used for agricultural and industrial zones. These groundwater and surface water are collected and transformed into purifying centers and then, drinking water is created. A water distribution network is designed to distribute the drinking water to urban demand zones. Next, the returned water from urban zones is collected by wastewater centers. In these centers, the returned water is

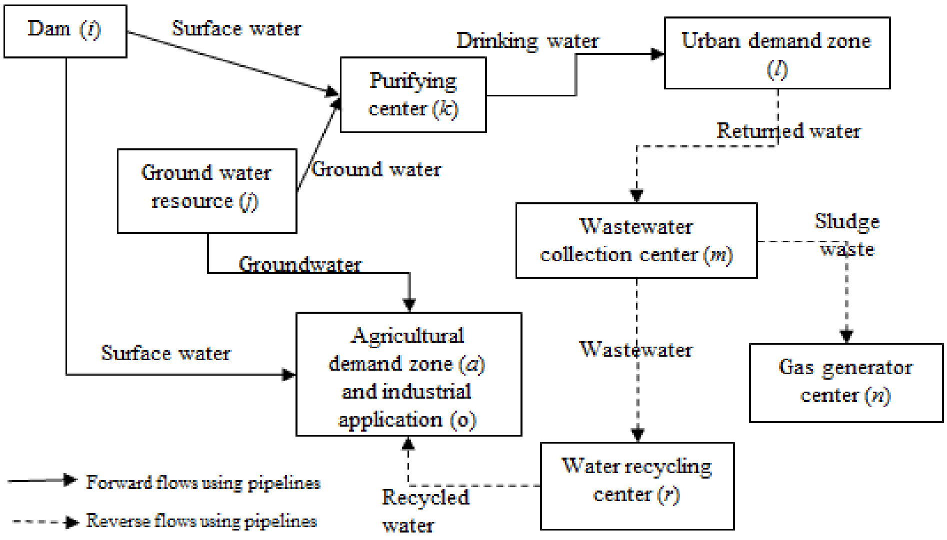

Figure 1. Proposed water network system [9]

assessed and then divided into sludge waste and wastewater. The sludge waste is transformed into biogas generator centers to create energy. The wastewater is evaluated by the water recycling centers. After recycling the wastewater, the recycled water is applicable to agricultural and industrial zones. All these mentioned operations are processed in our water network system.

The proposed water network system is evaluated by the triple bottom line approach for contributing to economic, environmental and social criteria, simultaneously. We are making the location, allocation and inventory decisions based on economic criteria to minimize the expected total cost. To address the environmental criteria, we have considered a maximum upper bound for environmental emissions generated by location, transition and processing different types of the water in our network. To consider the social sustainability, a minimal lower bound is considered for the number of jobs generated by the proposed water network system. In addition, a maximum upper bound is considered for lost working days in the water network system.

This water network is formulated by the concept of robust optimization proposed by Mulvey et al. [32]. The robust optimization aims to address the uncertainty and to control the possibility of worst-case scenarios. To illustrate this tool for the optimization, consider a minimization objective function $Z_s = fy + c_s x_s$, where Z_s is the objective function for each scenario, f denotes the coefficients of location decisions, y is the binary variable, c_s indicates the coefficients of allocation and inventory decisions, and x_s is the continuous variable for each scenario. Using this definition, the robust optimization model is as follows:

$$\min(\lambda \sum_{s\in S} \pi_s Z_s + (1-\lambda)\sum_{s\in S} \pi_s (Z_s - \sum_{s'\in S} \pi_{s'} Z_{s'})^2) \quad (1)$$

where λ shows the importance of each part of the total cost and π_s is the occurrence probability of each scenario $(s\ s' \in S)$, The constraints of the above objective function, are:

$$Ty + Ax_s \leq b_s \quad \forall s \in S \quad (2)$$

where T is the technical coefficient of locational decisions, A denotes the technical coefficient of allocation decisions and b_s is the budget. The robust optimization is generally an extension to the two-stage stochastic programming to control the worst-case scenarios in an efficient way. The robust optimization model proposed by Mulvey et al., [32], is more complex than a general type of a two-stage stochastic programming which is a mixed integer linear approach. It is because of the non-linearity in the objective function. This robust optimization model is linearized by Leung *et al.* [33] using one auxiliary variable. The objective function of this revised robust optimization model is:

$$Min \sum_{s\in S} \pi_s Z_s + \lambda \sum_{s\in S} \pi_s (Z_s - \sum_{s'\in S} \pi_{s'} Z_{s'} + 2\theta_s) \quad (3)$$

where θ_s is an auxiliary variable. This model is limited to the following constraints:

$$Ty + Ax_s \leq b_s \quad \forall s \in S \quad (4)$$

$$Z_s - \sum_{s'\in S} \pi_{s'} Z_{s'} + \theta_s \geq 0 \quad \forall s \in S \quad (5)$$

Equation (4) defines the budget constraint with regards to each scenario and Equation (5) ensures the deviation of scenarios must be positive based on statistical properties.

All in all, based on the description of the proposed water network and the concept of robust optimization model, this study follows the following assumptions:

- The proposed integrated network for the water supply and wastewater collection is a single-objective, multi-level, multi-period, scenario-based network design to address the triple bottom line concept.
- The proposed mode makes the location of facilities and their right allocation and the inventory status in each time period. These decisions are considered in an uncertain environment using the concept of robust optimization.
- The economic dimensions include the fixed establishment, transition, processing, holding and shortage costs.
- The environmental dimensions are to consider the effects of facilities establishment, processing, water transition by pipelines and extraction of groundwater on the environment. These environmental impacts are limited by a maximum upper bound.
- The social dimensions are to model the employment and lost workdays aspects.
- The water shortage is considered in the proposed model as an uncertain factor.
- It is assumed that there is one demand point in support of all industrial applications employed different types of water.
- Some parameters are multiplied by scenarios and considered the sign factor for these parameters.

To formulate the proposed water network using the robust optimization, the notations are defined according to litertature. In the mathematical model, the objective function aims to minimize the expected total cost including the shortage costs (Z^{SC}), holding costs (Z^{HC}), processing costs (Z^{PC}), transition costs (Z^{TC}) and the fixed opening costs (Z^{FC}) as well as the cost of each scenario given (f_s). This objective function is limited by a set of constraints including envioronmental and social constraints, inventory statuses, balance network constraints, capacity limitations, pipline assignment and locational constraints.

3. PROPOSED METAHEURISTIC ALGORITHMS

Since the water network design is a complex optimization problem and the exact solver is not able to handle large-scale problems [9], heuristics and metaheuristics are an alternative answer. The high performance of recent metaheuristics like RDA and KA, is a motivation for us to employ them in the area of water supply planning. This study for the first time applies RDA and KA and compares them with GA and PSO. Here, in this section, an encoding plan is proposed to show that how our metaheuristics can handle the constraints and decision variables. Then, the main loop for RDA and KA is explained. Since GA and PSO are well-known algorithms, more details about them are not provided and referred to [37, 38].

3. 1. Encoding Plan Metaheuristic algorithms use a continuous search space and the decision variables are continuous. However, in the proposed optimization model, we have integer and binary decision variables. These decision variables must get a feasible value to meet the constraints. Our encoding plan is planned by the random-key method [39]. Here, we firstly show that how we can find feasible values for the location decisions.

Consider that metaheuristics generate random continuous values between zero and one for location variables ($Y_k^K, Y_m^M, Y_n^N, Y_r^R, Y_p^P$). In our encoding plan, we sort these variables and select the lowest values based on the constraints (59) to (62). Figure 2 is an example for one of the decision variables (Y_k^K). Assume that we have five candidate points for purifying centers and three of them should be selected. In this regard, the lowest values are selected and they are one and other variables are zero.

For allocation and inventory decision variables, we need to do first the allocation decisions and the inventory decisions are repeated by each period. In our example, we want to allocate these selected purifying centers to urban demand zones. Figure 3 shows a priority-based representation to do the allocation decisions. Similar to location decisions, a set of random uniform distributed numbers for both contributions of assignment has been generated. Their sequence separately has been computed from the lowest amount to the highest one. Subsequently, the allocation based on this sequence and also their general order has been considered as detailed in this figure.

3. 2. RDA RDA is a recently-proposed algorithm by Fathollahi-Fard et al. [33]. RDA is an evolutionary algorithm and inspired by amazing behaviors of red deers for roaring, fighting and mating activities during the breading season. The RDA has been applied to many optimization models in different fields like pharmaceutical supply chains [40] and sustainable supply chains applied to aluminum industry [41], glass industry [42] and tire industry [43]. However, as far as we know, no study has applied this metaheuristic to the water supply and wastewater collection network models.

0.35	0.65	0.71	0.48	0.24

1	0	0	1	1

Figure 2. Encoding plan for locational variables

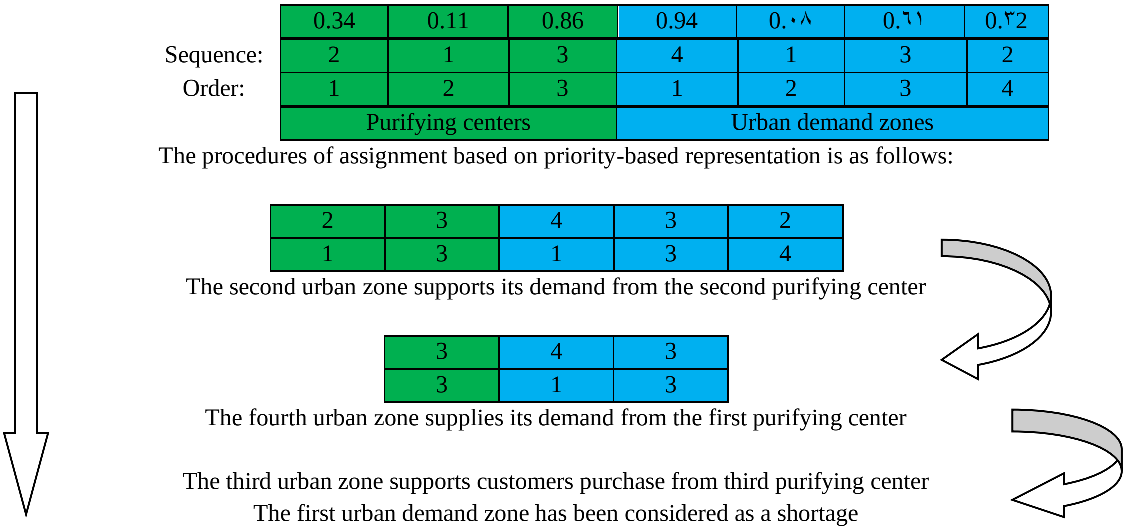

Figure 3. Encoding plan for the allocation decisions

Having a definition for the main loop of RDA, it starts with a set of random solutions (*nPop*). Based on the cost function, they are sorted and the best solutions are considered as male red deers (*Nm*) and the rest is hinds (*Nh*). In the first step, the male roars loudly to attract hinds and show their power to other males. In fact, the roar operator does a local search for each male. In the next step, the cost function of each male is reassessed. Then, the males are divided into two groups. Gamma percent of males are selected as male commanders and others are selected as stags. The fighting process is now done. In the fighting process, each commander fights with a stag randomly. This operator is an extension to the crossover operator in a greedy approach. In this regard, the winner is selected as the commander and the loser is selected as the stag. Each commander forms his harem which is a group of hinds. Each harem is the territory of the commander. The final step is to apply the mating operator. The commander mates with alpha percent of hinds in their harem. Then, the commander to promote its territory attacks to a harem randomly and mates with betta percent of hinds in this harem. Finally, the stags who have no harem, mates with his nearest hind. This mating creates some for commanders and stags. The selection of next generation is based on the best males and other solutions are selected by the roulette wheel selection to give a chance to all hinds and offspring randomly. All these steps are repeated per iteration once the maximum number of iterations (*MaxIt*) is satisfied. Having more details for implementation of RDA, the pseudo-code is given in Figure 4.

```
Set the parameters of RDA including nPop, MaxIt, Nm, Nh, alpha,
betta and gamma.
Generate a set of random solutions.
Sort them and divide them into Nm and Nh.
It=0;
While It< MaxIt
For each Nm
      MaleRD= Roaring (MaleRD);
End
Sort MaleRDs.
Select gamma percent of them as male commanders.
For each male commander
      Select one stag randomly.
      [winner, loser]= Fighting (male commander, stag);
      Male commander is the winner.
End
Generate harems for each male commander.
For each male commander
        Select alpha percent of hinds in his harem randomly.
        Select a harem randomly.
        Mate with betta percent in this harem.
End
For each stag
      Find the nearest hind to this stag.
      Mate this hind to this stag.
End
Save the best males and select the next generation.
Find the best solution.
It=It+1;
End
```

Figure 4. Pseudo-code for the RDA

3. 3. KA Keshtel is a dock in Anas family who is living in the north of Iran. Every year, this dock migrates from northern lands in Russia to the southern lands in the Caspian Sea. KA is inspired by an amazing feeding behavior of this dock. Hajiaghaei-Keshteli and Aminnayeri [34] proposed KA as a swarm-based optimization algorithm. The high performance of KA for solving complex optimization models like production scheduling [34], facility location [44] and closed-loop supply chains [42]. As far as we reviewed in the literature review, no study has applied this optimization algorithm for the water supply planning.

KA considers the search space as a lake. Like other metaheuristics, KA generates a set of random solutions as the initial population (*nPop*). They are landed in the lake. KA divides this set of solutions into three groups, i.e., *N1*, *N2* and *N3*. The first group is *N1* who is the best set of solutions. They are named as lucky Keshtels. They are lucky because they found a good source of foods. They are swirling around each other. This operator aims to improve the exploitive behavior of the algorithm. *N2* does a local search and they move around two nearest luck Keshtels. The last group is *N3* and they are flying and landing in other parts of the lake. It means that they are generated randomly per iteration. For the selection of next generation, we update *N1*, *N2* and *N3* and the best solution ever found. These activities are done per iteration to satisfy the maximum number of iterations (*MaxIt*). Having more details about the proposed algorithm, the pseudo-code is provided in Figure 5.

```
Set the parameters of KA including nPop, MaxIt, N1, N2 and N3.
Generate a set of random solutions.
Sort them and divide them into N1, N2 and N3.
It=0;
While It< MaxIt
For each N1
    Do the swirling operator and update it.
End
For each N2
    Move each search agent randomly with regards to the nearest
lucky Keshtel.
End
For each N3
    Generate each search agent randomly.
End
Merge N1, N2 and N3 and update them.
Find the best solution.
It=It+1;
End
```

Figure 5. Pseudo-code of KA

4. INTRODUCED CASE STUDY

Our case study evaluates the North Khorasan province in Iran. A geographical map for this province is depicted in Figure 6. North Khorasan province, which was formed in 2003 as a result of the division of the former Khorasan province into the center of Bojnord, is located in the northeast of Iran with an area of about 28434 square kilometers and constitutes 1.7% of the total area and is the 15th largest province in Iran. This share is more than the share of the province's population in the whole country, because the population of this province in 2010 was equal to 867727 people, i.e., 1.15 percent of the total population of Iran. Thus, the share of the province is larger than the share of its population in the country, and as a result, the population density in it with about 31 people is less than the average density of the country with 46 people in the same year. The characteristics of the area and units of the country divisions of North Khorasan province are shown in Table 1.

Given the strategic nature of the water resources allocation debate in North Khorasan province, a 25-year horizon for resource planning will be considered. Hence, 100 periods when each period will be considered as a chapter containing 90 days. Therefore, the timing horizon will include 7776000 seconds. To solve the scenarios of the developed model as a possible model, three general scenarios will be drawn: realistic, optimistic and pessimistic. In this regard, the probability of each scenario will be considered equal to one third. Possible scenarios have a direct effect on the theoretical parameters of demand, rainfall rate, steam rate and water loss rate, as well as the percentage of water return flows that are evaluated in energy recycling and conversion centers. To better understand these scenarios, consider that summer demand is naturally much higher than the rest of the seasons as a pessimistic scenario, but this demand is greatly reduced in the winter and is considered an optimistic demand. Spring and autumn demand rates can be thought of as realistic demand. This situation can be developed and generalized for other parameters such as steam, rainfall and surface water loss. Demand-related parameters for urban and ago-industrial applications will be estimated using previous studies and statistical analyzes. It should be noted the range of other parameters were simulated by the data set from the literature review [9]. Finally, the coefficient of robust optimization is set as 0.5. The upper bound for the environmental emissions is set as 188000 kg. The minimum number of jobs which is expected from the water network, is 3000 jobs and the maximum number of lost working days is expected to be 60000 days maximally.

5. COMPUTATIONAL RESULTS

Here, the model is implemented on a laptop using Intel(R) Core (TM) i7-10850H CPU @ 2.70GHz 2.71

TABLE 1. Characteristics of our case study

Demand zone	Area (km^2)	Number of cities	Capacity of dams ($10^6 \times M^3$)
Esfarayen	5019	2	232
Bojnord	3619	3	196.7
Jajrarm	3486	3	112
Shirvan	3945	4	85
Faruj	1615	2	3.3
Garmeh	2159	3	220.3
Maneh and Samalqan	6053	4	40
Raz and Jargalan	2538	1	67
Total	28434	22	956.3

Figure 6. Map of North Khorasan

GHz processor with 32.0 GB RAM. Metaheuristics were coded in MATLAB software. The CPLEX solver was used for GAMS 24.7.4 for finding the exact solution. Here, we firstly tune the algorithms and then, compare them based on different criteria. Finally, our case study is evaluated by some sensitivity analyses.

5. 1. Tuning Tuning the parameters of metaheuristics, plays a significant role in their performance [45]. If the algorithms are not tuned well, the comparison would be biased [46, 47]. There are some methods for tuning like Taguchi and response surface method. Here, we apply the Taguchi design method [48]. The main benefit of this approach is to reduce the number of tests to find the appropriate level for each parameter. We have considered three candidate values for each algorithm. Table 2 shows the parameters of each algorithm.

TABLE 2. Candidate values for each parameter

Algorithm	Parameter	Candidate values		
		Level 1	Level 2	Level 3
RDA	*nPop*	50	100	150
	MaxIt	100	150	200
	Nm (Nh= nPop- Nm)	10	20	30
	alpha	0.5	0.7	0.8
	betta	0.3	0.5	0.7
	gamma	0.6	0.7	0.8
KA	*nPop*	50	100	150
	MaxIt	100	150	200
	N1	0.2	0.3	0.4
	N2 (N3=1- N1- N2)	0.3	0.4	0.5
GA	*nPop*	50	100	150
	MaxIt	100	150	200
	Pc	0.5	0.6	0.7
	Pm	0.1	0.15	0.2
PSO	*nPop*	50	100	150
	MaxIt	100	150	200
	C1	1.75	2	2.25
	C2	1.75	2	2.25

For RDA, Taguchi suggests L_{27} as the orthogonal array and L_9 is considered for KA, GA and PSO. To tune the algorithms, we have considered the relative percentage deviation (RPD) index as formulated below:

$$RPD = \frac{Alg_{sol} - Best_{sol}}{Best_{sol}} \tag{6}$$

where Alg_{sol} is the output of each algorithm in each test and $Best_{sol}$ is the best solution ever found by this algorithm. As known, a lower value for the RPD brings a better performance of candidate values for algorithms' parameters. We have calculated the average of RPD for each algorithm and the results are given in Figure 7.

5. 2. Comparison Here, we do an extensive comparison among different criteria. In this regard, we first generate 20 different random test problems as given in Table 4. 10 small and 10 large instances were generated to analyze the complexity of our optimization model.

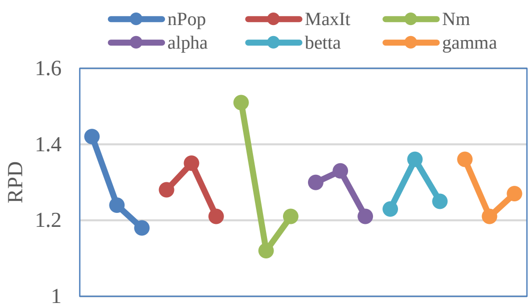

(a)

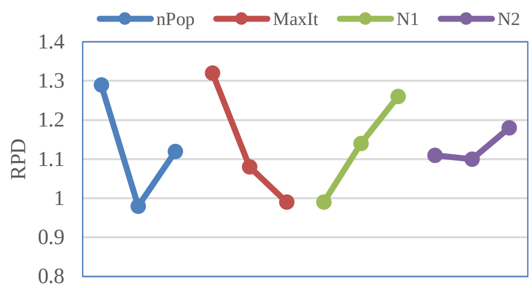

(b)

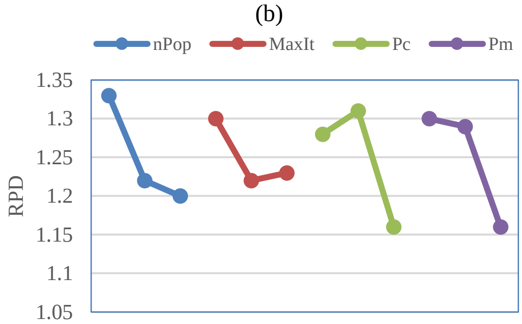

(c)

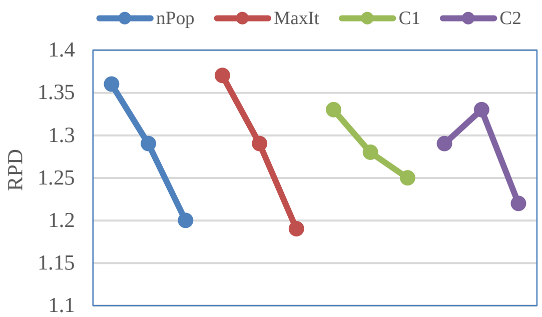

(d)

Figure 7. Results for mean RPD: (a) for RDA, (b) for KA, (c) for PSO and (d) for GA

TABLE 3. Tuned values for algorithms' parameters

Algorithm	Tuned parameters
RDA	*nPop=150; MaxIt=200; Nm=20; Nh=130; alpha=0.8; betta=0.3; gamma=0.7;*
KA	*nPop=100; MaxIt=200; N1=0.2; N2=0.4; N3=0.4;*
GA	*nPop=150; MaxIt=150; Pc=0.7; Pm=0.2;*
PSO	*nPop=150; MaxIt=200; C1=2.25; C2=2.25;*

TABLE 4. Our test problems

Complexity	Number of tests	(I, J, K, L, M, N, R, A, P, T)
Small	P1	(3, 6, 4, 4, 2, 2, 2, 4, 3, 4)
	P2	(3, 8, 6, 4, 2, 2, 2, 5, 3, 8)
	P3	(3, 8, 6, 6, 4, 2, 4, 6, 3, 8)
	P4	(5, 8, 6, 6, 4, 2, 4, 7, 3, 16)
	P5	(5, 12, 8, 8, 6, 2, 4, 8, 3, 3, 24)
	P6	(5, 12, 8, 8, 6, 4, 6, 9, 3, 3, 24)
	P7	(7, 14, 10, 9, 6, 4, 6, 10, 3, 3, 32)
	P8	(7, 14, 10, 9, 6, 4, 6, 5, 11, 5, 3, 32)
	P9	(9, 18, 12, 10, 8, 4, 6, 5, 12, 5, 3, 32)
	P10	(9, 18, 12, 10, 8, 4, 6, 5, 12, 5, 3, 48)
Large	P11	(12, 24, 16, 16, 12, 8, 10, 16, 6, 3, 64)
	P12	(12, 24, 16, 18, 14, 8, 10, 17, 6, 3, 64)
	P13	(12, 24, 18, 20, 18, 10, 14, 18, 6, 3, 72)
	P14	(12, 24, 18, 20, 18, 10, 14, 19, 6, 3, 72)
	P15	(15, 28, 20, 22, 18, 12, 16, 20, 6, 3, 80)
	P16	(15, 28, 20, 22, 20, 14, 18, 20, 8, 3, 80)
	P17	(15, 28, 24, 24, 20, 14, 18, 22, 8, 3, 84)
	P18	(18, 32, 24, 24, 20, 14, 18, 24, 8, 3, 92)
	P19	(18, 32, 28, 28, 22, 14, 20, 28, 8, 3, 100)
	P20	(18, 32, 28, 32, 24, 14, 22, 32, 8, 3, 112)

Results of the comparison are provided in Appendix (Table A1). We have run algorithms for 10 times and the best, the worst, the average and standard deviations for solutions are noted. The optimality gap from the exact solver and the CPU time are also noted in this table.

For the criteria of the best, worst and the average solutions, the RDA can be selected as the best algorithm in these metrics. After RDA, KA is highly efficient than PSO and GA. At the end, PSO is slightly better than GA.

Based on the criterion of optimality gap, Figure 8 shows a comparison among algorithms. It should be noted that the exact solver was not able to solve the test problem P9 to P20. From the criterion of optimality gap, RDA shows the best performance. KA and PSO are not better than RDA. Vice versa, the GA was the weakest performance.

Based on the CPU time for algorithms, there is a great similarity between the performance of algorithms. The behavior of algorithms is the same. However, GA is faster than other algorithms. Conversely, RDA needs more time in comparison with other metaheuristics. Finally, based on the standard deviation of algorithms, a statistical test using the interval plot is done. This analysis is provided in Figure 10. In this regard, we first normalize the standard deviation of metaheuristics and then run MINITAB software to calculate the interval plot based on 95% confidence level. As can be seen, RDA is highly better than other metaheuristics and shows a robust behavior in this comparison. After RDA, KA is better than GA and PSO. At the end, PSO shows the weakest performance in this comparison.

5. 3. Sensitivity Analysis Here, we analyze our case study by some sensitivity analyses. These analyses were run on GAMS software. First, the values of robust optimization coefficient are analyzed and changed from 0 to 1. The results were given in Table 5.

Results given in Table 5, indicate that an increase in the robust optimization coefficient not only increases the total cost uniformly, but also increases the complexity as the computational time is generally increased during variations.

In addition to the sensitivity analysis on the robust optimization, some sensitivity analyses are done to implement sustainable development goals. In this regard, the bounds for environmental emissions, job opportunities and lost working days are analyzed. In addition, we do sensitivity analyses for the maximal amount of environmental emissions. This bound is changed from 175000 to 200000 kg. Five tests are designed and analyses are reported. Accordingly, the behavior of total cost and computational time of these solutions, is reported in Table 6.

The results in Table 6 indicate that there is no feasible solution if we reduce the maximum bound of environmental emissions to 175000 kg. An increase to this factor provides two advantages. First, the total cost would be reduced and it shows that the total cost and environmental emissions have a conflict for finding the optimal solution. Another advantage is the reduction of time complexity and when this factor increases, the environmental constraints would be relaxed.

Another sensitivity analysis is done on the constraint of job opportunities. The minimum number of job opportunities is increased from 2000 to 4000. Five tests are considered. Table 7 shows the behavior of criteria. From results given in Table 7, there is no feasible solution for the minimum number of job opportunities which is equaled to 4000. While the number of job opportunities increases, the computational time increases and the

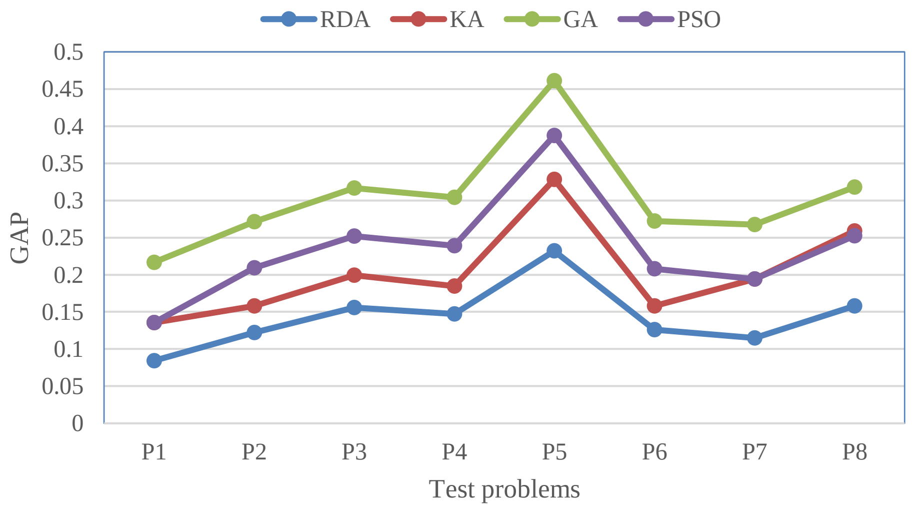

Figure 8. Comparison of algorithms based on the optimality gap

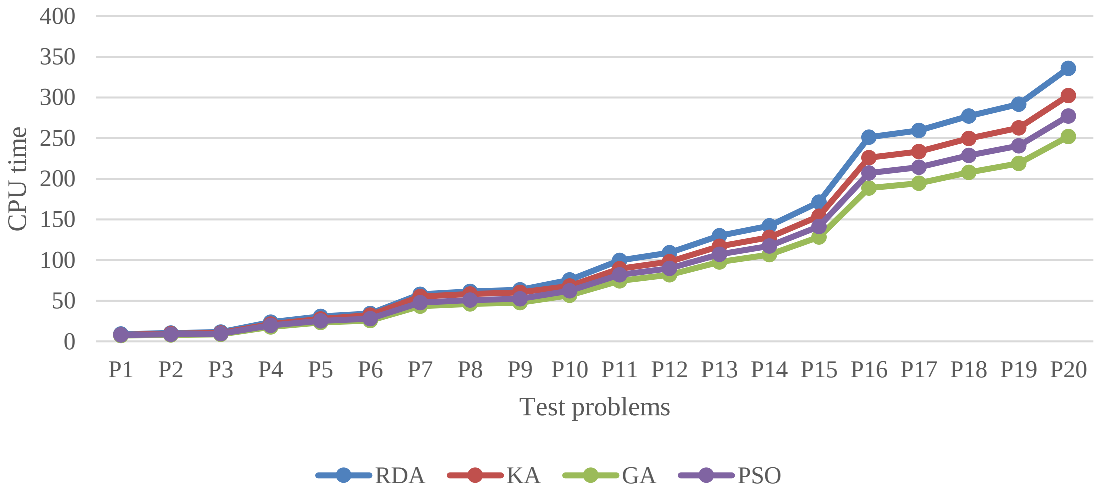

Figure 9. Comparison of algorithms based on the CPU time

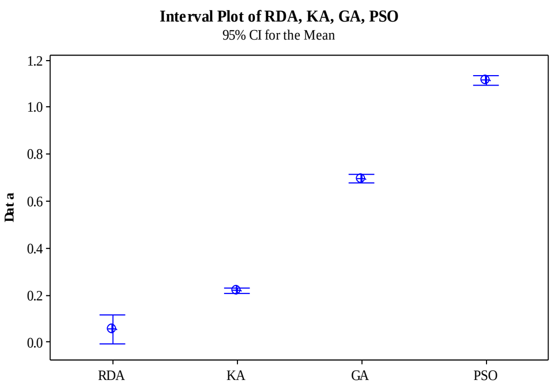

Figure 10. Interval plot for analyzing the metaheuristics

optimality is limited. Finally, the maximum number of lost working days is analyzed. This factor is changed from 40000 to 80000 days. Five tests are studied and results are reported in Table 8.

As given in Table 8, there is no feasible solution if we want to limit the number of lost working days to 40000. While the number of lost working days increases, the total cost is reduced and the optimality is improved. It goes without saying that an increase to the bound of lost working days, releases this social constraint and reduces the time complexity of the proposed optimization model.

TABLE 5. Results for the sensitivity analysis on the robust optimization

Robust optimization coefficient	Total cost	CPU time
0	8.42E+07	630.43
0.1	1.13E+11	784.25
0.2	2.26E+11	912.54
0.3	3.39E+11	892.75
0.4	4.52E+11	864.62
0.5	5.65E+11	899.54
0.6	6.78E+11	903.72
0.7	7.91E+11	913.62
0.8	9.04E+11	905.71
0.9	1.02E+12	907.13
1	1.13E+12	911.48

TABLE 6. Results for the sensitivity analysis on the environmental emissions

Maximum upper bound for environmental emissions	Total cost	CPU time
175000	Infeasible	0
180000	1.4562E+13	1000
188000	5.6534E+11	899.54
195000	2.7418E+11	912.28
200000	4.8219E+10	865.19

TABLE 7. Results for the sensitivity analysis on the job opportunities

Minimum number of job opportunities	Total cost	CPU time
2000	7.5843E+09	912.56
2500	3.2871E+10	987.39
3000	5.6534E+11	899.54
3500	7.9124E+11	1000
4000	Infeasible	0

TABLE 8. Results for the sensitivity analysis on the lost working days

Maximum number of lost working days	Total cost	CPU time
40000	Infeasible	0
50000	7.8324E+13	1000
60000	5.6534E+11	899.54
70000	6.8319E+11	912.33
80000	2.1743E+10	845.27

There are some limitations to this study and some recommendations can be suggested for future works. One suggestion is to develop a multi-objective decision-making framework and algorithms for our robust and sustainable water supply network design problem [49]. Other uncertainty models like fuzzy logic can be applied to our optimization model in comparison with the proposed robust optimization [50]. Finally, different recent and state of the art metaheuristics like social engineering optimizer [51] and adaptive evolutionary algorithm [52] should be tested on our optimization problem in comparison with our applied algorithms.

6. CONCLUSION AND FUTURE WORKS

In this paper, a robust optimization model was developed to address a comprehensive water network design problem. A sustainable water supply and wastewater collection network design problem was proposed and applied to the case study of North Khorasan province, Iran. The main novelty was the development a set of metaheuristics for the proposed sustainable water supply model. In this regard, RDA and KA were applied to this research area for the first time. We have compared these algorithms with two traditional metaheuristics, namely, GA and PSO. In this regard, their encoding plan was presented and then, the algorithms were tuned by Taguchi method. At the end, an extensive comparison based on different criteria was done and one finding was the high performance of RDA in comparison with KA, PSO and GA.

It goes without saying that the proposed robust optimization model as different from other similar models in the literature. The proposed optimization model aimed to minimize the total cost while the environmental pollution, job opportunities and lost working days were limited as new constraints to the model in addition to the constraints of water network design, inventory statuses, capacity limitations, pipeline assignments and locational decisions. The case study of North Khorasan province, Iran was solved and some sensitivity analyses were performed. Results confirm that the robust optimization coefficient is very important to manage the time complexity and solution quality. In addition, the role of environmental and social constraints, is highlighted to improve the optimality and solution time.

7. REFERENCES

1. Fathollahi-Fard, A.M., Hajiaghaei-Keshteli, M., Tian, G. and Li, Z., "An adaptive lagrangian relaxation-based algorithm for a coordinated water supply and wastewater collection network design problem", ***Information Sciences***, Vol. 512, (2020), 1335-1359, https://doi.org/10.1016/j.ins.2019.10.062
2. Yazdani, M., Kabirifar, K., Frimpong, B.E., Shariati, M., Mirmozaffari, M. and Boskabadi, A., "Improving construction and demolition waste collection service in an urban area using a simheuristic approach: A case study in sydney, australia", ***Journal of Cleaner Production***, Vol. 280, (2021), 124138, https://doi.org/10.1016/j.jclepro.2020.124138
3. Ali, S.M., Paul, S.K., Chowdhury, P., Agarwal, R., Fathollahi-Fard, A.M., Jabbour, C.J.C. and Luthra, S., "Modelling of supply chain disruption analytics using an integrated approach: An emerging economy example", ***Expert Systems with Applications***, Vol. 173, (2021), 114690, https://doi.org/10.1016/j.eswa.2021.114690
4. Shabbir, M.S., Mahmood, A., Setiawan, R., Nasirin, C., Arshad, M.A., Khan, S. and Batool, F., "Closed-loop supply chain network design with sustainability and resiliency criteria", Petra Christian University, (2021),
5. Yang, F., Fan, X.-Y., Jia, X., Klemeš, J.J. and Liu, Z.-Y., "An iterative design approach for water networks with multiple regeneration units", ***Journal of Cleaner Production***, Vol. 271, (2020), 122483, doi: 10.1002/apj.2420.
6. Fathollahi-Fard, A.M., Ahmadi, A. and Karimi, B., "Multi-objective optimization of home healthcare with working-time balancing and care continuity", ***Sustainability***, Vol. 13, No. 22, (2021), 12431, https://doi.org/10.3390/su132212431
7. Fathollahi-Fard, A.M., Dulebenets, M.A., Tian, G. and Hajiaghaei-Keshteli, M., *Sustainable supply chain network design*. 2022, Springer.1-3.
8. Fathollahi-Fard, A., Hajiaghaei-Keshteli, M. and Tavakkoli-Moghaddam, R., "A lagrangian relaxation-based algorithm to solve a home health care routing problem", ***International Journal of Engineering***, Vol. 31, No. 10, (2018), 1734-1740, https://www.magiran.com/paper/1901827?lang=en
9. Fathollahi-Fard, A.M., Ahmadi, A. and Al-e-Hashem, S.M., "Sustainable closed-loop supply chain network for an integrated water supply and wastewater collection system under uncertainty", ***Journal of Environmental Management***, Vol. 275, (2020), 111277, doi: 10.1016/j.jenvman.2020.111277.
10. Sakib, N., Hossain, N.U.I., Nur, F., Talluri, S., Jaradat, R. and Lawrence, J.M., "An assessment of probabilistic disaster in the oil and gas supply chain leveraging bayesian belief network", ***International Journal of Production Economics***, Vol. 235, (2021), 108107, doi: 10.1016/j.ijpe.2021.108107.
11. Goulter, I. and Morgan, D., "An integrated approach to the layout and design of water distribution networks", ***Civil Engineering Systems***, Vol. 2, No. 2, (1985), 104-113, https://doi.org/10.1080/02630258508970389
12. Goldman, N. and Saykally, R., "Elucidating the role of many-body forces in liquid water. I. Simulations of water clusters on the vrt (asp-w) potential surfaces", ***The Journal of Chemical***

Physics, Vol. 120, No. 10, (2004), 4777-4789, doi: 10.1063/1.1645777.

13. Samani, H.M. and Mottaghi, A., "Optimization of water distribution networks using integer linear programming", ***Journal of Hydraulic Engineering***, Vol. 132, No. 5, (2006), 501-509, https://doi.org/10.1061/(ASCE)0733-9429(2006)132:5(501)
14. Wang, L., Fang, L. and Hipel, K.W., "Basin-wide cooperative water resources allocation", ***European Journal of Operational Research***, Vol. 190, No. 3, (2008), 798-817, doi: 10.1016/j.ejor.2007.06.045.
15. Samani, H.M. and Zanganeh, A., "Optimisation of water networks using linear programming", in Proceedings of the Institution of Civil Engineers-water management, Thomas Telford Ltd. Vol. 163, (2010), 475-485.
16. Fattahi, P. and Fayyaz, S., "A compromise programming model to integrated urban water management", ***Water Resources Management***, Vol. 24, No. 6, (2010), 1211-1227, doi: 10.1007/s11269-009-9492-4.
17. Verleye, D. and Aghezzaf, E.-H., "Modeling and optimization of production and distribution of drinking water at vmw", in International Conference on Network Optimization, Springer. (2011), 315-326.
18. Eum, H.-I., Vasan, A. and Simonovic, S.P., "Integrated reservoir management system for flood risk assessment under climate change", ***Water Resources Management***, Vol. 26, No. 13, (2012), 3785-3802, doi: 10.1007/s11269-012-0103-4.
19. Kang, D. and Lansey, K., "Scenario-based robust optimization of regional water and wastewater infrastructure", ***Journal of Water Resources Planning and Management***, Vol. 139, No. 3, (2013), 325-338, https://doi.org/10.1061/(ASCE)WR.1943-5452.0000236
20. Zhang, W., Chung, G., Pierre-Louis, P., Bayraksan, G. and Lansey, K., "Reclaimed water distribution network design under temporal and spatial growth and demand uncertainties", ***Environmental Modelling & Software***, Vol. 49, (2013), 103-117, http://dx.doi.org/10.1016/j.envsoft.2013.07.008
21. Steinbrueckh, E., "Water scarcity and international conflict in africa, a game theory approach”", Università degli Studi di Perugia, Scienze Politiche, (2014),
22. Pérez, R., Sanz, G., Cugueró, M.-À., Blesa, J. and Cugueró, J., "Parameter uncertainty modelling in water distribution network models", ***Procedia Engineering***, Vol. 119, (2015), 583-592, doi: 10.1016/j.proeng.2015.08.911.
23. Mortazavi-Naeini, M., Kuczera, G., Kiem, A.S., Cui, L., Henley, B., Berghout, B. and Turner, E., "Robust optimization to secure urban bulk water supply against extreme drought and uncertain climate change", ***Environmental modelling & software***, Vol. 69, (2015), 437-451, https://doi.org/10.1016/j.envsoft.2015.02.021
24. Mo, S., Duan, H., Shen, B. and Wang, D., "Interval two-stage stochastic integer programming for urban water resource management under uncertainty", ***Journal of Coastal Research***, Vol., No. 73 (10073), (2015), 160-165, https://doi.org/10.2112/SI73-028.1
25. Degefu, D.M., He, W., Yuan, L. and Zhao, J.H., "Water allocation in transboundary river basins under water scarcity: A cooperative bargaining approach", ***Water Resources Management***, Vol. 30, No. 12, (2016), 4451-4466, doi: 10.1007/s11269-016-1431-6.
26. Schwartz, R., Housh, M. and Ostfeld, A., "Least-cost robust design optimization of water distribution systems under multiple loading", ***Journal of Water Resources Planning and Management***, Vol. 142, No. 9, (2016), 04016031, doi: 10.1061/(ASCE)WR.1943-5452.0000670.
27. Naderi, M. and Pishvaee, M., "Robust bi-objective macroscopic municipal water supply network redesign and rehabilitation", ***Water Resources Management***, Vol. 31, No. 9, (2017), 2689-2711, doi: 10.1007/s11269-017-1655-0.
28. Naderi, M.J. and Pishvaee, M.S., "A stochastic programming approach to integrated water supply and wastewater collection network design problem", ***Computers & Chemical Engineering***, Vol. 104, (2017), 107-127, doi: 10.1016/j.compchemeng.2017.04.003.
29. Ghelichi, Z., Tajik, J. and Pishvaee, M.S., "A novel robust optimization approach for an integrated municipal water distribution system design under uncertainty: A case study of mashhad", ***Computers & Chemical Engineering***, Vol. 110, (2018), 13-34, doi: 10.1016/j.compchemeng.2017.11.017.
30. Sahebjamnia, N. and Fathollahi-Fard, A., "A lagrangian relaxation-based algorithm to solve a collaborative water supply chain network design problem", ***International Journal of Emerging Trends in Engineering Research***, Vol. 6, (2018), 40-45, doi: 10.30534/ijeter/2018/01672018.
31. Abdul Ghani, L., Ali, N.a., Nazaran, I.S. and Hanafiah, M.M., "Environmental performance of small-scale seawater reverse osmosis plant for rural area water supply", ***Membranes***, Vol. 11, No. 1, (2021), 40, https://doi.org/10.3390/membranes11010040
32. Wolpert, D.H. and Macready, W.G., "No free lunch theorems for optimization", ***IEEE Transactions on Evolutionary Computation***, Vol. 1, No. 1, (1997), 67-82, doi: 10.1109/4235.585893.
33. Fathollahi-Fard, A.M., Hajiaghaei-Keshteli, M. and Tavakkoli-Moghaddam, R., "Red deer algorithm (RDA): A new nature-inspired meta-heuristic", ***Soft Computing***, Vol. 24, No. 19, (2020), 14637-14665, https://doi.org/10.1007/s00500-020-04812-z
34. Hajiaghaei-Keshteli, M. and Aminnayeri, M., "Solving the integrated scheduling of production and rail transportation problem by keshtel algorithm", ***Applied Soft Computing***, Vol. 25, (2014), 184-203, https://doi.org/10.1016/j.asoc.2014.09.034
35. Wang, S.-C., "Interdisciplinary computing in java programming, Springer Science & Business Media, Vol. 743, (2003).
36. Kennedy, J. and Eberhart, R., "Particle swarm optimization", in Proceedings of ICNN'95-international conference on neural networks, IEEE. Vol. 4, (1995), 1942-1948.
37. Altiparmak, F., Gen, M., Lin, L. and Karaoglan, I., "A steady-state genetic algorithm for multi-product supply chain network design", ***Computers & Industrial Engineering***, Vol. 56, No. 2, (2009), 521-537, https://doi.org/10.1016/j.cie.2007.05.012
38. Mousavi, S.M., Bahreininejad, A., Musa, S.N. and Yusof, F., "A modified particle swarm optimization for solving the integrated location and inventory control problems in a two-echelon supply chain network", ***Journal of Intelligent Manufacturing***, Vol. 28, No. 1, (2017), 191-206, doi: 10.1007/s10845-014-0970-z.
39. Zheng, J.-N., Chien, C.-F. and Gen, M., "Multi-objective multi-population biased random-key genetic algorithm for the 3-d container loading problem", ***Computers & Industrial Engineering***, Vol. 89, (2015), 80-87, https://doi.org/10.1016/j.cie.2014.07.012
40. Delfani, F., Kazemi, A., Seyedhosseini, S. and Niaki, S., "A green hazardous waste location-routing problem considering the risks associated with transportation and population", ***International Journal of Engineering***, Vol. 33, No. 11, (2020), 2272-2284, doi: 10.5829/IJE.2020.33.11B.18.
41. Yuan, G., Yang, Y., Tian, G. and Fathollahi-Fard, A.M., "Capacitated multi-objective disassembly scheduling with fuzzy processing time via a fruit fly optimization algorithm", ***Environmental Science and Pollution Research***, (2022), 1-18, doi: 10.21203/rs.3.rs-1075510/v1.
42. Hajiaghaei-Keshteli, M. and Fathollahi Fard, A.M., "Sustainable closed-loop supply chain network design with discount

supposition", ***Neural computing and applications***, Vol. 31, No. 9, (2019), 5343-5377, https://doi.org/10.1007/s00521-018-3369-5

43. Fathollahi-Fard, A.M., Dulebenets, M.A., Hajiaghaei–Keshteli, M., Tavakkoli-Moghaddam, R., Safaeian, M. and Mirzahosseinian, H., "Two hybrid meta-heuristic algorithms for a dual-channel closed-loop supply chain network design problem in the tire industry under uncertainty", ***Advanced Engineering Informatics***, Vol. 50, (2021), 101418, https://doi.org/10.1016/j.aei.2021.101418
44. Fard, A.M.F. and Hajaghaei-Keshteli, M., "A tri-level location-allocation model for forward/reverse supply chain", ***Applied Soft Computing***, Vol. 62, (2018), 328-346, https://doi.org/10.1016/j.asoc.2017.11.004
45. Mojtahedi, M., Fathollahi-Fard, A.M., Tavakkoli-Moghaddam, R. and Newton, S., "Sustainable vehicle routing problem for coordinated solid waste management", ***Journal of Industrial Information Integration***, Vol. 23, (2021), 100220, doi: 10.1016/j.jii.2021.100220.
46. Fathollahi-Fard, A.M., Woodward, L. and Akhrif, O., "Sustainable distributed permutation flow-shop scheduling model based on a triple bottom line concept", ***Journal of Industrial Information Integration***, Vol. 24, (2021), 100233, https://doi.org/10.1016/j.jii.2021.100233
47. Pasha, J., Dulebenets, M.A., Fathollahi-Fard, A.M., Tian, G., Lau, Y.-y., Singh, P. and Liang, B., "An integrated optimization method for tactical-level planning in liner shipping with heterogeneous ship fleet and environmental considerations", ***Advanced Engineering Informatics***, Vol. 48, (2021), 101299, doi: 10.1016/j.aei.2021.101299.
48. Karna, S.K. and Sahai, R., "An overview on taguchi method", ***International Journal of Engineering and Mathematical Sciences***, Vol. 1, No. 1, (2012), 1-7, https://www.researchgate.net/publication/265282800
49. Fazli, M., Fathollahi-Fard, A.M. and Tian, G., "Addressing a coordinated quay crane scheduling and assignment problem by red deer algorithm", ***International Journal of Engineering***, Vol. 32, No. 8, (2019), 1186-1191, doi: 10.5829/ije.2019.32.08b.15.
50. Moosavi, J., Fathollahi-Fard, A.M. and Dulebenets, M.A., "Supply chain disruption during the covid-19 pandemic: Recognizing potential disruption management strategies", ***International Journal of Disaster Risk Reduction***, (2022), 102983, https://doi.org/10.1016/j.ijdrr.2022.102983
51. Fathollahi-Fard, A.M., Hajiaghaei-Keshteli, M. and Tavakkoli-Moghaddam, R., "The social engineering optimizer (SEO)", ***Engineering Applications of Artificial Intelligence***, Vol. 72, (2018), 267-293, https://doi.org/10.1016/j.engappai.2018.04.009
52. Soleimani, H., Chhetri, P., Fathollahi-Fard, A.M., Mirzapour Al-e-Hashem, S. and Shahparvari, S., "Sustainable closed-loop supply chain with energy efficiency: Lagrangian relaxation, reformulations and heuristics", ***Annals of Operations Research***, (2022), 1-26, https://doi.org/10.1007/s10479-022-04661-z

Appendix A

The comparison of algorithms is provided in the results as reported in Table A1.

TABLE A1. Comparison of algorithms (B=best; W=worst; M=mean; ST=standard deviation; GAP=optimality gap from exact solver; CPU=computational time based on seconds)

Algorithm		P1	P2	P3	P4	P5	P6	P7	P8	P9	P10	P11	P12	P13	P14	P15	P16	P17	P18	P19	P20
RDA	B	1.34E+10	5.31E+10	5.62E+10	1.07E+11	1.76E+11	3.18E+11	4.61E+11	6.99E+11	9.38E+11	1.16E+12	1.57E+12	2.22E+12	4.78E+12	5.54E+12	5.75E+12	5.8E+12	6.06E+12	8.31E+12	1.07E+13	1.3E+13
	W	1.49E+10	5.89E+10	6.24E+10	1.19E+11	1.95E+11	3.53E+11	5.12E+11	7.76E+11	1.04E+12	1.29E+12	1.74E+12	2.46E+12	5.31E+12	6.15E+12	6.38E+12	6.44E+12	6.73E+12	9.22E+12	1.19E+13	1.44E+13
	M	1.41E+10	5.60E+10	5.93E+10	1.13E+11	1.86E+11	3.35E+11	4.86E+11	7.37E+11	9.90E+11	1.22E+12	1.66E+12	2.34E+12	5.04E+12	5.84E+12	6.07E+12	6.12E+12	6.39E+12	8.77E+12	1.13E+13	1.37E+13
	ST	5.98E+08	2.31E+09	2.45E+09	4.65E+09	7.69E+09	1.38E+10	2.0921E+10	3.19E+10	4.27E+10	5.29E+10	7.17E+10	1.02E+11	2.18E+11	2.53E+11	2.63E+11	2.65E+11	2.77E+11	3.8E+11	4.91E+11	5.93E+11
	GAP	0.0843	0.1222	0.156	0.147	0.232	0.126	0.115	0.158	-	-	-	-	-	-	-	-	-	-	-	-
	CPU	8.905	10.35556	11.41667	23.655	30.765	34.105	57.845	61.425	63.355	75.46	99.415	109.0045	129.9455	141.9591	171.1	251.144	259.444	277.1	291.564	335.864
KA	B	1.4E+10	5.41E+10	5.73E+10	1.09E+11	1.8E+11	3.24E+11	4.9E+11	7.48E+11	1E+12	1.24E+12	1.68E+12	2.38E+12	5.11E+12	5.93E+12	6.15E+12	6.2E+12	6.49E+12	8.89E+12	1.15E+13	1.39E+13
	W	1.54E+10	5.95E+10	6.30E+10	1.20E+11	1.98E+11	3.56E+11	5.39E+11	8.23E+11	1.10E+12	1.36E+12	1.85E+12	2.62E+12	5.62E+12	6.52E+12	6.77E+12	6.82E+12	7.14E+12	9.78E+12	1.27E+13	1.53E+13
	M	1.47E+10	5.68E+10	6.02E+10	1.14E+11	1.89E+11	3.40E+11	5.15E+11	7.85E+11	1.05E+12	1.30E+12	1.76E+12	2.50E+12	5.37E+12	6.23E+12	6.46E+12	6.51E+12	6.81E+12	9.33E+12	1.21E+13	1.46E+13
	ST	7.37E+08	2.92E+09	3.09E+09	5.89E+09	9.68E+09	1.75E+10	2.54E+10	3.84E+10	5.16E+10	6.38E+10	8.64E+10	1.22E+11	2.63E+11	3.05E+11	3.16E+11	3.19E+11	3.33E+11	4.57E+11	5.89E+11	7.15E+11
	GAP	0.135626	0.157764	0.199498	0.184525	0.328217	0.157804	0.194277	0.258941	-	-	-	-	-	-	-	-	-	-	-	-
	CPU	8.0145	9.32	10.275	21.2895	27.6885	32.39975	54.95275	58.35375	60.18725	67.914	89.4735	98.10409	116.9509	127.7632	153.99	226.0296	233.4996	249.39	262.4076	302.2776
GA	B	1.5E+10	5.94E+10	6.29E+10	1.2E+11	1.98E+11	3.56E+11	5.2E+11	7.83E+11	1.05E+12	1.3E+12	1.76E+12	2.49E+12	5.35E+12	6.21E+12	6.44E+12	6.49E+12	6.79E+12	9.3E+12	1.2E+13	1.46E+13
	W	1.74E+10	6.89E+10	7.30E+10	1.39E+11	2.30E+11	4.13E+11	6.03E+11	9.08E+11	1.22E+12	1.51E+12	2.04E+12	2.89E+12	6.21E+12	7.20E+12	7.47E+12	7.53E+12	7.88E+12	1.08E+13	1.39E+13	1.69E+13

	M	1.62E+10	6.42E+10	6.79E+10	1.30E+11	2.14E+11	3.84E+11	5.62E+11	8.46E+11	1.13E+12	1.40E+12	1.90E+12	2.69E+12	5.78E+12	6.71E+12	6.96E+12	7.01E+12	7.33E+12	1.00E+13	1.30E+13	1.58E+13
	ST	1.02E+09	4.06E+09	4.3E+09	8.2E+09	1.35E+10	2.43E+10	3.5523E+10	5.35E+10	7.17E+10	8.88E+10	1.2E+11	1.7E+11	3.65E+11	4.24E+11	4.4E+11	4.43E+11	4.64E+11	6.35E+11	8.2E+11	9.97E+11
	GAP	0.216742	0.271186	0.316726	0.304064	0.461039	0.272156	0.267396	0.317849	-	-	-	-	-	-	-	-	-	-	-	-
	CPU	7.21305	7.766667	8.5625	17.74125	23.07375	25.57875	43.38375	46.06875	47.51625	56.595	74.56125	81.75341	97.45909	106.4693	128.325	188.358	194.583	207.825	218.673	251.898
	B	1.4E+10	5.65E+10	5.98E+10	1.14E+11	1.88E+11	3.38E+11	4.9E+11	7.44E+11	9.98E+11	1.24E+12	1.67E+12	2.37E+12	5.08E+12	5.9E+12	6.11E+12	6.17E+12	6.45E+12	8.84E+12	1.14E+13	1.38E+13
	W	1.69E+10	6.84E+10	7.24E+10	1.38E+11	2.27E+11	4.09E+11	5.93E+11	9.00E+11	1.21E+12	1.50E+12	2.02E+12	2.87E+12	6.15E+12	7.14E+12	7.39E+12	7.47E+12	7.80E+12	1.07E+13	1.38E+13	1.67E+13
PSO	M	1.55E+10	6.24E+10	6.61E+10	1.26E+11	2.08E+11	3.73E+11	5.41E+11	8.22E+11	1.10E+12	1.37E+12	1.85E+12	2.62E+12	5.61E+12	6.52E+12	6.75E+12	6.82E+12	7.13E+12	9.77E+12	1.26E+13	1.52E+13
	ST	1.26E+09	5.07E+09	5.36E+09	1.02E+10	1.6856E+10	3.03E+10	4.39E+10	6.67E+10	8.95E+10	1.11E+11	1.4973E+11	2.12E+11	4.55E+11	5.29E+11	5.48E+11	5.53E+11	5.78E+11	7.93E+11	1.02E+12	1.24E+12
	GAP	0.135626	0.209125	0.251832	0.238861	0.387249	0.207833	0.194277	0.252209	-	-	-	-	-	-	-	-	-	-	-	-
	CPU	7.934355	8.543333	9.41875	19.51538	25.38113	28.13663	47.72213	50.67563	52.26788	62.2545	82.01738	89.92875	107.205	117.1163	141.1575	207.1938	214.0413	228.6075	240.5403	277.0878

Persian Abstract

چکیده

طراحی کارآمد یک سیستم آبرسانی و جمع آوری فاضلاب برای مقابله با عدم قطعیت طبیعی این سیستم و اهداف توسعه پایدار در کشورهای در حال توسعه مانند ایران اهمیت قابل توجهی دارد. برای پرداختن به عدم قطعیت طبیعی در تامین آب و چالش گرمایش جهانی، این طراحی باید قوی باشد و این انگیزه یک بهینه‌سازی قوی است. برای در نظر گرفتن معیارهای پایداری، این طرح باید تمام اثرات اقتصادی، زیست محیطی و اجتماعی را پوشش دهد. از این رو، این مطالعه راه‌حل‌های نوآورانه‌ای را بر اساس الگوریتم‌های فراابتکاری اخیر و سنتی برای تامین آب و سیستم جمع‌آوری فاضلاب قوی و پایدار توسعه می‌دهد. الگوریتم گوزن قرمز (RDA) و الگوریتم کشتل (KA) به عنوان الگوریتم های اخیر استفاده شده است. این الگوریتم‌های اخیر با روش‌های پیشرفته مانند الگوریتم ژنتیک (GA) و بهینه‌سازی ازدحام ذرات (PSO) مقایسه می‌شوند. کاربرد مدل و الگوریتم های ما، بر روی یک مطالعه موردی در استان خراسان شمالی آزمایش شده است. پس از انجام برخی تحلیل‌ها بر روی عملکرد الگوریتم‌ها و حساسیت‌های ما روی مدل، بحثی برای نتیجه‌گیری بینش‌ها و یافته‌های مدیریتی برای دست اندرکاران در سیستم کاربردی ارائه می‌شود.

AIMS AND SCOPE

The objective of the International Journal of Engineering is to provide a forum for communication of information among the world's scientific and technological community and Iranian scientists and engineers. This journal intends to be of interest and utility to researchers and practitioners in the academic, industrial and governmental sectors. All original research contributions of significant value focused on basics, applications and aspects areas of engineering discipline are welcome.

This journal is published in three quarterly transactions: Transactions A (Basics) deal with the engineering fundamentals, Transactions B (Applications) are concerned with the application of the engineering knowledge in the daily life of the human being and Transactions C (Aspects) - starting from January 2012 - emphasize on the main engineering aspects whose elaboration can yield knowledge and expertise that can equally serve all branches of engineering discipline.

This journal will publish authoritative papers on theoretical and experimental researches and advanced applications embodying the results of extensive field, plant, laboratory or theoretical investigation or new interpretations of existing problems. It may also feature - when appropriate - research notes, technical notes, state-of-the-art survey type papers, short communications, letters to the editor, meeting schedules and conference announcements. The language of publication is English. Each paper should contain an abstract both in English and in Persian. However, for the authors who are not familiar with Persian, the publisher will prepare the latter. The abstracts should not exceed 250 words.

All manuscripts will be peer-reviewed by qualified reviewers. The material should be presented clearly and concisely:

- *Full papers* must be based on completed original works of significant novelty. The papers are not strictly limited in length. However, lengthy contributions may be delayed due to limited space. It is advised to keep papers limited to 7500 words.
- *Research* notes are considered as short items that include theoretical or experimental results of immediate current interest.
- *Technical notes* are also considered as short items of enough technical acceptability with more rapid publication appeal. The length of a research or technical note is recommended not to exceed 2500 words or 4 journal pages (including figures and tables).

Review papers are only considered from highly qualified well-known authors generally assigned by the editorial board or editor in chief. Short communications and letters to the editor should contain a text of about 1000 words and whatever figures and tables that may be required to support the text. They include discussion of full papers and short items and should contribute to the original article by providing confirmation or additional interpretation. Discussion of papers will be referred to author(s) for reply and will concurrently be published with reply of author(s).

INSTRUCTIONS FOR AUTHORS

Submission of a manuscript represents that it has neither been published nor submitted for publication elsewhere and is result of research carried out by author(s). Presentation in a conference and appearance in a symposium proceeding is not considered prior publication.

Authors are required to include a list describing all the symbols and abbreviations in the paper. Use of the international system of measurement units is mandatory.

- On-line submission of manuscripts results in faster publication process and is recommended. Instructions are given in the IJE web sites: www.ije.ir-www.ijeir.info
- Hardcopy submissions must include MS Word and jpg files.
- Manuscripts should be typewritten on one side of A4 paper, double-spaced, with adequate margins.
- References should be numbered in brackets and appear in sequence through the text. List of references should be given at the end of the paper.
- Figure captions are to be indicated under the illustrations. They should sufficiently explain the figures.
- Illustrations should appear in their appropriate places in the text.
- Tables and diagrams should be submitted in a form suitable for reproduction.
- Photographs should be of high quality saved as jpg files.
- Tables, Illustrations, Figures and Diagrams will be normally printed in single column width (8cm). Exceptionally large ones may be printed across two columns (17cm).

PAGE CHARGES AND REPRINTS

The papers are strictly limited in length, maximum 6 journal pages (including figures and tables). For the additional to 6 journal pages, there will be page charges. It is advised to keep papers limited to 3500 words.

Page Charges for Papers More Than 6 Pages (Including Abstract)	
For International Author ***	**$55 / per page**
For Local Author	**100,000 Toman / per page**

AUTHOR CHECKLIST

- Author(s), bio-data including affiliation(s) and mail and e-mail addresses).
- Manuscript including abstracts, key words, illustrations, tables, figures with figure captions and list of references.
- MS Word files of the paper.

International **J**ournal of **E**ngineering, P.O. Box 13145-1659, Tehran, I.R. Iran
Materials and Energy Research Center, 5 Ahuramazda St., Alvand Ave., Argentina Sq., Tehran, Islamic Republic of Iran
www.merc.ac.ir - www.emerc.ac.ir

INDEXED IN EMERGING SOURCES CITATION INDEX CLARIVATE ANALYTICS

THOMSON REUTERS
WEB OF SCIENCE

INDEXED IN EMERGING SOURCES CITATION INDEX THOMSON REUTERS

Scopus®

CAS®
A DIVISION OF THE
AMERICAN CHEMICAL SOCIETY

ISC
Islamic World Science Citation Center

Crossref

SIS
Scientific Indexing Services

Google Scholar